

**Computer Technology in Welding  
and Manufacturing**

**&**

**Mathematical Modelling  
and Information Technologies  
in Welding and Related Processes**

Conference Sponsors

*Presidium of the National Academy of Sciences of Ukraine*  
*E.O. Paton Electric Welding Institute of NASU*

Information Support

*«The Paton Welding Journal»*  
*«Автоматическая Сварка» Journal*  
[www.nas.gov.ua/pwj](http://www.nas.gov.ua/pwj)

The E.O. Paton Electric Welding Institute  
The Welding Institute  
International Association «Welding»  
Local Charity Foundation «Welding Community»

# **Computer Technology in Welding and Manufacturing**

16th International Conference

&

# **Mathematical Modelling and Information Technologies in Welding and Related Processes**

3rd International Conference

**Proceedings of Joint International Conference**

*6–8 June 2006, Kiev, E.O. Paton Electric Welding Institute*

Edited by Prof. W. Lucas and Prof. V.I. Makhnenko



E.O. Paton Electric Welding Institute of the NAS of Ukraine  
Kiev 2006

(2006) The book contains papers presented at the Joint 16th International Conference «Computer Technology in Welding and Manufacturing» & 3rd International Conference «Mathematical Modelling and Information Technologies in Welding and Related Processes», covering the latest achievements in the field of mathematical modelling and computer technology for welding, cutting, surfacing and other advanced methods of materials processing. Prospects of application of welding technologies are considered. Authors of the papers are the known specialists from many countries all over the world. Kiev: E.O. Paton Electric Welding Institute, NAS of Ukraine, 328 pp.

Compiled by *W. Lucas, V.I. Makhnenko*

Publishing Project *A.T. Zelnichenko*

Editor *N.A. Dmitrieva*

CRC preparation *I.S. Batasheva, L.N. Gerasimenko, T.Yu. Snegiryova, A.I. Sulima*

Design *I.S. Batasheva*

State Registration Certificate DK 166 of 06.09.2000

**ISBN 966-8872-05-3**

© E.O. Paton Electric Welding Institute of the NAS of Ukraine, 2006

© International Association «Welding», 2006

---

Sent to press on 14.12.2006. 60×84/8 form. Offset paper. Offset print. Ukr. Pet. Font. 70.4 cond. print. sheets. 48.3 publ. print. sheets.  
Edition of 200 copies. Camera-ready copy: ITB Advertising Agency.  
Published by «Esse». 34 / 1, Vernadsky Ave., Kiev, 03142.

---

# CONTENTS

Welcome Address .....	9
<b>SESSION I</b>	
<b>COMPUTER TECHNOLOGY IN WELDING AND MANUFACTURING .....</b>	<b>11</b>
<i>Abdullah B.M., Smith J.S. and Lucas B.</i> Vision System for Monitoring Arc Welding Processes .....	13
<i>Bikbulatov D.V., Dyachenko V.I., Kunkevich D.P., Medvedev S.V. and Streltsov A.I.</i> Software-Methodical Means for Formation of Technological Documentation of New Generation .....	20
<i>Brightmore A. and Hole G.</i> Improving the Documentation of Welding at Heatric Ltd. by Using the Welding Coordinator Software System .....	23
<i>Chinery M. and Strachan J.</i> Taking Fabrication Management into the 21st Century .....	26
<i>Christiansson A.-K. and Gougeon P.</i> Sensor and Control System for Metal Deposition Using Robotised Laser Welding .....	29
<i>Cuiuri D. and Norrish J.</i> Versatile Welding Power Source Controller for Research and Product Development .....	32
<i>Gorbach V.D., Steshenkova N.A. and Ponikarovski R.F.</i> Software-Controlled Technologies of Adaptive Welding .....	40
<i>Hyeong-Soon Moon, Yong-Baek Kim, Jong-Joon Kim, Jong-Cheol Kim and Moo-Ryeong Park.</i> Automatic Pipeline Welding System with Self-Diagnostic Function and Laser Vision Sensor .....	46
<i>Keitel S., Ahrens C. and Aryus A.</i> Blended Learning for Welding Engineers: First Experience .....	51
<i>Kovalenko V.S. and Kolpakov V.V.</i> Virtual Enterprise Based on Highly Efficient Use of Industrial Laser Systems .....	55
<i>Kunkevich D.P., Medvedev S.V. and Yakovleva Zh.G.</i> Developed Computer Technology for Designing Assembly-Welding Technological Tooling .....	58
<i>Mavromatidis P. and Lucas J.</i> Modelling and Testing of Dielectric Heat Source Designs for the Microwave Thermal Spraying Process .....	63
<i>Melyukov V., Korepanov A. and Tyurin V.</i> Method of Optimum Control in Technological Processes for Welding and for Local Thermocyclic Treatment .....	68
<i>Nicholson A., Norrish J. and Di Pietro P.</i> Novel Offline Robot Programming Software .....	73
<i>Norrish J.</i> Model for Distance Learning of Welding Engineers and Some Experience with its Application .....	76
<i>Petrushina M.V.</i> Moving Heat Source Model Capabilities in LS-DYNA Parallel Version .....	80
<i>Pietras A., Zadroga L. and Mikno Z.</i> New Quality Inspection System for AC Resistance Welding .....	84
<i>Plotnikov A.M., Karpoushkina N.G. and Paute D.G.</i> Program-Technical Complex on the Base of Thermal Cutting Machines of RITM-Type for Optimal Nesting of Metal, Development of NC Programs and Cutting of Parts .....	91

<i>Pratt A., Norrish J. and Dunn L.</i> Computer Based Virtual Reality Training System for Welding .....	95
<i>Pretorius T., Woitschig J., Habedank G. and Vollertsen F.</i> Distortion Manipulation by Means of Thermal Generation of Residual Stresses .....	100
<i>Shapovalov E.V. and Kolyada V.A.</i> Technical Vision Means for Butt Following Systems Used in Welding Fabrication .....	106
<i>Sinitsky V.A.</i> Computer-Aided Technology for Checking of Shape Parameters of Welded and Pipe Structures in Shipbuilding with Use of Location Acoustic Measuring Stations .....	110
<i>Sung-Hoon Ko, Hyeong-Soon Moon and Jong-Cheol Kim.</i> Characteristics of Magnetic Field in Automated Multi-Torches FCAW .....	113
<i>Tapp J., Guy P. and Chawla K.</i> Weld Monitoring and Stability Indices .....	116

**SESSION II****MATHEMATICAL MODELLING AND INFORMATION TECHNOLOGIES  
IN WELDING AND RELATED PROCESSES .....**

121

<i>Afonin Yu.V., Bataev A.A., Burov V.G., Orishich A.M., Malikov A.G. and Shikakhalev E.G.</i> Physical Simulation of CO <sub>2</sub> Laser Welding of Al–Li and Ti Alloys, Low-Carbon and Stainless Steels .....	123
<i>Aleksandrov S., Hulka K., Morozov Yu. and Nazarov A.</i> Optimisation of Alloy Design for Good Weldment of HSLA Steels .....	130
<i>Berezovsky B.M., Pujko A.V. and Pilnik O.V.</i> Mathematical Computer Modeling and Optimization of Welded Joint Formation for Multi-Pass Welding of Gas Pipeline Fittings .....	136
<i>Bolshakov M.V. and Lukina G.N.</i> Mathematical Modelling of Cold Pressure Welding .....	143
<i>Borodianskiy K., Lugovskoy A., Mazurovsky V., Zinigrad M. and Gedanken A.</i> Modeling of the Weld Metal Microstructure .....	147
<i>Charles C. and Jarvstrat N.</i> Finite Element Modelling of Microstructure on GTAW Metal Deposition of Ti–6Al–4V Alloy .....	151
<i>Cherepanov A.N., Shapeev V.P., Fomin V.M. and Semin L.G.</i> Numerical Simulation of Heat Transfer and Structure Formation in Laser Welding of Aluminum Alloy .....	157
<i>Karkhin V.A., Khomich P.N. and Michailov V.G.</i> Prediction of Microstructure and Mechanical Properties of Weld Metal with Consideration for Real Weld Geometry .....	162
<i>Karkhin V.A., Levchenko A.M., Khomich P.N. and Michailov V.G.</i> Computer-Aided Express Determination of Diffusible Hydrogen in Deposited Weld Metal .....	167
<i>Korolyova T.V., Starodubtsev V.A., Stepanov B.V. and Yarochkin V.A.</i> Numerical Study of Influence of Edge Preparation Angle of Butt, Tee and Corner Joints on Microstructure and Mechanical Properties in FZ and HAZ on Low-Alloy Steels of General Designation .....	173
<i>Kovalev O.B. and Manajchev K.A.</i> Numerical Simulation of SHS Laser Welding of Metals .....	179
<i>Kriotsun I.V., Demchenko V.F. and Lesnoj A.B.</i> Model of Evaporation-Condensation Processes in Welding and Material Treatment .....	184
<i>Lomozik M.</i> Numerical Modelling of Thermal Cycles in Steel During Surfacing and Welding without Preheating and their Comparison with Experimental Data .....	188

<i>Makhnenko O.V.</i> Numerical Substantiation of Maximum Pressure in Pneumatic-Aquarium Method of Testing the Tightness of Heat Exchange Tubes and their Welded Joints of the PGV-1000M Steam Generator .....	196
<i>Makhnenko O.V.</i> and <i>Makhnenko V.I.</i> Forecasting of Durability of Welded Arch Pylon of Bridge over the River Moskva .....	202
<i>Makhnenko O.V.</i> and <i>Muzhichenko A.F.</i> Mathematical Simulation of Thermal Straightening of Cylindrical Shells and Shafts with General Distortion of Longitudinal Axis .....	208
<i>Makhnenko O.V.</i> , <i>Velikoivanenko E.A.</i> and <i>Pivtorak N.I.</i> Numerical Study of Formation of Lamellar Cracks in Welding of Shells of Manholes into Body of Reservoir RVS 75,000 m <sup>3</sup> in Town of Brody .....	213
<i>Makhnenko V.I.</i> Aspects of Predicting Safe Operation Period of Welded Joints with the Established Defects .....	219
<i>Makhnenko V.I.</i> Current Problems of Mathematical Modelling in Welding and Related Technologies .....	227
<i>Makhnenko V.I.</i> , <i>Milenin A.S.</i> and <i>Semyonov A.P.</i> Mathematical Modeling of Thermo-deformational and Physicochemical Processes during Welding of Lap and Butt Dissimilar Titanium-Aluminum Joints .....	234
<i>Makhnenko V.I.</i> , <i>Velikoivanenko E.A.</i> , <i>Rozyinka G.F.</i> and <i>Pivtorak N.I.</i> Numerical Investigation of Causes of Failure of Welded Pillars of Casting Stand Crosshead .....	240
<i>Maksymova S.V.</i> , <i>Khorunov V.F.</i> and <i>Zelinskaya G.M.</i> Amorphous Brazing Filler Alloys, Research and Modelling of their Structural State .....	247
<i>Mokrov O.</i> , <i>Pavlyk V.</i> and <i>Dilthey U.</i> Analysis of Thermo-Electrical Processes and Electrode Metal Transfer During Gas-Metal-Arc Welding with the Aid of Numerical Modelling .....	250
<i>Paton B.E.</i> , <i>Yushchenko K.A.</i> , <i>Kovalenko D.V.</i> , <i>Krivtsun I.V.</i> , <i>Demchenko V.F.</i> , <i>Kovalenko I.V.</i> and <i>Lesnoj A.B.</i> Role of Quasi-Keyhole and Marangoni Convection in Formation of Deep Penetration in A-TIG Welding of Stainless Steel (Phenomenological Model of A-TIG Process) .....	258
<i>Pavlyk V.</i> , <i>Mokrov O.</i> and <i>Dilthey U.</i> Integrative Welding Simulation: Example of GMA Welding .....	264
<i>Ploshikhin V.</i> , <i>Prikhodovsky A.</i> , <i>Ilin A.</i> , <i>Makhutin M.</i> , <i>Heimerdinger C.</i> and <i>Palm F.</i> Numerical Simulation of Solidification Cracking During Laser Beam Welding of Aluminium Alloys .....	269
<i>Saprykina G.Yu.</i> Conditions for Choosing Rational Parameters of Modes of Local Heat Treatment of Welded Joints .....	274
<i>Semmler U.</i> , <i>von Breitenbach G.</i> and <i>Sedlmaier A.</i> Finite Element Simulation of the Continuous RF and the HF Welding Process of Internal High-Pressure Tubes .....	279
<i>Seyffarth P.</i> , <i>Makhnenko V.I.</i> and <i>Velikoivanenko E.A.</i> Modelling Lateral Deformations in Welding without Tacking of Large Plates with Account of Frictional Forces Created by Stationary Clamps .....	286
<i>Shekera V.M.</i> Experimental Determination of Residual Stresses by Semi-Destruction Method in Conjunction with Numerical Simulation of their Development .....	292
<i>Sudnik V.A.</i> , <i>Erofeev V.A.</i> , <i>Richter K.-H.</i> and <i>Heins K.-U.</i> Numerical Modelling of the EBW Process .....	295
<i>Turichin G.</i> , <i>Lopota V.</i> , <i>Valdaytseva E.</i> , <i>Malkin P.</i> and <i>Zemlyakov E.</i> Numerical Solution of Inverse Problem for Laser and Hybrid Welding with LaserCAD .....	301
<i>den Uijl N.J.</i> Modelling the Influence of Resistance Spot Welding on Material Properties .....	306

## CONTENTS

---

<i>Velikoivanenko E.A., Rozynka G.F., Pivtorak N.I., Starodubtsev V.A., Stepanov B.V. and Yarochkin S.V.</i> Numerical Study of the Influence of Groove Angle of Butt, Tee and Corner Joints on Angular Distortions and Lateral Shrinkage in Arc Welding of Low-Alloyed Steels .....	314
<i>Zaitsev A.V. and Kovalev O.B.</i> Physical-Mathematical Model of Multiple Reflection of Radiation in Laser Welding, Cutting and Drilling the Metal .....	322
<b>NAME INDEX</b> .....	327



*To participants of the International Conference on Computer Technologies  
and Mathematical Modelling in Welding and Related Technologies  
Kiev, June 2006*

## **WELCOME ADDRESS**

*First of all, I would like to greet you at the E.O. Paton Electric Welding Institute of the National Academy of Sciences of Ukraine – the major science and technology centre of welding and related processes.*

*Current advancements in science, technology and manufacturing depend to an increasing degree upon the application of high technologies, based on extensive utilisation of computer engineering, mathematical modelling and advanced information technologies.*

*This equally applies to welding and related processes, where a great interest has been seen for the last decades in application of computer facilities at stages of research and development, manufacturing and operation of products.*

*International conferences focused on the above topics, which are held regularly by TWI in Great Britain, the University of Austria in Graz-Seggau, College of Judea and Samaria in Israel, and the E.O. Paton Electric Welding Institute in Ukraine, attract attention of a large number of specialists from all over the world. The Conference we are opening today is not an exception, as it gathered scientists and specialists from 15 countries of four continents of the Globe.*

*Issues we are to discuss can be somewhat conditionally divided into the following areas:*

- *Fundamental research of complex physical phenomena accompanying welding and related processes (surfacing, coating and special electrometallurgy), where the application of modern mathematical models and numerical implementation methods allows obtaining a number of new results, which are important for subsequent technological developments;*

- *Multi-variant design and development of rational technologies, based on application of computation-information systems and computer facilities;*

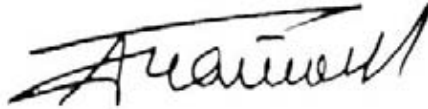
- *Production control, monitoring of manufacturing operations, inspection of quality of welded products, etc., where the required quality is ensured by modern computer systems based on appropriate control feedbacks, models and algorithms*

- *Prediction of safe service life of welded structures and products of related technologies at different stages of operation, based on monitoring of real service and loading conditions, as well as diagnostics of an actual state in terms of defects and degradation of resistance of materials to different types of fracture.*

*These areas are covered to different extents in papers to be presented at our Conference. I do hope the discussions will be fruitful, and will inspire you for further creative work.*

*I sincerely wish you every success, great achievements, efficient cooperation and mutually beneficial contacts, as well as pleasant stay in our beautiful Kiev.*

**Prof. Boris E. Paton**

A handwritten signature in black ink, appearing to read "Boris E. Paton". The signature is written in a cursive, flowing style with a prominent horizontal stroke at the top.

***SESSION I***  
***COMPUTER TECHNOLOGY***  
***IN WELDING***  
***AND MANUFACTURING***



# VISION SYSTEM FOR MONITORING ARC WELDING PROCESSES

B.M. ABDULLAH<sup>1</sup>, J.S. SMITH<sup>1</sup> and B. LUCAS<sup>2</sup>

<sup>1</sup>University of Liverpool, UK

<sup>2</sup>TWI Ltd., Cambridge, UK

This paper describes a vision-based approach for obtaining high quality images of the weld pool and the surrounding area. The objective is to provide reliable real-time measurements of the molten pool width for use with a process controller. The weld pool contains important information about the welding process, which can be used by the process controller to adjust the welding parameters and regulate the weld pool width in order to allow for consistent welds. To extract the information from the weld pool, a novel vision-based system is developed. The basis of the system is to capture clear, stable and high quality images of the welding process for image analysis and processing. The extreme intensity of the arc light makes it impossible to see through the arc to the weld pool. Therefore, for effective viewing and in order to do any kind of image processing, the arc light intensity must be reduced or eliminated.

Extensive experimentations have shown that the geometry, i.e. the size and shape of the weld pool, contains sufficient information on the weld penetration [1]. It is also known that the weld penetration is a major determinant of the weld quality. Thus, the geometrical features of the weld pool should be sensed and controlled [2]. The visual information that is accessible in real-time will also enable a quick reaction to various types of malfunctions. Figure 1 shows a high quality image of a TIG welding process in argon shielding gas [3].

The main difficulty encountered in vision-based sensing of the weld pool geometry is the strong interference from the arc light across a wide spectrum. Many attempts have been made in the past to find a method of sensing weld penetration so that it can be adequately controlled. The system developed by Kovacevic and Zhang is valued at \$100,000 [4]. From an industrial point of view, this is too expensive to apply in industry, so other alternatives are to be investigated. The reduction in the cost of cameras and illumination systems has allowed vision systems to be increasingly used as sensors to extract information about the weld pool. This information will be used to control the system and modify the welding parameters to maintain the required weld quality and productivity.

**Camera technology.** CCD and CMOS imagers have unique strengths and weaknesses that make them appropriate to different applications. Neither is categorically superior to the other, although vendors selling only one technology often claim otherwise [5]. In recent years some new CMOS sensors have appeared, which have lowered the technological gap between the two technologies. CMOS cameras use arrays of photodiodes as the imaging sensor. These sensors can be accessed to give an output voltage proportional to the instantaneous illumination. Hence there is no requirement for charge accumulation and

consequently these devices are not prone to blooming. With the CMOS cameras the electronics are configured to give a logarithmic response to the illumination. This allows a wider dynamic range to be viewed than can be observed with CCD cameras [6]. The benefits of a CCD sensor include better light sensitivity, better colours and sharper image and low background noise. Some drawbacks with the CCD technology include more expensive to produce, more expensive and complex to incorporate and blooming and smear; when there is a very bright object in the scene (e.g. welding arcs), the CCD may bleed causing vertical stripes below and above the object.

The CMOS technology is the standard technology in which almost all chips are made, including memory chips, microprocessors and more. This makes the technology much more affordable than the CCD. The benefits of the CMOS sensor include lower cost, anti-blooming, the ability to drain localized overexposure without compromising the rest of the image in the sensor. CMOS generally has natural blooming immunity. CCDs, on the other hand, require specific engineering to achieve this capability. Many CCDs that

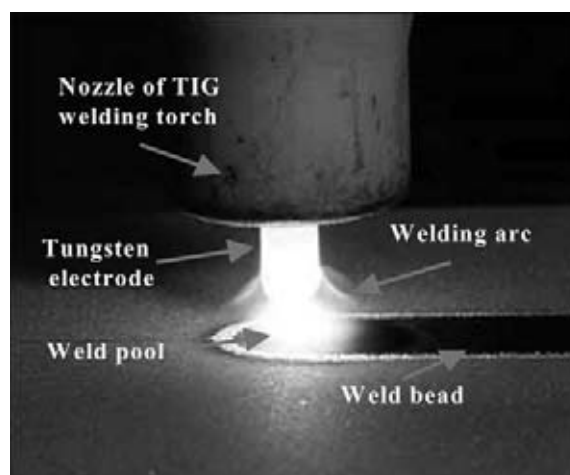


Figure 1. Characteristic appearance of the AC TIG arc

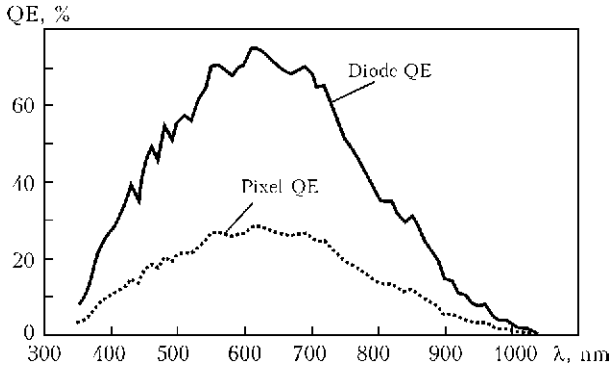


Figure 2. Quantum efficiency of a CMOS camera used

have been developed for consumer applications do, but those developed for scientific applications generally do not. The benefits also include fast shuttering speed, windowing and large dynamic range. The CMOS electronics are configured to give a logarithmic response rather than a linear response to the illumination [7]. Some drawbacks with CMOS technology include appearance of fixed-pattern noise in low light environments that can be seen as small dots or noisy lines in the image and higher noise ratio than CCDs.

**Quantum efficiency.** Quantum efficiency indicates the efficiency of the conversion of photons in electron hole pairs and the ability to collect these pairs. Typically the quantum efficiency is the ratio of the impinging photons on a pixel to the number of collected electrons. Figure 2 shows the quantum efficiency of the CMOS camera used in this study. The quantum efficiency of the pixel is equal to the quantum efficiency of the CMOS photodiode multiplied by the fill factor of the pixel.

**Optical emissions.** Arc light emissions have the potential as a welding information source. The emission varies with weld parameters; these parameters include current, voltage, electrode diameter and type, and shielding gas. Some researchers have applied spectra for weld monitors. In these studies, it was shown that the emission spectra can be used to detect changes in the welding arc. Other studies including this one incorporated welding spectra to enhance the image quality of the weld pool. Further studies investigated the possibility of sensing welding behaviours based on arc light [8]. In another research work, an arc light sensor was used to monitor the droplet transfer mode in GMAW [9]. Extensive research was also made by Richardson and Edwards towards the feasibility of arc light sensing, such as investigating the sensitivity and stability of arc light [10]. Similar work was carried out by Pengjiu and Zhang [11].

The spectra can be roughly predicted by two ways one is by using Wien's displacement law and the second is by combining the spectrum of the parent material (e.g. stainless steel) with the spectrum of the shielding gas [12]. According to Wien's displacement law, objects of different temperatures emit spectra that peak at different wavelengths. Using this law allows us to find the frequency (or wavelength) at which Planck's law has the maximum intensity.

Planck's law gives the intensity radiated by a blackbody as a function of frequency. Eq. 2 is Wien's displacement law, which is derived from Planck's law (Eq. 1):

$$B_{\nu}(T) = \frac{2h}{c^2} \frac{\nu^3}{e^{h\nu/(kT)} - 1}; \quad (1)$$

$$\lambda(B_{\lambda}) = \frac{hc}{4.965kT} = \frac{2.898 \cdot 10^{-3} K m}{T}. \quad (2)$$

Therefore, (2) can be approximated to the following form:

$$\lambda T \approx 30,000,000. \quad (3)$$

The melting point of stainless steel type 302 is 1420 °C (i.e. 1693 K), therefore according to Wien's displacement law, the wavelength where most energy is given off ( $\lambda_{\max}$ ) is

$$\lambda_{\max} = \frac{30 \cdot 10^6}{1693} = 1772 \text{ nm.}$$

Temperature of the arc varies from 5,000 to 30,000 K [8]. Therefore, the wavelength where most energy is emitted is

$$\lambda_{\max} = 100 - 600 \text{ nm.}$$

StellarNet optical spectrum analyser with a wavelength range from 300 to 850 nm was used to obtain the arc spectrum of TIG welding process on stainless steel in argon shielding gas. Figure 3, *a* shows the emissions emitted by the argon [13], and Figure 3, *b* and *c* shows the arc spectra as measured by the optical analyser with different current settings.

**Arc light elimination. Spectral filtering.** A typical spectral response range for a standard visible-light camera is 400–900 nm, falling sharply outside this range. On the other hand, laser illumination is at a very specific wavelength, with a typical wavelength much smaller than 1 nm. This is illustrated in Figure 4, *a*, which shows how the light from a laser light-source might compare with the arc light. However, if a BPF is used, then only the laser light will pass with some arc light. The result is a much-attenuated arc light with little effect on the laser light as illustrated in Figure 4, *b*.

**Temporal filtering.** More arc light will be captured if longer exposure time is used, this does not affect how much laser light is captured as long as the pulse width remains shorter than the exposure time. Laser light will only be attenuated if the laser pulse width is greater than the exposure time of the camera or if the laser is a continuous wave laser rather than a pulsed laser. The contributions to the image brightness from the laser and the arc light are illustrated in Figure 5.

**Vision system structure.** Initial investigations used infrared cameras and high band pass filters to allow the weld to be observed whilst eliminating the arc light [14]. However, these infrared cameras are

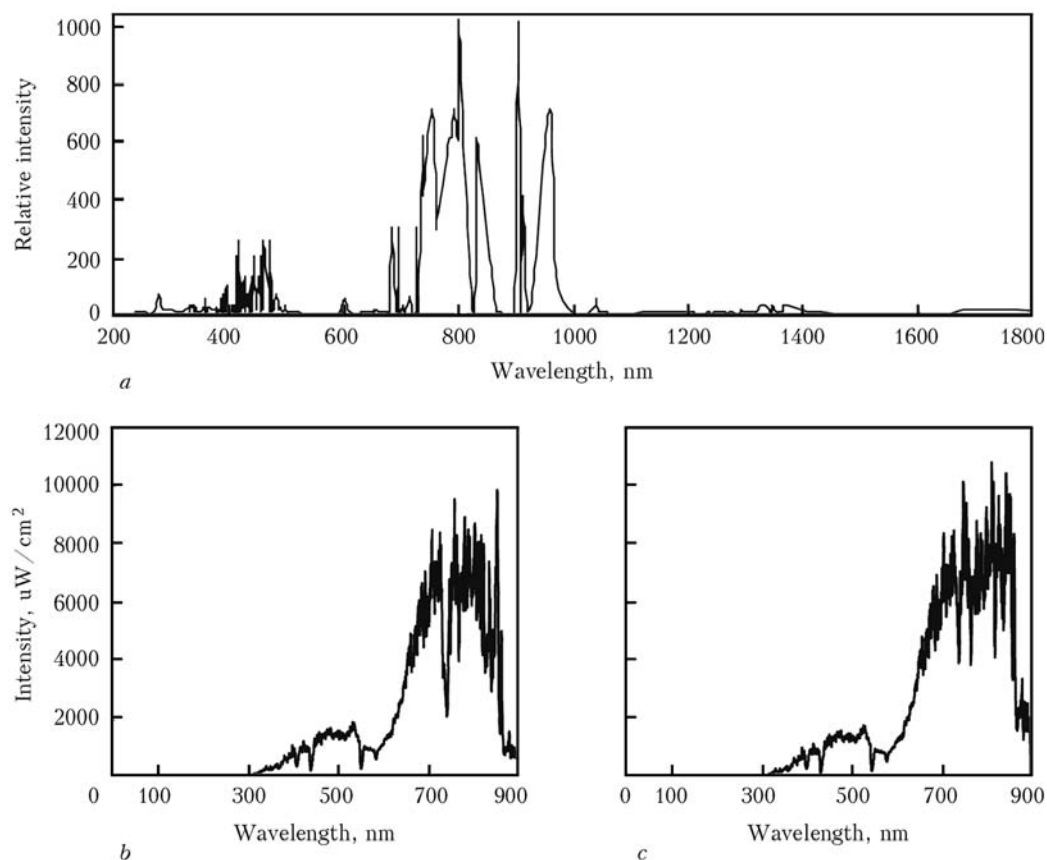


Figure 3. Argon (a) and arc spectrum in TIG welding at 100 (b) and 200 (c) A

expensive and bulky. Numerous other techniques for arc welding process automation have been studied. These range from an artificial intelligence based approach to automate process parameter selection [15, 16] to sensors for process monitoring and control [17] and advanced control strategies designed to process sensor information [18–20]. Recently, intensive research has been done to develop a system, which can be used for direct weld pool viewing. However, these techniques have been affected by the high expense of the components.

The laser light-source can either be mounted on the same side as the camera i.e. backward reflection, or opposite the camera i.e. forward reflection, as shown in Figure 6. More laser light is reflected to the camera when the laser is on the opposite side. Hence,

less laser energy is required. However, uneven reflection from the weld pool occurs, varying the angle between the laser beam and the workpiece can improve this. On the other hand, mounting the laser on the same side as the camera gives natural lighting with little glare but requires more laser energy, since most of the laser light reflects away from the camera.

**Laser-camera synchronisation. Trigger methods.** Figure 7, *a-d* shows four synchronisation methods that can be used to capture the laser pulse. In Figure 7, *a* the camera is driving the laser, a strobe output from the back of the camera is connected to the laser external input. In Figure 7, *b* the laser is driving the camera, this will also introduce a delay to the camera shutter, which can be overcome by introducing a pulse delay. In the third method, which is shown in Fi-

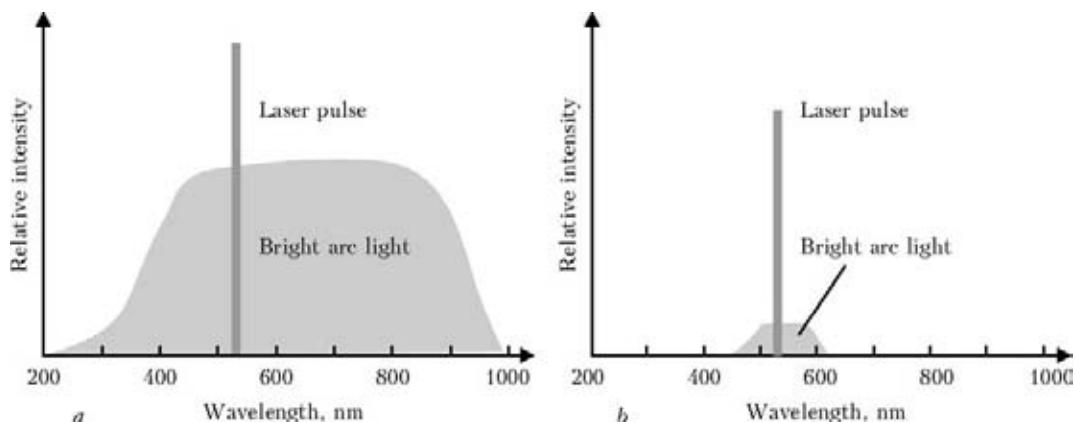


Figure 4. Comparison of light from laser light-source with arc light before (a) and after (b) filtering

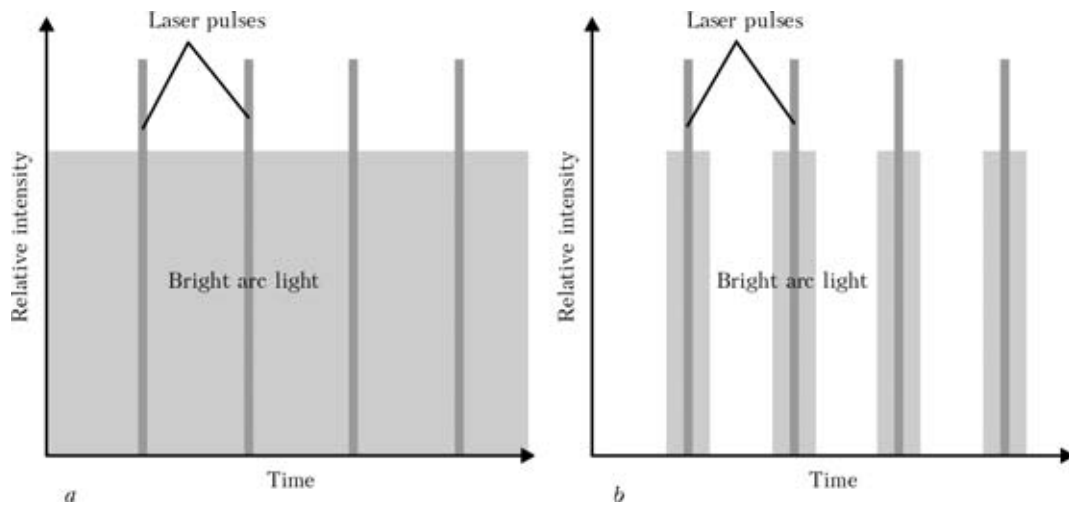


Figure 5. Contributions to the image brightness from the laser and the arc light before (a) and after (b) temporal filtering

Figure 7, c, both the camera and the laser are driven by an external master-triggering unit. This is the preferred method for synchronising pulsed lasers. Since both the camera and the laser are triggered at exactly the same time no delay is introduced. The frame rate, laser frequency and timing of the system can be controlled when connected to a pulse generator. The fourth method shown in Figure 7, d, is used when using a continuous wave laser as an illumination source. Both the camera and the laser are free running and are independently controlled.

**Trigger modes.** In the camera-controlled exposure mode, the exposure time is defined by the camera. For an active high trigger signal, the camera starts the exposure with a positive trigger edge and stops it when the programmed exposure time has elapsed. In the level-controlled exposure mode, the exposure time is defined by the pulse width of the trigger signal. For an active high trigger signal, the camera starts the exposure with the positive edge of the trigger signal and stops it with the negative edge. Figure 8 shows the timing diagram for capturing the laser pulse. The signal EXSYNC denotes the trigger signal that is provided by the I/O trigger. A pulse is sent

to trigger the FLASHLAMP signal. Another delayed pulse is then sent to trigger the Q-SWITCH and EX-SYNC signals.

**Results and discussion. Diode laser.** The results obtained using a diode laser as an illumination light source are shown in Figure 9. Its wavelength of emission is 808 nm and its peak power is 200 W. Although the peak power is relatively low but its pulse width is relatively long compared to other lasers, which can be manually set from 1 to 80  $\mu$ s. Pulse energy varies from 0.15 to 15 mJ depending on the pulse width, the longer the pulse width the higher the pulse energy. For maximum power a pulse width of 80  $\mu$ s was used, hence the exposure time was also set to 80  $\mu$ s.

**Nd:YAG laser.** This is a FlashLamp pumped Q-switch Nd:YAG laser with a frequency doubling option, pulse energy of 20 mJ and pulse width of 5 ns. Figure 10 shows the results obtained when the laser is operated at 532 nm.

**Copper vapour laser.** Although this is considered a pulsed laser but its repetition rate is 10 kHz, which means synchronising the laser pulse with the camera shutter is not possible due to the camera's limited frequency. The exposure time was set to 100  $\mu$ s; this

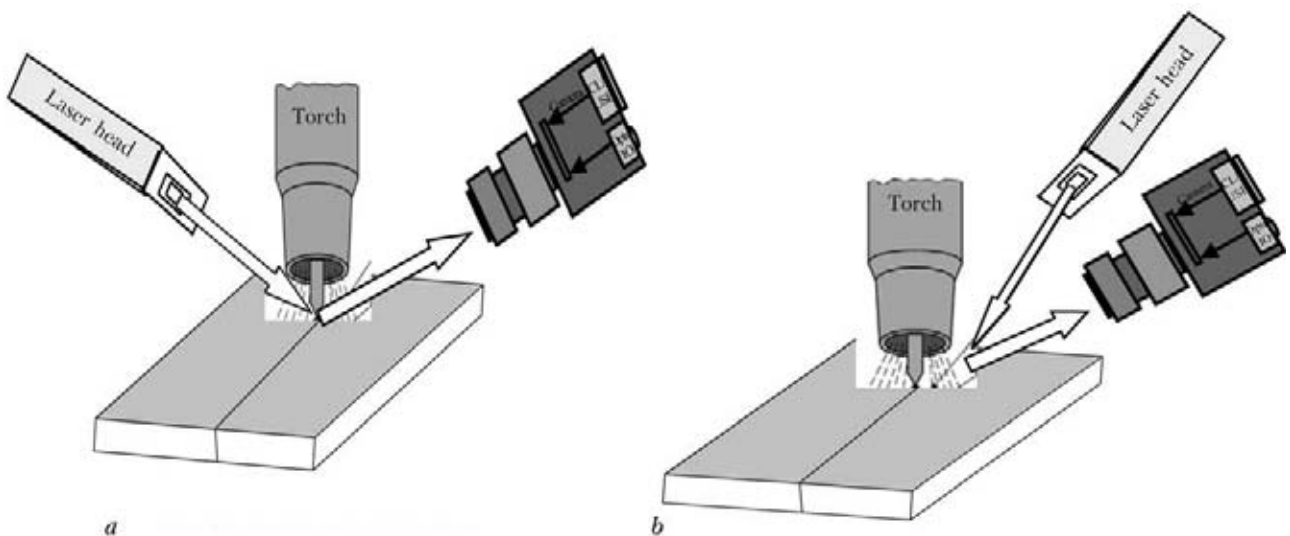
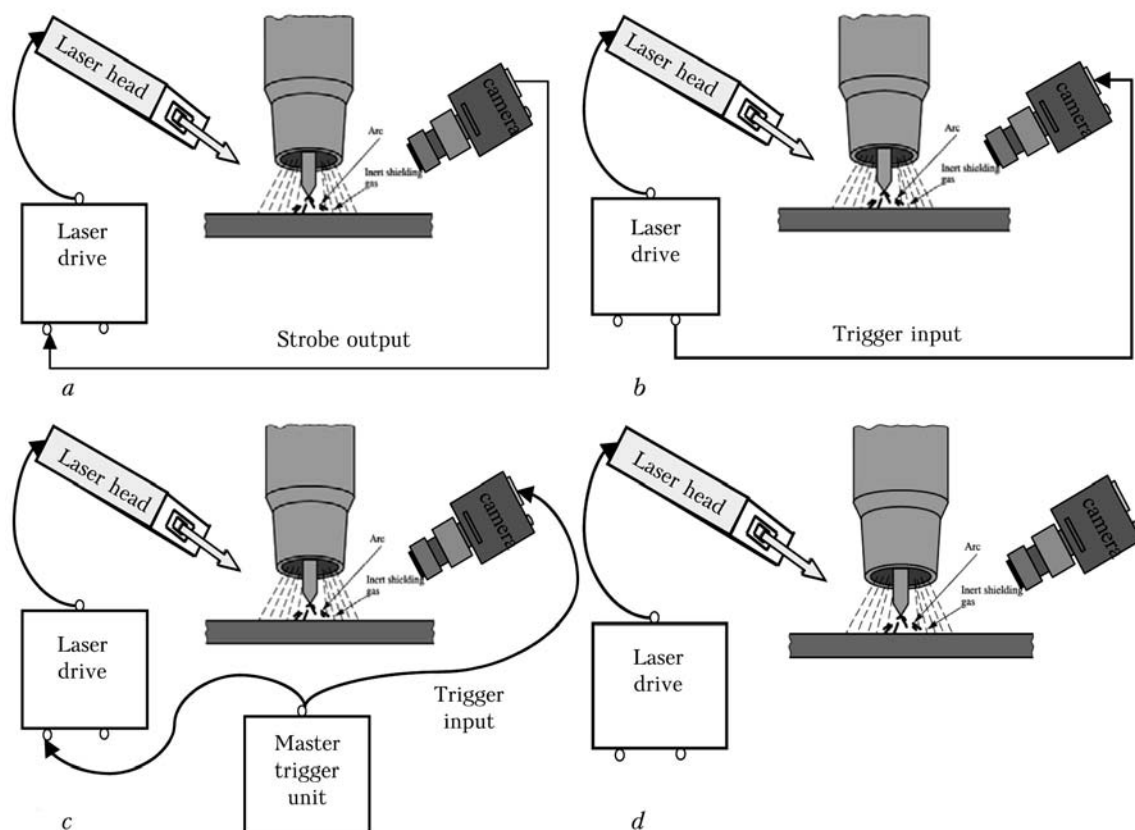


Figure 6. Forward (a) and backward (b) reflection





**Figure 7.** Synchronisation methods for capture the laser pulse: *a* – camera driving laser; *b* – laser driving camera; *c* – camera and laser driven by an external trigger; *d* – camera and laser driven independently

was the longest exposure time possible without capturing too much arc light. The pulse width is 5 ns, average power is 5 W, peak power is 70 kW and pulse energy is 2.75 mJ. Figure 11 shows the images obtained when the copper laser was used as an illumination source. They appear to be out of focus due to the narrow depth of field, which is caused by the aperture setting. The narrower the aperture the greater the depth of field, in this case the aperture was set to two resulting in a narrow depth of field.

*Continuous wave laser.* Figure 12 shows the images obtained using a high power Nd:YAG continuous wave laser as an illumination source. The emission wavelength is 1064 nm, i.e. operating at the end of the camera's spectral response, which is less than 0.5 % in Figure 2. The arc light is totally eliminated

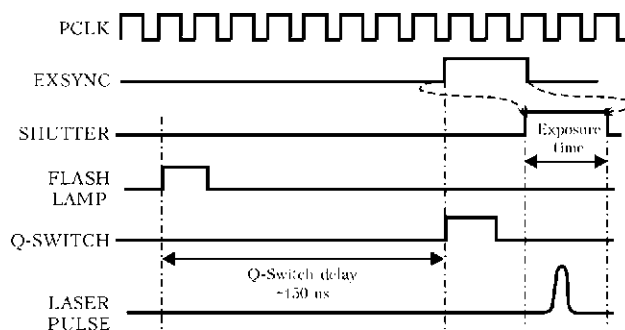


**Figure 8.** Camera-laser synchronisation diagram

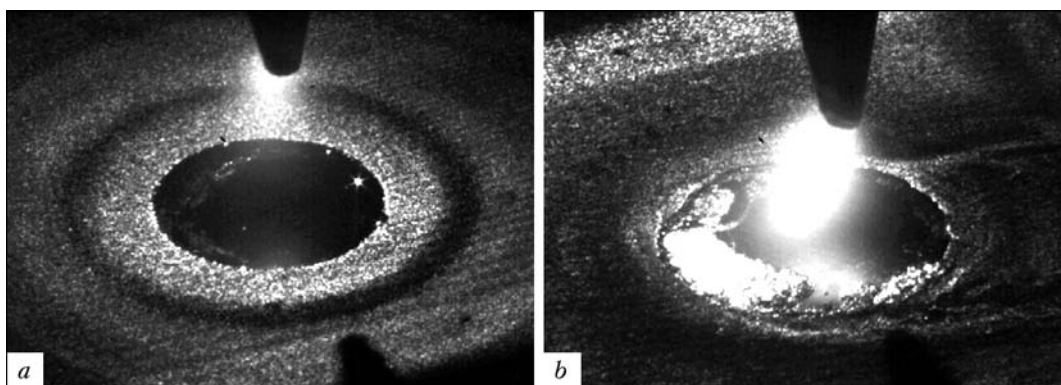


**Figure 9.** Use of diode laser as an illumination light source in TIG welding of stainless steel at 50 (*a*) and 100 (*b*) A with exposure time of 80 us

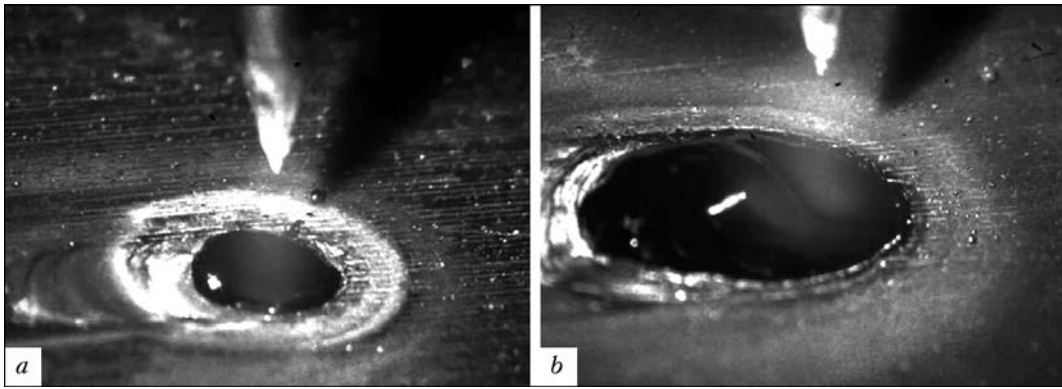


**Figure 10.** Use of Nd:YAG laser operating at 532 nm for TIG welding of stainless steel at 100 (a) and 150 (b) A with exposure time of 10 us and backward reflection

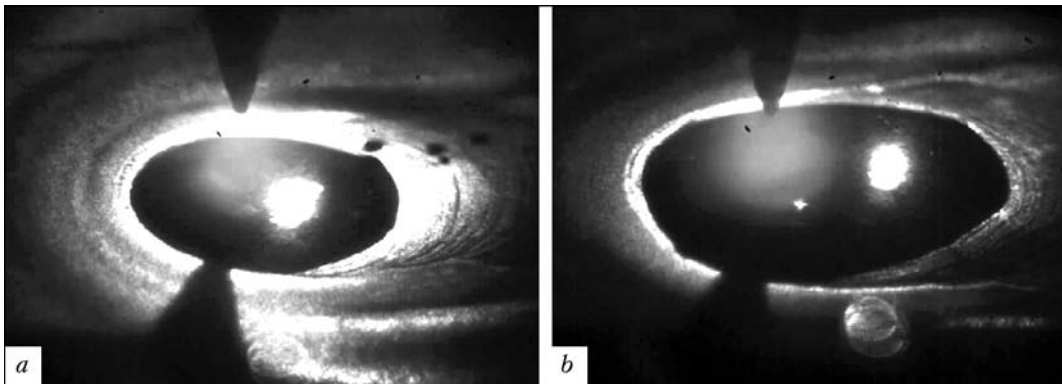


**Figure 11.** Use of copper laser as an illumination source in TIG welding of stainless steel at 150 (a) and 200 (b) A with exposure time of 100 us and forward reflection

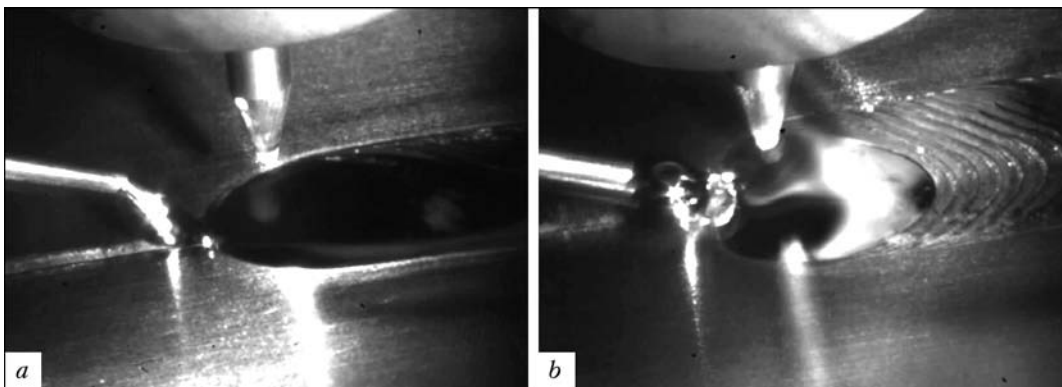


**Figure 12.** Use of high power Nd:YAG CW laser as an illumination source for TIG welding of stainless steel at 100 (a) and 160 (b) A with exposure time of 20 ms and backward reflection

due to spectral and temporal filtering and operating at the end of the spectral response where emissions are mainly from the weld pool.

## CONCLUSION

The vision system described has been shown to effectively remove arc light and produce reliable and high quality real-time welding images. The system incorporates a CMOS camera with a lens and narrow band pass filter along with a frame grabber and an illumination source. Several laser illumination light sources were used, pulsed and continuous wave. High quality images are obtained using relatively low power pulsed lasers. However, images with the same quality can be obtained using relatively high power CW lasers. Arc and weld pool emissions were studied to

enhance the image quality. It was found that arc emissions abound at the lower part of the spectrum, and the weld pool emissions abound at upper end of the spectrum, i.e. infra red region. The noise level is dependent on the shielding gas, if the shielding gas is argon then argon emissions, which abound at the 700 to 900 nm wavelength would increase the noise level at this region. Meanwhile, operating at wavelengths greater than 1000 nm is preferable since arc and argon emissions are low and weld pool emission are high but the camera's spectral response is low and therefore more laser energy is required.

1. Anderson, P.C.J. (1994) *A review of sensor systems for the top face control of weld penetration*: TWI Members Report 503.

2. Kovacevic, R., Zhang, Y.M., Li, L. (1996) Monitoring of weld joint penetration based on weld pool geometrical appearance. *Welding J.*, 75(10), p. 317–329.
3. Lucas, B. *TIG welding, a guide to best practice*: TWI report.
4. Kovacevic, R., Zhang, Y.M., Ruan, S. (1995) Sensing and control of weld pool geometry for automated GTA welding. *ASME J. Eng. for Industry*, 117(5), p. 210–222.
5. Litwiller, D. (2001) CCD vs. CMOS: Facts and fiction. *Photonics Spectra*, 35(1), p. 154–158.
6. Smith, J.S., Lucas, W. *Vision based control of arc welding processes*.
7. Lucas, J., Smith, J.S. (2001) *Sensors systems for visualisation of high pressure arcs and their workpieces*: GR/M32672, August.
8. Li, P.J., Zhang, Y.M. (2000) *Analysis of an arc light mechanism and its applications in sensing of the GTAW process*.
9. Madigan, R.B., Quinn, T.P., Siewert, T.A. (1989) Sensing droplet detachment and electrode extension for control of gas metal arc welding. In: *Proc. of 2nd Int. Conf. on Trends in Welding Research* (Gatlinburg), p. 999–1002.
10. Richardson, R.W., Edwards, F.S. (1995) Controlling GT arc length from arc light emissions. In: *Proc. of 4th Int. Conf. on Trends in Welding Research* (Gatlinburg).
11. Li, P., Zhang, Y.M. (2001) Robust sensing of arc length. *IEEE Transact. on Instrumentation and Measurement*, 50(3).
12. Wang, J. *Visual information acquisition and adaptive control of weld pool dynamics of aluminium alloy during pulsed TIG welding*.
13. *National Institute of Standards and Technology (NIST)*.
14. Lucas, W., Smith, J.S. (2000) Keeping an electronic eye on automated arc welding. *Welding and Metal Fabrication*, April.
15. Kim, I.S., Jeong, Y.J., Yarlagadda, P.K.D.V. (2003) Prediction of welding parameters for pipeline welding using an intelligent system. *Int. J. Adv. Man. Tech.*, 22(9/10), p. 713–719.
16. Balfour, C., Lucas, J., Maqbool, S. et al. (2000) A neural network model for MIG welding parameter prediction. In: *Proc. of 10th Int. Conf. on Computer Technology in Welding*.
17. Gao, J., Wu, C. (2002). Extracting weld penetration in tungsten-inert-gas welding. *Proc. of Inst. of Mech. Eng. Man.*, 216(2), p. 207–214.
18. Luo, H., Devanathan, R., Wang, J. et al. (2002) Vision based neurofuzzy logic control of weld pool geometry. *Sci. and Tech. of Welding and Joining*, 7(5), p. 321–325.
19. Zhao, D.B., Chen, S.B., Wu, L. et al. (2001) *Intelligent control for the shape of the weld pool in pulsed GTAW with filler metal*.
20. Zhang, Y.M., Kovacevic, R. (1998) Neurofuzzy model-based predictive control of weld fusion zone geometry. *IEEE Transact. on Fuzzy Sys.*, 6(3), p. 389–401.

# SOFTWARE-METHODICAL MEANS FOR FORMATION OF TECHNOLOGICAL DOCUMENTATION OF NEW GENERATION

D.V. BIKBULATOV<sup>1</sup>, V.I. DYACHENKO<sup>2</sup>, D.P. KUNKEVICH<sup>1</sup>, S.V. MEDVEDEV<sup>1</sup> and A.I. STRELTSOV<sup>1</sup>

<sup>1</sup>United Institute of Informatics Problems, NAS of Belarus, Minsk, Belarus

<sup>2</sup>Minsk Tractor Plant, Belarus

Traditional form of presenting technological documents for assembly-welding processes does not meet to full degree state-of-the-art requirements to its operative perception, correction, and bringing to commercial level status. GTD is a set of sketches and abstracts, a located on the process chart sketch, which shows mutual arrangements of parts in a structure, joints, which connect them, and sequence of assembly. After selection of an annotated item its characteristics appear in the dialogue window of the screen. Designation, mass, overall dimension of an item are indicated, and time of its installation on table and into a jig. For a welded joint its designation is given and mass, volume of built-up metal, welded joint length, main and auxiliary time are indicated. Software-methodical means are implemented in graphic environment Mechanical Desktop 6 under operational system Windows XP.

State standards of technological documents representation forms is conventional and integral part of welding production planning. There is too much text information on the traditional form of assembly-welding processes documents. It makes documentation difficult for perception, editing, mustering process plan is embarrassing.

There is base of development of perspective computer-aided welding process planning systems: constant decrease of computer hardware price and increase of computer productivity, approaching personal computer parameters to graph stations parameters, extension of computer graphic systems capabilities, solid modeling. In the CIS as well as beyond of its bounds, new approaches of welding production documents forming is found and developed [1, 2]. One of them is supported by INWELDEN system (INstrument of WELDing ENgineer) (Figure 1). This approach is based on virtual 3D models of assembly-welding structure, parts which assembly-welding structure-assembly-welding fixture (AWS-AWF) consist of welding seams.

Three problem types are considered in the CAD of assembly-welding process planning [3], namely calculation and optimization of arc and spot weld and heat treatment; process planning as sequence of location, clamping, sticking of assembly parts and seams laying; and automatic or automated forming of process documentation.

In this paper documentation forming is considered. Assumed welding conditions are calculated or are selected from reference book, assembly-welding sequence is determined by qualified welding engineer.

There is the tendency of organization of integrated systems of modern welding production preparing [4]. In accordance to this tendency, AWS and their technological environment (AWF and equipment) is con-

sidered as united technological assembly-welding system in its own stations space.

It expediently distinguishes next fixed stations of AWS-AWF system:

- start station of AWS as collection of its parts;
- terminal station of AWS on check operation;
- station as assembly-welding scheme;
- stations on the process operations which represents interaction and relations parts and seams with AWF units and welding tools (welding torch, welding pincers);
  - auxiliary (intermediate) stations, strains of AWS parts is taken into account;
  - stations of individual joint while multi-passed seams are laid on;
  - reserve and additional stations.

Pointed stations of assembly-welding system may be represented by graphic. Images are results of are supplied by welding parameters, rates of main and auxiliary welding materials expenses and other technological data. That image collection fully determines process; it is named graphic technology documentation (GTD). To develop scientific-methodological approaches experimental system INWELDEN-GTD was making.

3D models of AWS are initial information for system. Those models may be represented with STEP or SAT solid formats.

Subsystem FSS 01 is intended to set AWS in position, which suits for welding, as well as creating visual assembly-welding schemes in dialogue mode. Seams are drawn on the AWS model by means of this subsystem. Seams are automatically grouped according to types and calibres. Seams summary length is determined too.

Subsystem FSS 02 is used under two modes, namely creation of visual location-clamping scheme

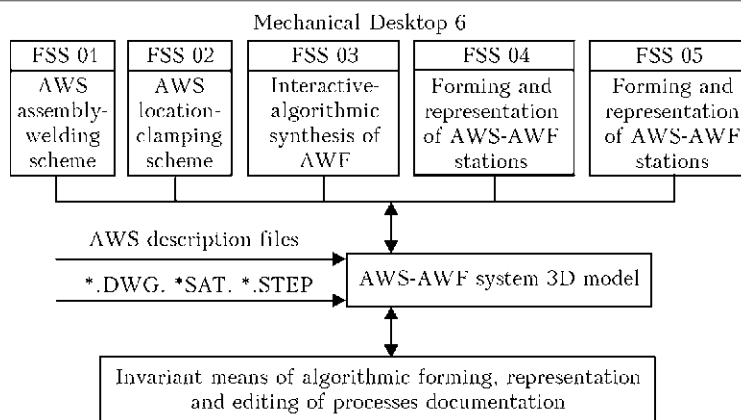


Figure 1. Scheme of program-methodical system INWELDEN-GTD

(principal fixture scheme) by means of placement locators and clamps signs on the AWS model; and forming output file which includes fixture units coordinates in the AWS coordinate system for further using in AWF synthesis subsystem (FSS 03).

Subsystem FSS 04 forms and represents stations of AWS-AWF system, which are requested by user (manufacturing engineer). AWS 3D model, AWS assembly-welding scheme are used by FSS 04.

Subsystem FSS 05 calculates expenses of electrodes, welding wire and shielding gas. Dimensions of seams are used. Data are placed into suitable fields of process blanks.

Program system INWELDEN functions are based on Mechanical Desktop 6 [5]. Its facilities are accessible for user. The results of any subsystems may be modified interactively.

GTD is an outline collection represented sequence of states to be passed toward terminal station. Outlines are supplied by annotations describing features of assembly-welding system units illustrated (Figure 2).

For outline creation AWVIEW command is used. Its running is started by suggestion to select objects for outline in the command line. Blank of GTD will be inserted and just formed outline will be placed and scaled on.

Every blank contains three outlines. New outlines are placed below of one existing. For scaling the biggest size of outlines collection bounding box is compared with correspondent size of blank. If active blank contains three outlines, new blank will be inserted in the right of active blank. If user wants to place in the current blank less than three outline, one may insert next blank in right of current one. It may be carrying out automatically by means of BLANK command. Next outlines will be placed in a new blank.

Second key operation of INWELDEN-GTD is annotating. There is AWANN command for its carrying-out. When it has started suggestion to select annotated object will appear in command line. Annotated object selection is followed by appearance of dialogue window which contains object features. For the parts name, code, mass property, bounding box dimensions, location time is represented. For the seam

notation, mass, welded metal volume, length and operation time are represented.

Auxiliary time for part clamping is determined taking into account clamp driver type (lever, screw, etc.), thread length (for screw clamps). Special tables are used. Welded metal mass is extracted from solid seam model.

INWELDEN-Seams module is provided for solid seam models creating. User should select seam type and its parameters from menu, mark start and end points on the AWS model, input weld parameters. 3D seam models including fusion zones and irreversible plastic deformation zones models are formed programmatically.

After INWELDEN-GTD subsystem had been exploited special GTD-blank was proposed. Certain semantic zones are its peculiarity (Figure 3).

Zone 5 may be detailed with additional blank containing corresponding semantic zones (Figure 4).

Offered blank application is considered. Welded structure example is introduced in Figure 5, and Figure 6 demonstrates special GTD-blank. Its zones contain GTD-information filled in by means of INSWAR-GTD.

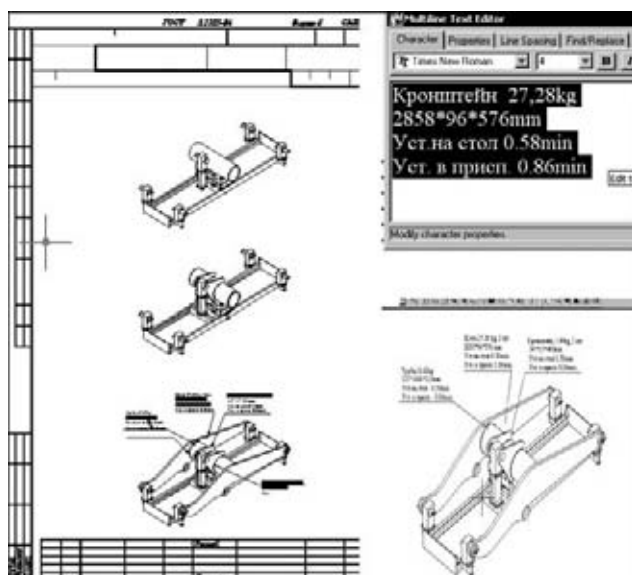


Figure 2. Example of graphic technology document based on standard outline blank

Location-clamping scheme	Assembly-welding scheme	Operation stations of AWS-AWF system
Fixtures, tools, attachment		Operation time
		Welding conditions
Checking circuit and check equipment		Welding material expenses
		AWS piece

Figure 3. Semantic zones of special GTD-blank

AWS-AWF system station on previous operation	AWS-AWF station with different welding tools positions	Zone of graphic and additional information
	Ration time	
	Material expense	

Figure 4. Semantic zones of additional GTD-blank

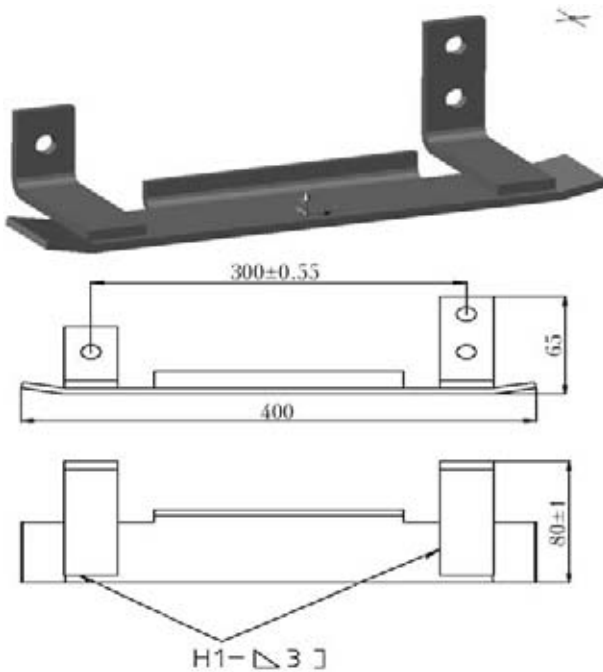


Figure 5. Welded structure

Proposed document forms have several advantages. Due to 3D image information is conceived easily

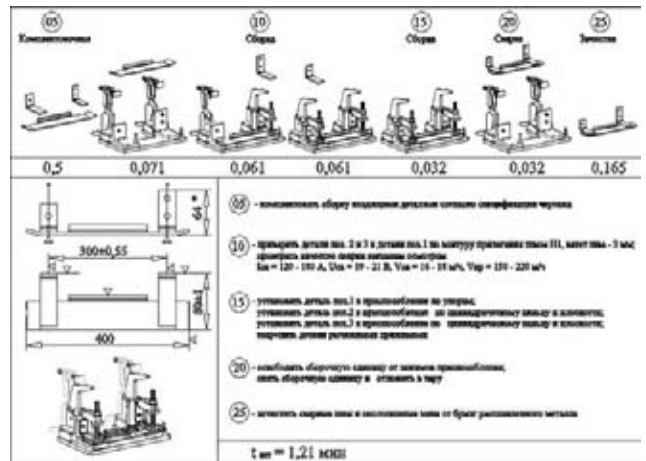


Figure 6. Example of special GTD-blank variant

then text, GTD is unambiguously assimilated by welder. Essential reduction of documentation count is other GTD advantage. Offered approach was tested at manufacturing enterprises of Belarus. Mentioned advantages have got confirmation and positive estimation of welding specialists.

Further investigations are appropriately realized in next general directions:

- perfection of program-information means of interactive-algorithmic documents forming;
- development and testing of variants of GTD-blanks;
- development of approach of welding process parameters determination for the purpose of reduction of interactive operations quote in documents forming.

1. Engh, E. (1996) The product model as a source for quality assurance and quality control – a new approach to product documentation. In: *Proc. of 6th Int. Conf. on Computer Technology Welding* (Cambridge), p. 1–12.
2. Medvedev, S.V. (1998) Formation of welding process documents. *Svaroch. Proizvodstvo*, 5, p. 37–40.
3. Babkin, A.S. (1996) Methods for problem solution in technological CAD of welding production (Review). *Ibid.*, 4, p. 20–23.
4. Medvedev, S.V. (1994) Principles of integrated system construction in welding production. *Ibid.*, 12, p. 26–28.
5. Polishchuk, V.V. (2001) *Mechanical Desktop*. Moscow: Dialog-MIFI.

# IMPROVING THE DOCUMENTATION OF WELDING AT HEATRIC Ltd. BY USING THE WELDING COORDINATOR SOFTWARE SYSTEM

A. BRIGHTMORE<sup>1</sup> and G. HOLE<sup>2</sup>

<sup>1</sup>TWI Ltd., Cambridge, UK

<sup>2</sup>Heatric Ltd., UK

The Heatric manufacture printed circuit heat exchangers (PCHEs), which are highly compact, highly robust heat exchangers, constructed from a process of chemically etching metal plates and diffusion bonding. This unique technology is well established in the upstream hydrocarbon processing, petrochemical and refining industries for applications ranging from gas compression cooling and gas dewpoint control offshore to ethylene oxide processing and hydrogen production. The welding of attachments, valves, frames, etc. is carried out using more conventional arc welding processes and is qualified mostly to ASME IX. Heatric has been using TWI Weldspec and Welderqual software for a number of years to manage its welding procedures and welder qualifications. This paper describes the implementation of TWI Welding software to manage all aspects of welding. It describes the process of implementation and the benefits gained from using the software. These benefits include savings in time in creating and managing welding procedures and welder qualifications; savings in time through the use of the electronic signature capability of the software; easier assignment of qualified procedures and personnel to production welds; ensuring the documentation is up-to-date by checking documents with the latest welding codes/standards; and better traceability of information through links between the Welding Coordinator and the Weldspec and Welderqual software. Finally, the paper describes how development of the system in the future will bring additional benefits to Heatric Ltd.

**Heatric and PCHEs.** Heatric is based in Poole, Dorset (Figure 1) in the UK and manufactures PCHEs. PCHEs are highly compact, highly robust heat exchangers, constructed from a process of chemically etching metal plates and diffusion bonding (Figure 2). This unique technology is well established in the upstream hydrocarbon processing, petrochemical and refining industries for applications ranging from gas compression cooling and gas dewpoint control offshore to ethylene oxide processing and hydrogen production.

PCHEs offer a number of advantages over conventional heat exchangers as follows:

- they are 4–6 times smaller than conventional shell and tube heat exchangers of the equivalent duty;

- they have a pressure capability in excess of 600 bar (9000 psi) and can cope with extreme temperatures, ranging from cryogenic to 900 °C;

- PCHEs can achieve thermal effectiveness of over 98 % in a single unit;

- they can incorporate more than two process streams into a single unit. This design feature has space and weight advantages, reducing exchanger size together with piping and valve requirements.

About 50 heat exchangers are built by Heatric each year, and a typical completed PCHE is shown in Figure 3.



**Figure 1.** The Heatric premises in Poole, Dorset, UK

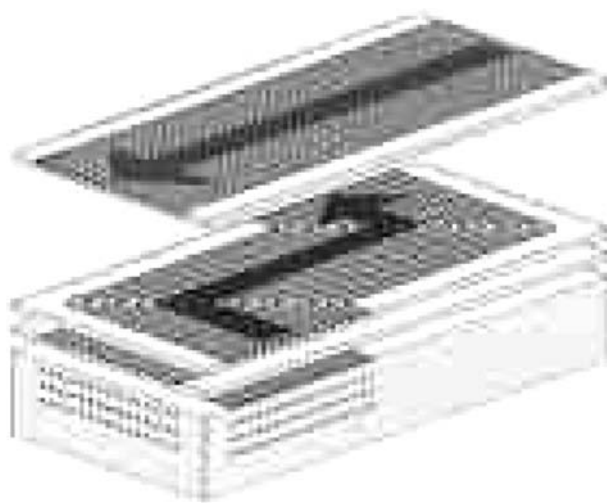


**Figure 2.** PCHEs are constructed from flat metal plates into which fluid flow channels are etched

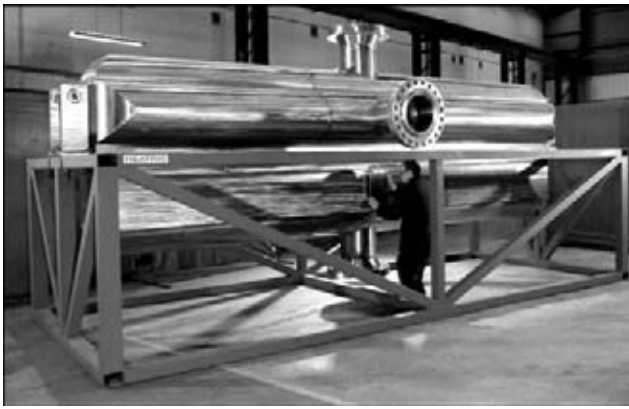


Figure 3. Typical completed PCHE

### Welding procedures and welder qualifications.

The welding of attachments, valves, frames, etc. is carried out using more conventional arc welding processes and is qualified mostly to ASME IX (Figure 4). Heatric has an ASME U-stamp as well as EN ISO 9001 accreditation. Heatric has been using TWI Weldspec and Welderqual software for a number of years to manage its welding procedures and welder qualifications and the use of the software is embedded in Heatric quality procedures.

Heatric has 16 full time welders and the welders have an average of 35 qualifications each (a total of 558 qualifications). This is a very large number of qualifications to create and keep track of. Heatric uses Welderqual's «File save-as» function to create multiple welder certificates only changing the document number and the welder's name on each certificate (for a screen shot from Welderqual see Figure 5).

On the welding procedure side, it used to take half a day to create a PQR using the previous paper system. Using Weldspec, this can be cut down to about 1 h and the WPS is created automatically by the software. In addition, the software checks all the latest code rules, so the ranges of approval and test requirements are generated automatically.

The company has about 90 WPSs, all backed up with a PQR. The welding procedures are a mix of



Figure 4. Welding headers to the exchanger core



Figure 5. Entering WPO generating ranges of approval

generic documents and some which are contract-specific. Weldspec's «File Save-as» function is used extensively to create contract-specific WPSs.

Heatric also makes extensive use of the both programs' electronic signature capability. On start-up, the user logs into the software with a user name and password. To sign a document, the user simply clicks in the relevant signature block. The software adds the user's name, signature graphic and date automatically and locks that document to prevent unauthorised editing. The QA Manager and Third-party inspector also add their signatures electronically.

The use of the login system prevents any unauthorised creation and editing of documents in any of the welding software programs.

The «Export to PDF» function is used by the contract engineers to e-mail documents to clients and customers for review. PDF versions of documents cannot be changed and are easily extracted from e-mails by client staff. Sending documents in this way is much more efficient than the previous paper method. PDF documents do not suffer from grease, fingermarks, tears and spatter burns.

Heatric only keep paper copies of welding documents as back-ups. The master copies are all electronic, within Weldspec and Welderqual. An efficient IT back-up policy means that electronic storage is much more effective than paper for disaster-recovery.

**Welding Coordinator.** After successfully integrating Weldspec and Welderqual within the Heatric working practices, the company investigated the use of the Welding Coordinator software to manage production welding information. Heatric previously used a paper-based Weld Log and NDT Record system on which information on weld numbers, processes, welders, filler materials and other QC information was recorded.

The layout editor built into Welding Coordinator was used to design a form which contained similar information to the paper form. The paper form was examined but it was felt that it did not need a complete redesign (Figure 6).



MMEGGITT		Project name Sheet No. Creation date Customer/Client PO Number Project Project No. Min NDT Op. Qual Doc Code/No.	WL-40276 1 11 Jan 2005 Parsons E&C Europe Ltd SAP - 450932906 Langley Receiving Facilities 190277 ASNT Level II	HEATRIC 46 Holton Heath, Poole, Dorset, BH 16 6LT Weld Log and NDT Record		Fabrication code Class Welding code Description Item No./Tag No. Visual Examination Visual Test Spec. DP Procedure DP Acceptance Stc.	ASME Section VIII 1 ASME Section IX Sales Gas Heat Exchanger E-02-101 WI-296 ASME V Art 9 WI-294 ASME V Art 6													
General	Process	Welder	Filler	NDT Weld																
Weld ID	WPS number	Region	Welders ID	Code 1	Code 2	Code 3	Fill-up date	Visual	Dye Pen	Full UT	TP Monitor	Spot X-ray	Full X-ray	Spot UT	Full UT	Ferrite Cert.	Hardness	NFI Cert.	PIM Cert.	
1011	WPS 1-1-25A	Cap	H05H02	K2P	LAL		20 Mar 2005	CM												
	WPS 1-1-25A	Root	H25H06	K2P			18 Mar 2005	CM												
1021	WPS 1-1-25A	Cap	H05H02	K2P	LAL		20 Mar 2005	CM												
	WPS 1-1-25A	Root	H25H06	K2P			18 Mar 2005	CM												
1031	WPS 1-1-25A	Cap	H05H02	K2P	LAL		20 Mar 2005	CM												
	WPS 1-1-25A	Root	H25H06	K2P			18 Mar 2005	CM												
1041	WPS 1-1-25A	Cap	H05H02	K2P	LAL		20 Mar 2005	CM												
	WPS 1-1-25A	Root	H25H06	K2P			18 Mar 2005	CM												
1051	WPS 1-1-25A	Cap	H05H02	K2P	LAL		20 Mar 2005	CM												
	WPS 1-1-25A	Root	H25H06	K2P			18 Mar 2005	CM												
2011	WPS 8-013-403	Root	H08	LHJ			03 Jun 2005	IS												
	WPS 8-013-403	Cap	H21H06	LEG			10 Jun 2005	BR					Required							
2012	WPS 8-013-403	Cap	H21H06	LEG			03 Jun 2005	IS												
	WPS 8-013-403	Root	H08	LHJ			10 Jun 2005	BR												
2013	WPS 8-013-403	Cap	H08	LEG			17 May 2005	IS					Required							
	WPS 8-01-403	Root	H08	K18			18 May 2005	IS												
2014	WPS 8-01-403	Cap	H08	K2P			28 Feb 2005	ML												
	WPS 8-013-403	Cap	H08	LEG			17 May 2005	IS												
2021	WPS 8-013-403	Cap	H08	LEG			19 May 2005	IS					Required							
	WPS 8-01-403	Root	H08	LEB			19 May 2005	IS												
2022	WPS 8-01-403	Root	H10	K0N			26 Feb 2005	GG												
	WPS 8-01-403	Cap	H10	K0K			26 Feb 2005	GG												
20111	WPS 8-01-410	Cap	HR	LAM			03 Jun 2005	IS												
	WPS 8-01-410	Root	H08	LHJ			20 Jun 2005	AS												
2021	WPS 8-01-410	Cap	H08	LAM			03 Jun 2005	IS												
	WPS 8-01-410	Root	H08	LHJ			20 Jun 2005	IS												
4011	WPS 8-013-403	Cap	H32	K2Z	LAM	K20	03 May 2005	CS												
	WPS 8-013-403	Root	H32	K2W			04 May 2005	CS					Required							
2031	WPS 8-013-403	Cap	H21H06	LEG			03 June 2005	IS					Required							
	WPS 8-013-403	Root	H08	LHJ			10 June 2005	BR												
2032	WPS 8-013-403	Cap	H08	LEG			03 June 2005	IS												
	WPS 8-013-403	Root	H08	LEB			17 May 2005	IS					Required							
2033	WPS 8-013-403	Cap	H08	LEG			18 May 2005	IS												

Figure 6. Electronic Weld Log and NDT record

The system was implemented on number of computers and information is entered into the system whenever it is generated. This includes welders entering visual test information into the system as soon as welds are completed. This, in turn, means that live progress reports can be generated on heat exchanger projects.

One key aspect of the Welding Coordinator system that Heatric make extensive use of is the instant traceability that the system gives between welds and associated information, such as welding procedures and welders. Clicking on a WPS number on a Weld

Log in Welding Coordinator, for example, displays that document directly from Weldspec.

**Future work.** Currently, Heatric are still monitoring the use of the Welding Coordinator system. The electronic system was used successfully in parallel with the paper system on four projects. As the systems continue to be used, more of the systems' functions will be implemented, including the following:

- automatic generation of welder performance reports directly from the system;
- automatic NDT requisitions;
- automatic updating of welder qualifications in Welderqual.

# TAKING FABRICATION MANAGEMENT INTO THE 21st CENTURY

M. CHINERY and J. STRACHAN  
TWI Ltd., Cambridge, UK

As the business world moves at an ever-increasing pace, pressures increase to complete projects faster, to ever stricter quality requirements. To compound the situation law suits against faulty manufacture are becoming increasingly common so the need to prove the quality of workmanship is vital. All of these factors lead to a situation where areas of business must improve to even retain market share, let alone improve the business position. This paper will address the impacts of changes in the modern working environment and discuss how fabrication project management and quality assurance could use the latest technologies to meet the high demands placed on industry today. We identify the advantages and shortfall of existing methods of managing welding projects, welder qualification and welding certificates, proposing improvements to these systems with respect to issues including sharing data, task scheduling, process optimisation and quality assurance. In an increasingly technologically orientated world, new electronic devices could provide us with an elegant solution to many of the problems discussed. Powerful, portable equipment such as mobile phones and palmtop devices, combined with implementations of modern communications standards (existing wireless technologies such as 802.11a, 802.11b and Bluetooth, and emerging standards including Zigbee and WiMax) could allow us to push forward fabrication management to a new level. The paper considers the advantages and possible safety issues that could arise in the use of these technologies, presenting a «visionary case-study» of a technologically advanced welding project, which in reality could be implemented today. We also look at longer term ideas such as extending technologies to address site safety issues, identifying possible problem areas by monitoring project failure and repair data.

## Fabrication management today

Fabrication project management has traditionally been an area where good traceability, progress reporting and review of historical data is very important. At present there are many different solutions to this problem. Technology moves at a very fast pace but in some areas we can be slow to make the most of the advancements to improve the way we complete tasks in the world. This paper will discuss the various methodologies that are currently used today, explain some of the new technologies that have been developed and then give an example case study of how we can utilise new technology to make business more cost effective, improve manufacturing quality, and increase traceability.

Of the existing solutions to the fabrication management problem, a paper based system is the most common. In a paper based system, the company designs a paper document in order to record information regarding the project in question (typically a table of welds, material information, welding procedure information and NDT results). A paper based system offers the advantages of being very cheap to create, no specialist skills are required to design and use it, the information is stored in one location and many people can view the information. However, this is a very dated system and has some major drawbacks. Although all necessary information is recorded, the process is very time consuming to mine information from – to find information concerning a particular weld could take a vast amount of time as the data must be checked by hand. As the document can only physically be in one place it cannot be updated by

people in different locations at once which for large scale projects makes for serious difficulties. Backing up information in paper based systems must be done manually which can lead to human error as if this is forgotten and the original is lost/misplaced all the data is lost.

With the introduction of computers an obvious next step was to use them to aid in this process. As computer systems have been around for a considerable amount of time there are various different solutions currently available.

The cheapest solution to this is by adapting an existing package to meet the needs of fabrication project management. By using a spreadsheet package such as Microsoft® Excel a weld data sheet can be created quickly, the set up time is fairly small and the initial cost outlay is minimal as most working environments will currently already use a spreadsheet package. By having a computerised system saving of information is much more straight forward – many different people are able to look at an up to date view of the data at once. By being computerised the system can easily be backed up as well as being able to historically view the state of the information at any date. Finding information is also much more straight forward as the computer will take the work out of searching as the package will most likely come with a built in search facility. On the negative side if computer systems are not present the start-up cost can be vast, and if the employees do not currently have IT skills training maybe required. By using an off the shelf package that is not specifically designed for this purpose it may not be possible to create weld data sheets to the

exact specification wanted, or extract the information in the way desired.

To move on from this, the next stage of a computer based solution would be to use an off the shelf package designed specifically for weld data. An example of an existing product designed specifically for this purpose, is the TWI's Welding Coordinator™ software (Figure 1). Off the shelf fabrication management packages are designed to meet the needs of industry and specifically create weld data sheets, welding procedures and welder qualifications. These products typically make setting up the weld data sheet very simple and allow quick up times because of the similarity in layout to the traditional paper based system. The off the shelf packages will often all integrate with each other so when creating a fabrication map you will be able to search records of welders and procedures to find a suitable procedure and welder at the touch of a button. This can save a lot of time, and greatly improve traceability compared to the paper based approach.

Due to the system being designed for fabrication projects, reporting systems will often be built in. This will allow the information about the welds, the welders and procedures to be extrapolated into a report to give information on which procedures are being used most, the most productive welders, the highest quality welders and also identify that the correct amount of NDT is being performed in order to meet the required standards. On the negative side these products are generally quite expensive and require time to set up. They also could possibly require some changes in working practice to take full advantage of the new features, and this could impact productivity in the short term whilst the company is getting to grips with the new working practices.

The most expensive solution to quality assurance is to have a bespoke software solution created. This will involve working on a tailored solution for a specific business that will fit in their working practices and give all reporting and support they require. This will hopefully mean the system will become automatically productive and improve the business and the quality of their product. With all the diversity of fabrication projects and the differing requirements even within a company for specific products it can be difficult to find an off the shelf solution that will not be a hindrance to working practices. The bespoke solution should hopefully remove this problem from the equation. If a very effective piece of software is developed and allows a company to produce higher quality products due to better quality assurance this will then give them an advantage over their rivals, and allow the business to profit. If the company has a bespoke solution that they have funded to be produced they will then own the rights and keep the advantage over their rivals.

Unfortunately producing a bespoke solution can be very costly and be impossible to justify the huge costs to fund. While it may exactly meet their needs

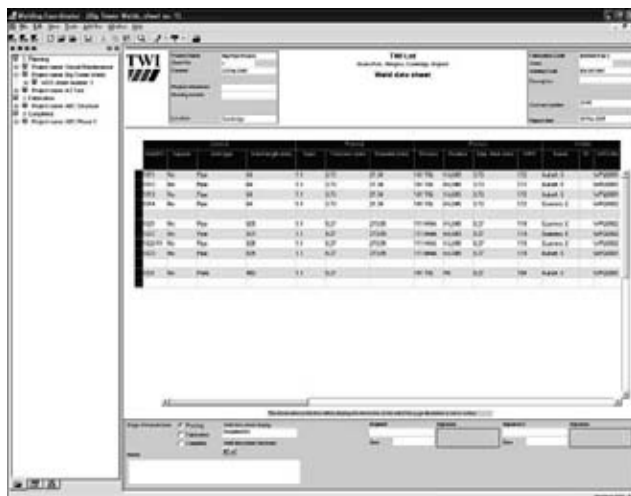


Figure 1. Welding Coordinator™ software

a cheaper solution may not meet their exact specifications but offer enough functionality to be chosen as the most appropriate solution. A major drawback of a bespoke solution could be that as a business changes and the ways they work, a bespoke solution if incorrectly engineered could be too tightly coupled to the old ways of working that using it in the future becomes impossible. This could lead to a very expensive development becoming redundant and a wasted investment.

All of these present solutions have their place in the business world, however, on the largest projects with the most information that are safety critical it is very important to find the best solution possible.

#### Other technologies and software

In addition to the fabrication management solutions discussed previously, there are several other software solutions available, addressing other parts of the fabrication lifecycle.

**CrackFirst™.** The CrackFirst™ system (Figure 2) is a device for monitoring and reporting the fatigue damage that a structure has suffered. CrackFirst™ indicates the portion of the design life that's been consumed and enables engineers to estimate its remaining life, using Bluetooth to communicate wirelessly with a base station, allowing engineers to view the results. The system won the Worshipful Company of Scientific Instrument Makers Annual Achievement Award in 2005.

**Crackwise®.** Crackwise® is decision support software designed to assist engineers in evaluating the integrity of pipelines, pressure equipment and structures containing flaws. Crackwise® applies BS 7910:2005, and is the leading fitness for purpose software.

**Riskwise™.** Riskwise™ is Risk Based Inspection/Risk Based Maintenance software for process plant, boilers, tanks, pipelines, and gas turbines. Riskwise™ advises users when components are reaching the end of their design life, and need to be inspected or replaced. As well as these industry specific solutions, in this paper we are also concerned with the

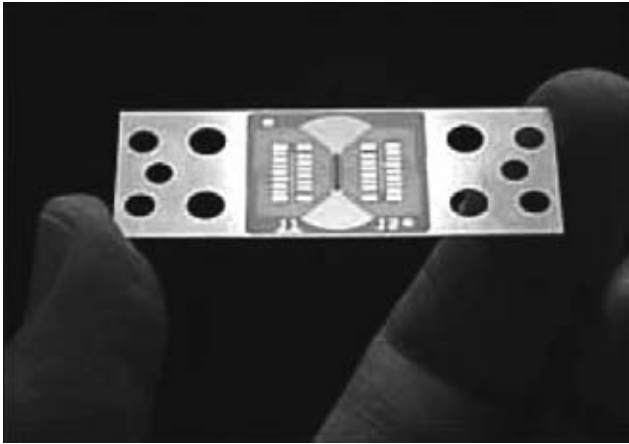


Figure 2. CrackFirst™ sensor

standardisation of mainstream computer hardware and technologies.

**Wireless technologies.** Wireless LANs (802.11b and 802.11g wireless networks) are now more reliable, easier to implement, and at a lower cost than ever. This is an important advance in communication technologies as it allows people to connect to networks and communicate with others whilst on the move. Another important wireless technology is Bluetooth – a short range wireless communication protocol. Bluetooth is now a globally accepted standard, with over 5 mln Bluetooth devices shipping every week at the end of 2005.

**Portable devices.** As wireless technologies develop, devices making use of them improve and get cheaper. Notebooks, powerful PDAs and other handheld devices make use of both Bluetooth and 802.11 wireless protocols. The continually falling costs of this hardware mean that for some companies, it is now financially viable to equip all members of staff with a mobile device, allowing communication at all times from all points on site.

#### Case study

The case study presents a purely hypothetical fabrication project, suggesting how the technologies and software discussed in this paper could be used to overcome problems faced by the construction and maintenance teams working on the project.

We will consider an oil rig, because of the safety critical nature of the structure, and the difficulties involved in construction and maintenance:

- adverse weather conditions mean a high level of maintenance is required, and make it difficult to check for damage and carry out maintenance;
- sheer size of the structure means high stress levels and a large area to maintain;
- areas that experience most stress are the most difficult to access;
- safety is a top priority as people live on the structure.

For simplicity, some of the problems involved in the fabrication lifecycle of the oil rig are broken down below, with suggested solutions from the technologies we have discussed.

*Problem:* size of the structure makes it hard to manage all of the required documentation.

*Solution:* electronic fabrication management system:

- at the most basic level a system such as Welding Coordinator™ would offer traceability of construction and maintenance of the structure;
- system could be used to trace anything from filler batch numbers used from a particular joint, through to welder qualifications and NDT reports.

*Problem:* data cannot be automatically entered into the fabrication management system.

*Solution:* wireless access points around the site allowing users to connect to the network from all locations:

- welders can update the system when they have completed a weld, the system can then automatically ask an NDT inspector to check the joint;
- PDAs could be used around the site by NDT inspectors to find the joint (using GPS) and to send NDT data back to a central location over a wireless connection;
- welding managers can monitor fabrication in real time using a laptop anywhere on site.

*Problem:* routine inspections do not flag up joints under more stress than expected.

*Solution:* CrackFirst™ on all critical joints allow engineers to view real time results but routine maintenance is also very important. RBI software such as Riskwise™ would allow engineers to schedule inspections based on the design life and calculated stress and fatigue on the components of the structure:

- while Riskwise™ is very comprehensive, it doesn't provide us with real time information on the state of joints;
- CrackFirst™ on all critical joints would allow engineers, or automatic decision support software to schedule early maintenance to a particular joint;
- using Bluetooth, CrackFirst™ systems could automatically communicate with a base station, reporting the current fatigue of a joint.

*Problem:* most critical joints are in hard to access areas.

*Solution:* CrackFirst™ and Bluetooth:

- Bluetooth enables CrackFirst™ devices to reports results from the most awkward locations;
- Bluetooth enabled handheld devices allow welders and NDT inspectors to ensure they are looking at the right joint.

## CONCLUSION

The necessity of traceability in fabrication management systems will continue to grow. From the ideas presented in the case study, we can see that technologies and software available today can be used to make a more complete fabrication management system. With the correct design, implementation and training, today's solutions could combine to provide full site wide fabrication management, with an incredibly high level of traceability and reliability.

# SENSOR AND CONTROL SYSTEM FOR METAL DEPOSITION USING ROBOTISED LASER WELDING

A.-K. CHRISTIANSSON<sup>1</sup> and P. GOUGEON<sup>2</sup>

<sup>1</sup>University West, Sweden

<sup>2</sup>Industrial Materials Institute, Canada

Metal deposition is in this paper a technique for building metal structures according to a 3D-CAD-drawing using robotised laser welding technology, and can thus be considered as a kind of free form fabrication for metal. The component structure is built-up layer by layer by using robotised welding and wire filler material. The technique has shown to be very successful when skilled welders continuously control the parameters, and the main objective of this research is automation of the process. This includes selection of a sensor system as well as development of an adequate control strategy. The proposed sensor system measures metal temperature before and after a new layer is laid on former layer in order to obtain controlled material properties. The sensor system also measures the built geometry after and before a layer is produced and acquires on-line images of the scene close to the weld pool to detect disturbances in the process. The control system takes decisions based on the sensor information and modifies the nominal wire feed, heat source power and welding speed.

There are a number of different techniques for free form fabrication (FFF) for metal, each with their own specific characteristics. Applications of these techniques are mainly rapid prototyping, rapid manufacturing and tool repairing as described in the annual Wohlers report [1]. They are sometimes named according to the process involved or to the deposition type (e.g. [2]) for a review of these techniques. Robotised fusion welding was successfully used in [3]. Cladding is the often used term when the power source is a laser beam [4], while metal deposition (MD) seems to be a more general term for any type of welding energy source.

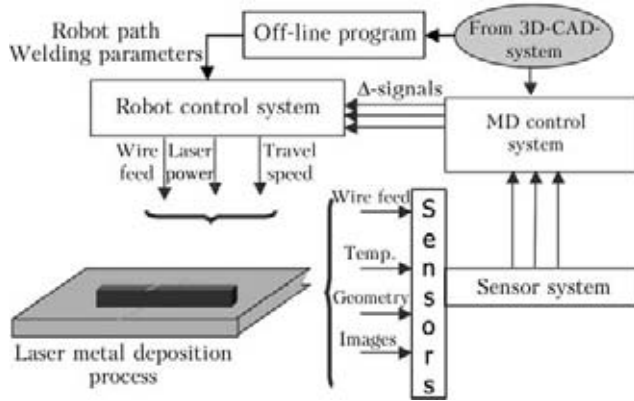
Most references found for processes building metal structures are for processes using metal powder and special nozzles for powder feeding in the melt pool [5] using a 2 kW CO<sub>2</sub>-laser. They show promising results for different metals. In [6] however wire is used motivated as in our project in order to give higher deposition rates by using a simpler feeding mechanism. A comparison of material properties resulting from powder and wire feed is made in [7] for a 1.5 kW diode laser, and for a combination of wire and powder in [8]. Directed light fabrication (DLF) and laser engineering net shape (LENSTM) were developed for powder melting in Los Alamos and Sandia laboratories and practical issues regarding these are discussed in e.g. [9]. Specific thermal issues regarding the LENS process are studied in [10]. Some projects use CNC-machines to move either the power source or the work piece. One such example is [11], which investigates a CO<sub>2</sub>-laser melting powder. This system makes use of a sensor- and feedback system for on-line change of the process parameters. Since analytical modelling of the deposition process is complicated, [12] uses fuzzy-logic control, which does not need an exact analytical model of the process. Direct metal deposition (DMD) is the name for the POM-group system

using CO<sub>2</sub>-laser and powder fed through a special designed concentric nozzle. There are some dedicated and specialised FFF-machines for metal like [13], which produces a metal 3D structure from a CAD-drawing using a controlled electron beam (EB) to melt metal powder in a closed vacuum chamber.

Rolls-Royce has successfully developed a robotised TIG welding process using metal wire. Their process is called shaped metal deposition (SMD), and it is now commercially available. This process is semi-automatically controlled by using a monitoring system that allows the operator to change parameters when necessary. The current project is inspired of the success of this SMD-process. However, to be able to obtain even higher deposition rates and less heat input into the metal a laser source replaces the TIG-source, and the process is aimed to be fully automated. This automation is the main issue for this paper which presents a joint work by University West and Volvo Aero Corporation, Sweden, and Rolls-Royce plc and KUKA Robot, UK, within the EU FP6 VITAL (EnVIronmentALLY Friendly Aero Engines) project. The power sources in the project are Nd:YAG-lasers and the material is titanium for making parts in new aero engines. The use of a laser as power source implies possible higher deposition rates and introduces less energy into the base material than in TIG welding. The spot size needs to be relatively large – compared to standard laser welding – to obtain efficient melting of the wire and also be able to use larger wire diameter. To obtain this larger spot one possibility is to work with a defocused laser. Another possibility is to adapt the optics in the laser head in order to have a larger spot size at the focal plane.

## Project background

Metal deposition is in this work a technique for building features of titanium on titanium through wire melted by an Nd:YAG-laser source. The wire is fed to the base material in the weld pool at a certain angle to the laser beam. The metal is melted and added to the base plate as beads side by side and layer by layer



Simplified overview of the proposed sensor and control system for metal deposition

with the goal to form the designed geometry. Some specific simplified features like bosses and flanges are defined in the VITAL project. The current work is aimed for automating the process for titanium features, more specifically to develop a sensor and control system so as to be able to automate the MD process. Equipment includes the laser power source, an industrial robot, sensors and control system(s). Parameters to be measured during the process have to be measured using non-contact type sensors to give robustness and flexibility to the control, meaning sensors will mainly be optical ones. The MD has to be made in a controlled atmosphere to avoid oxidation, and for this a chamber was built that is filled with argon gas around atmospheric pressure.

Prior to the deposition process can start an off-line program (OLP) must be made for the specific 3D-CAD-geometry to build. This OLP gives nominal data for the process parameters, however out of the scope for this paper.

The sensor and control system will be built as modular as possible to allow for different types of robots, laser sources, different geometries and sizes, etc. It can also easily be modified for different situations and be easily expandable. It is worth noting that some machining might be needed to obtain the final geometrical finish.

The paper discusses the need for sensors and control strategies to obtain a fully automated process and avoid the need for continuous monitoring and actions by an operator. This means that the task for the control system is to introduce modifications to the nominal OLP-parameters so as to meet up for disturbances or unforeseen process behaviour. The target for the project is to produce add-ons on metal parts to be used in aero engines, which is why demands are high and the process needs to be verified. It is not allowed to modify process parameters in this kind of applications outside a specific range, which is why it is important to have full traceability of the changes made by the control system.

**Limitations.** In the initial stage of the project, the size of the features is initially limited to some 10 cm in all dimensions and simple geometries are considered. The CAD-geometry is assumed to be pre-processed using OLP into a robot-path and initial

nominal weld parameters. As a starting point the robot is assumed to be well calibrated and able to exactly follow the programmed path. The paper does not consider other possible interesting applications for the process such as modifications of existing products, tool repair, etc.

#### Sensor system: an overview

The sensor system consists of three main parts (described in subsections below and illustrated in Figure: sensors for off-line measurements to give a general view of the process during operation and for development and evaluation of trials; sensors for on-line measurements for control (the main part of the work); a computerised measurement system to analyse and store data (the measurement system shall communicate with the control systems for robot movement, for wire feed and for laser power).

**Sensors for off-line measurements.** The sensors for off-line measurements are not central for the control system, but of utmost interest to obtain controlled conditions for the process. This in turn is needed to be able to rely on the feedback control.

It is strongly recommended to analyse the laser beam quality on a regular basis to avoid disturbances due to varying beam quality, however not on-line. The spot size where the wire is introduced needs to be constant and to have uniform energy distribution.

Since the process must be performed in a controlled atmosphere and with laser safety regulations there is need to monitor the overall scene. At least one CMOS-camera shall be connected to a monitor just outside the environment for the operator to monitor and to the measurement system for recording. The choice of camera depends on distances and other local constraints at either partner, but demands are not very specific which is why a standard camera could be used.

A 3D-scanning needs to be performed on the built feature from time to time during process, however with laser source switched off or with the laser beam away from the reflective surfaces, and always at the end of the process to verify that the built feature fulfils the CAD-model. This is not time critical, but possibility to automate the scanning to some extent would be helpful. It is however observed that the shiny titanium is very difficult to scan successfully without manual touch up, and it is therefore initially not intended to be automated. This measurement is outside the VITAL project.

It has been shown to be most critical to measure temperature during the process in order to control the microstructure in the built feature. For this an IR-camera has been used during initial trials. To protect the camera from the laser power and to keep the oxygen outside the controlled atmosphere a Ge-window has been mounted on the chamber wall with the camera placed outside. This camera will however not be used regularly during parts production.

**Sensors for on-line measurements.** On-line sensors are the main part of this work. The wire feed rate has shown to be most critical to control, and thus also to measure. This can be done with a contact measurement close to the feeding equipment, e.g. using a potentiome-

ter affected on the axis by the feed motor. This signal can also be obtained directly from a high quality wire feeding equipment. Depending on situations, a more precise feed rate measurement can be achieved by using the observed images of the wire tip as seen by a CMOS-camera fixed on the robot arm.

The surface temperature of the titanium part under process needs to be measured in order to maintain product quality. For this purpose a pyrometer is mounted on the robot arm to measure the temperature just before a new layer is laid and also just after. The surface temperature before deposition must not be too high, since that could imply that the whole structure collapses. It must not be too low either, since that could imply bad material properties like bad adhesion. The temperature just after deposition is an important parameter controlling the material properties. In case of too hot, the control system shall cause a pause in the deposition, and in case of too cold, the control system shall lead to a heating path without wire feed or an increase of the laser power. Within a certain temperature range this pyrometer signal shall not lead to modifying the process parameters. The pyrometer emissivity calibration needs to be taken care of, however the situation will be rather constant during the process and thus the need for recalibration is minor during deposition.

The part geometry needs to be captured by measurement and we propose to do it by using two laser lines: one projected in front of and behind the weld pool. Both laser diodes are to be placed on the robot arm in order to illuminate the part without any shadowing during the robot move. Both projected lines and the weld pool are captured by a camera equipped with a filter of the same wavelength as the laser lines, and an image processing will give as output the height of the last layer and the width of the weld pool, which correspond to the bead width. The measurement idea is similar to what is used in a triangulation seam-tracker, however the built profile is of interest here – not to follow a seam. The camera should preferably be placed in the optics at the top of the laser head viewing the scene through a beam splitter. This avoids the high power laser to enter the camera sensor and also protects the camera from the hot process.

The content of oxygen when welding titanium must be held below a certain limit to avoid oxidation. For this purpose an O<sub>2</sub>-sensor is mounted close to the weld pool.

#### Control system and database

There are mainly two levels of control system, one that is closely related to the robot and welding basic functions, and one that is supervisory taking care of the modifications of the normal robot and welding parameters, called MD-control in the Figure. The MD-control is a multivariable control system that holds both a sequence program that handles each layer correct and also a feedback control algorithm that calculates how the process parameters shall be modified based on the sensor information.

This MD-control system shall give deviation signals to the robot control system, which in turn needs to be capable of handling such modifications. The modifications are change in wire feed, change in laser power and change in travelling speed. These changes in parameters

need to be logged in a database in order to have full traceability of the process. The project uses a general measurement and data processing software – LabView – to take care of both sensor signals and control algorithms. The reason for this is to make an open architecture and take advantage of standard functions. This applies to both communications between system parts using standardised signal interface, signal conditioning, filtering, data logging, alarming, sequence program, control algorithm, etc. and eliminates the use of difficult-to-handle specialized solutions.

The process is considered to be multivariable and needs to be sequentially programmed in order to take into consideration a number of functions that need to be executed in sequence. One typical example is that the sensor information will be discarded when the program «knows» that this information is incorrect, as in sharp corners. The multivariable control considers the combined influence of all available sensor information.

#### Summary

The paper proposes a sensor- and control system to be used for automated MD using robotised laser welding of titanium wire on titanium. This system is inspired by how experienced welders work, and one important issue has been to design a modularised system that assures traceability of the result using standardised computer hard- and software. Just as experienced welders increase their knowledge with time also the control system is prepared for adding new functions when there is a need for this.

**Acknowledgment.** *This work has been performed within the EU FP6 programme VITAL, project number AIP4-CT-2004-012271.*

1. Wohlers, T. (2005) *Wohlers annual report 2005: rapid prototyping, tooling and manufacturing, state of the industry.*
2. Mazumder, J., Dutta, D., Kikuchi, N. et al. (2000) Closed loop direct metal deposition: art to part. *Optics and Lasers in Engineering*, **34**, p. 397-414.
3. Ribeiro, F., Norrish, J. (1997) Making components with controlled metal deposition. In: *Proc. of IEEE Int. Symp. on Industrial Electronics*.
4. Toyserkani, E., Corbin, S., Khajepour, A. (2004) *Laser cladding*.
5. Kai, Z., Weijun, L., Xiaofeng, S. Research on the processing experiments of laser metal deposition shaping. *Optics & Laser Technology* (in press).
6. Choi, D.-S., Lee, S.H., Shin, B.S. et al. (2001) Development of a direct metal freeform fabrication technique using CO<sub>2</sub> laser welding and milling technology. *J. Materials Proc. Technology*, **113**, p. 273-279.
7. Syed, W.U.H., Pinkerton, A.J., Li, L. (2005) A comparative study of wire feeding and powder feeding in direct diode laser deposition for rapid prototyping. In: *Applied Surface Sci. Proc. of Europ. Materials Res. Soc.*, **247**, p. 268-276.
8. Syed, W.U.H., Pinkerton, A.J., Li, L. Combining wire and coaxial powder feeding in laser direct metal deposition for rapid prototyping. *Applied Surface Sci.* (in press).
9. Lewis, G.K., Schlienger, E. (2000) Practical considerations and capabilities for laser assisted direct metal deposition. *Materials & Design*, **21**, p. 417-423.
10. Griffith, M.L., Schlienger, M.E., Harwell, L.D. et al. (1999) Understanding thermal behavior in the LENS process. *Ibid.*, **20**, p. 107-113.
11. Choi, J., Chang, Y. (2005) Characteristics of laser aided direct metal/material deposition process for tool steel. *Int. J. Machine Tools and Manufacture*, **45**, p. 597-607.
12. Hua, Y., Choi, J. (2005) Adaptive direct metal/material deposition process using a fuzzy-logic controller. *J. Laser Appl.*, **17**, p. 200-210.
13. Gibbons, G., Hansell, R. (2005) Direct tool steel injection mould inserts through the Arcam EBM free-form fabrication process. *Assembly Automation*, **25**, p. 300-305.

# VERSATILE WELDING POWER SOURCE CONTROLLER FOR RESEARCH AND PRODUCT DEVELOPMENT

D. CUIURI and J. NORRISH

University of Wollongong, Australia

The diminishing cost and increasing speed of microprocessors has made them ubiquitous in modern welding control equipment, whether it is mass produced or custom made for research purposes. Flexible, programmable controllers for gas metal arc welding research at the University of Wollongong are described. This equipment has been used to conduct both government funded research and industry funded development of specific process control algorithms for implementation onto existing commercial equipment platforms. An overview of various equipment architectures is given, with examples of embodiments that have been used over a period of nine years for various projects, including implementation of conventional power sources with accurately controlled inductance, resistance and OCV; replication of pre-existing controlled short-circuiting transfer techniques; investigation of benefits of adding fast current turnoff capability to the process; testing and development of alternative methods of controlled short-circuiting transfer; research to combine short-circuiting transfer and dynamic reversing wire feed systems; and twin wire pulsed transfer welding research.

In order to effectively conduct both basic research and process parameter development, a flexible welding power source controller is essential. The central controller should be easily programmed, and should have sufficient processing speed to meet the likely welding process control requirements.

The interfacing equipment should be capable of electrically isolating the output command signals applied to the power sources being controlled. It should also provide clean and responsive feedback signals that can be reliably used to control the process.

The associated data acquisition system is required to faithfully capture and analyse the feedback signals from the process, so that detailed analysis of the process can be made with confidence.

This paper describes how such a flexible controller has been designed and used within a variety of equipment architectures to investigate and improve a number of gas metal arc welding control techniques. The auxiliary equipment that is controlled and co-ordinated by the controller is also described.

**Description of controller.** The welding controller is based on a DSP processor board that is installed into a desktop computer (PC). The processor has a 32 bit floating point core capable of 50 MFLOPS (million floating point operations per second). Hardware on the board is configured to generate an interrupt every 40  $\mu$ s (25 kHz), and this is used as the basis for repeated execution of the various process control programs. Once initiated, this execution is independent of the host PC's operating system. Other functions, such as data transfer to the PC and auxiliary «background» calculations, are performed in the free time between servicing the process control program interrupts. The control program is programmed in C high level language. An appropriate proprietary compiler is used to produce the downloaded executable file. The availability of floating point operations

allows for fast, simple code which uses engineering units (such as Volts, Amperes and metres per minute).

The controller's function is adaptable to a range of welding processes and different equipment that may be fitted to the welding test facility. This is done by changing the control software that is executed by the processor board. Corresponding changes are made to the operator's graphical user interface (GUI) software that is executed in the host PC, so that the appropriate parameters can be modified and monitored during welding trials. Changing between control techniques is a matter of loading the relevant software package into the DSP board, and executing the associated operator interface software. The changeover time is very short, and this is extremely valuable for back-to-back comparison of competing control techniques. The simple changeover is also convenient where a number of people are using the same facilities for different projects.

Figure 1 shows the host PC, electrical interface equipment, and other equipment that is associated with the test facility.

The user interface (GUI) offers a medium through which welding parameters are transferred to the DSP controller, and also is used to display the process data and status. It is programmed in C<sup>++</sup>, and is compiled using a commonly available compiler with convenient debugging facilities. The GUI also incorporates the mechanism that selectively downloads the DSP executable and initiates the execution within the DSP board. Program download and data exchange is performed through dual port RAM, a shared area of memory that is accessed by both processors. Low level arbitration is transparently performed by the hardware. An additional level of software arbitration is incorporated into both PC and DSP programs, to ensure that consecutive transfers of data always contain fresh data. The facility for data recording is con-



tained in both DSP and GUI programs. This feature is not intended to replace the general data acquisition function, which is performed by a separate dedicated system with significantly greater storage capacity. Instead, DSP data recording is used as a fault-finding or debugging tool for process development. This software has the advantage of access to all data within the DSP controller, not just the basic external signals. By collecting, logging and analysing this data, subtle errors in the programming code can be uncovered, feedback noise and incorrect A/D conversion can be checked, and access can be gained to multiple real-time internal calculations which would otherwise be inaccessible. This has been a useful tool in the development of complex control processes. A typical interface screen is shown in Figure 2. It shows the various process parameters that are adjustable. Parameters are altered as required through pull-down menus and dialog boxes.

The flexibility of the overall system is illustrated by the examples in subsequent sections.

**Description of welding test facility.** An example of the architecture of the welding test facility is shown in Figure 3. Due to its flexibility, the «slave» equipment within the facility can vary, but the controller and interfacing equipment is relatively static. Figure 3 shows the configuration for a twin wire system, which is one of several options investigated. This application illustrates the most intensive requirement for analogue I/O.

The arc power required by the welding processes is supplied by either one or two current-controlled power sources having a high dynamic response. These can be either commercial inverter-based power sources, or custom units that have been constructed at the University of Wollongong for welding research. The mechanical feeding of the electrode (or electrodes) can be performed by a range of alternatives. For commercial single-wire processes, a commercial wire feed



Figure 1. Equipment including controller host PC (left) and interfaces (bottom)

der with external control of the feed rate can be used. For research-oriented tasks, a custom feed unit with closed-loop speed control is used. For high-current deposition with CO<sub>2</sub> shielding gas, a dynamic reversible wire feed system is available [1]. As shown in Figure 3, a dedicated twin-wire feed unit (non-reversing) is connected. The position and height of the welding torches are fixed above a moving welding table, to which the workpiece is clamped. The main advantage of this arrangement is the ease with which detailed photographic work can be carried out [2]. The travel speed of the welding table is regulated by a variable speed drive.

#### Conventional GMAW power source emulation.

One of the earliest tasks undertaken with the flexible controller was to emulate the operation of a conventional constant-voltage (CV) power source, but in a manner that enabled precise and repeatable adjustment of the electrical parameters independently of the «slave» power source that is being used in current-controlled mode. The model of an ideal CV power source is shown in Figure 4.

The controller can be programmed to produce the required output current by using the following equations:

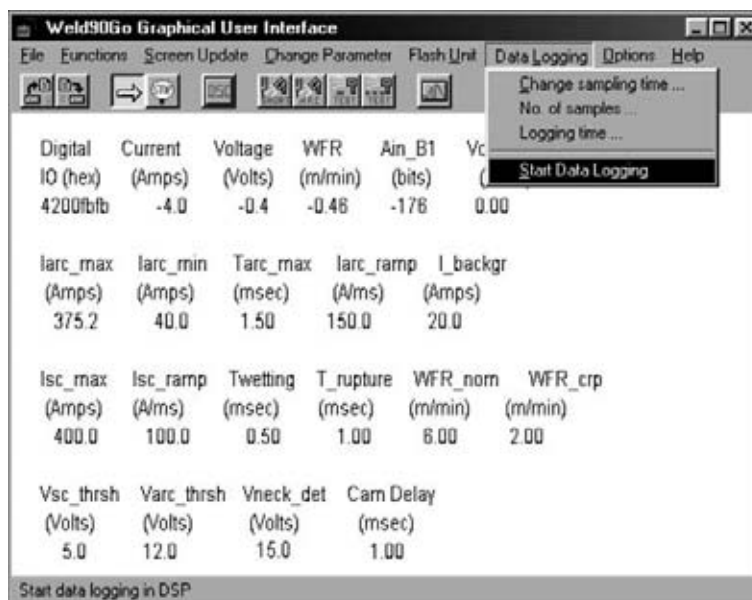


Figure 2. Typical user interface screen

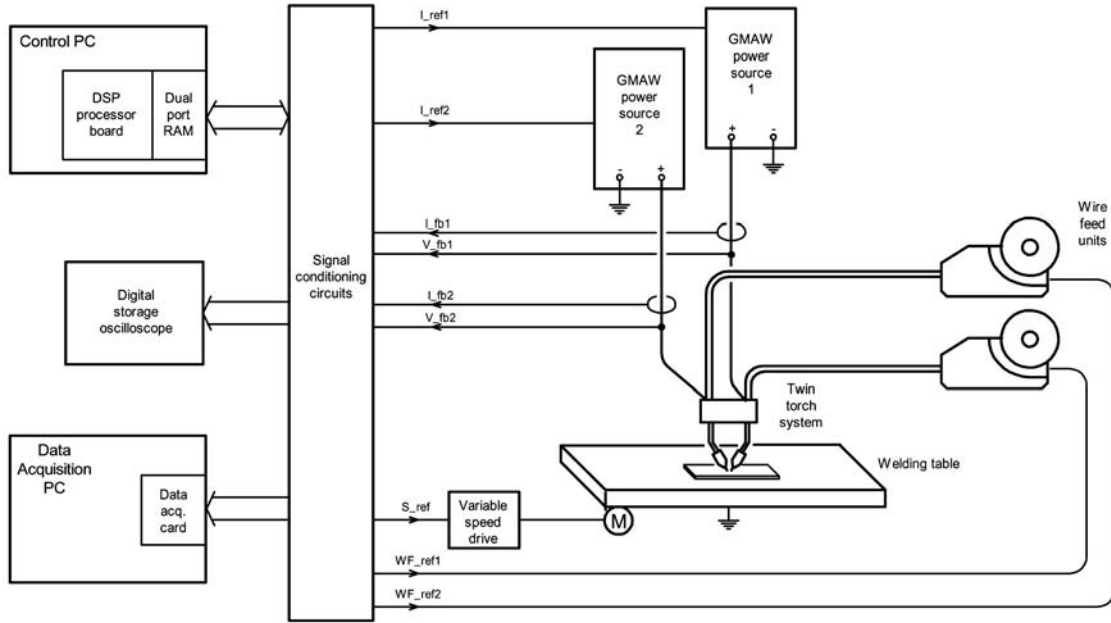


Figure 3. Test facility configuration diagram for twin-wire system

$$\Delta I = \frac{(V_{o.c} - V_{fb}) - I_{fb}R_{slope}}{L_m} T_S;$$

$$I_{next} = I_{fb} + \Delta I,$$

where  $T_S$  is the sampling and controlling period of the controller;  $\Delta I$  is the change in current for a particular period; and  $I_{next}$  is the current reference supplied to the power source for the next controlling period.

By using this approach, it is possible to emulate other output circuits of more complex design [3].

**Control of the GMAW short-circuiting transfer process.** Methods for regulating short-circuiting transfer using current control were first investigated in the late 1960s and early 1970s [4, 5]. The first major development involved control of the current waveform [5]. The process stability is remarkably improved by this method, and is attributable to the use of a controlled current waveform and the ability to rapidly turnoff the welding current just before the end of the short-circuiting period. However, stability could not be maintained for large variations in contact tip to work distance (CTWD) because the prediction of the short-circuiting event was performed by a simple voltage comparison. In the late 1980s and early 1990s, various developments allowed for much more reliable prediction of the short-circuiting rupture event [6, 7] and also allowed for an economical method of fast

current turnoff [8] using inverter-based power sources.

Detailed investigations of the current-controlled short-circuiting GMAW process have been conducted using the controller described above [9]. To simplify programming, the process control software has used a state-based programming approach. In this concept, the welding process is considered to proceed in a finite number of sequential steps or states. The current supplied to the process by the power source is regulated in different ways, depending on the state of the weld. The transition between states is determined mainly by voltage changes within the welding process, and sometimes by pre-determined time limits. As an example, for the short-circuiting GMAW process described in [7], the state diagram and corresponding current and voltage waveforms are shown in Figure 5. This approach simplifies the control of the process, and allows greater flexibility than that possible solely by programming separate voltage-current characteristic into the controller [10].

Having investigated and quantified the performance of this control method, it is then possible to devise and test a simpler method of process control that captured most of the benefits of the more elaborate method, but without the added complexity of a fast current turnoff switch and a short circuit rupture premonition circuit. This method [11] minimises spatter by limiting the short-circuiting current to low values, and allowing surface tension between the weld pool and molten droplet to perform a greater proportion of the metal transfer process. This allows the current at the point of short circuit rupture to be low, thereby reducing spatter and physical disturbance to the weld pool at the start of the arcing period. The program state diagram and typical waveforms are shown in Figure 6.

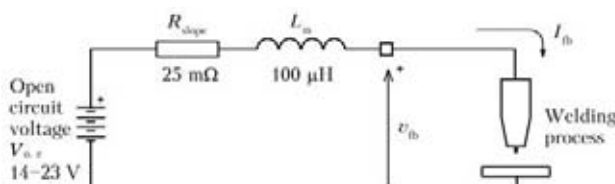


Figure 4. Model of ideal CV power source

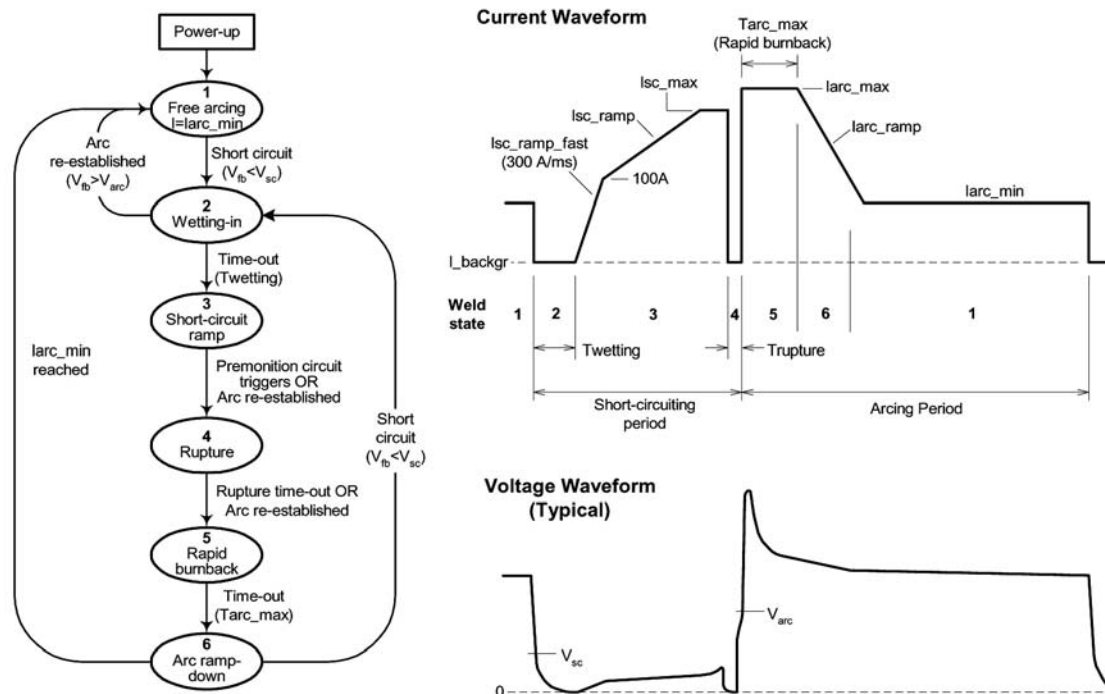


Figure 5. DSP program state diagram and typical waveforms for short circuit GMAW method 1

The straightforward implementation of this process control method to standard inverter-based power sources has made this project attractive to industry. Consequently, a significant part of the industry-funded project was devoted to establishing robust parameters for a variety of electrode types (low alloy steel, stainless steel and silicon-bronze) and argon-based shielding gases. The control method has also been patented by the industry sponsor [11]. To bring the concept closer to production, a stand-alone flexible

DSP-based controller was designed and constructed (Figure 7). This design encapsulates the control and interface functions of the laboratory system, retains the programming flexibility, and provides a more rugged package for field trial.

**Short-circuiting transfer with dynamic reversible electrode feed.** The methods of controlled short-circuiting transfer discussed in section above have focused on manipulating the current to achieve the desired process behaviour, while feeding the electrode

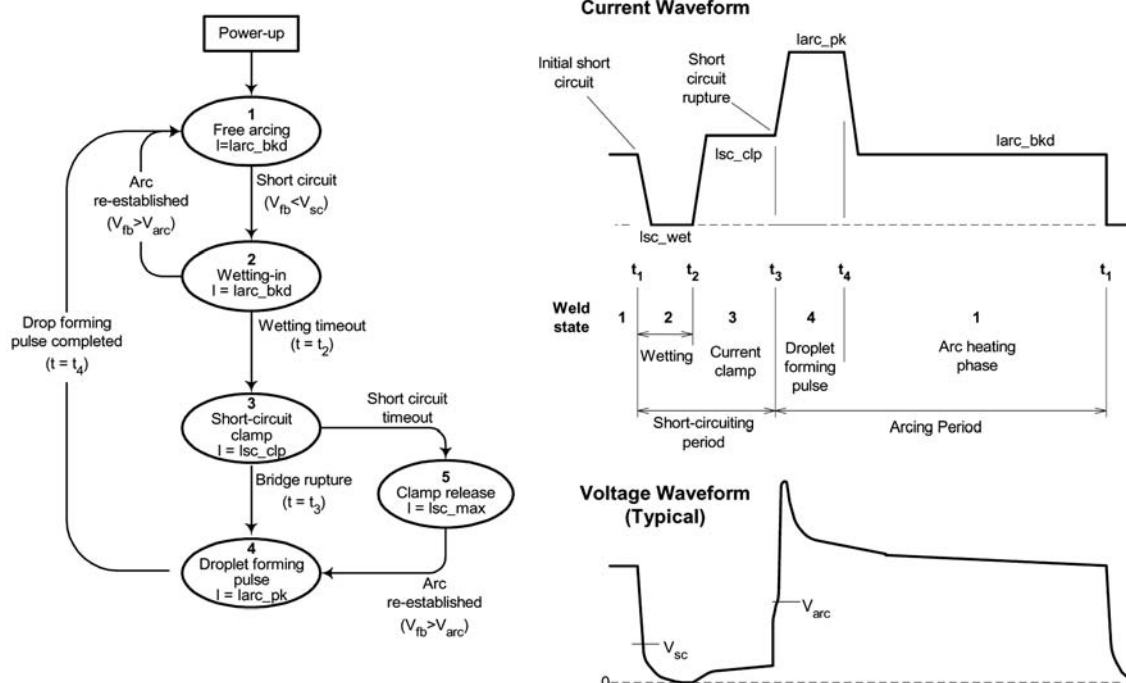


Figure 6. DSP program state diagram and typical waveforms for short circuit GMAW method 2



Figure 7. Field-trial version of flexible controller

at a constant rate. An alternative is to mechanically adjust the instantaneous electrode feed rate to improve the process, while using relatively simple power sources. Earlier attempts involved the unidirectional stepped feeding of wire [12]. This approach used step feeding to dictate the short-circuiting frequency of the process. More recently, Huisman [13] has described in detail the operation of a dynamic wire feeding system which rapidly reverses the direction of the electrode at the start of the short circuit. In this system, the dipping frequency is not enforced. Instead, the control system merely responds to the incidence of a short-circuiting event. The withdrawal of the electrode away from the weld pool guarantees that the rupture of the short circuit can successfully occur even at low currents for large electrodes, with minimal disturbance to the weld pool. Once the arc is re-established after the short circuit, the wire is fed forward at the desired feed rate. Tests in [13] were conducted at relatively low wire feed rate and constant

current (150 A) with a 1.6 mm steel electrode in Ar + 3 % CO<sub>2</sub> mixture.

At the University of Wollongong, research has been undertaken where the dynamic control of the electrode feed is combined with the advanced current waveform control [1]. The objective of this approach is to develop a means of stable metal transfer at high deposition rates with low spatter and high stability when using 100 % CO<sub>2</sub> as a shielding gas. In CO<sub>2</sub>, it is possible to reach high deposition rates (above 3 kg/h) only by using pulsed-spray transfer. However, the dissociative nature of CO<sub>2</sub> at high temperatures generates asymmetrical arc forces that destabilize the process and generate very high spatter as metal is transferred in free-flight across the arc [1].

These issues are avoided by using short-circuiting transfer, and the use of a reversing electrode feed system ensures that the short circuit reliably ruptures, even at high average wire feed rates. With a 1.2 mm electrode, average feed rates of 10 m/min to 13.5 m/min (5.3–7.1 kg/h) were achieved with very low spatter and high stability. The current waveform and wire feed profiles are shown in Figure 8. The equipment used in this research is shown in Figure 9. Because of commercial interest, the control method has been protected by patent [14].

**TWIN wire pulsed GMA welding.** With the need to increase travel speeds and deposition rates in manufacturing, the twin-wire process operated in pulsed-spray mode has been successfully adopted in many applications [15]. While single wire pulsed-spray transfer is well studied, multi-wire systems are less

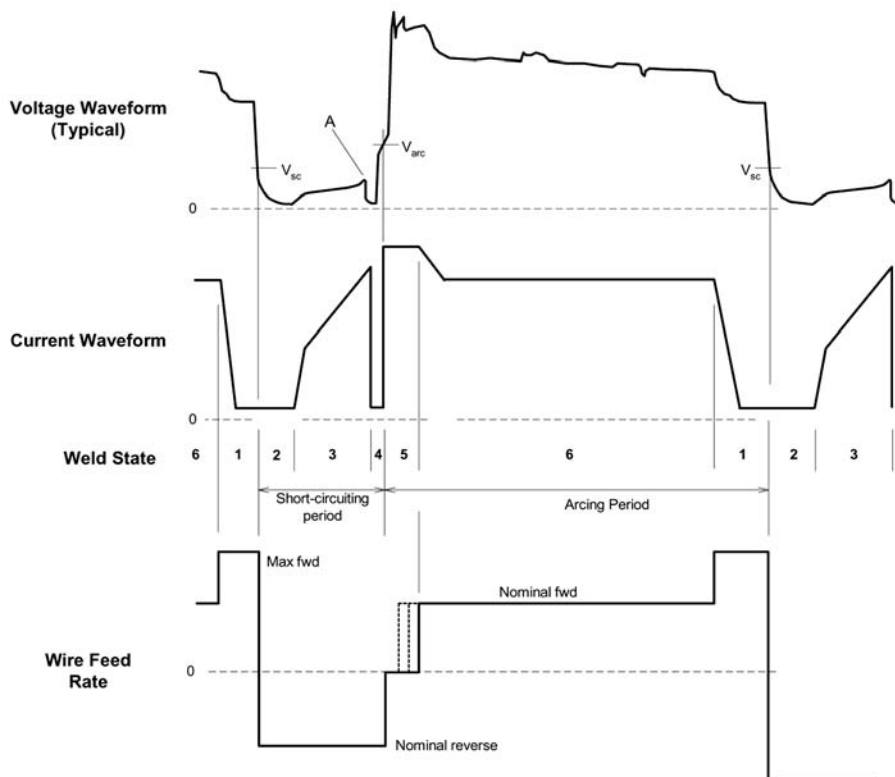


Figure 8. Typical waveforms for current, wire feed rate and welding voltage

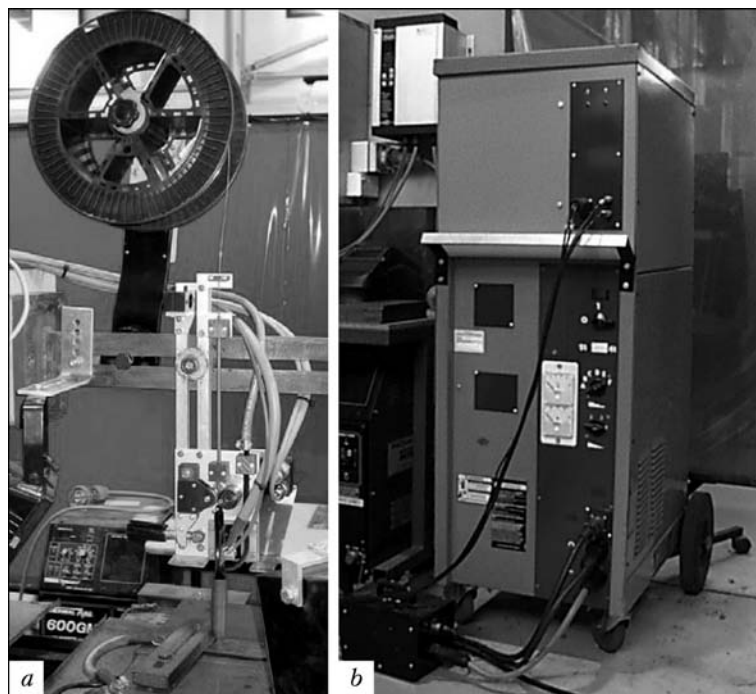


Figure 9. Reversing wire feed unit and custom power source with fast current turn-off

well known. A major hurdle to research and development is the difficulty involved in constructing the torch and electrode feed system, and the coordination of the independent power sources to avoid electromagnetic interference between the adjacent arcs.

The use of a versatile controller with sufficient I/O capability greatly simplifies this task, and lowers the entry barrier to this area of study. This allows

more time to be dedicated to the control software, which presents its own unique problems when two electrodes are involved.

Magnetic interaction between the arcs is minimised by introducing a preset time delay between the pulsing period of the two electrodes. This requires the pulsing frequency for both electrodes to be the same. Independent arc length control for each elect-

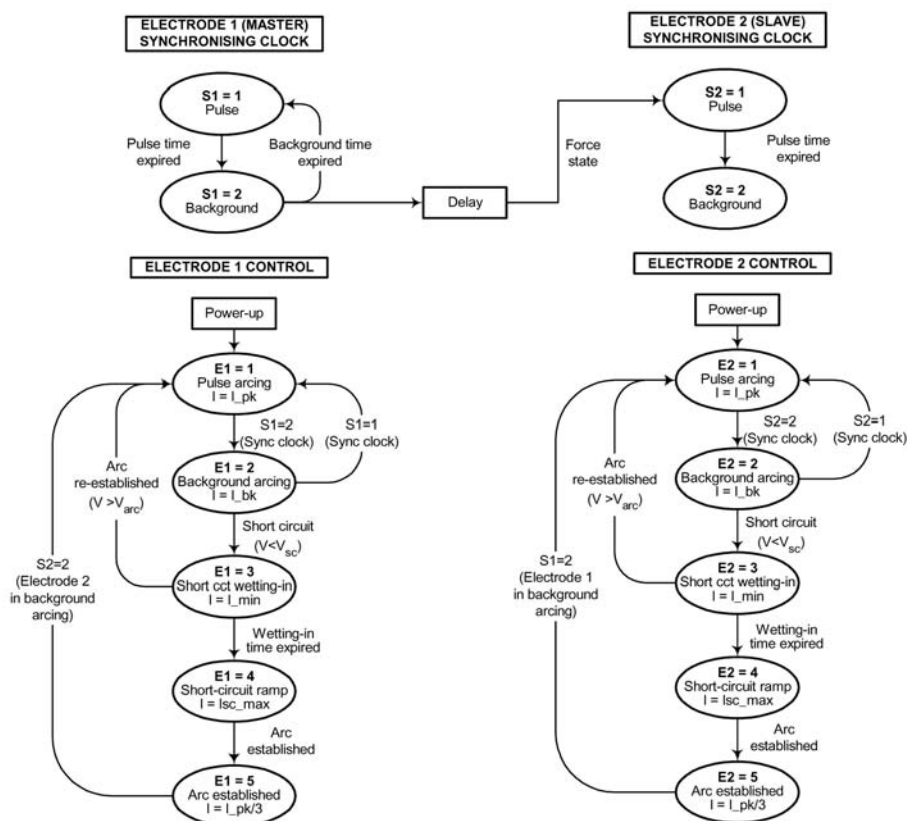


Figure 10. Program state diagram for twin-wire GMAW

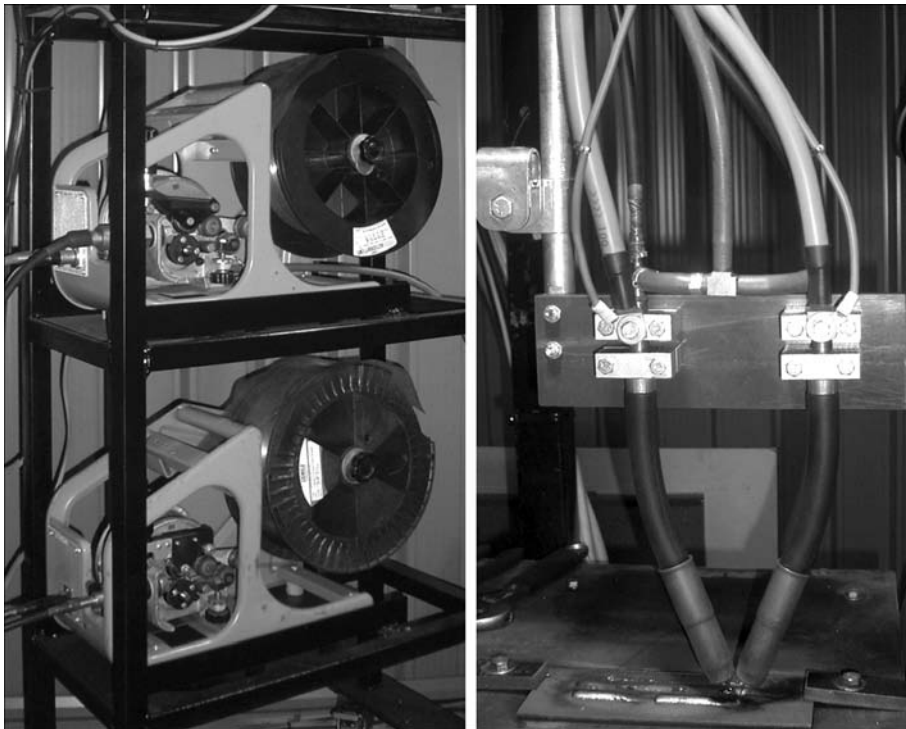


Figure 11. Twin-wire feed units and experimental torch

rode must therefore be performed through adjustment of the background current, rather than adjustment of the background time [16]. With this approach, control of the twin-wire system is relatively straightforward, provided that both electrodes operate in open-arc conditions.

However, complications arise where one electrode is in short circuit while the other is in open-arc mode. This situation can occur either at the start of the weld, or during the weld if there is a step reduction in CTWD. In either case, the control scheme must place priority on not disturbing the open-arc electrode that

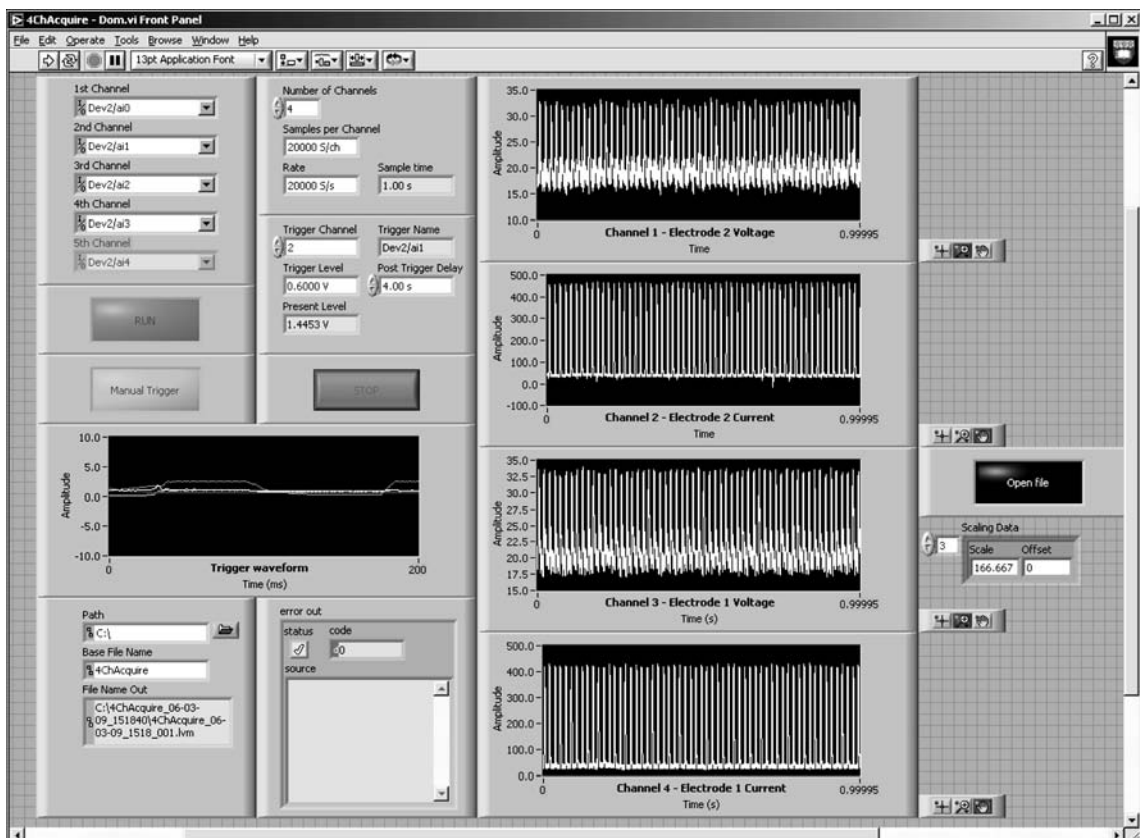


Figure 12. Typical data acquisition control panel for twin-wire GMAW

is operating in a stable condition. To avoid disturbance, the large current pulse that is usually applied to the short-circuiting electrode as a rupture occurs is delayed if the open-arc electrode is in the pulsing period. Once the pulsing period of the open-arc electrode expires, a current pulse is applied to the electrode that is emerging from the short circuit, to increase the arc length and establish a stable open-arc condition.

This control technique produces rapid and reliable arc starting, and recovers well from disturbances during the welding process. Figure 10 shows the program state diagram for this method, and Figure 11 shows the wire feed units and twin-wire torch that have been used in preliminary trials.

**Data acquisition facilities.** A data acquisition system with suitable sampling rate and memory depth is necessary for evaluation and comparison of welding conditions, irrespective of the welding process being investigated. The system that is currently being used is based on a low-cost PC-based acquisition card with eight 16-bit analogue input channels and a maximum sampling rate of 200 kS/s for all channels. For the twin-wire process, four channels are being sampled at 20 kS/s over 10 s for most welding trials. The sampled data is streamed to disk, so the memory depth is ultimately limited by the storage capacity of the host PC.

A generic acquisition software package has been written at the University of Wollongong that is readily modified by individual researchers to suit their particular application. It contains the usual facilities such as adjustment of sampling rate, data scaling, triggering level, triggering delay, and automatic file saving for repeated welding trials. Figure 12 is a typically adapted operator panel from this software.

## CONCLUSION

A programmable welding controller has been designed and used for research and development of GMAW processes. The flexibility of the facility is gained from the modularity of the hardware and also from the extensive software control and monitoring of almost all aspects of its operation. The development and

application of control algorithms can be easily implemented. The performance of the process can be readily evaluated due to the comprehensive monitoring capabilities. These features make the versatile controller and associated test facility an indispensable tool for welding research.

1. Cuiuri, D., Norrish, J., Cook, C. (2001) New approach to controlling unstable gas metal arc welding. In: *Proc. of WTIA 49th Annual Conf.* (Adelaide, Australia, Oct. 8–10, 2001).
2. Cuiuri, D., Norrish, J., Cook, C. (2002) A flexible computer-controlled experimental power source for welding research. In: *Proc. of 12th Int. TWI Conf. on Computer Technology in Welding and Manufacturing* (Sydney, Australia, Aug. 26–30, 2002).
3. Aberg, P. (1992) Computerised power sources make optimised welding characteristics more easily accessible. *Svetsaren*, 46(1).
4. Smith, A.A. (1966) Features of short-circuiting CO<sub>2</sub> arc welding with a duplex power source. *British Welding J.*, April, p. 215–223.
5. Boughton, P., MacGregor, G.J. (1974) Control of short circuiting in MIG welding. *Welding Res. Int.*, 4(2), p. 31–53.
6. Ogasawara, T., Maruyama, T., Saito, T. et al. (1987) A power source of gas shielded arc welding with new current waveforms. *Welding J.*, 66(3), p. 57–63.
7. Stava, E.K. (1993) A new, low-spatter arc welding machine. *Ibid.*, 72(1), p. 25–29.
8. Nakanishi, S., Nakajima, Y., Kawano, H. et al. *Method and device for controlling welding power supply to avoid spattering of the weld material*. US Patent 4,544,826.
9. Cuiuri, D. (2000) *Control of the short circuit gas metal arc welding process using instantaneous current regulation*. PhD Diss. UOW.
10. Ou, Z., Wuang, Y., Ushio, M. et al. (1999) New concept for the characteristic of an arc welding power source. Report II: New development of arc control system for CO<sub>2</sub> welding. *Transact. of JWRI*, 28(1), p. 5–8.
11. Norrish, J., Cook, C., Cuiuri, D. et al. *Welding control system*. US Patent 6,512,200.
12. Jingzhong, W., Ddojun, C., Xintao, W. et al. (1984) Study on the dynamic process of half-cycle pulsed wire feeding CO<sub>2</sub> welding. In: *Proc. of Int. Conf. on Quality and Reliability in Welding* (Hangzhou, China, Sept. 6–8, 1984), p. XVII 1-1–1-6.
13. Huismann, G. (2000) Effect of the welding current on the material transfer in short circuit MIG welding. *IIW Doc.* 212-979-00.
14. Norrish, J., Cook, C., Cuiuri, D. et al. *Control method and system for metal arc welding*. PCT WO 03/101658.
15. Michie, K., Blackman, S., Ogunbiyi, T. (1999) Twin-wire GMAW: Process characteristics and applications. *Welding J.*, 78(5), p. 31–34.
16. Middleton, P., Oliveira Santos, J.F., Quintino, L. (1992) Synergic algorithms to relate wire feed rate to arcing current for conventional GMA welding. *Joining Sci.*, 1(2), p. 87–93.

# SOFTWARE-CONTROLLED TECHNOLOGIES OF ADAPTIVE WELDING

V.D. GORBACH, N.A. STESHENKOVA and R.F. PONIKAROVSKI  
Central Research Institute of Shipbuilding Technology, St.-Petersburg, Russia

In this paper the results of the work are set forth on development of experimental model of automatic welding machine provided with geometrical and technological adaptation systems. The automatic machine is intended for consumable electrode gas-shielded welding in all spatial positions of the most demanding metalworks having a large thickness. The problems arisen in the process of design, manufacture and test of the automatic welding machine are formulated and methods of their solution are determined. The advantages of software-controlled adaptive welding technologies are outlined and prospects of adaptive welding equipment improvement are evaluated.

One of the trends in growth of reliability and service life extension of metalworks is application of adaptive welding technologies with guaranteed level of high quality of welded joints independent of continuously changing welded joint geometry and welders' qualification.

The Central Research Institute of Shipbuilding Technology (CRIST), Russia, has developed automatic welding machine «Junior» provided with geometrical and technological adaptation systems. The automatic machine is intended for consumable electrode gas-shielded welding of butt joints in various spatial positions.

In the automatic welding machine a unique welding technology with the use of the «cross-hill» method developed by the CRIST has been implemented (Figure 1). The essence of this technological version consists in the weld formation in single pass over the full cross section due to complicated movement of welding head.

The adopted technology has the following advantages:

- welding can be done in all spatial positions, including of non-rotary joints with radius of curvature exceeding 2.5 m;
- insignificant angular deformations;
- possibility for welding a wide range of steel and alloy grades, including titanium-based alloys;
- single-pass welding of butt joints 10–50 mm thick;
- wider, in comparison with other welding methods, range of permissible gap sizes: the tolerance zone is 4 mm;
- no need for manipulators or rotators.

The following algorithm serves as the basis for the control system:

- radiative videosensor block with immediate advance, determined by a distance of the sensor block from welding torch, provides scanning of welded joint line;

- received numerical information is delivered to the computing module of the automatic machine control system; then the parameters of welding conditions are computed with the «cross-hill» algorithm: a number of beads laid out on the layer to provide the groove filling in coordinates are determined with regard of welding current and welding speeds ensuring the obtaining of high quality welded joint;

- information about the parameters of welding conditions is transferred by the actuating mechanism;
- welding is executed;
- parameters of welding conditions and layer coordinates are recorded in the database.

The whole cycle from reading of groove elements to correction of welding process parameters takes 0.03–0.05 s. With regard to actual welding speeds of 5–8 mm/s in welding of the «cross-hill» beads, such rate of correcting data input exceeds many times the minimum required rate.

The developed automatic welding machine consists of the following modules (Figure 2):

- welding tractor installed on a guide and provided with five drives to ensure the welding tractor and welding head linear and oscillatory transfer and across the butt and the welding wire feed;
- adaptive radiator-videosensor block to provide collection and transfer of information about the actual condition of the welded joint;
- automatic machine control systems combining in themselves two levels of control: lower level presented by a controller, control power source and the machine drives, and the upper level processing information obtained from the sensor block and correcting the welding process parameters;
- welding power source.

Optimization of welding conditions using the automatic machine with adaptive control system demands that the welding conditions satisfy the following needs:

- ensuring the highest productivity;
- correspondence of thermal cycle to technological properties of steel to be welded;
- holding of weld pool on the deposited surface.



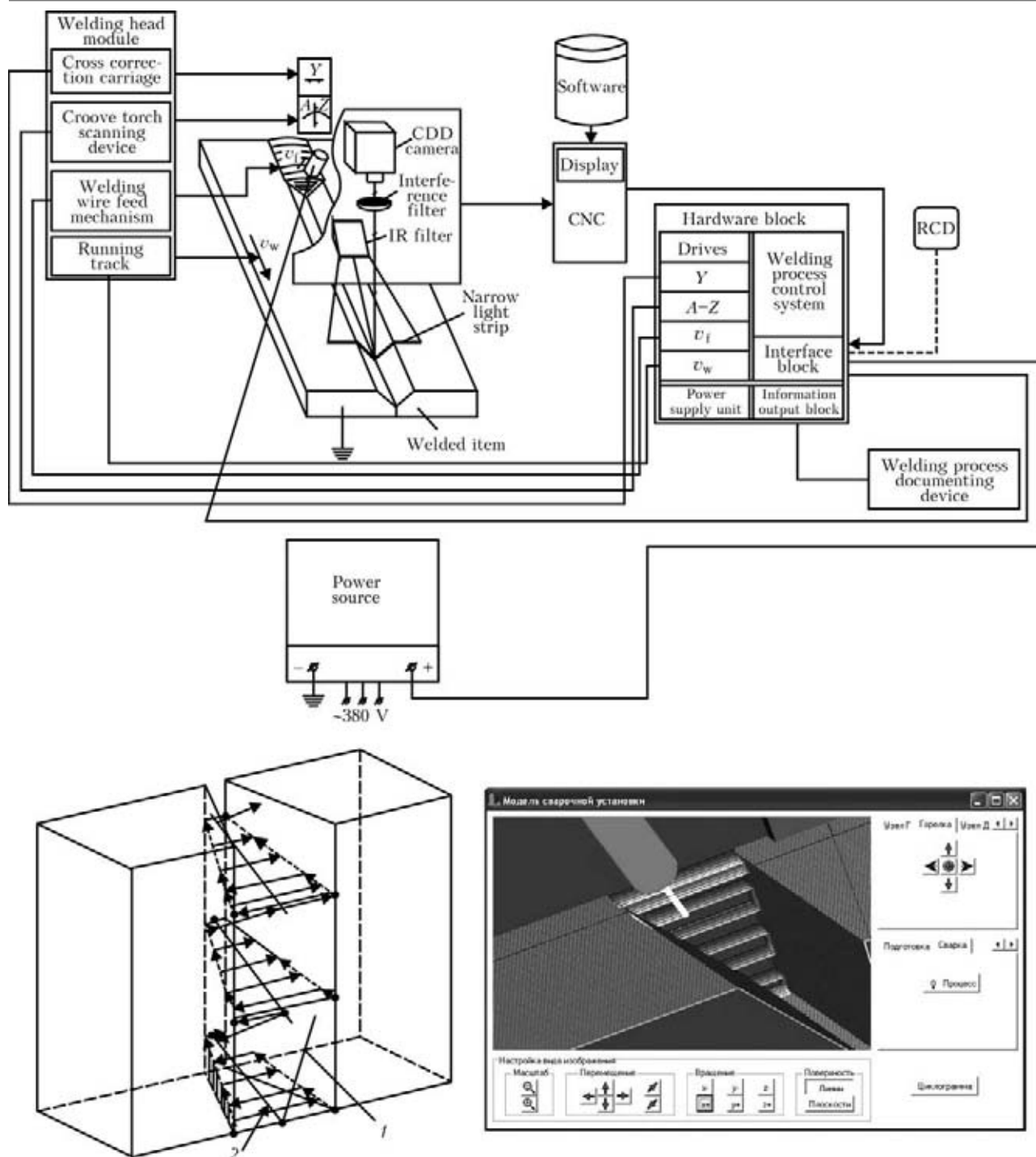


**Figure 1.** Scheme of «cross-hill» method of welding: 1 – initial position of tool prior to start of welding; 2 – bisectrix of groove angle; CNC – computer numerical control system; Y, Z,  $v_f$ ,  $v_w$  – actuating mechanism drives: cross correcting carriage (Y), torch scanning device by the depth of weld joint (Z), cross-scanning device (A); RCD – remote control desk

In order to achieve the highest productivity it will be enough to select the filler wire of maximum diameter and preset for execution by the automatic machine the maximum allowable values of current and voltage (Table).

Such conditions should be used in welding of joints when the weld pool is in the lower position and technological properties of the base metal do not require the cooling speed quotation and restriction of metal

stay time at a higher than the adjusted for this steel grade temperature.

At the weld formation by the «cross-hill» method a multiple repetition of procedure for deposition of subsequent layer on the previous one takes place (Figure 3).

Surface area of deposited layer  $F_{d,1}$ ,  $cm^2$ , is determined from formula

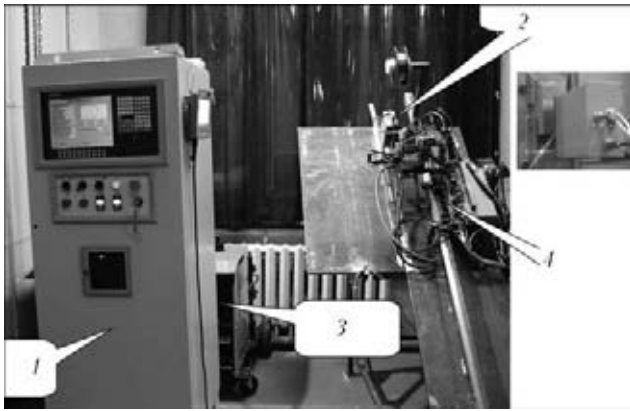


Figure 2. Adaptive automatic welding machine «Junior»: 1 – control system; 2 – sensor block; 3 – power source; 4 – welding tractor

$$F_{d,1} = \frac{S(b + S \operatorname{tg} \alpha)}{\cos \beta}, \quad (1)$$

where  $S$  is the plate thickness, cm;  $\delta$  is the deposited layer thickness, cm;  $\alpha$  is the groove bevel angle, deg;  $\beta$  is the «vertical hill» inclination, deg;  $b$  is the root gap, cm.

The weld formation by the «cross-hill» method demands the use of such welding condition, which provides the weld pool holding on the inclined plane. Choice of the condition for deposition of the first layer does not involve difficulties. This is possible to perform in experimental way on the basis of data of the Table. However, the deposition of subsequent layers will be executed over the surface having a residual temperature  $T_{res}$

$$T_{res} = T_0 + \Delta T, \quad (2)$$

where  $T_0$  is the reference temperature, °C;  $\Delta T$  is the temperature of layer at the moment of starting the second layer deposition, °C.

At the deposition of subsequent layers the residual temperature  $T_{res n}$  will be increased, i.e. an effect of automatic heating will take place:

Range of acceptability of welding current and arc voltage

Filler wire diameter, mm	Type of wire	Type of base metal			
		Carbon steels		Low-alloy steels	
		$I_w^{DCRP}, A$	$U_a, V$	$I_w^{DCRP}, A$	$U_a, V$
1.0	Solid	80–300	18–32	80–280	18–28
1.2		120–380	18–34	120–350	20–33
1.4		150–420	22–36	–	–
1.2	Flux-cored	110–300	21–32	110–300	21–32
1.4		130–320	22–32	130–320	22–32
1.6		150–380	24–32	150–360	24–34

$$T_{res n} = T_0 + \sum_{i=1}^n \Delta T_i. \quad (3)$$

In consequence of heat accumulation in the surface layer one should expect a growth of welding pool volume and deterioration of conditions for the pool holding on the inclined plane. As a result of action of automatic heating on the vertical weld formation, an increase in angle  $\beta$  will be provided. This, in its turn, will cause a change in weld geometry (shape): as it is shown in Figure 4, increase in weld height  $h$  will occur.

For estimation of this process intensity it will be of interest to determine the dynamics of temperature rise in automatic heating under various conditions of the deposited layer formation.

Computation methods of defining the temperature in the welded joint points, being used in engineering practice, are not applicable for this welding method, as they all are built-up for some different conditions of heat input and distribution.

For estimation of heat distribution in welding process using the «cross-hill» method we shall consider the action of instantaneous heat source over the surface of semi-infinite body.

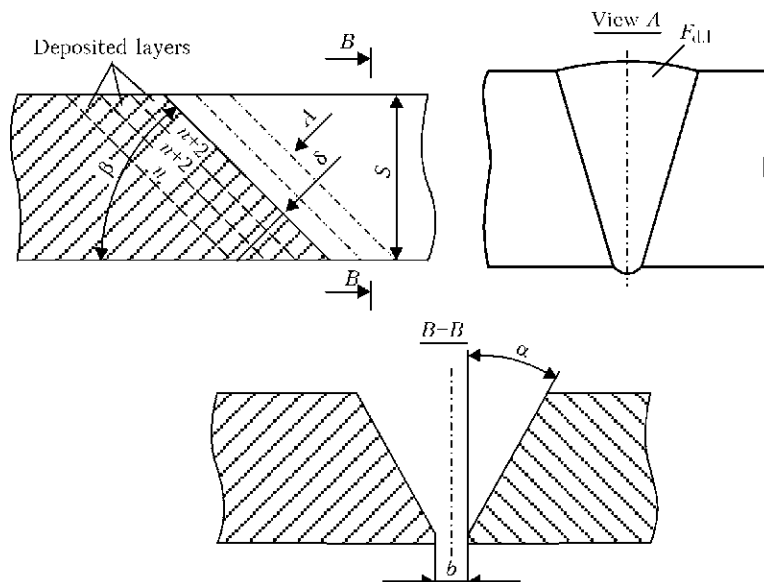


Figure 3. Deposited layers as weld composition parts formed by the «cross-hill» method (for designations see the text)

Assume that per unit of the end surface of  $S$  in thick plates to be welded with instantaneous source, the amount of heat  $Q$  is input, which is determined from the equation

$$Q = \theta \delta, \quad (4)$$

where  $\theta = 9000 \text{ cal/cm}^3$  [1] is the heat content of  $1 \text{ cm}^3$  of weld metal corresponding to the used type of welding;  $\delta = 0.1\text{--}0.3 \text{ cm}$  [2] is the deposited layer thickness, cm.

At the moment of heat input a temperature in a zone of instantaneous source action is  $T_{\text{melt}}$ . The input heat is distributed in semi-infinite body according to the Fourier differential equation having a solution towards the temperature for  $t$  time of the body selected points with coordinates  $X, Y, Z$  of the following type:

$$T = \frac{2Q}{c\rho(4\pi at)^{3/2}} e^{-\frac{R^2}{4at}}, \quad (5)$$

where  $R = \sqrt{X^2 + Y^2 + Z^2}$  is the distance between the point to be considered and the heat input spot;  $Q$  is the amount of heat derived from formula (4),  $\text{J/cm}^2$ ;  $c$  is the specific heat,  $\text{J}/(\text{kg}\cdot\text{K})$ ;  $a$  is the heat conduction coefficient,  $\text{W}/(\text{m}\cdot\text{K})$ ;  $t$  is the time from the moment of heat input, s.

The temperature field from the instantaneous heat source as some time  $t$  passes from the moment of heat input is shown in Figure 5.

Formula (5) is true in the case of semi-infinite body, in practice we have dealings with plates of restricted thickness, i.e. the body is infinite in merely one of the directions. Assume that these limits are adiabatic. Then, the temperature of this limit must be twice higher than the temperature calculated from formula (5). We assume also that there is no heat exchange of welded joint with the environment. These assumptions give an error, which reduce the degree of risk when taking the decision. The error value is insignificant as the heat transfer in the environment at temperatures below  $300 \text{ }^\circ\text{C}$  is less than 2% [3].

For the zone of beginning the welding  $X = Y = Z = R = 0$ . Thus, an increment of weld surface temperature in the zone of beginning the next layer deposition is

$$\Delta T = \frac{4Q}{c\rho(4\pi at)^{3/2}} = \frac{\theta \delta}{2c\rho(\pi at)^{3/2}}. \quad (6)$$

The time for one deposition of the «cross-hill» layer is defined by deposit mass and actual welding current:

$$t = \frac{3600M}{\alpha_s I_w}, \quad (7)$$

where  $M$  is the mass of deposited layer metal, g;  $I_w$  is the welding current, A;  $\alpha_s$  is the deposition factor,  $\text{g}/(\text{A}\cdot\text{h})$ .

The temperature calculation has been made for automatic heating of the next layer of the «cross-hill»

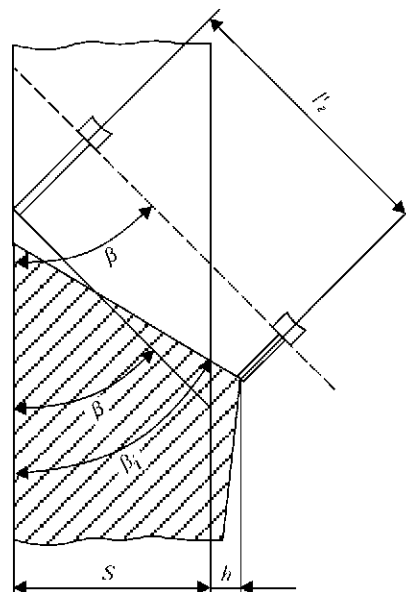


**Figure 4.** Variations in the weld formation at increase in weld pool fluidity as a result of automatic heating:  $\beta$  — angle between back surface of parts and welding tool movement trajectory plane;  $\beta_1$  — angle between actual surface of deposited layer and back surface of parts;  $h$  — weld height;  $l_2 = S/\cos \beta$  — range of welding tool movement along the plane of its movement trajectory

for specimens with a thickness of 20, 30 and 40 mm in welding of 20 layers with the use of experimental data obtained during technological trials of automatic welding machine «Junior». The calculations have been provided for layers of the «hill» 1, 2 and 3 mm height. In this case the welding current values allow performing the «cross-hill» welding, have been selected on the basis of experimental data.

The analysis of received data (Figure 6) shows that the minimum temperature of automatic heating will take place using the welding conditions corresponding to the minimum welding current and maximum thickness of deposited layer. For accepted values of welding current, when carrying out the analysis, an interval of allowable welding speeds amounts to 0.3–1.2 cm/s.

The relationship between the intensity of automatic heating process and welding tool movement

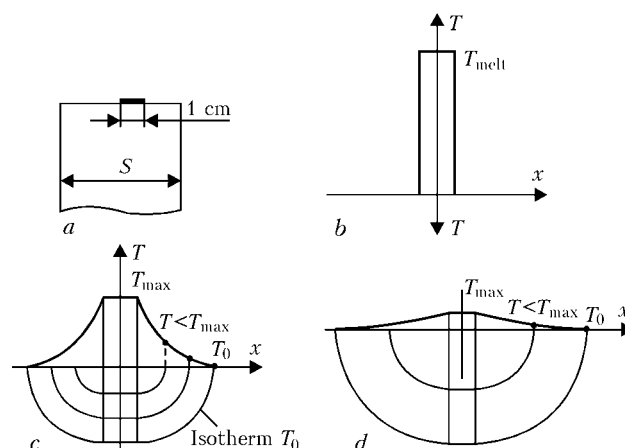


**Figure 5.** Heat distribution in semi-infinite body (a) at  $t = 0$  (b),  $t = t_1$  (c) and  $t = t_2 > t_1$  (d)

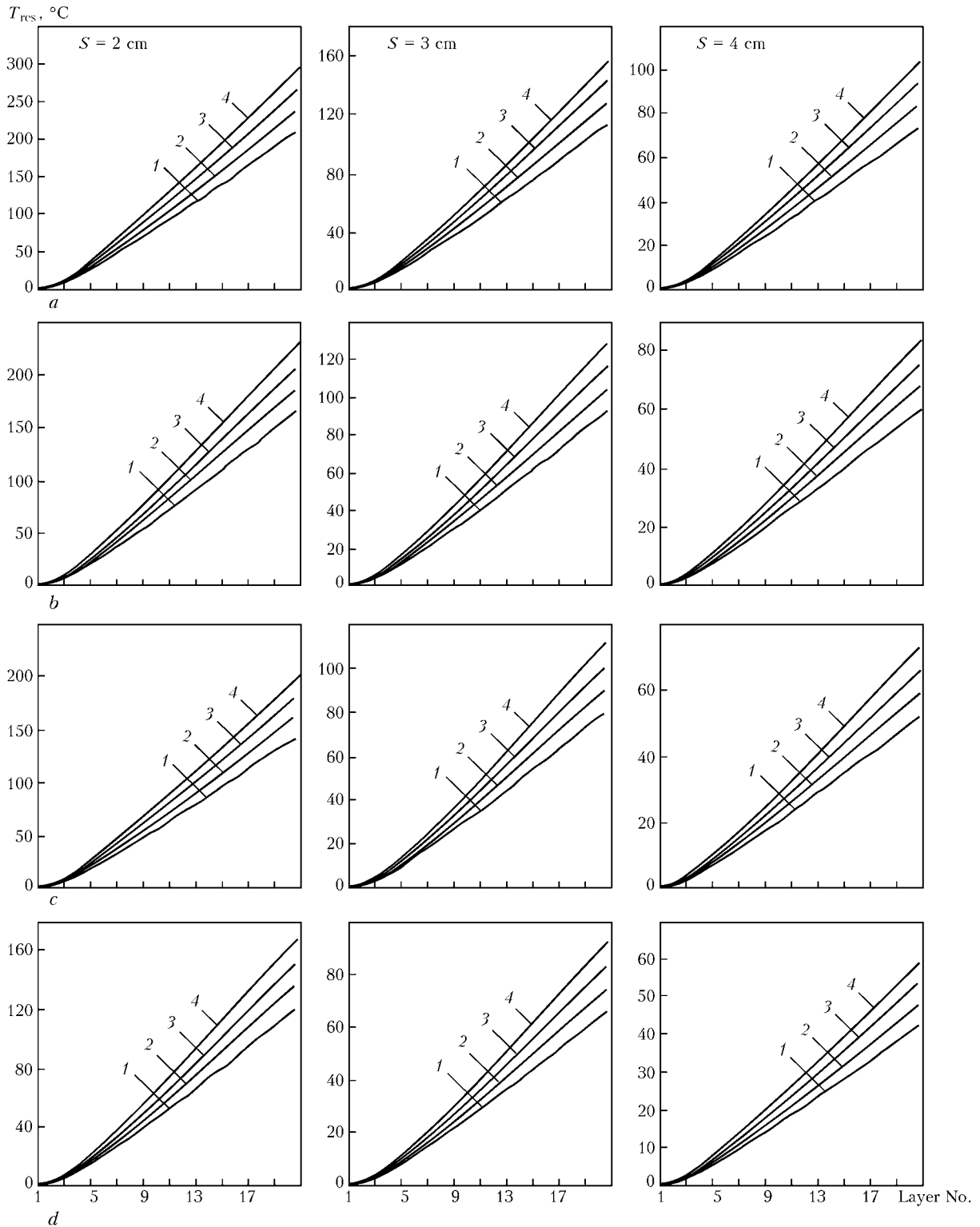


**Figure 6.** Relationship between automatic heating temperature and numbers of deposited layers 0.1 (a), 0.15 (b), 0.2 (c) and 0.3 cm (d) thick at  $I_w = 120$  (1), 130 (2), 140 (3) and 150 (4) A and different plate thickness  $S$

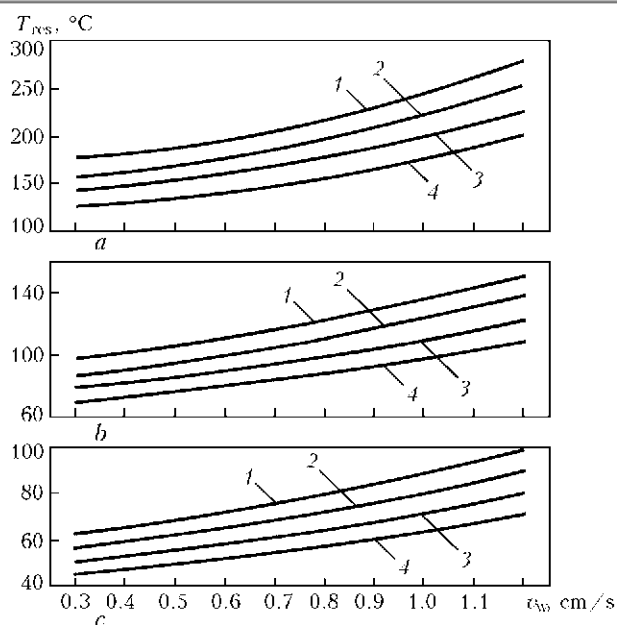


**Figure 7.** Relationship between temperature of automatic heating and welding speed in deposition of the 20th layer at  $I_w = 150$  (1), 140 (2), 130 (3) and 120 (4) A for  $S = 20$  (a), 30 (b) and 40 (c) mm

speed has been analyzed for the interval of welding speed values from 0.3 to 1.2 cm/s and is presented in schedules (Figure 7).

Based on the results of made computations, the algorithm of welding technological process loaded in the automatic machine software, has been corrected, namely:

- from calculated values of welding current by actual groove section a minimum value is selected;
- welding torch travel speed according to the automatic heating minimization conditions should not exceed 0.8 cm/s.

Consideration of such phenomenon as automatic heating made it possible to provide the weld formation when using the «cross-hill» method with even height of weld reinforcement.

1. Kuzminov, A.S. (1974) *Welding deformations of ship structures*. Sudostroenie.
2. Petrov, G.L., Tumarev, A.S. (1977) *Theory of welding processes*. Moscow: Vysshaya Shkola.
3. Dyurgerov, N.G., Sagirov, Kh.N., Levikin, V.A. (1985) *Equipment for consumable electrode pulsed arc welding*. Moscow.

# AUTOMATIC PIPELINE WELDING SYSTEM WITH SELF-DIAGNOSTIC FUNCTION AND LASER VISION SENSOR

HYEONG-SOON MOON, YONG-BAEK KIM, JONG-JOON KIM, JONG-CHEOL KIM and MOO-RYEONG PARK  
Hyundai Industrial Research Institute, Korea

Automatic welding has been used frequently on pipeline projects. The productivity and reliability are most essential features of the automatic welding system. The mechanized GMAW process is the most widely used welding process and the carriage-and-band system is most effective welding system for pipeline laying. This application-oriented paper introduces new automatic welding equipment for pipeline construction. It is based on cutting-edge design and practical welding physics to minimize downtime. This paper also describes the control system designed and implemented for the automatic welding equipment. The system has the self-diagnostic function which facilitates maintenance and repairs, and also has the network function via which the welding task data can be transmitted and the welding process data can be monitored. The laser vision sensor was also designed for narrow welding groove in order to implement higher accuracy of seam tracking and fully automatic operation.

Automatic welding has been used frequently on offshore pipeline projects. The productivity and reliability are most essential features of the automatic welding system. It has been proved that the carriage-and-band system is most effective on pipeline lay barges. Currently, many pipe laying contractors rely on automatic welding by using their own proprietary equipment or renting it at a high cost.

The aim of this work is to develop a new generation automatic pipeline welding system based on cutting-edge design and practical welding physics to minimize downtime caused by weld defects and machine faults on the barges. To achieve this, the self-diagnostic function has been developed so that the system can automatically detect faults status for each control board and cable connection.

The system consists of dual torches, a mechanized carriage with five axes (four for dual torch up/down and left/right motion, one for travel motion), a guide ring, a main control unit, a wire feeder box and two welding power sources.

The developed system has various features to make a weld effectively. In addition to the self-diagnostic function, the system offers through-the-arc weld seam tracking, a laser vision sensor, a remote pendant, a remote jog and remote monitoring function. Process monitoring and job data transfer are possible using delicate software running on a Windows system via LonWorks network.

The laser vision sensor was specially designed for narrow welding groove in order to implement higher accuracy of seam tracking and fully automatic operation. Front and rear torches can be controlled individually, and weaving frequency and width can be set separately on both torches. Arc amperage is maintained in each torch within a specified range through either the arc sensor or laser vision sensor. We adopted the advanced motor control technology to move the carriage under a smooth speed profile around pipe circumference.

The mechanized carriage has been designed to have a slim, ergonomic design and less weight so that the operator can handle easily. Utilizing CAD software, a unique, patented clamping handle design was obtained.

### System configuration

For offshore pipeline installation, a number of equipment should be adequately considered such as lineup, welding, NDT and coating stations on a lay barge. Figure 1 shows a layout of automatic welding production line on a lay barge. The number of welding stations depends on the thickness of a pipe or welding speed. In pipeline welding process, two welding carriages with controllers traveling on a guide ring are necessary to weld girth welds in the 5G position simultaneously. Each welding carriage is controlled by fully computerized control system around pipe circumference.

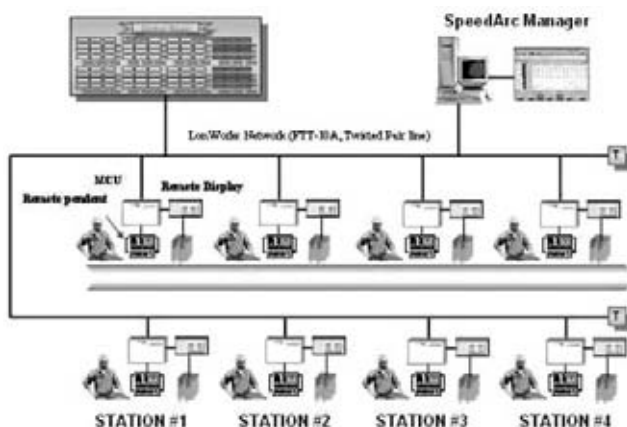


Figure 1. Layout of automatic welding production line on lay barge

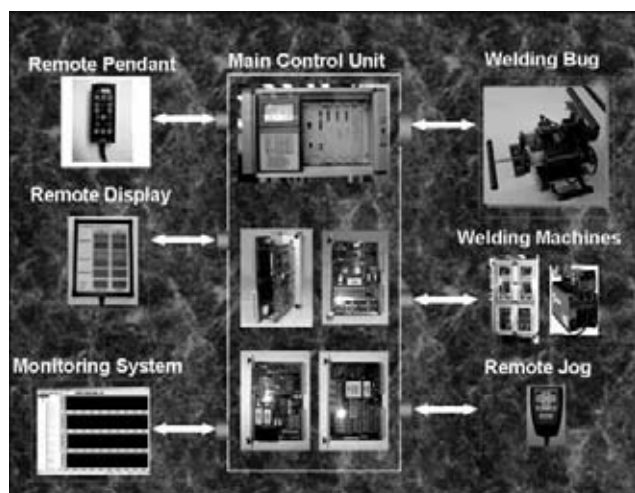


Figure 2. Block diagram of system configuration

The components of the welding system consist of mechanized carriage with dual welding torches, a guide ring, a main control units, a wire feed box and two power sources. Figure 2 shows components of the welding system.

**Automatic welding system**

The feature of the developed automatic welding system is outlined below:

Pipe size, inch .....	above 8
Travel speed, mm/min .....	0-4500
Torch distance (adjustable), mm .....	55
Oscillation speed at 2 mm oscillation width, Hz .....	5
Oscillation width, mm .....	0-50
Torch up/down stroke, mm .....	50
Welding position, deg .....	1
Torch type .....	water- or air-cooled
Carriage weight, kg .....	15

**Welding carriage.** Offshore pipe laying is achieved consecutively during 24 hours a day. So durability, reliability and easy maintenance should be considered in design of the carriage. The mechanized orbital carriage developed consists of total five axes, four axes for dual torch up/down and oscillation motion and one for travel motion. The weight of carriage is crucial point because welding helpers normally manipulate the carriage more than 400 times in a day. Figure 3 shows the picture of automatic welding carriage developed.

**Main control unit.** The main control unit has various functions as follows and is shown in Figure 4.



Figure 3. Automatic welding carriage developed



Figure 4. Main control unit

The features of main control unit can be summarized as follows:

- fully micro-processor control;
- multi-processor system;
- process monitoring, logging and saving function;
- accurate arc control;
- through-the-arc tracking;
- self-diagnosis function;
- automatic torch alignment.

The self-diagnosis function of the system monitors various faults caused by the system, and judges fault status of hardware malfunctions. So the fault diagnosis can minimize down time caused by the system problems.

**Remote pendant.** The welding operator handles a remote pendant most frequently for welding database selection and carriage operation. Therefore, the remote pendant should be designed so that the operator

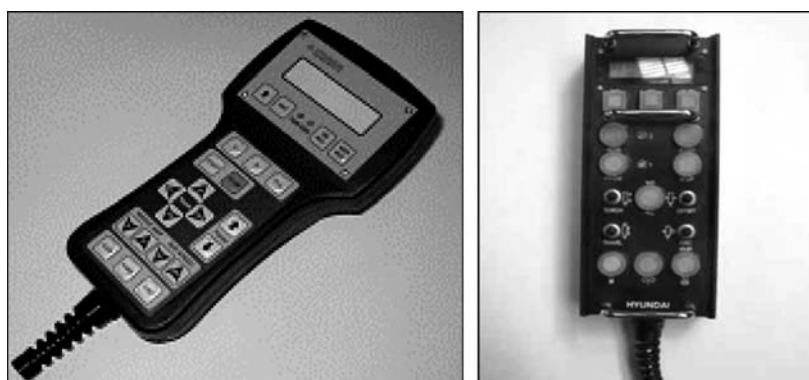


Figure 5. Types of remote pendant developed

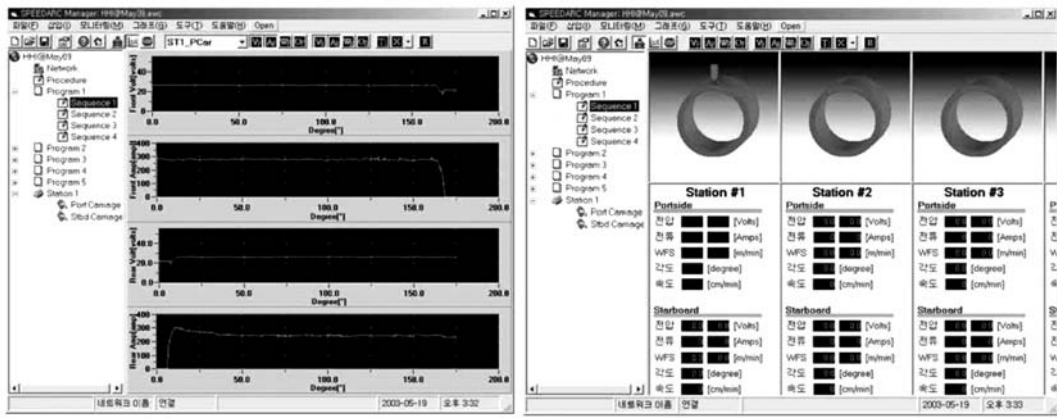


Figure 6. Remote weld and production monitoring

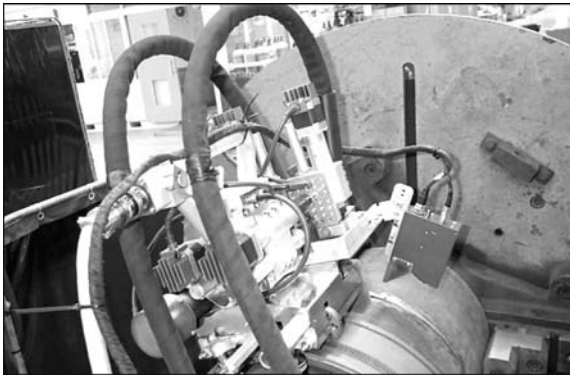


Figure 7. Laser vision sensor developed

can use very easily. Figure 5 shows the developed remote pendent.

**Network monitoring and welding database.** There are at least eight main control units and each main control unit uses different welding parameters.

All main control units developed can be connected each other via local operating network or Ethernet. Remote monitoring software (SpeedArc Manager) has functions such as welding database management, remote weld monitoring and remote fault diagnosis function. The SpeedArc is a user-friendly application applying a graphical user interface. It allows fast development of welding procedure. It manages welding database and allows easy management of weld passes and conditions according to carriage angle. Figure 6 shows some sample screenshot of SpeedArc software.

**Laser vision sensor.** The term «Automatic welding» has been used to describe pipeline GMAW process for over 30 years but none of the systems are actually automatic. The carriage in use is actually mechanized and requires a high degree of welder skills. The daily productivity depends on welder skills. The welder continually monitors the position of the weld tip and makes corrections to keep the weld tip center

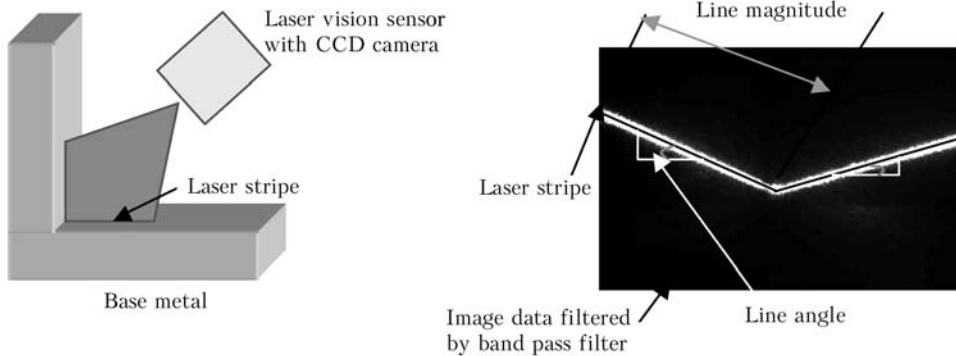


Figure 8. Extraction of line characteristics for fillet joint

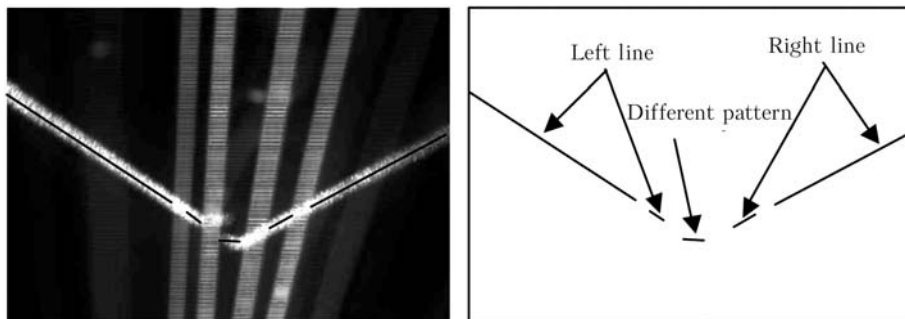


Figure 9. Result of image processing after eliminating the arc noise



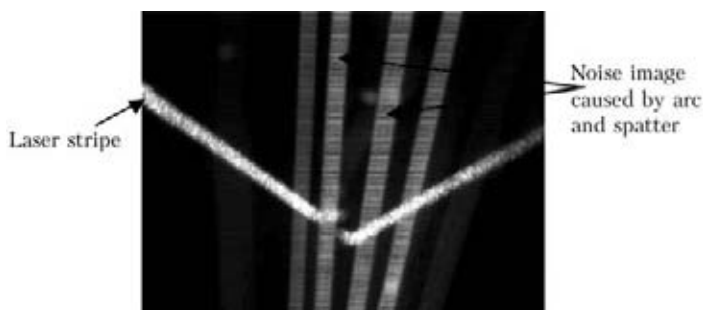


Figure 10. Captured image data with noise original image for fillet joint

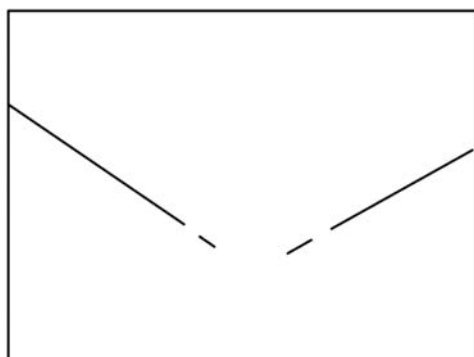


Figure 11. Reconstructed image data



Figure 12. Final result of image processing

on the welding bead. The travel speed of welding carriage is higher than that of normal GMAW carriage and highly skilled welder can operate it without any welding defect.

The laser vision sensor was specially designed for narrow welding groove in order to implement higher accuracy of seam tracking and to eliminate lack-of-fusion defects. Figure 7 shows laser vision sensor developed.

Arc spatter, sunlight or welding environment influence against image processing results because these have same wavelength of semiconductor laser used for laser vision sensor. To eliminate various kinds of noise images and detect accurate weld profiles by filtering the noise images, a new type of image processing algorithm was developed. A new pattern matching algorithm for detection of weld center position was developed based on [1]. The developed pattern matching algorithm focuses on minimization of image pro-

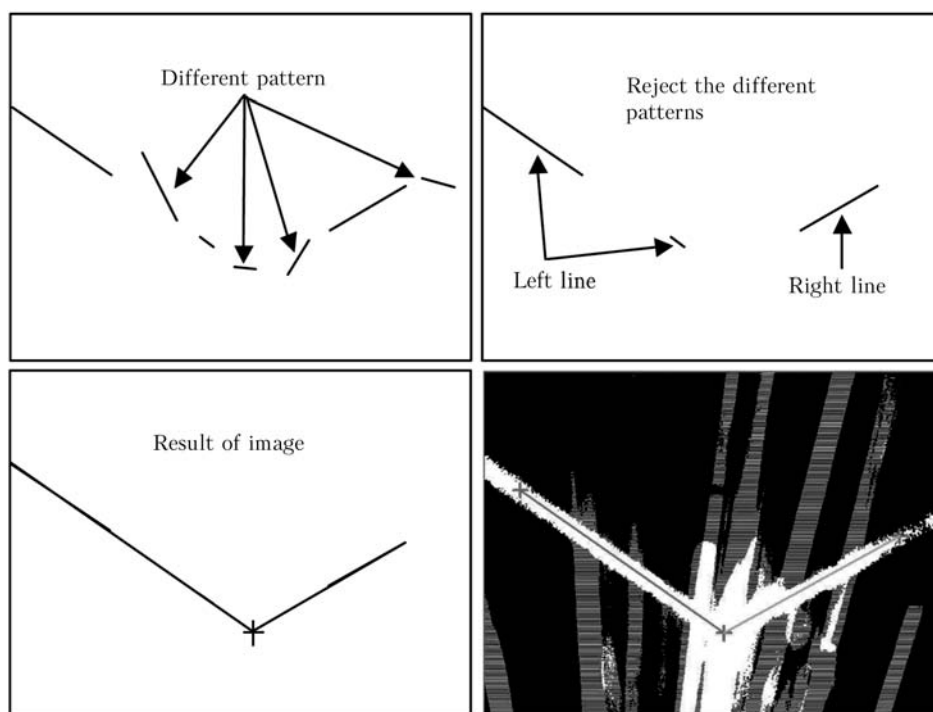


Figure 13. Example of image processing

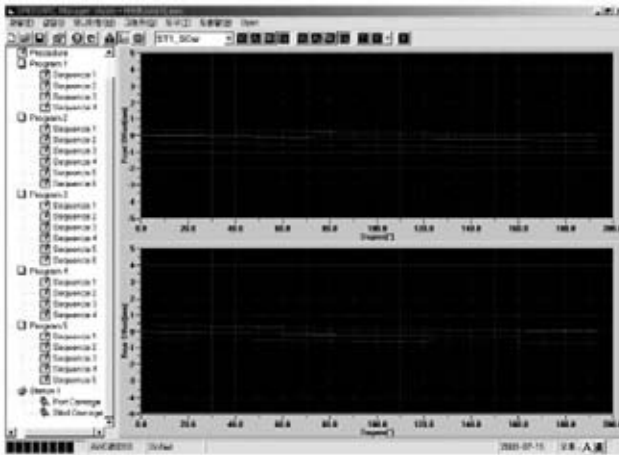


Figure 14. Result of weld seam tracking

cessing time and error caused by arc noise. The pattern matching algorithm contains the followings:

- save the original image without noise and extract line characteristics (Figure 8): line angle, line type, line magnitude;
- eliminate noise images (Figure 9) caused by open arc and surroundings from captured image (Figure 10);
- reconstruct the image data reflected from weld groove exactly to match original weld profile (Figure 11);
- examine the reconstructed image data with the line characteristics saved before welding (the new pattern matching algorithm);

- if there exists any matching point between the reconstructed image and the line characteristics, determine the weld seam position (linear regression) (Figure 12).

Figure 13 shows typical example of the proposed image processing algorithm. In this case, various type of noise are involved, however, the weld seam center is exactly detected.

The result of seam tracking is shown in Figure 14. It shows center points of front and rear torch.

## CONCLUSIONS

The automatic welding system for pipeline construction has been developed and applied for Chunxio, China, and PTT, Thailand, pipeline projects in 2004 and 2005.

The developed automatic welding system was designed to minimize downtime caused by weld defects and machine faults during production. To do this, the main control unit has self-diagnostic function and can automatically detect faults status of each control board and cable connections.

The mechanized carriage has been designed to have a slim, ergonomic design and less weight so that the welder can handle it more easily.

The laser vision sensor has been used for welding seam tracking. The GUI software for welding database management and welding state monitoring was successfully applied to actual project.

1. Pierre, S., Martin, D.L. (1989) Joint recognition and tracking for robotic arc welding. *IEEE Transact. on System, Man and Cybernetics*, 15(4), p. 714–728.

# BLENDING LEARNING FOR WELDING ENGINEERS: FIRST EXPERIENCE

S. KEITEL, C. AHRENS and A. ARYUS  
SLV Duisburg, Germany

Since 2001 nearly 500 students have taken the advantage of studying welding by distance learning courses offered through the GSI. 47 of them have participated in «Blended Learning» in DVS Welding Designer Courses. In August 2005 – after preliminary authorisation of the International Authorisation Board (IAB) – a newly developed blended learning course for International Welding Engineers (IWE) and International Welding Technologists (IWT) started in Germany. In this work our experience with this new form of learning after about one year upon the beginning of the course shall be presented. The training courses offered by the SLV have been approved by the State Central Agency for Correspondence Learning by the personnel certifying committee, DVS-PersZert, and by IAB of the International Institute of Welding. Parallel to the IWE/IWT distance learning courses, training as an International Welding Designer (IWD), an International Welding Specialist (IWS) as well as training on economic efficiency (CONTIUNUED) are being offered as a computer based training in Germany at present. Internationally, the IWE training Part 1 is being offered by the GSI and its partners in English, Italian and French.

## History of development and utilization of CBT programmes in the education on welding by the SLV Duisburg

The GSI GmbH (Gesellschaft fuer Schweisstech-nik International mbH) offers neutral expertise for individuals, crafts enterprises and industrial companies, authorities and research committees. It is a merger of high-performance welding institutes with an experience of 80 years of the individual institutes in joining, cutting and inspection technology. The objective of the GSI is the common education and consulting as well as the transfer of technology in Germany and abroad [1].

The GSI was founded in 1999 by the DVS – Deutscher Verband fuer Schweissen und Verwandte Verfahren e.V. (German Association for Welding and Related Processes) first by merging of four SLVs (Welding Institutes).

Based on their longstanding experience in welding, cutting and inspection technology, the GSI is the competent partner on the field of theoretical and practical education and training.

The development and the utilization of computer based training (CBT) programmes in welding educa-

tion have an almost 20-years tradition within the SLV Duisburg and therefore the GSI mbH.

As early as in the year 1988 a first project for an educative film of the Institute for Vocational Training (Institut fuer Berufliche Bildung) was developed by the SLV Duisburg. It was the description of the transfer of droplets through different types of arcs.

In the year 2001 the CBT programme IWE Part 1 was approved by the State Central Agency for Correspondence Learning (Zentralstelle fuer Fernunterricht – ZfU). The programme had been developed by the SLV Duisburg. In the mean time several hundreds of participants in the IWE courses (welding engineer courses) have completed part 1 as a distance learning course.

Also in 2001 the SLV Duisburg marketed the distance learning course International Welding Specialist Part 1 (CBT IWS Part 1). This development was mainly based on the experience and scope of the distance learning course CBT IWE Part 1 (Figure 1, 2). For this target group, however, the contents had been considerably reduced and presented easier to understand. In addition, the illustrations and animations had been revised and improved.

In the year 2003 the SLV Duisburg included its CBT course IWE Part 1 in English into its scope of training courses. This distance learning course has since been made use of worldwide.

In 2004 the first Blended Learning (BL) Course of the SLV Duisburg was offered, the IWD Course G1. This course consists of a CBT-part and phases of classroom learning. The build-up of the IWD Courses is shown in Figure 3.



Figure 1. Graphical user interface CBT IWE Part 1



Figure 2. Graphical user interface CBT IWS Part 1

In 2005 the GSI developed the IWE Course Part 3 (main course) as a BL Course [2].

**Blended learning in the IWE-education of the GSI mbH**

In this paragraph the build-up, concept and background of the application of BL in the international education of welding engineers will be explained. The structure of the training in the distance learning part and the classroom learning part in the SLV will be shown. The IIW IWE blended learning was developed

by the GSI mbH under the responsibility of the SLV Duisburg.

In practice, it has shown that the educational success of the participants is the same as that of the participants learning in classrooms.

**Training concept IWE Part 1.** In the year 2000 the SLV Duisburg developed a distance learning course for the IWE Part 1 which has been offered since 2001. Since part 1 comprises the so-called fundamentals, a concept particularly based on the computer (CBT) has been realised. The participants of the distance learning course receive the complete scope of the course on a CD together with the appropriate training software. The participants are guided by a tutor and have to do some homework depending on their learning progress which will be evaluated. This distance learning concept IWE Part 1 has been accepted by ZfU in Germany and nationally been authorised under No.663901.

Since the introduction of the distance learning course IWE Part 1, approximately 280 participants have been guided by the SLV Duisburg, more than 180 of which have terminated the distance learning course and officially completed it by doing an examination. The examination for part 1 can be taken at every GSI SLV in Germany.

**Training concept IWE Part 3.** The distance learning course for the IWE Part 3 has been set up as a BL concept strictly in compliance with IIW-Guideline IAB-195-2004 [3] being currently the most modern design of a distance learning course system. It is particularly suitable for training subjects having to teach a high extent of practice-related knowledge as it is the case with the education of welding engineers. BL is a combination of distance and classroom learning. In addition to a plain part of distance learning, the participants get the opportunity during their phase of classroom learning to consolidate their knowledge and to understand the practical subject matter by practical training. At the same time the periods of classroom learning guarantee the obligatory participation in the practical training required according to the IIW-guideline.

The distance learning concept of the GSI for IWE Part 3 comprises the division of the periods into distance and classroom learning. Therefore, part 3 comprises of about 150 h distance learning and of about 150 h classroom learning, plus 2 h each of a written examination at the end of each module. There are various dates for the oral final examinations offered by the SLVs concerned. The CBT-documents have been developed by the lecturers and the staff in charge from all eight GSI-SLVs and coordinated and supervised by the SLV Duisburg. The required phases of classroom learning however are exclusively offered and conducted by the SLVs in Duisburg, Halle, Hannover and Munich. Having passed the examination, the candidate will be awarded the diploma by the national board. Currently, the candidate will receive

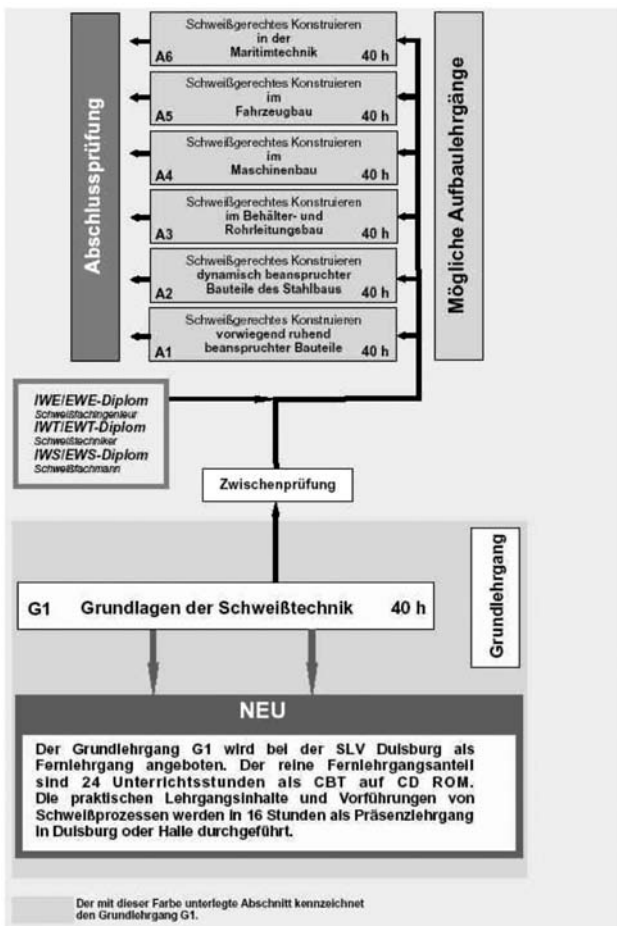


Figure 3. Build-up of the International Welding Designer Courses of the DVS (basic course G1 is offered as blended learning)

3 diplomas: one by the DVS, one by the EWF and one by the IIW.

**Distance learning material.** *CD CBT IWE Part 3.* For the part of distance learning the participant will receive a CD for CBT, a book comprising the most essential standards as well as the documents for the phases of classroom learning (Figure 4).

*Recommended course of studies, media features and options.* The CBT-material has been set up using the market leading, well-proven and approved software «Authorware» by the company Macromedia, which has been furnished with every function necessary for sequential learning. The participant will receive extensive information on the content, the recommended learning (course of studies) as well as the programme together with a description (Figure 5). Menu guidance of the software is self-explaining. The modules have been numbered according to the guideline and have been divided into individual sub-groups. Printer options, text search, notepad and bookmark options have complemented the tools necessary for organised and structured learning. The course of studies constitutes an aid for the participant to find his way through the relatively comprehensive documents. Here, he will receive the information how to structure his studies. The sequence of learning may be organised by the participant on his own complying with his own needs. It is recommended, however to follow the course of studies.

**Control of the study progress.** At the end of each teaching unit multiple choice tests for self-control and control of the study progress have been entered. The participant will have the opportunity to read again the respective teaching units and to understand the correct answers. In addition, the participant within the frame of tutorial assistance will, either upon approximately 4 weeks of commencing the correspondence learning course or upon his own request, be sent some homework provided with trial tests, in order to carry out a performance test. The completed homework shall be returned to the tutor after 2 weeks upon receipt. Within a further week it shall be controlled, evaluated and the participant will receive the result of his trial test.

**Attendance of participants.** If required the participants will have the opportunity to enter into contact with the tutors, either via phone (at standard prices), via fax, via e-mail or personally.

On the Internet Homepage of the GSI a portal will be opened where the participant can log himself into using an admission number. On this site, a forum will be installed where a fixed schedule of times will be published during which the participants may enter into contact with their co-students and the responsible tutor. In addition to this, there is an agenda with the topics and the teaching unit, particularly reviewed by the tutor. Attendance to the forum is optional. The option of attending a forum offers the participants additional opportunities of learning, e.g. to ask questions and therefore to get a better understanding.



Figure 4. Graphical user interface CD CBT for Blended Learning IWE Part 3

Further, the distance learning course participant has the opportunity to communicate with his co-students.

**Group of participants.** Admission to the participation in the GSI IWE Distance Learning Course Part 3 has been regulated following guideline DVS-EWF/IIW 1173 and corresponds – according to its designed concept – to the admission to the standard IWE classroom courses in Germany. The stipulations of guideline IAB-195-2004 and guideline DVS-EWF/IIW 1196 March 2005, as well as of the German additional regulations will be complied with.

**Quality assurance, system analysis and corrective actions.** Based on their experience with almost 500 participants in various training courses obtained so far, GSI has introduced a system of permanent control and guidance of the participants. Error messages by the participants and the tutors in charge will be collected via an organizer and forwarded through the responsible lecturer to the CBT development team. According to the experience gained in Duisburg

Kapitel	Lehrstoff	Bearbeitungs- woche für CBT	Fernlehrgangs- teil CBT UE T3	Bemerkung	Unterrichtseinheit in der Präsenzphase separat Lehrgangstermine
Hauptgebiet 1: Schweißprozesse und -ausrüstung	1.4 – Der Lichtbogen	W 1	2	ist Wiederholung von T 1	1
	1.5 – Strichproben für alle Lichtbogenschweißen			Wiederholung von 1.3 ist separat	1
	1.3 – MAG-Schweißen	W 1	2	weiter 1.2b 1.1	2
	1.8 – MIG/MAG- und Füllmetallschweißen	W 1	4	weiter über 1.4 bearbeiten	2
	1.9 – Lichtbogenhandschweißen	W 1	4	weiter über 1.4 bearbeiten	2
	1.10 – Unterpunktschweißen			4 UE aus Teil 1 und weiter überarbeiten	2
	1.11 – Widerstandsschweißen	W 2	4		4
	1.12 – Sonderschweißprozesse	W 2	8		2
	1.13 – Schneiden und andere Nebenbearbeitungsverfahren	W 3	4	die ersten 2 h sind Wiederholung aus T1	
	1.14 – Beschichtungsschneiden	W 3	2		
	1.15 – Mechscherste Verfahren und Rüderschweißen	W 4	6		2
	1.16 – Hart- und Weichlöten	W 3	4		1
	1.17 – Kunststoffschweißen	W 4	4		1
	1.18 – Schweißprozesse für moderne Werkstoffe				2
1.19 – Laborübungen oder Fertigungsübungen im Modellbau			14 UE Übungen	10	
Wiederholung für Hauptgebiet 1			Die Präsenzphase ist wie separate Lehrgang WS	4	
<b>Summe</b>			44		36

= Information für den Fernlehrgangsteil  
 = Information für den Präsenzlehrgangsteil

Figure 5. Course of studies: example main subject 1

so far, the quality of the distance learning course has been constantly improved.

**Curricula.** All participants will receive a recommendation on the course of studies. Since the distance learning concept, however offers the participant the most possible flexibility, this recommendation serves as a didactic aid only. Fixed curricula will be set up for the phases of classroom learning which will be handed over to the participants prior to commencing these modules. The participation in the classroom phases is obligatory for the participant. Attendance to the module will be controlled by an attendance list. In case of absence of more than 10 %, admission to the final examination will not be given.

### **Experience with the BL Course IWE Part 3**

The fact that this distance learning course could be developed within 1.5 years has certainly been influenced by various positive factors within the GSI:

- existing of high-quality and well-proven documents for IWE Courses standardized within the GSI;
- existing of experience obtained from other distance learning courses (IWE Part 1 in German and English, IWS Part 1, IWD G1, CONTINUED);
- business plan with estimation of costs and profit;
- existing of competent IT experience (in 5 projects);
- allocation of tasks to expert lecturers and software specialists;
- close co-operation with all persons involved;
- working in the IIW IAB (as chairman of the IAB A) and in the working group distance learning courses;
- strong support by the GSI managing director and the branch managers.

In the mean time, as many as 12 participants of the distance learning courses have completed the whole course. A further more than 20 participants

have made use of this flexible possibility of learning during the classroom phases in Halle, Munich and Duisburg. Almost all participants also make use of the forum, i.e. the direct contact with the main tutor and the four subject tutors, thus offering the necessary feedback for constantly improving the course. The classroom phases in particular are felt to be of decisive importance. Almost all users of the BL concept have already passed IWE Part 1 as a distance learning course. After part 2 which in general has been conducted in the nearest of the 8 GSI SLVs, the participants, for the first time, will enter into personal contact to each other and to the lecturers. Therefore, very interesting discussions and a strong team spirit will arise.

Summarized it can be stated that in the final examination the same results are obtained as in the «normal» classroom courses. It must be stated, that the extent of guidance by tutors, however is more intensive.

### **Outlook**

Blended learning has obviously proven itself as a new concept of learning in Germany. After the starting phase, it seems to turn out that approximately 20 % of all participants are choosing this way of learning. The rest of the participants – probably due to the large number of training houses in Germany (overall 10 SLVs in Germany), are further choosing a classroom course in the form of a day, evening or weekend course. It must also be stated, however, that the development of such a concept needs a large extent of time and money, thus not being possible to be offered by any institution.

1. *Documents of the GSI mbH.*
2. *Training course concept GSI distance learning IWE Part 3.*
3. *Guideline DVS-IIW/EWF 1173 and IAB-195–2004.*

# VIRTUAL ENTERPRISE BASED ON HIGHLY EFFICIENT USE OF INDUSTRIAL LASER SYSTEMS

V.S. KOVALENKO and V.V. KOLPAKOV

Laser Technology Research Institute of NTUU «KPI», Kiev, Ukraine

Some aspects of scientific, academic and industrial potential of Ukraine integration into European community based on the Laser Technology Research Institute (LTRI) Internet resources are discussed in this paper. Being the most highly developed country from the post Soviet republics, Ukraine has the significant scientific, academic and industrial fundament for laser technology development and its implementation into industry. The country has quite numerous parks of industrial laser systems belonging to different institutions and companies which are not used efficiently. To some extent the similar situation is typical for other countries. The concept of more efficient use of sophisticated industrial laser systems based on opportunities of web-technologies is proposed.

Global economy development discloses new challenges for human activities. Advent of information technologies, airspace developments, new success in health care, new results in biotechnology and other science and technology achievements are possible among others due to fundamental changes in manufacturing science and possibilities to use new approaches in product developments [1]. Laser technology born in the middle of the last century continues to bring new challenges and to open new horizons for scientists and manufacturers up to now.

Nevertheless it is quite common practice that some sophisticated industrial equipment at small companies and different research institutes and universities can not be used 24 hours a day 7 days per week. At the same time such equipment is quite expensive and it is difficult to get fast money return. The solution of the problem may be found by combining unique opportunities of laser technology – high productivity, versatility and flexibility – with ultra fast communication possibilities of modern information technologies. The wide range of industrial laser applications (hole piercing, welding, cutting, hardening, cladding, rapid prototyping, marking etc.) may be realized using quite limited variety of different available industrial and experimental systems.

The virtual enterprise may be proposed as an effective means to get constant flow of orders to keep industrial laser systems close to 100 % efficiency. The structure and some features of such enterprise are discussed. It includes the databank of equipment owners from different institutions both from Ukraine and outside the country, the range of technological parameters of every particular piece of equipment, availability of materials to be used for product manufacturing, data on optimal working conditions, set of special treatment recommendations, etc.

**Globalization is a strategic goal.** The world economy is moving towards globalization in the last few decades. This became possible due to intense develop-

ment of information technologies and other advanced technologies [2]. Generally speaking the globalization is based on advanced manufacturing technologies, information technology, and modern communication systems.

As a result of globalization processes in industry the customer may gain the following benefits:

- productivity increase;
- final product variety rise;
- product cost decrease.

The classic economy law says that the manufacturing cost of product is decreasing with the amount of manufactured products in a batch. But the modern society is very much interested in the product variety rise. As Prof. K. Hitomi from Kyoto University, Japan, stated in his book «Manufacturing Systems Engineering», NY, 1975, «about 80 % of components in modern industry were manufactured in amount not exceeding 50 pieces in a batch». This caused the product individualization, impossibility to use mass production (expensive moulds, dies, automatic lathes, etc.) in products manufacturing. Such trends are becoming even more accentual now.

Thus the solution to overcome the discrepancy between the need of the product variety increase and product cost decrease may be found in application of more versatile and flexible technologies and equipment like laser industrial systems and corresponding technologies.

**Laser technology — universal solution.** Among the varieties of laser technology there are more than 20 different industrial applications, such as hole piercing, welding, cladding, hardening, surface alloying, cutting and material shearing, micro- and nanomachining, marking, engraving, sheet material deformation, combined or hybrid processing, and others.

Mentioned processes may be realized practically using the same piece of equipment and generally speaking by simple change of main working conditions: focused laser radiation power density and the duration of irradiation.

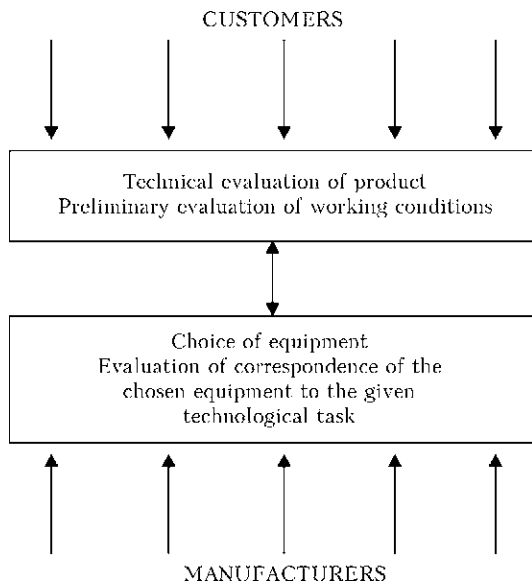


Figure 1. Interactions between customer and manufacturer

**Laser-aided manufacturing in Ukraine.** First research activities in laser aided manufacturing in Ukraine date back to 1964 and had been initiated at the Kiev Polytechnic Institute (now National Technical University of Ukraine «KPI»), in the E.O. Paton Electric Welding Institute and at other institutions. There was a splash of increased interest to this advanced technology in the last two decades. The interesting feature of this process is the appearance of the number of small private organizations, different job-shops and the development of new R&D activity in a number of universities and research institutes (total around 50). Along with traditional industrial laser applications (cutting, surface treatment, welding, cladding, marking, cleaning, etc.) some new fields are emerging such as rapid prototyping, micro- and nanoprocessing, and development of the new types of lasers.

From the very beginning of the laser era, activities on the development of academic programs in laser technology were initiated at KPI. Thus, at KPI, the first graduates of this course received their Engineering Diploma in 1966–1967 from the Mechanical Engineering Department. This course has the official status of the new specialty «Technology and Equipment for Laser Processing» and created in 1984. The corresponding academic program started first in the

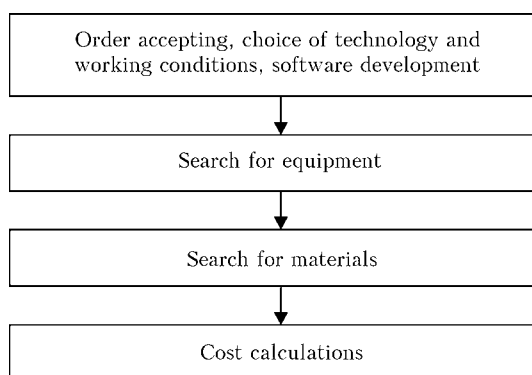


Figure 2. E-enterprise service

FSU and in Ukraine at KPI in Kiev and at the Bauman Institute in Moscow.

During the last years the academic program is being adapted to the Bologna Agreement concept, the main goal of which is the integration of the national education systems into the European and global one.

From that time up to now more than 800 engineers and masters (both from Ukraine and other 32 countries) in laser technology graduated KPI. For the last decades 27 PhD theses and 6 DSci theses of researchers in laser technology had been successfully defended.

The developed technology and equipment are quite widely used at different plants – Arsenal, Bolshevik, Aviant (Kiev), Malysheva Plant, Tractor Plant (Kharkov), AvtoKraz (Kremenchug) and many others. At these plants, soviet-made CO<sub>2</sub> and Nd:YAG lasers are mainly used for components welding, hardening, cladding, material cutting, etc. Last time more than 60 new industrial laser systems had been purchased by companies from foreign manufacturers – Trumf, Bistronic, Rofin Sinar, etc. The number of small private organizations and different job-shops appeared at the market in the last few years, with their activities focused on sheet material shearing, welding, and components restoration by cladding, marking and engraving, etc.

**Role of Laser Technology Research Institute in promoting the integration processes.** The international collaboration in the field of laser technology has improved significantly for the last decade. Different mechanisms are involved in stimulating such moves. Apart from bilateral agreements on scientific collaboration between Ukraine and different countries, there is a number of direct ties between universities and laser centres (for example, LTRI has such agreements with Okayama University (Japan), Ohio State University (USA), Zhejiang University (China), etc.). A number of projects is financed by NATO, by different institutions of EU (INTAS, EURIKA, etc.), and by the Scientific and Technological Centre of Ukraine.

It is obvious that the globalization goes hand in hand with the integration process. We witness such integration in every field of human activity, in different regions, in America, Europe and Asia. Ukraine, as a country located in the very geographical centre of Europe, is trying to be an integral part of the European community and supports different integration initiatives.

Prof. V. Kovalenko (NTUU) and Prof. A. Grabchenko (Kharkov NTU) had been invited by EU officials as coordinators from Ukraine to develop the National Manu Future Technological Platform. Based on the achieved results and gained experience in advanced technology R&D activity this Manu Future Technological Platform of Ukraine has been developed recently and proposed for integration in EU Manu Future Platform. Laser-aided manufacturing is considered as a key technology of this concept.

In spite of chronic financial problems, Ukrainian experts in laser technology are becoming regular par-



ticipants of different international professional institutions: LIA, CIRP, IEEE, LEOS, LAS, etc. and their events: ICALEO, ISEM, and CIRP General Assemblies, etc.

Thus it was quite natural that due to the gained experience in research, academic and industrial activity, not only in Ukraine but internationally as well, the concept of virtual enterprise based on more efficient use of industrial laser systems was proposed and developed at LTRI.

#### Functions and structure of virtual enterprise.

The main function of the proposed e-enterprise is to become the integrating unit between the customer needs and the manufacturers proposed service [3]. The generalised idea of these interactions is demonstrated in Figure 1.

To realize this interaction the following steps should be developed in the framework of the e-enterprise:

- database of accessible production facilities;
- database of the necessary fixtures and materials;
- orders acceptor;
- structure of the close-loop virtual manufacturing.

The e-enterprise may propose the service shown in Figure 2.

The web-site of LTRI for electronic processing of orders includes the following program modules [4, 5]:

- presentation of general information in the form of HTML-files with possible inclusion of active advertising pages;
  - formation and processing of the database of orders with active acceptance modules;
  - information about customer;
  - formation and processing of a data file from/for the database of orders using active modules of acceptance of information on the characteristics of the product suggested for manufacturing;
  - processing the file of order payment and issuing a command for manufacturing and realization of products;
  - support and recording of receiving of the order by the user.

During construction of a virtual manufacturing the last listed items should be complemented with evaluation of accessibility of equipment, which enables fulfilling the order and calculation of the possible manufacturing time, and preparation of technical documentation for manufacturing and transfer for performance.

The electron version of database on available equipment was created at LTRI to make possible to accept orders from customers both from Ukraine and outside – the post Soviet countries and some countries of EU. According to the e-enterprise structure accepted orders are processed at the e-enterprise and are transferred to the chosen manufacturer to perform the

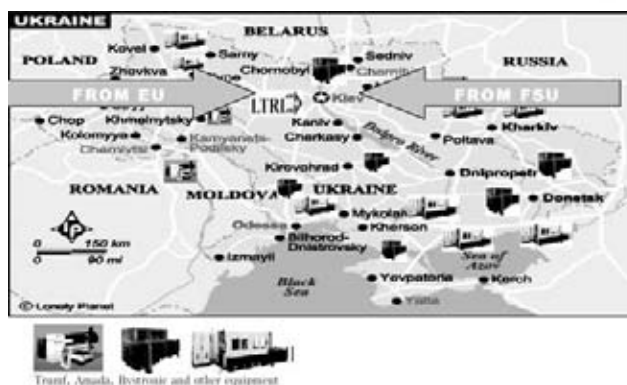


Figure 3. Scheme of connections of interested sides via LTRI

necessary laser operation. The scheme of connections is demonstrated in Figure 3. It is accentual to note that when it is necessary, the additional e-education program may be supplied as well.

## CONCLUSIONS

1. The combination of advanced processing technology with information technology is crucial factor in development of globalized society.
2. Research, industrial and academic activity in laser technology in Ukraine has the obvious trend to globalization.
3. E-enterprise based on more efficient use of laser technology is the right solution to solve the problems in the modern industry.
4. The proposed principles of web-enterprise may be spread out on other technologies based on different types of unique equipment.
5. The discussed concept of e-enterprise is developed at LTRI as ingredient part of the National Manufacturing Future Technological Platform.

**Acknowledgements.** The authors would like to acknowledge the financial support of this research in the framework of the project No. GO127-2006, sponsored by the Ministry of Science and Education of Ukraine.

1. Kovalenko, V.S., Anyakin, M.I. (2002) Manufacturing technology in the information age. In: *Proc. of 35th CIRP Int. Seminar on Manufacturing Systems* (Seoul, Korea, May 12–15, 2002).
2. Westkamper, E. (2002) Platform for the integration of assembly, disassembly and life cycle management. *Annals of CIRP*, 51(1), p. 33–36.
3. Kolpakov, V.V., Kovalenko, V.S., Zhuchenko, A.I. (2005) Information on-line system to choose equipment and working conditions for laser material processing. In: *Abst. of 2nd Int. LTWMP Conf.* (Katsiveli, Crimea, Ukraine, May 23–27, 2005), p. 38.
4. Kovalenko, V.S., Kolpakov, V.V. (2004) Use of web-technologies to improve the competitiveness of Ukrainian engineering plants. *The Paton Welding J.*, 7, p. 32–38.
5. Kovalenko, V.S., Mamalis, A., Kolpakov, V.V. (2005) Web-technologies application to increase the efficiency of laser industrial systems. In: *Proc. of 2nd Int. LTWMP Conf.* (Katsiveli, Crimea, Ukraine, May 23–27, 2005), p. 64–66.

# DEVELOPED COMPUTER TECHNOLOGY FOR DESIGNING ASSEMBLY-WELDING TECHNOLOGICAL TOOLING

D.P. KUNKEVICH, S.V. MEDVEDEV and Zh.G. YAKOVLEVA  
United Institute of Informatics Problems, NAS of Belarus, Minsk, Belarus

Computer technology and supporting it software-methodical complex INWELDEN for automated multi-version designing of assembly-welding technological tooling are considered. INWELDEN was successfully used for equipping welded structures of tractor cabs at the Minsk Tractor Plant, and designing and preparing for production of soil-cultivating machines. The term of development of assembly-welding tooling reduces 1.5–4 times.

Initial data for fixture design are assembly-welding structure (AWS) volumetric model in solid format, technological process and welding assembly scheme. By means of 3D marks that correspond to standard conventional signatures for supports and clamps (GOST 3.1107–81) welded structure parts mounting and fixing scheme is formed.

On the next stage the formed mounting and fixing scheme constructive fulfillment is made. During this stage mounting or fixing element from the constructive elements (CE) database is put in the conformity with every mark. Displacement parameters are automatically taken off from the conventional marks substituted by CE.

Placed in conformity with basing scheme functional CE are algorithmically composed into fixture structure by body the later being rectangular, round or arbitrary form plate or frame and beam structures from standard and normalized rolled metal.

60–70 % of technological preparation labour-intensiveness (laboriousness) is expended on designing,

matching and assembly-welding fixtures (AWF) making processes. In [1, 2] the importance of skillfully developed AWF is emphasized, there is direct relation between welded assembly quality and fixture design levels.

Computer technologies for designing technological tooling for AWS base on the method of interactive-algorithmic synthesis of special WAF designs in space of incomplete description CE extensive databases [3–5].

The last version of system INWELDEN (INstrument of WELDing ENgineer) has contemporary user interface, its realize is based on Mechanical Desktop 6 (Figure 1).

CE database is continuously increased. Now it includes more than 500 items and reflects traditions of several industries such as automobile, agriculture machine building, as well as experience of production and design engineers of welding departments.

Every fixture unit model is to include description of principal bases – the faces by means of it will be

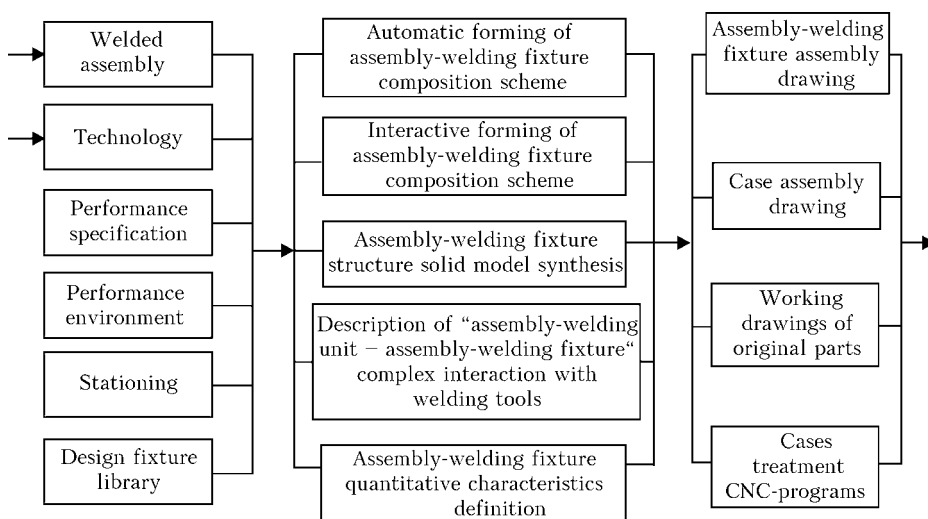


Figure 1. Mechanical Desktop 6

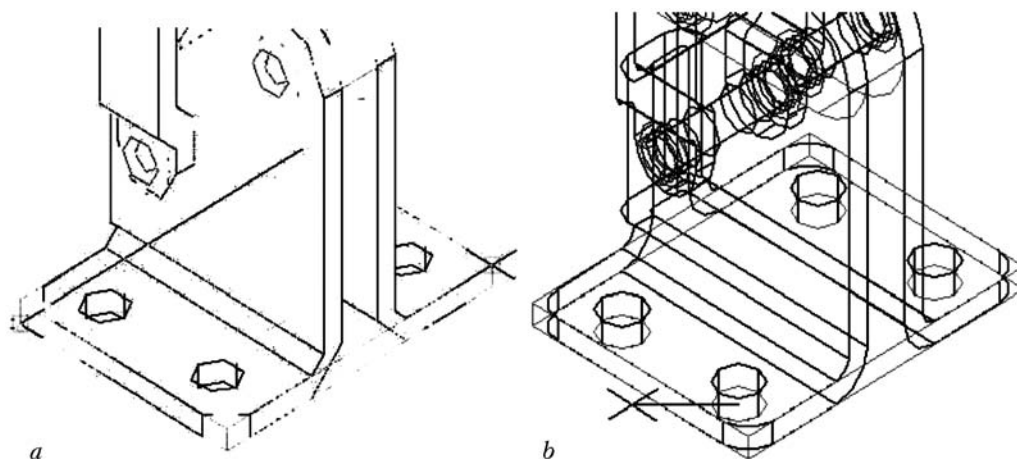


Figure 2. Picking up principal bases of fixture units: *a* – plane base; *b* – mounting hole

mounted onto fixture. Is considered two kind of principal bases, namely plane base (Figure 2, *a*) and mounting hole (Figure 2, *b*).

Solid model of AWS is principle data for fixture design (Figure 3). Contemporary graphic systems allowed creation models of height complexity parts and connection thereof in assemblies by means of coordinates or object snap. By means of graphic exchange formats (STEP, SAT etc.) solid model may be transform into system from any graphic system.

Carried out investigations showed that the processes of analysis of manufacturability and assemblability AWS, principal technology, assembly-welding and location-clamping schemes creating processes, as well as process of interactive-algorithmic fixtures and jigs design may be realized in the context united 3D models of AWS, AWF and attachment. The possibility of operating assembly-welding system component models provides really computer embodiment of principals of constructive-technological welded assembly design.

User interaction with design system starts from set up of preferred state object and locating-clamping scheme formation. During development of module «Stationing» attention was focused on flexibility of scheme graphic model. Locator and clamp signs are used to forming location-clamping scheme (Figure 4). As united graphic object, any sing may be moved, rotated, copied in AWS model space. Placement of

signs around of 3D graphic model is not difficult for trained users. Thus, the wide set interactive tools compensate for a deficiency in automation procedures.

During location-clamping scheme forming any sign may be redefined. It means that sign contents may be changed while insert point and orientation will be saved. It provides at principal scheme level to show and to estimate different variants of constructive embodiment.

The programs of automated design are supplied with information about fixture technical conditions of its manufacturing and utilized from spatial block «Performance specification». It includes information about codes and names of object and fixture, power of issue, fixture type, power drive type, fixture body material etc. Active editing of these data is possible with window dialogue (Figure 5).

INWELDEN may be used in algorithmic mode or interactive-algorithmic mode. In algorithmic mode the system analyzes location-clamping scheme, selects suitable CE from database and places them in geometry synthesis space. Along with geometric form the results of this step are saved in ASCII-file (<Project\_Name>.KSP). That representation is named as



Figure 3. Welding construction solid model

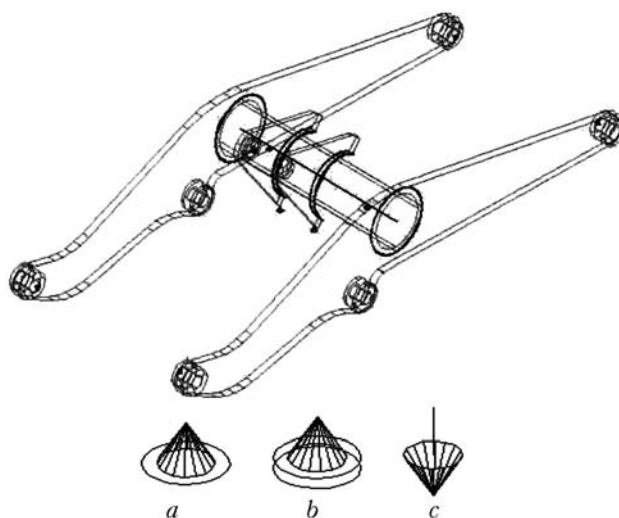


Figure 4. Welded structure basing example: *a* – locator sign; *b* – flexible locator sign; *c* – clamp sign

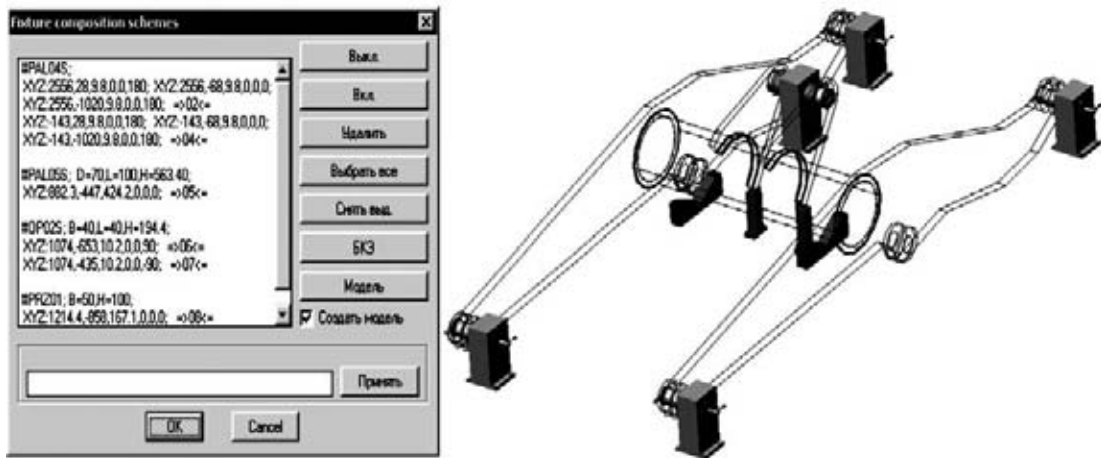


Figure 5. Example of assembling scheme and its embodiment

assembling fixture scheme and may be modified in dialogue form (Figure 6).

For CE selecting several criteria are used: necessary clamping forces for any parts, clamp driver type, necessary response speed and forces direction. Clamping force power is determined by means of experiment-calculated dependences and rule of thumb as well as stochastic similarity dependences, the manufacturing experience and traditions taking into account too.

Body type and dimensions are selected algorithmically based on performance specifications. Body model is united together with CE models algorithmically.

In interactive-algorithmic mode referred operations are carried out by designer of assembly-welding attachments. The results of automatic fixture design may be edited at 3D models level or at level of drawings.

Special format is used for CE description in assembling scheme:

```
#<KENAME>(:TPR)(,<P1>=<P1>),...
(<P1>=<P1>),...(<Pn>=<Pn>);
XYZ:X,Y,Z(Ax,Ay,Az),
```

where <KENAME> is the CE identifier; TPR is the version; <Pi> is the parameter identifier; Pi is its mean; XYZ is the key word for coordinates input; X, Y, Z are the insert points; Ax, Ay, Az are the angels of rotation about coordinate axes.

Assumed AWS parts usually are placed up to fixture body. This placement provides good position object for welding, better condition for forming seams and their accessibility for welding tools. Because direct contact elements of fixture correspond to geometry of AWS parts, plane constructions of body are considered. They appear as mono plate or frame welded structure.

Mentioned body type is widely used. Their design is easier to formalize. Such body types are usually used in industry: rectangle plate with certain thickness; circular table, the diameter is dependant of fixture dimensions; free form plate; rectangle frame make

up from channel or tube roll-metal; frame with spine bulk; rotated frame with spine bulk; and table support appeared as channel bulk.

The body as rotated frame with spine bulk is shown in Figure 7, a. It consists of two channels. Distance between channels comes to 580 mm. Non-rotated fixture with body as rectangle frame is shown in Figure 7, b, body as plate — in Figure 7, c. 10–25 mm plate thickness is assumed. These bodies are applied for fixtures for small objects functions.

Contact between CE and body may be realized directly or by means of adapters, which should carry out compensation and adjustment functions.

If adapter height is less than 80 mm, then it will be making as seamless part with through holes. If adapter height is more than 80 mm, it will be making as two plate connected with strengthening member. Strengthening member as 12 mm sheet is used in welded adapter if its height is less than 150 mm (and more than 80 mm). If height of adapter is more than



Figure 6. Example of computer-aided design task

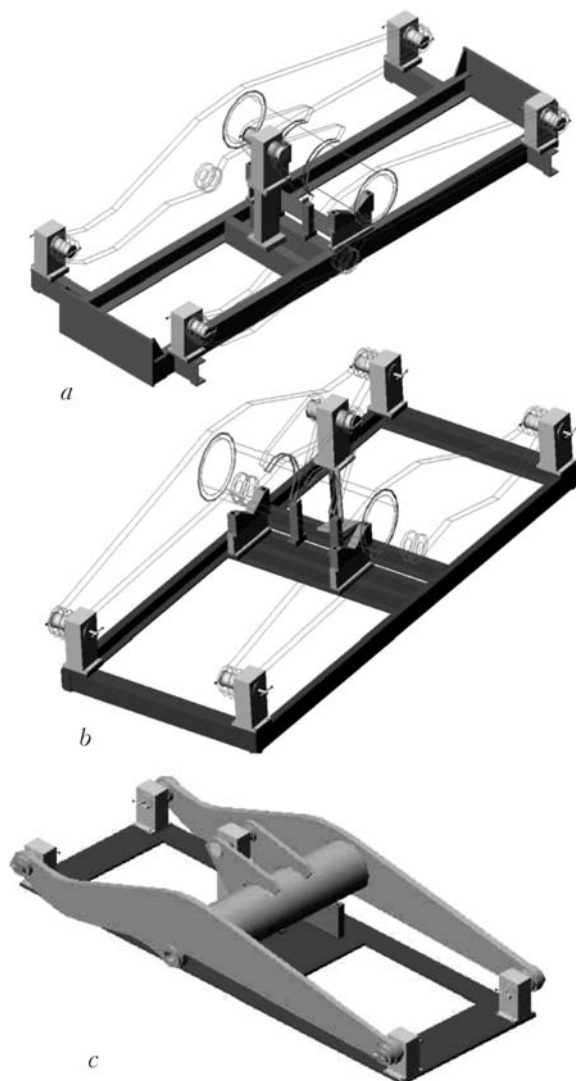


Figure 7. Fixtures with different body types

Характеристики ССП	
Габаритные размеры, L x D x H	2069 x 1462 x 517.5
Координаты центра масс СС	
Координаты центра масс ССП	1242.2, -2.68, -95.95
Координаты центра масс СС-СП	
Производственная площадь, кв.м	4.19
Масса, кг	413.36
Площадь предохраняемых поверхностей, кв.м	12.35
Коэффициент утяжеления конструкции, %	
Расход проката (Швеллер N 10) ,лог. м	22.56
Количество привалочных пластинок корпуса	38
Количество библиотечных констр. элтов	38
Трудоёмкость, н/час	35.15
Стоимость, у.е.	289.35
<input type="checkbox"/> Сохранить в KSP файле	<input type="checkbox"/> Сохранить в новом файле

Figure 8. Quantitative INWELDEN welding-assembly fixture characteristics

150 mm it is defined from performance specification. Material may be channel, tube (rectangle or cilinder). There is information about channel version or tube dimensions in this line. If there is not mentioned line in performance specification file, adapter material will be assume as one of body. Adapter is situated among clamping holes. Space for spanner should be reserved among adapter and holes. If selected by this manner material is not suitable, then smaller version of material will be selected.

Insertion adapters in fixture model are finished fixture design processes.

Several characteristics are used for quantitative assessment of fixture variants (Figure 8). Computer-aided technology INWELDEN (Figure 9) allows one to form basic part of design documets in algorithmic mode. Using system INWELDEN to equip production of AWS of agriculture mashinery revealed positive

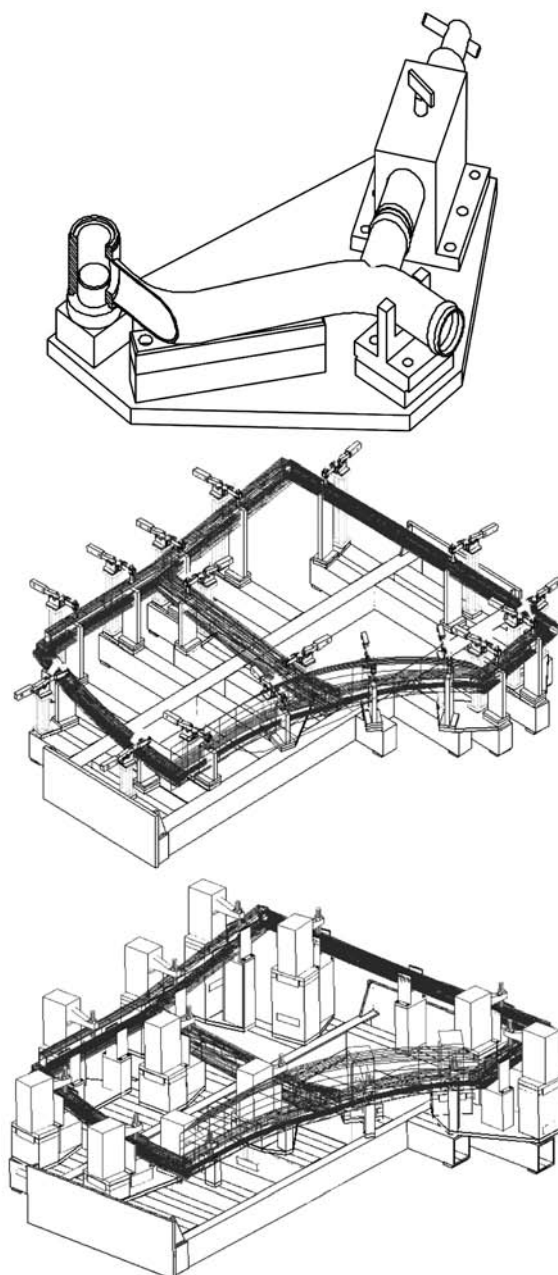


Figure 9. Examples of INWELDEN computer-aided fixture design

and negative sides of scientific approach, as well as allows directions of further investigation to be defined:

- development intelligent procedures to forming CE models and fixture assembling schemes;
- continuous perfection CE database for constructive implement and for applied materials;
- extending sphere of algorithmical fixturing synthesis in the context adjusted by user program-information multimedia environment;
- development of stress-strain state estimation methods with supercomputer systems (www.skif.basnet.by).

## CONCLUSIONS

1. Program facilities INWELDEN provides possibility of variant design of fixtures and jigs for equip arc welding production processes.

2. United 3D model of AWS, AWF and non-regular attachment provides to connect assemblability analysis, selection of preferred object state for assembling and welding, forming and realization of propo-

sitions for welded assembly manufacturability improvement.

3. Reduction of fixture design period is achieved. It comes to 1.5–4 times in comparison with interactive design (using only universal graphic facilities); result quality is improved due to multi-version design, the principal mistakes revealed on body fabrication stage (tooling body with coordinate drilling machine) are eliminated.

1. Medvedev, S.V. (2005) Constructive-manufacturing principles of welded structure designing at supercomputer environments. In: *Transact. of Tula State University on Computer Technologies in Joining of Materials*, Vol. 3; *Proc. of 1st Int. Sci.-Eng. Internet Conf. on Computer Technologies in Joining of Materials*. Tula: TulGU, p. 70–76.
2. Medvedev, S.V., Rakovich, A.G. (1997) Computer technology of welding-assembly fixture design. *Avtomatich. Svar-ka*, 7, p. 33–38.
3. Medvedev, S.V. (2000) *Computer technologies of assembly-welding attachment design*. Minsk: IIK.
4. Medvedev, S.V., Kunkevich, D.P. (2001) Experience of effective computerized design of assembly-welding jigs. *The Paton Welding J.*, 3, p. 39–43.
5. Denisov, L., Medvedev, S. (2003) A differentiated approach to the computer design of welded structures. *Welding Int.*, 17(11), p. 899–904.

# MODELLING AND TESTING OF DIELECTRIC HEAT SOURCE DESIGNS FOR THE MICROWAVE THERMAL SPRAYING PROCESS

P. MAVROMATIDIS\* and J. LUCAS

\*University of Liverpool, UK

The microwave thermal spraying process is a unique spraying technique whose novelty is focused on the use of a microwave powered heat source. This enables the construction of long heat exchangers that significantly reduce the power consumption and operational costs. However, the presence of a metal heat exchanger and a variety of dielectric materials in different shapes and forms, inside the microwave cavity, combined with the heating process make theoretical calculations of microwave propagation and electric field distribution complex and tedious. Furthermore, the harsh environment of microwaves, due to the radiation interference with electronic devices, and the induction of high temperatures make any sensing mechanism or visual inspection within the cavity system, while in operation, unreliable and sometimes impossible. Therefore, the investigation of multiple novel microwave heat sources was undertaken using the high frequency structure simulator. This resulted in an approximate identification of potential flaws in the designing process and helped with the selection of the right materials. Thus the microwave thermal spraying process was designed and constructed using an enclosing dielectric heat source, which has provided stability of operation, reliability and elimination of arcing effects.

All existing metal spraying processes are based on the use of high-pressure gas and a short heat interaction to bring the powder particles at a high velocity and temperature and project them onto a well prepared (thermally and chemically) surface [1]. The microwave thermal spraying technique, on the other hand, is a direct, continuous melting spray technique using a different approach to create the bond between injected particles and the surface. It brings the thermal and kinetic energy in a balance to increase the coating efficiency. It uses a high and long thermal interaction path to heat the coating powder above melting point and then project them onto the substrate surface creating a weld-bonded coat. Moreover it uses microwaves as the power source and significantly reduces the power consumption of the process. In the early stages of the research, microwaves were used to produce heat by means of a gas discharge heat source [2, 3]. This design worked but subject to temperature limitations. The instabilities of the plasma discharge, the fragile nature and the limited endurance to high temperatures of the construction material, created the need for a stable and compact design. This approach is based on the use of lossy dielectrics [4] in the microwave resonance cavity [5] as the heat source and a metal spiral shaped tube as a heat exchanger. This design faced different problems as electrical breakdown between the metallic constructed spiral and the cavity walls occurs at high microwave power levels. The microwave dielectric heating was further developed and with the use of the high frequency structure simulator (HFSS) a valuable insight of the microwave interaction within the cavity was provided that could not be otherwise visualised. It provided crucial explanation, revealed weaknesses and validated assumptions.

**Microwave thermal spraying process.** The main focus on the on the production of the microwave spraying system is in the construction of the microwave

heating system of the overall process. The heat source is chosen to be a hot-pressed silicon carbide. The silicon carbide is chosen not as a compact structure but porous, with 2 mm diameter holes alongside, exactly the same structure used in catalysts. A bulk material requires high power levels in order to allow uniform power distribution and hence uniform heating. By using a less dense material the power is uniformly distributed due to higher penetration depth [6] and the induced heat is distributed faster by means of conduction, from unavoidable hot spots to lower temperature points where the field is weaker bringing the whole structure in a thermal equilibrium. The induced temperature is then conducted to a heat exchanger which is a confined path and through which nitrogen gas is streamed. The heat exchanger has a spiral configuration so that the flowing nitrogen is subject to heating for a long period of time. The use of nitrogen as the carrier gas significantly reduces the cost of operation, whereas the use of a long interaction path introduces a more efficient heating technique reducing energy losses and therefore overall power consumption. The gas flowing at a constant rate will pick up the heat energy from the walls of the heat exchanger by means of convection and will act as the transfer medium. When the nitrogen carrier gas is successfully heated to the required temperature the coating powder is introduced in its stream before entering the heat source. The fine powder is carried in the gas stream through the heat source where it is provided with the essential melting temperature and the resulting molten particles are then propelled to the substrate surface. The whole process can be described as a conversion of microwave energy to useful heat through a workload medium and can then be directed and managed according to the application requirements.

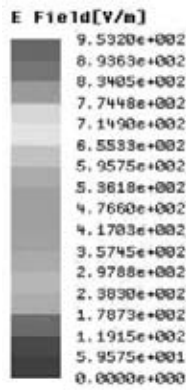


Figure 1. E-field notations

**High frequency structure simulator.** The HFSS is an electromagnetic field simulator allowing for the design of 3D devices in a graphical operating environment [7]. It can give a visual representation of the field distribution and emulate laboratory measurements to provide verification of the results. One advantage of the HFSS is that it allows for complex geometries to be defined with a simple and common graphical interface. The interaction of these volumetric models with frequency can then be simulated at a user defined frequency. Each geometrical object has to be assigned to a specific material like vacuum, air or a dielectric either through the existing database or by manually defining the material properties. The magnitude of the E-fields can be viewed by creating imaginary planes vertical and horizontal to the design's cross section and plotting them along their path. The field variations are graphically represented with changes in colour following a value pattern according to the notations shown in Figure 1.

The first step in the designing process is to model the waveguide and cavity assembly. The model of the waveguide system consists of a rectangular waveguide with cross sectional area of  $86 \times 43$  and 246 mm length. The circular cavity has 97 mm diameter and 292 mm length. Both waveguide components are filled with air. Figure 2 shows the electric field strength across the system in a 3D view. The magnitude of the electric field draws weaker when entering the circular cavity, which is an expected effect as microwaves are propagated to a wider dimension waveguide and the field is stretched.

**Silicon carbide heat source centred inside the spiral flow structure.** One of the early microwave spraying designs was the direct contact SiC heat source surrounded by the spiral heat exchanger as seen in Figure 3. The SiC acting as a heat source absorbs the microwave power and conducts the heat to the spiral flow structure to be convected by the

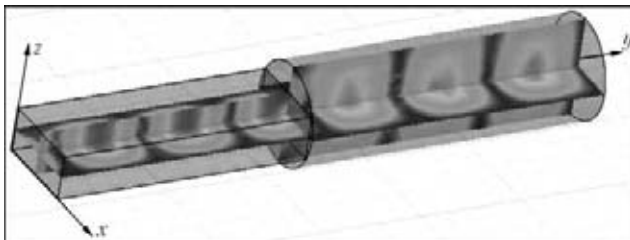


Figure 2. 3D view of the field strength in waveguide system

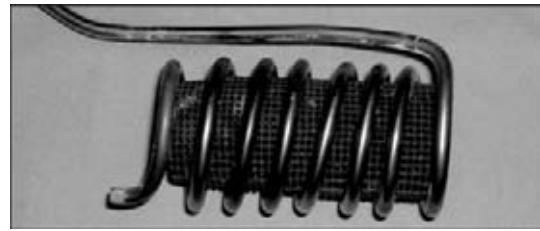


Figure 3. Direct contact SiC heating system

gas stream flowing through. The heat exchanger is selected to surround the spiral because the surface of the SiC is expected to have higher microwave absorptivity than the rest of the mass and hence induce higher temperatures. This will optimise the heat efficiency of the system and reduce heat losses.

As a first step this heat exchanging assembly is investigated in the circular cavity with only air as an in-between medium. In the simulation model the spiral is designed as one object and defined as stainless steel. The spiral structure made of a 5 mm diameter rod has overall inner diameter of 45 mm with 7 spirals having space gaps of 10 mm. A SiC rod of 44 mm diameter and 80 mm length is then centred in the spiral configuration and the overall assembly is placed inside the circular cavity filled with air as seen in Figure 4. The model is then simulated at 2.45 GHz frequency. The 3D field distribution can be seen in Figure 5.

As it can be seen from Figure 5 the field strength initially reduces when entering the circular cavity but substantially increases around the load. Some intense field can be spotted inside the SiC which is a desired effect as it will be induced into heat when absorbed by the dielectric. However, there is also high field intensity around the spiral structure mainly concentrated at the edges of the overall load stretching to the cavity walls. Since the spiral is a metallic structure the effect of an arcing across the spiral and the cavity is imminent. This assumption is validated by experimental results as the SiC direct contact heat source failed at a power level of only about 900 W. The hottest point, where meltdown of the tubing occurred, was at the end facing the microwaves where the gas stream should theoretically be cold. The E-field concentrated on the edges will significantly heat the surface of the dielectric at these points, but because the spiral flow structure is in direct contact with the surface it will dissipate most of the heat prevailing heat conduction to the overall mass of the dielectric that will uniformly distribute the temperature. Hence, the spiral structure at these points becomes substantially hot. Furthermore, these high field strength spots are observed between the spiral and the cavity walls, and since air is the only in-between medium, electrical breakdown between the two will

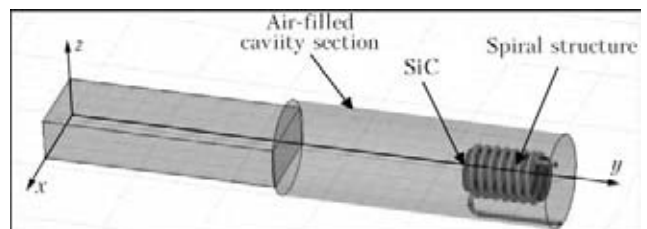


Figure 4. Design of the SiC rod centred in spiral flow structure



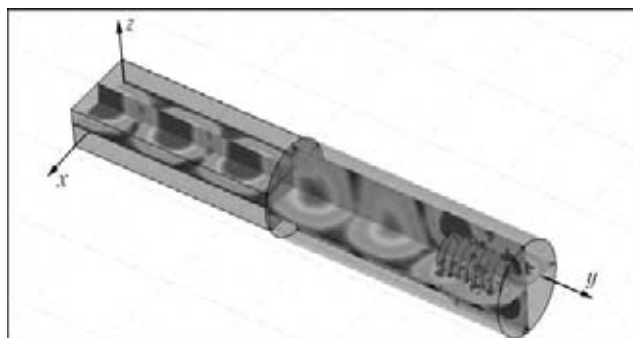


Figure 5. 3D view of the field strength in waveguide system

be induced even at low power levels. The metal structure is constantly subject to arcing as microwave power increases and therefore localised melting on the spiral is unavoidable and cause.

In further development, the above heating system design is placed in an alumina powder filled cavity. Because the cavity is only partially occupied with alumina, the circular waveguide is divided into two sections, one of 162 mm length filled with air and the other 130 mm length filled with alumina powder, as seen in Figure 6. The presence of alumina powder between the cavity walls and the spiral structure significantly reduces the field strength, as shown in Figure 7, minimising the generation of arcs. Although most of the field is concentrated in the centre of the SiC, small spots of high field strength can still be detected around the spiral as seen in Figure 8, that are sufficient enough, at high power levels, to initiate a dielectric breakdown. It should also be taken into consideration that these simulations are an approximation and in practice the positioning of the spiral and the dielectrics inside the cavity vary within a couple of centimetres and if the spiral structure is closer to the cavity wall, the E-field spots on that side will be more intense. Nevertheless, even one detected spot is enough to create an arc, at high power, and threaten the metallic structure of the heat exchanger as it has been observed in experimental work.

**Enclosing heat source.** In order to seal the metal heat exchanger from microwave exposure and prevent any arcing, in the final design of the microwave ther-

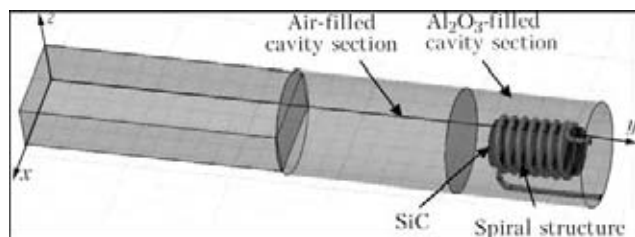


Figure 6. Design of  $\text{Al}_2\text{O}_3$ -filled cavity with the SiC centred in spiral flow structure

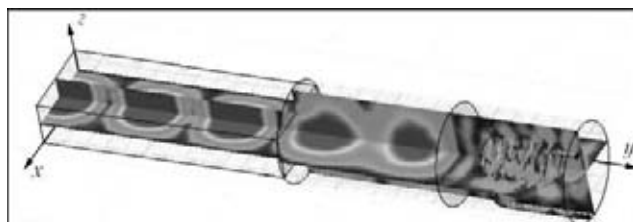


Figure 7. 3D view of the field strength

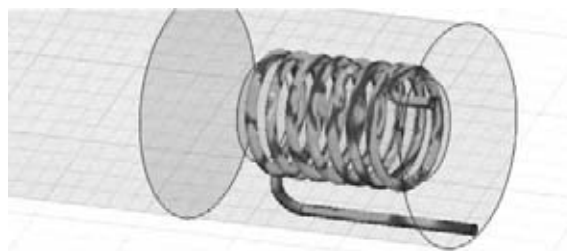


Figure 8. Field strength plot along the spiral length

mal spraying system, the whole spiral configuration is enclosed within the dielectric heat source. A SiC tube is used, with the one end sealed with a SiC disc. In order to avoid uneven distribution of temperature, due to the cooling effect of the inlet tube, the later is designed to cross through the centre of the spiral configuration as depicted in Figure 9. Therefore, the flow path structure can be pushed inside the dielectric and all the spirals to their external perimeter are in contact with the heat source, as shown in Figure 10. A big source of heat losses is the heat energy escaping from the cavity walls. The temperature induced in the dielectric will conduct throughout the whole material to bring it in equilibrium. Although the spiral flow path will absorb the temperature from the centre of the dielectric, a large amount of heat energy on the surface of the dielectric will conduct to the cavity walls and from there to the environment constituting heat losses.

The filling medium within the heat source is selected to be alumina powder (Figure 11, *a*). The SiC powder has higher thermal conductivity and would be more appropriate to use but if it melts it solidifies in a strong mass that cannot be removed and in the case of failure the whole assembly would have to be disposed. The alumina powder, on the other hand, if it melts and solidifies it can easily be broken and the various parts of the assembly can be freed. Therefore the heat source and the spiral flow structure can be reused, depending on the position of the failure.

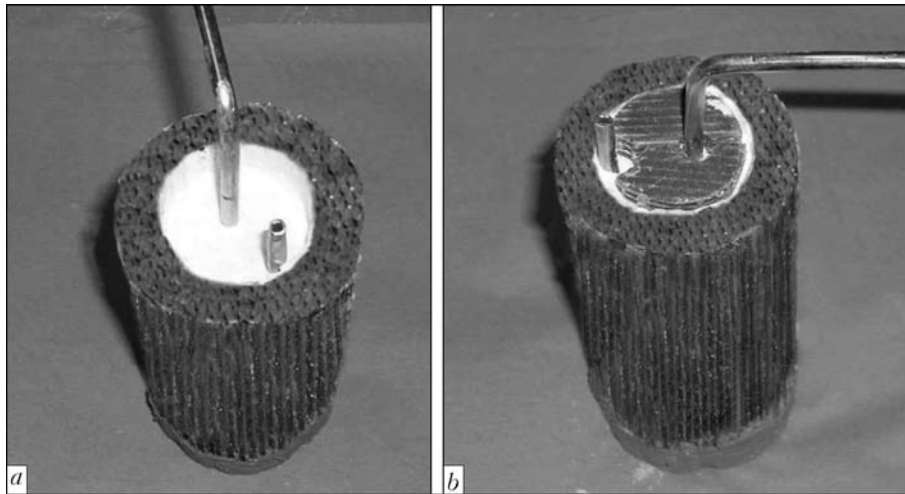
Another SiC disc is further used to seal the front end of the dielectric tube, as shown in Figure 11, *b*. This way the alumina powder is firmly trapped inside and furthermore the spiral is protected from arcing effects. Because the open end of the dielectric tube is close to the end of the cavity, the electromagnetic field will be intense at that point. Arcing is therefore possible between the short circuiting flange of the



Figure 9. Spiral flow path with inlet tube running through the centre



Figure 10. Spiral structure pushed inside SiC tube



**Figure 11.** SiC tube with spiral structure filled with  $\text{Al}_2\text{O}_3$  powder (a) and sealed with SiC disc (b)

cavity and the spiral structure as it can easily penetrate through the alumina powder. The SiC disc will ensure that there is no arcing reaching the spiral inside the dielectric tube.

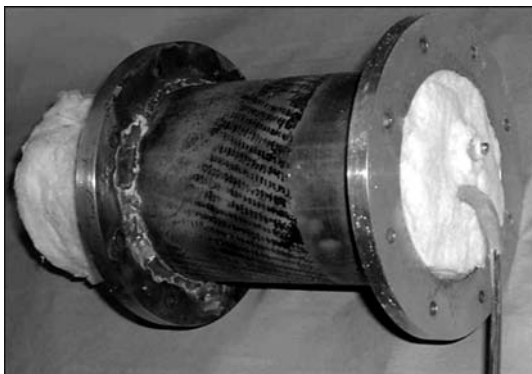
In order to minimise the losses from the perimeter of the SiC tube a heat insulator is used to surround the dielectric and fill the gap between the later and the cavity walls (Figure 12). This heat insulator is a superwool blanket. Its exact dielectric properties are unknown because it is a synthetic material. However, considering that it is made 60–70 %  $\text{SiO}_2$  that has a dielectric constant of 3.8, 25–35 %  $\text{CaO}$  with dielectric constant of 11.8,  $\text{MgO}$  with 9.7 and traces of  $\text{Al}_2\text{O}_3$  with 9.0 the overall material is expected to have a small dielectric constant. This was verified by experimental results that showed no interference with the microwave electromagnetic field.

The spiral heat exchanger built for the modelling purposes consists of 7 spirals with 10 mm gap in-between and 25 mm diameter (Figure 13). The gas inlet crosses through the inside of the spiral structure and bends to form a helix configuration. Once the spiral was designed, it was placed inside a SiC tube of 98 mm length, 32 mm inner diameter and 14 mm thickness with both ends sealed. The inside gap that is not occupied by the volume of the spiral is defined as alumina. The assembly was then placed in a circular cavity (Figure 14) and simulated at the microwave frequency of 2.45 GHz. The

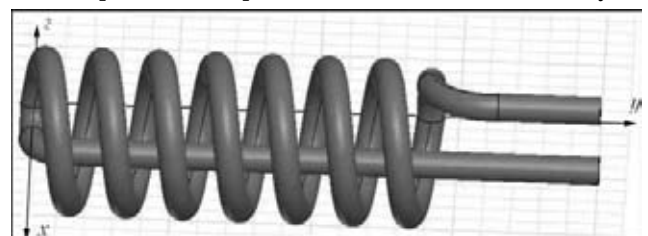
field distribution along the horizontal and vertical plane is depicted in Figure 15.

Figure 15 shows that the E-field in the second section of the cavity is non uniform and high field strength spots are scattered around and inside the SiC. Because the SiC is a dielectric, there is no threat of an electrical discharge across the cavity walls, so the microwave power is dissipated as heat on the walls of the dielectric. This means that substantial energy is consumed on the surface of the SiC. Therefore, most of it will be wasted as heat losses on the cavity walls rather than being conducted throughout the dielectric material. More high field spots are located inside the SiC and around the spiral that would normally suggest a risk of an electrical discharge. However, because the spiral structure consists of one bulk material and is isolated from any other conducting material, like the cavity walls, such threat is diminished. This leaves only the threat of a corona discharge. In practical experiments, though, no such effect was observed so it can be assumed that most of the power is induced as heat in the dielectric.

In order to suppress the heat losses and as applied in practice, an insulating material is used wrapped around the SiC. The enclosing dielectric heat source, in the practical experiments, was surrounded by a



**Figure 12.** Heat source wrapped with superwool heat insulating blanket within the cavity



**Figure 13.** Spiral structure

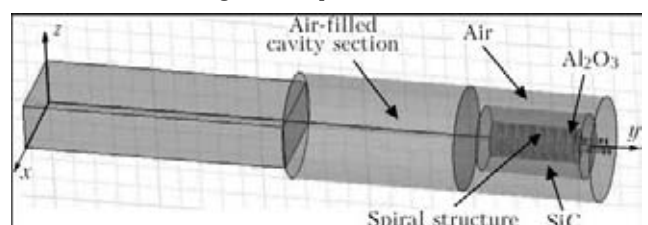


**Figure 14.** Design of SiC enclosing spiral flow structure

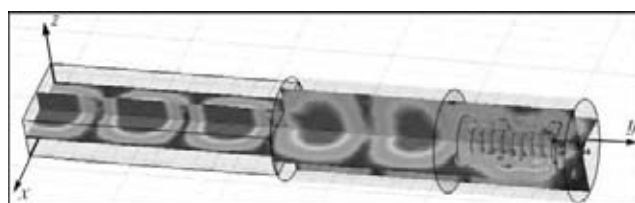


Figure 15. 3D view of the field strength

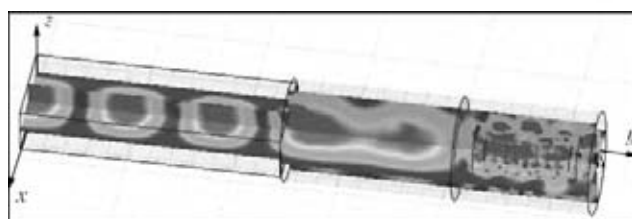


Figure 17. 3D view of the field strength in final design

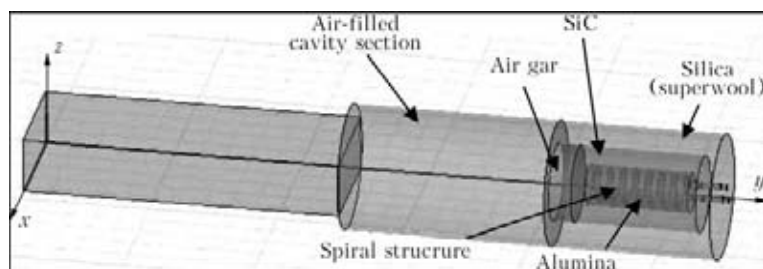


Figure 16. Design of silicon carbide enclosing spiral flow structure wrapped in silica

superwool blanket. This insulating material appears as a dielectric inside the cavity that effects the E-field distribution. In order to simulate the impact of the superwool blanket on the microwave field, the SiC heat source is surrounded by a silica material. In practice, the insulating material is wrapped around the SiC and also covers the front end where the nozzle is exerted. A gap of air is therefore left in the back end facing the power source as it is the only point not occupied by the superwool, as seen in Figure 16. Although the insulating blanket is made of many materials for ease of design and with approximation the material is selected to be  $\text{SiO}_2$  as it is the dominant constituent (60–70 %). The introduction of the silica around the silicon carbide (Figure 17) significantly changes the pattern of the E-field.

Inside the cavity the E-field appears to be concentrated mainly in the centre of the dielectric load and across the  $yz$ -plane centred to the cavity. Although on the horizontal sides of the cavity the field is weak, on the top and bottom sides of the  $yz$ -plane there is high field intensity. Outside the SiC it seems to be spreading almost radial across the cavity walls. It can be visualised as if the field is confined inside the cavity along a  $yz$ -plane centred to the cavity, inside the SiC tube. As discussed previously the high field strength around and inside the SiC is unlikely to create an electrical discharge. The silica surrounding the SiC does not have a high enough dielectric to induce heat and since it is a heat insulator it can be assumed that the power is consumed in the SiC and induced into heat which is mainly conducted inwards towards the spiral. In this heating technique more power is wasted as heat losses but it can still operate at higher power levels keeping the system within the limits of an energy efficient thermal spraying method as it can produce a nitrogen gas flow temperature of about  $700^\circ\text{C}$  with power consumption of about 2 kW. The energy losses are a necessary compromise to ensure stability of operation.

## SUMMARY

The microwave thermal spraying technique utilizes the dielectric properties to produce heat with low power consumption and a metallic spiral heat exchanger to provide a long and uniform distribution of heat in a flow of gas and powder mixture. The presence of a metal spiral inside a microwave cavity, however, significantly distorts the electric field. This results in the creation of high field strength spots scattered inside the cavity and posing a threat of electrical discharge. However, with consideration of practical experiments and simulations, in the case of the enclosing dielectric these spots are eventually consumed in the high dielectric material inducing heat and at the same time isolating the metal heat exchanger from microwave exposure. Any spot outside the silicon carbide can be considered either as an eventual heat loss. Finally the presence of a dielectric medium in the cavity such as alumina provides a more uniform distribution of the field strength. In the case of the superwool blanket used in the final design, its use significantly distorts the E-field but in essence it reduces the heat losses without compromising the microwave absorption of the dielectric and consequently the induced heat. The system stability has been tested with the production of low melting temperature coatings such as babbitt and tin.

1. (1999) *Thermal spraying: new construction and maintenance*: EM 1110-2-3401, Jan. 29, 1999. U.S. Army Corp. of Engineers, p. 6.1–6.6.
2. Mavromatidis, P., Shaw, A., Al-Shamma'a, A.I. et al. (2004) 2.45 GHz microwave plasma system for high velocity thermal spraying. *J. Materials Proc. Techn.*, **153/154**, p. 294–299.
3. Mavromatidis, P., Al-Shamma'a, A., Lucas, J. (2003) High velocity thermal spraying using 2.45 GHz microwave plasma. In: *Proc. of 16th Int. Symp. on Plasma Chemistry* (Tarormina, Italy, June 22–27, 2003).
4. Langton, L.L. *Radio-frequency heating equipment*. Sir Isaac Pitman & Sons Ltd., p. 14–15.
5. Baden Fuller, A.J. *Microwaves: an introduction to microwave theory and techniques*. 3rd ed. Pergamon Press, p. 68–69.
6. Meredith, R. *Engineers Handbook of industrial microwave heating*. IEE, p. 3, 21–23, 32–33.
7. (2003) HFSS software for next-generation design. *Microwave J.*, **46(1)**, p. 148–152.

# METHOD OF OPTIMUM CONTROL IN TECHNOLOGICAL PROCESSES FOR WELDING AND FOR LOCAL THERMOCYCLIC TREATMENT

V. MELYUKOV<sup>1</sup>, A. KOREPANOV<sup>1</sup> and V. TYURIN<sup>2</sup>

<sup>1</sup>Vyatka State University, Kirov, Russia

<sup>2</sup>N.A. Dollezhal Research and Development Institute of Power Engineering, Moscow, Russia

In treatment of materials with concentrated energy sources, there are problems caused by the increase of the process productivity and the need to ensure high accuracy of a number of parameters. Many of these treatment processes are carried out under non-optimum conditions which do not utilize efficiently the energy and functional possibilities of concentrated sources, nor ensure the quality parameters of treatment which could be achieved otherwise. Analysis of the approaches and methods of determining the conditions show that determination of the mode is in its formulation an inverse problem. In formulating the problem of determining the conditions, the source of the thermal process must be determined from the required properties of the material or from the given temperature field, constructed taking into account these properties. In cases in which the aim of solving the problem is to determine the treatment conditions, the inverse thermal conductivity problem can be formulated as a problem of the optimum control of the thermal process. As an example of using the methods of the optimum control of the thermal processes, it is convenient to examine a welding process with following local thermal or local thermocyclical treatment of the welded joint.

In welding and other types of treatment of materials with concentrated energy sources, there are problems caused by the increase of the process productivity and the need to ensure high accuracy of a number of parameters. Many of these treatment processes are carried out under non-optimum conditions, which do not utilize efficiently the energy and functional possibilities of concentrated sources, nor ensure the quality parameters of treatment which could be achieved otherwise. In particular, the problem of determination of effective conditions and welding mode is especially acute when developing technological processes for new materials which have been examined insufficiently.

## Problem of determination of welding mode

In developing technological processes for welding, the conditions are often determined by empirical methods, which depend on the experience and knowledge of the technologist. This is followed by their verification. In this case, it is necessary to use handbook data and recommendations or specify the parameters on the basis of the technological experience followed by their correction on full-size specimens.

**Direct thermal conductivity problem.** The parameters are determined in many cases by calculation methods developed on the basis of the theory of thermal welding processes with taking into account the non-linear condition [1–3]. These methods make it possible to determine the welding conditions on the basis of computing experiments by solving a direct thermal conductivity problem.

The procedure used to select the required conditions on the basis of numerical modeling of a direct problem of thermal conductivity requires repeating

its solution for every given mode. Since the calculation model does not contain dependences which justify accurate and reliable selection of the type of source and its parameters with an allowance made for the requirement on the quality of processed material, the range of application of the calculation methods in developing technology and determining the conditions is restricted. In addition, it is necessary to correct the selected conditions by experiments on full-size specimens. This method of selecting the welding modes is ineffective when developing new technologies and under conditions of small-series and single-item production.

Determination of the welding conditions on the basis of solving the direct problem of thermal conductivity has now been used for many years when examining welding processes and developing technology. However, the absence in the solution of the dependence of the source parameters on the temperature field in the treatment zone and on the properties of the processed material does not make it possible to obtain effective sources with the optimum effect.

**Problem of welding process optimum control.** In solving the direct thermal conductivity problem, the reason-consequence relationship typical of the actual welding process the source-temperature field, is not disrupted. However, analysis of the approaches and methods of determining the conditions show that determination of the mode is in its formulation an inverse problem whose typical feature is the disruption of the reason-consequence relationship of the actual thermal process. In formulating the problem of determining the conditions, the source of the thermal process must be determined from the required properties of the material or from the given temperature field  $T'$ , constructed taking into account these properties [4, 5].

In cases in which the aim of solving the problem is to determine the treatment conditions, the inverse thermal conductivity problem can be formulated as a problem of the optimum control of the thermal process. At present, the methods of the theory of optimum control have been developed most extensively for linear systems. This makes it possible to formulate and solve the problems of controlling the welding processes on the basis of linear models. Taking into account the non-linearities to increase the accuracy of the calculation model by 5–10 % almost completely eliminates the possibility of optimizing the process, the search for new sources and the optimum treatment conditions.

In formulating the problem of optimizing the thermal welding process on the basis of the model of the linear inverse problem of thermal conductivity, the problem can be solved using methods of the theory of optimum control of systems with distributed parameters. With the restriction  $0 \leq q \leq q_{\max}$  for the variation of the power in accordance with the actual energy characteristics of the concentrated energy sources, the problem of optimum control of the thermal welding process in relation to its formulation can be solved using the maximum principle, the moment methods and finite functions. In contrast to the problems of classic variation computation, optimum control  $q$  is determined in a restricted region from zero to  $q_{\max}$  and is of the piecewise-continuous type with a finite number of interruption points of the first kind. The property of the inertialess, almost instantaneous and jump-like variation of the individual parameters of concentrated energy sources makes it possible to model more accurately these parameters in the group of piecewise-continuous or piecewise-constant functions. These properties are shown in most cases by the electron beam and the laser radiation.

#### Optimising of process for circumferential welded joint

With welding circumferential joint of pipes the heat flow circuits in direction of the welded joint and forms a closed circuit. The effect of closed heat flow influences on the heat weld process and this influence depends on values of radius  $r$  and thickness  $s$  of pipe wall. The influence becomes impotent if ratio  $s/r$  remains 0, 1 and more. In order to stabilize a heat regime and dimensions in the cross section along the entire circumferential joint it is necessary to use the mathematical model of thermal process in a moving cylindrical coordinates  $y, \theta, r$  (Figure 1) and to optimize the welding process. The cylindrical coordinates  $y, \theta, r$  are attached to welding source, which move at constant speed  $V$ .

**Mathematical model of thermal process.** Let us assume that the heat input per unit thickness of pipe wall is constant; then heat conditions are the same throughout the thickness  $s$ , and the function of temperature  $T$  must be independent on  $r$ , i.e.  $\partial T / \partial r \equiv 0$ . In this case function  $q$  of the volume source must be also independent of  $r$ . From this we may infer that

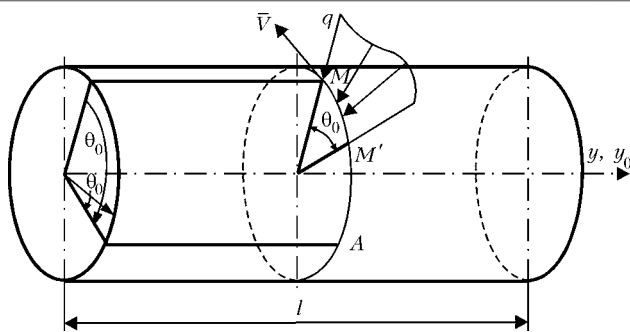


Figure 1. Scheme of pipe and cylindrical coordinate system

in this problem the radius  $r$  is constant and its value must be equal the medium radius of pipe.

Taking into account this simplification we have 2D heat process of circumferential welded joint. The mathematical model of this process in cylindrical coordinates  $y, \theta$  is a non-stationary equation of heat conductivity with boundary conditions of the second kind.

The differential equation of heat is expressed with partial derivative of  $T(y, \theta, t)$  with respect  $y, \theta, t$  and the function  $q$  must be in the equation. In this case we get [6]

$$\frac{\partial T}{\partial t} = a \left( \frac{\partial^2 T}{\partial y^2} + \frac{1}{r^2} \frac{\partial^2 T}{\partial \theta^2} \right) - \frac{V}{r} \frac{\partial T}{\partial \theta} + \frac{q}{c_v}; \quad (1)$$

$$T(y, \theta, 0) = \varphi(y, \theta);$$

$$\lambda \left( \frac{\partial T}{\partial y} \right)_{y=0} = q_1(\theta, t); \quad -\lambda \left( \frac{\partial T}{\partial y} \right)_{y=l} = q_2(\theta, t). \quad (2)$$

where  $T(y, \theta, t)$  is the temperature of welded pipes which is a uniform distribution through thickness of pipe wall;  $q(y, \theta, t)$  is the power density of volume moving source;  $V$  is the speed of a moving source;  $\theta$  is the angle of rotation of the welding source;  $r$  is the medium value of pipe radius.

**Equation solution.** The solution of the equation (1) with the boundary conditions (2) is obtained by use of integral Fourier transformation:

$$T_{n, m}(t) = \int_0^l \int_{-\pi}^{\pi} T(y, \theta, t) e^{-in\theta} \cos \mu_m y dy d\theta, \quad (3)$$

where  $l$  is the total length of two pipes;  $i$  is the imaginary unity;  $\mu_m = \pi m / l$ ;  $m = 0, 1, 2, \dots$

The solution of equation (1), reduced to the form of an integral equation, can be written in an abbreviated form as follows:

$$G(y, \theta, t) = \int_0^t \int_0^l \int_{-\pi}^{\pi} q(\eta, \alpha, \tau) K(y, \theta, \alpha, t, \tau) d\tau d\eta d\alpha, \quad (4)$$

where  $K$  is the kernel of the integral equation. This kernel is a cosin series. The function  $T(y, \theta, t)$  and boundary conditions go in the expression of function  $G(y, \theta, t)$ .

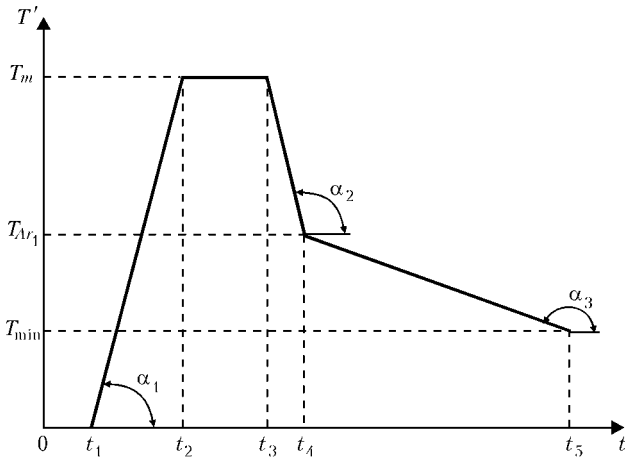


Figure 2. Simple thermal cycle

The temperature  $T(y_0, \theta_0, t)$  in non-moving system of coordinates  $y_0, \theta_0$  which is attached to the pipe may be determined from (4) using the transformations of coordinates

$$y = y_0, \quad r = r_0, \quad \theta = \theta_0 + \frac{Vt}{r}. \quad (5)$$

**Given temperature distribution.** In order to formulate the problem of optimum control of a welding process it is necessary to construct a given temperature distribution taking into account required properties which determines a weldability of materials to be welded and a quality of the weld metal. The heat conditions and the dimensions in every cross section along the entire joint must be stabilized during welding process. For stabilization of these conditions the required thermal cycle must be done in every point of the welding zone. In this case the welding thermal cycle must determine a maximum temperature of heating and a rate of heating or cooling in every point.

**Model of required thermal cycle.** In this case we shall set the main parameters of welding thermal cycle. As an example we take the model of simple thermal cycle (Figure 2) which was proposed by Prof. Rykalin [1].

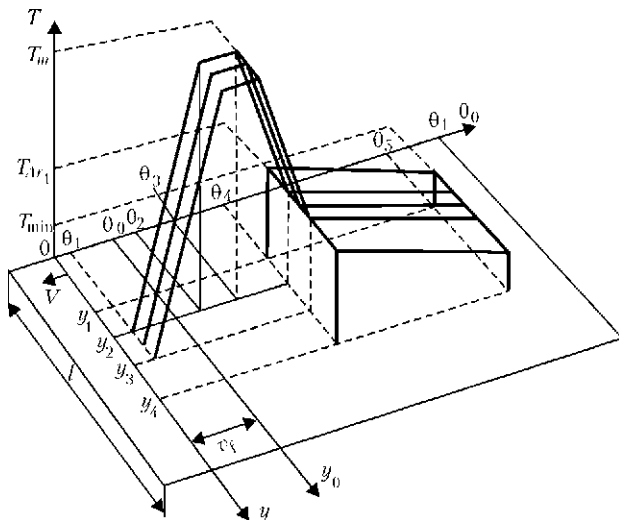


Figure 3. Given temperature distribution

Let us set values of the main parameters:  $T_m, T_{Ar1}, T_{min}, \omega_1, \omega_2, \omega_3$ , where  $\omega_1, \omega_2, \omega_3$  are the rates of heating ( $\omega_1$ ) and cooling ( $\omega_2, \omega_3$ ) during welding;  $T_m$  is the maximum temperature of heating, for example, a fusion temperature;  $\text{tg } \alpha_1 = \bar{\omega}_1$  is the given rate of heating up to the temperature  $T_m$  during the period of time  $t_2 - t_1$ ;  $\text{tg } \alpha_2 = -\omega_2$  is the given rate of cooling down to the temperature of a phase transition  $T_{Ar1}$  during period of time  $t_4 - t_3$ ;  $\text{tg } \alpha_3 = -\omega_3$  is the given rate of cooling to the temperature  $T_{min}$  of thermal treatment of a weld.

The time of heating and cooling may be defined from the next formulas:

$$t_2 - t_1 = T_m / \omega_1, \quad t_4 - t_3 = (T_m - T_{Ar1}) / \omega_2, \\ t_5 - t_4 = (T_{Ar1} - T_{min}) / \omega_3. \quad (6)$$

On the other hand, the parameters  $\omega_1, \omega_2, \omega_3$  may be determined from (6) if the values of the periods  $t_2 - t_1, t_4 - t_3, t_5 - t_4$  and the parameter  $T_m, T_{Ar1}, T_{min}$  are set.

Many steels, particularly, carbon ones, may be welded only in such a manner as there is no tendency to form by quick cooling (quenching) a hard and brittle constituent. The weldability of such steels depends upon the factors which govern the heat distribution and, primarily, the rate of cooling from  $T_{Ar1}$  to  $T_{min}$ . To prevent the appearance of hard and brittle constituent it is necessary to keep the rate of cooling  $\omega_3$  below the «critical cooling speed». Using this and any other conditions we can construct at every point of the weld zone the model of the required thermal cycle  $T'(t)$  which secures the weldability and quality of the weld metal.

**Function of the given temperature distribution.** On the pipe surface let us pick out a line which is normal to the pipes butt and is attached to the pipe. This line parallels the axis  $y$ . At every point of the line the required thermal cycles are constructed taking into account the width of the weld and the dimensions of the heat-affected zone. Constructing such thermal cycles at every point of this line we get a composition of the required thermal cycle  $T'(y, t)$ . After that using the transformation of coordinates (5) and formulas (6) we get the function of the given temperature distribution (Figure 3) which can be written as follows:

$$T'(y, \theta) = \begin{cases} \bar{\omega}_1 \frac{r}{V} (\theta - \theta_1), & \theta \in (\theta_1, \theta_2), y \in (y_1, y_2) \\ \bar{\omega}_1 \frac{r}{V} (\theta_2 - \theta_1) = T_m, & \theta \in (\theta_2, \theta_3), y \in (y_1, y_2) \\ \bar{\omega}_1 \frac{r}{V} (\theta_2 - \theta_1) - \bar{\omega}_2 \frac{r}{V} (\theta - \theta_3), & \theta \in (\theta_3, \theta_4), y \in (y_1, y_2) \\ \bar{\omega}_1 \frac{r}{V} (\theta_2 - \theta_1) - \bar{\omega}_2 \frac{r}{V} (\theta_4 - \theta_3) - \bar{\omega}_3 \frac{r}{V} (\theta - \theta_4), & \theta \in (\theta_4, \theta_5), y \in (y_3, y_4), \end{cases} \quad (7)$$

where  $\theta_1, \theta_2, \theta_3, \theta_4$  are the angular coordinates of the weld zone along circumferential joint. The values of this coordinates are got from the third formula of (5) at the moments of time  $t_1, t_2, t_3, t_4$  accordingly. The diagram of the distribution  $T'(y, \theta)$  and the axes  $y, y_0$  shown in Figure 3 are drawn conditionally on the plane for visual imagery.

**Formulating the problem of optimizing.** The solution of the differential equation of heat conductivity (1) written as the form (4) of integral equation permits to formulate the problem of optimizing and to use the maximum principle for the systems with distributed parameters [7]. The maximum principle is a method of the theory of optimum control. This principle may be used to solve the problems of control with the restrictions. Such problems with the restriction are so called incorrect problems which may be solved using the maximum principle [8].

The power of the welding source has the finite value and consequently the power density must satisfy the condition

$$0 \leq q(y, \theta) \leq q_{\max}, \quad (8)$$

where  $q_{\max}$  is the maximum value of the power density of the chosen weld source.

Let us formulate the problem of the optimum control as a correct problem by Tikhonov: «a simple thermal cycle is given taking into account the required properties of the welded joint. Using the equation (4) and the condition (8) the function  $q(x, y, t)$  of a moving welding source is to be found with the condition of the smallest deviation of calculated temperature  $T(y, \theta, t')$  from the given temperature  $T'(y, \theta)$ , where  $t'$  is the time of welding».

The smallest differences  $T'(y, \theta) - T(y, \theta, t')$  are determined by minimum of the quadratic functional [8]

$$J = \int_{-\infty}^{\infty} \int_0^l [G'(y, \theta, t') - G(y, \theta, t')]^2 dx dy \quad (9)$$

where  $G'(y, \theta, t')$  is determined by replacing in  $G(y, \theta, t')$  the function  $T(y, \theta, t')$  by the given temperature distribution  $T'(y, \theta)$ .

**Optimizing problem solution.** The function  $G'(y, \theta, t')$  is of the piecewise-continuous type with interruptions of the first kind, but  $G(y, \theta, t')$  is the continuous function. The control  $q(y, \theta, t)$  with the restriction (8) does not provide the identity

$$G'(y, \theta, t') = G(y, \theta, t').$$

Then the minimum of the functional (9) determines the optimum control  $q(x, y, t)$ ,  $t \in (0, t')$ . According to the maximum principle the optimum con-

trol under which the functional (9) reaches minimum is determined by the solution of integral equation. The solution of this integral equation leads in its turn to the solution of the system of non-linear algebraic equation [9]. As a result of the solution we get the function of optimum control:

$$q(y, \theta, t) = \frac{1}{2} q_{\max} + \frac{1}{2} q_{\max} \text{sign} \times \sum_{n=0}^p \sum_{m=0}^d \cos \mu_m y e^{-ab_{n,m}(t'-t)} \times \left[ \gamma_{1n,m} \cos n \left( \theta - \frac{V}{r} (t' - t) \right) + \gamma_{2n,m} \sin n \left( \theta - \frac{V}{r} (t' - t) \right) \right] \quad (10)$$

where  $\gamma_{1n,m}$ ,  $\gamma_{2n,m}$  are the solution of the system of  $(p+1)(d+1)$  non-linear algebraic equations. The expression (10) is the solution of the degenerated problem of optimum control which we get supposing for  $n$  and  $m$  the finite value  $p$  and  $d$  accordingly.

**Practical result.** The N.A. Dollezhal Research and Development Institute of Power Engineering uses the method of mathematical modeling and optimum control when developing technological process and local thermocyclic treatment of zirconium-niobium canals for operating nuclear power plants and research reactors. Welded joints of zirconium alloys work in corrosive medium, under pressure and at high temperatures [10].

The welded joint is the zone of structural heterogeneity and non-uniformity of the elastoplastic state. The problem of increasing the corrosion resistance and plasticity of welded structures of zirconium alloys is solved by modern scientific and technological methods using numeral modeling of the optimum mode for electron beam welding and following local thermocyclic treatment of the circumferential welded joint with the same electron beam.

The given temperature distribution (7) for welding and thermocyclic treatment must be constructed with taking into account of the corrosion resistance of the welded joint and plasticity of the zirconium materials. The plasticity and corrosion resistance are greatly affected by residual stresses. The most uniform distribution of the maximum heating temperature in the cross section of welded zone tail part, the smallest

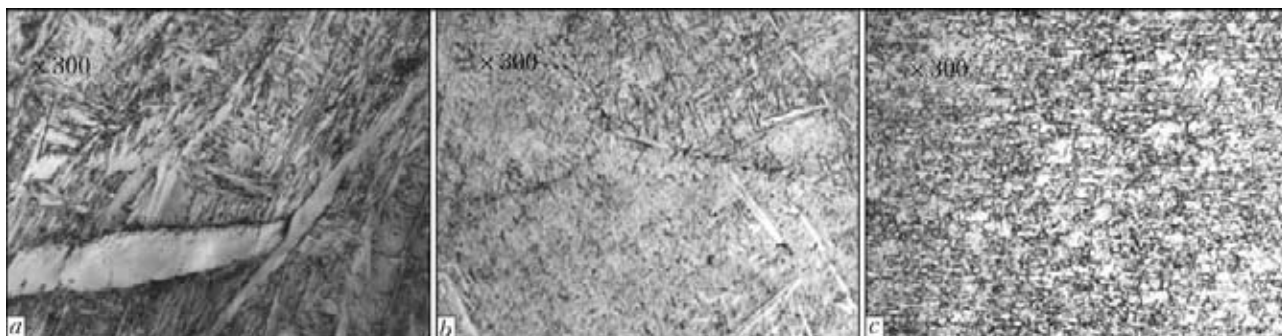


**Figure 4.** Results of metallography of the zirconium-niobium alloy welded joint: *a* – weld metal microstructure; *b* – weld metal microstructure after local thermocyclical treatment; *c* – HAZ metal microstructure after local thermocyclical treatment

width of the heat-affected zone and, correspondingly, the minimum heat input during welding. All these ensure the decreasing of the residual stresses in welded joint [11].

When local treatment performed, the electron beam is the surface source. It is known that the surface source has the optimum distribution of the power density  $q$ , i.e. the optimum form of the heat spot [11], there can be most uniform temperature distribution with respect to the thickness. In this case for the calculation of the optimum surface source we can use for the first approximation the mathematical model (1) and (2) with the volume source.

The maximum temperature  $T_m$  of heating, when performing the local thermocyclic treatment of zirconium-niobium alloy, assumes equal 900 °C and  $T_{\min} = 500$  °C.

The micrographs of structure of welded joint of the zirconium-niobium alloy are shown in Figure 4. Figure 4, *a* is the microstructure of weld metal after electron beam welding. This microstructure indicates the grains of welded metal and the rough martensite needles. Figure 4, *b*, *c* shows the microstructures of welded metal and of heat-affected zone metal after the local thermocyclic treatment of circumferential joint with the same electron beam. The grains of metal are smaller, the boundaries of martensite needles are dispersed, and  $\beta$ -phase of niobium is picked out.

## CONCLUSION

The optimum control of electron beam welding with following local thermocyclical treatment of welded joint made possible to reduce the heat treatment in furnace and at the same time to increase the quality of zirconium manufactures [12, 13].

1. Rykalin, N.N. (1951) *Calculations of thermal processes in welding*. Moscow: Mashgiz.
2. Uglov, A., Ivanov, V., Tuzhikov, A. (1980) Heat calculation of moving source taking into account the temperature-dependent coefficients. *Fizika i Khimiya Obrab. Materialov*, 4, p. 7–11.
3. Sudnik, W.A. (1985) Digitale und experimentelle Temperaturverteilung in der Schwei zone bei Einwirkung des defokussierten Energiestromes. In: *DVS-Berichte 99*. DVS, p. 158–161.
4. Melyukov, V.V. (1996) Optimising the thermal regime of the welding process. *Welding Int.*, 10(7), p. 571–573.
5. Melyukov, V.V. (1985) Optimum control of heat processes under the effect of concentrated energy fluxes on materials. In: *Effect of concentrated energy fluxes on materials*. Moscow: Nauka, p. 92–98.
6. Lykov, A.V. (1967) *Heat conductivity theory*. Moscow: Vysshaya Shkola.
7. Butkovsky, A.G. (1975) *Methods of controlling systems with distribution parameters*. Moscow: Nauka.
8. Tikhonov, A.N., Arsenin, V.Ya. (1988) *Methods of solving incorrect problems*. Moscow: Nauka.
9. Berezin, I.S., Zhidkov, N.P. (1962) *Computation methods*. Vol. 2. Moscow: Fizmatgiz.
10. Zajmovsky, A.S. et al. (1982) *Zirconium alloys in nuclear power engineering*. Moscow: Energoizdat.
11. Melyukov, V. (1997) Effect of the optimum thermal welding condition on residual strains and stresses in welded joints in Zr-2.5 % Nb alloy. *Welding Int.*, 11(8), p. 639–641.
12. *Patent 2259264 RU*. C1 2005.
13. *Patent 2259906 RU*. C1 2005.



# NOVEL OFFLINE ROBOT PROGRAMMING SOFTWARE

A. NICHOLSON<sup>1</sup>, J. NORRISH<sup>1</sup> and P. Di PIETRO<sup>2</sup>

<sup>1</sup>University of Wollongong, Australia

<sup>2</sup>ANSTO, Australia

This work was initiated to address the problem of automated weld repair of hydro turbine cavitation damage. An extensive review of the application requirements was undertaken [1] which highlighted the need for a new approach to robot programming. This led to the development of a novel rapid programming technique based on a vision system which involved the development of algorithms to correlate robot and vision system coordinates, communication links to the system hardware, and a software environment to «manage» the process. The complete system was successfully validated by representative trials on a full-size hydro turbine mock-up. This paper describes the software used to implement the vision based offline programming system.

Automated in-situ weld repair has been recognized for some time to potentially overcome issues relating to OH&S, poor weld quality, and excessive outage time. The advantages of using an automated system include the removal of the operator from a hazardous area, greater availability to repair zones, improved control of weld bead deposition, and ultimately reduced repair costs due to reduced downtime. A major obstacle for robotic repair is the time required to generate the robot program.

Prior investigations [2, 3] have indicated that robotic welding is a feasible option for reclamation of worn components, however, the time needed to develop a robot program has restricted robotic welding systems to applications with high production runs, justifying the programming effort with repeat execution of the one program. Where individual components need to be welded in various locations, each with unique wear patterns, tailored programs need to be generated quickly and easily. Traditionally, offline programming has used computer-aided design (CAD) data to assist in generating the weld paths necessary to perform repair operations, and the robot trajectories are simulated in software before downloading to the robot controller. Problems arise with this method when the damaged areas are unknown in size and location (and are undefined in the CAD model), direct weld path generation is impossible. Also, discrepancies with real world dimensions and CAD dimensions often lead to misplaced or poorly defined trajectories. These problems restrict the feasibility of robotic welding for smaller production runs, and, as a result, robotic welding systems have found limited acceptance in this market.

An offline programming methodology has been developed in this work that addresses certain shortcomings of robotic welding systems as described in the available literature. The methodology developed involves capturing image data from a torch-mounted camera and using software to assist the operator to identify damage and define a region for repair, calculating the necessary weld path strategy, automating

the robot program generation process, providing inter-cellular equipment communications, and monitoring and adaptively controlling the welding process.

**Control module.** For this application it was necessary to provide a PC-based control system for the cell in order to integrate monitoring and control of the robot, profile measurement, and control of the GMAW package. Although a specific software solution was developed for interfacing equipment in the robotic welding cell, it is likely that the approach could be adapted to other welding and non-welding applications involving the networking of processing equipment. Further detail can be found in [4].

**Surface mapping.** Various options were investigated in an attempt to automatically map the profile of the worn area and convert this directly into a robot program. Although techniques such as laser profilometry were considered, the initial study identified tactile scanning and video imaging as the most cost-effective and practical options. Touch-sensing was found to be effective but scan rates were low and would be impractical for large complex wear-damaged areas. Instead, a vision system which incorporated some touch-sensing functionality in the robot program was used. A CCD camera provides a very fast means of acquiring 2D information, and when used in conjunction with touch-sensing, 3D information can be constructed relatively quickly. Furthermore, program translations are possible since information about the TCP coordinates can be obtained from the robot controller. In this way, touch-sensing was used to calibrate programs written offline. Excellent accuracy is achieved due to this automatic self-calibration using touch-sensing. An alternate approach detailed in [5] mathematically calculates the workpiece position based on the focal lengths of two CCD camera lenses, and the distance between the two CCD chips.

**Image acquisition and processing.** To avoid problems with damage characterization and provide consistent target identification several programs were developed for live image acquisition and processing. Work initially concentrated on the recognition of the damage itself, but the inherent problems associated

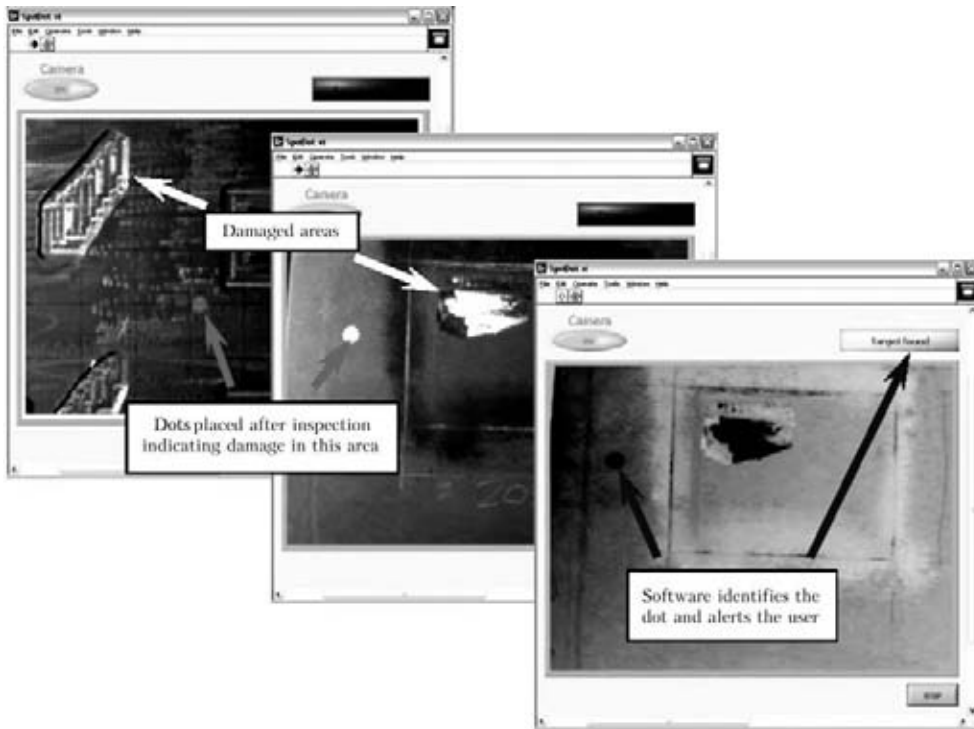


Figure 1. Small dots placed to indicate nearby damage

with object recognition (such as lighting) made this quite difficult. Rules must be defined for damage recognition, but the problem with evaluating damage in general is that damage is always unique in size and shape, so to program a set of rules to detect arbitrary areas of damage is almost impossible. There are different ways to handle this problem however. One method investigated was to place a small circular dot sticker near a damaged area on the workpiece (Figure 1).

The recognition of small dots is relatively easy to program into software. The dots all being the same size and shape makes defining rules for the recognition straight forward. Alternatively, there are certain filtering functions that can be performed on the image to help identify features that cannot be easily found otherwise. Techniques like this simplify the recognition of damage, but a higher level of intelligence (i.e. human intervention) is still required for absolute assurance that what is found is indeed damage. Shadows, surface marks, or slight deviations of surface profile all may be erroneously identified as damage. In this work, the identification of

damage is left up to human intelligence. If the small dot is placed near a damaged area, the recognition algorithm informs the operator that damage is in camera view, and to take a photo.

**Rapid weld path generator.** A new visual programming technique was developed in this work that allows an operator to visually program the robot on a PC using a mouse and associated software. Facilities for surface profile acquisition and manipulation of the welding path based on the wear pattern and profile are features of the software. In this paper, the acronym RAPID stands for Rapid Adaptive Programming using Image Data [6]. The RAPID Weld Path Generator program is explained below.

After starting the software the user imports an image taken from the torch-mounted camera. Image axes are created according to the robot position relative to the workpiece. The viewing window size is used as axes limits in the software, effectively calibrating the image.

With the image loaded in the GUI, the user defines a region around the damaged area using the mouse. The coordinates of the mouse clicks in the GUI are recorded and certain operations are performed to pick out valid points and discard invalid points, leaving only the peripheral points to form a closed boundary around all internal points. The input parameters are required for the weld bead geometry and location calculations to be made, after which the weld paths required to fill the region are generated.

**Weld bead geometry.** For GMAW, flux in wires and/or spatter reduce the volume of metal being transferred to the weldment. Grouping these into an efficiency factor  $\eta$ , the volume of metal per unit time being transferred to the weldment with efficiency  $\eta$  is equal to the volume of metal in the weld per unit time. Assuming a semi-circular cross-sectional area of



Figure 2. Main GUI showing generated weld paths

the weld bead, travel speed  $v_{tr}$ , wire diameter  $d_w$ , and wire feed speed  $v_f$ , this leads to

$$W_{bead} = d_w \sqrt{\frac{2\eta v_f}{v_{tr}}} \quad (1)$$

The offset between consecutive welds is calculated using the percentage overlap input value. For an overlap of  $\alpha$  %, the offset is

$$W_{bead} \times (100 - \alpha) \% \quad (2)$$

These calculations are necessary for the next step, determining the welding path locations. The information needed to cover a region with parallel weld beads are the start and finish points for every weld bead, and the offset between consecutive beads. The start and finish points will lie on the boundary defined by the peripheral points, and the offset is determined from Eq. 2 (Figure 3).

**Weld bead locations.** Given that the region to be filled will consist of a set of parallel weld beads, a baseline weld (from which all other welds will be offset) can be determined by creating a line function through the baseline points and offsetting this function (in image coordinates) by a portion of the calculated bead offset. The intersections of these weld path functions with perimeter functions constructed from line segments between boundary points determine the endpoints of the welds. Once all start- and stop-weld positions have been determined, the weld paths are superimposed over the area defined by the user in the GUI (see Figure 2). A robot program is then compiled which can be transferred to the robot controller for execution using the developed communications and control software.

**Discussion.** Due to the nature of cavitation damage, every repair situation will be different depending on the location, size, depth, orientation, and extent of the damage. Therefore, in-situ robotic repair of hydro turbine runners requires a robotic system capable of fast reprogramming and adaptive control. In the current work it was decided that the most critical aspect was the ability to develop a programming technique which made «one-off» tasks feasible or cost-effective. While the feasibility has been greatly improved with the techniques presented in this work, certain limitations have been identified, such as the curved/inclined plane problem as discussed in [7] (although suggested solutions are also presented). There also appears to be an inherent problem with image acquisition when structured light is not used. Great care is needed to achieve consistent and uniform illumination and even then, automatic feature recognition is still extremely unreliable with contrast variations likely to be experienced in this application. For these reasons it was decided to incorporate manual selection of the damage area. Manual selection is simple and quick, taking only a few seconds. It also avoids problems in damage characterization and hence erroneous auto-identification. While this involves an extra step it is far more robust.

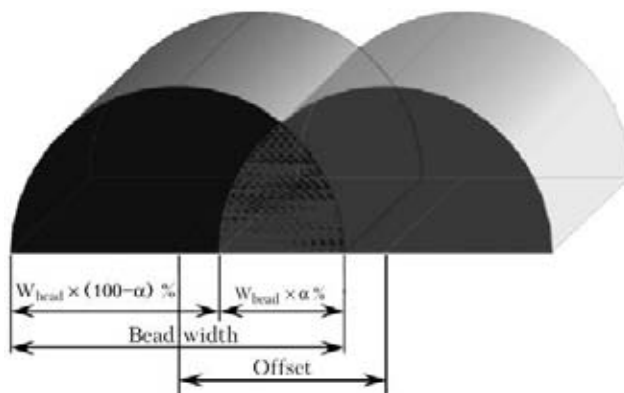


Figure 3. Weld bead offset illustration

## CONCLUSION

A novel programming methodology for robotic weld reclamation of worn components has been developed in this research. The literature available indicates the current feasibility and limitations of the technology, and in an attempt to alleviate some of the associated problems in «one-off» applications, a new adaptive technique was developed. This novel programming technique can generate complex robot programs in seconds rather than hours. Good quality GMAW positional welds have been produced using this rapid programming technique. The methodology and system have been successfully demonstrated in the laboratory. The technique developed is suitable for the target application, hydro turbine cavitation repair, and may be extended to many other wear replacement scenarios commonly found in industry. The technique has potential for direct application to generic weld programming as well as wear replacement.

**Acknowledgements.** The authors would like to thank colleagues at UOW for their assistance in preparing this paper. The authors would also like to acknowledge the support of the Australian Power Generation Industry and the Cooperative Research Centre for Welded Structures (CRCWS) for funding the research. The CRCWS was established and is supported under the Australian Government's Cooperative Research Centres Program.

- Nicholson, A. et al. (2002) In-situ weld repair of hydro turbine runners: A study of current practice and the feasibility of automation. In: *Proc. of IIW Asian Pacific Int. Congress* (Singapore, Oct. 29–31, 2002), No.54.
- Derwort, E. (2004) *The refurbishment of crawler shoes using robotic technology*: Dissert. UOW.
- Hydro-Quebec*. The SCOMPI™ technology for hydraulic turbine maintenance. Acc. 01/02. [www.ireq.ca/an/expertise/generation/index\\_scompi.html](http://www.ireq.ca/an/expertise/generation/index_scompi.html)
- Nicholson, A. et al. (2004) A PC based solution for integrated robot welding gell control: IIW Doc. XII-1828-04. In: *Proc. of IIW Com. XII on Arc Welding Processes and Production Systems* (Osaka, Japan, July 12–14, 2004).
- Tung, P.-C. et al. (2004) An image-guided mobile robotic welding system for SMAW repair processes. *Int. J. Machine Tools and Manufacture* (to be publ.).
- Nicholson, A. et al. (2005) Rapid adaptive programming using image data (RAPID). In: *Proc. of 53rd WTIA Ann. Conf.* (Darwin, Australia, Oct. 10-13, 2005), No.24.
- Nicholson, A. (2005) *Rapid adaptive programming using image data*: PhD Thesis. UOW.

# MODEL FOR DISTANCE LEARNING OF WELDING ENGINEERS AND SOME EXPERIENCE WITH ITS APPLICATION

J. NORRISH

University of Wollongong, Australia

The University of Wollongong (UOW) and the Cooperative Research Centre for Welded Structures (CRCWS) has developed a distance delivery program closely aligned to the syllabus prescribed by the International Institute of Welding (IIW) for the International Welding Engineer Diploma. The post graduate program is delivered by means of learner directed texts supplemented by multimedia content and four intensive one-week «summer» schools. Tutorial support is offered via the Internet. The paper will describe the format and methodology adopted and will review the benefits and limitations of the approach. The program has been running for the last 5 years and some experience gained from its application will be discussed.

The move to uniform international qualification standards in welding were originally recognized in Europe in the late 1980s prompted by the harmonization of standards in the European Community. Subsequently the systems developed have been adopted by international welding bodies [1]. The need for professionally qualified welding engineers has been recognized by International standards ISO 3834 [2] and the requirements for Welding Coordinators are set out in EN 14731-97 [3]. This requirement was also recognized in Australia in 1994 by the creation of two postgraduate courses (one at the University of Adelaide and the other at UOF). Both courses followed the European Welding Federation (EWF) prescribed syllabus and were accredited by TWI in the UK under the EWF scheme.

These courses were run for 5 years and following completion of their studies several candidates successfully completed the European Welding Engineer (EWE) examinations set by TWI and were awarded the EWE qualification.

Whilst the recognition of the qualification and the demand for the courses increased, the number of students who were able to complete the courses was restricted in Australia by demographic considerations\*. These conditions made it difficult for students to attend either of the two instructional nodes and the relatively small numbers made it uneconomical to replicate the courses at other locations.

In order to cater for the widely distributed student population the CRCWS and UOW developed a flexible (distance) delivery alternative to the on campus course. This course which was launched in 2000 uses the latest techniques of learner directed teaching and

web-based technology. The course is offered as a post graduate diploma leading to the award of the UOW Graduate Diploma in Materials Welding and Joining and may be converted to a Master of Welding Engineering on completion of an additional dissertation.

It was agreed by IIW in 2001 that the course would be run on a trial basis to assess the suitability of this mode of instruction for education of IIW International Welding Engineers (IWE). The course was initially audited by the Australian Authorized National Body (ANB) of IIW and representatives of IIW commission XIV to ensure that the prescribed syllabus was met and the instructional methods were appropriate. A full «report of distance learning project» was prepared and submitted to the ANB and the IIW assessor in November 2000. At the time of commencement of the trial the course was unique and no guidelines for IIW compliance were available. During the last 5 years the IIW has recognized the importance of this mode of delivery and appropriate guidelines were developed and published as IAB 195-2004 [4] in December 2004. Following this initial approval the course has been operated for the last five years. Details of the course structure and teaching methods are given below.

### Flexible delivery mode

Flexible delivery combines the most appropriate teaching materials to enable students to study in their own time at remote locations. In the case of the Materials Welding and Joining Course the backbone of the teaching material is in the form of 12 learner directed texts or «study guides». Unlike books or lecture notes the study guides are designed to direct the student through the learning material (which may include external readings). To check student progress informally but frequently, self assessment questions are used. More formal assessment by the tutor is provided by the submission of written assignments. Each of the 12 study guides was originally backed by a web-based tutor. The web component was a purpose designed teaching package that allows the student

\*Australia has a small population and a large land mass and many students need to study part-time whilst maintaining paid employment.

Structure of Materials Welding and Joining Course

Module (IIW)	Subject	Reinforcement (residential school)
A. Welding processes and equipment	Introduction to materials welding and joining (901) Fusion welding, part 1 (902) Non-fusion processes (903) Fusion welding, part 2 (904)	Welding processes and automation (917)
B. Materials and their behaviour during welding	Introduction to materials and ferrous weldability (905) Ferrous metals, nickel alloys and wear (906) Non-ferrous metals and non-metals (907)	Weldability and wear (918)
C. Construction and design	Construction and design, part 1 (908) Construction and design, part 2 (909)	Design of welded structures (915)
D. Fabrication application engineering	Fabrication and applications engineering, part 1 (910) Fabrication and applications engineering, part 2 (911) Fabrication and applications engineering, part 3 (914)	Fabrication case studies and NDT (916)
Thesis Option – Master of Welding Engineering, students only		
Practical course – mandatory for IWE		

access to an expert tutor via a bulletin board but also allows the tutor to update course material continuously, supply links to information resources, supply electronic reference material, set quizzes to check progress and offer tips on learning techniques and presentation. To supplement and reinforce the text and web material 4 one-week residential units are included in the course. These «summer schools» are attended after completion of the subjects which make up each of the four modules of the IIW syllabus, which are welding processes and equipment (including welding automation), behavior of metals during welding (including surface engineering), design of welded structures, and fabrication and application engineering.

The face to face study during these intensive four weeks on campus allow presentation of multimedia material (video and computer software), laboratory classes, lectures from industry experts, industry site visits, group case studies, revision and tutorials. Each residential school includes a written examination which includes material from the previous module.

In addition some 60 hours of practical welding is required by IIW and this is currently available from one of the many approved local providers. In Australia the Technical and Further Education (TAFE) colleges provide this form of vocational training. In summary the course structure consists of 12 texts based distance delivery modules (learner directed texts), 4 weeks of on-campus delivery, web-based support and assessment, and 2 weeks of practical welding training.

The details are given in the Table, where the 9xx numbers are university subject codes.

**Text-based modules.** Each text-based module was derived from the previous on campus teaching material and is the equivalent of 30 hours of face to face on-campus contact. Like the on campus study it also requires the equivalent of 90 hours self study and assignments. The study guides are written by authors from the university and industry. Guided study of additional resource materials (text books and papers) is incorporated into the texts. These supplementary

materials are provided in the form of recommended text books, 22 technical notes (from the Welding Technology Institute of Australia), copies of relevant technical articles, and Australian standards.

The enrolled students are all provided with free access to «Australian Standards On-Line» which enables them to view and download all Australian and some international standards.

The UOW Centre for Educational Development and Interactive Resources (CEDIR)\* produces the final printed material; providing guidance on educational techniques prior to production.

**Practical welding training.** The 60 hours practical training is an optional (but highly recommended) requirement for the Graduate Diploma and Master of Welding Engineering qualifications at UOW but mandatory for IIW-IWE candidates. In Australia the format of TAFE course NBB 09 offers a suitable basis for this training. Alternatively students may satisfy the practical training requirements by completing vocational welding certificates 1-9 of Australian standard AS 1796 or its equivalent.

**On-campus component.** Some elements of the course require «hands on» experience and reinforcement which can only be gained in a laboratory, workshop or classroom environment. In the case of the UOW courses these include advanced welding process demonstrations, robot programming exercises, metallography and metallurgical examination of weld samples, and exposure to NDT techniques. In addition experts from such diverse industrial areas as construction standards, steel production, pressure vessel design, ECA and NDT provide lectures which illustrate the practical application of the course material. The students also participate in case studies which involve team work and real industrial problems.

**Web-based support.** A web-based support system was originally established using a purpose designed

\*UOW has considerable experience in flexible delivery methods and produces and offers a large number of distance learning courses.

educational authoring tool (WebCT) and this incorporated:

- update information and technical support on the coursework;
- multi-choice assessment tests and progress on student feedback;
- bulletin board for student queries.

This component of the course enabled interaction between students and teachers and was intended to take the place of normal face to face tutorials.

**Course duration.** The original on-campus course was conducted over 1 year but it was expected that the flexible delivery program would normally be completed in 2 years unless the student had no other commitments when it would still be possible to complete in 1 year.

**Assessment.** The introductory subject (ENGG 901) may be taken as a preliminary to the main course (e.g. as an undergraduate elective) and is assessed by assignments, a web-based quiz and a 2-hours examination.

Course assessment for the remainder of the course is continuous and based on two substantial essay assignments per subject, case studies and a 2-hour written examination on completion of each module (A–D) residential school. The final composite course mark for the University award is based on a weighted average of assignment, case study and examination results. Each subject is worth 3 credit points. The UOW Master of Welding Engineering is assessed in the same way but an additional 12 credit point dissertation is required.

For the IIW diploma it was originally decided in consultation with the ANB that the students needed to complete the graduate diploma course and University examinations before attempting the independent examination. This IIW examination consists of 4 two-to-three-hour written papers and a 1-hour oral examination. It was intended that the IIW written papers should be taken progressively immediately after each of the residential schools. In February 2004 the University and the ANB set combined written examinations followed by the IIW oral exam. All examinations complied with the IIW guidelines but were marked independently to meet the formal requirements of the University and IIW.

**Entry requirements.** The normal entry requirements are a first degree (equivalent to a 4-year bachelor degree) in an engineering or related science subject. These entry requirements are mandatory for IWE candidates although mature students may submit a compendium of evidence of prior experience and training for entry to the University Graduate Diploma (it is however made clear to students gaining entry to University courses via this route that it is not possible for them to apply for the IWE diploma).

**Student management.** Student management is achieved by a formal computer-based system at the University (student management package). In addition departmental staff maintain regular contact with the

students to issue course material, collect assignments and monitor progress. The student contact is facilitated by an integrated group email (student on line service SOLS) and progress and assessment results are posted on the same system.

#### **Progress**

Over the last 3 years the number of registered students has remained at between 15 and 20. A continuous intake policy has been maintained with students able to enrol at any time. Most students are «mature» and industry based with considerable welding technology and management experience. Although a large number of final year undergraduates have undertaken the introductory elective only a small number have progressed to the post graduate course.

The standard of coursework submitted by the students for the continuous assessment has been excellent. In most cases the assignments have been very well researched and indicate a firm grasp of the underlying principles. Similarly in the case studies students have demonstrated an awareness of the procedures and standards and have produced sound proposals. Although performance in multi-choice quizzes has been good the performance in the 2-hours closed book written examinations has been disappointing. The most common problems seem to be associated with poor examination technique. In spite of specific mentoring students continue to have difficulty in addressing the questions and providing sufficient depth in their answers. These performance characteristics may be associated with the fact that most of the students were undertaking welding engineering tasks similar to those posed in the assignments in their daily employment whereas most mature students were inexperienced or unfamiliar with examination technique.

The majority of students have been in full time employment whilst completing the course. This has led to extended periods of enrolment occasional withdrawal from the course and requests for deferment.

Many of these extended periods of study have been due to the employer changing the student role, often increasing his responsibilities or posting the student to a remote location or overseas project, in one case the student has deferred due to a period of military service.

**Delivery techniques.** Surveys of past and current students indicate that the text-based study guides and supporting material are well received since they allow considerable flexibility in study methods. The performance of the web-based component has been disappointing in spite of the fact that the product used is a state of the art proprietary package which has been well proven elsewhere. The main problem with this component appears to be student access to high bandwidth internet connections as well as the updating overhead for the teachers. Bandwidth is a particular issue when it is attempted to post complex graphics or video on the web-site. As a result many students do not utilize this facility but prefer to use e-mail to contact the tutor and other students. The main ad-

vantage of such a web-based system remains the bulletin board which allows student/student/teacher interaction.

**Amendments to techniques and procedures.** Since video information is extremely useful to reinforce an understanding of welding the bandwidth restrictions were viewed as a serious limitation of the web delivery approach. As a result it was decided to commit such material to CD-ROM or DVD. A trial of this approach was undertaken using a CD-ROM to provide all of the support material for the «Introduction to Materials Welding and Joining». The CD is accessed by a common web browser and would be easily transferable to a web platform. It incorporates course notes, animation and video footage. The CD has been trialed by over 200 undergraduate engineering students in Australia and the response has been extremely positive.

In reviewing the progress of the course several steps have been proposed in an attempt to improve quality, availability and completion rates; these include the adoption of a 6 session academic year with strong inducements to the students to complete at least 1 subject and preferably 2 subjects per session (8 weeks), use of a simple bulletin board and e-mail for student communication, and use of CD-ROM based supplementary material for high bandwidth material (video and animations).

## CONCLUSION

The flexible delivery approach has been well received by Australian industry and industry based students. The quality of work produced by the students in assignments and case studies has been excellent. The course completion rate has however been disappointing as has the uptake of IWE examination options. The poor completion rate has been attributed to diversion of employment and attempts to improve the situation by closer surveillance and reduced session durations have recently been implemented. Trials of supplementary CD-based multimedia content has proved very popular.

**Acknowledgement.** *The author would like to acknowledge the assistance of many colleagues at the University of Wollongong and the Centre for Educational Development and Interactive Resources for assistance in development of this course and the Co-operative Research Centre for Welded Structures for its financial support. The CRC was established and is supported by the commonwealth of Australia.*

1. Quintino, L., Ferraz, R. (2005) International education, qualification and certification systems in welding. In: *Proc. of Int. Congress* (Tel-Aviv, Israel, 2005), p. 24–41.
2. *ISO 3834:1999* Quality Requirements for Welding.
3. *ISO 14731:1997* Welding Coordination: Tasks and Responsibilities.
4. *IIW Guideline IAB 195–2004*.

## MOVING HEAT SOURCE MODEL CAPABILITIES IN LS-DYNA PARALLEL VERSION

M.V. PETRUSHINA

United Institute of Informatics Problems, NAS of Belarus, Minsk, Belarus

By means of Goldac moving heat source model incorporated in LS-DYNA, the processes of heat residual stress and strain formation are simulated for a frame. Heating and cooling process dynamics was studied taking into account convection and radiation losses and phase (melting and solidification) changes. Qualitative and quantitative results were obtained for residual stresses and strains for different directions and sequences of welds laying on. In conclusion a method of residual stress influence on the modal properties of the considered welded structure estimation was proposed.

**Moving heat source.** By means of Goldac moving heat source model incorporated in LS-DYNA the processes of heat residual stress and strain formation are simulated for a frame. Heating and cooling process dynamics was studied taking into account convection and radiation losses and phase (melting and solidification) changes. Qualitative and quantitative results were obtained for residual stresses and strains for different directions and sequences of welds laying on. In LS-DYNA 971 version the possibility of parallel coupled thermal analysis is incorporated for the moving heat source model.

The examples with box and frame structures were considered. The stress and strain fields for the fillet and circular welds correspondently are obtained using

Goldac moving heat source [1] (Figures 1, 2) and by welding process simulation by modeling laser interaction with the sample [2]. The results were compared and rather good correlation was found in the resulting shapes of plastic zones and their dimensions. Also weld end effects were revealed in both types of thermal-stress simulations.

Coupled thermal-stress analysis were carried out using moving heat source, the stresses and strains were found. This type of analysis helps to appreciate the shape and dimensions of plastic zone that occurred in standard welded joints, to find the peculiarities of different extent welds and determine weld ends effects. Thus, in spite of using artificial analytical formulas for the dimension of plastic zone applicable only for the simple joints that do not contain information about end effects it is possible to use information from virtual tests. These two types of information about plastic zone dimensions were compared for standard joints (Figure 3). The information obtained from numerical tests is trustworthy and applicable to all kind of joints and welding process conditions, contains additional information absent in the traditional plastic zone calculation recommendations, has explicit 3D character and can further be used in the modified shrinkage force method [3].



Figure 1. Goldac moving heat source on T-joint

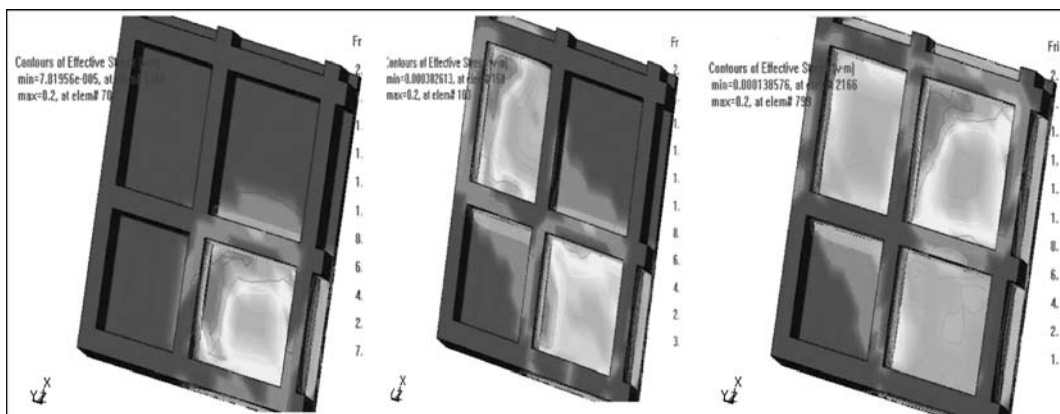


Figure 2. Von-Mises stress distribution in box structure during welding process simulation using moving heat source



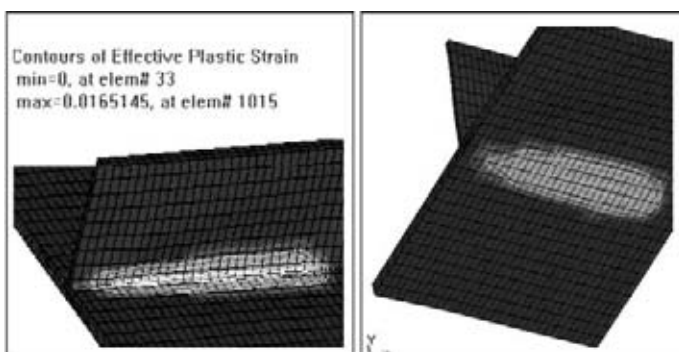


Figure 3. Fillet weld plastic zone obtained with Goldac moving heat source simulation

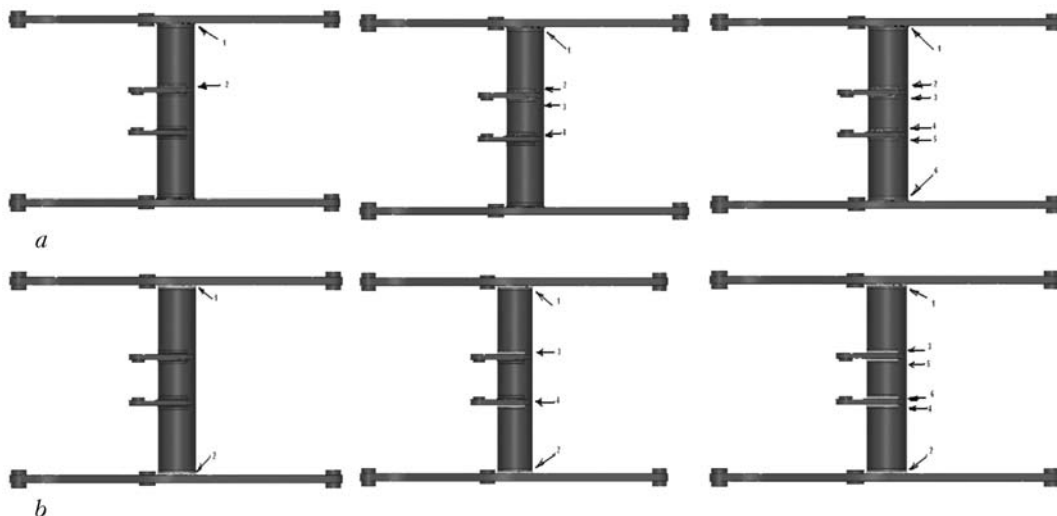


Figure 4. Sequences of weld laying on for the frame structure: *a* – consequent not optimal sequence; *b* – sequence which leads to lower result deformations

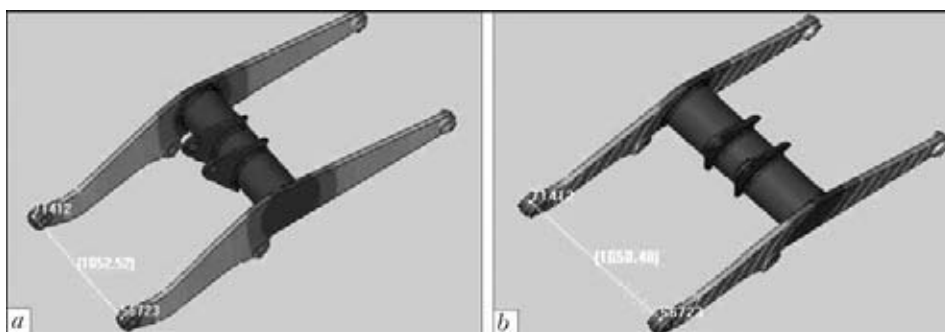


Figure 5. Sequences of weld laying on for the frame structure (*a* and *b* are the same as in Figure 4)

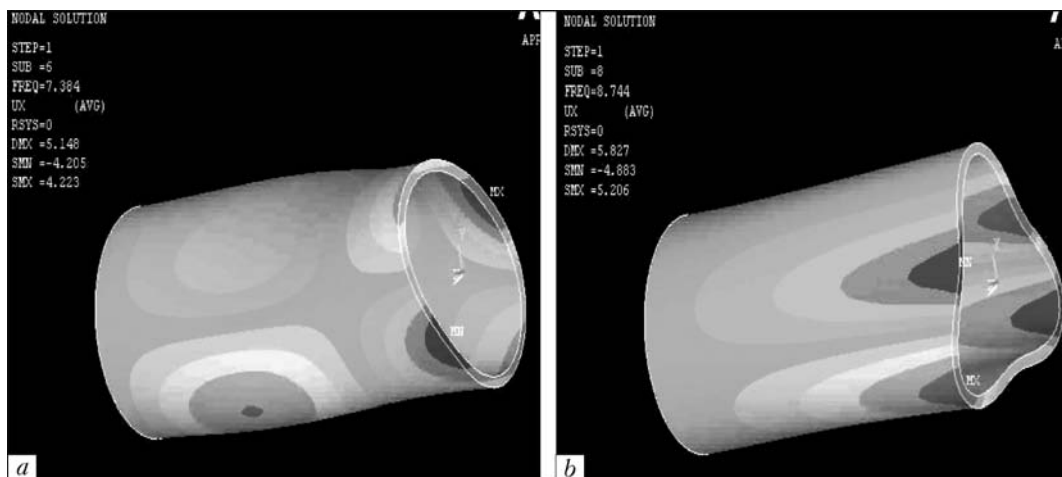


Figure 6. Typical mode shapes of the first 20 natural frequencies: *a* – 6th mode shape; *b* – 8th mode shape

**Weld sequences.** These two simple structures (box and frame ones) are also good examples to study weld sequence influence on the result structure deformations and stresses. Figure 4 shows the different sequences of weld laying on for the frame structure.

Figure 5 shows the difference in the result displacements. It can be seen that the second variant deformations are less. Coupled thermal analysis mppersion implemented in 971 version of LS-DYNA make it possible to carry out numerical simulation for the geometrically complicated and complex welded structures repeatedly changing welding condition parameters and welding directions and sequence. The frame presented in Figure 5 is quite simple. It contains six circular welds.

**Welded structure modal properties dependence on internal residual stress presence.** Though it is known from practice that modal properties of some welded structures undergo noticeable changes after joining (for instance, the fact that multiple welded pipes to the basic tube «clink» after welding), one

pays almost no attention to that phenomenon in comparison to the strength problems encountered during and after welding. One of the objective of this paper is to examine the consequences of welding process on modal properties of different nature welded structure.

Elaborated method [3, 4] of the residual welding stress simulating based on the shrinkage forces is used. The results are obtained in LS-DYNA and ANSYS-Multiphysics [5] finite element analysis package deployed on the SKIF family supercomputer [3].

Let us first consider a cylindrical welded structure constrained on the bottom and carrying one circled weld. It is a simplest example that can slightly model a cylindrical reservoir. First we find the values of natural frequencies for the cylinder without weld. These values for steel material with  $\rho = 7700 \text{ kg/m}^3$ ,  $E = 210$ ,  $\nu = 0.3$  are in the second column of the Table. The typical mode shapes of the first 20 natural frequencies are shown in Figure 6.

Using the elaborated shrinkage forces method [3, 4] the residual welding stresses and displacements

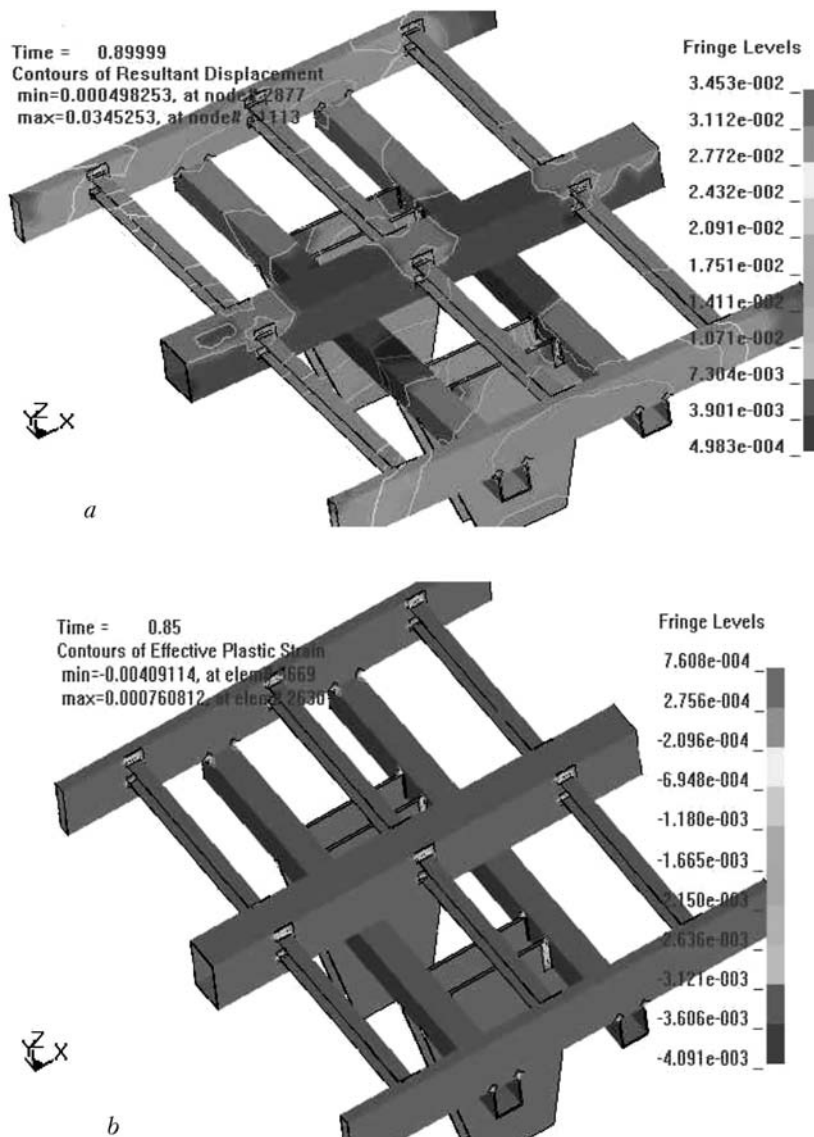


Figure 7. Deformation (a) and plastic strains (b) in welded structure

Natural frequency values for cylinder and frame structures without and with welding residual stresses

Mode shape No.	Natural frequency value, KHz			
	Cylinder		Frame structure	
	Without weld	With weld	Without weld	With weld
1	3.426	3.425	0.68393	0.069808
2	3.434	3.432	0.12399	0.123986
3	3.434	3.432	0.12845	0.128437
4	3.446	3.444	0.14505	0.144725
5	7.381	7.373	0.14785	0.147702
6	7.384	7.377	0.15912	0.159043
7	8.096	8.096	0.16237	0.162285
8	8.744	8.743	0.17804	0.178017
9	8.987	8.987	0.18074	0.180725
10	10.220	10.215	0.18778	0.187719
11	10.405	10.400	0.19042	0.190322
12	11.949	11.945	0.19499	0.194979
13	11.949	11.945	0.21547	0.215449
14	13.063	13.063	0.21742	0.217588
15	14.096	14.090	0.23950	0.239554
16	14.202	14.195	0.29163	0.291834
17	14.778	14.772	0.30160	0.301331
18	14.785	14.779	0.35751	0.357496
19	16.780	16.780	0.36984	0.369585
20	16.846	16.846	0.40026	0.399796

were simulated. The results for the natural frequencies for the welded cylinder are in the second column of the Table.

As can be seen from the Table, the natural frequencies obtained for the welded cylinder are slightly less than for the cylinder without weld. The value of

this difference depends on the mode shape type. Considered geometry has an axis of symmetry both for the cylinder and for the circular weld. Therefore there are some frequencies mode shapes of which correspond to the oscillations in the axis of symmetry direction that remain unchanged.

The presented example of a frame welded structure corresponds to real parts of agricultural machines. The frame was fixed on the bottom. Using the elaborated shrinkage forces method [3, 4] the residual welding stresses and displacements were simulated (Figure 7) and its natural frequencies were found for the model without and with welds (see the Table).

As can be seen from the Table, the sign of the changes in natural frequencies of the frame due to welding residual stresses is arbitrary and does not correlate with frame mode shapes. One can suppose that the character of the welding residual stresses influence on the welded structure modal properties depends on the complexity and shapes of the structure. Thus in some cases it is possible to say about the tendency of frequency shifts for a range of frequencies such as related to the one type of mode shapes. These phenomena can be anticipated in the structure analyses with the system symmetry presence. In other cases the influence of the welding residual stress can have no explicit dependencies.

1. Petrushina, M.V., Nikolajchuk, V.V. (2004) Modelling of shrinkage forces and moving heat sources for prediction of residual welding strains. In: *Mathematical Modelling and Information Technologies in Welding and Related Processes: Proc. of 2nd Int. Conf. (Katsiveli, Crimea, Ukraine, Sept. 13–17, 2004)*. Kiev: PWI, p. 225–229.
2. Petrushina, V., Pogudo, E.L., Chivel, Yu.A. (2006) Spherical powder sintering process simulation under laser pulse radiation. *Vysokotemp. Termofizika*, 44(1), p.148–152.
3. Medvedev, S.V., Petrushina, M.V., Tchij, O.P. (2004) Modeling of welded structures residual strains. In: *Proc. of 8th Int. LS-DYNA Users Conf.* (Dearborn, USA, May 2–4, 2004). Livermore Software Techn. Corp., p. 7–29.
4. Medvedev, S.V. (2002) Computer modeling of residual welding strains in technological design of welded structures. *Welding Int.*, 16(1), p. 59–65.
5. *Release 10.0 Documentation for ANSYS*.

## NEW QUALITY INSPECTION SYSTEM FOR AC RESISTANCE WELDING

A. PIETRAS, L. ZADROGA and Z. MIKNO  
Instytut Spawalnictwa, Gliwice, Poland

In the Instytut Spawalnictwa, Gliwice, the new system for monitoring of the parameters and quality inspection of the spot and projection welds made on the conventional AC welding machine was elaborated. In this paper the new system is presented. The LOGWELD system is enable to measure and check welding parameters (current, electrode force and voltage) and on the base of its run can elaborate the information about the quality of the joint. In the Instytut Spawalnictwa the research procedures and structure of the research stations for spot and projection welding were modified in such a way, which enables to record, process and transfer of measurement data from the LOGWELD device to the master computer. In this computer further data processing is conducted on the base of the new algorithms, which using the current flow, dynamic resistance and voltage profile recorded during welding, can estimate the dimensions of nugget and strength of the joint. This system enables to control welding condition in real time and furthermore for automatic inspections of welding quality.

### Model station for AC resistance welding

The modern station for resistance welding is based on standard welding machine ZPa-80 produced by ZAS ASPA in Poland. The welding machine is equipped with sensors and converters of important parameters of resistance welding processes, i.e. voltage, current, and electrode force. Computer system enables the measurements and recording of these important parameters. General structure of the station is shown in Figure 1 in a block diagram.

The system is controlled by the industrial computer equipped with controlling software and interface for measuring of electrode current and voltage. In Figure 2 there is a measuring and recording device LOGWELD designed for measuring, recording and transferring of selected results to managing computer, which communicates via internet network with computers in cooperating firms. Computer network was

constructed and activated in order to connect resistance welding stand with any computer at the Instytut Spawalnictwa. The system can collect research data.

During the works on model station at the Laboratory following specialised computer programs were developed [1]:

- program for recording and preliminary analysis of electrical characteristic, which controls the system of measurement and inspection of welding quality;
- program for final analysis of collected results of measurements.

The first program is installed on the LOGWELD device. Its task is to aid and accelerate recording of electrical characteristics, enable to preliminary monitor of measuring results and storage data on the computer disc.

The second program is installed on the computer in the technologist's office and its task is to analyse

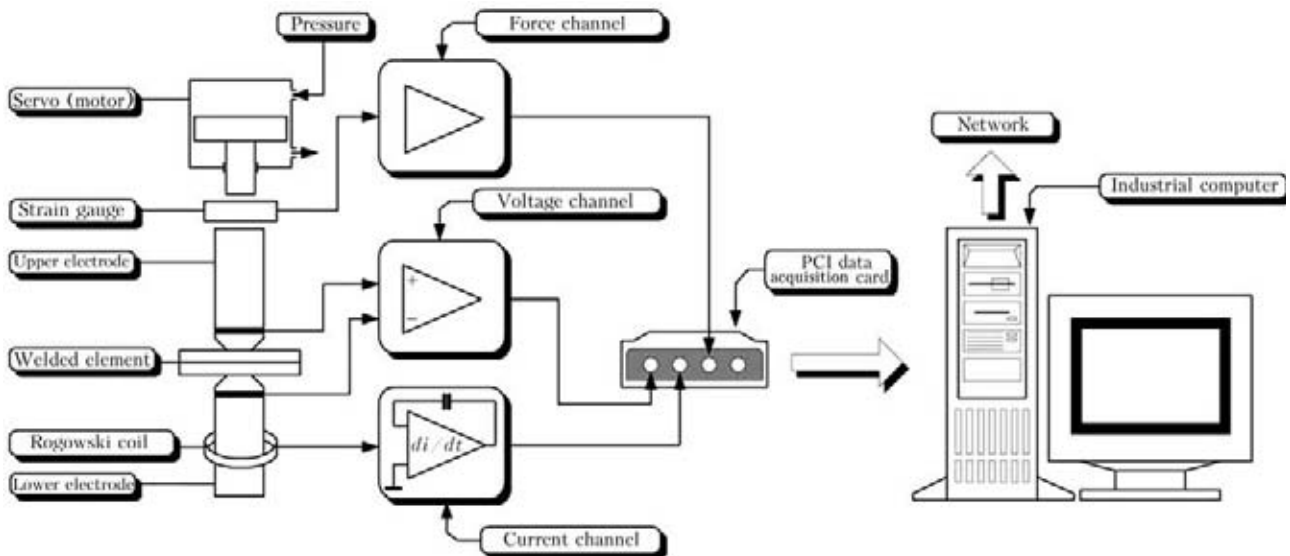


Figure 1. Block diagram of the measuring and recording of resistance welding parameters system



Figure 2. LOGWELD measuring and recording device

in details gathered data with use of algorithms designed for each technology of resistance welding. The algorithms take into consideration the needs occurring during quality inspection and research works.

Current version of the LOGWELD control program makes possible visualisation on the computer screen the characteristic of analysed parameters in graphic form (numerical and text fields) and adjustable elements such as slides and push-buttons.

In the Instytut Spawalnictwa Laboratory during past two years execution the system of distant quality inspection of resistance welding with use of developed device and software was tested while welding of just after welding [2]. Developed system enables the technologist to estimate quality of the resistance welding process in the distance, on the production stands in firms cooperating with the Instytut Spawalnictwa Laboratory, thanks to transferring data via computer network. The specially prepared data, recorded in production process, are processed and analysed with use of specialised research software.

#### Quality inspection of welds

The quality inspection of spot and projection welding made at AC welding machines, were conducted in support of measurements of process parameters, recorded with the use of LOGWELD device and mec-

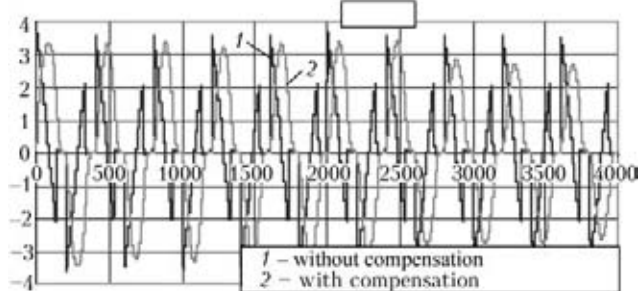


Figure 3. Exemplary run of the voltage with and without compensation

hanical examination of joint and metallographic examinations of welds. In the paper selected results of investigations concerning to spot welding are presented.

**The objective of researches.** The objective of researches was to elaborate methods of the quality assessment of spot and projection welding in support of recorded electrical characteristics of process parameters. During the researches relationships between actual electrical characteristics of welding parameters and the quality of obtained welds were searched.

**Research program.** Research program enclosed:

- recording of welding parameters;
- investigations of influence of the welding current and welding force on the run of recorded welding parameters and the properties of welded joints;
- investigations of mechanical properties of welds in the shearing test;
- investigations of mechanical properties of welds in the peel test;
- assign of the function approximating selected characteristic of process parameters;
- assign of the basic quantities characterized the quality of the welding process.

In order to compensate the voltage subjected interferences of the current flow, the additional measuring system was used in the welding area. Exemplary run of the voltage with and without the compensation is shown in Figure 3.

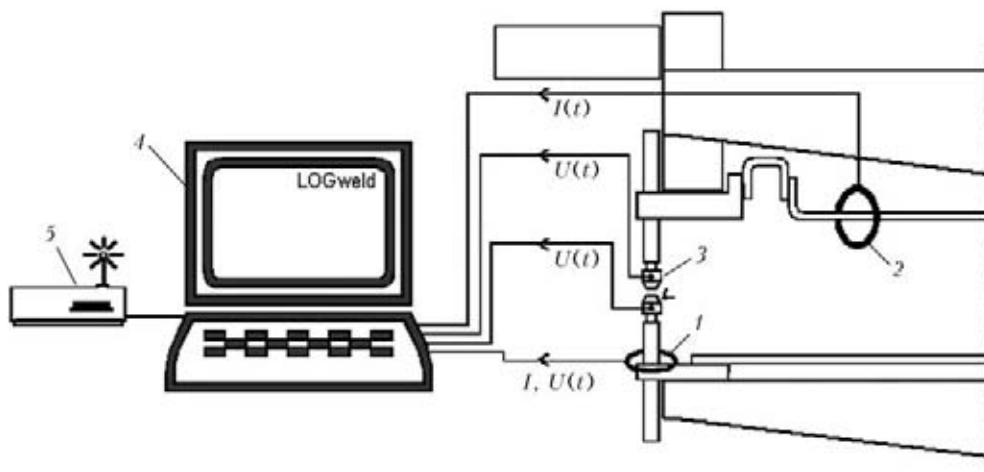


Figure 4. Test stand for measuring and recording of resistance welding parameters system: 1 – voltage channel with compensation circuit; 2 – current channel; 3 – voltage channel; 4 – LOGWELD system based on the industrial computer board; 5 – RF/IF transceiver

Processing, calculations and the analysis of measuring data were conducted with the use of Excel 2000. During the precise regulation of the welding force, device of TECNA 1416 was used. The measuring scheme is shown in Figure 4.

**Materials used for investigations.** For quality investigations in spot welding, sheets of 08J grade low-carbon steels 0.8 and 1.0 mm thick, electrolytic galvanized of about 9 μm Zn layer, were used. The welding machine was equipped in cup electrodes made of copper alloy of A2/1 class, CRM 16 grade, hardness HV 130 and appropriate electrical conductivity 45 MS/m (about 80 % of IACS). The diameter of electrode tips was selected in dependence of the thickness of welded sheets with formula  $d_e = 5\sqrt{\delta}$  mm, where  $\delta$  is the thickness of welded sheets.

**The way to conduct the investigations.** For spot welding sheets of dimensions  $30 \times 150 \times \delta$  were used. The distance between particular welds were about  $5d_e$  ( $d_e$  is the diameter of the electrode tips), that eliminated the influence of shunt current. Before welding, the surface of sheets were cleaned with the use of flannel cloth.

Optimal welding parameters were established experimentally using the work mode of the control system permitted for the stabilization of the welding current. Investigations were conducted at electrodes partially used up, with which 800 welds were made at optimal parameters before.

After preliminary series of welds was made, investigations of weld quality at different current and variable welding force were started.

The welding quality during the investigations was evaluated on the basis of visual test, run of electrical parameters, recorded with the use LOGWELD device, technological peel test, and shear strength test.

For every set of parameters, at least three welds were made, at the time the current and voltage were recorded. On the basis of recorded current and voltage runs of the following quantities were analyzed:

- peak current  $I_p$  [kA] (the quantity determined with the use of program of LOGWELD device);
- effective current  $I_{eff}$  [kA] (the quantity determined with the use of program of LOGWELD device);

- peak voltage  $U_p$  [V] (the quantity determined with the use of program of LOGWELD device);
- dynamic resistance  $R_d$  [μΩ] (the quantity determined with the use of program of LOGWELD device);
- energy supplied to the joint  $E = \Sigma UIt$  (calculated quantity);
- analytical coefficient  $K = I^2 R_d$  (calculated quantity);
- analytical coefficient  $M = I^2 t$  (calculated quantity).

Because particular quantities demonstrate large oscillation during formation of the weld, each run of quantities, taking into consideration in the analysis of the welding process, was approximated with the method of minimum of the mean quadratic deviation with the function  $F = f(t)$ . The correlation coefficient  $R$  of the function  $F = f(t)$  was calculated by formula (example for resistance):

$$R = \sqrt{\frac{\sum_{i=1}^n (R_{di} - R_d)^2 - \sum_{i=1}^n (R_{di} - R_{Di})^2}{\sum_{i=1}^n (R_{di} - R_d)^2}}$$

where  $R_{di}$  is the value of particular measurement data (resistance) recorded with the device or calculated direct from the measurement data;  $R_{Di}$  is the dependent variable in defined point;  $R_d$  is the mean value.

For each function the value of correlation coefficient  $R$  was higher than 0.9.

**Results and research analysis of resistance welding**

**Control and quality assessment of the weld formation process in support of dynamic resistance analysis  $R_d$ .** In result of tests and investigations it was found that important in the analysis is the run of the quadratic function approximating the run of dynamic resistance during modifications of resistance connected with the process of formation of the weld nugget and the coefficient  $a$  of linear function ( $f(t) = at + b$ ) assigned from the selected range of time interval (Figure 5).

Maximum of the quadratic function approximating the run of dynamic resistance is in the field in

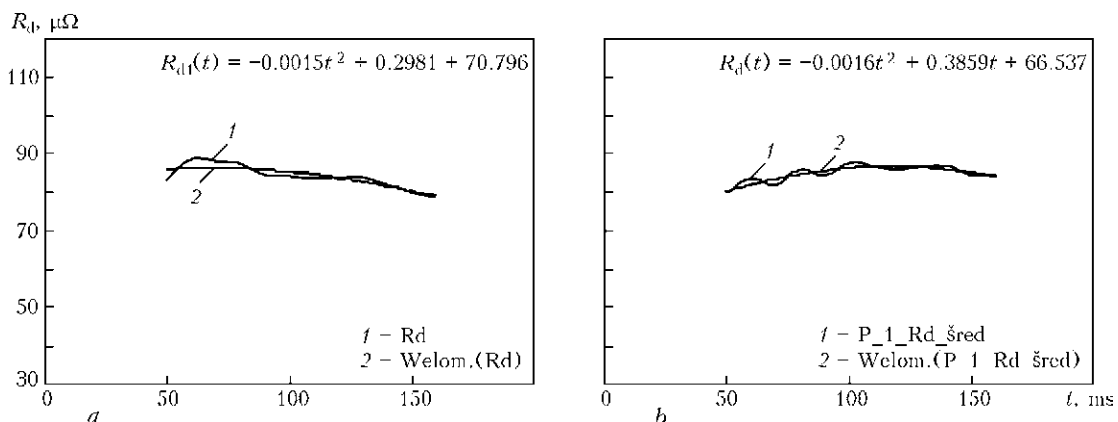


**Figure 5.** Exemplary run of dynamic resistance with the quadratic function approximation for joint performed with the use of most advantageous welding conditions (a) and too low welding current (b)

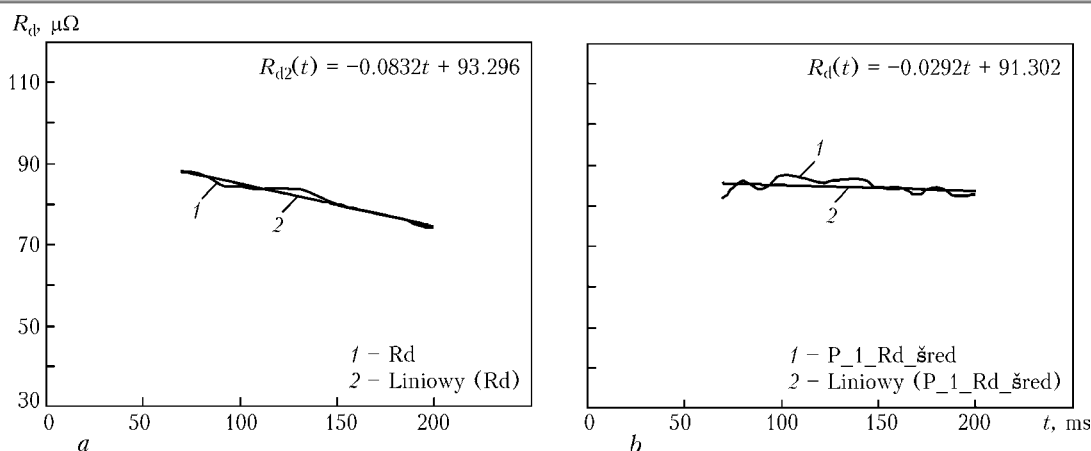


**Figure 6.** Exemplary run of dynamic resistance with the linear function approximation for joint performed with the use of most advantageous welding conditions (a) and too low welding current (b)

which initiation of the process of fusion of metal in the faying surface succeeds. For sheets 0.8 mm thick, the maximum is situated in the time interval from 50 to 150 ms, whereas for sheets 1.0 mm thick — in the time interval of 80–150 ms. The run of function is evidence of the process of weld formation. The earlier the maximum of the function approximating the run of dynamic resistance occurs, the faster conditions in the faying surface for fusion of metal are being create, and the longer is time for expansion of weld nugget.

The linear function approximates the run of dynamic resistance in the final interval of welding time (Figure 6). For 0.8 mm sheets, the linear function approximates the run of resistance in the time interval from 70 to 200 ms, whereas for 1.0 mm sheets — from 100 to 200 ms. The coefficient  $a$  of the slope of the function depends on the thickness of sheets. Decreasing character of function indicates at loss of resistance in welding area, what testify about quantity (volume) of fusion metal in the faying surface.

In results of investigations it was found that the higher absolute value of the coefficient  $a$  of the linear function (the function is decreasing), the larger amount of metal in the faying surface undergoes a fusion. In case, when the linear function approximating the run of resistance is growing, it testifies about defective run of welding process.

*Sheets 0.8 mm thick.* In case of carry out welds with the most advantageous parameters, the maximum is being achieved after 90 ms (about 45 % of the total welding time,  $t_{total}$ ). The coefficient of the linear function  $a = -0.090$  (peel diameter  $d_p = 4.6$  mm, shearing force of weld  $F_{sh} = 332$  daN).

During welding of sheets with the high current, the maximum is being achieve already after 75 ms (40 %  $t_{total}$ ),  $a = -0.177$  ( $d_p = 6.1$  mm,  $F_{sh} = 340$  daN).

The low welding current causes formation of the maximum only after 120 ms (60 %  $t_{total}$ ), for  $a = -0.020$  ( $d_p = 3.1$  mm,  $F_{sh} = 230$  daN).

Welds made at high welding force achieve the maximum of function only after about 110 ms (59 %  $t_{total}$ ), for  $a = -0.030$  ( $d_p = 1.7$  mm,  $F_{sh} = 265$  daN).

At low welding force displacement of the maximum of the function approximating the run of dynamic resistance to time 85 ms takes place (42 %  $t_{total}$ ), for  $a = -0.100$  ( $d_p = 5.2$  mm,  $F_{sh} = 340$  daN).

*Sheets 1.0 mm thick.* In case of carry out welds with the most advantageous parameters, the maximum is being achieve after 119 ms (about 60 %  $t_{total}$ ), for  $a = -0.241$  ( $d_p = 6.3$  mm,  $F_{sh} = 558$  daN).

During welding with high current, dynamic resistance achieves the maximum of the function after 107 ms (about 53 %  $t_{total}$ ),  $a = -0.957$  ( $d_p = 6.1$  mm,  $F_{sh} = 550$  daN).

In case of welding with a low current, the maximum of resistance is being achieve after 133 ms (about 66 %  $t_{total}$ ), and  $a$  obtains the value of  $-0.086$  ( $d_p = 3.0$  mm,  $F_{sh} = 490$  daN).

At high welding force the function approximating a dynamic resistance, achieved the maximum only after time 135 ms (about 67 %  $t_{total}$ ), for  $a = -0.056$  ( $d_p = 3.7$  mm,  $F_{sh} = 535$  daN).

At low welding force, the time to achieve the maximum of the function is cutting down till 106 ms (about 53 %  $t_{total}$ ), for  $a = -0.324$  ( $d_p = 6.0$  mm,  $F_{sh} = 550$  daN).

**Control and quality assessment of the weld formation process in support of energy supplied to the weld.** The energy supplied to the welding area (Figure 7) was assigned from the definition of energy

$$E = \int_0^t p(t)dt, \text{ where } p(t) \text{ designates the instantaneous}$$

power assigned as the product of the instantaneous values of the current and voltage, measured with the frequency 20,000 Hz. In the result of test and investigations it was testified that the coefficient  $c$  of the slope of the linear function ( $f(t) = ct + d$ ) assigned in the entire range of the welding process.

The angle of linear function (the coefficient  $c$  of function ( $f(t) = ct + d$ )) testifies about increase of the energy supplied to the weld and indirectly about the quality of the joint.

The most advantageous welding conditions for sheets 0.8 mm thick have characterized by the function

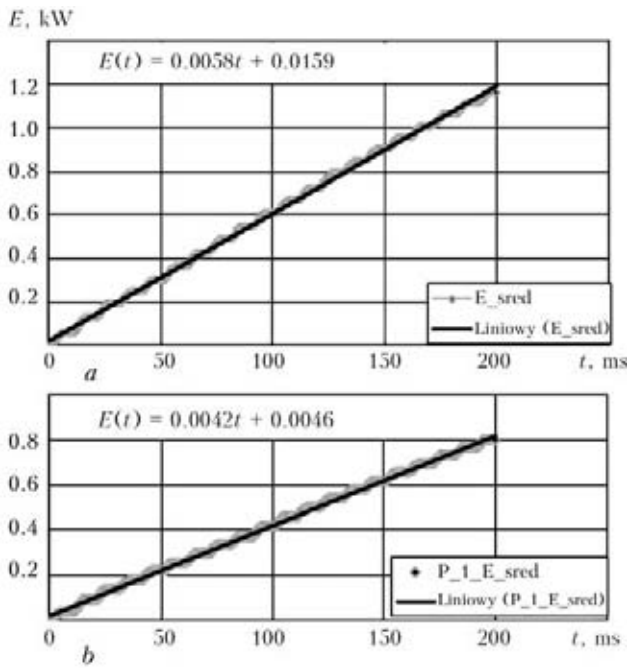


Figure 7. Exemplary run of energy supplied to the weld with approximating linear function for joint performed with the use of most advantageous welding conditions (a) and low welding current (b)

coefficient  $c$  from 0.0052 to 0.0054, whereas for sheets 1.0 mm thick – by the value of 0.006.

*Sheets 0.8 mm thick.* For welds carried out with high welding current the coefficient  $c$  of linear function describes the increase of the energy supplied to the weld was  $c = 0.0063$ , whereas with the low welding current  $c = 0.004$ .

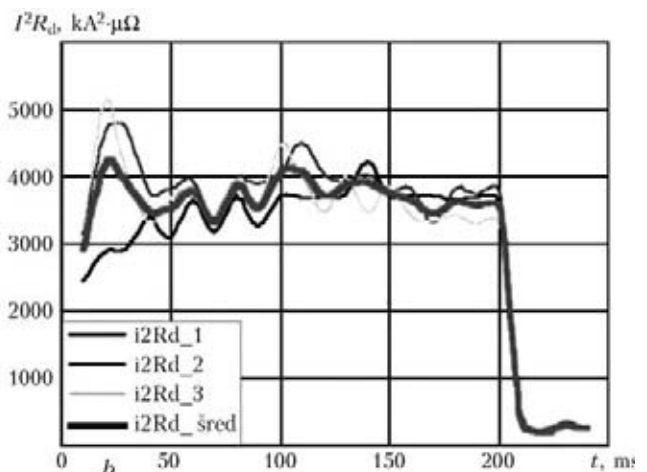
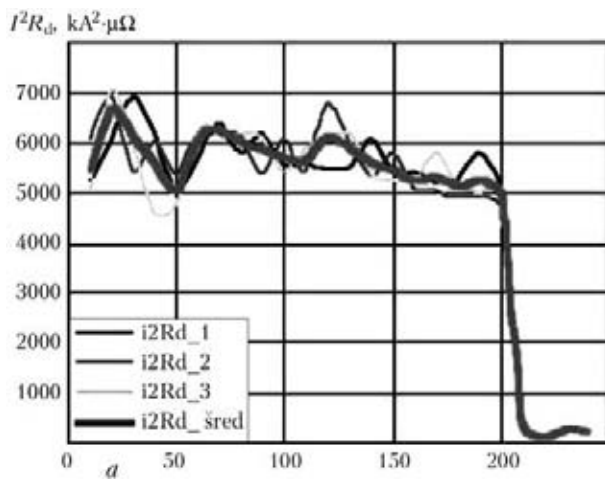


Figure 8. Exemplary run of computational coefficient  $K$  for joint performed with the use of most advantageous welding conditions (a) and low welding current (b)



Figure 9. Macrostructure of spot welded joint with correctly formed nugget of diameter close to electrode lap diameter ( $d_j = d_e = 5\sqrt{\delta}$ ):  $I = 8.3$  kA,  $t = 20$  pulses,  $P = 190$  daN ( $\times 40$ )

For welds carried out with high welding force the coefficient  $c$  of linear function describes the increase of the energy supplied to the weld was  $c = 0.0044$ – $0.0046$ , whereas with low welding force  $c = 0.0054$ – $0.0056$ .

*Sheets 1.0 mm thick.* For welds carried out with high welding current the coefficient  $c$  of linear function describes the increase of the energy supplied to the weld was  $c = 0.007$ , whereas with the low welding current  $c = 0.0037$ .

For welds carried out with high welding force,  $c = 0.0052$ , whereas with low welding force  $c$  was from 0.0066.

**Control and quality assessment of the weld formation process in support of analysis of the computational coefficient  $K = I^2R_d$ .** The computational coefficient  $K$  is strictly connected with actual value of the welding current and dynamic resistance of the welding area. The coefficient  $K$  is calculated from the quadratic of the effective current and from dynamic resistance assigned from the peak values of the current and voltage, measured in every half-period. Exemplary runs of changes of computational coefficient  $K$  during the welding process are shown in Figure 8.

During the work of the control system with stabilization of the welding current, the run of the coefficient  $K$  is strictly correlates with the run of welding power.

**Metallographic examinations.** Metallographic examinations were carried out on chosen welds in series, in purpose to determinate the correlation between the welding parameters and the quality of joints, and the structure of spot joints on 08J grade





**Figure 10.** Macrostructure of spot welded joint with small weld nugget of about 2.0 mm in diameter:  $I = 7.3$  kA,  $t = 20$  pulses,  $P = 190$  daN ( $\times 40$ )

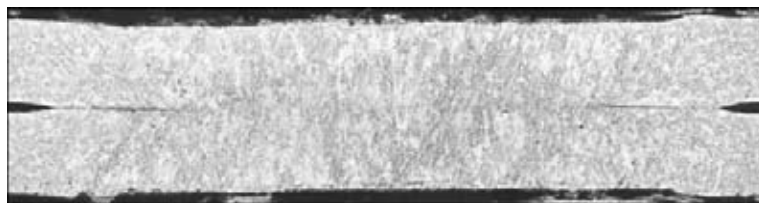


**Figure 11.** Macrostructure of spot welded joint with small weld nugget of about 3.0 mm in diameter:  $I = 7.3$  kA,  $t = 20$  pulses,  $P = 150$  daN ( $\times 40$ )

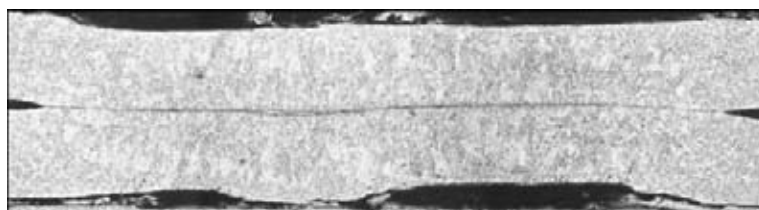


**Figure 12.** Macrostructure of spot welded joint with lack of weld nugget:  $I = 7.8$  kA,  $t = 20$  pulses,  $P = 300$  daN ( $\times 40$ )

steel sheets 0.87 mm thick, welded at different welding parameters. Chosen results of metallographic examination (Nital etching) are shown in Figures 9–12.

### Summary

Analysis of all data of the runs of electrical parameters and the statistic investigations have shown that during the resistance welding process the most advantageous is to control the run of dynamic resistance and the energy supplied to the welding area. The runs of these parameters the most adequate inform about the quantity of the heat input to the weld, the time of initiating the weld nugget formation, quantity (volume) of molten metal in the faying surface and indirectly about strength properties of welds.

In case of use the runs of the energy coefficient  $E$  for the current control of the welding quality, the most advantageous is analysis of inclination angle of linear function approximated increase of supplied energy  $E$  in welding (the coefficient  $c$ ) and the value of the total energy  $E_c$  supplied in the welding area. In the initial half-periods of the current flow, reliable randomness in the run of the value of energy, following from the matching of the electrodes to the sheets and from the process of current stabilization by the control system of the machine. For correctly made weld, the coefficient of the function should be  $c = 0.0055\text{--}0.0060$  (for 0.8 mm sheets) and  $c = 0.0067$  (for sheets 1.0 mm thick).

The value of the total energy supplied to the joint, calculated in the entire range of current flow, should amount for 0.8 mm sheets  $E_c = 1.15$  kW, for sheets 1.0 mm thick,  $E_c = 1.25$  kW.

In case of analysis of the run of dynamic resistance, selection of the range of the run of actual values of

resistance, took into account during the quality assessment of welding is very important. Initial decrease of dynamic resistance is connected with matching of the contact surface of the welding area (electrodes to the sheets and sheets in the faying surface) and changes of actual values of current and voltage, which may have the source in the stabilization processes realized automatically by the control system of the machine. In results of carried out analysis of the run of actual values of dynamic resistance, calculations of different approximating functions and computer simulation it was found that the most adequate for quality assessment is the range of the welding time, in which changes of dynamic resistance connected with the heat of metal in the faying surface and with the process of formation of the weld nugget proceed. These changes are situated in the range from 50 to 150 ms of the run time of the heat process.

For chosen range the quadratic function approximating the run of dynamic resistance was assigned. The function run testifies about the process of weld formation. The maximum of quadratic function approximating the runs of dynamic resistance is placed in the area, in which the initiation of fusion metal process in the faying surface took place. From the comparison of the runs of approximating function and results from the strength test follows that the earlier maximum of the function approximating the run of dynamic resistance occurs, the faster conditions for fusion metal in the faying surface are being created and the longer remains the time for increase the dimension of the weld nugget, guaranteed the appropriate strength.

From the investigations results follows that for correct performed welds the approximating function

achieves the maximum value for the time below 100 ms. In case of welding with the low current or with high welding force, time, for which the approximating function achieves the maximum value, displaced to the value exceeding 110 ms.

The additional, good quality indicator of forming weld is the run of the linear function approximating the run of dynamic resistance in the final time interval of welding. Decreasing character of the function indicates at decrease of resistance in the welding area what testifies about quantity (volume) of fusion metal in the faying surface.

In results of investigations and calculations it was found that for sheets 0.8 mm in thickness it is the best to approximate with the use of linear function the resistance run in the time interval of 70–200 ms, whereas for sheets 1.0 mm thick in the time interval from 100 to 200 ms. The higher is the absolute value of the coefficient of the linear function  $a$  (function decreases), the higher quantity of metal in the area of the faying surface fuses. This coefficient  $a$  depends on the sheets thickness. In case if the linear function approximating the run of resistance is increasing, it testifies about defective run of the welding process.

In case of the projection welding initial decrease of dynamic resistance is connected with matching of the contact surface of the welding area and with dynamic projection deformation in the initial stage of current flow. The runs of dynamic resistance of welding area in projection welding of bars and sheets are insignificantly different. Each of the technology requires an individual approach to determine the coefficients of the quality control. From our research results that the quality control should consists the following measurements: initial resistance  $R_{d\text{ in}}$  measured in 10 ms of current flow, dynamic resistance after stabilize the run  $R_{d\text{ stab}}$  measured in 30 ms of current

flow, and the change of the run of dynamic resistance  $R_d(t)$  in the time interval from 30 ms to the end of the current flow.

## CONCLUSIONS

For the quality assessment of the spot welding three quality factors should be take into account:

- time, for which square function approximating the run of dynamic resistance, takes the maximal value;
- value of coefficient of the linear function  $a$  approximating the run of dynamic resistance in the range of 70–200 ms;
- value of coefficient of the linear function  $b$  approximating the run of the supplied energy  $E$ , calculated as the product of the actual current values and the voltage.

For the quality assessment of the projection welding following factors should be take into account:

- value of coefficient of the linear function  $b$  approximating the run of the supplied energy  $E$ , calculated as the product of the actual current values and the voltage;
- value of the total energy supplied to the weld  $E_c$ ,
- value of dynamic resistance  $R_d$  assigned in 10 ms of the time of the welding current flow;
- value of dynamic resistance  $R_d$  assigned in 30 ms of the time of the welding current flow;
- value of coefficient of the linear function  $a$  approximating the run of dynamic resistance in the range from 30 ms to the end.

1. Zadroga, L., Pietras, A. (2004) *Studies and research in the quality control of resistance welding*: Work package Da-100. Gliwice: Instytut Spawalnictwa.
2. Pietras, A., Zadroga, L., Mikno, Z. et al. (2002–2005) *Project INSPAW*. WP 6. Polish Welding Centrum of Excellence.

# PROGRAM-TECHNICAL COMPLEX ON THE BASE OF THERMAL CUTTING MACHINES OF RITM-TYPE FOR OPTIMAL NESTING OF METAL, DEVELOPMENT OF NC PROGRAMS AND CUTTING OF PARTS

A.M. PLOTNIKOV, N.G. KARPOUSHKINA and D.G. PAUTE

FSUE Central Research Institute of Shipbuilding Technology, St.-Petersburg, Russia

The complex includes thermal cutting machines of RITM-type and upper level CAD system RITM-RASKROY. A new generation of TCMs is provided with modern control systems, characterized by using of industrial computers and digital valve-type servo actuators, as well as components available in European electronics market. This is an open architecture control system, which allows using modular design to satisfy customers' requirements. Functional software allows flexible setting of control system. The machine can be adjusted for gas, plasma and combined cutting. CAD RITM-RASKROY is purposed for nesting of metal plates and development of NC programs for cutting. The system provides automatic nesting of material, interactive drawing of nesting plates, cutting routes, output of NC programs for nesting and cutting using necessary formats and codes. Nesting can be done for thermal and mechanical cutting, panel and sheet-type for cold pressing.

Central Research Institute of Shipbuilding Technology (CRIST) has been producing thermal cutting machines since the beginning of 1970s. We have manufactured over 1000 machines (Cristall and Granat types), being now in operation at shipbuilding enterprises as well as in other industrial sectors in Russia. In parallel we developed automated means for metal plates nesting and elaboration of NC programs for parts cutting-out using various hardware and operational environments. Automated operator stations for nesting and preparation of NC programs were delivered to the customers both along with machines and separately.

One of the most vital activity for CRIST is now series production and delivery of program-technical complexes on the base of RITM-type thermal cutting machines [1] for optimal nesting, preparation of NC programs and parts cutting-out. Delivery set of the complex includes upper level CAD system RITM-RASKROY [2].

**Thermal cutting machines of RITM-type.** RITM-type machine [1] is actually a kind of «processing center», allowing up to five processing operations to be performed, namely oxygen cutting, plasma cutting, marking, nesting and grooving for welding (with oxygen or plasma).

Control system, employed in a cutting machine, has great effect upon processing quality. During recent decades several generations of NC systems for cutting machines have been changed. First NC systems were created on the base of ferrite-transistor modules (FTM) and were classified as NC-type. Operational algorithm of such devices is built-in in the circuit and cannot be changed after their manufacturing. NC programs from perforated tapes were inserted with photo readers. NC-type systems had poor reliability and did not allow changing of operational algorithm and technical parameters of cutting machine. Components for such systems

were taken out of production in the beginning of 1980s. However, many enterprises continue to operate such thermal cutting machines, exploiting skills of experienced maintenance personnel. Control circuit of electric drives was also built of the base of FTM, and was introduced as a pulse-phase system, controlled with unitary code (pulse sequence).

In 1980s CRIST conducted research on NC control systems on the base of medium integration level ICs, however only pilot samples were manufactured. At the same time a decision was taken to apply commercial NC control systems from other manufacturers. Concern LEMZ on the base of NC system 2R32 has developed and delivered device 2R32T for thermal cutting machines. This device was later modernized and got index RM33. These systems were of CNC class. Their operational algorithms were program-based and written to the memory, thus could be further modified. Control circuit for DC electric drives, developed by CRIST, were based on transistor-type pulse-width converter. Further, since own-made drives did not show sufficiently high reliability, valve-type electric drives of EKRU-1 type, developed in Cheboksary, were employed.

Unfortunately, new researches on thermal cutting machines were closed in CRIST since the end of 1980s. A decision to resume development and manufacturing of new generation of thermal cutting machines was taken in 1997. By that time electronic products from leading international manufacturers were available in Russian market, so that they could be used for Russia-made NC systems. In such a situation, one of two possible approaches for designing of NC systems could be accepted.

The first approach presumed integrated development of a control system (CS) on the base of own circuit design, including local specialized controllers for electrical automatics and electric drives. Such approach requires considerable time for design and stand trials of pilot samples of separate units and modifications

of machines. This is a practice of world leading companies, such as ESAB, Messer Griesheim, etc., which can afford expensive R&D works, returning investments due to low production cost of series manufacturing.

Another approach presumes development of CS on the base of standard commercial components, such as NC CS, industrial computers and controllers, servo drives, power sources and circuit components. In this case expenses are minimal and production cost is comparably low, since components with same performance parameters are available from various manufacturers with considerable difference in their price.

We in CRIST have chosen the second option, since manufacturing of large series of machines is not economically effective by now. Furthermore, the customers require various types of cutting machines, which can vary sometimes quite considerably. During recent three years CRIST has manufactured 11 machines, with only three of them of the same type.

Our specialists did not accept using commercially available NC systems, because as a rule they are intended for a certain group of machine tools, mainly metal processing ones (such as laths, milling machines, processing centers, etc.). To employ them for CS of thermal cutting machines certain expenses are required for software and hardware adjustment. Moreover, this presumes usually a certain hardware redundancy of the NC system. All this makes control system much more expensive, taking also into account that commercial NC systems are mainly supplied by leading electronic manufacturers (like Siemens, Fanuc and others), and their items are more expensive due to an internationally recognized brand name.

We develop NC systems on the base of IBM compatible industrial computers and specialized standard modules, such as input-output modules for discrete data, control modules for servo drives, etc. Hardware configuration is specific for each particular task, thus excluding unnecessary hardware redundancy and reduces price of the NC system. These electronic components are supplied by dozens international manufacturers, therefore an optimal price/quality ratio can be selected.

Another major component of CS is servo drive. Mostly, thermal cutting machines are equipped with commercial Germany- and Japan-made valve-type servo drives. Valve-type (synchronous) electric mo-

tors show high reliability and practically do not require any maintenance.

With this approach to design of CS for thermal cutting machines, our specialists implemented manufacturing of state-of-the-art thermal cutting machines with reliability and performance parameters comparable to analogs, manufactured by well-known international manufacturers. At the same time, price and operational expenses of our machines are much less.

Main performance parameters of RITM-M thermal cutting machines are as follows:

Thickness of plate to be cut, mm:	
for plasma torch (depending	
on power source type) .....	1-100
for gas torch .....	5-200
Plate width, m .....	2.5-5.0
Plate length, m .....	2-34
Number of torches (carriers), pcs .....	up to 4
Torch travel speed, m/min .....	0.1-12.0
Voltage, V .....	380
Program tracing accuracy, mm .....	±0.35

The machines can be modified for gas, plasma and combined cutting. We produce machines with up to four torches, including wide-portal modifications (Figure 1).

**RITM-RASKROY automated system.** RITM-RASKROY automated system is intended for nesting of metal plates and preparation of NC programs for metal cutting with CNC-controlled machines. RITM-RASKROY provides:

- automatic nesting for thermal and mechanical cutting;
- interactive correction of nesting plates;
- interactive setting of parts cutting sequence;
- compiling NC programs for cutting and nesting using required codes and formats;
- drawing out process documents for nesting plates.

A basis of automatic nesting program for thermal cutting is heuristic models of tight allocation of arbitrary shaped figures, accumulating main techniques of manual nesting from previous practice of shipbuilding yard specialists. Heuristic model is understood as mathematic model and its software implementation, built on the base of analogy between actions undertaken by an operator during actual nesting process and functions, performed with a PC program. The model is based upon preliminary tight allocation of small parts groups in rectangular figures (fragments of nesting plates) and subsequent arrangement of such rectangular figures within the preset frames of given material piece. Result of automatic nesting process is presented in Figure 2.

There is a separate option for mechanical cutting with a guillotine with reading data from parts database (initially the program operated independently without the database and without forming nesting plates with graphic processor, only rectangular blanks were arranged with registry of their arrangement on the nesting plate).

Result of nesting process for mechanical cutting is presented in Figure 3.



Figure 1. RITM-M gas cutting machine with 1-4 torches

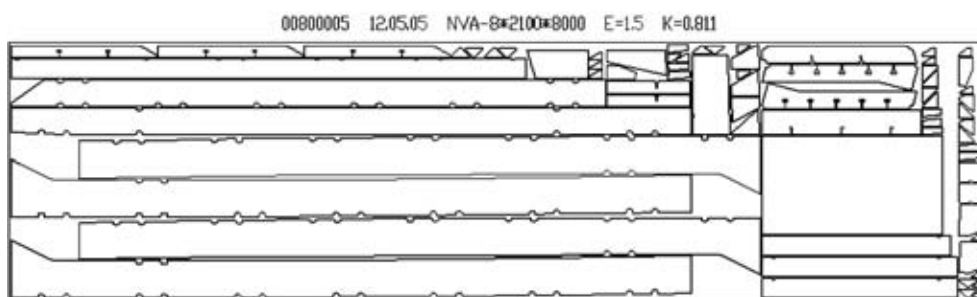


Figure 2. Example of nesting plate for thermal cutting

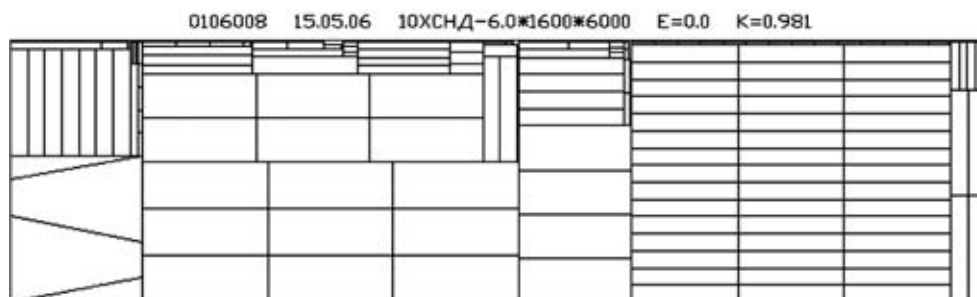


Figure 3. Example of nesting plate for mechanical cutting

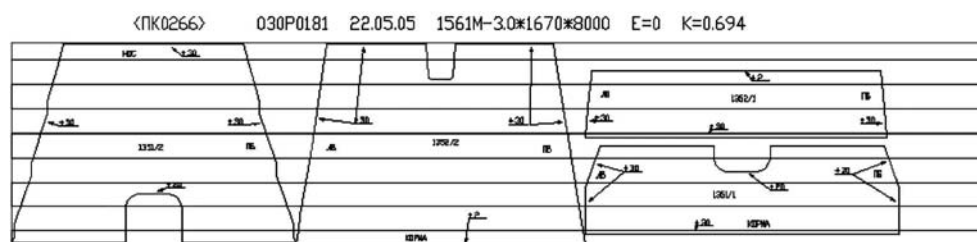


Figure 4. Example of panel nesting plate

Two new nesting options are added to the system: nesting of panel parts with panel view setting in dialog box (Figure 4), and nesting for pressing parts for serial items with compulsory cuts for guillotine. This embodiment is intended mostly for engineering industry (Figure 5).

Combination of automatic nesting with user-friendly interactive mode reduces labor intensiveness of NC programs preparation.

Functions of interactive nesting are as follows: definition of periodical arrangement of parts in arbitrary area or strip; gathering group of parts and performing operations to them; various movements/shifts (orthogonal, parallel, along the vector, etc.); rotation of parts and parts group; design of matching of two and more parts; rotation of nesting plate by 180°; registering of usable scrap in nesting plate; in-process monitoring of nesting ratio.

RITM-RASKROY system allows designing of any technologically reasonable route, in particular: cutting of parts along their contour with automatic definition of piercing points, inlet and outlet from the contour; cutting of two and more parts with one kerf (combined kerf); combination of several parts into one continuous contour with «bridges» to reduce number of pierces; setting of bridges on parts contours.

Default route setting is also widely used, i.e. piercing of outer contour — on continuation of first contour segment, piercing of inner contour — inlet

to contour along the radius with outlet from the circle, tracing outer contour clockwise and inner contour — counterclockwise. For each nesting plate kerfs length is calculated, as well as travel length, number of pierces, and nesting ratio (Figure 6). All data are recorded to project database.

The following options for correction of cutting route are provided by the system: deleting of the route or its segments; correction of contour cutting (changing of rout direction and shifting of piercing point to any point of the contour); correction of travel between parts (changing of travel portion to a kerf and back, deleting of travel portion, setting of kerf in a free area).

We continuously increase a list of postprocessors for output of NC programs upon requests of our customers: machines RITM, ALFA, GRANAT, KRIS-

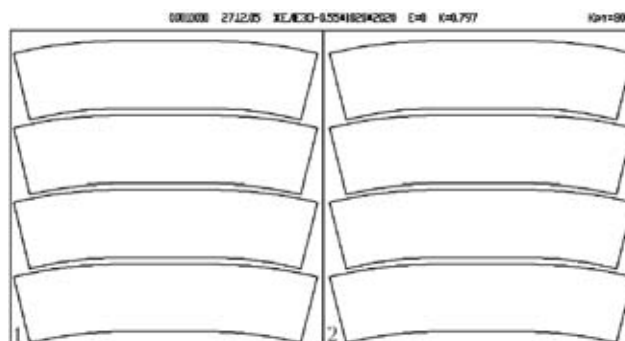


Figure 5. Nesting for pressing

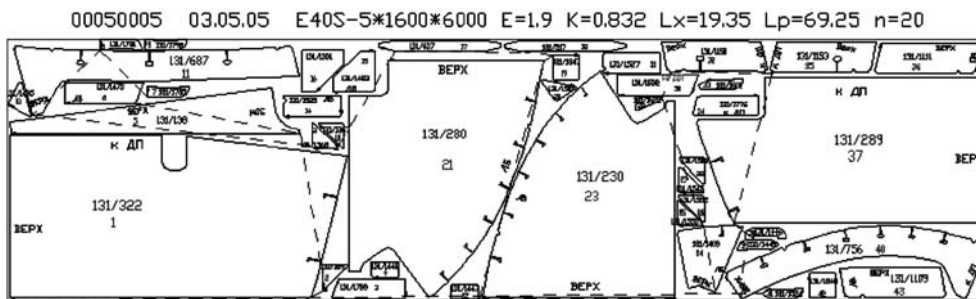


Figure 6. Nesting plate with preset cutting route

TALL, PELLA PLZ (Russia), MESSER GRIESHEIM (Germany), KOMET (Ukraine), etc.

Along with NC program for cutting a control program can be developed for parts marking. This program is usually combined with cutting program, but can be delivered separately upon customer's request.

New option of the module is automatic activation of kerf half-width monitoring when setting cutting route [3]. This option allows NC programs to be generated with inclusion of processing commands 29 (command to shift to the left from molded line), 30 (command to shift to the right from molded line), and 38 (command to cancel shifting). These commands provide additional convenience, since the same NC program can be used for various kerf widths, which are set from machine control panel or by NC program command.

Program complex has two options to match equidistant line with parts contours, namely automatic compensation of kerf half-width during arrangement of parts, and compensation of kerf half-width during cutting by inserting process commands 29, 30 and 38 into NC program.

First option was traditionally implemented in our country due to absence of NC devices for thermal cutting machines, where no process commands, except for «torch ON» and «torch OFF», were used.

At present the task to set the equidistant line in nesting plate is resolved, thus allowing this line to be set both during nesting of parts and during setting of cutting route.

The system includes a procedure for checking cutting control programs, which is automatically set to recognize code VII and decode codes VII to format DXF AutoCAD and then displaying drawing of control program on the screen. It is possible to check NC program step-by-step on the screen with marking of current frame and simulation of torch movement along the entire plate. This can be useful for online checking of NC program.

Along with NC programs, RITM-RASKROY system prepares all set of process documents, including nesting registers, process nesting charts, parts register in nesting plates, metal consumption register, etc.

Program system RITM-RASKROY is operating under Windows 2000/XP on the base of graphic processor AutoCAD 2002/2005. FoxPRO is used for design textual databases.

At present we have prepared English version of the system for AutoCAD 2005.

To learn RITM-RASKROY operation training system is prepared. This system simplifies for the user training on operation of RITM-RASKROY. It includes a set of major functions and operations, requires to be fulfilled to obtain a final result — NC program for heat cutting machine and drawing out process documents.

Demo version of the system shows its new features and options.

Software of RITM-RASKROY system is used in various educational institutions in Russia for training of students.

## CONCLUSION

This year, CRIST has delivered program modules of RITM-RASKROY system to several customers in Russia (Oktyabrskaya Revolutsiya Shipyard, Blagoveshchensk, Far East Plant Zvezda, Bolshoj Kamen, Zelenodolsk Design Bureau, Yaroslavl Shipyard).

In 2005, CRIST manufactured and delivered for Admiralty Yards (Saint Petersburg) machine PITN-M-PKP-2.53R (with three-torch block), which provided simultaneous cutting and edges grooving for welding. Implementation of such machines allows increasing productivity of pre-production facilities at shipyards. For JS Severstal we delivered three machines RITN-M-KP5000 for cutting metal for large-diameter pipes (Kolpino, Saint Petersburg).

We developed procedures for reduction of gas content in the edges of cut metal and for protection against emission and reduction of noise during plasma cutting. Our specialists proposed and implemented protection with so-called «water-hood».

In 2004–2005, we applied considerable efforts to enlarge the range of our thermal cutting machines. For example, we designed and manufactures a new portal for RITM machines, reducing metal content by 20 % and thus reducing its production cost by 30 %.

The CRIST specialists also developed modernization of old cutting machines of Kristall and Granat type.

Program-technical complexes on the base of thermal cutting machines RITM, made by CRIST, are successfully operated in various industrial sectors of Russia, proving their high reliability and efficiency.

1. Semenyuk, V.F. (2004) Modern approach to design of control systems for thermal cutting machines. *Shipbuilding Technology Rev.*, **12**, p. 154–155.
2. Karpoushkina, N.G., Plotnikov, A.M. (1998) Nesting of plate metal by automated system Ritm-Hull. *Sudostroenie*, **3**, p. 46–49.
3. Karpoushkina, N.G. (2004) New features of «Raskroj» module in automated system Ritm-Ship. *Ibid.*, **6**, p. 67–70.

# COMPUTER BASED VIRTUAL REALITY TRAINING SYSTEM FOR WELDING

A. PRATT, J. NORRISH and L. DUNN  
University of Wollongong, Australia

A virtual reality training system for welding is being developed at the University of Wollongong. The system is intended to be used in vocational institutions such as technical colleges, as a method of training introductory welding to inexperienced welders in a safe and cost effective manner. An overview of the justification for the training package has been given previously but a clear advantage of the computer based approach is the ability to incorporate diagnostics and feedback to the trainee based on accepted models of the process. This paper describes the software framework of the system and indicates how this may be used to deliver the required feedback and instruct the operator in the choice of operating parameters. The system enables both manipulative skills and cognitive skills associated with welding to be developed. The manipulative skills are often the most time consuming aspect of training whilst the correct setting of equipment determines the ultimate weld quality.

The justification for the development of virtual reality (VR) training systems for welding may include factors such as:

- international shortage of skilled manual welders [1] caused in part by the de-industrialisation of developed countries and automation of welding. This is compounded by an aging work force of skilled manual welders and a perception that the occupation of manual welding is hazardous and that it requires extensive training;
- current training for manual welding involves intensive practical skill development [2]. The manipulative skills required for manual metal arc welding (MMAW) and gas metal arc welding (GMAW) are difficult to obtain and this is compounded by the use of protective filters, that necessarily restrict the welder's vision;
- in the initial training for welders there is a large amount of wastage of material in terms of scrap test pieces and consumables. In Australia it is estimated that it costs A\$ 70,000 per annum, per student for materials and this averages out at approximately \$ 300 per welding certificate [2];
- vocational training of this type also requires skilled instructors who must often divide their time between many students;
- manual welding is hazardous and during the early stages of training there is a greater risk of injury due to the student being unfamiliar with operating techniques. Therefore there is a need for a training system to allow welders to gain the basic skill set of welding before they are exposed to the hazardous welding environment;
- VR systems have been used successfully for training in other environments such as pilot training and surgery.

A review of VR systems for welding has previously been published [1]. This was based

on currently available information. A summary of the findings is shown in Table 1. At the time of this review it appeared that most of the systems were «experimental» prototypes although it is believed that some may now be commercially available. The systems generally address the need for manipulative skill training but some have been more focused on assessment as a means of skill improvement.

## Demonstration system development

Having reviewed the current systems it was decided that a simple low cost system would best serve the requirements for assessment and preliminary training in Australia. This was based on the fact that the system needs to be widely available in regional centres and if successful, students would quickly progress to real practical trials.

The proposed components of the target system are shown in Figure 1. In operation it would be expected that the student be presented with a virtual welding task and would be required to select consumables and equipment settings prior to attempting the manipulative part of the exercise.

The tasks are based on the existing training manuals developed by the Welding Technology Institute

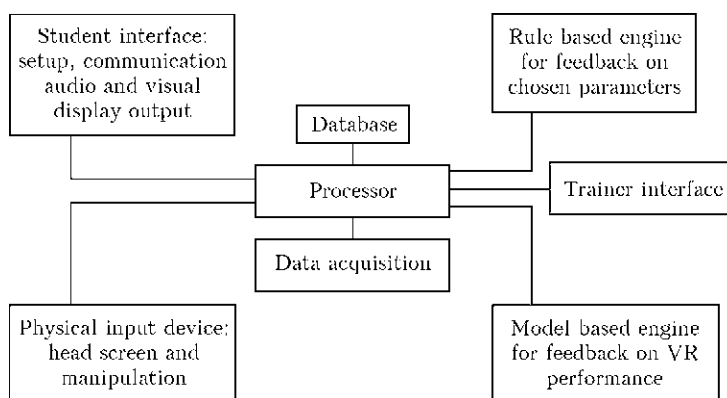


Figure 1. Schematic view of proposed system

**Table 1.** Summary of some current VR systems for welding

System and reference	Description	Comment
WAVE [4]	Flat panel display, sensors mounted on torch with pick ups on large frame, client server architecture for monitoring and control	Good display and 3D motion sensing but no force feedback. Appears to be large, fixed installation and costly. Portable version now available
University of Chiba [5]	«Mixed reality» system with video, audio and tactile feedback. Helmet mounted display and ARToolKit augmented reality software	Comprehensive. Could be portable but complex hardware appears to be laboratory prototype
US Navy [6]	Artificial neural network based process models	Little information available, aim to produce VR welding cell for shipyards
ARS CAVE system (Fronius) [7]	3D animation, VR application: an SGI Onyx «A 6-DOF (degree of freedom) tracker»	Process animation system
Harbin welder training simulator [8]	Physical simulation of workpiece with magnetic/hall effect sensors. MCS-51 microcontroller	Arc light and sound feedback but no weld pool image
University of Bremen [9]	Intelligent welding helmet, augmented reality system with information feedback	Welder information feedback rather than VR training system
Toshiba [10]	Video, infrared and eye tracking cameras for motion analysis fed to computer – Mahalanobis–Taguchi analysis used for skill assessment	Currently a skill assessment package good benchmarking system but quite complex

of Australia (WTIA) and Australian Technical and Further Education (TAFE) colleges [3].

**Graphical user interface.** The main user interface serves several purposes and takes the form of a PC monitor; preferably an LCD display. On initiating the program a «management» screen appears, this allows the student to record his personal details which are entered in the database. A unique password and ID is also allocated to the student. The student may then select the exercise which is required to perform. The tasks are sequential and the student is alerted to the fact that there is no successful record of the prerequisite task if this is the case. Having selected an exercise an appropriate parameter input screen is generated. This screen allows the student to choose optional process inputs and welding parameters. The student choices are expected to be based on prior instruction delivered in the form of lectures or written material such as the MMAW Training Manual [3]. The rule based engine generates errors and advisory feedback based on these inputs before allowing progress to the next stage. For simple MMAW choices include electrode type, polarity, electrode size, elec-

trode angle and welding current. Following successful input of the parameters the student may progress to the «weld» stage and the screen shows a 3D image of the welded joint to be tackled.

**Physical input device.** In view of cost constraints a simple physical input device consisting of a WACOM™ tablet and stylus was chosen. The stylus is mounted in a simulated MMAW electrode holder or GMAW torch and the tablet is mounted in a frame which may be orientated into the principal welding positions. The WACOM device allows position, speed and orientation of the tool to be acquired. For initial trials a simple tablet and pen were used with a separate PC display although as shown in Figure 2, a combined interactive display is available. Initially a fixed stylus has been used and this satisfactorily simulates the GMAW process whereas for MMAW it would be more realistic to drive the stylus (which represents the electrode) upwards to simulate electrode burn off. A normal welding head-screen equipped with headphones and a clear filter lens is worn by the student.

**Parameter selection.** The initial parameter selection may be illustrated by reference to the first exercise from the WTIA Basic Training Manual for MMAW [3]. This requires the student to make a single bead-on-plate run on flat plate in the downhand or flat position. The student is given the choice of electrode type, polarity, diameter and current. The chosen parameters are compared with the database and appropriate response is given (Table 2). The student needs to amend any errors before progressing. Acceptable choices are recorded for use in the real time model.

**Real time VR simulation.** When the student selects «weld» from the parameter selection screen the screen display changes to show a 3D image of the joint. In the case of the exercise above the image is a flat plate with a line indicating the desired position

**Figure 2.** WACOM™ interactive display device



**Table 2.** Parameter input choices for exercise 1 and response to «errors»

Process: MMAW		Exercise: 1. Bead-on-plate	
Parameter	Options	Choice	Comment
Electrode type	Cellulosic		This is a deep penetration electrode – unsuitable
	Basic		This is a high quality electrode – unnecessary
	Rutile (4112)		Correct
	Iron powder		This is a high deposition electrode – unnecessary
Electrode polarity	DCEP		Preferred
	DCEN		This electrode is flexible and useable on DCEN and AC
	AC		
Electrode diameter, mm	Choose diameter between 1.6 and 6.4 mm	1.6–2.4	Too small for chosen bead size
		3.2	Correct; select appropriate current
		4.0	Correct; select appropriate current
		4.8–6.4	Too large requires higher current
Current, A	Choose current in the range 50 to 250 A	50–90	Too low
		90–130	OK for 3.2
		130–180	OK for 4.0
		180–250	Too high

of the weld bead. For the real time simulation of MMAW the «arc» is initiated when the stylus is brought into contact with the workpiece then lifted slightly. At this point the display image is darkened to simulate the use of a self darkening filter and a «weld pool» image develops simultaneously and the process clock is started. As the student moves the stylus along the line the speed is calculated and the bead width is estimated from the likely burn off rate using an equation based on the classical burn off relationship:

$$MR = \alpha I + \frac{\beta I^2}{a},$$

where  $I$  is the current;  $l$  is the electrical stick-out or electrode length from the arc to the electrode holder;  $a$  is the wire cross sectional area;  $\alpha$  and  $\beta$  are the constants.

In MMAW the arc heating term  $\alpha I$  is assumed to remain constant but electrode length and resistivity are changing as the electrode melts and the temperature of the remaining electrode increases. Decreasing electrode length  $l$  reduces the resistive heating effect

**Table 3.** Postweld reporting

Parameter	Deviation	Report
Arc length	Too short (less than 3 mm)	Irregular build-up of the weld metal. Stubbing and sticking tendency
	Too long (more than 4 mm)	Causes coarse ripples and a flatter bead than normal. Arc extinguishes (arc outs reported)
Travel speed	Too high	Gives a narrower, thinner deposit, with longer than normal length. Travelling to fast may cause lack of fusion with the parent metal. Estimated width reported. Lack of fusion reported if heat input below threshold
	Too low	Wider, thicker deposit, shorter than normal length may allow the slag to flood the weld pool causing difficulty in controlling deposition. Estimated width reported
Current	Too low	Tends to cause the weld metal to pile up in irregular ripples without adequate penetration into the parent metal. Current which is too low makes the slag difficult to control. Slag may be trapped between ripples. Lack of fusion reported if heat input below threshold
	Too high	Gives a deposit that is flatter and wider than normal with deeper penetration into the parent metal. Ripples are coarse and evenly spaced. If the current is too high, excessive spatter occurs
Line following	Inconsistent	Deviation from straight line reported
Electrode angle		Deviation from correct angle reported
Heat input		Heat input is calculated on basis of current assumed voltage and travel speed reported for information

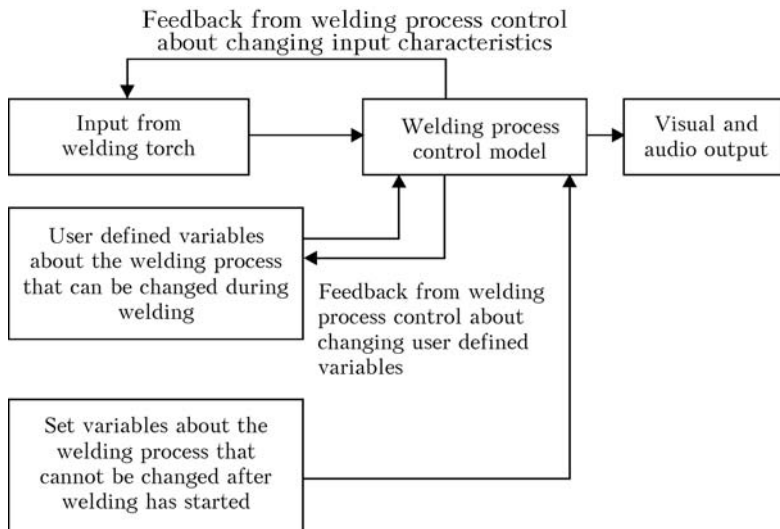


Figure 3. Software structure

whilst the increase in temperature increases the resistivity and hence the melting rate of the electrode. In practice with plain carbon steel electrodes the effect is minimal unless the electrode diameter is too small. With high resistivity stainless steel electrodes an increase in burn off rate is often experienced and the travel speed may have to be increased to compensate and this must be accommodated in the model. For the purposes of the real time model the deposited weld cross section is assumed to be semicircular with a radius  $r$  (whilst in plan view the weld pool has an elliptical shape). Then the volume of metal deposited,  $\text{mm}^3/\text{min}$ , is given by

$$MR = S \frac{\pi r^2}{2},$$

where  $S$  is the travel speed,  $\text{mm}/\text{min}$ ;

$$W = 2r = 2 \sqrt{\frac{2MR}{\pi S}}$$

is the bead width.

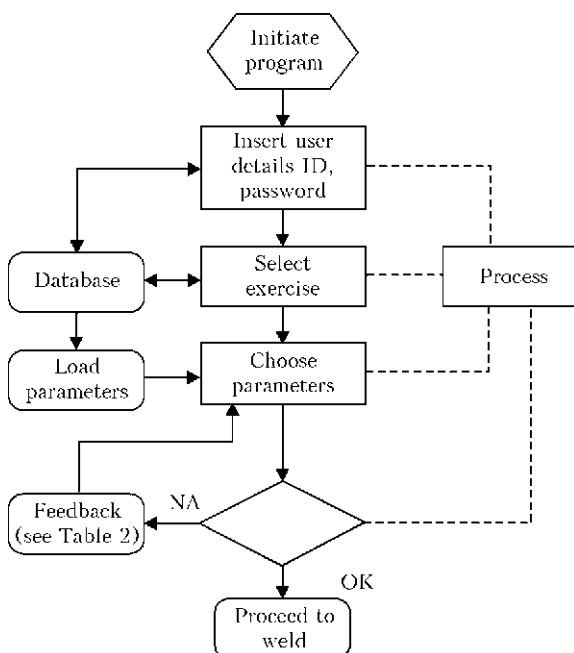


Figure 4. Pre-weld software flow chart

The weld pool dimensions are primarily influenced by current and travel speed; whilst a theoretical weld size could be derived using heat flow equations, in the VR simulation it is required to display the «apparent» weld pool size as it would appear to the welder through a conventional welding helmet. In the present system typical apparent pool sizes and their dependence on current and travel speed were determined empirically by using a CMOS camera mounted in the welding helmet. The «arc length» is monitored by the stylus separation from the tablet and the arc sound is modified according to arc length. Again this is currently achieved by sampling typical sounds at varying arc lengths and presenting these as .wav files through the helmet mounted head set. If the arc

length is less than the preset minimum, stubbing or sticking are reported. When the arc length is excessive a potential arc outage is recorded. If the arc outage lasts for more than 2 s the run is terminated (it is assumed that the arc has been broken intentionally).

The trajectory of the electrode end is recorded and deviations from the chosen path are reported as a percent variation from a straight line.

**Feedback and reporting.** The errors are currently reported after the simulation is complete although there is provision for alarms or voice prompts to be activated by serious deviations from acceptable conditions. Immediately after the VR weld run is completed the monitor shows a 3D simulation of the completed weld bead. The contents of typical reports are listed in Table 3. These reports are presented in the form of text as indicated in the Table.

**Software design.** The software used needs to present a simple user interface for data input, realistic graphical displays for visualisation of the weld pool and finished bead, data acquisition, data storage, and real time feedback capabilities. To this end it was chosen to write the application in JAVA whilst JAVA 3D was used to produce the advanced graphics.

A client server application is necessary to allow the trainer access to the trainee records and to monitor progress. This is implemented using a local area network (either hard wired Ethernet or wireless).

An overview of the basic software structure is shown in Figure 3.

There are three basic software modules: pre-weld management module, online monitoring module, and postweld analysis and reporting module.

The structure of the pre-weld module software is shown in Figure 4.

The online model can be considered as a «black box» containing predetermined information about the welding process. This «black box» takes the input characteristics of the welding process from the trainee and outputs the characteristics of the weld.

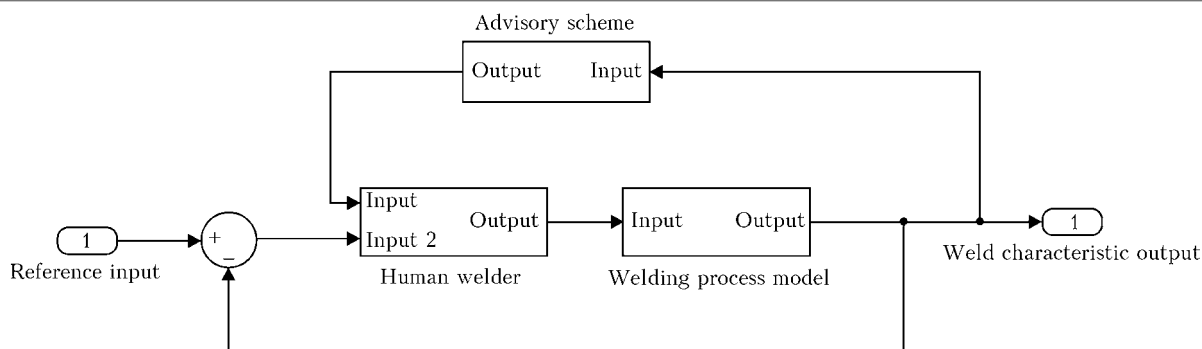


Figure 5. Control diagram for the welding process

The system can be looked at from a standard classical control point of view similar to that applied to welding when using an automated welding control scheme. In this sense the plant is the welding model and the human user and the advisory scheme combine to form the feedback controller of the system changing the input of the system based on the output.

Figure 5 shows the control scheme with the manual welder and advisory scheme replacing the controller used in the automated environment.

The difference between the rule base used in the industrial environment and the advisory scheme used to give feedback to the user operating the system is that in the industrial environment variables signals are used to directly control the welding process by using mathematical rules whereas the advisory scheme needs to give feedback to the user in an understandable language. The user will then need to change the input variables based on learnt information. The advisory scheme for the VR training system has to interpret the different signals from the welding process model and give feedback in the form of text based descriptors, e.g. «a problem in current welding process, advise changing the following variables inputs» (see Table 3). Postweld analysis and reporting also relies on the monitored performance as illustrated in Table 3.

### Discussion

The system developed uses simple low cost components and common software packages. It is capable of offering preliminary assessment and training in the manipulative skills required for welding with potential to reduce normal welding material costs and the safety hazards associated with initial training. The user interface is flexible and it would be possible to introduce safety training segment into the pre-weld interface to check the trainee's appreciation of the hazards.

### CONCLUSION

The demonstration system has been developed to satisfy the requirements set out in the Australia Basic Skill Training Manual for MMAW welders. The initial bead-on-plate exercise is described above by way of illustration but work is ongoing to incorporate many more of the 34 exercises listed. These exercises

include pad, butt and fillet welds in all of the principal joint orientations with several electrode types.

It is believed the low cost and portability of the system will enable its widespread use for vocational training locally and in regional centres. The possibility of remote monitoring also improves the support available to teachers.

The system has been demonstrated to technology students in high schools and may be used to stimulate an interest in vocational training. The adoption of such systems may also address the skill shortage currently being experienced internationally.

**Acknowledgement.** *The work reported here was carried out by Alexander James Pratt before his untimely death in December 2005 and is dedicated to his memory. His co-authors would like to acknowledge the efforts made by Alex to develop the system. We would also like to acknowledge the support received from the Welding Technology Institute of Australia, Wollongong TAFE, TAFE SA and the Australian Research Council for sponsorship under the Linkage Project scheme.*

- Dunn, L.J., Norrish, J. (2002) A virtual reality training kit for arc welders. In: *Proc. of 50th WTIA Annual Conf. and 12th Int. TWI Conf. on Computer Technology in Welding and Manufacturing*. Vol. 2. Paper 72. WTIA.
- Dunn, L., DiPietro, P. (2003) *Virtual reality training system for arc welders*: Linkage Grant. Australian Res. Council.
- (1983) *Manual metal arc welding: basic training manual*. WTIA.
- [http://wave.c-s.fr/documents/WAVE\\_flyer\\_eng.pdf](http://wave.c-s.fr/documents/WAVE_flyer_eng.pdf) (accessed March 2006).
- Kobayashi, K., Ishigame, S., Kato, H. (2003) Skill training system of manual arc welding — by means of face-shield-like HMD and virtual electrode. In: *Proc. of IFIP 1st IWEC Conf.* (2002, Norwell, USA). Kluwer A.P., p. 389–396.
- <http://www.nsrp.org/onr/shipbldg/initiative.html> (accessed March 2006).
- [http://www.aec.at/en/futurelab/projects\\_sub.asp?iProjectID=2703](http://www.aec.at/en/futurelab/projects_sub.asp?iProjectID=2703) (accessed March 2006).
- Chuansong, W. (1992) Microcomputer-based welder training simulator. *Computers in Industry*, 20(3), p. 321–325.
- Tschirnerl, P., Graser, A. (2002) Optimisation of manual welds using virtual and augmented reality. In: *Intelligent Technology in Welding and Joining for the 21st Century: Proc. of Int. Welding/Joining Conf.* (Gyeongju, Korea, Oct. 28–30, 2002), p. 289–294.
- Sakuma, M., Tsuboi, R., Kubo, K. et al. (2004) *Development of welder's training support system with visual sensors*: Welding Guide Book V. JWS.

# DISTORTION MANIPULATION BY MEANS OF THERMAL GENERATION OF RESIDUAL STRESSES

T. PRETORIUS, J. WOITSCHIG, G. HABEDANK and F. VOLLERTSEN  
BIAS Bremer Institut fuer angewandte Strahltechnik, Germany

Thermal treatments of steel components with the goal of hardening often result in distortion by releasing the residual stresses which were brought into the specimen during the preceding processing steps. The goal of the presently presented work is the minimization of this distortion. By generating definite residual stress fields and investigating the resulting distortion, the distortion mechanism can be observed in detail. A flexible and reproducible way to generate such residual stress fields inside a specimen is by means of thermal treatment with a laser beam. For the presently presented work a high power laser system combined with a scanner system was used. This allows for a wide range of parameters for the heat treatment and therefore different types of residual stress fields can be produced. The activated mechanisms in this process are the temperature gradient mechanism and the martensite expansion mechanism. To achieve results that are both detailed and verified, computer simulations as well as experiments were carried out using an idealised tooth of a gearwheel (finger sample) as a model system. The simulation method includes the cooling of the samples after the laser heat treatment as well as the subsequent process step the hardening heat treatment. With this procedure the influence of the thermal treatment on the distortion of the specimen can be observed. This distortion is controllable and therefore it can be used to attempt to compensate distortion that is caused otherwise.

**Motivation.** The correction and elimination of distortion is very costly. This means that the prevention or compensation of distortion in the production process of components is preferable. Causes of distortion can be found in every step of the manufacturing process chain. In Figure 1 the simplified production process chain according to [1] of steel components (e.g. gear wheels) is illustrated.

A lot of parameters influence the distortion of a component [2]. The casting of the alloy produces a distortion potential due to an inhomogeneous distribution of alloying elements. The following mechanical and thermal process steps influence the material distribution and induce residual stress. Manufacturing tolerances and temperature gradients during heat treatments are further causes of distortion potential. Towards the end of the process chain – in the hardening heat treatment – the distortion potential is released. The final step – grinding – can only be used to correct very small distortion.

The goal of the collaborative research center «Distortion Engineering» of the German Research Foundation (DFG) is a detailed investigation of every step

of the production process chain, which enables the understanding of the development of the distortion potential and thus enables the development of distortion compensation methods. The gained knowledge about the development of the distortion potential can be used to manipulate and eliminate this potential before the hardening heat treatment. For the development of the process step «distortion potential manipulation» (see Figure 1) it is necessary to modify the distortion potential of the components in a well-defined and flexible way. This could be done with a local heat treatment using a high power laser beam (CO<sub>2</sub> or Nd:YAG) combined with a scanner system. The local heat treatment modifies local stresses and possibly the local microstructure in the components [3–7]. This alteration of the distortion potential of the component and can thus be used to try to compensate distortion which is cause elsewhere.

This paper investigates the local laser beam heat treatment and the effects on samples that are stress-free before the treatment. To achieve results that are both detailed and verified, experiments as well as computer simulations were carried out, which include the local heat treatment together with the hardening heat treatment to release the altered distortion potential.

**Model geometry.** An idealised tooth of a gearwheel (finger sample) was used as a model system. The geometry is shown in Figure 2. The total size of the sample is L60 × W17 × H17 mm. The size of the finger is L40 × W17 × H5 mm. The transition between finger and block is shaped with a radius of 0.8 mm. The material chosen for the samples is steel 20MnCr5. This material is also used by the other subprojects of the collaborative research center «Distortion Engineering». The relevant material parameters of this alloy are investigated in detail in the collaborative research center [8].

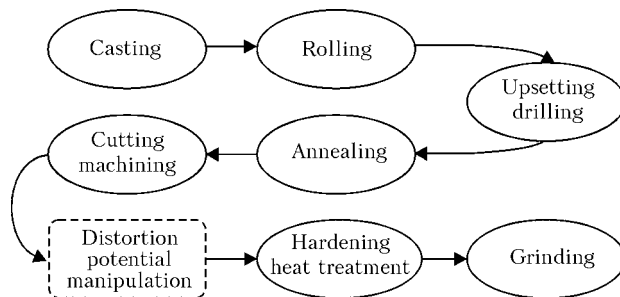


**Figure 1.** Simplified production process chain for steel components (e.g. gear wheels) with distortion manipulation enhancement

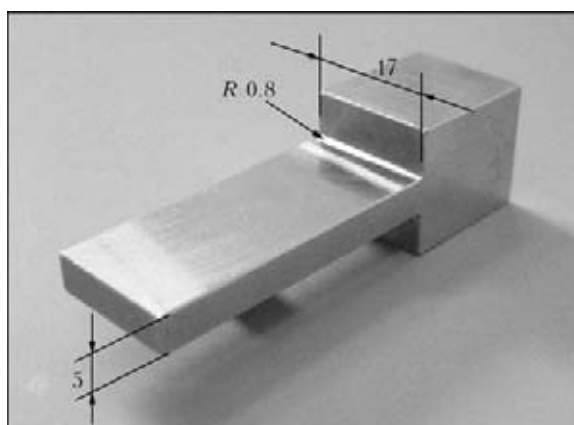


**Figure 2.** Geometry of the 20MnCr5 steel samples used in experiments

**Distortion potential manipulation.** For the presented work two high power laser systems (CO<sub>2</sub> with a maximum power of 6 kW and Nd:YAG with a maximum power of 4 kW) combined with scanner systems were used. This allowed a wide range of parameters for the heat treatment and therefore it was possible to produce different types of residual stress fields. The use of a Nd:YAG-laser has the advantage that a graphite coating on the surface of the specimens is not necessary. Using a CO<sub>2</sub>-laser such a coating is necessary to achieve a reasonable absorption of the laser light.

In Figure 3 the experimental setup is illustrated. The laser beam was moved parallel to the transitional edge between finger and block. This resulted in a heat treatment line perpendicular to the finger. The described setup allowed for systematic investigations with respect to different process parameters (laser power, number of scans, laser beam spot size). For later attempts to compensate the distortion potential nearly any shape of the heat treatment zone can be generated.

**Hardening heat treatment.** The temperature cycle of a hardening heat treatment is shown in Figure 4. It consists mainly of a slow heating, a carburisation (not shown), hold at high temperature and a fast cooling. Especially the fast cooling can produce distortion by itself, which is not in the scope of the investigations of work for this paper. This heat treatment process step is used for the release of the distortion potential (which is mainly due to residual stresses) and therefore a stress relief annealing instead of the hardening heat treatment can be used to investigate the changes of the distortion potential due to the local laser heat treatment. The temperature cycle of such a stress relief annealing is also shown in Figure 4.

**Thermal forming mechanisms.** Changes of residual stresses of first order are always accompanied by macroscopic geometrical changes. Within the scope of this work, three thermal forming mechanisms have to be taken into account, namely residual stress relaxation mechanism (RSM) [9], temperature gradient mechanism (TGM), and martensite expansion mechanism (MEM).

In the first approach described in this paper, no residual stress was induced into the initial samples.

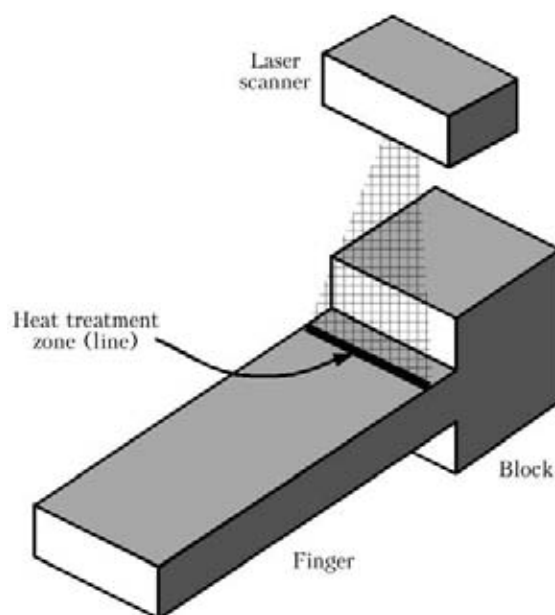


**Figure 3.** Schematic illustration of the local laser heat treatment

Therefore, the experiments were focussed on TGM and MEM.

TGM is illustrated in Figure 5, *a* (it is described in detail in [10]). At the beginning of the local heating a temperature gradient perpendicular to the surface of the zone is induced. The different thermal expansions in the upper and lower regions lead to a bending of the sheet away from the heat source. The magnitude of this bending depends mainly on the thickness of the sheet [11]. The heating of the material does not only result in a thermal expansion but also in a decrease of the yield stress in the heated region. The thermal expansion increases until the thermal stresses equal the yield stress of the material. Afterwards the thermal expansions will be converted into plastic up-setting. When the heating ends the cooling of the deformation zone causes a contraction, which is larger in the plastically deformed region. The contraction overcompensates the bending away from the heat source and leads to a bending towards it.

MEM was so far not considered in thermal forming, but is relevant concerning the aspects of this work. It is illustrated in Figure 5, *b*. Different time-temperature cycles in the upper and the lower region of the heated zone lead to phase changes. A phase change from ferrite to austenite in the upper region induces a local shrinkage of the material. After the laser is switched off, the material cools down and a

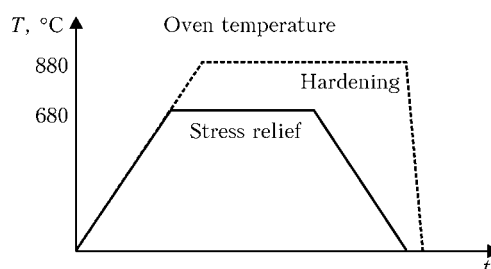


**Figure 4.** Schematic temperature cycle of hardening heat treatment and stress relief annealing

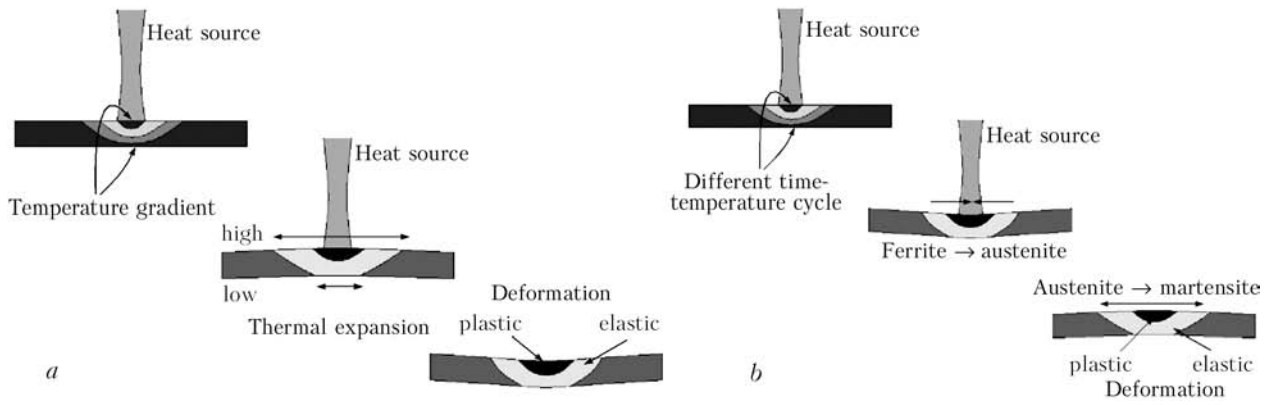


Figure 5. Schematic illustration of TGM (a) and MEM (b)

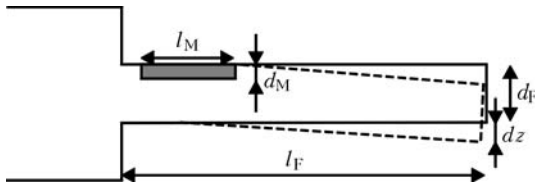


Figure 6. Schematic illustration for bending of finger due to MEM phase change from austenite to martensite occurs. This causes an expansion of the material in the upper region. This expansion overcompensates the shrinkage due to the temperature gradient mechanism and thus results to the sample bending away from the laser beam.

The maximum geometrical variations  $dz$  at the end of the finger due to MEM can be calculated if the stiffness of the finger is neglected and a complete transformation of the grey zone is assumed (Figure 6). The corresponding maximum possible bending angle can be derived from  $\tan \alpha_{\max} = \Delta l_M / d_F$ . The maximum geometrical variation is given as  $dz_{\max} = l_F \sin \alpha_{\max}$ . If a heated zone of width 6 mm is assumed, theoretically a maximum geometrical variation at the end of the finger of 95  $\mu\text{m}$  due to phase transformations is possible.

**Experimental investigations.** To investigate the influence of the laser heat treatment on the samples a line on the outer surface of the samples was measured before and after the laser heat treatment (Figure 7). The geometry measurements were carried out using a tactile coordinate measurement system (accuracy  $1.7 \mu\text{m} + 0.3 \mu\text{m}/100 \text{mm}$ ).

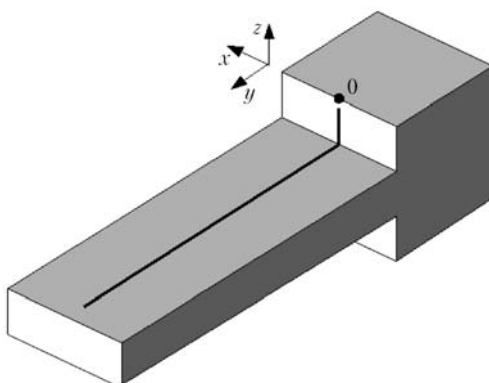


Figure 7. Position of the coordinate measurement line

Using a  $\text{CO}_2$ -laser and varying the heat input into specimens with finger thickness of 5 mm resulted in different bending angles and directions. For a laser beam velocity of 1000 mm/s, a laser spot diameter of 6 mm, laser beam powers up to 1500 W and up to 300 cycles of the laser beam a bending of the finger toward the laser beam can be observed. Therefore TGM is activated within this parameter range. For laser beam powers equal or higher than 1900 W and cycle numbers of 600 or more a bending of the finger away from the laser beam can be observed. In this parameter range the higher energy input leads to phase changes in the heated region and MEM is additionally activated additionally to TGM. The bending direction therefore depends on the relation of the deformation caused by MEM and TGM. In the observed cases (with high energy input) the deformation caused by MEM is greater than that caused by TGM, and therefore led to a bending of the sample away from the laser beam. The results of the coordinate measurements for such a case are shown in Figure 8. At the end of the finger a downward bending of  $\sim 8 \mu\text{m}$  can be observed.

**Simulation.** The computer simulation was used to investigate the temperatures, the phase transformations and the stress field of the specimen. The simulation was done using the software package SYSWELD on a PC with two Intel Xeon 2.8 GHz processors. The

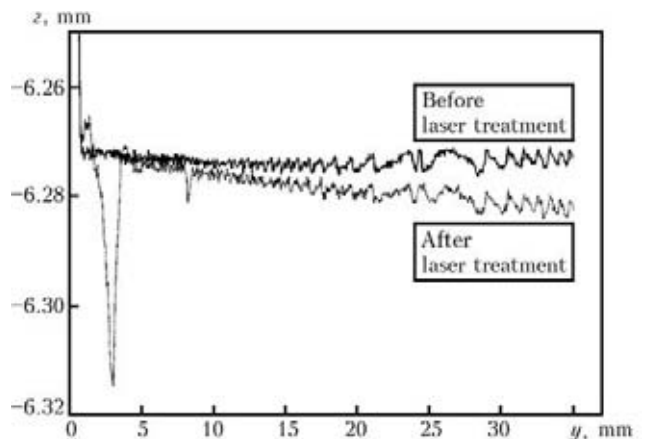


Figure 8. Result of coordinate measurements at laser beam power of 1900 W; number of scans of  $2 \times 320$ ; 2 and 6 mm distance between center of laser beam and edge of the block; laser beam spot diameter of about 6 mm

calculation was explicitly time-dependent and includes the movement of the laser beam along the heat treatment line. Temperature-dependent material parameters were used, they are detailed in [8]. The element mesh used for the simulations of the finger sample is shown in Figure 9. It is locally refined in the transition region between the finger and the block and in the laser heat treatment zone. The mesh includes about 12,000 elements of 8 node brick type. As boundary conditions a constant energy transfer in the actual laser spot area (with Gaussian distribution) for the laser beam was used. For the rest of the surface of the sample energy losses due to convection and radiation were calculated (convection coefficient of  $10 \text{ W}/(\text{m}^2 \cdot \text{K}^{-1})$ ).

One result of the simulations is the time-dependent temperature field. In Figure 10 the surface temperatures after 5 and 20 cycles of the laser beam are shown. Due to the time-dependent modeling of the laser beam motion the calculation time for simulating 20 cycles (thermal and mechanical calculations) was about 34 h.

It can be seen in Figure 10 that the cross sectional temperature distribution along the irradiation path is almost constant. This is a result of the high scanning speed of the laser. The cylindrical shape of the temperature distribution allows a simplification of the simulation, which will be detailed in the following.

*Accelerated simulation.* As earlier mentioned, it is not necessary to simulate the movement of the laser beam in detail, since the resulting cross sectional temperature distribution along the irradiation path is al-

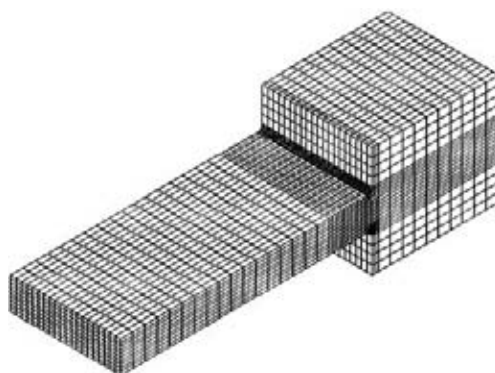


Figure 9. Element mesh of the finger sample

most constant. A line or area heat source can be used alternatively. With this approach the explicit time dependency of the fast laser beam motion vanishes, which accelerates the calculation significantly. In Figure 11, *a*, the temperatures of a cross sectional cut through the temperature field using a moving heat source (diameter of 6 mm) is shown. The result of a simulation, which uses a static equally distributed area heat source of width 6 mm and length 17.5 mm (equal to width of the finger) is shown in Figure 11, *b*.

A detailed comparison according to [9] of the temperatures of the described explicit time-dependent simulation  $T_{\text{mov}}$  and the static simulation  $T_{\text{st}}$  is shown in Figure 12. The values of curve *A* were taken on a line perpendicular to the surface from the upper (depth is 0 mm) to the lower surface (depth is 5 mm) of the finger at the center of the heat treatment line.

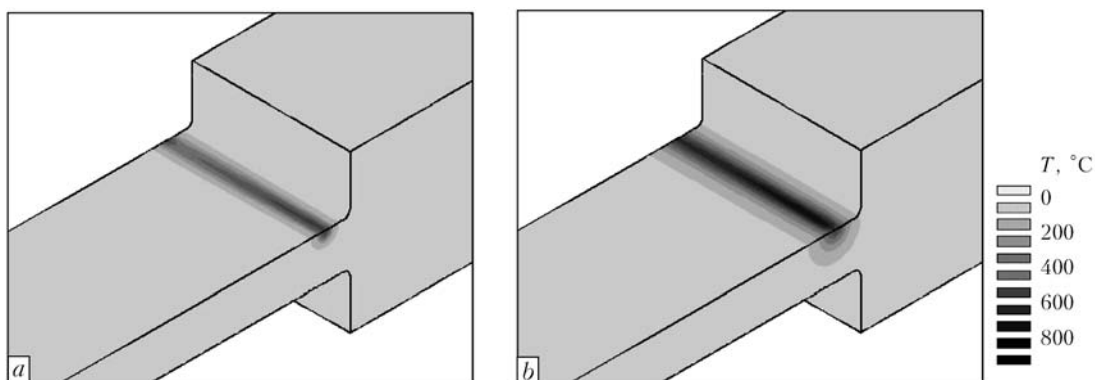


Figure 10. Surface temperature after 5 (*a*) and 20 (*b*) cycles of the laser beam at beam power of 1000 W, laser beam spot diameter of 0.85 mm and laser beam velocity of 1000 mm/s

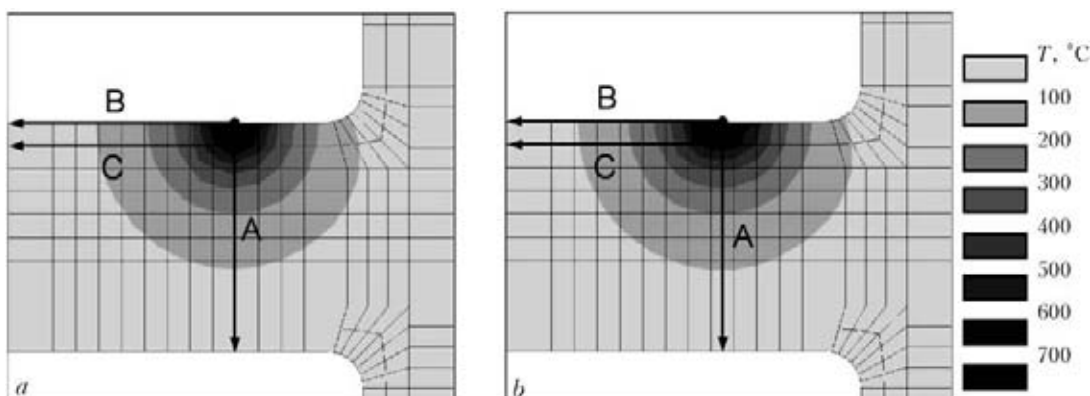
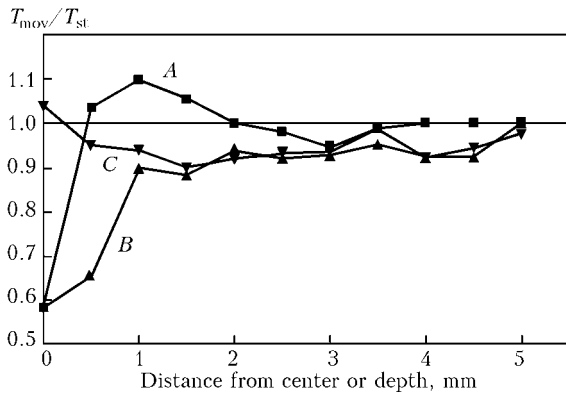


Figure 11. Cross sectional cut through the temperature field of simulation using a moving (*a*) and area (*b*) heat source 6 mm width



**Figure 12.** Comparison of temperatures on vertical (A) and horizontal (B) line at upper surface, and horizontal (C) line 0.5 mm below upper surface (see Figure 11)

The values of B and C were taken on a line in direction of the *y*-axis at a distance of 0–5 mm of the center of the heat treatment line at the upper surface of the finger (B, depth is 0 mm) and 0.5 mm below the upper surface of the finger (C, depth is 0.5 mm). Larger temperature differences can only be observed directly in the region of the two different heat sources (distance of < 1 mm). For the rest of the sample the differences are below 10 %. The maximum geometry change after 20 cycles of the laser beam is 0.23 mm in the case of the moving laser beam simulation and 0.25 mm for the simulation using the constantly heated area. This also corresponds to an error of < 10 %. The calculation time for this simulation was ~ 0.3 h, which is about 100 times faster than in calculation using a moving laser beam. The simplified method allows simulation that correspond to hundreds of cycles of the laser beam, as used in the experiments.

*Simulation of the laser heat treatment and stress relief annealing.* The accelerated simulation method allows the calculation of laser heat treatments with a duration (cycle numbers up to several hundreds) as used in the experiments. To investigate the influence on the distortion potential, it is necessary to simulate also the cooling of the specimen and the stress relief annealing. In Figure 13 the distribution of the temperatures at the laser heat treatment area is schematically

illustrated. The laser beam treatment of 5 s duration and transferred power of 1000 W heats the specimen locally (width of laser treatment area is 6 mm) as indicated underneath the diagram. The maximum temperatures reached were about 1400 °C, which is in agreement with the experimental observation of a slight surface melting. After this the calculation is carried on for a time period of 600 s in which only radiative and convective losses were used as boundary conditions. At the end of this cooling phase the specimen has a nearly uniform temperature of about 40 °C. In the final stress relief calculation the boundary conditions were set according to the oven conditions: heat transfer coefficient of 100 W/(m<sup>2</sup>·K), and heating/cooling rate of 5 K/min. The slow heating and cooling rates result in very small thermal gradients during this phase. Therefore the existing residual stresses can be released without generating new sources of distortion potential. A high cooling rate, as part of a hardening heat treatment, would induce high thermal gradients, which could act as distortion potential for themselves.

The calculated geometry changes at the end of the finger during the process were (*dz* is the deviation from a straight finger, i.e. the position at the start of the process):

- $dz (t = 5 \text{ s}) = -0.39 \text{ mm}$ , i.e. at the end of the local laser heat treatment: downward bending due to the thermal expansion of the upper side of the finger;
- $dz (t = 7 \text{ s}) = +0.23 \text{ mm}$ , i.e. at the beginning of the cooling phase: phase transitions and high temperature changes at the upper side of the finger lead to a temporary upwards bending of the finger;
- $dz (t = 600 \text{ s}) = -0.016 \text{ mm}$ , i.e. at the end of the cooling phase: all thermal expansions have been abated, the remaining small downwards bending implies that the MEM has been activated;
- $dz (t = 20000 \text{ s}) = -0.017 \text{ mm}$ , i.e. at the end of the stress relief annealing nearly no further geometry changes can be observed.

The observed geometry changes already indicate the activation of the MEM, whereas the effects due

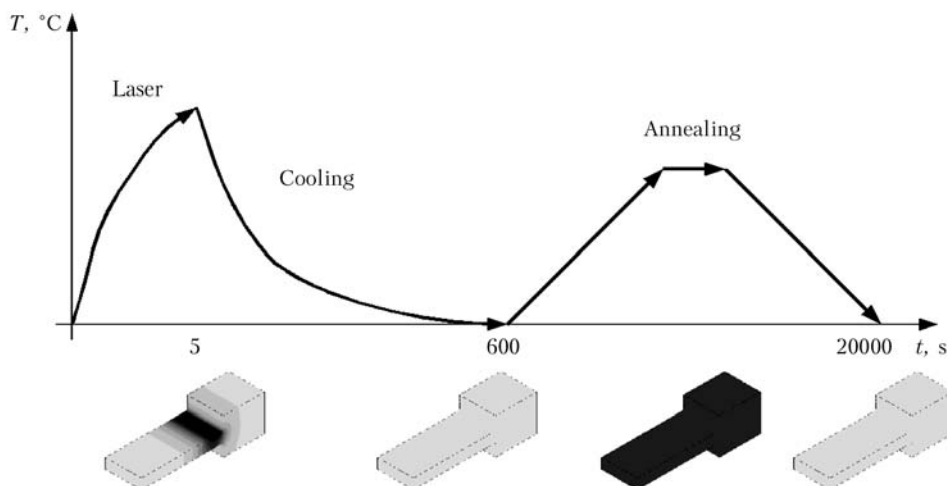


**Figure 13.** Schematic illustration of temperature development at the laser heat treatment position



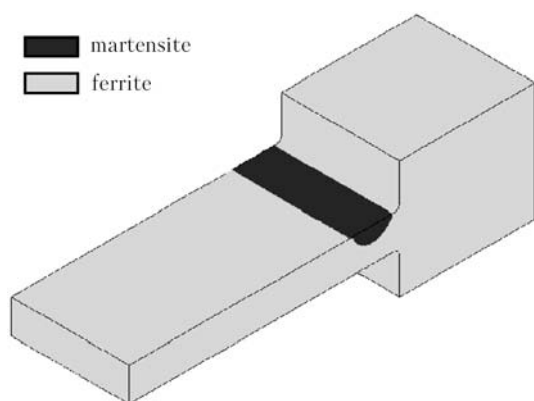


**Figure 14.** Simulated phase distribution after process with laser heat treatment of 5 s, power of 1000 W, treatment area width of 6 mm

to the TGM with the used parameters have only minor effects. The phase distributions after the process (Figure 14) confirm the activation of the MEM. Therefore the MEM was established by simulation for the first time. Up to now only theoretical and experimental investigations [12] have been done according to the MEM.

**Conclusion and outlook.** A method has been developed to model the additional step in the production process chain of steel components, the «distortion potential manipulation» step using a local laser heat treatment. The simulation includes the cooling after the laser heat treatment and a following stress relief annealing which is used as a replacement for the hardening heat treatment process step to release the distortion potential. Experiments and simulation calculations with laser heat treatment parameters which activate the martensite expansion mechanism yielded similar results. Therefore it was possible to confirm the activation of the MEM by simulation for the first time.

Further calculations will be used to investigate the complex behaviour at the beginning of the cooling

phase after the local laser heat treatment and to identify process parameters which activate mainly the TGM, which is more flexible in order to change the distortion potential of the specimens.

**Acknowledgements.** This work has been funded by the German Research Foundation through SFB 570 (Collaborative Research Center «Distortion Engineering»), Subproject B8 «Thermal Induced Prestressing for Distortion Minimization». The authors wish to acknowledge the DFG for their support.

- Hoffmann, F., Kessler, O., Lubben, T. et al. (2002) Verzugsbeherrschung in der Fertigung. *HTM*, 57(3), p. 213–217.
- Volkmath, J. (1996) Eigenspannungen und Verzug. *Ibid.*, 51(3), p. 145–154.
- Hamann, C., Rosen, H.-G. (1990) Relaisfederjustierung mittels gepulster Nd:YAG-Laser. In: *Proc. of Laser'89 Conf.* Berlin: Springer, p. 661–665.
- Rosenthal, A.R. (1992) *Eigenspannungsinduzierung durch Laserstrahlung in scheibenförmige Werkzeuge.* Duesseldorf: VDI.
- Geiger, M., Glasmacher, M., Pucher, H.-J. (1994) Quality assurance for laser beam microbonding in electronic production. *Prod. Engineering*, 84(1), p. 209–214.
- Tonshoff, H.K., Berndt, A.H., Rosenthal, A.R. (1994) Laser based cutting, tensioning and straightening of saw blades – a flexible production line. In: *Proc. of LANE'94 Conf.* Bamberg: Meisenbach, p. 337–343.
- Vollertsen, F., Geiger, M. (1997) Laserstrahljustieren mechatronischer Komponenten. In: *Laser – Von der Wissenschaft zur Anwendung.* Strahltechnik, Band 10. Bremen: BIAS, p. 309–320.
- Lowisch, G., Dalgic, M. (2005) Influence of the temperature on stress-strain curves of a bearing steel and a case hardening steel using pearlitic and austenitic structure. In: *Proc. of IDE Conf.* (Bremen, Sept. 2005), p. 325–333.
- Vollertsen, F. (1996) *Quantitative process modelling.* Sheet metal. Univ. of Twente, p. 411–422.
- Vollertsen, F. (1996) *Laserstrahlumformen – Lasergestützte Formgebung: Verfahren, Mechanismen, Modellierung.* Bamberg: Meisenbach.
- Geiger, M., Vollertsen, F., Amon, St. (1991) Flexible Blechumformung mit Laserstrahlung – Laserstrahlbiegen. *Blech, Rohre, Profile*, 38(11), p. 856–861.
- Pretorius, T., Habedank, G., Woitschig, J. et al. (2006) Thermal generation of residual stress fields for purpose of distortion minimization. *Mat.-wiss. u. Werkstofftech.*, 37(1), p. 85–91.

# TECHNICAL VISION MEANS FOR BUTT FOLLOWING SYSTEMS USED IN WELDING FABRICATION

E.V. SHAPOVALOV and V.A. KOLYADA

E.O. Paton Electric Welding Institute, NASU, Kiev, Ukraine

Control of welding unit positioners consists in formation of control actions for actuators, response to which would guarantee passage by a welding tool of a spacial trajectory with assigned accuracy. If such trajectory is not known in advance, it is advisable to use tracking systems for directing a welding tool at a joint. Three methods of analysis of 3D scenes by technical vision means are known: use of structured illumination, stereo-analysis by means of binocular TV-systems, and determination of a distance pattern by means of scanning distance finders. The method of structured illumination, known as a method of light section, which consists in projection on the surface of items being welded of a narrow light band with its further registration by a video camera, is most widely used. One of shortcomings of the method of light section is its inapplicability for tracking a joint without edge preparation, in which a gap is close to zero. Producers of technical vision means for welding production produce sensors with field of vision only 5 mm for maximum magnification of the image of the butt joint zone. As a result a sensor gets sensitive to the defects of welded surfaces (scratches, flux particles, etc.). At the E.O. Paton EWI a method for tracking a weld without edge preparation is developed. The method is based on mathematical processing of images of welded surfaces illuminated by laser radiation with a wide directivity diagram. This method is applicable for any metal surfaces, allows processing up to 30 frames per second and generating a control signal for each frame.

Numerous problems connected with automation of welding processes and related technologies are encountered now. One of the main components in any currently available welding unit is a system of butt joint parameter data acquisition. Preference is given to data acquisition systems based on technical vision means (TVM).

The most widely accepted are optical systems based on the method of structured illumination. Systems of structured illumination project the light onto the butt and then determine the groove shape and distance to the butt by triangulation method. The projected beams most often form a light plane. Such systems can be applied both for following a butt with grooved edges, and for controlling the welding process parameters based on the obtained information on the groove geometry. Two types of butt following systems with linear illumination were developed: for butt following in welding of longitudinal welds on large-sized pipes, and for following the weld reinforcement during automated ultrasonic testing (AUT).

In case of square butt welding of parts with a gap close to zero, application of TVM with structured illumination is inefficient. To solve such a problem a special optical following system was developed, the operating principle of which is based on processing of digital images. A scattered laser illumination of the working zone is used to increase the contrast of the input video signal.

**Automatic following of weld reinforcement.** During AUT of longitudinal welds on pipes transverse displacements of the weld relative to the ultrasonic transducers arise, which essentially influence the testing quality. A two-channel system of following the

weld reinforcement bead was developed for HK-360 ultrasonic testing system, the description of which is given in [1]. The number of channels in the following system corresponds to the number of independent racks with ultrasonic transducers of NK-360 system. The main objective of the following system is detection of transverse displacement of the center of weld reinforcement relative to a certain fixed position and formation of transverse correction signals. Correction signals are fed to the master controller of AUT unit, which directly controls the drives of horizontal displacement modules of the rack with ultrasonic transducers. The following system consists of three main components, namely two TV optical sensors based on laser triangulation method, and following system controller based on an industrial computer. The method of laser triangulation is considered in [2]. The generalized block-diagram of a two-channel following system is shown in Figure 1. The following system has two independent similar control circuits, closed via the TV sensors. The display is used at adjustment and checking of the following system.

The optical TV sensor includes two main components: laser line generator, which projects a narrow light band on the pipe surface, and video camera which records the image of the light band projection. Each image frame is sent to the controller of the following system for processing. The result of image processing is evaluation of transverse displacement of the weld reinforcement center. The following system controller also has the function of interacting with the master controller of AUT unit by receiving/sending discrete information and control signals.

Software of each channel of the following system is designed for solving the following subproblems: digitizing the video signal obtained from the TV op-

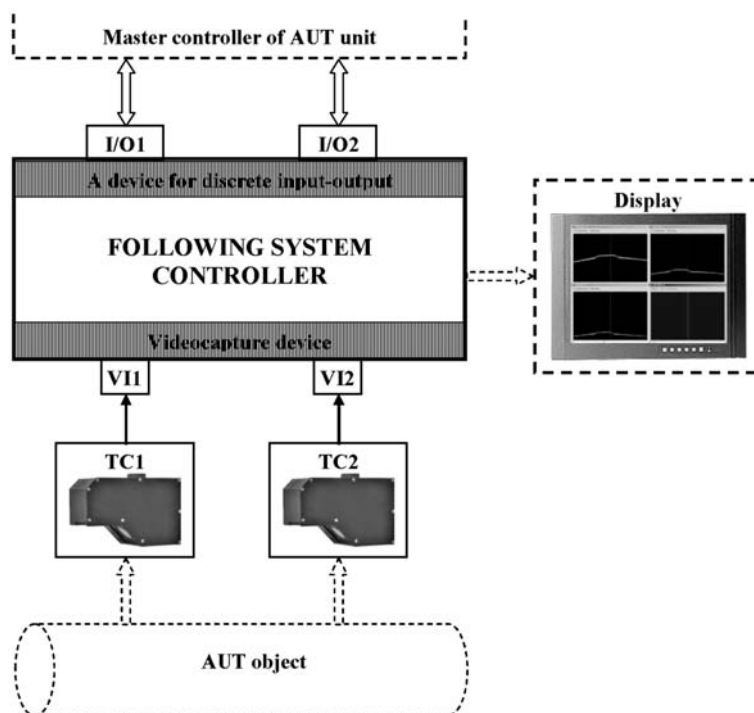


**Figure 1.** Block-diagram of 2-channel following system: I/O1, I/O2 – discrete inputs/outputs for the 1st and 2nd channels; VI1, VI2 – video inputs for the 1st and 2nd channels; TC1, TC2 – TV sensors

tical sensor, preprocessing of the digitized video signal, taking decisions on the obtained signal characteristics, assessment of transverse displacement of the weld reinforcement center, and interaction with the main controller of AUT unit.

Video signal digitizing is performed using a video capture device, included into the hardware of the following system controller. In the digital form each frame captured from the video flow is a matrix of integer numbers, where the element index corresponds to the position of points in the image, and the element value is directly proportional to the pixel brightness.

The main objective of the procedure of image preprocessing consists in separation of the contour of the light band projection. The contour is a curve, which corresponds to the nature of the surface of the object of measurement.

Based on the results of image preprocessing, signal analysis is performed using a set of decision functions. Analysis result is a decision on the degree of the derived contour curve correspondence to weld reinforcement. If the curve contour corresponds to the reinforcement, further frame processing is performed, otherwise processing is interrupted, and the system gives a signal about a failure in the following process.

At evaluation of transverse displacement of the weld reinforcement center the following operations are performed:

- determination of points in the image, which correspond to the edges and center of the weld reinforcement bead;
- transformation of point coordinates from the image coordinate system into the real space coordinate system, i.e. transition from image pixels to millimeters;

- determination of the magnitude and direction of the transverse displacement of the weld reinforcement center relative to the reference point of the following system (reference point is set during adjustment).

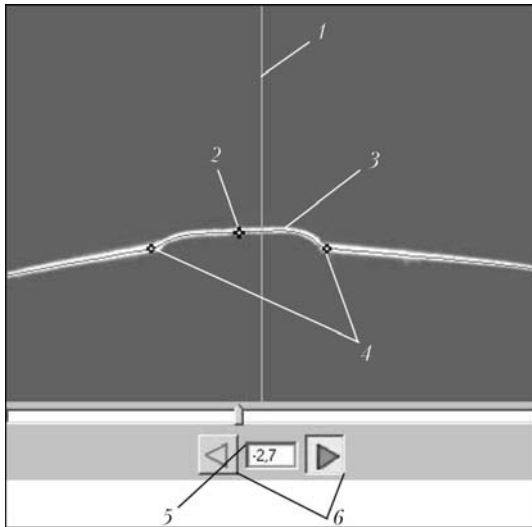
To achieve the transition from the image pixels to millimeters of the real space, the procedure of sensor calibration is first performed using a reference. The applied method of calibration is presented in [3].

Figure 2 gives the results of image processing and evaluation of transverse displacement of the reinforcement bead center.

Each channel of the following system has a certain insensitivity zone, this allowing avoiding the self-oscillation mode at appropriate adjustments of the transverse correction drive. The size of the insensitivity zone determines the accuracy of the following process.

The two-channel system of following the weld bead reinforcement has been successfully tested and is functioning as part of AUT units NK-360 in the Vyksun Metallurgical Works Company, Russia.

**Following systems for pipe production.** Two types of following systems were developed, namely for mills for internal and external welding of large-sized pipes. In welding of an outer longitudinal weld the groove is V-shaped with partial filling after the technological pass. In case of welding of the inner weld a square edge butt with a gap close to zero is used. Different types of butt joints led to application of various approaches in development of following systems for mills for external and internal welding. In the general form both types of the systems have a similar structure. The main differences consist in the structural features and principle of operation of TV sensors, and, as a result, in the algorithms for video signal processing for different types of systems. In



**Figure 2.** Results of image processing: 1 – axis determining system reference point; 2 – reinforcement bead center; 3 – contour of light band projection; 4 – reinforcement bead edges; 5 – mismatch value, mm; 6 – indications of correction direction

the following system for mills for external welding a TV sensor is used, which is based on the classical method of laser triangulation. A combined approach is used in the TV sensors for mills for internal welding. Here, laser triangulation is complemented by the method of diffuse illumination, which was developed specially for detection of the transverse displacement of the butt with a «zero» gap [4]. Both types of the following systems allow evaluation of both the transverse (horizontal), and vertical relative displacements of the butt. The lag of the following system is directly proportional to the distance between the TV sensor and welding tool. The main problem which was solved in development of the structures of TV sensor cases was moving the TV sensors as close as possible to the welding point, allowing for the design features of welding heads.

The generalized schematic of the butt following system is shown in Figure 3. The controller is an industrial computer, fitted with the devices of video capture, discrete input-output, and appropriate software. The video capture device is designed for entering

and digitizing the video signal from the TV sensor. The device of the discrete input-output forms control signals for the drives of welding tool position correction and takes commands from the operator panel. The graphic display connected to the controller, is used for visualization of the process of butt following and displaying the welding parameters. The sound alarm device is designed for generating a sound signal in case of system failure. Output discrete signals «Right», «Left», «Upwards», «Downwards» represent the corrective actions for the respective drives. Input signals are as follows: «Auto» (switching on of automatic butt following); «Switch off horizontal correction» (switching off of automatic correction along a horizontal); «Switch off vertical correction» (switching off the automatic correction along the vertical); «Nulling» (setting the system reference point).

General principle of the following system operation can be presented as follows. After switching on the controller and loading the software, the following system is in the standby mode. If adjustment or repair of the welding head was conducted, it is necessary to perform the operation of «nulling». Welding operator using the manual correction means aligns the electrodes with the butt center and presses the «Nulling» button, so that the following system «memorizes» the zero horizontal and vertical displacements of the welding tool relative to the butt. After pressing «Auto» button on the operator panel, the system goes into the mode of automatic following along the horizontal and vertical. During automatic following correction actions «Right», «Left», «Upwards» and «Downwards» are issued, depending on the direction of displacement of the butt center relative to the system reference point, which was set during the «nulling» operation.

System discrete inputs «Switch off horizontal correction» and «Switch off vertical correction» are connected in parallel to the respective buttons of the horizontal and vertical manual corrector. If during automatic following the welding operator has pressed the horizontal corrector button, the following system switches off the automatic horizontal correction, but

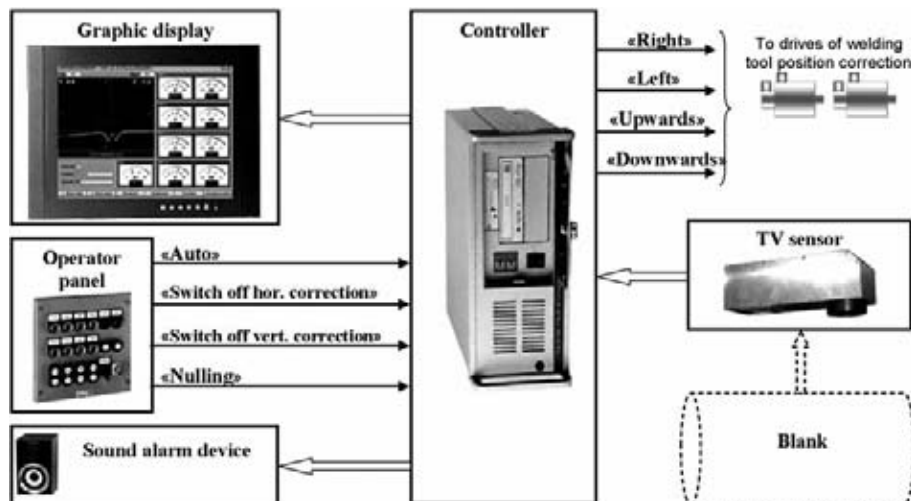


**Figure 3.** Block-diagram of butt following system

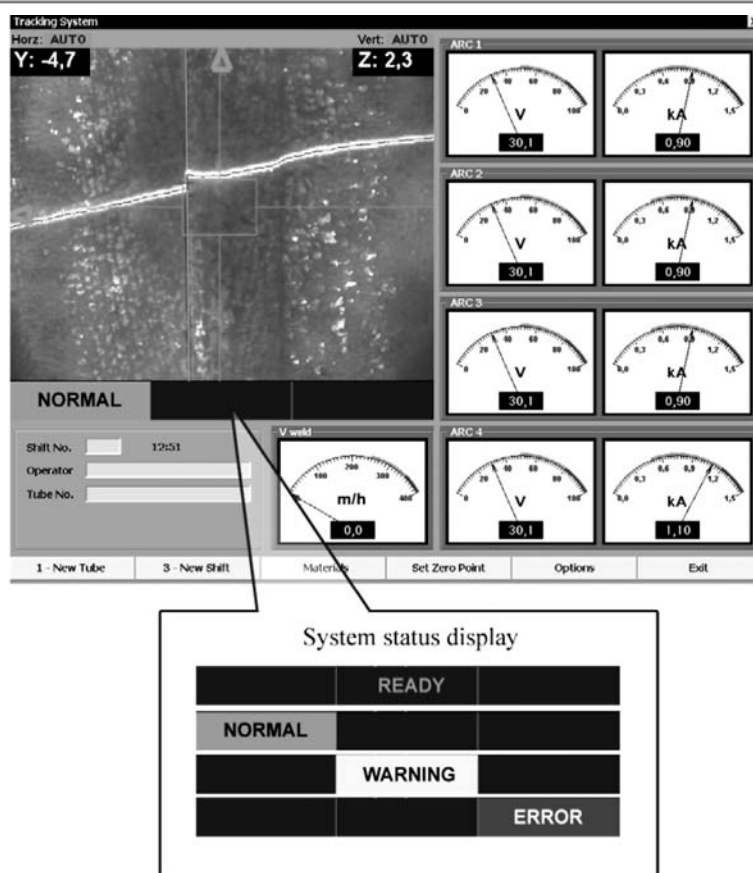


Figure 4. Main dialogue window of following system software

still continues controlling the vertical and otherwise. At simultaneous or successive pressing of the buttons of the horizontal and vertical manual corrector the following system goes into the standby mode.

If in the process of automatic following the system cannot find the butt for some time, a visual message on the critical error (failure) and a sound alarm is issued. For rejecting the critical error and switching the system into the standby mode it is necessary to press one of the buttons of the manual corrector.

A special graphic interface was developed for interaction of the welding operator with the following system. Dialogue windows of the software of following systems for the mills for internal and external welding look similar (Figure 4).

Located in the left part of the dialogue window is a rectangular area for displaying the graphic information, associated with the butt following process. Coordinate axes are applied on the initial video signal, which determine the system reference point, indicators of the correction direction and «crosshair» designed for indication of the found position of the butt center in the image. «Hor.» and «Vert.» indicators are designed for displaying the current mode of controlling the horizontal and vertical correction («MC» is the mode of manual control of correctors, and «Auto» is the automatic correction mode). Current values of horizontal and vertical displacements of the butt center in millimeters are also displayed (fields Y and Z). Indicator of system condition is used for

displaying the following messages: «Readiness» (system is ready for switching on the automatic correction mode); «Norm» (following process runs normally); «Attention» (warning about system malfunction); «Failure» (critical error, i.e. further automatic following is impossible). Graphic models of the indicators are designed for displaying the current parameters of the welding mode, fed from the welding unit.

Systems of following for mills for internal and external welding of longitudinal butt joints on large-sized pipes have been put into production in Khar'tsyzsk Pipe Plant Company, Ukraine.

## CONCLUSION

Means of technical vision are one of the most important components used in automation of production processes. Their flexibility and versatility allows solving a broad range of problems related to welding fabrication. Improvement of the hardware and software related to automatic following of the butt is a promising direction in development of modern science and technology.

1. Najda, V.L., Mozzhukhin, A.A., Lobanov, O.F. (2004) New generation of equipment for automated ultrasonic testing of welded pipes. *The Paton Welding J.*, **9**, p. 57–61.
2. Boillot, J.P., Noruk, J. (2002) The benefits of laser vision in robotic arc welding. *Welding Tech.*, **8**, p. 33–34.
3. Kiselevsky, F.N., Kolyada, V.A. (2005) Calibration of triangulation optical sensors. *The Paton Welding J.*, **5**, p. 48–49.
4. Kiselevsky, F.N., Butakov, G.A., Dolinenko, V.V. et al. (2003) Optical sensor for butt following at gap sizes close to zero. *Ibid.*, **2**, p. 48–50.

# COMPUTER-AIDED TECHNOLOGY FOR CHECKING OF SHAPE PARAMETERS OF WELDED AND PIPE STRUCTURES IN SHIPBUILDING WITH USE OF LOCATION ACOUSTIC MEASURING STATIONS

V.A. SINITSKY

FSUE Central Research Institute of Shipbuilding Technology, St.-Petersburg, Russia

The article is devoted to research and development of a new advanced method and the location acoustic measuring station (LAMS) equipment to provide geometrical parameters control of ship articles and structures which has no analogs in domestic industry and abroad in the form of complete industrial standards of technological control equipment. A principle of acoustic location which underlies in the station operation is a contact-probe excitation of spherical waves and determination of control point coordinates of multi-microphone receiving aerial with further automatic embedded computer calculation of sizes and forms of articles with drawing construction. The advantages and prospects of the LAMS equipment introduction into the shipbuilding yards pipe shop have been outlined.

FSUE CRIST in cooperation with INFIIS, Moscow, has recently carried out a number of research work to develop a new advanced method and equipment for measuring of geometric parameters of ship-borne items and structures. Either in Russia or abroad no analogue equipment for this technique has been developed up to the stage of production pieces for process monitoring [1–3].

We have manufactured and tested at the shopfloor of shipbuilding yards a samples of fast-operating LAMS, which allows replacing manual tools, appliances (such as templates and brackets) and optical devices during dimension checking operations.

The LAMS operates on the basis of acoustic location, i.e. contact acoustic emitter (a bar with two electrical loud speakers) positioned in test points of the item, excites spherical acoustic waves and thereafter a multi-microphone antenna defines coordinates of test points with carrying further automatic estimations of shape and dimensions of the items in the preset coordinate system, with use of built-in PC, and generation of a drawing.

The item to be measured, e.g. a pipe, is secured on a platform in the shop. Thereafter we mark test points: for each control section of the pipe two point should be marked within the limits of 60–90° sector. Then the operator takes the acoustic bar and sets its tip sequentially to each of test point on the pipe surface, and presses the start button, which is connected to the electronic unit with a cable. The electronic unit generates strong exciting impulses, which are coming to two emitters on the bar with intervals of 0.1 s. At the same time each emitter generates spherical acoustic wave, which passes through the air and the electronic unit starts time measuring devices, connected to microphones of the receiving antenna.

Acoustic wave front from each emitter is received with antenna microphone and then converted into electric impulses for each measuring channel, which stop operation of time measuring devices, defining time intervals  $t_1, t_2, t_3$  between the moment of acoustic wave generation and reaching of this wave front to the microphones.

With a special program, a PC estimates distances  $L_1, L_2, L_3$  between geometrical centers of bar emitters and each of the microphones, using the formulas:

$$L_1 = t_1 C; \quad L_2 = t_2 C; \quad L_3 = t_3 C,$$

where  $C$  is the sound velocity in the environment air (with correction for air temperature), and then calculated coordinates  $X, Y$  and  $Z$  of geometrical emitters center in the coordinate system of the antenna (transverse  $X$ -axis crosses centers of two lower microphones, vertical  $Y$ -axis crosses  $X$ -axis in the middle between lower microphones, longitudinal axis is  $Z$ ).

Then a mathematic description is elaborated for a straight line, crossing coordinates of geometrical centers of bar emitters, and a known distance from bar tip to the center of the nearest emitter is marked on this line, allowing us to obtain coordinates of test points of the measured item, scanned with the bar tip.

Appearance and composition of LAMS is presented in Figures 1 and 2, respectively.

## Specification of station (average standard set)

Measuring range with distance from its front to acoustic antenna no more than 2 m, m:	
triangle-type measuring antenna (side size 700 mm) .....	2 × 1 × 1
triangle-type measuring antenna (side size 1500 mm) .....	4 × 2 × 2
Measurement allowance for difference in any two-point coordinates in measuring range, mm:	
measuring range 2 × 1 × 1 m .....	max. 1.0
measuring range 4 × 2 × 2 m .....	max. 1.5



Figure 1. Appearance of LAMS

Measurement coordinate system — right-hand rectangular: .....	longitudinal Z-axis, transverse X-axis, vertical Y-axis
Measurement time for point coordinates, s .....	2
Indication of measured coordinates of test points:	not less than 4 digits after decimal point, 2 digits after digital point
Sources of acoustic waves: contact electrodynamical probe .....	single-pulse laser
Sensitivity of acoustic sensor, mV/Pa .....	5–10
Power supply, V:	
network .....	220
portable battery .....	12

Areas of application of the LAMS were explained to representatives of three leading shipyards during presentation of the equipment:

- checking shape of sections of hull plating parts along templates control lines during bending with presses. The results are compared with the task drawing and displayed on PC monitor;
- checking shape of profile metal bents during forming frame-type parts with special bending machine and bending presses;
- final checking of parts bent with presses without use of frame templates;
- checking shape of pipelines, their wire templates, mutual positioning of welded flanges and pipe ends.

It was recommended to start implementation of LAMS in pipe shops of shipyards. This recommendation was given due to the following reasons:

- FSUE CRIST has developed an automated systems «Ritm-Sudno. Pipes», allowing to fulfill the following tasks: express processing of measuring data with use of PC, built-in in the LAMS, automatic generation of 3-projection drawing of measured pipe with all necessary dimensions, generation of axonometric pipe image and elaboration of control program for CNC-controlled pipe bending machine;
- majority of insert pipes can be placed within local measuring range of  $2 \times 1 \times 1$  m;
- checking technique allows preliminary measuring of pipe diameter and distance between end points (tying length) with mechanical instruments, thus al-

lowing to compare measuring results, obtained with the LAMS, to the calibration standards and to achieve required accuracy of measurements in case of environmental changes;

- there is a possibility for considerable economy by rejecting wire templates and generation of control programs for CNC pipe bending machines on the base of digital data from the LAMS, especially for manufacturing of insert pipes.

All the above-mentioned advantages were proved during trials of the LAMS in pipe shop at the shipyard for the purpose of checking shape and dimensions of bent pipes, where for each particular pipe a chart drawing was generated for subsequent processing with pipe bending machine (Figure 3).

During 2006, FSUE CRIST intends to manufacture and deliver to pipe production facilities a pilot LAMS, suitable for further series production. A number of effective technical solutions were implemented for this station.

Multi-microphone LAMS antenna is equipped with electret microphones-sensors with preamplifiers. Their adjustment and tuning can be done on a simple stand of «optical bench» type with reference bases. Sensors are controlled with one of software operations, displaying on the monitor not only coordinates

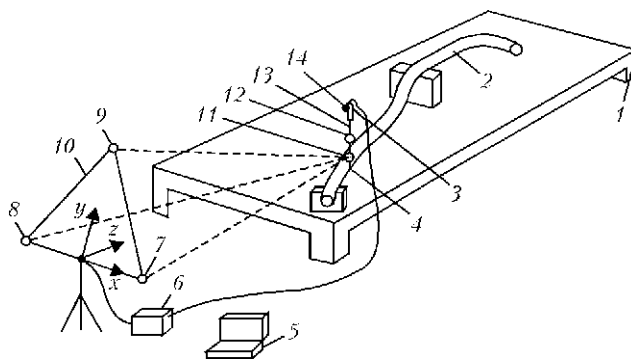


Figure 2. Composition of LAMS: 1 — platform; 2 — pipe; 3 — bar handle; 4 — bar tip; 5 — PC; 6 — electronic unit; 7–9 — microphones; 10 — receiving antenna; 11, 12 — electrical loudspeakers; 13 — acoustic bar; 14 — start button

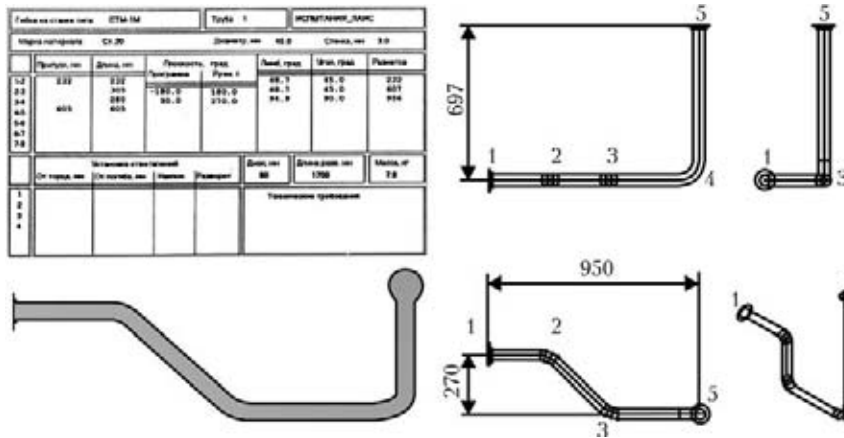


Figure 3. Example of the LAMS output measurement data

of test points X, Y, Z, but also convergence (in mm percent) of distance rays from centers of three main and one auxiliary microphones for each point, calculated by triangular method.

Effects from fluctuation of temperature, humidity, dust and wind is eliminated through automatic testing of the station during measurement process with taking as a reference value a known distance between two acoustic emitters of the bar of special reference base, located within the measuring range. Averaging of multiple measuring results for each test point also helps to obtain this objective, since processing speed of the LAMS allows one to carry out multiple measurements fast.

As acoustic emitters small-sized high-frequency electrical loudspeakers are used, with optimal distance between their centers of 350–400 mm, and distance between the bar end and center of the nearest emitter can vary between 50–120 mm, thus allowing data to be taken from test points located out of the line-of-sight coverage of the microphones.

Obtained by the LAMS data can be transferred to the user on a floppy disk, CD, flash memory card or through the cable. Data configuration is fully complied with design feature of pipe bending machines and pipe bending standard, being used with system «Ritm-Sudno. Pipes», developed by FSUE CRIST and with guiding document «Ship Systems and Systems of Ship-Borne Power Plants. Requirements to Design, Manufacturing and Installation of Pipes in Accordance with Sketches and Drawings with Coordinates of Pipeline Routes».

For making design of insert pipe route onboard a vessel under construction using LAMS, plugs with punches in the center are inserted in the flanges, subject for connection. Tip of the LAMS bar is placed in the punch mark, thus allowing coordinates of flange opening centers to be defined.

By moving the bar tip along the proposed route of the insert pipe, the LAMS defines digital trajectory, considering calibration reference base, located within the measuring range. On the basis of obtained digital data a final shape of the pipe is generated with the PC along with processing program for pipe bending machine. After manufacturing the pipe is connected with flanges on the stand and shifted onboard to the installation site.

Advantages of the LAMS in comparison with other measuring systems are high measuring speed (up to 2 s for 1 point), measuring in the coordinate system of receiving antenna without requirement of reference bases, easy maintenance, not requiring tiresome manual operations and high qualification of servicing personnel, low cost in comparison with tacheometers and measuring equipment with angular sensors.

1. Syasko, V.A., Sinitsky, V.A. (2003) Use of laser-acoustic method and high-speed measuring station for checking dimensions and shape of ship articles and structures. *Shipbuilding Technology Rev.*, Issue 10.
2. Benditsky, A.A., Shelemin, E.B. *Method for measuring distance to the object*. Summary of inv. USSR author's cert. 1835048. Int. Cl. G01D17.00. Publ. 15.08.93.
3. Benditsky, A.A. (1994) Optical and acoustic location — a new method for definition of object coordinates. *Measuring Eng.*, Issue 7.



# CHARACTERISTICS OF MAGNETIC FIELD IN AUTOMATED MULTI-TORCHES FCAW

SUNG-HOON KO, HYEONG-SOON MOON and JONG-CHEOL KIM

Hyundai Industrial Research Institute, Korea

In order to reduce the prime cost and to improve productivity in heavy industries, a variety of attempts are developing including automatic equipment and new welding technology. Among them, multi-torches welding process comes to rise as a crucial step due to its high productivity. However it is difficult to set up proper welding parameters since the arcs of each electrode interfere with each other. To enhance quality and reliability in multi-torches welding, the study on characteristics and the interference of multi-torches arcs should be given priority over all others. In this study, the arc shapes were photographed by using high-speed camera to measure the length and width of arc. The arc shape was also formulated with a simple equation in terms of welding parameters. Based on the magnetic field around the arc calculated using finite element method, the effect of arc shape on the magnetic flux was evaluated. The minimum distances between arcs to avoid interference for various welding parameters could be determined using the results of the analysis.

Since welding is the principal manufacturing process in ship building industries, studies are continuously accomplished to reduce the prime cost and to improve productivity in welding process. Since fillet flux-cored arc welding (FCAW) holds 70 % of welding process in ship building, it is a world-wide tendency that introduces welding automatic equipment and develops welding technology used for automatic equipment in FCAW. The twin tandem FCAW process among such researches has been supplied widely and is increasingly used due to its triple high productivity compared with single-torch process. Recently, a three torch welding technique in FCAW was developed to increase welding speed and was almost put to practical use [1]. In general, welding process using multi-torches can be operated in comparatively higher welding speed and help to decrease welding deformation, as it has higher electrode melting rate and lower heat input compared with single-torch process [2]. However it is needed to establish a reliable automated equipment of high cost and it is difficult to set up proper welding parameters since the flow of molten metal shows a complex behavior because of relatively long weld pool and the interference of each arc. To enhance quality and reliability in automated multi-torches FCAW, the study on characteristics and the interference of multi-torches arcs should be given priority over all others.

In this study, the arc shapes were photographed by using high-speed camera to measure the length and width of arc. The arc shape was also formulated with a simple equation in terms of welding parameters. In order to study the mutual interference of arcs in the FCAW system with multi-torches, the magnetic flux densities on FCA weldment were evaluated using electro-magnetic field analysis. Based upon the results of the finite element analysis, the effect of arc shape on the magnetic flux was also evaluated, and the minimum space of torches which can prevent mutual interference of arcs was established.

**Photography of arc. Equipment.** As shown in Figure 1, the equipment to capture the photograph of arc consists of a rotating positioner, a welding machine and high-speed camera system. The high-speed camera is located at the same height with welding arc. Panasonic RF600 as the welding machine, AWS E70T-1 as the welding electrode, and CO<sub>2</sub> as the shielding gas, were used for this experiment.

## Analysis of arc shape

It is difficult to represent an arc shape with a few of photographs while the length and width of arc are continuously changed by the molten metal transfer in FCAW. In this study, the average arc shape was determined by using a statistical method which analyzes a number of photos taken with the high-speed camera. The deflection of arc is defined as the length between arc center and electrode center on the surface of base metal, as shown in Figure 2.

The outline of the arc can be extracted using threshold image processing from photos of arc captured from photographed movie, and the length and the deflection of arc are easily measured (Figure 3).

**Regression model of arc shape.** Welding voltage is the sum of voltage of cable, electrode and arc (1), if welding current is constant, welding voltage is proportional to arc length, therefore, arc length is gene-

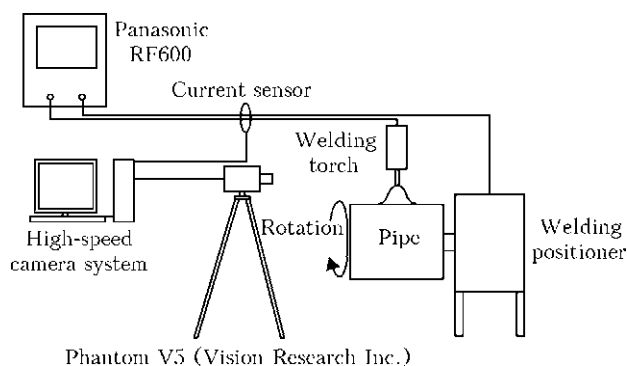
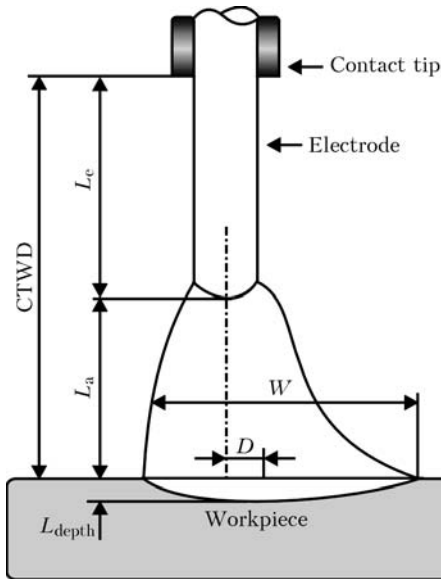


Figure 1. Schematic diagram of experimental equipment



**Figure 2.** Model of arc shape:  $L_e$  – electrode extension length;  $L_a$  – length from the tip of electrode to base metal;  $W$  – arc width;  $D$  – arc deflection

rally expressed the function of welding voltage and current (2) [3]:

$$V = V_0 + (R_c + R_e + R_a)I + E_a L_a, \quad (1)$$

$$L_a = \frac{V - V_0 - (R_c + R_e + R_a)I}{E_a}, \quad (2)$$

where  $V$  is the welding voltage;  $V_0$  is the initial constant of voltage;  $R_c$  is the resistance of cable;  $R_e$  is the resistance of electrode;  $R_a$  is the resistance of arc;  $E_a$  is the intensity of electric field.

The constants in above equations are determined by experiment and are affected by metal transfer mode, shielding gas etc. [4]. However equation (2) proposed for an ideal symmetric arc model does not reflect the effect of arc deflection due to moving electrode. In order to estimate accurate arc length in moving electrode conditions, a modified approach is required to take account of arc deflection. Arc shape is generally affected by many factors, such as welding

Experimental models and results of Taguchi method

$I$ , A	$U$ , V	$v$ , m/min	$L_a$ , mm	$D$ , mm
300	32	1.0	2.6	0.9
	35	1.5	4.2	0.3
	38	2.0	4.8	0.5
360	32	1.5	2.7	0.6
	35	2.0	3.1	0.3
	38	1.0	3.4	0.5
420	32	2.0	1.4	1.5
	35	1.0	1.1	2.0
	38	1.5	3.0	0.6

voltage, current, type of shielding gas, welding speed, distance between contact tip and base metal, material and diameter of electrode and flux. However, main factors among them are welding voltage, current and speed. The effects of main factors on arc length were evaluated using Taguchi method, and the length and deflection of arc was interpolated based on the experimental results. The experimental models and results of Taguchi method are shown in the Table.

**Electro-magnetic field analysis**

It can be estimated that the induced electro-magnetic field formed around arc and base metal interferes the arc in multi-torches welding process. To calculate the distribution of the electro-magnetic field, the finite element method (FEM) was used. The models of cylinder and truncated cone were utilized as arc shape for FEM analysis (Figure 4, a), and mesh design of arc (Figure 4, b).

To analyze electro-magnetic field, first of all, the current distribution in arc and base metal has to be calculated. The current flows not only through the shortest path from electrode to ground but through the entire base metal (Figure 5). Because current density around arc and ground is relatively high, magnetic field induced by current affects only neighboring arcs in multi-torches welding process.

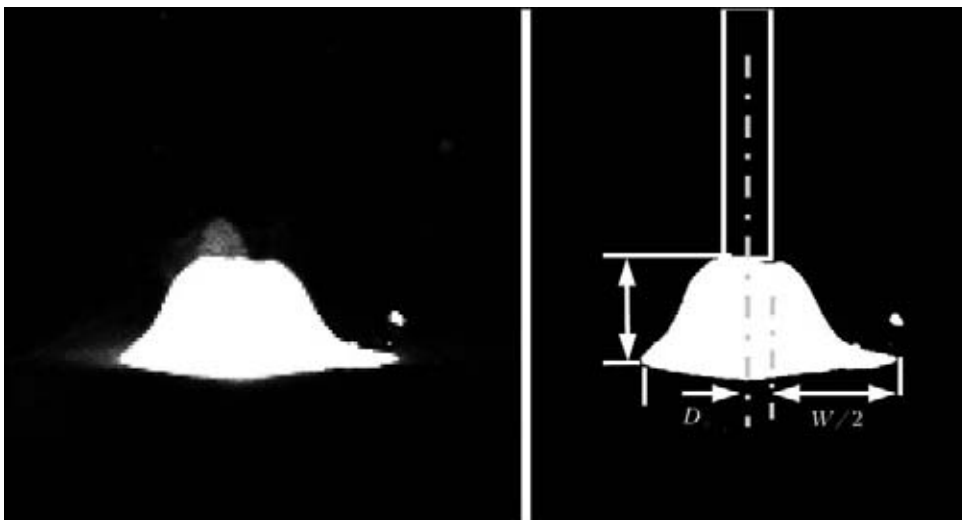


**Figure 3.** Measurement of arc shape from arc image

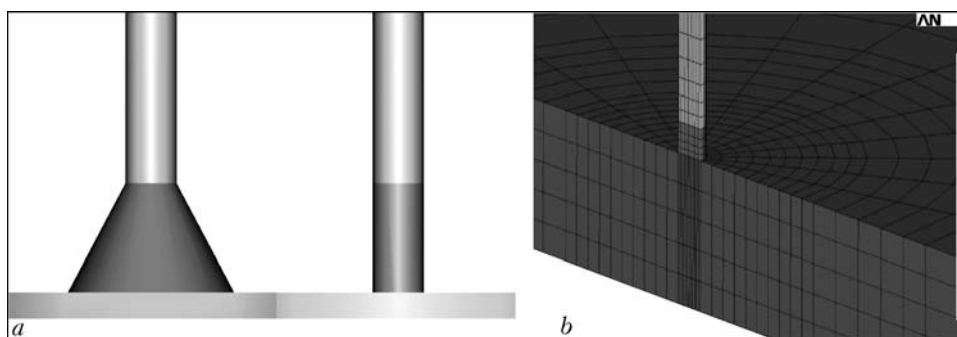


Figure 4. Model of assumed arc shape (a) and mesh design of arc (b)

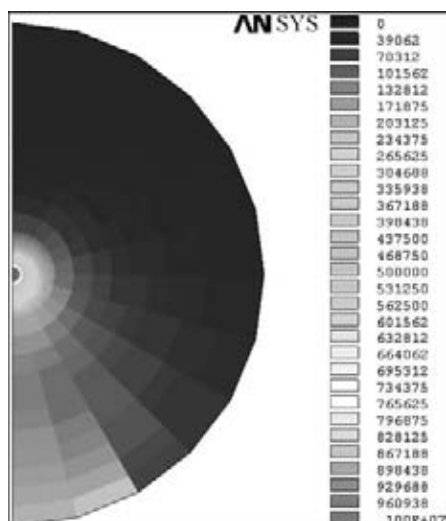


Figure 5. Contour of 400 A current density, A/mm<sup>2</sup>

Induced magnetic flux density calculated by FEM is shown in Figure 6, when arc length is 3 mm long and 400 A of welding current flow. The magnetic flux density on the electrode and base metal is very high because permeability of metal is higher than that of air and that on air around electrode is relatively low and uniform. However the magnetic flux density on arc is more complex and higher, because of high current density and low permeability than that of air.

The distance from arc center to the position, where magnetic flux density is 50 Gs, was 17.6 mm in the direction of ground and 15.4 mm in the opposite direction of ground. In the direction of ground, as the directions of magnetic flux induced by current flowed on base metal and electrode corresponded, magnetic flux density was slightly higher than that in other direction. For various arc lengths, Figure 7 shows the maximum distance from arc center to position at magnetic flux density of 50 Gs. Because of very low variance of distance, the effect of arc length change can be neglected when distance from electrode center is over 10 mm.

## CONCLUSION

In order to prevent interference of arcs in multi-torches FCAW, the characteristics of induced magnetic field were evaluated using the finite element method and the statistic analysis. Arc shape was determined using the statistic analysis from a number of photog-



Figure 6. Contour of magnetic flux density at current of 400 A

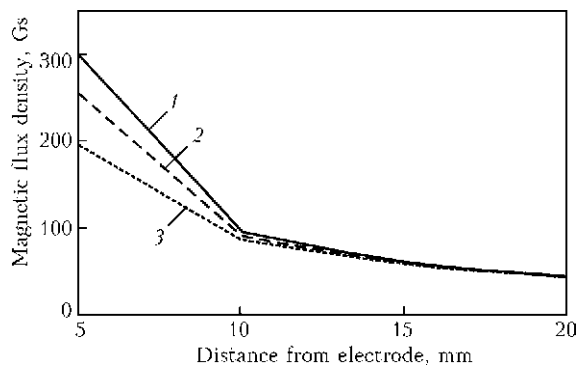


Figure 7. Effect of 5 (1), 3 (2) and 1 (3) mm arc length on magnetic flux density

raphs which were captured in high-speed movie and the regression model of arc shape was proposed as a function of welding voltage, current and speed. The induced magnetic field around the arc was calculated using the FEM and the minimum distances to avoid interference of arcs for various welding currents could be determined using the results of the analysis. This research will be applied to the development of arc sensor for multi-torches welding.

1. Mulligan, S.J., Melton, G.B. (2002) Assessment of the tandem MIG-MAG welding process. In: *TWI Report 745*.
2. (1996) *Patent 8-224667 Japan*.
3. Lancaster, J.F. (1986) *Physics of welding*. 2nd ed. Pergamon Press.
4. Ushio, M., Mao, W. (1996) An analysis of the dynamic characteristics of the arc sensor for DC MIG/MAG welding in open arc model — a study on the improvement of the sensitivity and the reliability of the arc sensor in GMA welding. Report 2. *J. JWS*, 14(1), p. 108-111.

# WELD MONITORING AND STABILITY INDICES

J. TAPP, P. GUY and K. CHAWLA

Triton Electronics Ltd., UK

With the development of current welding power sources and control techniques there is an increased need for faster and more intelligent monitoring systems. This paper discusses some of the requirements for monitors capable of determining welding waveforms. Further, some analysis procedures are discussed both for the description of the welding waveform and to assess arc stability. Arc weld monitoring started some thirty or forty years ago when power source waveforms were uncomplicated and average welding parameters were required. The main goal of weld monitoring was to ensure a welding procedure was accurately recorded and then replicated. Even today this quality function is still required despite onboard power source data monitors. The basic arc weld monitor offers an independent, external record of the weld. Over time these monitors have acquired data storage and communications functions. Most welding waveforms are 400 Hz or slower and it is now possible to digitally record these with faster arc welding monitors. Typically, these systems operate at 5 kHz or more per channel. However, the more advanced power sources now control the waveform to improve the welding characteristics, such as reduced spatter or greater tolerance to standoff variation. This is often achieved with a small pulse overlaid on the main waveform, to accurately describe these small pulses faster data logging is required, and monitors are available with a logging frequency of 100 kHz. If basic monitors were developed to provide procedure quality control so the faster monitors have become tools that can analyse small fluctuations in the welding waveform. Many authors have detected quality indicators from these fluctuations, initially for arc stability, where consumable performance can be objectively assessed and welding parameters compared. However, some models claim to be able to detect weld defects caused by surface preparation, root gap shielding gas failure as just some examples. The techniques range from looking at transient features on a welding waveform to developing a programme based on Chaos theory to identify potential errors or instabilities. This paper offers a brief overview of some of these techniques.

As modern power sources become more complex and welding is more controlled so it is important that weld monitors are developed with greater capability both for accurately capturing the waveform and for describing the data in ways that are relevant to welding. This paper is split into three sections, the first describes what is required for a fast welding monitor. The second illustrates how this system can be applied to a quality control database so increasing producti-

vity and accuracy. The third looks at some stability indices and shows how these can be used to describe the welding process and opens up the opportunity for automatic parameter determination and fault detection.

**Welding monitor.** Historically welding monitors have been used for the verification of welding parameters and so only need to record average data. These have been termed basic monitors [1] and have been the following characteristics: average values of current, voltage; very robust construction; heat input calculation, and portable and battery powered. All monitors comply with standard accuracies listed in Table 1.

To accurately monitor a welding waveform it is important to monitor with a higher frequency than the underlying process waveform. Figure 1 shows that if frequency determination is required then logging at twice the process frequency is sufficient, however if amplitude determination is required this needs to be increased to 10 or more times the process frequency.

Typical frequencies associated with arc welding processes are listed in Table 2. These will range from a few Hertz to around 400 Hz found in AC and spray

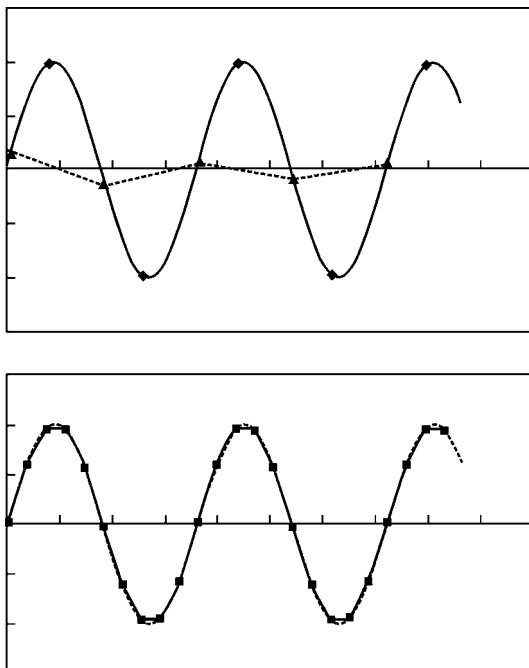


Figure 1. Illustration of monitoring frequency

Table 1. Validation accuracies for power sources BS 7570 2000 «Code of Practice for Validation of Arc Welding Equipment»

	Standard grade power sources	Precision grade power sources
Quantity	Accuracy	Accuracy
Current meter	± 2.5 % of maximum rated welding current	± 1 % of maximum rated welding current

**Table 2.** Process frequencies

Process	Variation	Main frequency, Hz	Monitor frequency for process determination, Hz × frq
GTAW	DC	NA	1000
	Pulse	0.1–10	1000 × 100
	AC	50–400	1000 × 20
GMAW	Dip	100–300	6000 × 20
	Globular	10–50	1000 × 20
	Spray	250–400	8000 × 20
	Pulse	50–300	5000 × 20
	AC	50–400	8000 × 20

applications. Hence any fast monitor should be capable of monitoring in excess of 8000 Hz per channel recorded. This should guarantee a 20 to 1 ratio and so allow full mapping of the waveform.

**The AMV 4000.** This is a PC based fast welding monitor (Figure 2) fulfilling the requirements listed in Table 2.

The monitoring software is designed to be easy to use both for production welding and research applications. The fundamental concept is that the data logging is handled by the AMV 4000 but the remaining data interpretation and handling is modular. The code is constructed in such a way that additional modules can be added for quality control or process stability. Figure 3 shows how the 3 areas interact.

The process analysis is expected to include routines for describing the waveform such as stability analysis. The bespoke code can include control strategy based on either the raw data or the process analysis or both together.

*Setting-up the AMV4000.* The AMV 4000 can be set-up either simply just by entering the process and channels to monitor. The data acquisition rate and process related factors (including heat input efficiency) are automatically set. This screen is shown in Figure 4. The number of channels to be monitored is also set on this screen along with standard QC information such as operator and procedure name. The



**Figure 2.** AMV 4000

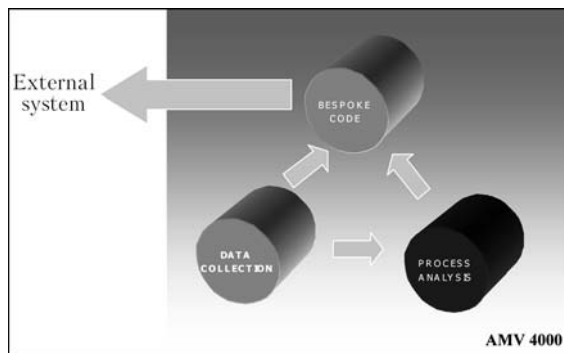


**Figure 3.** AMV 4000 code regions

AMV 4000 can also be tailored to a specific welding requirement in which case the advanced set-up routine is used. Figure 5 shows this screen. The main considerations are as follows.

*Set sample rate.* This determines the overall sample frequency. The maximum is 100 kHz, so if all 8 channels are recorded then each is sampled at 12.5 kHz per channel. If only 2 are recorded then each is sampled at 50 kHz.

*Set trigger channel.* By default the AMV 4000 triggers if it senses more than 5 V and 20 A but this can be changed if required. Any single channel can be selected and the trigger value set. Only current and voltage are used jointly though.

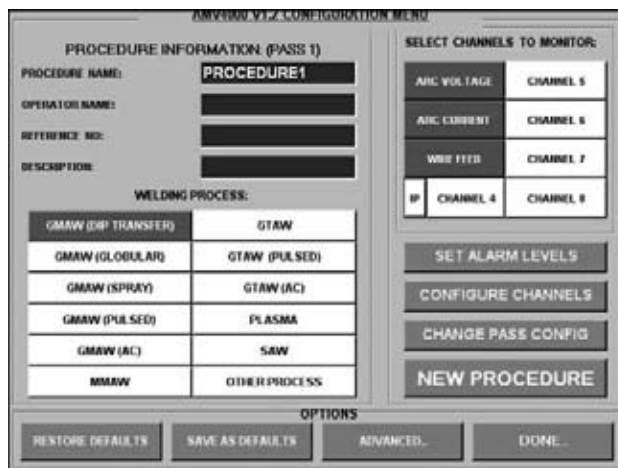


**Figure 4.** Configuration screen

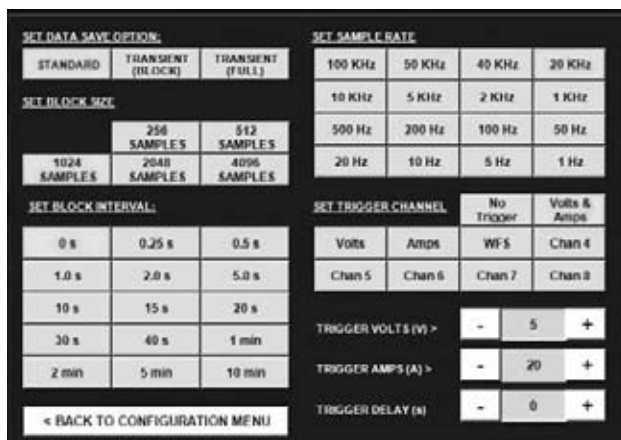


**Figure 5.** Advanced screen

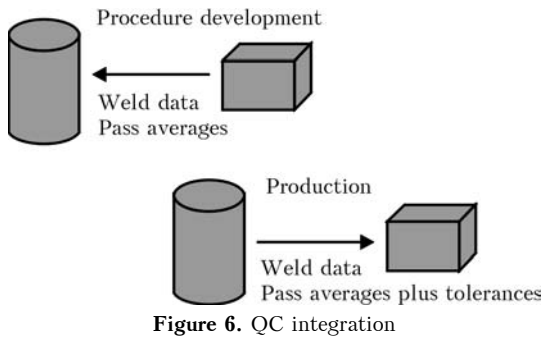


Figure 6. QC integration

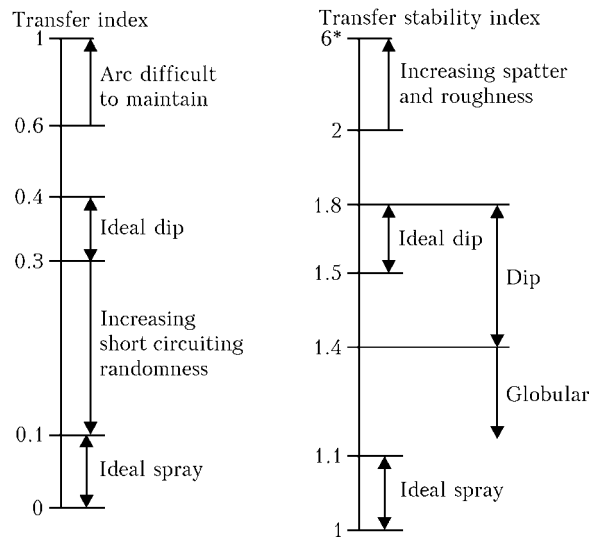


Figure 8. Cranfield stability indices

TRITON ELECTRONICS LTD AMV4000 V1.2 - PROCEDURE SUMMARY FILE										
PROCEDURE NAME: SA4678										
OPERATOR NAME: SIMON JONES										
REFERENCE NUMBER: 234875										
DESCRIPTION: PIPE WELD										
DATE STARTED: 01/06/2006										
TIME STARTED: 17:12:41										
DATE COMPLETED: 01/06/2006										
TIME COMPLETED: 17:16:10										
PASS NUMBER	ARC VOLTAGE	ARC CURRENT	WIRE FEED	TEMP	Interpass or Standard	PROCESS	WELD LENGTH	ARC DURATION	HEAT INPUT	ARC ENERGY
1	60	596.2	0	0	Standard	GTAW	500	27	1.1592	1.932
2	60.4	599.6	15.5	88.79108	Interpass	GMAW (SPRAY)	500	39.1	2.2656	2.832
3	60.3	598.7	15.4	88.79108	Interpass	GMAW (SPRAY)	500	22	1.2704	1.588

Figure 7. Pass welding data

**Block size.** This determines how many samples are collected in one block. Once the block is full all calculations are performed such as average values, peak values and stability index.

**Set block interval.** The blocks can be continuous (i.e. 0 block interval) or they can be separated by up to 10 min. This is really only interest when monitoring a stable welding process that is extremely long.

**QC integration.** During weld procedure trials the AMV 4000 can save weld procedure information direct to a welding procedure database, this improves both productivity and accuracy.

Secondly the welding database can apply applicable tolerance values from international standards (Figure 6). The AMV 4000 stores pass information in a similar format to normal reporting systems with average pass data and process type recorded along with heat input. The AMV 4000 also contains limit

values and these can be adjusted manually from the limit screen (Figure 7).

**Stability.** The AMV 4000 will collect large amounts of data that can be difficult to decipher and many stability indices have been developed. Two particular indices are the Cranfield models and Weldprint.

**Cranfield stability models.** These models [2] use a number of ratios to describe determine the transfer mode. These ratios are TI transfer index, TSI transfer stability index, and DCI dip consistency index.

The first two ratios can be compared on the ranges illustrated in Figure 8.

Some examples of how these ratios can be applied are shown in Figure 9.

Figure 9, *a* shows a waveform within the ideal dip conditions but Figure 9, *b* indicates a dip condition where indices are borderline dip. This was also evident from the running condition of the arc and there was

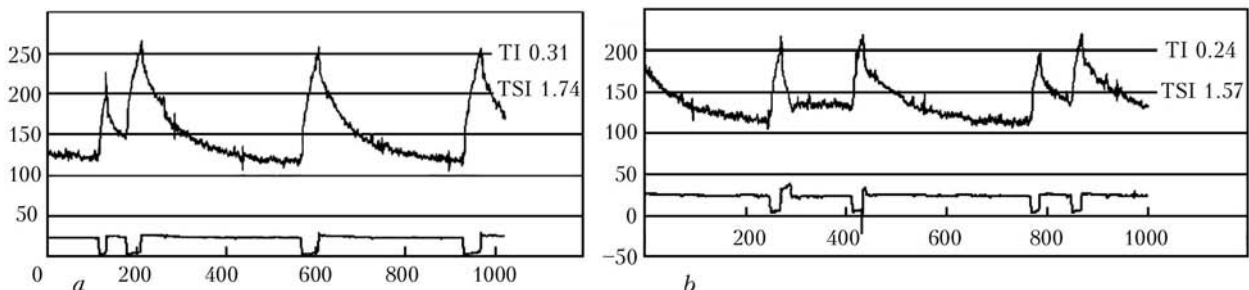


Figure 9. Examples of Cranfield stability indices

more spatter and a less regular bead appearance. Hardly an exhaustive test but it does indicate that a single number can describe a welding waveform, or the mode of metal transfer can be inferred from some comparatively simple ratios.

*Weldprint.* Weldprint [3] has been developed for a number of years and has a successful track record for analysing stability and even detecting potential fault conditions within the arc itself. Weldprint uses Chaos theory to check how similar the monitored waveform is to a sample waveform and can establish a stability number from this. It can go further and from the stability estimate if there is a potentially faulty weld. The example in Figure 10 shows how spatter build up affects weld quality (or stability).

## CONCLUSION

The AMV 4000 is a dedicated fast welding monitor based on PC technology. It accurately monitors all welding process waveforms and comes with an easy to select menu to ensure the optimised settings are possible for each process type. It is possible to add modules for QC and stability applications to the

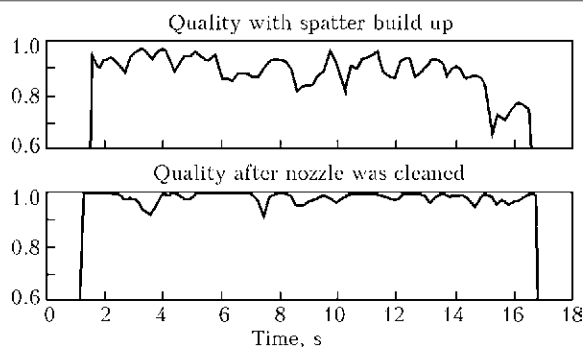


Figure 10. Weldprint quality index

AMV 4000 monitoring software. Some examples have been discussed; however the options to tailor the monitor and decision making process to individual applications is infinite.

1. Tapp, J., Yapp, D. (2004) Techniques and instruments for monitoring arc welding processes. In: *Proc. of 14th Int. Conf. on Computer Technology in Welding and Manufacturing* (Sheffield, UK, June 15–17, 2004).
2. Ogunbiyi, B., Norrish, J. (1996) Monitoring indices for metal transfer in the GMAW process. *Sci. and Techn. of Welding and Joining*, 2(1), p. 33–35.
3. Hughes, P. (2005) In: *WTI Corp. Presentation*, August.





***SESSION II***  
***MATHEMATICAL MODELLING***  
***AND INFORMATION***  
***TECHNOLOGIES IN WELDING***  
***AND RELATED PROCESSES***



# PHYSICAL SIMULATION OF CO<sub>2</sub> LASER WELDING OF Al-Li AND Ti ALLOYS, LOW-CARBON AND STAINLESS STEELS

Yu.V. AFONIN<sup>1</sup>, A.A. BATAEV<sup>2</sup>, V.G. BUROV<sup>2</sup>, A.M. ORISHICH<sup>1</sup>, A.G. MALIKOV<sup>1</sup> and E.G. SHIKAKHALEV<sup>1</sup>

<sup>1</sup>Institute of Theoretical and Applied Mechanics, RAS SB, Novosibirsk, Russia

<sup>2</sup>Novosibirsk State Technical University, Russia

The paper presents the results of experimental simulation of the laser welding of the metals most widespread in the manufacturing processes of aviation, chemical, and oil industry. Butt welding involved the samples of Al-Li alloy 01420T, titanium alloy VT20, low-carbon steel St20 and stainless steel 12Kh18N10T. We investigated the welding modes with the most optimum neutral gas (He) velocity and pressure, physical and chemical structure and microhardness of the welded joint, and also mechanical strength of the samples after the laser action of continuous radiation with the power up to 3 kW, wave length of 10.6  $\mu\text{m}$ . The continuous electric discharge CO<sub>2</sub> laser with the convective cooling of the process medium and maximum power of 8 kW was used as a laser radiation source [1]. In the experiments, the laser radiation level of 3 kW was limited by the long-term beam strength of the ZnSe lens with the focal distance of 254 mm. The most promising results for the microstructure, microhardness and plasticity have been obtained in welding of titanium alloy and stainless steel. It has been demonstrated that the low-carbon steel welding process must be followed by the heat treatment to produce a grinded ferrite-pearlite structure in the welding zone, which provides a high complex of mechanical properties. The obtained results can be used as recommendations for the welding process improvement under certain technological conditions, and also to produce an adequate mathematical model of the laser welding.

**Description of experimental laser facility and techniques of welded sample tests.** At the beginning of 1980s, the process of laser welding of different materials has been studied in Russia and other countries [2]. It has been founded that the effectiveness of heat utilization in the laser welding process is much higher than in the electric arc process, and the strength of the welded joint does not differ much from the base metal strength. The basic advantages of the laser welding, as well as the presence of CO<sub>2</sub> laser technological complexes, stimulate the mastering of this technology at the wave length of 10.6  $\mu\text{m}$  in various industries, in particular, in atomic and chemical industry for welding stainless steel, in aviation industry for welding light aluminum alloys, in oil industry for joining carbon steel big-diameter tubes. In laser welding we applied the continuous electric discharge CO<sub>2</sub> laser with the self-filtering resonator and working radiation power of 5 kW (Figure 1). The active medium is excited by a self-maintained discharge of the direct current in a transversal gas stream. The electrode system consists of two tube cathodes and a flat anode between them. The electrodes are water-cooled and form two discharge gaps. The laser generates a flat-polarized beam with the polarization plane inclined to the horizon at the angle of 45°.

The welding equipment in Figure 1 includes the laser itself with the outlet ZnSe window with the diameter of 50 mm, radiation calorimeter gate set directly near the outlet window, rotating mirror transferring the beam from the horizontal plane to vertical one, welding cap with the exchangeable ZnSe lens, mechanism for linear motion of the samples being

welded, and control board, which provides a certain sequence of remote gate opening, protection gas supply, technological support plate motion.

The technological sketch of the welding is shown in Figure 2. The beam with the flat polarization of 30 mm in diameter is focused by the ZnSe lens with the focal distance of 254 mm. The major experiments were performed at the radiation power of up to 3 kW with the welded plates up to 6 mm thick. To protect the lens, helium was supplied coaxially with the beam through the nozzle 4 under the pressure of 1 atm. The angle of incidence onto the welded metal 1 is 80°. The angle has been chosen for practical reasons: at high angles, part of the reflected radiation falls onto the central nozzle; at low angles, the molten metal flows out from the fusion zone. While welding, the sample is set onto the technological plate 3 fabricated to hold the plates being welded. The support plate has a gro-



Figure 1. CO<sub>2</sub> laser welding equipment

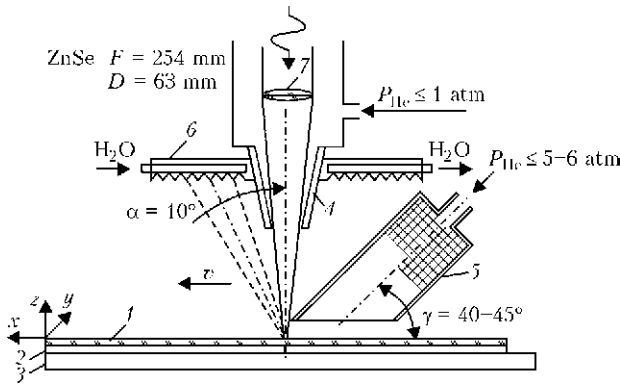


**Figure 2.** Welding technological sketch: 1 – welded unit; 2 – refractory substrate; 3 – support plate; 4 – central nozzle; 5 – side nozzle; 6 – reflected radiation absorber; 7 – focusing lens;  $\alpha$  – angle in the  $yz$ -plane;  $\gamma$  – angle in the  $xz$ -plane;  $v$  – beam velocity

ove of 10 mm width and 2 mm depth, wherein helium is supplied to protect the bottom run. The reflected radiation is absorbed by the water-cooled screen 6. The welding was carried out in the shielding helium medium. The shielding gas was supplied through the side window 5, its flow rate reduced to the normal atmosphere did not exceed 60 l/min. The side nozzle of 20 mm in diameter was inclined to the welded plates surface at the angle of 40–45°.

**Welding of Al-Li alloy 01420T.** Figure 3 shows the cross section of a weldpool.

For the butt welding, the optimum helium pressure range is 4–6 atm (sections 2 and 9 in Figure 3, *a*). When the pressure decreases, we observe the overburning (joint 4 in Figure 3, *a*), when the pressure increases, the weldpool boils, pores occur in the junction, scores on the surface.

With the pressure of 5.5 atm, the optimum welding speed was 4.5–5.5 m/mm (see Figure 3, *b*, sections 6–8). Reduction of the speed results in the alloy overburning (see sections 1 and 2), speed increase causes a cone-shaped weldpool (sections 14–17), no beaded weld (sections 16,17 at  $v = 6.5$  and 6.3 mm/mm).

For the lap welding, the optimum speed was 2.5–2.7 m/min, the joint quality being satisfactory (see Figure 3, *c*, samples 5–7). Reduction of the speed first causes bubbles (sections 10, 11), and then the overburning (sections 12 and 13).

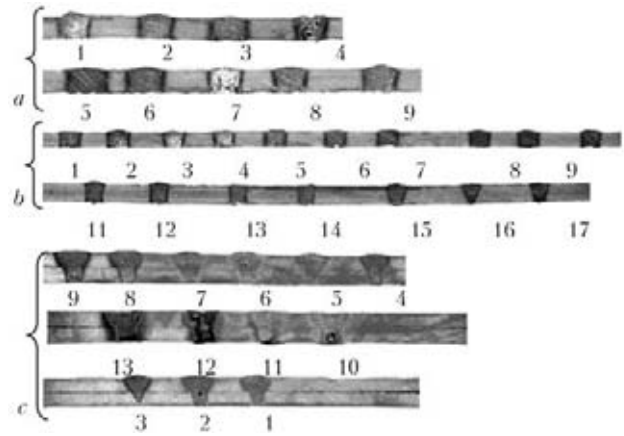


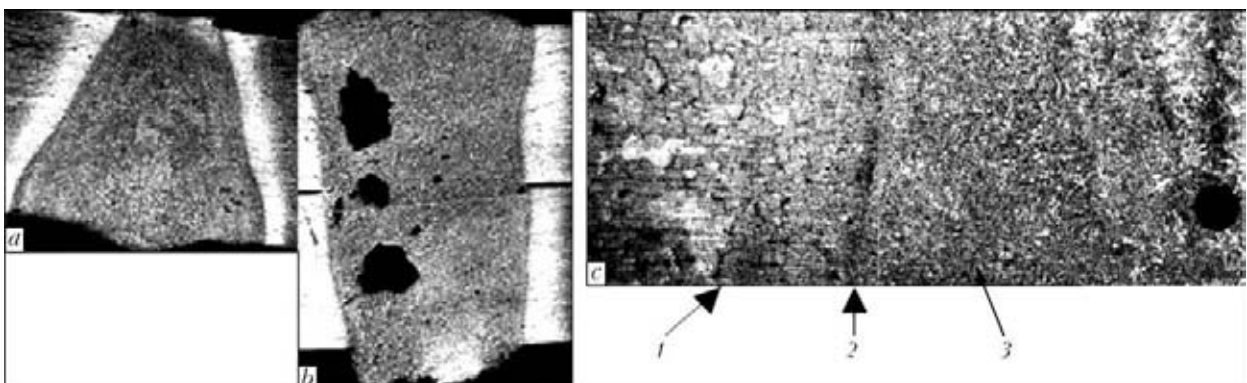
**Figure 3.** Weldpool cross section in butt (*a, b*) and lap (*c*) welding depending on helium pressure with the constant beam velocity of 4.1 m/min (*a*), on beam motion velocity with the constant helium pressure of 5.5 atm (*b*) and on velocity at helium pressure of 6 atm (*c*)

**Mechanical strength of the welded joints.** The static strength of the butt-welded samples was in optimum modes of 0.8 of the solid sample strength ( $\sigma \approx 460$  MPa). The fatigue strength tests for the butt-welded samples have shown not bad results. According to the tests, the lap welding shows worse strength characteristics. We assume the main reason is in insufficiently dense adjacency of the units. Pores caused by an air layer and magnesium combustion, occur in the partition points of the welded plates.

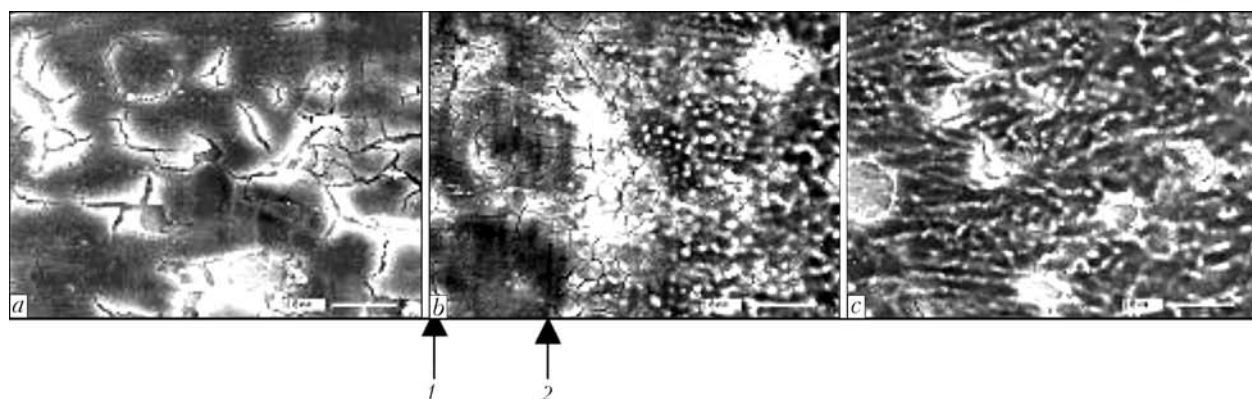
**Study of the welded joint zones in laser welding.** The quality of the laser-welded samples was evaluated by the width of the welding zone, its microstructure and changing microhardness during the transition from the base material to the welding zone. The study of the microstructure was performed in the optic (Figure 4) and scanning microscope (Figure 5).

Table 1 presents the average width of the fusion zone for the half-ready products, used for the mechanical test samples. The measurements were carried out in three sections of the regions.

As is seen from the Table, the region width changes from sample to sample, as well as the shape, which is likely to result from the unstable work of the source. The comparison between the size and quality of the fusion zones makes us to assume that the samples 1-2



**Figure 4.** Microstructure of transition zone between the base metal and melt (*a, b* –  $\times 50$ ) and of welding zone (*c* –  $\times 250$ ) in butt- (*a*) and lap-welded (*b*) joints: 1 – zone of thermal action on the melt boundary; 2 – beginning of the fusion zone; 3 – fusion zone



**Figure 5.** Microstructure of welded joint zones: *a* – initial material beyond the thermal action; *b* – arrows 1–2 – HAZ on the melt boundary, arrow 2 – fusion zone beginning; *c* – fusion zone

**Table 1.** Average width of fusion zone on the half-ready products used for mechanical test samples

Half-ready product No.	Fusion zone size, mm		
	Wide area	Central area	Narrow area
1-2	1.56	1.02	0.24
3-2	1.64	1.14	0.58
5-6	1.40	1.18	1.02
8-2	1.50	1.16	1.14
11-2	1.42	1.20	1.03
15-2	1.42	1.30	1.38
4-5*	2.03	1.35	1.35

\*Lap-welded, the rest being butt-welded.

and 3-2 have more strength joints (see Figure 4, *a*). This is proven by the mechanical test results. The fusion zones of these samples possess the minimum porosity. The highest porosity is seen in the samples 8-2 and 15-2.

In the sample 4-5, which is lap-welded, we see especially high porosity. During the high-temperature action, the size of the pores increased significantly (see Figure 4, *b*). This was to a great extent a reason of the low strength of the joint, i.e. 0.4 of the strength of the base material.

The character of the changing microstructure during the transition from the base material to the welded region is of great interest for the analysis of the laser welding process, as well as the microstructure in the region itself. These are appreciable reasons of the inner tensions in the junction.

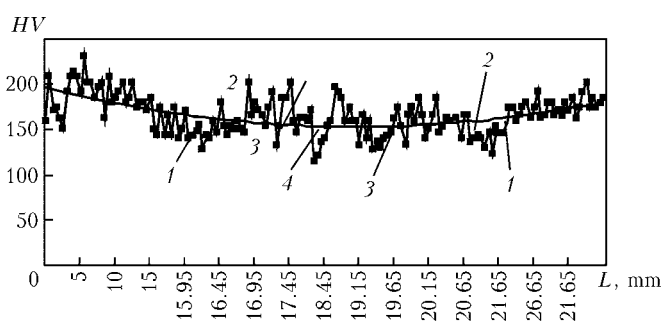
In Figure 4, *a* and *c*, the character of section itching shows that there are the regions of thermal action from the side of the welded material. Figure 4, *c* presents the transition region microstructure at the high resolution. It is evident that in the HAZ (gap between arrows 1 and 2) the size of the grain is smaller than in the initial material. This points to the fact that this region was heated up to the one-phase state temperature, and this was followed by the re-crystallization. The micropores (arrow 2) are seen at the transition boundary. Region 3 is the zone of the melt solidification.

Figure 5 demonstrates the microstructures of initial material, transition region in the point with minimum amount of pores and fusion zone in the same places, obtained by the scanning electronic microscope. It is obvious that the initial alloy presents a two-phase system, the second phase is situated mainly near the grain boundaries as volume of various shapes. The two-phase structure retains in the HAZ, transition region, and fusion zone. The dispersion and uniformity increase.

Figure 6 shows the character of microhardness variation regarding the material state, namely in initial state (up to the first arrow on the left), in the HAZ (distance between the first and second arrows), in transition region, and fusion zone (distance between the third and fourth arrows), then the inverse sequence.

The decrease of microhardness in the HAZ and fusion zone, where the grain size is smaller, and the second-phase dispersion degree is higher, may be caused either by the porosity, accompanying the process of melt crystallization, or by the failed aging of the alloy after the quenching.

*Previous conclusion.* The results of structural and mechanical researches of the quality of the butt-welded samples show the promising future of this method in the practical application. The further efforts, in our opinion, should be directed to choose the mode providing the width of the fusion zone of about 1 mm, to study the conditions of the following heat treatment for making the structure equilibrium. This processing must guarantee the microhardness not worse than that of the initial material.



**Figure 6.** Microhardness variation in welded joint zones: 1 – material initial state; 2 – HAZ; 3 – transition region; 4 – fusion zone

**Table 2.** Mechanical properties of 12Kh18N10T base metal and butt-welded joints at welding speed of 1 m/min

Sample type	$\sigma_t$ , MPa	$\sigma_{0.2}$ , MPa	$\delta$ , %	$\xi$ , %
Stainless base metal	628	364	57.0	42.0
Real joint	365	327	7.4	9.3
Ideal joint	647.6	362.7	51.4	42.9

Note.  $\delta$ ,  $\xi$  – relative reduction in area and elongation of the cross section, respectively.

**Experimental study of the 12Kh18N10T steel welded samples.** The quality of the welded joints was estimated by the strength indices (ultimate strength, yield strength), by the results of microhardness measurement and by the data obtained from the metallography.

The investigations included two stages. The first stage contained the study of the welded joints produced by through melting of a whole plate of steel 12Kh18N10T (for simplicity, we called these joints «ideal» ones), and butt-welded joints of two plates (these joints were called the «real joints»). The joints for strength tests were welded at the power of 3 kW and speed of 1 m/min. The joints prepared for the metallographic tests were welded at the same power but with various speeds (0.4–1.5 m/min). The plate thickness was 3 mm. The results of the strength tensile tests are presented in Table 2.

As is seen from the Table, the samples with the «ideal» joints showed sufficient ultimate strength  $\sigma_t$ . In addition, the joint has a «strengthening» region – a small bulge above the plate surface. This bulge is likely to be the reason why the samples broke not by the welded joints. The samples with the «real» joints demonstrated poor strength indices. The ultimate strength was almost twice lower as compared to that of the «ideal» joints.

With the purpose to remove possible residual stress in the welded joints, several samples underwent heat treatment (normalization). The samples were heated up to 600 °C, and held at this temperature for about 2 h, and then were cooled in air. This action did not influence the strength test results.

To measure the microhardness and perform metallographic analysis, we prepared sections. The microhardness was measured in lengthwise and transversal directions on the joint. The base metal microhardness was at the same level as the welded joint microhardness. As the rate rises, the microhardness decreases

**Table 3.** Mechanical properties of 12Kh18N10T steel welded joints

Welded joint thickness, mm	$\sigma_t$ , MPa	$\sigma_{0.2}$ , MPa	$\delta$ , %	$\xi$ , %
3 (with milled edges)	561.45	330.8	26.2	35.1
4 (with polished edges and one-side fusion)	557.6	312.3	53.6	46.1
4 (with milled edges and one-side fusion)	569.4	318.4	57.7	42.0

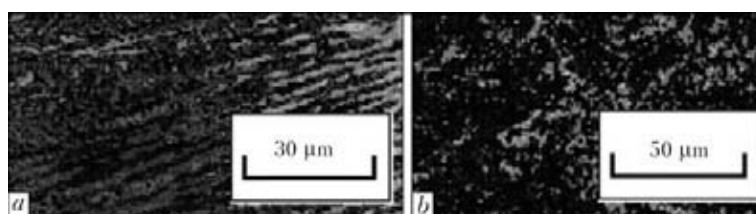
(plasticity rises), but after normalization the microhardness partially recovers. In the samples with the «ideal» joint, no pores nor shrinkage cracks are observed. Pores are the cavities in the structure. Shrinkage cracks are caused by the tensions appearing in the joint at the course of nonuniform cooling. We do not observe them, it means that the speed mode of the welding is correct. The joint structure is uniformly dendritic (Figure 7). Dendrites present metal grains which have grown during crystallization in the direction perpendicular to the heat abstraction, and have taken a fiber shape. Such a structure is typical for the cast state of any steel. The metallography proves good quality of the joint.

Hence, during the first stage we have revealed that extra measures must be taken to prepare the samples to the welding with the object of advancing the low-quality «real» joints to the «ideal» joints level.

The second stage of the investigations included necessary modifications of the welding technology and optimum welding mode to reduce the joint width for the thicknesses of 3 and 4 mm. The working table of the laser facility was modified in such a way that the bottom run turned out to be protected with the helium medium as well. Besides, samples clamping during the welding was simulated. It allowed reducing the gap between the butt ends of the welded plates. Also, to reduce the gas, for comparison of various degrees of mechanical processing, some samples have milled edges, and the other – polished.

We have drawn the dependence: as the speed and power rise, the joint width decreases. It is natural that the joint width decrease is allowed only while the through melting retains. The strength tests demonstrate the good quality of the welded «real» joint (Table 3).

Table 3 shows that the ultimate strength of the welded joint is on the level of the ultimate strength of the junction with the «ideal» joint. Then, the re-

**Figure 7.** Dendritic colonies in the apex (a) and on the edges (b) of joint

**Table 4.** Porosity of the 12Kh18N10T steel welded joints 100 mm length

Porosity	Needed	Result
Largest nodule size, mm	0.6	0.3
Amount of nodules and agglomerations in any section	11	8
Total area of nodules and agglomerations in any section, mm <sup>2</sup>	2.5	≈ 1.5
Largest size of single large nodules, mm	3	Escaped detection

duced gap between the welded plates resulted in the appeared strengthening region in the «real» joint, too. Hence, we have reached that the real butt joint breaks not by the joint.

The reduced width of the joint causes faster and more directed metal melting, which promotes the shape factor formation. X-ray transmission was used to study the porosity of the welded joint 100 mm length. The results are presented in Table 4.

It is seen from the Table that the optimum welding mode ( $v = 1.1$  m/min,  $W = 2.76$  kW) for the samples 4 mm thick produces the welded joint of the category 1.

**Conclusions.** The performed investigations allow concluding:

- CO<sub>2</sub> laser radiation of the power up to 3 kW can be successfully used for welding of stainless steel up to 6 mm thick;
- previous experiments have demonstrated that to form more narrow welded joint on the thin plates of 1–2 mm and to reach deeper penetration of them, the laser radiation must be focused on the bottom plane of the plates. With the bigger thickness, the focus is risen to the corresponding level. In such focusing conditions, the threshold power necessary for the welding process start is 0.6–0.8 kW;
- optimum modes of the butt welding have been found for the plates 3 and 4 mm thick. For the 4 mm thickness and radiation power of 2.8 kW, the optimum welding speed is 1.1 m/min. The strength and plasticity of the welded joint almost coincide with these parameters of the base metal. As the speed increases, the penetration becomes incomplete, as the speed decreases, we observe higher microhardness and lower plasticity of the welded joint. With the thinner welded plates, the welding speed increases pro rata;
- increased power and correspondingly welding speed for a sample of assigned thickness changes the welding mode to the «shape factor» melting. The role of thermal conductivity in the heat balance of the

**Table 5.** Scarf welding modes for the VT20 alloy sheets 2 mm thick at laser power of 1.5 kW with modes 1–5

Welding modes, m/min				
1	2	3	4	5
0.40	0.64	0.85	1.06	1.30

welding process reduces, and we obtain maximum narrow joint;

- welded joint does not require any additive heat treatment. Normalization, i.e. heating up to 600 °C for 2 h and cooling in air, increases the joint microhardness by 20 %, and strength properties of the joint do not change;

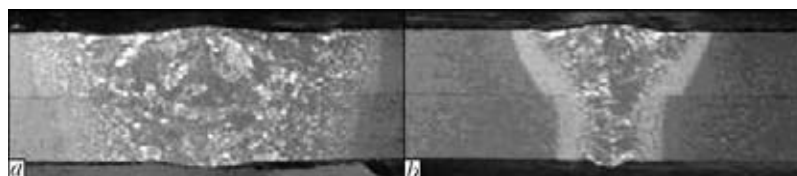
- optimum modes produce the butt-welded joint of good quality, the porosity of the weldpool corresponds to the category 1 of OST 9539.

**Laser welding of titanium alloy.** The samples were obtained from scarf welding of sheets of alloy VT20 (6Al–2Zr–1Mo–1V) 2 mm thick.

**Technological parameters.** Analyzing the reference literature, we can see that titanium alloys demonstrate high tendency to pore formation at increased temperatures. The major reason is hydrogen and oxygen. The laser processing is accompanied by the strong convective motion of the substance. This motion results in the gas penetration into the liquid metal, and appeared bubbles have no time to go onto the surface due to the high-speed crystallization. That is why especial attention was paid to the joint protection from oxidation during the welding process. The shielding gas was helium, supplied not only to the joint apex but also to the bottom run. Besides, the gas was supplied up to complete metal cooling. The beam power in scarf welding of the plates 2 mm thick was of 1.5 kW. The welding speed varied from 0.4 to 1.3 m/min.

The joint outlook is shown in Figure 8. It is evident that the joint width decreases as the welding speed increases. From the technological point of view, the 5th mode is the most advantageous (Table 5), due to the small geometrical dimensions of the joint. The widths of the joint in the top section and the HAZ are 2.6 mm and 375 μm, correspondingly (see Figure 8). Besides, the joint has necessary strengthening in the top and bottom sections prescribed by the standard regulations for welded articles, and profitable formation of the joint is guaranteed.

**Microhardness research.** The numerical estimation of the mechanical properties of the produced welded joint called for the investigations of the microhardness. The microhardness was measured in the sam-

**Figure 8.** Structure of joints 1 (a) and 5 (b) acc. to Table 5

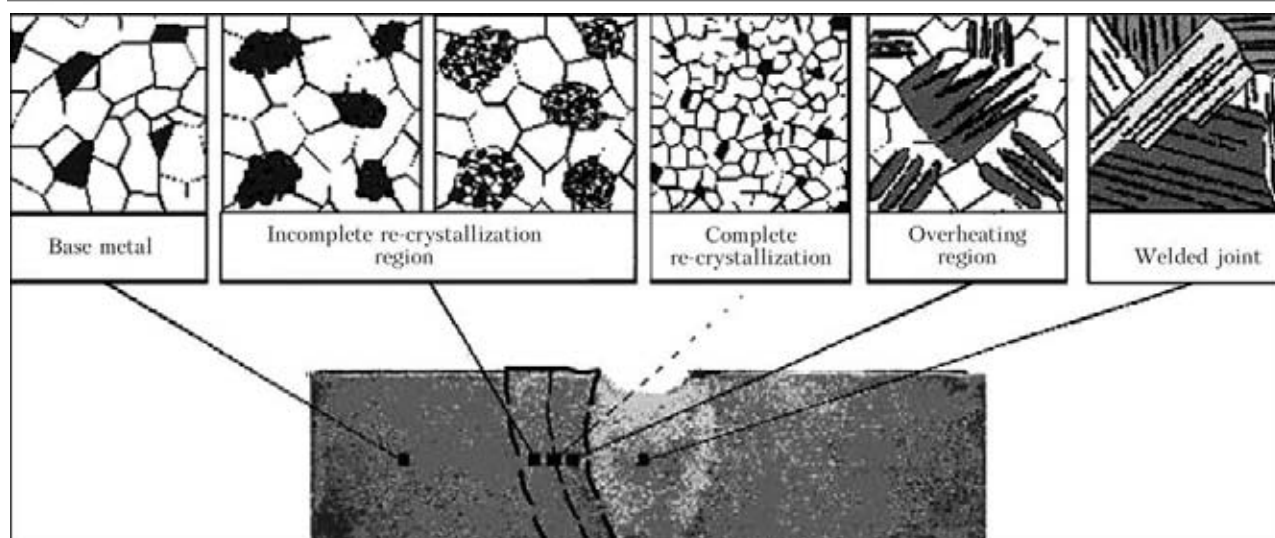


Figure 9. General scheme of structural changes in the welded joint metal

ple 5 acc. to Table 5. The result showed that the welded joint microhardness retained at the base metal level. Its average value was 3600 MPa. Besides, during the tensile tests, the material broke not by the joint, but in the base metal region. This investigation allows us to conclude that the welded joint possesses favorable mechanical properties.

**Conclusions.** The following conclusions can be drawn from the performed investigations:

- needed joint protection from the ambient medium together with optimum welding power and speed, and also assigned focus position permit to reach the high quality of the welded articles, both from the viewpoint of geometrical characteristics and strength;
- higher welding speed allowed the material porosity to be avoided, which is the most widespread defect of the welded junctions in titanium alloys;
- joint and base metal microhardnesses are similar at the level of 3600 MPa;
- optimum scarf welding mode has been found for the sheets 2 mm thick, namely  $W = 1.5$  kW;  $v = 1.3$  m/min; beam focus being in the bottom run. The joint width is not more than 3 mm.

**Peculiarities of the joint formation in laser welding of carbon steels.** Mechanical properties of welded structures depend on the joint and the adjacent HAZ microstructure [3, 4]. These sections of welded junctions normally have heterogeneous structure, which results from the essential difference in temperature and cooling conditions in different junction regions. The welded joint structure has been studied extensively for a number of technological welding processes. Special conditions are realized at the laser heating of half-ready products. The present work is devoted to the study of the structure of the laser-welded joints of carbon steels.

The St20 plates 4–10 mm thick were used as a subject of inquiry. The radiation power was 3 kW, the rate of half-ready product motion about the laser beam varied from 0.1 to 0.6 m/min. The major researching techniques were optic metallography and microhardness tests. Structural researches are carried

out in the microscope NU-2E with the magnification of  $\times 50$ – $\times 1000$ . The microhardness was estimated in the device of PMT-3 type. The loading on an indenter was 0.98 N.

In spite of the simple chemical composition of the steel 20, the welding process produces a complex structure of the welded joint and adjacent region of the HAZ. This structure demonstrates many defects, which weaken the joint. A peculiarity of the HAZ typical for the laser processing is its small width as compared to the electric arc welding.

The general scheme of the structural changes in the metal after laser welding is shown in Figure 9. Five metal regions with clearly differing structure are evident. In the welded joint, crystallization arises directly from the liquid state, and actually secondary crystallization, i.e. re-crystallization of the solid-state metal realizes in the HAZ.

The base metal did not undergo any structural changes during the welding and has a typical ferrite-pearlite structure. The average size of a ferrite grain is 30  $\mu\text{m}$ , that of pearlite colony is about 10  $\mu\text{m}$ . This structure provides high plasticity typical for the low-carbon steels, and this plasticity allows the structure brittle failure to be avoided.

First structural changes are observed in the incomplete re-crystallization region (Figure 10), wherein the solvability of carbon in ferrite rises because of the heating, and it results in carbon diffusing from the pearlite colonies in ambient ferrite. The pearlite colonies loose carbon and dissolve. When the material cools down, new small pearlite colonies and ferrite grains form at the site of the former ones. In Figure 9 one can see that the re-crystallization degree rises as the welded joint is approaching, i.e. together with the temperature growth.

Sizes of new ferrite grains and pearlite colonies in the incomplete annealing are about 5 and 4  $\mu\text{m}$ , correspondingly. The most part of initial ferrite grains retain in the material.

In the next region located closer to the welded joint (see Figure 9), we observe complete re-crystal-



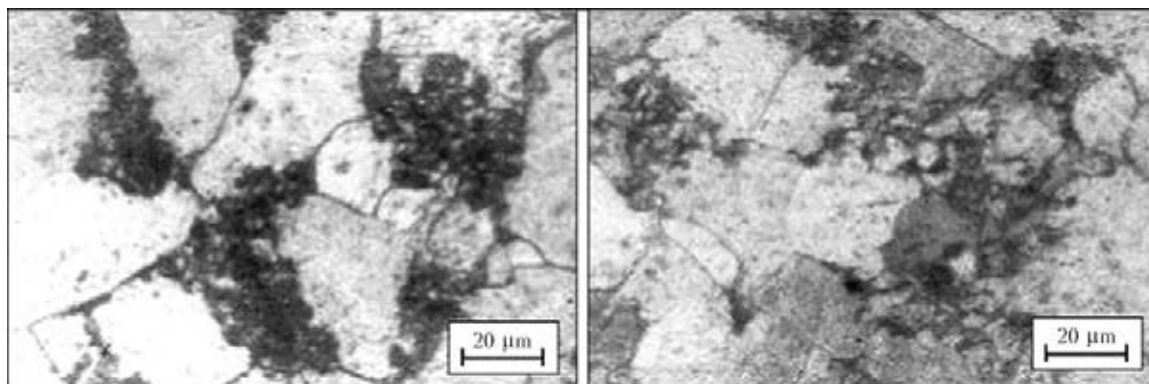


Figure 10. Incomplete re-crystallization region

lization of the structure, caused by the heating of the steel above temperature  $A_{c3}$ . In this region, the ferrite-pearlite structure forms, which differs from the base metal by the smaller size of the structural components and hence by higher mechanical properties. The average size of the ferrite grains in the complete re-crystallization region is  $7\ \mu\text{m}$ , that of pearlite colonies is  $5\ \mu\text{m}$ .

The region of macrocrystalline structure directly borders with the welded joint. Its rough structure is governed by the metal overheating up to the temperatures approaching the melting point of the base metal. The presence of the crystals of Widmanstaetten needle ferrite up to  $60\ \mu\text{m}$  length is a striking property of the overheating. The feature of this type structure is a low level of plasticity. The pearlite formations are predominantly elongated in this region.

The last region among those presented in the scheme (see Figure 9) is the welded joint region. It demonstrates the macrocrystalline clearly oriented ferrite-cementite structure with the Widmanstaetten type of ferrite. Crystal length reaches  $80\ \mu\text{m}$ . This indirectly characterizes the size of the former austenite grain, from which ferrite crystals appeared.

We see from the performed structural analysis that the HAZ must not be treated as a uniform layer with

solely negative properties (low shock viscosity, plasticity and crack resistance). The HAZ includes the regions with favorable structures, i.e. regions of incomplete and complete annealing, which show better indices comparing with the initial structure.

From the viewpoint of providing a high complex of mechanical properties, it is desirable to extend the region with the grinded ferrite-pearlite structure and to remove the region of the Widmanstaetten ferrite. Complete removal of the Widmanstaetten ferrite formation during the welding process has been unsuccessful. A possible way of welded joint quality improvement is an extra heat treatment. With the laser technology applied, this processing can be done through the repeated laser action with the modes guaranteeing steel austenization and relatively slow cooling to produce the structure of the ferrite-pearlite type.

1. Afonin, Yu.V., Golyshev, A.P., Ivanchenko, A.I. et al. (2004) Generation of radiation with high-quality beam in continuous  $\text{CO}_2$  laser of 8 kW power. *Kvant. Elektronika*, 34(4), p. 307–309.
2. Grigoriantz, A.G. et al. (1980) Comparison of laser and arc welding. *Svarochm. Proizvodstvo*, 9, p. 1–3.
3. Grigoriantz, A.G., Shiganov, I.N. (1988) *Laser welding of metals*. Moscow: Vysshaya Shkola.
4. Kovalenko, V.S. (1989) *Laser technology: Guide for universities specializing in machines and technology of high-effective processing*. Kiev: Vyshcha Shkola.

## OPTIMISATION OF ALLOY DESIGN FOR GOOD WELDMENT OF HSLA STEELS

S. ALEKSANDROV<sup>1</sup>, K. HULKA<sup>1</sup>, Yu. MOROZOV<sup>2</sup> and A. NAZAROV<sup>2</sup>

<sup>1</sup>Niobium Products Company GmbH, Duesseldorf, Germany

<sup>2</sup>I.P. Bardin Science Research Institute for Ferrous Metallurgy, Moscow, Russia

A deterioration of the toughness in the HAZ can often be correlated with local brittle zones, caused by an enrichment of alloying elements as a result of the solidification process. Especially the enhanced shrinkage during the peritectic reaction in steels with more than 0.09 % C promotes interdendritic segregation. For a defined cooling rate (heat input, preheating, wall thickness) and carbon content there exists an optimum alloy content, which guarantees the transformation into a fine acicular bainitic microstructure, exhibiting the best toughness and a moderate strength compared to microstructures of coarse ferrite, granular bainite or martensite. Such considerations for the microstructure-property relationships are valid also for the base and weld metal. During research there were studied the weldability of several grades of steels by the method of imitation of temperature-time modes in HAZ, allowing thermo-kinetics parameters in HAZ to be reproduced at various types of welding. The research were carried out on various steel grades from X52 up to X80 with the carbon contents from 0.19 up to 0.03 %. The target of the research was to evaluate the influence of a chemical composition on steel weldability and to define the parameters of welding providing optimum properties of metal in HAZ. As results of research was developed low carbon bainitic HSLA steels which allows the safe and economic usage of even higher strength steels than actually applied in welded structures.

A reduction in wall thickness can be achieved by applying materials with higher strength. This reduction is highest, when only uniaxial stresses like in pipelines occur. By doubling the yield strength there, half of the wall thickness is sufficient to carry the load [1]. But also with other stresses deriving from bending or torsion loads, the weight reduction is still remarkable [2]. This economic result is demonstrated by the ex-

ample of beams with different strength levels (Figure 1) confirming that a higher strength of the steel allows the usage of lighter profiles.

Such remarkable weight reduction compensates by far the higher costs for the high-strength low-alloy (HSLA) steel. Furthermore, the lower weight reduces fabrication costs such as transportation and handling. Especially the efforts for welding are drastically reduced, i.e. related to the reduction in wall thickness, the reduction in the weld metal volume amounts to an exponent of two and the weld metal volume determines the production time needed for the fabrication of a component. As a result, the yield strength increase from 355 to 460 MPa results in material savings of about 30 % and the overall costs for the whole structure may be reduced by about 14 %, even if the price per ton for the higher strength steel is 30 % higher [4].

These obvious economic merits can only be used, if the structure is safe. Besides the necessity to avoid any brittle fracture at operating temperature also sufficient ductility to withstand the propagation of ductile cracks is requested. This is obtained with «clean steel», exhibiting low levels of sulphide and oxide inclusions, and also by reducing the volume fraction of the second-phase pearlite, consequently asking for a low carbon content. Therefore, modern HSLA steels rely on grain refinement as the major strengthening mechanism, since it is the only metallurgical method to improve both strength and toughness. The thermo-mechanical rolling process, often in combination with accelerated cooling (TMCP), is the practical realisation of this goal [5].

Besides other welded pipelines are an important application of HSLA steels in Russia, with sometimes more severe property demands than in other parts of

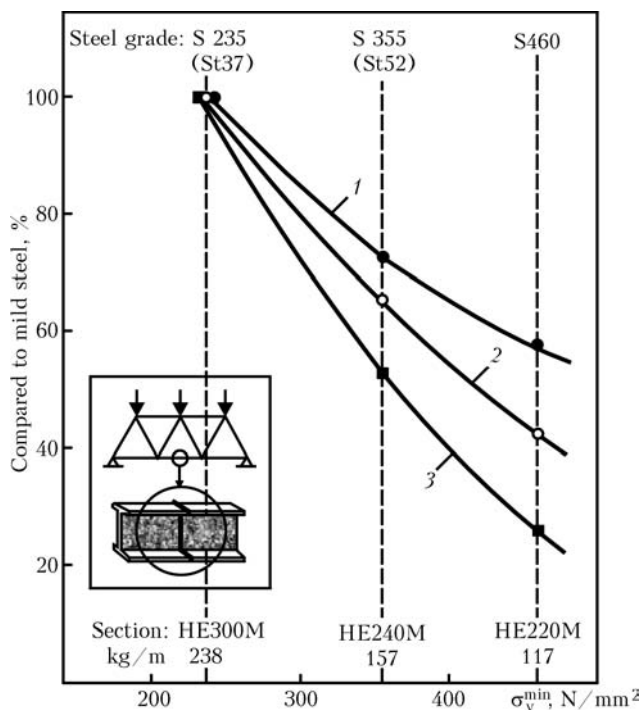
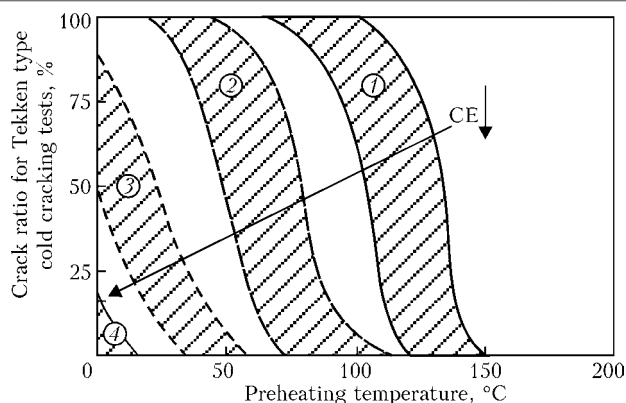


Figure 1. Weight and cost reduction by using HSLA steels (tension member for a load of 7000 kN) [3]: 1 – material costs; 2 – weight; 3 – weld metal volume

the world, including wall thickness up to 50 mm and strength of grade X80 and higher to allow a pressures of 100 atm and higher (up to 250). Furthermore, new pipelines in Siberia and seismic regions of Transbaikaliya as well as off-shore pipelines ask for increased requirements to the pipes, including the welds. While some years ago the impact toughness of welds at the fusion line was specified by Mesnager U-notch specimens, now GAZPROM and TRANSNEFT and other major consumers of pipes specify the impact toughness at the fusion line and in the center of the seam by Charpy V-notch specimen and the impact toughness level should be not less than  $59 \text{ J/cm}^2$  for gas pipes and  $39 \text{ J/cm}^2$  for oil pipes.

**Weldability considerations.** For a given welding process and wall thickness (heat input) of steel structures, the chemical composition of steel, described by a carbon equivalent formula, determines if a crack-free structure can be obtained without using expensive preheating. Figure 2 shows the development of off-shore plate grade 50 for the last decades, which finally resulted in the application of low carbon thermomechanically rolled plate, which do not need pre-heating.

The toughness in the HAZ depends on the effective grain size and the amount of local brittle phases, the later being a result of the local chemical composition as results of segregations [6]. Figure 3 explains the reason for segregations originated during the solidification of steel. It is known that primary segregations can be caused by interdendritic inclusion of the liquid phase, which is naturally enriched in carbon and the



**Figure 2.** Effect of carbon equivalent on pre-heating temperature for crack-free weldments 40–60 mm thick of steel with  $R_e > 355 \text{ MPa}$  [4] at welding heat input  $12 \text{ kJ/cm}$ : 1 – normalized structural CMn steel with  $C \leq 0.20 \%$ ,  $CE \leq 0.46 \%$ ; 2 – normalized structural CMnNb steel with  $C \leq 0.17 \%$ ,  $CE \leq 0.43 \%$ ; 3 – normalized off-shore CMn(Ni)NbTi steel with  $C \leq 0.13 \%$ ,  $CE \leq 0.42 \%$ ; 4 – TMCP CMn(Ni)NbTi steel with  $C \leq 0.10 \%$ ,  $CE \leq 0.38 \%$

other alloying elements. During the peritectic reaction, which takes place in steel with carbon levels of 0.09–0.53 %, an additional shrinkage occurs as a result of the transformation from the cubic body-centred  $\delta$ -ferrite into the cubic face-centred austenite. The relatively highest shrinkage of this kind occurs with the highest amount of  $\delta$ -ferrite already formed before the start of the peritectic reaction, i.e. with steels of about 0.10 % C. The additional shrinking mechanism with the peritectic reaction is also known to be responsible for enhanced surface cracks in continuously cast steel with such carbon levels of 0.09–0.12 %, a

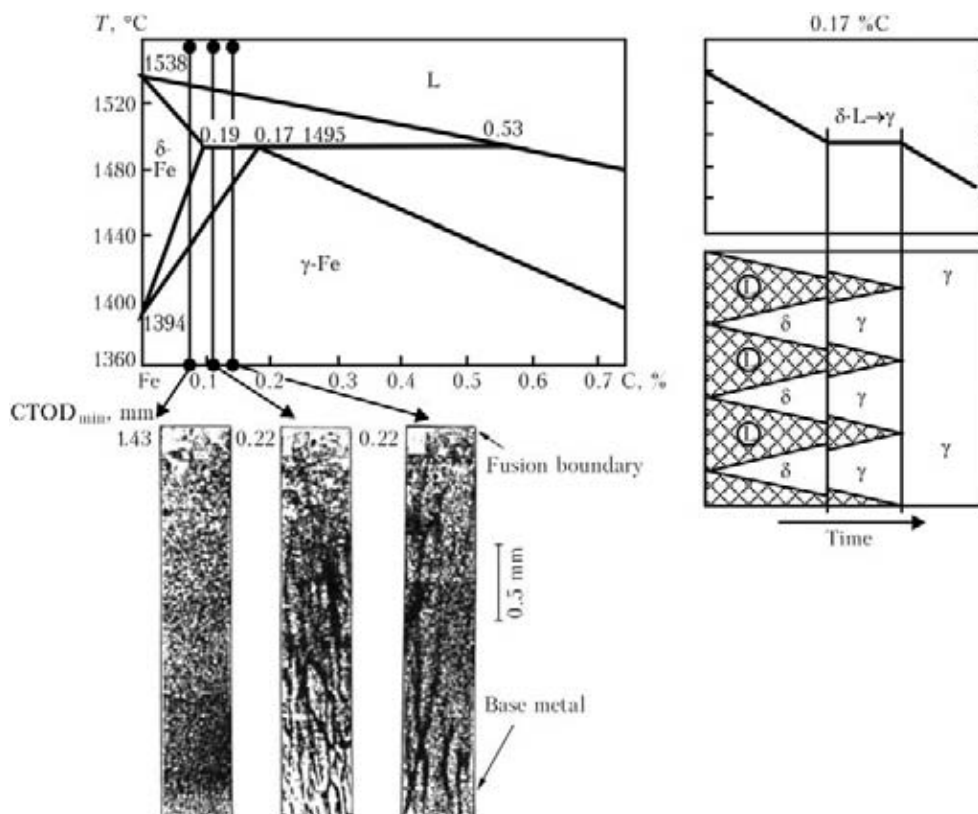


**Figure 3.** Segregation caused by peritectic solidification and decrease in HAZ toughness caused by LBZ [7, 8]

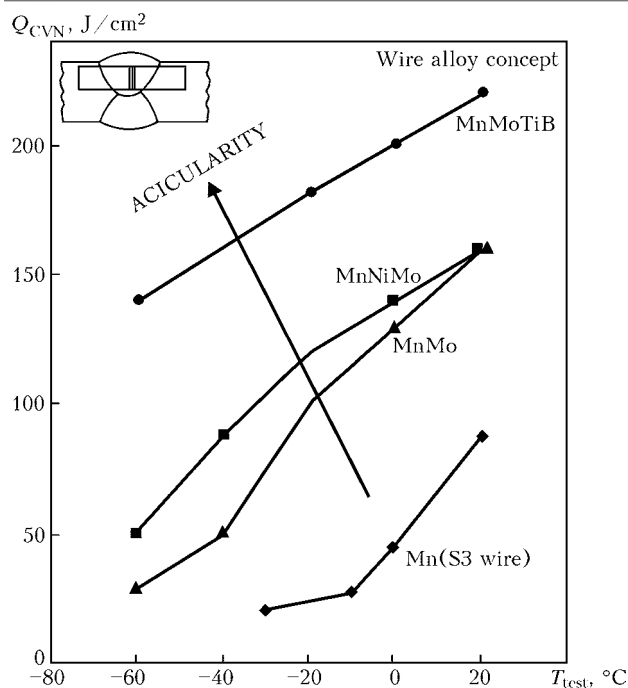


Figure 4. Toughness of weld metal on X70 pipe steel [13]

practical reason, why such alloy design is often avoided. The primary segregation of carbon itself will be reduced during the further solidification and during hot rolling, but such a homogenisation is marginal for the substitutional elements in solid solution owing to their slow diffusibility.

In HSLA steels manganese is the major alloying element, being often about 1.5 %, and its interdendritic enrichment determines the secondary segregation and in the final product. Often the segregated zones exhibit a manganese enrichment corresponding to a segregation ratio of two. Manganese is an austenite-stabilising element and forces the carbon to diffuse into the region of ultimately transformed austenite. Since both elements carbon and manganese add to hardenability, a higher amount of local brittle zones (LBZ) in the HAZ is observed in such regions corresponding to the originally primary segregations.

Besides understoichiometric Ti/N additions refined the austenite grain in the HAZ [9], the HAZ microstructure showing the optimal toughness is a low carbon fine acicular bainite, while coarse ferrite site plates and martensite constituents deteriorate the toughness. Besides the welding conditions, also the steel chemical composition determines the transformation temperature and thus the microstructure and properties in the HAZ [10–11].

The most relevant welding procedure for HSLA steel is fusion welding with consumables via automatic or manual processes. The development of suitable consumables has to take into consideration, that a certain percentage of the base metal will be dissolved in the weld metal. Besides the role of carbon and the other alloying elements in microstructure and toughness as already discussed before precipitation hardening and possible further embrittlement owing to the microalloying elements (titanium, vanadium or ni-

bium) during a follow up thermal cycle of multi-pass welding has to be taken into consideration [12]. For good weld metal toughness a low inclusion level is a pre-requisite. Furthermore one aims to obtain an acicular microstructure. Figure 4 exhibits one example, i.e. the weld metal toughness of the longitudinal seam of large diameter pipes, where typically about 60 % of the chemical composition of the weld metal derive from the dissolution of the parent plate material. It is obvious that the impact energy of the weld metal is remarkably improved, when using welding wires with a high alloy content. The best result after high speed AC/DC welding is achieved with a molybdenum-boron containing wire, where the nitrogen content has been fixed by titanium, together with a fully basic flux.

**Investigation of weldability.** Besides full tests of bridge or pipe welded joints, the simulation of the welding processes is a cheaper method and gives scientifically clear results. One successful method was developed at the I.P. Bardin Moscow State Science-Research Institute for Ferrous Metallurgy and is especially used for the development and quality control of new steels for large diameter pipes. It includes different methods, such as classification of the microstructure and the HAZ hardness and toughness as results of the steel chemical composition and the cooling rate from peak temperature.

*Description of the method.* The technique is based on the simulation of a welding thermal cycle for the grain-coarsened HAZ, which often represents the area of lowest toughness.

The used equipment is a dilatometer, which allows high-speed induction heating to peak temperature of 1300 °C (corresponding almost to maximum temperature in a HAZ). Then the specimens are cooled with different cooling rates in inert gas (Ar, He) jets. Cooling rate is measured in the temperature range of 800–700 °C and can be varied from 0.6 to 350 °C /s. The specimens for the dilatometer are hollow cylinders with an outside diameter of 6 mm and wall thickness of 1 mm, however for toughness test and resistance to SCC V-notch specimens of 5 × 10 × 55 mm are common, and also other types of samples are possible.

This method allows determining on the steel weldability (loss of strength, susceptibility to cold cracking, impact toughness of simulated HAZ, etc.) and correlating the HAZ properties with its microstructure and the cooling rate, which is directly related to the heat input during welding. As result of the investigations one obtains the phase transformation for continuous cooling (CCT-diagram for welding), a description of the microstructure, hardness and impact toughness of metal (as diagrams plotted over the cooling rate). Furthermore, also the determination of crack tip opening displacement (CTOD) can be carried out.

These tests of samples with simulated HAZ are more severe and more precise than tests of real welded joints, since they evaluate only the properties of a

defined condition in the HAZ without any participation of neighbouring zones of the metal, which might be less affected by heat input during welding, as it is natural when testing real welded joints.

The simulated cooling conditions of the HAZ for different welding modes are the basis for the analysis and classification of weldability of various steel grades.

*Some results of the investigations.* A big variety of steels has been investigated by using the simulated HAZ method, especially in order to gain a better understanding of microstructure and property formation during the welding of large diameter pipes in the pipe mill and during pipe laying. As an example CCT-diagrams of different steels are shown in Figure 5, indicating that different steels exhibit different microstructures for the different welding processes.

For good toughness of steel and the HAZ metal, a low-carbon microalloyed steel is beneficial for the large diameter pipes austenite transformation in HAZ metal during welding of 0.03C-Mn-Cr-Ni-Cu-Nb steel differs from other steels: the ferrite formation takes place only at cooling rates lower than 1.5 °C/s and pearlite formation is observed at cooling rates below 1 °C/s.

In this steel, the diffusion controlled transformation with formation of polygonal ferrite and pearlite is completely suppressed at cooling rates of actually applied welding processes in the pipe mill and during pipe laying. At cooling rates obtained in practice (partial or complete) bainite transformation takes place in a temperature range of 620–550 °C and cooling rates from 0.7 °C/s and more. Furthermore, high-temperature martensite transformation is observed in the temperature range of 520–400 °C and cooling rates above 70 °C/s. As a consequence of the favorable morphology of austenite transformation products (lath bainite, acicular ferrite), this steel exhibits high Charpy toughness values at subzero temperatures to as low as –60 °C under any automatic submerged arc welding conditions.

In contrary, as a consequence of the relatively high carbon content and the unfavorable heterogeneous structure, the 0.19C-Mn-Si steel HAZ exhibits an insufficient Charpy impact toughness at temperatures below 0 °C. A certain increase in Charpy toughness at –20 °C is achieved at cooling rate, corresponding to automatic submerged arc welding schedule. For this steel the required level of critical hardness  $HV_{10}$  350 that guarantees absence of cold cracks (hydrogen induced embrittlement) corresponds to cooling rate of 50 °C/s, while this critical hardness value has never been observed with the 0.03C-Mn-Cr-Ni-Cu-Nb steel not even at the highest cooling rates typical for welding with low heat input.

Impact toughness of 0.1C-Mn-Nb steel HAZ is in between the described steel grades, but the absolute level is still rather low.

Recent development work was concerned with high-strength pipeline grades (X80 and higher),

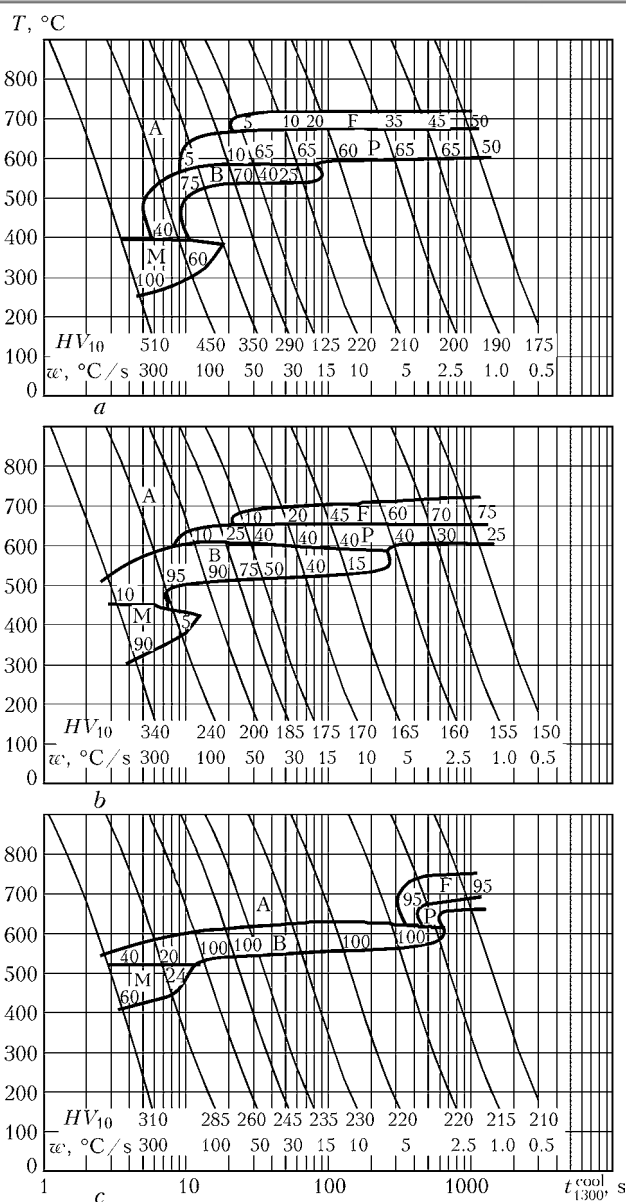


**Figure 5.** Welding CCT diagrams for pipe steel of 0.19C-Mn-Si (a), 0.1C-Mn-Nb (b) and 0.03C-Mn-Cr-Ni-Cu-Nb (c) grades

which included the investigation of weldability for the developed 0.05C-Mn-Mo-Ni-Cu-Nb steel. At cooling rate of 2.5 °C/s the microstructure consists of 100 % low-carbon upper bainite. The temperature of bainite transformation start is about 600 °C, and the martensite formation temperature is close to 450 °C. A microstructure consisting of 100 % low-carbon bainite is observed up to cooling rate of about 70 °C/s, while at cooling rate 100 °C/s about 85 % of martensite and 15 % of bainite are observed (Figure 6). Only at low cooling rate 0.1 °C/s the microstructure of the simulated HAZ exhibits polygonal ferrite with small amount (10–15 %) of upper bainite. At cooling rate 1 °C/s the microstructure is mainly bainitic (not more than 10 % of ferrite), and gets fully bainitic with further increase in cooling rate.

The hardness of 0.05C-Mn-Mo-Ni-Cu-Nb steel HAZ at the highest investigated cooling rate of 300 °C/s was  $HV_{10}$  340 with 100 % martensite microstructure. These hardness data indicate that at low

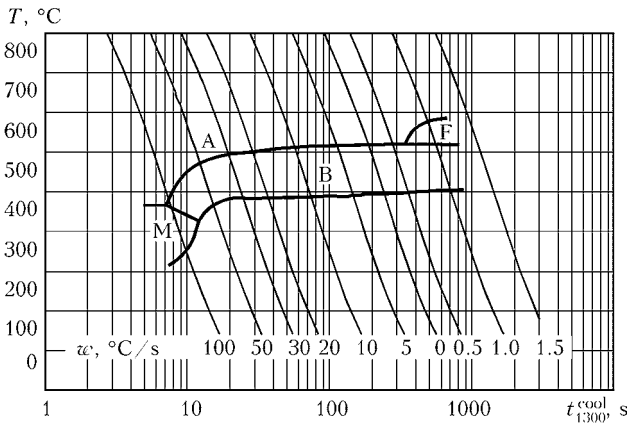


**Figure 6.** Welding CCT-diagrams for 0.05C-Mn-Mo-Ni-Cu-Nb pipe steel

cooling rates a certain deterioration of strength in the HAZ occurs compared to the strength in the base metal. But the same result indicates also that the steel is not susceptible to cold cracking in HAZ at all investigated cooling rates (welding conditions). Furthermore, at all cooling rates investigated for welding simulation the metal is characterized by a high level of impact toughness. The 0.05C-Mn-Mo-Ni-Cu-Nb steel confirms excellent the weldability obtained in low-carbon steel with an optimized composition, which includes the addition of molybdenum to increase the stability of austenite in the HAZ.

To summarize, the CCT-diagrams show a clear correlation of the percent of microstructural constituent and the carbon content for a certain cooling rate. While the 0.19C-Mn-Si steel exhibits a coarse and heterogeneous microstructure for all cooling rates, the low-carbon (0.03–0.05 % C) steels with higher alloy additions show a microstructure of low-carbon bainite for a wide range of cooling rates (3–90 °C/s). With the low-carbon steels, which also exhibit a low carbon equivalent, much better toughness (resistance to crack formation and propagation) is obtained in the HAZ (Figure 7).

Toughness increase in steels with structure of low-carbon acicular bainite is a result of the low carbon content itself and the fine effective grain size of the bainitic microstructure. The average bainite «grain» size (the width of bainite lath) is remarkably finer than that of ferrite grain. However, when instead of ferrite-pearlite structures «grainular» bainite is formed, and no toughness improvement is obtained. The HAZ toughness also can be improved by the addition of titanium and niobium, refining austenite grain. Another factor is the ability of niobium in solid solution to reduce the temperature of  $\gamma \rightarrow \alpha$  transformation thus increasing the amount of acicular microstructural constituents.

Investigations of phase transformation of hot-deformed austenite (reheating to 1150 °C,  $\epsilon = 20\%$  at 1000 °C and 50 % at 850–800 °C) have shown that the same steels, which exhibit a favourable transformation for the conditions in the HAZ, also show a favourable transformation behaviour under conditions of thermomechanical rolling TMCP, resulting in ferrite-bainite or bainite microstructure over a wide range of cooling rates, increasing the stability of production process.

Furthermore, Figure 8 shows examples of industrial trials for the production of modern low-carbon niobium-microalloyed steels. They were carried out at the wide-strip mills of SEVERSTAL and MMK works to produce X70 steel grade with a thickness of up to 16 mm for spiral-welded pipes with a diameter of 1220 mm for Volzhsk Tube Works. They all exhibited low carbon levels combined with increased alloy additions ((0.04–0.06)C-Mn-Mo-Nb-V and (0.04–0.06)C-Mn-Cr-Ni-Cu-Nb-V) thus guaranteeing high impact toughness values in the welded joints, besides the excellent properties of the base metal.

The decrease in carbon from 0.19 up to 0.03 % in the HSLA steel pipes widens the range of favourable cooling rates (15–300 °C/s) for hardness values,

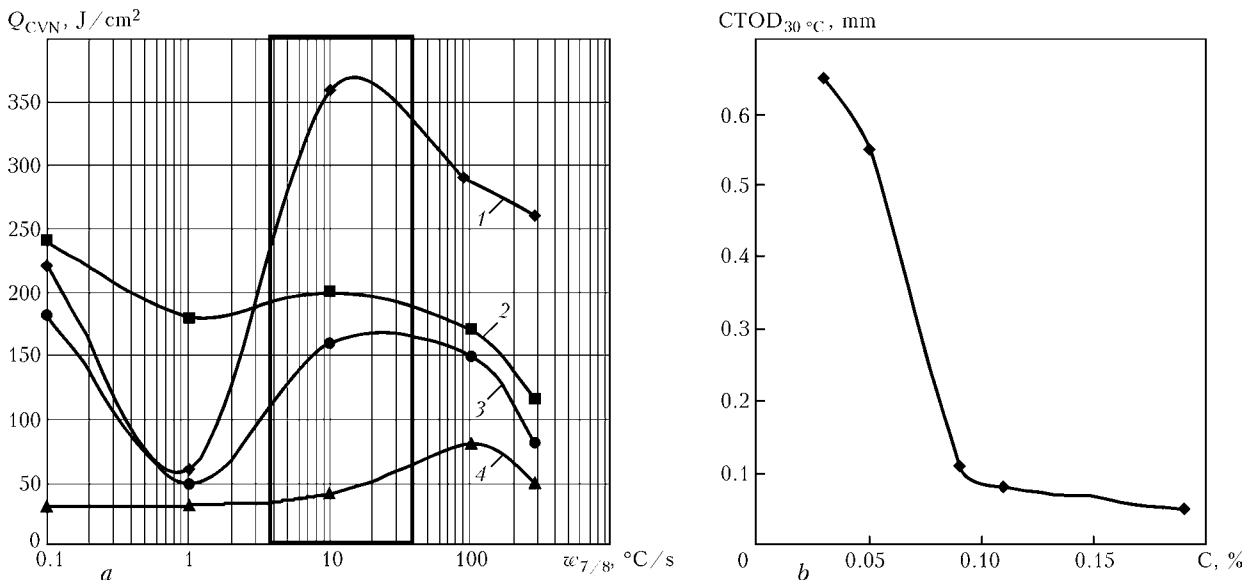


**Figure 7.** Effect of carbon content on Charpy V-notch impact toughness (a) for 0.03 (1), 0.05 (2), 0.06 (3), 0.10 (4) % C, and CTOD value (b) of the HAZ on pipe steels

which do not exceed the critical value of  $HV\ 350$ , avoiding cold cracks.

This simulation method was also used for investigation on susceptibility to SCC of pipeline steels. The technique developed by the I.P. Bardin Institute includes static bending of the samples in air and in low-acid (pH 5.1) corrosion medium with a slow strain rate to failure. The integral fracture energy at testing in medium  $-\Delta\Sigma^{SCC}$  is a parameter of evaluation of susceptibility of steel to SCC. It is known that the fracture energy in corrosion medium for the HAZ is lower than in the pipe base metal, thus the HAZ is more prone to crack nucleation under influence of stresses and corrosive media. The studies showed that the highest resistance to SCC was obtained in a steel with 0.055 % C, exhibiting a mainly acicular ferrite microstructure, and being microalloyed with niobium and small additions of nickel and copper. The highest susceptibility to SCC appeared steel with 0.1 % C, where the HAZ microstructure consists of ferrite and coarsened upper bainite.

## CONCLUSIONS

1. The fundamental relationships between chemical composition, microstructure and toughness apply not only for the base metal itself, the HAZ and weld metal. Especially when the economic high heat input welding processes are applied, a low carbon level, far below the 0.09 % C level, is a pre-requisite for sufficient HAZ toughness.

2. A low carbon fine-grained acicular bainite offers the best opportunity to obtain a high strength steel, suitable for safe welded structures. When applying the thermomechanical rolling process, which prepares a high amount of nucleation sites for the phase transformation, the effective grain size of bainite is typically as small as  $1\ \mu\text{m}$  [14]. Besides an improved toughness, the fine-grained bainite adds also to strength increase by both, further grain refinement and higher dislocation density compared to microstructure of polygonal ferrite plus pearlite.

3. There are two ways of obtaining a bainitic microstructure, either increasing the steel hardenability by adding more alloying elements or by increasing the cooling rate. Many modern rolling mills comprise accelerated cooling with a rate of about  $20\ ^\circ\text{C}/\text{s}$  for material 20 mm thick or even direct quenching with  $35\ ^\circ\text{C}/\text{s}$  or more for the same thickness plate. In order to obtain the demanded strength level, alloy design and cooling rate have to be balanced. Low-carbon bainitic HSLA steels open the possibility to apply

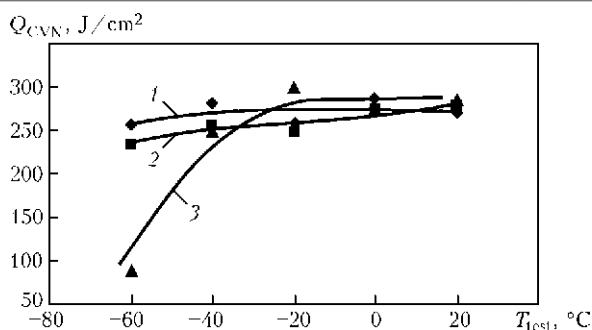


Figure 8. Impact toughness of welds on 0.05C-Mn-0.20Ni-V-Nb (1), 0.04C-Mn-0.30(Cr + Ni + Cu)-V-Nb (2) and the Severstal 0.06C-Mn-Cr-Ni-Nb-V ( $P_{cm} = 0.17$ ) steel spiral pipes 1220 mm diameter on fusion line

steels of higher strength than actually common in welded structures, with increased safety and economy.

4. The method of simulation of welding thermal cycles for HAZ, developed by the I.P. Bardin Institute, allows weldability of steels to be evaluated by considering the phase transformations and testing the strength loss, susceptibility to cold crack formation, impact toughness and crack resistance.

5. The best HAZ properties are obtained in steels with a microstructure of low-carbon bainite, and the most suitable shape of the CCT-diagram shows a wide bainite transformation field. Such shape is obtained with low carbon and a balanced alloy design.

6. High strength and thick wall pipe steel with excellent toughness in the base metal and improved weldability have been developed and industrially produced, exhibiting high values of Charpy impact toughness in the welded joints.

1. Lessels, J. et al. (1987) *HSLA steels*. Chapter 7. Brussels: IISI.
2. Younger, D.G. (1975) In: *Metal Progress*, 107(5), p. 43.
3. (1989) *TradeARBED S.A.*, HISTAR. Luxembourg.
4. Hubo, R., Hanus, F. (1994) In: *Stahlbau*, 63, p. 84.
5. (1994) CBMM/NPC. *Niobium Inform.*, 7.
6. Matsuda, F. et al. (1996) In: *Welding in the World*, 37(3), p. 134-154.
7. Harrison, P.L., Hart, P.H.M. (1990) *Metallurgy, welding and qualification of microalloyed (HSLA) steel weldments*. Miami: AWS, p. 626-658.
8. Heisterkamp, F., Hulka, K., Batte A.D. (1990) *Ibid.*, p. 659-681.
9. Tanaka, J. (1988) In: *Proc. of World Materials Conf.* (Chicago).
10. Lotter, U., Kawalla, R. (1990) In: *Steel Research*, 61(10), p. 518-522.
11. Batte, A.D., Kirkwood, P.R. (1988) *Microalloyed HSLA steels*. ASM Int., p. 175-188.
12. Garland, J.G., Kirkwood, P.R. (1975). In: *Metal Constr.*, 7, p. 320-330.
13. Christmann, H. et al. (1990) *Pipeline Techn.* Oostende, p. 4.25-4.33.
14. Graf, M.K., Hillenbrand, H.G., Peters, P.A. (1986) *Accelerated cooling of steel*. Warrendale: TMS, p. 165-179.

# MATHEMATICAL COMPUTER MODELING AND OPTIMIZATION OF WELDED JOINT FORMATION FOR MULTI-PASS WELDING OF GAS PIPELINE FITTINGS

B.M. BEREZOVSKY, A.V. PUJKO and O.V. PILNIK  
South-Urals State University, Chelyabinsk, Russia

The following procedure was offered for constructing complex mathematical models for bead formation in the groove and temperature fields in welded joints as applied to multi-pass arc welding of metal plates and pipes of large thickness. The system of models is open to further modification and allows specifying individual sub-models on the basis of more precise methods of modeling and calculation of the major processes taking place during the formation of multi-pass welded joints. Within the framework of the offered approach software has been developed making it possible to study, during the stages of scientific research and process engineering, the main peculiarities of welded joint formation, the shape of the surface and penetration zone of the individual beads forming in the groove, and also the thermal cycles of HAZ various points.

The gas pipeline fittings are important structural components ensuring to a considerable degree the serviceability of gas mains and reliability of their operation. Tees and pipe-bends with metal thickness of 16–65 mm are most frequently used fittings (Figure 1).

The technological peculiarities of the fabrication and installation of gas pipeline fittings depend on the conditions under which the process is organized. Under the stationary conditions of their fabrication the most productive methods of welding are used, in particular, multi-pass submerged-arc welding. During their installation in the field the multi-pass manual arc welding process using coated electrodes is mainly employed. The application of mechanized methods of

welding under the stationary conditions of fabrication makes it possible to reduce appreciably the effect of the welder's skill factor and considerably increase the productivity of the welding process, the quality and reliability of products.

A large variety of requirements, particularly stringent in the case of heavy metal, are imposed on the welded joints of gas pipelines. The reason for this is that gas pipelines are operated under the unfavorable conditions of high pressures and low temperatures.

*Making a multilayer weld without lacks-of-fusion or slag inclusions.* Under conditions of stationary fabrication of gas pipeline fittings all welded joints undergo a 100% ultrasonic inspection. In this connection it is important that the welding processes employed should be robust to the occurrence of defects in welds, particularly, various inclusions and lacks-of-fusion. The currently available publications on this issue present a wide range of opinions on the reasons for the occurrence of lacks-of-fusion and slag inclusions [1]. For example, in the opinion of the author of [2] lacks-of-fusion occur owing to the insufficient amplitude of electrode wire oscillation or because of excessive welding speeds.

*Bringing down to a minimum residual stresses induced by welding.* Thick metal to be welded involves problems with regard to the formation of residual welding stress fields and distortions in a workpiece both during and after welding. These problems can be solved on the basis of modeling fields of temporary and residual stresses taking into account the properties of the material being welded, their dependence on temperature, and a number of other factors [3–5].

*Prevention of technological cracks in weld and HAZ metal.* Cold crack formation is prevented by ensuring a favorable thermal cycle of both weld and HAZ metal [1, 3]. When welding special steels using high-strength low-alloy consumables which improve

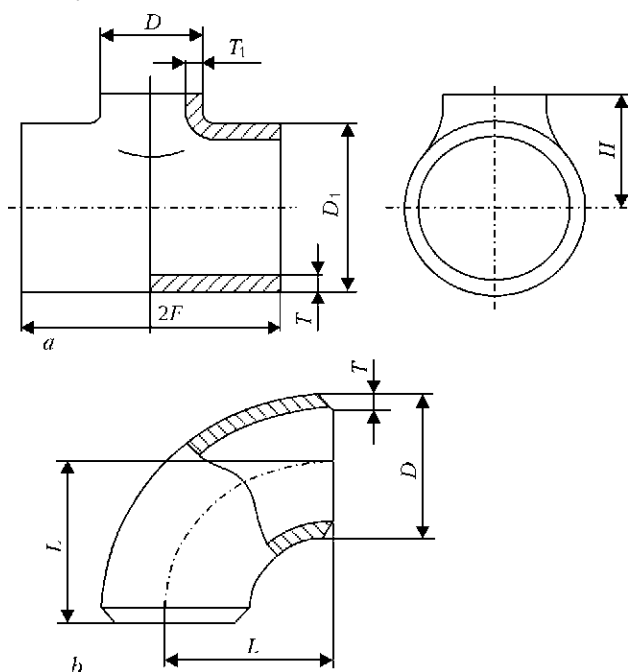


Figure 1. Main fittings of gas pipelines: a – tee; b – pipe-bend



the performance properties of welded joints, with the purpose of preventing the occurrence of cold cracks, preheating or sometimes accompanying heating is applied. Refusal from preheating is possible in cases of application of double-arc or multi-arc welding, and also when regulating thermal cycles by various techniques, for example, by depositing individual layers in a particular order (rational filling of the groove) [1].

*Ensuring achievement of required mechanical properties for HAZ metal.* Multi-pass submerged-arc welding operations account for about 28 % of all welding operations [6]. Most frequently this method of welding is applied when more stringent requirements are imposed with regard to the impact strength of the weld metal at low temperatures or for high-carbon, low- and high-alloy steels to improve the structure of weld and HAZ metal. For this purpose it is important to create favorable microstructures of the weld and HAZ metals, making it possible to achieve high mechanical properties of welded joints [7]. In a number of cases when special steels and alloys sensitive to a thermal cycle of welding are welded, the rate of heat input and the section of beads in the groove should be minimal, therefore edge preparation and multi-pass welding are applied even for joining components of small thickness. It is accounted for by the fact that welded joints of structural alloyed steels tend to form cracks and the impact strength of weld metal decreases.

#### Challenges and principles for optimization of arrangement of beads in the groove

The examination performed by the authors of [8] of the places where extensive slag inclusions are predominantly located in multi-pass welded joints in plates 38 mm thick and having X-shaped grooves (Figure 2, *a*) has shown that defects occur mainly at the edges of beads (Figure 2, *b-d*).

Similar problems are encountered when welding various materials, for example, aluminum alloys. In particular, when fabricating critical thick-walled welded structures from aluminum alloys designed for use under unfavorable conditions, a variety of defects occur in them [9].

These defects act as stress concentrations under load. Particularly dangerous are internal defects occurring in multi-pass welds in the form of lacks-of-fusion which cannot be always detected when X-ray tests are performed on welded joints, and ultrasonic testing is inapplicable in many cases.

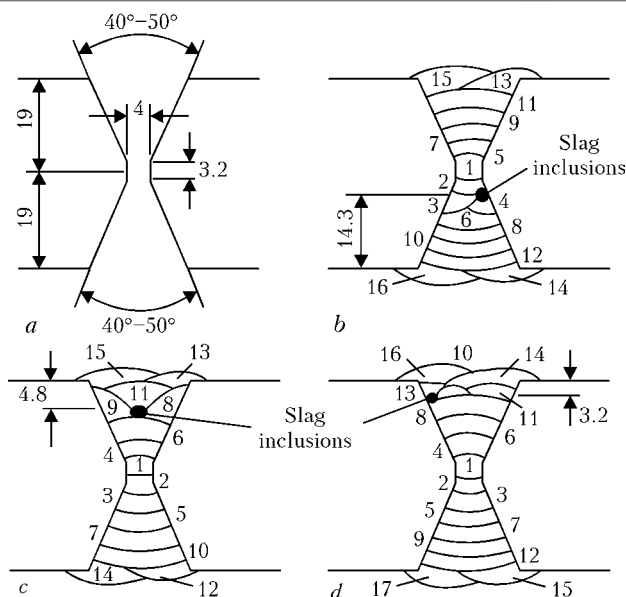


**Figure 2.** Preparation of edges for welding (*a*) and sites of slag inclusions in the middle of the plate (*b*), near the surface (*c*) and between the beads (*d*) in multi-pass weld [8]

Most frequently lacks-of-fusion occur when there are overlaps beyond weld toes (Figure 3, *a*), and also when penetrations are distinctly centrally and dagger-shaped (Figure 3, *b, c*).

When conventional melting techniques are used, metal penetration is maximum along the axis of a weld, and it is insignificant in the peripheral sections accounting for up to 40 % of bead width. Such a pattern of penetration during bead formation in the groove results increasingly in lacks-of-fusion between deposited beads. For example, when the basic technique was used for welding high-strength steel structures [10] the V-groove between workpieces was filled in four passes according to the diagram with austenite electrode wire 5 mm in diameter under different welding conditions for the root and filling beads (Figure 4).

One of the main reasons for such defects to occur is the adverse shape of the surface of the second bead especially at the sites of its transition to the edges of the parent metal, and also the shape of the third bead. Therefore, to prevent such defects as slag inclusions, it is necessary to deposit non-convex beads and ensure smooth transition to the parent metal. In so doing instead of depositing the third and fourth beads according to the basic welding technique, it is more expedient to finish the filling of the groove with the final wider third bead.

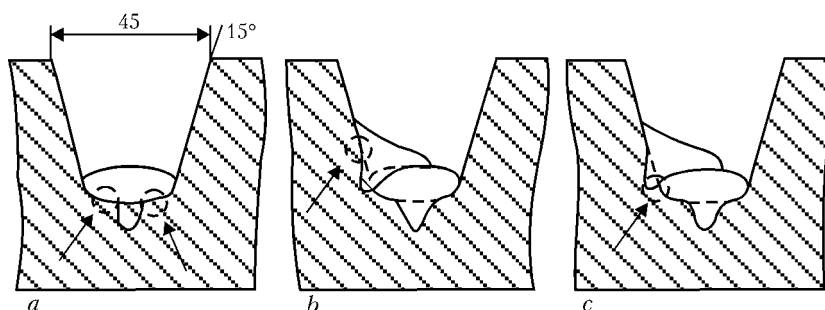


**Figure 3.** Localized lacks-of-fusion occurring in multi-pass welding of aluminum alloys [9]

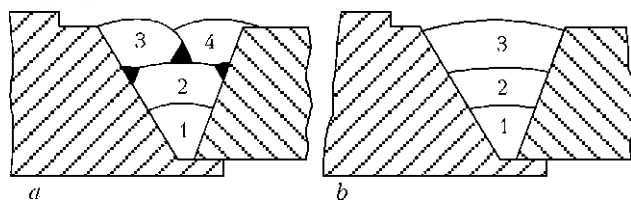


**Figure 4.** Location of slag inclusions in multi-pass weld (a) and arrangement of beads when using transverse oscillations of electrode (b) [10]

In this connection, it is important to ensure optimum control over the multi-pass welding process, i.e. to optimize arrangement of beads in the groove and to prevent slag inclusions and lacks-of-fusion. In particular, the principal technical and economic parameters of the welding technique essentially depend on the shape and geometric parameters of edge preparation [11–13]. As the thickness of workpieces to be welded increases and V- and X-grooves are used, the arrangement of beads becomes more complicated to a considerable degree. This is particularly so with big included angles and fluctuations of the shape and geometric parameters of grooves [14].

#### Challenges of multi-pass welding optimization.

The application of numerous criteria of quality to multi-pass arc welding of thick metal, the difficulty of accounting groove preparation deviations along the axis of a weld on the arrangement of beads and geometric parameters of a weld complicate the development of effective models and software, allowing the choice optimum technological options.

If for single-pass arc welding a significant amount of various procedures for calculating and optimizing the weld formation process has been developed, for multi-pass welding such procedures are almost non-existent. Therefore, in most cases developers of the welding processes for heavy-gauge metal are compelled to limit themselves only to setting the arrangement of beads in the groove and the range of changes to the key welding parameters (welding current, arc voltage, welding speed, etc.) for several beads in a particular layer of a weld [15].

The technological preparation of the welding process for heavy-gauge metal structures including the use of welding robots, calls for determination of a much greater number of welding parameters [6]. The shortage of effective mathematical models for multi-pass welding complicates development of the expert systems used for solving problems with regard to optimization of the multi-pass welding process [16], and also the software to control welding robots used for welding critical of heavy-gauge metal structures [17].

The author of [18] underlines that the main obstacle to the automation of multi-pass welding of thick metal under the conditions of significant fluctuations with regard to fit-up accuracy and geometric parameters of the groove is the lack of algorithms and programs for groove filling. In this connection welding robots widely used in many practical applications find limited application when thick metal structures are welded. For this purpose, it is possible to use expert systems integrated

into the robot control system. That said, it is necessary to take into account the fact that during the welding process the welding circuit buses experiences the action of various random factors upon itself: the error of fit-up, temporary distortions of the workpiece, various vibrations, fluctuations of parameters of welding conditions, and a lot of other factors. In addition, it is also necessary to take into account various technical and economic limitations.

A special feature of multi-pass arc welding is that the errors made when depositing the first and all subsequent beads can accumulate and eventually affect the final shape of a weld. Therefore, with groove dimensions varying any bead can be deposited in the groove under essentially different conditions for two identical workpieces. It can lead to adverse situations when undercuts occur in the groove sidewall or on the edges of the previous beads, and also an excessively sharp angle is formed between the profiles of adjacent beads, which may result in insufficient penetration during the next bead deposition.

The work [15] reviews the main provisions of the strategy acceptable for the robotized multi-pass process used for welding heavy metal. This strategy is focused on the use of robots having computer vision, seam tracking system and certain level of artificial intellect, sufficient for solving problems involved in multi-pass welding of heavy-gauge metal on the basis of selecting a particular sequence of arranging beads in the groove.

As the welding process control circuit includes weld models, any mathematical dependencies describing relationships between the shape and the dimensions of the bead in the groove on the key parameters of the welding conditions are necessary for realization of any strategy. The authors of [15] suggest using for this purpose the regression models obtained experimentally with design of experiments techniques.

In [19] a way of optimizing the process of automatic multi-pass CO<sub>2</sub> welding with wire of 1.6 mm in diameter is described. Calculations resulted in the optimization of welding parameters for the first and subsequent two passes ensuring qualitative filling of the groove. Examples have been given of the optimization of parameters of multi-pass welding used for sheets 25 mm thick with groove angles of 60° and 45°.

**Use of welding process control systems.** Adaptive multi-pass welding systems are beginning to be used on an increasingly broader scale when fabricating welded structures for complex critical products [20]. The modern intellectual adaptive welding systems are being integrated into installations for multi-pass welding thick-walled products. They provide the high quality of welds matching the high efficiency of the welding process. These systems possess high flexibility and fast adaptability to any welding procedure, and can also make up for any inaccuracies in fit-up. The systems also control distribution of metal in grooves of various sections with due regard for possible variations of the area of their section.

The intellectuality of these systems is provided with the help of mathematical models and also by modern software and hardware complemented by means of technical sight, measuring the shape of the groove and its cross-section area. The contour of the groove surface is analyzed by powerful processors, capable of calculating precisely the necessary amount of metal deposited for any complex groove and to coordinate the position of a welding torch when performing a welding operation [21].

### Theory

It was shown that irrespective of the groove angle, thickness of the metal plate and shape of the groove there are general regularities for the formation of layer beads in the groove [21–23]. Most effective can be the approach under which recommendations are given not with respect of specific ranges for allowable alteration of welding conditions, but for general parameters of the welding process, giving technologists sufficient leeway in selecting ways of achieving the values of these parameters with due regard of other conditions and restrictions.

The analytical mathematical model of formation of a layer of metal in welding or surfacing is described in detail in [21–23]. It uses the mathematical model of formation of a horizontal bead on an inclined plane. The model includes the basic geometric parameters of the bead in the groove, in particular, its width  $B$ , the area of section  $F_b$  and the angle of plane inclination  $\tilde{\theta}$ . The physical properties of metal are taken into account by the value of the capillary constant

$$\alpha_c = \sqrt{\sigma/g(\rho_1 - \rho_2)}, \quad (1)$$

where  $\sigma$ ,  $\rho_1$ ,  $\rho_2$  are the values of surface (interphase) tension of the weld pool liquid metal, its density and density of a shielding gas or a flux, respectively.

According to the model of formation of a horizontal bead on an inclined plane, the shape of the bead surface for the given calculating diagram is determined by the area of its section  $F_b$ , width  $B$ , angle of plane inclination  $\theta$  and capillary constant of weld pool liquid metal  $\alpha_c$ .

For the description of the surface shape of an individual bead sets of equations have been obtained determined by the basic geometric parameters of the bead. One of the possible variants of a set of equations can be represented as follows:

$$b_0 \cos \theta = \int_0^{\varphi_n} \frac{\cos \varphi d\varphi}{\sqrt{z_0^2 + 2(1 + \cos \varphi)}} - \int_0^{\varphi_v} \frac{\cos \varphi d\varphi}{\sqrt{z_0^2 + 2(1 + \cos \varphi)}}, \quad (2)$$

$$b_0 \sin \theta = \sqrt{z_0^2 + 2(1 - \cos \varphi_n)} - \sqrt{z_0^2 + 2(1 - \cos \varphi_v)}, \quad (3)$$

$$f_0 \sin \theta = \cos(\theta - \varphi_v) - \cos(\theta - \varphi_n), \quad (4)$$

where  $b_0$ ,  $f_0$  are the dimensionless values of the bead width and the area of its cross section calculated with the following formulae:

$$b_0 = \frac{B}{\alpha_c}; \quad f_0 = \frac{F_b}{\alpha_c^2}, \quad (5)$$

where  $\varphi_n$ ,  $\varphi_v$  are the boundary angles in boundary points  $M$  and  $N$  of the bead contour.

For example, from this model it follows that the primary factors determining the shape and dimensions of a bead deposited next to the groove sidewall are the height of the melting away of edge  $C_M$ , width of the melting away of groove  $B_1$ , and also the amount of metal deposited per one pass of  $F_b$ .

If area  $F_b$  depends only on the electrode diameter and the ratio of its feed speed and the welding speed, parameter  $C_M$  strongly depends not only on the rate of heat input, but also on the distance between the electrode tip and prepared edge (Figure 5, *a*). As distance  $L_e$  increases with value  $F_b$  of bead 1 remaining constant, there is a reduction of parameter  $C_M$ : the height of melting away of decreases, and the width of melting away of  $B_1$  increases.

As a certain value is achieved, the bead next to the sidewall changes its shape and becomes convex. As this takes place, the left edge this bead sinks, forming a hollow which is subsequently difficult to penetrate when depositing the bead of the following layer. As a result lack-of-fusion between the bead and the left sidewall of the groove (see Figure 5) is likely to occur. With  $L_e$  too small, excessive melting of the left edge of the groove occurs, and according to the model, on the left sidewall of the groove an undercut occurs, which is not filled with deposited electrode metal. As a result as the left bead of the next layer is deposited, lack-of-fusion between the bead and the left edge of the groove also occurs.

An analysis has shown that the most desirable shape of an individual bead forming in a groove is concave or convexo-concave. From an offered principle of physical-geometric modeling [22] and multi-pass welding optimization such general recommendations can be formulated as follows: at any ratio of welding conditions for an established current structure of deposited beads, the values of the bead width  $B$  and the area of deposited bead  $F_b$  for obtaining the concave or convexo-concave shape of the bead, the height of the melting away of the edges should be within optimum limits. At the same time it is necessary to take into account the fact that if the surface of the bead is too concave, undercuts of the bead edges being welded occur.

Such a pattern of occurrence of lacks-of-fusion, resulting from an analysis of process of bead formation with the help of the mathematical model, conforms to the regularities of the occurrence of defects in a multi-pass weld observed in practice.

Thus, in multi-pass welding the shape of the surface of the bead deposited per each pass is determined by a ratio of its width, the amount of metal deposited

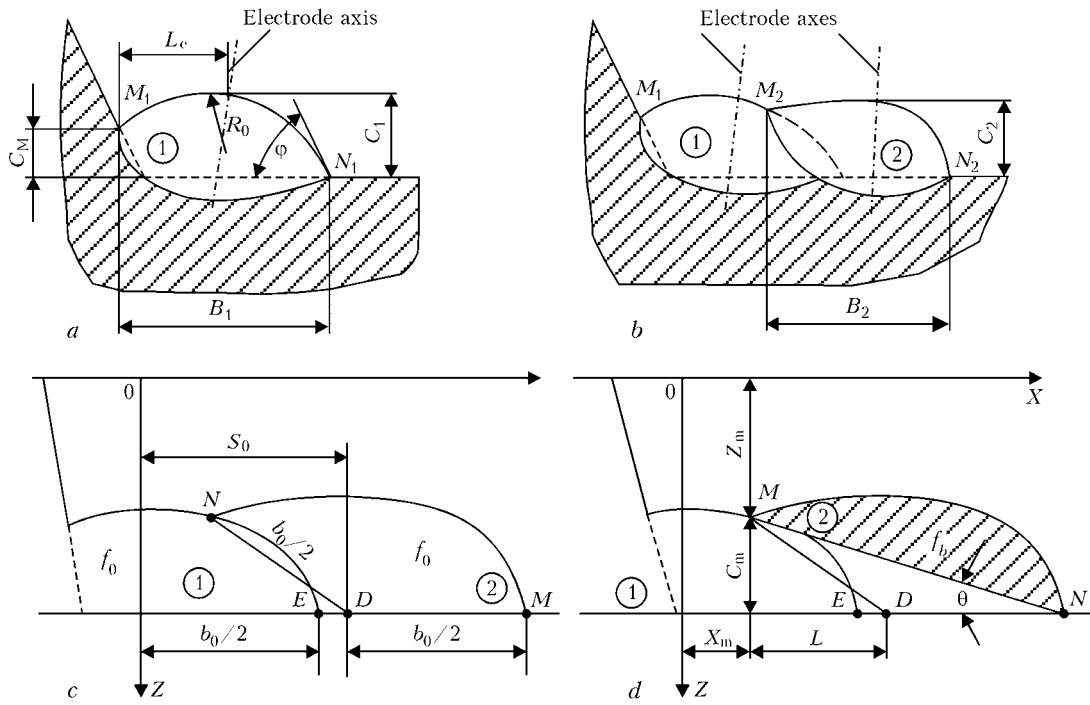


Figure 5. Scheme for modeling and basic geometric parameters of the bead deposited next to the sidewall and the second adjacent bead (for designations see the text)

per one pass and the height if the melting away of the edges. There is an optimum range of ratios of these parameters in which the surface of a bead is concave and has no undercuts of edges of the parent metal and overlaps in the bottom part of the bead.

**Computer program for simulating arrangement of beads in a groove.** This software package allows simulating the process of groove filling on the PC screen (Figure 6). In the software package for modeling arrangement of beads a database is built in. The database allows storing information about various options of the technique including both values of geometric parameters of the groove and all parameters of welding conditions, among them the characteristics of electrode positioning in each pass.

**Discussion of modeling results**

Figure 7 shows two adverse situations resulting from modeling on the PC screen the process of bead formation in the groove. In the first situation (Fi-

gure 7, a), with a relatively small amount of weld metal the deposition of a weld on the sidewall of a groove having a significant angle of inclination has led to an undercut in the top part of the bead. It is possible to remove this undercut by reducing the bead width, the area of the metal deposited or the angle of inclination of the groove. A more radical way is prevention of situations whereby a bead is placed on a contour with a big angle of inclination.

In the second case (Figure 7, b) a significant amount of metal deposited in the bead next to the wall has caused occurrence of an overlap on the horizontal part of the groove while the left part of the bead has formed a relatively favorable shape on the left sidewall of the groove. To eliminate this overlap it is necessary to reduce essentially the amount of metal deposited per one pass.

Figure 7 shows an option of modeling the arrangement of beads in a groove with a relatively favorable formation of the first layer consisting of three beads.

One the measures of quality of the formation of beads in a groove is the angle of intersection of the contours of adjacent beads. The closer is the value of this angle to 180°, the smoother is the contour of the beads in the groove and the lower is the likelihood of occurrence of lacks-of-fusion in a multi-pass weld when welding heavy-gauge metal. For example, the form of third bead in Fi-gure 7 can be improved by increasing the arc voltage or introducing the transverse oscillations of the electrode.

The validity of this approach was tested for cases when welds of different types were formed with the groove having different geometric parameters and miscellaneous welded materials. A good agreement has

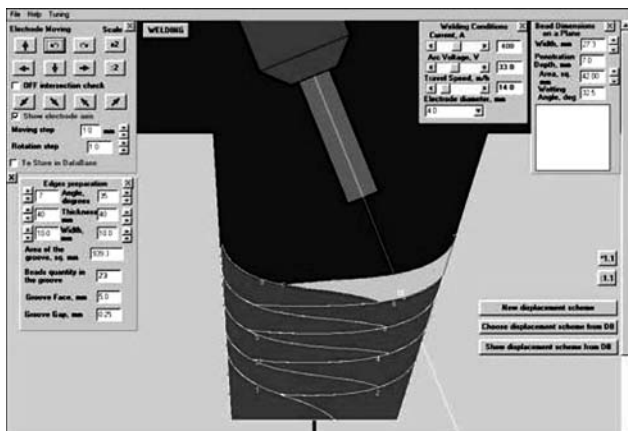
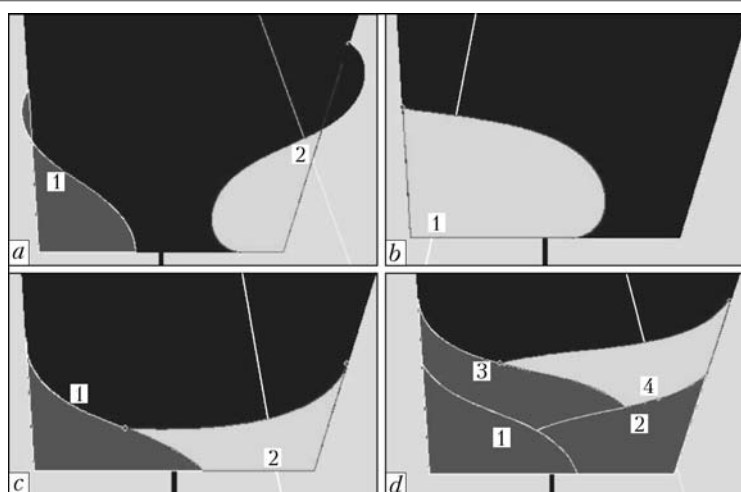
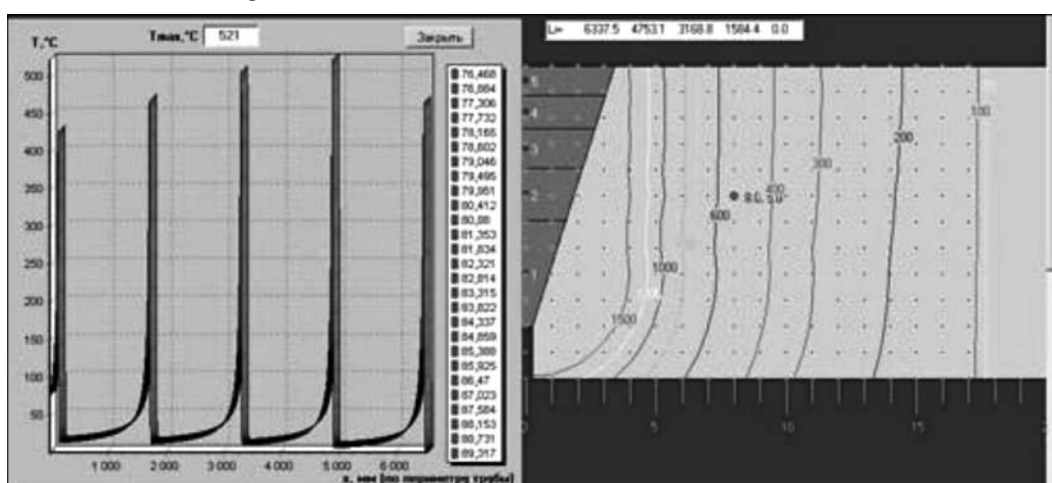


Figure 6. Main window of the software package for simulating arrangement of beads in groove



**Figure 7.** Shapes of surfaces of beads designed according to theoretical model with their adverse shape because of undercuts and overlaps (*a, b*) and with their favorable arrangement (*c, d*)



**Figure 8.** Thermal cycles of a welded joint HAZ

been reached between the theory and the experiments in terms of quality and quantity [21–25].

This method of modeling and the computer program allow study at the design stage of the arc multi-pass welding process the basic regularities for arrangement of beads in a groove and choice the best option from among those considered.

**Modeling and calculation of temperature fields in workpieces during multi-pass welding.** The sub-model of arrangement of beads in a groove makes it possible to estimate the reliability of the chosen scheme of arrangement to the occurrence of lacks-of-fusion or slag cavities. The result of its application is the information about the coordinates of each bead in the groove on which depends the character of the temperature field in the immediate proximity to multi-pass weld. Based on the known coordinates of beads in the groove it is possible to calculate the total temperature field in a pipe being welded, and also the thermal cycles of any HAZ point (Figure 8).

In this work for this purpose used computational methods of various levels of complexity. The simplest method consists in using schemes of point heat sources moving with uniform speed successively one after another. The distance between the sources along the

perimeter of the pipe depends mainly on the diameter of the pipe and welding speed. The arrangement of the sources in the section perpendicular to the axis of the weld is determined by the arrangement of beads in the groove.

At the second higher level of modeling, schemes of distributed heat sources have been applied. It makes it possible to estimate more precisely a temperature field in a welded joint HAZ.

At the third level of modeling temperature fields numerical methods of calculation (a finite difference method) were applied. They make it possible to improve the accuracy of modeling by considering during calculations of such factors as the dependence of the thermal and physical properties of metal on temperature and the heat of phase transitions such as melting-solidification. Knowledge of a thermal cycle of any HAZ point makes it possible to calculate its phase and microstructural composition, and also the distribution of mechanical properties in HAZ metal.

## CONCLUSIONS

1. The procedure offered for constructing comprehensive mathematical models of bead formation as applied to multi-pass arc welding of heavy-gauge metal makes

it possible to simulate with the help of the computer program the major phenomena occurring when multi-layer welded joints are fabricated.

2. This method of modeling and its computer implementation allow one to provide the most graphic visual simulation of all process peculiarities on the PC screen in order to select the optimum options of the multi-pass arc welding process for heavy-gauge metal.

1. Nazarchuk, A.T., Sterenbogen, Y.A. (1984) About optimization of arc welding process by means of a rational filling of the groove (Review). *Avtomatich. Svarka*, **11**, p. 46–49.
2. Hunt, J.F. (1982) Welding steam headers by narrow-gap GMAW. *Weld. Des. and Fabric.*, **55**(12), p. 49–52.
3. Makhnenko, V.I., Shekera, V.M. (1972) Peculiarities of stress and strain kinetics during filling of groove. *Fizika i Khimiya Obrab. Materialov*, **2**.
4. Boerjesson, L., Lindgren, L.-E. (2001) Simulation of multipass welding with simultaneous computation of material properties. *J. Eng. Mater. and Technol.*, **123**(1), p. 106–111.
5. Lindgren, L.-E. (2001) Finite element modeling and simulation of welding. Parts 1–3. *J. Thermal Stresses*, **24**, p. 141–192, 195–231, 305–334.
6. Weisselberg, A., Schmidt, R. (1982) Rechenprogramm fuer das UP-Mehrlagenschweissen. *ZIS-Mitteilungen*, **24**(12), p. 1354–1362.
7. Hantsch, H., Million, K., Zimmerman, H. (1982) Submerged-arc narrow-gap welding of thick-walled components. *Welding J.*, **61**(7), p. 27–34.
8. Harrison, J.D., Gurney, T.R. (1967) Some fatigue tests on 1 and 1/2 in. thick butt welds containing continuous slag lines. *British Welding J.*, **14**(3), p. 121–131.
9. Kiselyov, S.N., Khavanov, V.A. (1967) Effect of technological factors on weld quality for aluminum alloys of Avial-type. *Avtomatich. Svarka*, **9**, p. 51–52.
10. Stikhin, V.A., Berezovsky, B.M., Popkov, Y.A. et al. (1985) Application of transverse electrode oscillations during submerged-arc welding of multi-pass welds. In: *Transact. of Chelyabinsk Polytechnic Institute on Welding Engineering*, p. 98–103.
11. Liptak, J.A. (1961) Gas metal-arc welding aluminum with large-diameter fillers. *Welding J.*, **40**(9), p. 917–927.
12. Mueller, R. (1962) Zweckmassige Nahtorbereitung bei den verschiedenen Schweissverfahren und Beanspruchungsarten. *Schweissen und Schneiden*, **14**(10), p. 435–451.
13. Hinkel, J.E. (1970) Joint designs can be both practical and economical. *Welding J.*, **49**(6), p. 449–454.
14. Pouillard, E. (1961) Le soudage de plaques epaisses en acier au manganese-molybdene-vanadium. *Rev. Metallurgie*, **58**(9), p. 765–778.
15. Smati, Z., Alberry, P.J., Yapp, D. (1985) Strategies for automatic multipass welding. In: *Proc. of 1st Int. Conf. on Advanced Welding Systems* (London, Nov. 19–21, 1985), Paper 22, p. 219–237.
16. Anik, S., Dikicioglu, A., Akbas, N. (1994) Expert system for narrow-gap welding. In: *Proc. of 5th Int. Conf. on Comput. Technol. Weld.* (Paris, June 15–16, 1994), Paper 4.
17. Yada, T., Nakamura, U., Tomidokoro, S. et al. (1985) Development of a multipass arc welding robot for joining heavy plates. *Welding J.*, **64**(2), p. 51–56.
18. Roman, M. (1998) Automating multipass welding – the trials and tribulations. *Weld. and Join. Eur.*, Oct., p. 27–28.
19. Galopin, M., Laroche, Y., Cote, J.L. et al. (1990) Optimisation du mode operatoire en soudage multipasse a l'arc electrique. *Soudage et Techniques Connexes*, **44**(5/6), p. 33–40.
20. Ekeloef, B. (1993) Weld fill qualification – a matter for the adaptive butt-welding system. *Svetsaren*, **47**(1), p. 4–7.
21. Wu, J., Smith, J.S., Lucas, J. (1996) A weld bead placement system for multipass welding. *IEE Proc. on Science, Measurement and Technology*, **143**(2), p. 85–90.
22. Berezovsky, B.M. (1996) The mathematical model for optimization of weld shape formation in various positions of arc welding. In: *Proc. of 6th Int. Conf. on Comput. Technol. Weld.* (Lanaken, Belgium, June 9–12, 1996), Paper 12. Cambridge: TWI.
23. Berezovsky, B.M. (2002) *Mathematical models of arc welding*. Vol. 1: Mathematical modelling and information technologies, models of weld pool and weld formation. Chelyabinsk: SUSU.
24. Berezovsky, B.M. (2003) *Mathematical models of arc welding*. Vol. 2: Mathematical modeling and optimization of different types of weld formation. Chelyabinsk: SUSU.
25. Berezovsky, B.M., Stikhin, A.V. (1991) Optimisation of formation of a metal layer in arc deposition. *Welding Int.*, **5**(11), p. 888–891.

# MATHEMATICAL MODELLING OF COLD PRESSURE WELDING

M.V. BOLSHAKOV and G.N. LUKINA

National University «Lvivska Politehnika», Lvov, Ukraine

A model of the contact interaction in cold pressure welding is proposed. The problem of residual stresses influence on strength of cold-welded joints in terms of fracture mechanics was solved. It is shown that the cold-welded joints, which are formed between the metals inclined to brittle fracture, may be destroyed by the residual stresses after load removal. The quantitative criteria which connect cold weldability with mechanical properties, elastic constants and value of applied compression stress are established.

In 1948 in journal «Materials and Methods» a new method of welding without heating was presented by Sowter. The method has come to be known as cold welding. The basic parameter in cold welding is pressure or derivative value of plastic deformation  $\varepsilon_{\min}$  that suffices for the strong welded joints creation. There is a significant difference in value  $\varepsilon_{\min}$  for various metals, but some of them, for example steels and even pure iron, can not be welded by cold pressure welding.

In analyzing the various solid-state welding methods, including cold pressure welding, it is essential to distinguish between adhesion (or seizure) and welding phenomena. Adhesion is a process of elementary bonds formation when two solids are brought into contact by force  $P$ , while welding is a process of creation of strong welded joints which have a capacity for work. So we can say that the welding is the integral of adhesion over surface.

By now a great body of experimental data occur about different factors which influence on cold weldability of the metals and alloys. There are many hypotheses which attempt to explain the physical nature of the cold welding. The critical review of all the hypotheses was made in [1], where their contradiction to a great deal of experiments is pointed out. Moreover, all the hypotheses have qualitative character.

The adhesion and cold welding are very important in advanced technology and industry. Their positive role takes place in different solid-state welding processes. Adhesion adversely affects in operation of the friction couples and the machine contacting parts. Particular attention to the problem is given in context of space investigations [2] that corroborate adhesion between juvenile surfaces of similar and dissimilar metals. As it has been shown, these processes are not dependent on either mutual solubility or crystal lattice type of the metals. Some investigators note an influence of the residual stresses on cold weldability particularly of the metals that are prone to brittle fracture.

For a point of departure one can accept that as a result of great deformation in the contact zone the residual stresses spring up. The stresses will try to rupture the adhesive bonds during unloading. The danger of such rupture is intensified by hard cold working and the lack of adhesion, which are the sharp stress concentrators. The theoretical analysis has shown that at the periphery of discrete contacts the residual stresses approach infinity. Therefore periphery joints will rupture if they do not have ductility to adapt themselves to the new geometry of separated interface.

**Modelling.** A quantitative estimation of the joints viability having regard to the stresses level may be conducted in terms of fracture mechanics.

Let us look at a model in which two semi-spaces  $z > 0$  and  $z < 0$  are deformed together by force  $P$  (Figure 1, *a*). For a simple case let us assume that the seats of adhesion are disposed hexagonally on the plane  $z = 0$  (Figure 1, *b*). The area in the plane  $z = 0$  at which contact and adhesion occur is denoted by  $S$  and single seat radius equals  $b$ . All over the area  $S$  the normal stresses equal

$$\sigma_{zz} = p(x, y); \quad p \leq 0. \quad (1)$$

So, the whole contact area  $S$  may be considered as a welded metal and outside of  $S$  the lack of adhesion by size  $l$  occurs. It is suggested that in  $z = 0$  the

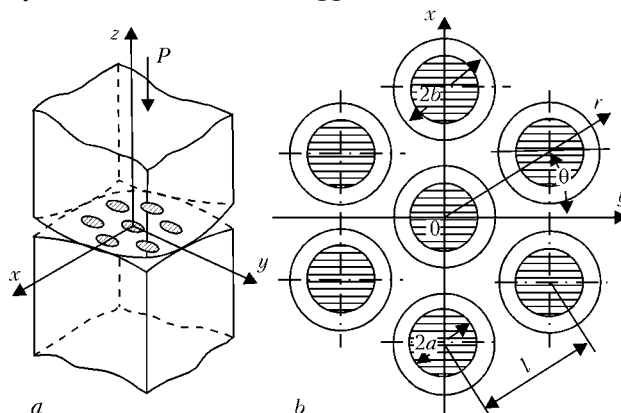


Figure 1. Calculated model: *a* – contact of semi-spaces; *b* – hexagonal disposition of adhesion seats

tangential stresses are  $\tau = 0$ ; during deformation the area  $S$  is kept flat; during unloading ( $P \rightarrow 0$ ) the brittle fracture may take place if the stress intensity factor (SIF) of the welded metal exceeds its critical value  $K_c$ , that depends on pressure value  $p(x, y)$ , scheme of deformation and properties of the metals. The value of  $K_c$  can be obtained experimentally.

During unloading when  $P = \int_S p(x, y) dx dy \rightarrow 0$ ,

the adhesion area will decrease from  $S$  to  $S_K$ . We consider the intermediate case when the force  $P$  decreases to  $P^*$  and adhesion area will equal  $S^*$ . The stresses into this area may be imagined as

$$\sigma_{zz} = p + p_*, \quad (2)$$

where the stresses  $p_*$  are determined from condition that in the area  $S$  the following expressions take place:

$$\begin{aligned} W|_{(x, y) \in S_*} &= c = \text{const}; \quad \sigma_{zz}|_{(x, y) \in S - S_*} = -p; \\ P_* &= \int_{S_*} (p + p_*) dx dy, \end{aligned} \quad (3)$$

where  $W$  is the normal displacement.

One can see from (3) that to determine the force  $P^*$  it is necessary to solve a contact problem in theory of elasticity for semi-space  $z \leq 0$  if in the area  $S^*$  acts a stamp (or several stamps) which has the flat interface; the total force acting to the stamp is recognized; normal stresses  $p(x, y)$  act out of stamp in the area  $S - S^*$ .

The area  $S$  is total combination of the circles with radius  $b$  periodically located in plane  $z = 0$ . By symmetry, it would suffice to determine the stress under one of the stamps, suggesting that during unloading the circle shape of the stamps is preserved. As in [3], we should take into consideration that the adhesion seats have centers at the origin of the coordinates and at the points  $r_n = nl$ ;  $\theta_{n, m} = 2\pi m/6n$  ( $m = 1, 2, \dots, 6$ ;  $n = 1, 2, \dots$ ) and value of the force applied to single circle at the end of loading equals  $P_0$ .

The radius  $a$  of welding area can be determined provided that applied to the stamp load equals  $P_0^*$  ( $P_0^* < P_0$ ).

In this instance, the contact problem boils down to the determination stresses under circle stamps with radius  $a$ , provided that the load  $P_0^*$  is applied to each of the stamps, and outside of these stamps additional load acts. For the stamp with center at the origin of coordinates the stress value can be found from relation

$$\sigma_{zz} = -p \quad (4)$$

when  $a < r < b$ .

According to [3], in such problems to the stresses determination in area  $r < a$ , we may allow changing all the rest load-carrying stamps by the centered forces. In this case, stresses under the stamp are defined as

$$\begin{aligned} \sigma_{zz} &= \frac{Ec}{\pi(1-\mu^2)\sqrt{a^2-r^2}} - \frac{P_1^*}{\pi^2\sqrt{a^2-r^2}} \times \\ &\times \sum_{n=1}^N \sum_{m=1}^{6n} \frac{\sqrt{l_n^2-a^2}}{r^2-2rl_n \cos(\theta-\theta_{n,m})+l_n^2} - \\ &- \frac{1}{\pi^2\sqrt{a^2-r^2}} \int_0^{2\pi b} \int_a^b \rho p(\rho, \varphi) \frac{\sqrt{\rho^2-a^2} d\rho d\varphi}{r^2-2r\rho \cos(\varphi-\theta)+\rho^2}, \end{aligned} \quad (5)$$

where  $c$  is the stamp displacement;  $l_n = nl$ ;  $P_1^* = P_0^* - \int_0^{2\pi b} \int_a^b r \rho dr d\rho$ ;  $N$  is the integral number tending to infinity;  $E$  is the elasticity modulus;  $\mu$  is the Poisson's ratio.

Based on Eq. (5) the stresses  $\sigma_{zz}^0 = \frac{1}{2\pi} \int_0^{2\pi} \sigma_{zz} d\theta$  averaged over  $\theta$  are available

$$\begin{aligned} \sigma_{zz}^0 &= \frac{Ec}{\pi(1-\mu^2)\sqrt{a^2-r^2}} - \frac{6P_1^*}{\pi^2\sqrt{a^2-r^2}} \sum_{n=1}^N n - \\ &- \frac{\sqrt{l_n^2-a^2}}{\sqrt{a^2-r^2}} \int_a^b \frac{\rho p_0(\rho) \sqrt{\rho^2-a^2}}{\rho^2-r^2} d\rho, \end{aligned} \quad (6)$$

where  $p_0(\rho)$  is the pressure averaged over  $\theta$ .

The constant  $c$  is defined provided that the main vector of forces applied to the stamp is known (equal  $P_0^*$ ). Whence it follows that

$$\begin{aligned} \sqrt{a^2-r^2} \sigma_{zz} &= \frac{P_0^*}{2a\pi} + \frac{6P_1^*}{\pi^2} \sum_{n=1}^{\infty} n \times \\ &\times \left( \frac{1}{a} \arctg \frac{a}{\sqrt{l_n^2-a^2}} - \frac{\sqrt{l_n^2-a^2}}{l_n^2-r^2} \right) + \frac{2}{\pi} \int_a^b \rho p_0(\rho) \times \\ &\times \left( \frac{1}{a} \arctg \frac{a}{\sqrt{\rho^2-a^2}} - \frac{\sqrt{\rho^2-a^2}}{\rho^2-r^2} \right) d\rho. \end{aligned} \quad (7)$$

Considering that  $p_0(\rho) = q = \text{const}$ , then the SIF  $K = \lim_{r \rightarrow a} \pi \sqrt{r-a} \sigma_{zz}^0$  averaged over  $\theta$  will equal

$$\begin{aligned} \sqrt{2a} K &= \frac{P_0^*}{2a} + \frac{6P_1^*}{\pi l} \sum_{n=1}^{\infty} n \times \\ &\times \left( \frac{1}{\alpha} \arctg \frac{\alpha}{\sqrt{n^2-\alpha^2}} - \frac{1}{\sqrt{n^2-\alpha^2}} \right) + \\ &+ qb \left( \frac{1}{\beta} \arctg \frac{\beta}{\sqrt{1-\beta^2}} - \sqrt{1-\beta^2} - \frac{\pi}{2} \beta \right), \end{aligned} \quad (8)$$

where  $\alpha = a/l$  and  $\beta = a/b$ .

Taking into account that at the end of unloading  $P_0^* = -\pi a^2 q$  and  $P_1^* = -\pi b^2 q$ , the terminal radius of the adhesion seats  $a = r_K$  can be found. The series involved in Eq. (8) at small  $\alpha$  ( $\alpha$  is always less than 0.5) by the expansion its into powers of  $\alpha$  and summation of the originated series can be written as



$$\sum_{n=1}^{\infty} n \left( \frac{1}{\alpha} \operatorname{arctg} \frac{\alpha}{\sqrt{n^2 - \alpha^2}} - \frac{1}{\sqrt{n^2 - \alpha^2}} \right) = \quad (9)$$

$$= f(\alpha) = -0.548\alpha^2 - 0.325\alpha^4 - 0.127\alpha^6.$$

It is of interest to investigate the case when  $r_K = b$ . From (8) follows that

$$|q|\sqrt{b/2} [\pi/2 + 6\alpha f(\alpha)] \leq K_c. \quad (10)$$

Let us denote by  $\sigma$  the stresses in the plane  $z = 0$  on the assumption that contact is ideal (that is to say that the stresses over the entire plane are evenly distributed). Considering that in our case between  $q$  and  $\sigma$  there is dependence  $q = \sqrt{3}\sigma/2\pi\alpha^2$ , the condition (10) would be expressible as

$$\frac{\sqrt{3}}{2\pi\sqrt{2}} \sqrt{l}\sigma \left[ \frac{\pi/2 + 6\alpha f(\alpha)}{\alpha^{1.5}} \right] \leq K_c. \quad (11)$$

As has been shown in [4] there is approximate relationship between dimensions of current contact area  $S(t)$  and its maximum value  $S_m$ :

$$S(t)/S_m \approx 1 - e^x, \quad x = \frac{4\sigma}{3\sigma_{0.2}}. \quad (12)$$

For accepted contact area the following equations is true:

$$S(t)/S_m = 12\pi\alpha^2/\sqrt{3}; \quad \alpha = \sqrt{\sqrt{3}(1 - e^x)/2\pi}. \quad (13)$$

From (11) it follows that during and after unloading of the cold-welded joints their failure will not occur if the following inequality is obeyed:

$$\sqrt{l}F(\sigma) \leq K_c, \quad (14)$$

and in its turn

$$F(\sigma) \frac{\sqrt{3}}{2\pi\sqrt{2}} \sigma \left[ \frac{0.5\pi + 6\alpha f(\alpha)}{\alpha^{1.5}} \right]. \quad (15)$$

The Eq. (14) relates the properties of the welded metals ( $\sigma_{0.2}$ ,  $K_c$ ), the lack of adhesion size  $l$  and the compression stresses  $\sigma$  to the failure probability of the welded joints by the residual stresses due to unloading. The function  $F(\sigma)$  is monotone-increasing (Figure 2) and

$$F(\sigma_{0.2}) = 0.8\sigma_{0.2}. \quad (16)$$

We emphasize that mechanical properties of the cold-welded metals should be determined by standard methods using hard cold-worked samples.

**Influence of tangential stresses.** The danger of failure of the joints of metals which are prone to brittle fracture is intensified by the tangential stresses resulting around the circle contact with diameter  $d_0$  and area  $S_0$ . The value of the stresses depends on maximal normal stresses  $\sigma_{\max}$  in the center of contact, which is equal [5]

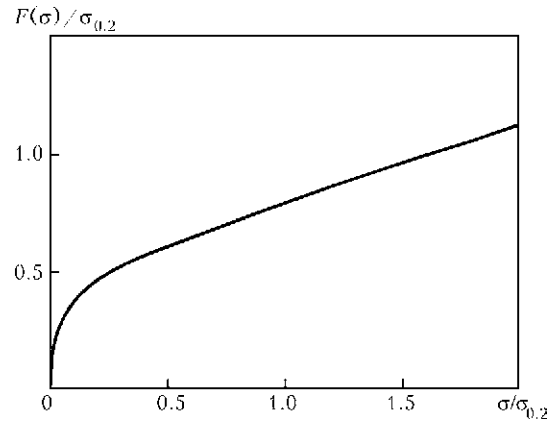


Figure 2. Form of function  $F(\sigma)$

$$\sigma_{\max} = \frac{3P}{2\pi d_0^2}, \quad (17)$$

$$\tau_{\max} = 1/3\sigma_{\max}(1 - 2\mu), \quad (18)$$

but as  $P = \sigma_S S_0$ , then

$$\tau_{\max} = 0.12\sigma_S(1 - 2\mu). \quad (19)$$

The value of the stresses for brittle metal having high value of yield strength  $\sigma_S$  and low value of Poisson's ratio can exceed the tensile stresses of the adhesion seats. As a result the adhesive bonds will failure already during the welding process.

**Role of elastic constants.** Analyzing fracture toughness of the body-centered metals, Crutchley and Reid [6] connect cold brittleness with their elastic constants. It has been shown by them that with increase of the bulk modulus  $B$  to the shear modulus  $G$  ratio the ductile-to-brittle temperature is reduced. The reason is that with increase of the ratio  $B/G$  the part of the elastic energy accumulated by a crystal at expense of the shear deformation increases in comparison with the energy accumulated at expense of the cubical expansion. Expressing the ratio  $B/G$  in term of the theory of elasticity one can connect the cold brittleness with Poisson's ratio  $\mu$ :

$$\frac{B}{G} = \frac{2(1 + \mu)}{3(1 - 2\mu)}. \quad (20)$$

On a basis of the way of looking, the experiments in cold welding and ultrahigh vacuum adhesion of various body-centered metals was carried out [7]. It has been shown that another quantitative cold weldability criterion may be represented by inequalities

$$B/G \geq 2.5 \text{ or } \mu \geq 0.32. \quad (21)$$

If pressure welding occurs at high temperature (resistance welding, diffusion bonding, friction welding etc.) the residual stresses relax and can not destroy the joints. In these cases the most important factors are problems of oxidation, surface film removal and also diffusion and recrystallization, that influence the structure and properties of interfacial zone.

**CONCLUSIONS**

1. The residual stresses due to elasto-plastic deformation during cold welding may exceed the strength of the adhesion seats and destroy a welded joint.

2. The brittle fracture danger of welded joints is aggravated by cold working of contact zone and the availability of the lacks of adhesion, which are the sharp stresses concentrators.

3. The proposed model of cold pressure welding is realized by means of the fracture mechanics mathematical apparatus, and permits to obtain the quantitative criterion of cold weldability estimation. The criterion connects weldability with the metal properties (yield strength, critical SIF) and the dimension of possible lack of adhesion.

4. The given concept connecting the cold weldability of the metals with their tendency to brittle

fracture is in good agreement with experiments in cold welding and adhesion of pure surfaces of the body-centered metals.

1. Strojman, I.M. (1985) *Cold welding of metals*. Leningrad: Mashinostroenie.
2. (1967) *Adhesion and cold welding of materials in space environment*. No. 431. Philadelphia: ASTM.
3. Galin, L.F. (1980) *Contact problems in theory of elasticity and viscous elasticity*. Moscow: Nauka.
4. Kochergin, K.A. (1970) *Pressure welding*. Leningrad: Mashinostroenie.
5. Timoshenko, S.P., Goodier, I.N. (1970) *Theory of elasticity*. New York: McGraw Hill.
6. Crutchley, D.E., Reid, C.N. (1968) Mechanical properties of the chromium monocrystals. In: *Proc. of 6th Plansee Seminar* (Reutte, June 24–28, 1968).
7. Bolshakov, M.V. (1980) An investigation of adhesion of the body-centered metals in ultra high vacuum. *Physical and Chemical Mechanics of Materials*, 2(16), p. 94–97.

# MODELING OF THE WELD METAL MICROSTRUCTURE

K. BORODIANSKIY<sup>1</sup>, A. LUGOVSKOY<sup>1</sup>, V. MAZUROVSKY<sup>1</sup>, M. ZINIGRAD<sup>1</sup> and A. GEDANKEN<sup>2</sup>

<sup>1</sup>College of Judea and Samaria, Ariel, Israel

<sup>2</sup>Bar-Ilan University, Ramat-Gan, Israel

A computer model for the prediction of weld structure and phase composition for fusion welding process based on a modified Schaeffler diagram has been developed. The model takes into account the non-equilibrium crystallization of metals and strengthening phase formation processes in the weld with any level of alloying and permits calculation of the quantities of each phase formed regardless the concentration level of alloying components. Chemical composition of new flux-cored wire for build up layers with good shock-abrasion resistance properties using the proposed model have been calculated. A calculated phase microstructure of the build up weld made by the computer was presented. Flux-cored wires were fabricated from a cold-rolled ribbon (1008 steel) and filled with a powder mixture. Low carbon steel (A 516) was used as the base metal. The samples were prepared by 3-layered build up. The prepared samples were tested using elemental analysis, hardness measurements, and metallographic tests were performed. The results of the mentioned tests confirmed the correct calculation of the model.

Fusion welding is a very complicated process because of the formation of the multi-component weld pool. This is multiphase system with a non-uniform temperature field and complex mass and heat transfer processes which are occurring on the metal-slag and metal-gas boundaries and determine the chemical composition of the weld metal and as the result determine its mechanical properties.

The mechanical properties of the weld deposit are determined not only by the chemical composition of the metal and of the build up wire, the nature of the crystallization of the weld has also a great influence on its properties.

More than 50 years, Schaeffler diagram is an important tool to predict Cr-Ni austenite, austenite-ferrite or austenite-martensite weld metal with carbon content of up to 0.12 %. Chemical composition of alloying elements is a main regulator for receiving required microstructure according to Schaeffler diagram. However, it does not allow determining the composition and volume of carbide phases. Furthermore, if carbon content in weld is over 0.12 % (for example, in the case of hardfacing), the forecast agreement with actual data is markedly reduced due to an intense consumption of carbon and carbide-forming elements by the process of carbide formation. Firstly, it could be attributed to the fact that the carbide formation process in weld is not taken into consideration (as mentioned above) and, secondly, it is caused by using constant empiric coefficients in the equations determining chromium ( $Cr_{eq}$ ) and nickel ( $Ni_{eq}$ ) equivalents.

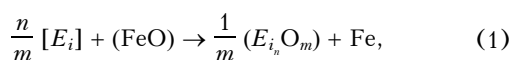
Schaeffler diagram was modified and presented in our previous works [1, 2] to provide a more accurate prediction of weld structure as follows:

- taking into consideration of the carbide formation process;
- implementation of variable coefficients in  $Cr_{eq}$  and  $Ni_{eq}$  equations (the coefficients should depend on

the concentration and mutual influence of alloying components, and on the carbide formation process in the weld metal);

- incorporating of phase percentage lines for interphase areas (i.e. the areas which contain two or more phases, as performed by Schaeffler diagram for austenite-ferrite area).

**Model of weld metal microstructure and chemical composition prediction.** The chemical composition of the weld metal is determined by the original chemical composition of the welding consumable, the base metal and the build up wire, and by the nature of the physicochemical interactions between the molten metal and the slag. The chemical composition of a weld deposit can be predicted by a procedure based on a kinetic analysis of the simultaneous diffusion-controlled reactions that occur between the molten metal and the slag [1, 3-5]. This procedure takes into account the mutual influence of the reactions and the diffusion of all the reactants in the metal and the slag. The oxidation of the elements in the molten metal can be represented by the reaction



where  $E_i$  denotes the  $i$ -element dissolved in the molten metal (Mn, Si, W, Mo, V, etc.); and  $E_i O_m$  denotes the  $i$ -element oxide in the molten slag.

Calculation of reaction (1) rates for each element does not present any difficulties. However, a separate analysis of each reaction does not correspond to the real processes occurring in the weld pool. The mutual influence of both the components of the interacting molten phases and the heterogeneous reactions taking place in these complex systems, must be considered. Within the approach developed, the rates  $V_{E_i}$  of the reaction (1) for all the metal components with con-

sideration of their mutual influence are defined by the expression

$$V_{E_i} = \frac{x^m - K_i^m \frac{(E_i O_m)}{E_i}}{\frac{x^m}{V_{E_i}^l} + \frac{K_i^m \frac{(E_i O_m)}{E_i}}{V_{E_i O_m}^l}}, \quad (2)$$

where  $x$  is the ratio between the concentration of iron oxide in the slag and the concentration of iron in the molten metal on the boundary between the interacting phases;  $V_{E_i}^l$  and  $V_{E_i O_m}^l$  are the limiting diffusion fluxes of the components of the molten phases;  $[E_i]$  and  $(E_i O_m)$  are the initial concentrations (wt.%) of the elements and their oxides in the molten phases, respectively;  $K_i$  is the equilibrium constant of reaction (1) for the  $i$ -component of the molten metal; and  $n$  and  $m$  are stoichiometric coefficients.

Taking into account that  $V_{E_i}$  are the rates of passage of the  $i$ -element from the molten metal into the molten slag or vice versa, we can use them to calculate the corresponding concentrations of the elements in the metallic and slag phases as functions of time. As the result, for the current and final compositions of the molten metal, in accordance with [4] we have

$$[E_i]^\tau = \frac{V_d[E_i]_d\tau + V_{bm}[E_i]_{bm}\tau + 100 \cdot M_{E_i} A_p \int_0^\tau V_{E_i} d\tau}{V_{\text{cryst}}\tau}, \quad (3)$$

where  $A_p$  is the interfacial interaction area;  $V_{\text{cryst}}$  is the rate of crystallization of the weld pool;  $M_{E_i}$  is the

molar mass of the  $i$ -element;  $V_d$  and  $V_{bm}$  are the rates of supply of the welding wire and base metals to the weld pool;  $[E_i]_d$  and  $[E_i]_{bm}$  are the concentrations of the  $i$ -element in the wire and base metal (wt.%).

This chemical composition is the starting point for determining the quantitative and qualitative composition of the phases of the build up metal.

The calculated (according to (3)) alloying element is distributed between matrix phases and carbide phases. First, each element forms carbide due to its carbide-forming ability as it was partially explained in [4]. The carbide-forming ability increases along the series consisting of Fe, Mn, Cr, Mo, W, Nb, V, Ta, Ti, Zr, and Hf, in good agreement with the results of [6–9]. Second, the remaining amount of the element dissolves in the matrix due to its solid solution behavior.

**Creation of shock-abrasion resistance build up metal.** The task of this work is developing of a new flux-cored wire for shock-abrasion resistance. The inverse problem of flux-cored wire computation has been solved (using mentioned model) which can provide us with the required chemical composition of build up metal and as the result it can give us the required mechanical properties, in our case shock-abrasion resistance properties. These required properties are achieved by austenite-martensite matrix structure with 10 wt.% of carbides uniformly distributed in it.

Austenite face centered cubic structure allows holding a high proportion of carbon in its solution. In our case austenite is used for shock resistance because of its energy absorbance ability. Martensite is body centered tetragonal where the carbon atoms constitute

**Table 1.** Composition and properties of flux-cored wire «pr.11» for shock-abrasion resistance (computer output), composition of base metals and build up layers (wt.%)

FCW												
Component	Density, g/cm <sup>3</sup>	Quantity in 100 kg, kg						Relation in the flux dray mixture, %				
Graphite (g17)	0.530					1.170					8.870	
Cr powder	3.480					2.080					15.850	
FeV-55	4.300					1.490					11.350	
Nb powder	3.830					1.730					13.150	
Ni powder	2.960					3.760					28.600	
Qz	1.900					0.580					4.440	
Rutile 0156	2.440					0.870					6.650	
CaFF18	1.390					0.870					6.650	
K <sub>2</sub> CO <sub>3</sub> 25	0.700					0.580					4.440	
Base materials and build up layers												
	C	Si	Mn	Cr	W	V	Mo	Ti	Al	Nb	Fe	Ni
A 516	0.280	0.300	1.000	0	0	0.001	0	0	0	0	98.350	0.001
Wire band	0.080	0.030	0.500	0.120	0.015	0.010	0.100	0.010	0.010	0.005	98.820	0.250
Required weld	1.100	0.400	0.500	1.800	0	0.700	0	0	0.001	1.300	91.197	3.000
Layer 1	0.995	0.155	0.605	1.625	0.012	0.683	0.066	0.048	0.015	1.294	91.444	2.977
Layer 2	1.185	0.118	0.500	2.057	0.015	0.864	0.083	0.059	0.019	1.637	89.608	3.768
Layer 3	1.236	0.097	0.473	2.171	0.016	0.912	0.088	0.063	0.020	1.731	89.129	3.978

**Table 2.** Atomic radii of metals with FCC lattice structures [10]

Element	Atomic radii, Å
$\gamma$ -Fe	1.27
Cr	1.28
V	1.36
Ni	1.24
Nb	1.47

a supersaturated solid solution and as a result it has the hardest and strongest microstructure. Therefore in our case martensite will be good for abrasion resistance according to its mechanical properties. The stable carbide phase brings the better toughness and abrasion resistance and also ensures uniform distribution of the hardness properties.

The way achieves the required properties partially explained here.

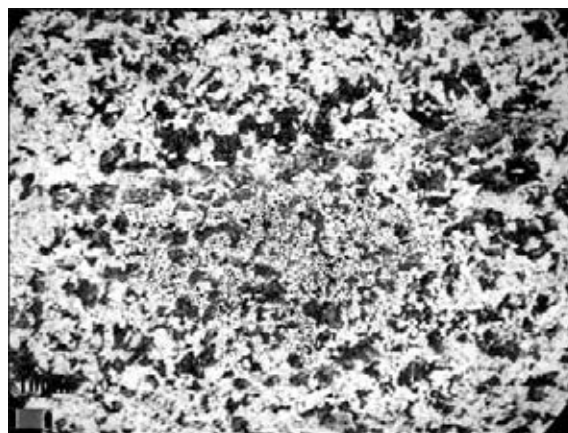
A cold-rolled ribbon (1008 steel) was filled with a powder mixture due to the calculated result presented in Table 1. In final «pr.11» wire the main alloying elements were graphite (carbon), ferrovandium, chromium, niobium (columbium), and nickel powders. From Hume–Rothery rules and [10] (Table 2) it is known that the crystal structures of the solute and the solvent must be the same, in our case the mentioned alloying elements should be dissolved in FCC structure (austenite phase structure). It is also known that the size difference between solute and solvent must be  $< \sim 15\%$ .

In our case chromium and nickel dissolves well in the austenite formed matrix. However, niobium because of its high difference in atomic radii as compared to  $\gamma$ -iron, and vanadium because of its different lattice structure, poorly dissolve in austenite. Therefore, by the end of the primary crystallization of a melt containing sufficient quantity of carbon (which is the case) both niobium and vanadium form disperse primary carbides of the type MC (NbC and VC) uniformly distributed in austenite matrix, which ensures good abrasion resistance [1]. By the end of the secondary crystallization, some amount of niobium and vanadium will stay dissolved in residual metastable austenite because of the high rate of cooling of build up layers. During impact loading this metastable austenite will dispart into alloyed martensite and carbide phases, which will additionally increase shock-abrasion resistance of the build up metal [2].

These alloying elements were supposed to increase the strength and toughness of the build up metal and

**Table 3.** «Pr.11» phase microstructure based on the model calculation

Type of structure	Structure fraction, %
Austenite	33.37
Martensite	56.14
Carbide	10.49

**Figure 1.** Base metal A 516 microstructure

this assumption was examined and the obtained results described below.

**Experiment.** The required properties for shock-abrasion resistance were the input in our computer program. The output is presented in Table 1 where we can see the needed alloying elements and their content in flux and final wire in wt.%. The Table presents also chemical composition of the base metal (A 516), wire band (cold-rolled ribbon, 1008 steel) and alloying elements the band was filled with.

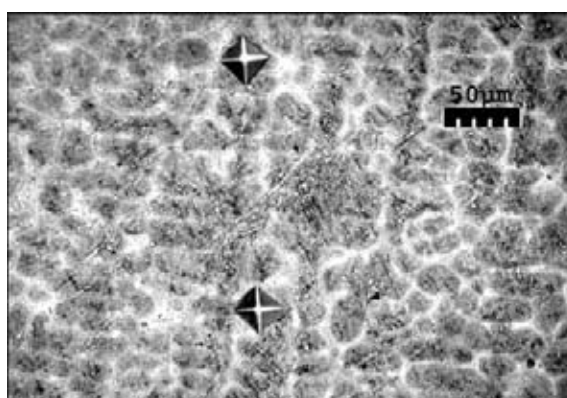
Flux cored wire with diameter 1.7 mm was prepared on a drawbench.

Next step in this work was manufacturing of the samples by build up process which was preformed by welding machine Kemppi FU 30, PS 3500. The samples were prepared by 3 layers build up metal. The technological parameters of the build up process were as follows: current 200 A, voltage 28 V, feed speed 130 m/h, travel speed 30 m/h, reverse polarity.

The samples were tested on home made shock-abrasion machine. The samples were subjects of the mechanic impact loading with the simultaneous continuous sea sand strew (85 g/min) of pre-tested sand passed through 60 Mesh sieve.

**Results and discussion.** A 12.5 mm thickness sheet of low carbon steel A 516, consisting 73 % of ferrite and 27 % of pearlite structure, was used as the base metal. Its microstructure is presented in Figure 1.

Phase composition of the microstructure of build up metal «pr.11» calculated with the help of the presented model is given in Table 3.

**Figure 2.** Surface build up metal microstructure

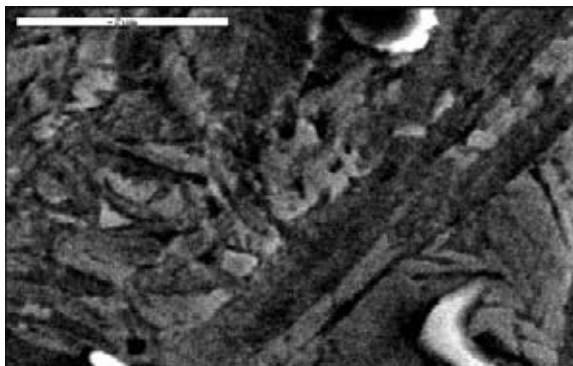


Figure 3. SEM-microstructure of surface build up metal

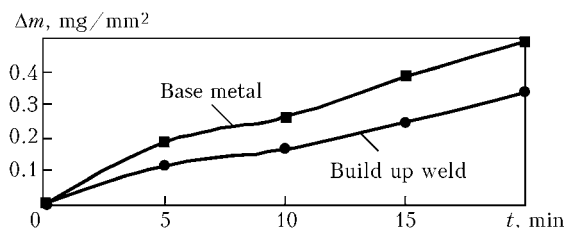


Figure 4. Shock-abrasion test results as a function of time

Surface of the 3rd layer build up metal microstructure is presented in Figure 2. In this Figure we can see martensite microstructure areas on the grain boundaries. As the result of formation of the microstructure areas, ferrite microstructure area decreased. The same area is presented in Figure 3. On the SEM-image we see the same microstructures (see Figure 2), the needle-like areas presents a martensite phase structure. The carbide inclusions (white areas on the image) dissolved in austenite microstructure.

The results of elemental analysis (EDS) of the matrix are shown in Table 4 in comparison with the results, calculated using the described model.

Hardness tests were made by the Rockwell hardness tester. The hardness of 3rd layer of build up metal was *HRC* 43 that is better result than *HRB* 90, the hardness of the base metal A 516 and emphasizes the good shock-abrasion resistance.

The results after shock-abrasion tests are presented in Figure 4. Tested samples were weighted every 5 min and the results of samples weight loss per shocked area were plotted as a function of time, i.e.

$$\frac{\Delta m}{A} = f(t). \quad (4)$$

The calculated results show that using the build up metal, shock-abrasion resistance increases by 33 %, which is in a good agreement with the declared aim of the current work. The presented test results of «pr.11» shock-abrasion resistance are very close to the computer-calculated results using the presented model. They confirm the correct calculation of the model. The computer calculation using the presented model can solve a big variety of problems like abrasion

Table 4. Results of EDS analysis and model calculations of weld metal chemical composition, wt.%

Element	EDS	Model
Si	0.21	0.097
V	1.03	0.7
Cr	2.92	2.171
Fe	92.26	89.129
Ni	1.58	3.978
Nb	2.00	1.731
Total	100	97.806

or impact only resistance, corrosion resistance, etc. The problems can be solved for build up processes as well as for welding of different metals or welding of poorly weldable metals.

## CONCLUSION

An approach for developing build up materials and a model of metal microstructure and chemical composition of a build up metal has been improved. The flux-cored wire improving the shock-abrasion resistance was produced in accordance with calculated composition using the proposed model. Build up samples have been prepared using this wire. Full-scale testing and investigation have been performed.

The presented results are confirming the adequacy of the computer calculation using the mentioned model.

The shock-abrasion resistance build up metal is only one of the possibilities which can be solved using the presented computer model.

- Mazurovsky, V., Zinigrad, M., Leontev, L. et al. (2004) Physicochemical analysis and phenomenological model of secondary crystallization of a metal in the course of welding. *Glass Physics and Chemistry*, 31(6), p. 73.
- Mazurovsky, V., Zinigrad, M., Leontev, L. et al. (2004) The main principles of development of modern surfacing materials. *Metal Technology J.*, 7, p. 34.
- Mazurovsky, V., Zinigrad, M., Zinigrad, A. (2002) Mathematical model of weld microstructure formation. In: *Computer technology in welding and manufacturing*. Sydney: TWI.
- Mazurovsky, V., Zinigrad, M., Leontev, L. et al. (2003) *The phenomenological model of non-equilibrium crystallization and strengthening phase formation processes in the weld*. Ariel: Isr.-Rus. Bi-Nat. Workshop.
- Zinigrad, M., Mazurovsky, V., Borodianskiy, K. (2005) Computer simulation of the primary crystallization processes of a metal during welding. In: *Proc. of Int. Conf. on Welding and Joining, Frontiers of Materials Joining*. Tel-Aviv.
- Gulyaev, A. (1977) *Physics of metallurgy*. Moscow: Metallurgiya.
- Oyama, S. (1996) *The chemistry of transition metal carbides and nitrides*. London: Blackie Acad. and Prof.
- Hugosson, H. (1999) *Theoretical studies of phase stabilities and electronic structure in molybdenum carbide*: Lic. thesis in physics. Uppsala.
- Grossman, J., Mizel, A., Cote, M. (1999) Transition metals and their carbides and nitrides: Trends in electronic and structural properties. *Physical Rev. B.*, 60(9), p. 6343.
- Goldshstein, M., Grachev, S., Veksler, Yu. (1985) *Special steels*. Moscow: Metallurgiya.

# FINITE ELEMENT MODELLING OF MICROSTRUCTURE ON GTAW METAL DEPOSITION OF Ti-6Al-4V ALLOY

C. CHARLES and N. JARVSTRAT

University West, Sweden

Titanium alloy Ti-6Al-4V is widely used in aero-engines because of its excellent strength, toughness, and corrosion resistance. The use of metal deposition (MD) technology is receiving increased interest due to its cost saving potential when manufacturing complex shapes. The main difficulty in producing high quality titanium alloys is to control the microstructure for the required properties. MD is essentially a multi-pass welding method, and can be used for building features such as bosses and flanges on fabricated components. There are different MD methods, however, the scope of this paper is MD with gas-tungsten-arc welding (GTAW) and wire feeding. A microstructure evolution model is necessary to provide input to a more physical-mechanical constitutive model. Further, it is necessary to accurately keep track of the temperature history when modelling this microstructure. The model should cover each step of the process considered: rapid solidification, cooling, and heating. The finite element method (FEM) is chosen to keep track of the temperature history. This work is part of the development of a complete virtual fabrication chain of compatible simulation models within the European research project VERDI (<http://www.verdi-fp6.org/>). A set of microstructure evolution sub-routines is being adapted for use in the FE commercial software MSC.Marc. Grain growth and phase content evolution are modelled according to a point-wise logic. The diffusional  $\beta \rightarrow \alpha$  phase transformations are described using a modified Johnson-Mehl-Avrami theory. The microstructures of a simple metal deposited feature are discussed in relation to this model, and some numerical approaches are presented.

The aero-engine industry has shown an interest in the development and understanding of metal deposition processes since the beginning of the 1980s. The saving in buy-to-fly material cost is of great interest, especially when using advanced and expensive materials such as titanium alloys. Laser metal deposition (LMD) has drawn much attention lately, and several LMD processes with metal powders have been commercialised in the last few years. However, the use of powders has less potential deposit output and demands a specific cleaning system. In this study, metal wire is fed through a conventional wire feeder and deposited as features on a metal plate using a standard GTAW power source. The power source is used to electrically heat and melt the metal wire, which then solidifies to form a fully dense layer. The addition of multiple layers produces a fully dense part having a near-net shape. In the current work, the most used titanium alloy Ti-6Al-4V [1] is deposited to form a single linear wall structure using the MD process.

Ti-6Al-4V alloy is a HCP- $\alpha$  and BCC- $\beta$  two-phase heat-treatable alloy, which exhibits a variety of microstructures dependent on the conditions experienced during cooling transformation from the high-temperature  $\beta$ -form to the low-temperature  $\alpha$ -form of the alloy, and for the reverse transformation upon reheating. During the MD process, steep temperature gradients and multiple thermal cycles lead to considerable microstructural changes within a very short time. Therefore, and since physical and mechanical properties are known to be sensitive to the microstructure, it is necessary to consider the effects of phase transformations.

A first model of the microstructure is proposed based on the diffusional theory. The thermal history, inducing phase transformations, is calculated using the FEM with the commercial software MSC.Marc. The modelling of the microstructure takes into account heating, cooling, as well as successive reheating

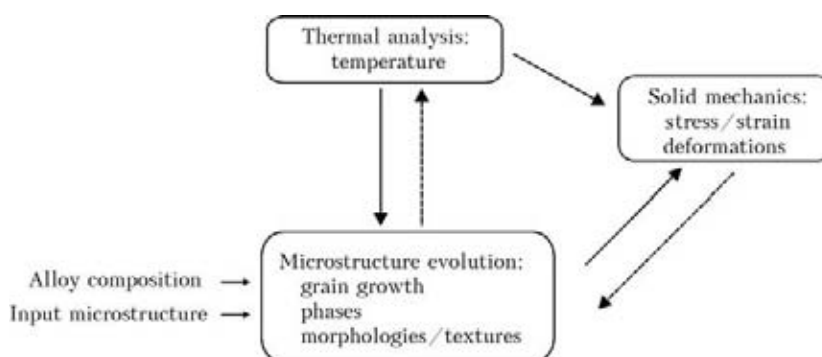


Figure 1. Flowchart of the thermal-microstructural modelling

**Table 1.** Chemical composition of the plate and wire, wt.%

	Al	V	Fe	C	O	N	Y	Ti
Plate	6.010	3.87	0.18	0.009	0.14	0.006	< 50 ppm	Balance
Wire	6.045	3.89	0.12	0.022	0.15	0.004	< 0.001	Balance

involved in the process of MD. In this paper, only the microstructure modelling strategy is presented.

### Numerical strategy

The MD process will be modelled in the traditional semi-decoupled thermal-microstructural-mechanical approach, as depicted in Figure 1. In this paper, only thermal and microstructural analyses are discussed. However, the ultimate goal of the FE simulations is to achieve a fully coupled simulation where metallurgical evolutions are stored and handled in parallel to mechanical deformations and thermal history throughout the manufacturing chain, giving an accurate account of product properties after the conceived production.

### Experimental setup

**Material.** The base plate 2 mm thick and measuring  $100 \times 210$  mm is made of Ti-6Al-4V alloy. The microstructure of the as-received plate (Figure 2, *a*) was a typical mill-annealed textured plate, consisting of primary  $\alpha$ -grains surrounded by a transformed  $\beta$ -structure. The chemical compositions of both the commercial grade Ti-6Al-4V alloys used in the plate and the feeding wire were according to aerospace specifications and are specified in Table 1.

**Metal deposition.** During the MD, the plate was held in place by a fixture with 3 contact points on each side (Figure 3, *b*). To avoid bending of the plate, it was also supported from below at one centrally located point. Six thermocouples of K type

(NiCr/NiAl) were spot welded on the top surface of the plate, positioned at a distance of 4, 4.5, 5, 6, 7 and 8 mm from the centre of the weld, and distanced 2 mm from each other in a direction parallel to the weld. Figure 4 shows the thermocouples in place after the building of the MD wall. The entire GTAW metal deposition sequence was performed within a chamber (see Figure 3, *a*) to prevent formation of  $\alpha$ -case and oxidation. A protective atmosphere of less than 20 ppm of oxygen was maintained by injecting argon into the chamber. An 8-layered wall, 8 mm wide was built next to the thermocouples (see Figure 4). The final wall measures 8 mm high by 120 mm long.

### Thermal model

The commercial FE software MSC.Marc is used for simulating the temperature field evolution during the MD operation. A 3D model is used to represent the experimentally investigated geometry.

There are two alternatives for modelling the weld heat source: a complete description of the plasma arc and molten weld pool or a simpler model for heat transfer distribution between the torch and the work-piece. In this study, one of the methods for the second approach listed by J.A. Goldak [2] was used. A circular Gaussian surface distribution has been chosen for modelling the heat source from the weld, because the GTAW pool penetration is shallow. User subroutines previously developed by a co-worker [3] were

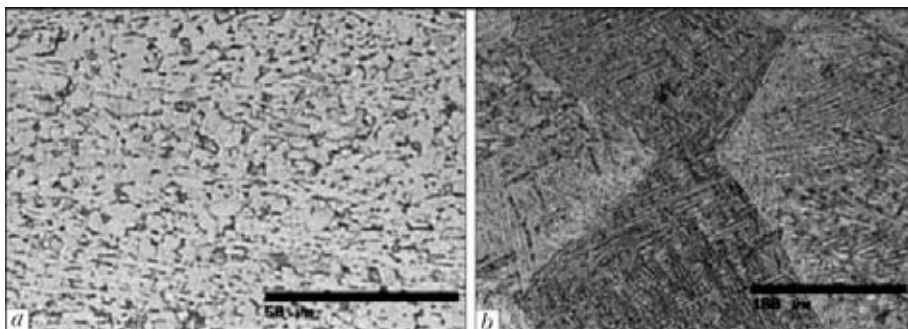


**Figure 2.** Original plate morphology: *a* – unaffected zone; *b* – HAZ

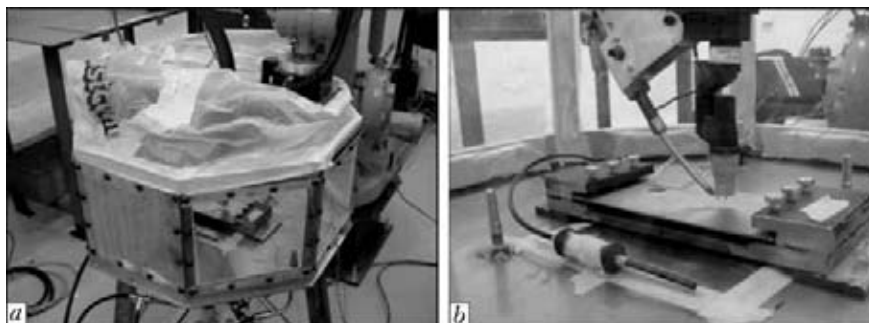


**Figure 3.** Setup of the Ti-6Al-4V plate: *a* – atmospheric chamber; *b* – weld torch, fixture and plate



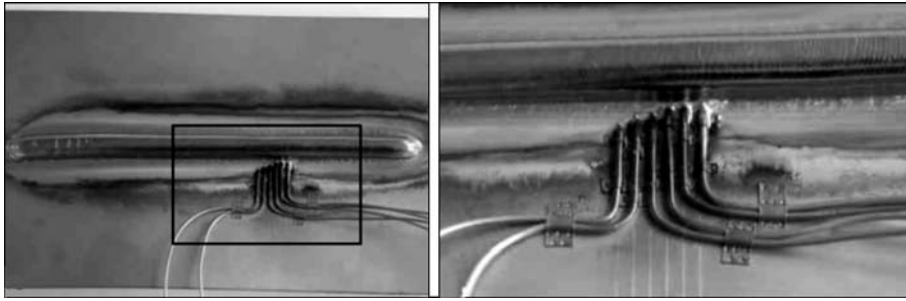


Figure 4. Position of the thermocouples close to the 8-layered MD wall

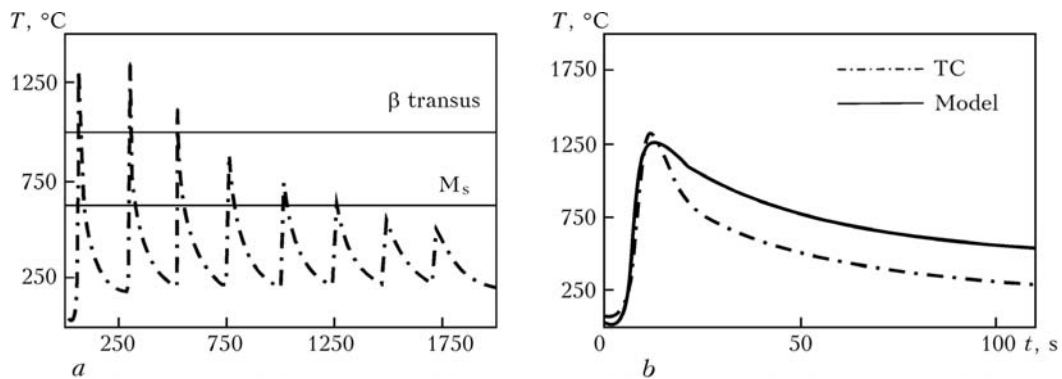


Figure 5. Temperature variations at 0.5 mm distance from the side of weld: *a* – experimentally measured temperature; *b* – comparison between predicted and measured temperature for the first weld pass

employed to simulate the heat source motion. The heat flux [4] is expressed as

$$q = q_0 e^{-\alpha_q r^2}, \quad (1)$$

where  $q$  represents the heat transfer to the plate  $q_0 = \frac{\eta EL\alpha_q}{\pi}$ ;  $E$  and  $I$  are the welding parameters voltage and current;  $\eta$  is the efficiency factor;  $\alpha_q$  is the concentration factor; and  $r$  is the radial distance from the centre of the heat source.

The thermal properties, specific heat and conductivity, were considered temperature dependent in the model [5]. The latent heat of melting has been accounted for separately in the model for temperatures between the solidus (1600 °C) and the liquidus (1670 °C). Natural film convection has been retained as boundary conditions on the entire plate surface, since the workpiece is maintained in an atmosphere controlled chamber during the MD. The heat conduction into the fixture has been neglected in these calculations due to its very small contact area with the plate. Consequently, the conduction of the heat within the base plate is the principal cooling factor considered in these simulations.

In order to model successive material layers while building up the wall, the mesh for the plate as well as for the complete wall must be established before the simulation. All the wall elements are then initially deactivated to ensure that they do not contribute to the heat load calculation. A new wall layer is subsequently activated in the mesh after each heat source pass [6]. Material properties and thermal boundary conditions are assigned to the elements at activation.

**Results.** Experimentally measured temperatures variations at the 0.5 mm distance from the weld during the MD are shown in Figure 5. Each temperature peak represents the thermocouple response as the heat source passes the thermocouple. The rapidly decreasing temperature after the peaks is caused by cooling from the surrounding material when the heat source moves away from the thermocouple during fabrication of an individual layer. The general decreasing trend in the temperature peaks is the result of the distance from the heat source increasing with each new layer. Notice that the reheating is extremely rapid, bringing the metal to temperatures higher than the  $\beta$ -transus several times.

The predicted top temperature is in good agreement with the measured temperature at the side of the weld (Figure 5, *b*). The discrepancy between measurements and simulation appearing during the cooling is probably mainly due to insufficient accuracy in thermal boundary conditions of the FE-model.

Figure 6 shows a typical heat distribution from a simulated weld pass, in this case without filler material from the 3D FE-model at a time of 40 s into the first pass. The white area in the centre represents temperatures higher than 1670 °C (liquidus temperature) and can be interpreted as the weld pool.

#### Metallographic description

The microstructure of the Ti-6Al-4V deposited metal needs to be examined in further detail. This is achieved by optical microscopy of deposited metal cross-sections. The following section contains a preliminary characterisation and comments on the MD microstructure. The samples shown were prepared using conventional grinding and polishing techniques and etched by a 2 % Kroll solution.

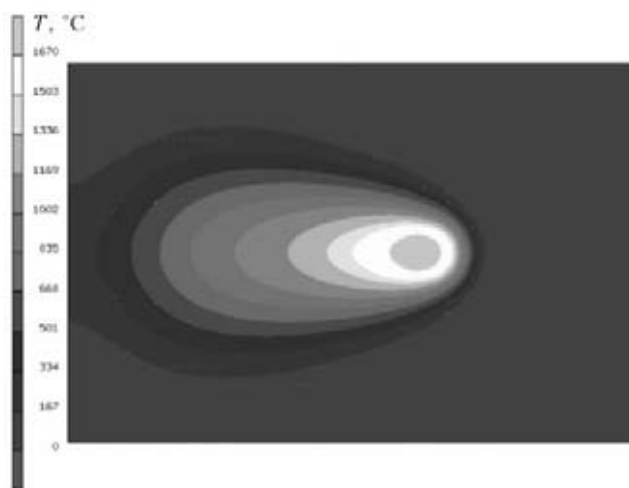


Figure 6. Contour plot of predicted temperature

**Macrostructural features.** Figure 7 represents a transversal and a longitudinal macrograph of the deposit, showing the presence of macroscopic banding between layers. Interestingly, the structure consists of 8 deposited layers but only 6 layer bands were observed. We interpret this as the band formations being caused by reheating during the deposition of the following layer. Also, the spacing between bands was measured to be  $0.6 \pm 0.1$  mm at the weld centreline, but the last visible layer was measured to be 1.3 mm corresponding to the sum of the last two deposited layers.

The presence of large columnar prior  $\beta$ -grains in the deposit is shown in Figure 7. They are nearly perpendicular to the plate and cross multiple deposited layers and layer bands. At their maximum, the size of the prior  $\beta$ -grains almost reaches the height of the entire structure. This is probably caused by continued grain growth in the new weld pool due to the unidirectional heat conduction during cooling. At the intersection of the first layer with the plate, the prior  $\beta$ -grain morphology changes from equiaxed to columnar (Figure 8).

In comparison with welding, a well defined heat-affected zone (HAZ) associated with the fusion zone (FZ) can be seen on the side of the deposit at the junction with the plate. Figure 9 shows the changing microstructure from the unaffected plate to the HAZ.

**Microstructure.** The plate exhibits a variety of microstructural morphologies dependent on the distance from the MD wall. The as-received plate mi-

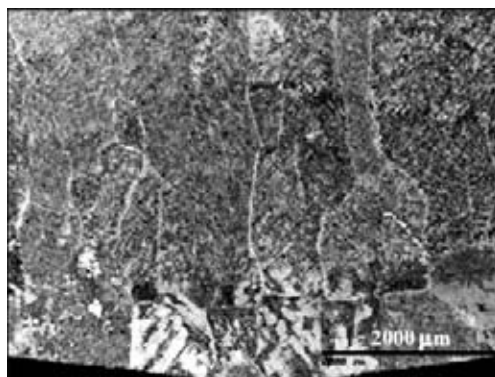


Figure 8. First two layers with plate, and changes in the prior structure of the  $\beta$ -grains from the plate to the deposited layers

crostructure was presented in Figure 2, *a*. The microstructure consists of equiaxed  $\alpha$ - in a transformed  $\beta$ -matrix, typically referred to as the  $\alpha + \beta$  microstructure. The  $\alpha$ -grains become larger and more acicular closer to the HAZ and FZ (see Figure 9). The prior  $\beta$ -grains are outlined by the presence of a continuous  $\alpha$ -phase at the grain boundaries (see Figure 2, *b*).

The deposit microstructure between the layers shows a basket-weave Widmanstaetten morphology (Figure 10). The banding morphology presents a difference in the  $\alpha$  size between the dark and the lighter bands. The lighter band microstructure in Figure 10, *c* presents a larger  $\alpha$ -platelet size than the darker band morphology in Figure 10, *b*.

Based on the current understanding of the as-deposited Ti-6Al-4V alloy microstructure, microstructural features are identified for quantification and as parameters (state variables) for the microstructural model.

#### Microstructural modelling

In this work, the main aim of the microstructural modelling is to provide information capable of parametrising mechanical properties in order to predict mechanical behaviour, distortions, residual stresses, and fatigue of aero engine components based on the manufacture processes employed. As a result, scalar quantities assignable to integration points in an FE calculation are needed. Obvious choices are the constituent phase fractions and associated size quantities. It is less obvious, however, which level of detail should be chosen for constitutive phase selection, as is the choice of size quantities. The  $\alpha$ - and  $\beta$ -phases should certainly be included, and the prior  $\beta$ -grain size is known to significantly influence material pro-

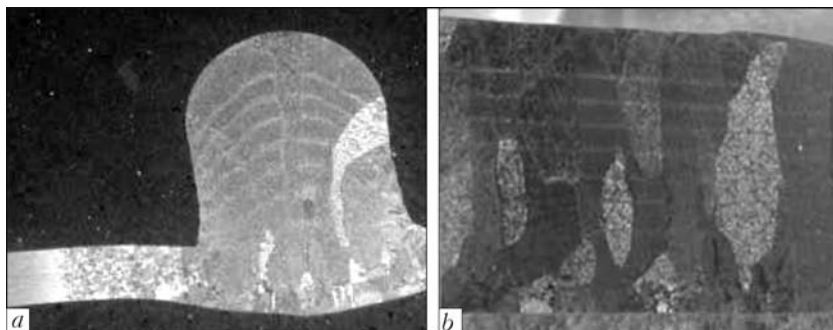


Figure 7. Macrographs of the Ti-6Al-4V deposited metal: *a* – transversal section; *b* – longitudinal section

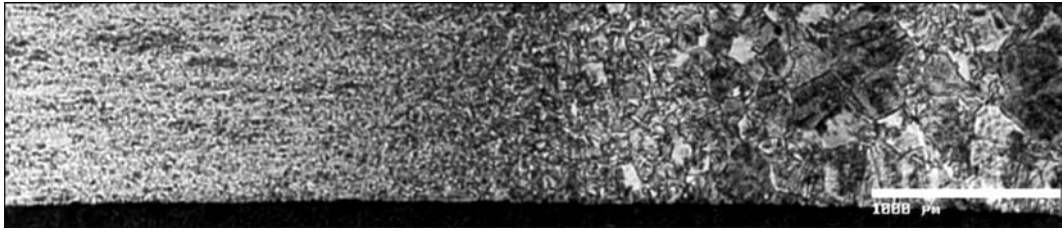


Figure 9. Changing microstructure from the base plate to HAZ

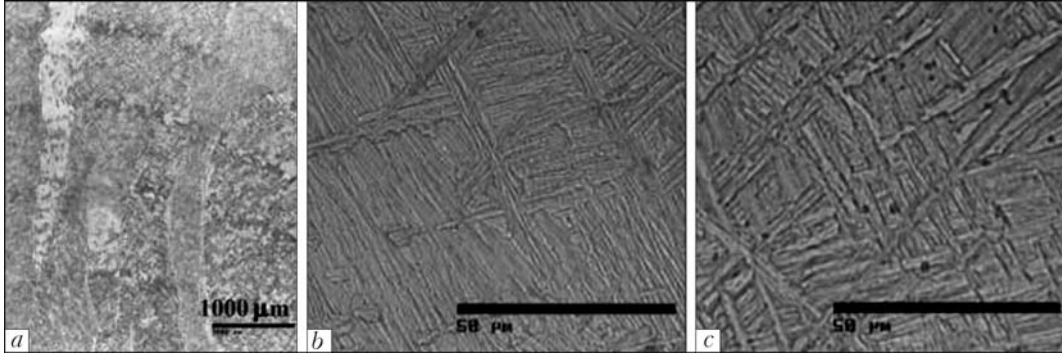


Figure 10. Banding structure crossed by prior  $\beta$ -grain boundaries (a), morphology in dark (b) and lighter (c) band

properties even after complete  $\beta \rightarrow \alpha$  transformation. We have, as a preliminary assumption, chosen to distinguish between several different  $\alpha$ -types, and, while retaining information about  $\beta$ -grain size, also adding size information about the  $\alpha$ -phases according to Table 2.

It has been established that phase transformations occurring during rapid cooling of titanium are of two principal types, namely diffusion-dependent and diffusion independent (martensitic). Phase transformations can be described graphically in transformation diagrams, the most common being the TTT (time-temperature transformation) or IT (isothermal transformation) diagram, and the CCT (continuous cooling transformation) diagram. Both contain essentially the same information, but this information has to be transformed into equations as discussed below; for this purpose, the TTT/IT diagram provides more readily translatable data.

As a first step, three different diffusional transformations ( $D^1$ ,  $D^2$ , and  $D^3$ ) and one martensitic (M) are considered.  $\alpha \rightarrow \beta$  transformation will be modelled, while the back-transformation  $\beta$  to  $\alpha$  will be considered independent of the type of a until contrary evidence is available. These transformation models are summarised in Figure 11.

For diffusion controlled transformations, the Johnson–Mehl–Avrami equation [7, 8] is adopted, which

for pure and isothermal transformation from phase  $j$  to phase  $k$ , can be written as

$$v_j = e^{-B_{jk} t^{N_{jk}}} v_j^0 v_k^{eq}. \quad (2)$$

Here  $v_k = (1 - e^{-B_{jk} t^{N_{jk}}}) v_j^0 v_k^{eq}$  is the current fraction of phase  $k$ ;  $v_j$  is the current fraction of phase  $j$ ;  $B_{jk}$  and  $N_{jk}$  are the temperature-dependent material constants that can be determined, e.g. from a TTT diagram;  $t$  is the time since start of transformation;  $v_j^0$  and  $v_k^{eq}$  are the initial fractions of phase  $j$  and the equilibrium fraction of phase  $k$ , respectively.

For the martensitic transformation, it is common practice for titanium to assume instantaneous transformation at cooling rates higher than around  $410 \text{ }^\circ\text{C/s}$  [9]. We will, however, employ the for steel established Koistinen–Marburger equation [10], which for transformation of phase  $j$  into phase  $k$  in the absence of diffusional transformations can be written as

$$v_j = e^{-0.003(T_{ms} - T)} v_j^0. \quad (3)$$

Here  $v_k = (1 - e^{-0.003(T_{ms} - T)}) v_j^0$ ;  $T_{ms}$  is the start temperature for martensitic transformation;  $T$  is the current temperature; the constant  $-0.003$  is taken from [11] and used instead of  $-0.011$  as commonly employed for steels.

Table 2. Microstructure parameters and morphology description

Phase constituents			Type	Size parameters	
$\alpha$	Diffusional	$\alpha^{gb}$	Grain boundary	Mean diameter	$d^{gb}$
		$\alpha^c$	Intragranular, basket-weave Widmanstaetten	Needle mean diameter, colony size	$d^c$
	Martensitic	$\alpha^m$	Massive, martensitic	Platelet thickness	$d^m$
$\beta$		$\alpha$	Prior $\beta$ -grain	Mean grain size	$d^\beta$

From \ to	$\alpha^{sb}$	$\alpha^c$	$\alpha^m$	$\beta$
$\alpha^{sb}$				$D^1$
$\alpha^c$				$D^1$
$\alpha^m$				$D^1$
$\beta$	$D^2$	$D^3$	M	

**Figure 11.** Schematic table of the preliminary included phase transformations (for notation see Table 2)

**Numerical considerations.** In order to discretise the transformation equations (2) and (3), the general case with several ongoing phase transformations should be considered, possibly simultaneous, and with phase contents changing due to other transformations and temperature variations during the process. Thus, the discretisation is performed using the assumption that the current fraction of the resultant phase is taken relative to the total content of transforming and resultant phase, rather than using the equations directly with the original content of the transforming phase. This assumption implies that transformation into other phases will remove possibly transformed material, regardless of when and at which temperature the transformations occur. With these assumptions, equation (2) can be written directly in incremental form without a detour through differential form:

$$\Delta v_k = -\Delta v_j = \left(1 - e^{-B_{jk}(t_c + \Delta t)^{N_{jk}}}\right) (v_j^n + v_k^n) v_k^{eq} - v_k^n; \quad (4)$$

$$t_c = \left[ -\ln \left( 1 - \frac{v_k^n / v_k^{eq}}{v_j^n + v_k^n} \right) / B_{jk} \right]^{1/N_{jk}}.$$

Here, superscript  $n$  denotes values at the beginning of the increment. In the same way, martensitic transformation according to equation (3) can be written in incremental form as

$$\Delta v_k = -\Delta v_j = (1 - e^{-0.003(-\Delta T)}) (v_j^n + v_k^n), \quad (5)$$

where  $-\Delta T$  is the step in increased undercooling below the martensite start temperature  $T_{ms}$ . When heating occurs, or when above martensite start temperature, no martensitic transformation is assumed to occur.

### Discussion and future work

A strategy has been presented for modelling temperature and microstructure, with the vision of achieving a complete coupled model for the MD process. Metallographic observations of the titanium alloy Ti-6Al-4V has been employed to determine representative parameters, such as  $\alpha$ -phase contents and associated geometrical size parameters. The prerequisite for applying the methodology is to determine

parameters for the microstructure kinetics. Available TTT diagrams are not detailed and may need some elaboration for use in these models. Thermodynamics and diffusional phase transformation software (ThermoCalc [12], JMatPro [13]) might be able to extend the existing microstructural data. The FEM allows using isothermal kinetics data by time and space discretisation.

In the near term, further 3D thermal simulations will be performed, and the microstructural model implemented as a subroutine including latent heat generation for the thermal calculations. The boundary conditions used will be reassessed, in particular with regards to the convection parameter, but possibly also including heat conduction to the fixture. Further, the microstructural evolution will be used in predicting the varying mechanical model parameters, e.g. by using the rule of mixtures on temperature-dependent flow stress of each constituent phase. Finally, the model will be developed to address the influence of morphology parameters, such as grain size, and to predict product fatigue resistance.

**Acknowledgments.** The authors acknowledge the financial support from the European 6th Framework Programme through the research project VERDI (Virtual Engineering for Robust manufacturing with Design Integration).  
http://www.verdi-fp6.org

1. Donachie, M.J. (2000) *Titanium: A Technical Guide*. 2<sup>nd</sup> ed. ASM Int.
2. Goldak, J.A., Akhlaghi, M. (2005) Ch. III: Thermal analysis of welds. In: *Computational welding mechanics*. New York, p. 71-118.
3. Ericsson, M. et al. (2005) Three dimensional simulation of robot path, heat transfer and residual stresses of a welded part with complex geometry. *Int. J. Joining of Materials*, 17(2), p. 42-51.
4. Radaj, D. (1965) In: *Heat effects of welding*. Springer, p. 18-67.
5. Pederson, R. (2004) *Microstructures of Ti-6Al-4V and Ti-6Al-2Sn-4Zr-6Mo and their relationship to processing and properties*: PhD thesis. Lulea: University of Technology.
6. (2005) *MSC.Software*. Vol. D: User subroutines and special routines. In: *Help documentation*.
7. Avrami, M. (1939) Kinetics of phase change. I: General theory. *J. Chemical Physics*, 7, p. 1103-1112.
8. Avrami, M. (1940) Kinetics of phase change. II: Transformation-time relations for random distribution of nuclei. *Ibid.*, 8, p. 212-224.
9. Ahmed, T., Rack, H.J. (1998) Phase transformations during cooling in ( $\alpha + \beta$ ) titanium alloys. *Materials Sci. and Eng. A*, 243(1/2), p. 206-211.
10. Koistinen, D.P., Marburger, R.E. (1959) A general equation prescribing the extent of austenite-martensite transformation in pure iron-carbon alloys and plain carbon steels. *Acta Metallurgica*, 7, p. 59-60.
11. Fan, Y., et al. (2005) Effect of phase transformations on laser forming of Ti-6Al-4V alloy. *J. Applied Physics*, 98(1), p. 013518.
12. *Thermo-Calc Software*. Stockolm.
13. *Thermotech. JMatPro*.

# NUMERICAL SIMULATION OF HEAT TRANSFER AND STRUCTURE FORMATION IN LASER WELDING OF ALUMINUM ALLOY\*

A.N. CHEREPANOV, V.P. SHAPEEV, V.M. FOMIN and L.G. SEMIN  
Institute of Theoretical and Applied Mechanics, RAS SB, Novosibirsk, Russia

2D quasi-stationary model of thermophysical processes in laser butt welding is proposed. Model is based on quasi-equilibrium description of processes of multi-component alloys melting and solidification with formation of two-phase zone. Numerical modeling of butt welding of aluminum alloy two plates is performed. Values for all necessary physical constants were taken from known sources.

In the last years the increasing attention is paid to development of technology for laser welding of metalware. Among advantages of this technology are local character of the heat impact, minimal thermal deformation, broad range of adjustment of laser radiation energy parameters, high productivity of the process. However, the use of the lasers (especially, the powerful CO<sub>2</sub> lasers) in different materials bonding is restrained by low stability of the welded joint properties. Due to specifics of the welding process, experimental study and definition of the optimal technological parameters are accompanied by essential methodical difficulties and considerable expenses. In this connection, development of adequate mathematical models and numerical algorithms for their computer realization is an important issue, because the method of computer mathematical modeling allows one to investigate effectively the complex physico-chemical and thermomechanical phenomena in the weldpool as well as in the near-weld zone, and to determine the efficient weld modes guaranteeing a high-quality joint. In the present study we propose a 2D quasi-stationary model of thermophysical processes in laser butt welding of metal plates and present a method for numerical modeling.

**Problem formulation.** Rectangular parallelepiped-shaped plates of the same thickness are butt-joined along narrow sides. Upper surface of the plates is blown by inert gas to avoid oxidation. Laser beam axis is in the plane of the butt and is perpendicular to the surface of the plates. We consider a case when the power density of laser radiation exceeds the threshold limit, and the process of the joint formation is accompanied by intensive evaporation of the material with formation of the vapour keyhole. The model is based on quasi-equilibrium description of processes of multi-component alloys melting and solidification with formation of two-phase zone. According to this

model, there is no supercooled fluid or superheated solid phase in the two-phase zone. There is a thermodynamic equilibrium between compounds of the non-solidified melt and crystals emerging from it. However, due to the low diffusive mobility of the dissolved components in the solid phase the substance distribution in the growing crystals is non-uniform, and the complete equilibrium in the system is not reached.

Figure 1 shows schematically the welding domain. As an origin of Cartesian coordinates the intersection point of laser beam axis and upper surface of plates was taken. The direction of  $z$ -axis is along laser beam axis,  $x$ -axis lies along butt in direction opposite to direction of laser beam motion,  $y$ -axis is normal to the butt. In coordinates chosen the laser beam is motionless and plates move with welding speed  $v$ . Vapour keyhole 2 is forming in vicinity of laser beam 1 and is adjacent with the molten pool 3. The latter is adjacent with subdomain 4, where the material is in two-phase state, and finally it surrounded by the material in solid state. Shape and location of these curvilinear boundaries (keyhole surface and boundaries between different phases) depend on laser power, thickness of the plates, material properties and other parameters of the problem.

In the mathematical model corresponding to the physical model mentioned above heat transfer process in welding is described by quasi-stationary heat conduction equation, and heat exchange with ambient medium and between subdomains in different phases

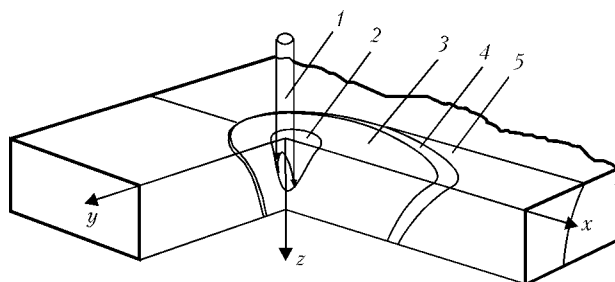


**Figure 1.** Scheme of deep penetration butt welding: 1 – laser beam; 2 – keyhole; 3 – liquid phase; 4 – two-phase zone; 5 – weld

\*This study was performed under financial support of RFBR grants Nos. 06-01-00080-a and 05-01-00311.

is described by different non-linear boundary conditions of heat balance.

In order to simplify this complex problem let us average 3D heat conduction equation over  $y$ -coordinate. As a result we obtain following equation:

$$c_{ei}v \frac{\partial T}{\partial x} = \lambda_i \left( \frac{\partial^2 T}{\partial x^2} + \frac{\partial^2 T}{\partial z^2} \right) - \frac{\lambda_i}{l_T^2} (T - T_a), \quad (1)$$

where effective heat capacity  $c_{ei}$  is given by formula

$$c_{ei} = \begin{cases} c_{iD1}, & T < T_e, \\ c_{2D2} \left( 1 + \frac{\kappa}{c_2} \frac{\partial f_l}{\partial T} \right), & T_e \leq T \leq T_{l0}, \\ c_{3D3}, & T_{l0} < T. \end{cases} \quad (2)$$

Here subscript  $i = 1, 2, 3$  denotes parameters of solid, two-phase and liquid states of metal, respectively;  $c_i, \lambda_i, \rho_i$  are the specific heat capacity, heat conduction and density of  $i$ -th phase;  $\kappa$  is the specific melting heat;  $T_{l0}, T_e$  are the temperatures of the beginning and the end of solidification;  $l_T = 2\sqrt{a_i\tau}$  is the heat-wave propagation length for the time  $\tau = 2r_F/v$ ;  $a_i$  is the thermal conductivity of  $i$ -th phase;  $T_a$  is the characteristic temperature of the plate outside the region of averaging;  $f_l(T)$  is the liquid portion in two-phase zone.

Boundary conditions are derived from the conditions of heat balance at boundaries. On the top surface  $z = 0$  in the domains of solid, solidified, liquid and two-phase state of alloy we specify following condition:

$$\lambda_{iT} \frac{\partial T}{\partial z} \Big|_{z=0} = (\alpha_k + \alpha_{ri})(T|_{z=0} - T_g), \quad (3)$$

$$x > r_F \quad (i = 1, 2, 3).$$

Here  $\alpha_k$  is the convective heat-transfer coefficient caused due to inert gas flow;  $T_g$  is the gas temperature;  $\alpha_{ri}$  is the radiative heat-transfer coefficient of  $i$ -th phase determined by relation  $\alpha_{ri} = \varepsilon_i \sigma_0 (T|_{z=0}^2 + T_g^2) \times (T|_{z=0} + T_g)$ , where  $\varepsilon_i$  is the specific emissivity factor of  $i$ -th phase;  $\sigma_0$  is the Stefan-Boltzmann constant. Similar condition is specified on the bottom boundary.

The condition of heat balance under the laser radiation ( $x < r_F$ ) on the keyhole surface is

$$-\lambda_3 \nabla T \vec{n} = \vec{q} \vec{n} - L \dot{m} + \delta q_c, \quad (4)$$

where  $\dot{m}$  is the mass rate of evaporation from unity surface;  $L$  is the specific evaporation heat of alloy;  $\vec{q}$  is the absorbed flux of laser radiation taking into account multiple reflections inside keyhole;  $\delta = 0$  on the front keyhole wall,  $\delta = 1$  on the rear one;  $q_c$  is the convective heat flux from the front keyhole wall to the rear wall, which is determined by relation  $q_c = c_3 \rho_3 v_r (T_1 - T)$ , where  $T_1$  is the averaged temperature on the front wall;  $v_r$  is the average velocity of liquid melt during flow around keyhole, which was estimated according to [1, 2]. The intensity of laser

radiation is described by normal Gaussian distribution  $I(x, z) = I_0 \exp(-2x^2/r_z^2)$ , where  $I_0 = 2W/(\pi r_z^2)$ ;  $W$  is the laser power;  $r_z$  is the laser beam radius at the depth  $z$ , which is determined by formula

$$r_z = \sqrt{r_F^2 + \left( \frac{z - Z_F}{\pi r_F} \lambda_0 \right)^2}, \quad (5)$$

where  $r_F$  is the laser beam radius in focal plane;  $Z_F$  is the focus location with respect to top surface of welded plates;  $\lambda_0$  is the wave length of laser radiation. Then the expression for flux absorbed by keyhole surface element will be given by the following formula:

$$q(x, z) = \frac{2W_{abs}}{\pi r_z^2} \exp(-2x^2/r_z^2), \quad (6)$$

where  $W_{abs}$  is the total value of all multiple absorbed power. When determining  $W_{abs}$ , we assume that remaining power after first reflection is distributed uniformly over keyhole surface. Power absorbed by keyhole walls is calculated approximately by formula  $W_{abs} = A_{eff}W$  using effective coefficient of absorption  $A_{eff} = \beta A + A_e(1 - A)$ , where  $A$  is the absorption coefficient;  $A_e$  is the equivalent absorption coefficient for multiple reflected laser radiation;  $\beta = 1$  under laser beam and  $\beta = 0$  beyond it.

On the inter-phase boundaries heat flux balance and continuity of temperature should be satisfied.

Below we expound numerical modeling of welding by finite-difference method omitting some minor details. Due to the fact that locations of keyhole surface and inter-phase boundaries depend on unknown solution and due to non-linearity of boundary conditions, the numerical algorithm is iterative with nested loops. For the convenience of program realization, all iterations in outer loop are divided into stages.

On the first stage (without keyhole) the computational domain  $G$  is rectangle in the plane of plates butt. Its sides are given by relations  $z = 0, z = h, x = -l_1, x = l_2$ , where  $l_1$  and  $l_2$  are the distances from the left and right rectangle sides to the laser beam axis. Choice of these quantities depends on the laser power and the welding speed. The main requirement on  $l_1$  is that it would be possible to specify the temperature on the left boundary equal to the ambient temperature. That is, as a boundary condition on the left side we suppose

$$T|_{x=-l_1} = T_\infty. \quad (7)$$

As moving off the molten pool to the right, the temperature in section parallel to  $z$ -axis equalizes. On the right side of the domain besides specifying Dirichlet condition with temperature  $T_\infty$  other boundary conditions were tested. In particular, temperature value was selected from test calculation in rectangular domain with large  $l_2$  without keyhole. Here we omit the description of quite simple method of checking the appropriateness of choosing this temperature value.

**Approximation of equation and some aspects of numerical algorithm.** The domain is covered by rectangular grid  $G_h$  with nodes  $(ih_1, jh_2)$ ,  $i = 0, 1, \dots, n_1$ ;  $j = 0, 1, \dots, n_2$ , where  $h_1$  and  $h_2$  are grid steps. Different variants of finite-difference scheme for pseudo-unsteady method were used to solve the problem numerically. One of these schemes is following:

$$\begin{aligned} & \frac{T_{i,j}^{n+1} - T_{i,j}^n}{\tau} + v \frac{T_{i+1,j}^{n+1} - T_{i-1,j}^{n+1}}{2h_1} = a_i \times \\ & \times \left( \frac{T_{i+1,j}^{n+1} - 2T_{i,j}^{n+1} + T_{i-1,j}^{n+1}}{h_1^2} + \frac{T_{i,j+1}^n - 2T_{i,j}^n + T_{i,j-1}^n}{h_2^2} \right) - \\ & - \frac{a_i}{l_T^2} (T_{i,j}^{n+1} - T_a). \end{aligned} \quad (8)$$

Convergence of numerical solution was observed, in particular, by convergence of the quantity  $\max_{i,j} |T_{i,j}^{n+1} - T_{i,j}^n|$ . The scheme (8) is implicit in  $x$ -direction and explicit in  $z$ -direction. It solved iteratively by Thomas algorithm for systems with three-diagonal matrices along coordinate lines  $x = \text{const}$  at each  $j$ .

In the present study boundary conditions on external and internal (inter-phase) boundaries are approximated with first order. It is necessary to know values of normal components and boundary curvature in particular node in order to set up boundary conditions. Since all internal boundaries are certain isotherms, they can be found by interpolation based on computed temperature values at grid nodes. Inter-phase boundary  $z = Z_l(x)$  between liquid phase and two-phase zone is to be determined by liquidus isotherm  $T = T_{l0}$ . Inter-phase boundary  $z = Z_e(x)$  between two-phase zone and solid phase is to be determined by isotherm corresponding to eutectic temperature  $T = T_e$ . In the computer program the process of constructing these isotherms is automatized.

On the inter-phase boundaries we require continuity of temperature and heat balance condition. On the boundary  $z = Z_l(x)$  heat balance condition is

$$\left. \frac{\partial T}{\partial n} \right|_{z=Z_l^+} = \left. \frac{\partial T}{\partial n} \right|_{z=Z_l^-}. \quad (9)$$

On the boundary  $z = Z_e(x)$  heat balance condition will take the following form:

$$\left. \frac{\partial T}{\partial n} \right|_{z=Z_e^+} = \left. \frac{\partial T}{\partial n} \right|_{z=Z_e^-} + \text{Pe St} \frac{\partial Z_e / \partial x}{\sqrt{1 + (\partial Z_e / \partial x)^2}}. \quad (10)$$

In these formulae indices + and - denote that temperature derivatives are taken from different sides of the curve. The last term in (10) relates to crystallization heat, Pe is the Peclet number; St is the Stefan number.

In order to approximate (9) and (10) we approximate curves  $z = Z_l(x)$  and  $z = Z_e(x)$  found on the grid solution by broken lines which pass over grid nodes. To do this, we take the node which is nearest to the curve under consideration passing between pair

of nodes. The nodes chosen are linked by parts of coordinate lines or cell diagonals in such a manner that broken line obtained will have no right angles. In the present study when approximating  $\partial T / \partial n$  on internal and external boundaries, the derivatives  $\partial T / \partial x$ ,  $\partial T / \partial z$  were approximated with first order taking the value of temperature in grid nodes from the corresponding side of a curve. The ends of these curves lie on external boundary and therefore conditions for external boundary are specified there. In order to accelerate iterations fictitious time finite-difference derivative of temperature was added into all finite-difference boundary conditions. As in equation (8), the sign at these derivatives was taken in such a way as to increase absolute value of diagonal element in corresponding row of matrix in the system of linear algebraic equations (SLAE).

The process of constructing the keyhole was composed of several stages. On the first stage the problem was numerically solved in rectangular domain without keyhole. Initial temperature for iterations was taken equal to ambient temperature. After the maximum of residual of substituting numerical solution into finite-difference equations over all grid nodes became less than some specified value, the isotherms of boiling, liquidus and eutectic were found. Thus, some rough approximations for temperature distribution and internal boundary positions were found and used as initial approximation for further stages.

In the present study the method of iteration was chosen where solution of problem with nonlinear mixed boundary condition on each iteration over whole domain was reduced to solution of SLAE. It consists of some known techniques.

First of them is linearization of nonlinear equations. For example, nonlinear coefficient  $\alpha_{ri}$  in boundary condition (3) is approximated on the solution computed on previous iteration.

On the second stage the domain is divided into subdomains. They differ either by heat conduction coefficients or by combination of boundary conditions on the ends of each coordinate line  $x = \text{const}$  which set ends against the boundaries of particular subdomain, and at the same time grid lines  $x = \text{const}$  do not intersect subdomain boundaries inside the subdomain. Number of subdomains depends on presence of keyhole and on positions of liquidus and eutectic curves.

During carrying out the iteration over whole domain (global iteration) system (8) is solved sequentially in all subdomains by Thomas algorithm along  $x$ -axis at every index  $j$  possible for each particular subdomain. Temperature values on the boundaries of each subdomain are taken from previous iteration. After iteration is finished, solution correction in all boundary nodes is performed. In each boundary node boundary condition is resolved with respect to temperature value at this node. Thus its correction is found through temperature values at neighbour nodes obtained at the current iteration. This corrected value is used at the next iteration.

Collection of methods described allowed obtaining quite simple method of numerical model realization.

**Keyhole modelling.** Constructing the keyhole and modeling physical processes on its boundary is the most complex part of solving the problem. Here we do not consider and do not simulate hydrodynamical instability of the free keyhole boundary. First of all, we model heat transfer through it and its shape which would guarantee heat balance on the surface and would approximately guarantee the equilibrium of surface tension force and pressure of metal vapour. Let us note that solution behavior on the keyhole boundary plays leading part in iteration process. The solution converges, first of all, in vicinity of keyhole and then in the rest of domain. The size and the shape of keyhole affect shapes and locations of isotherms in domain.

On the first stage the heat conduction coefficient was taken equal to that for liquid metal for whole domain. It is easy to understand that maximal value of  $z$ -coordinate on the boiling isotherm is the lower estimation for keyhole depth. If it is deeper than plate thickness, then it is clear that laser breaks plates through.

The shape of vapour keyhole depends, first of all, on the process of vaporization of liquid metal from the surface, vapour pressure, surface tension and hydrostatic force. The latter is relatively small for the narrow plates. Its inclusion appears to have little effect upon the shape of keyhole and eventually on the temperature field. The vapour pressure consists of saturated vapour pressure and recoil of vapour flowing out from the keyhole. The surface tension, being in proportion to the surface curvature forces the surface to become flat. In the whole, it tends to return the keyhole surface to the plane of plate surface ( $z = 0$ ) with zero curvature. Hence the surface tension is equilibrated by the vapour pressure within the keyhole which depends on the process of liquid metal vaporization. Moreover, with the surface tension and vapour pressure being absent, the shape of vapour hole was totally governed by the process of vaporization which is taken into account in the boundary condition (4).

At the second stage, when constructing the boundaries of keyhole, the temperature field obtained at the first stage is used. The shape of the front keyhole boundary (ahead of moving the laser beam) is matched so that the boundary condition (4) is fulfilled at this boundary first. If during welding the laser is the only energy source then the greatest quantity of the external heat flux into the domain passes through the close vicinity of laser beam axis at the front wall of the keyhole. The temperature such achieved depends on the wall slope angle. In controlling the keyhole wall slope relative to  $x$ -axis, the governing factor is the following physical process consisting of two mechanisms affecting the wall slope. These latter effect the slope in the opposite directions and are balanced at some slope value. As the greatest part of energy absorbed by the wall is in proportion to the cosine of

the slope to  $x$ -axis then, with laser power exceeding critical one, decrease in the slope results in the increase in metal vaporization, with the following increase in the keyhole depth, which leads to increase in the wall slope. But this slope increase is restricted.

First, with low plate thickness the break-through will take place, which is undesirable during welding. Second (and the main), the slope angle exceeding a certain value corresponding to given parameters of the problem (laser power, plate thickness, etc.) results in decrease in energy absorbed through the unity of wall surface thus leading to the wall temperature decrease and the keyhole depth decrease. The mechanism mentioned is accounted for in equation (4) by the first and the second terms in its right-hand side. The third term in right-hand side is negligible compared to these two.

Note that energy distribution in radius of laser beam presents pronounced peak with maximum at beam axis, which is essential. Therefore the greatest part of the front wall in  $z$ -direction is in the vicinity of beam axis. Moreover, at the upper plane of the plates ( $z = 0$ ) the front wall is approximately believed to begin from the point ( $x = -r_F, z = 0$ ).

Now the problem of construction of front wall at the second stage of iterations is reduced to finding the smooth curve with maximum of the slope angle at the beam axis ( $x = 0$ ) beginning at the point ( $x = -r_F, z = 0$ ) and ending at the point where it touches the circle of radius  $r_d$ . This radius is obtained from the estimation of the keyhole bottom curvature from the requirement of the balance of surface tension and vapour pressure. In so doing the keyhole depth ( $z = z_{\max}$ ) is determined from the condition that on this curve the relationship (4) is valid for the temperature, with the temperature  $T|_{z=z_c} = T_{sat}$  where  $T_{sat}$  is the boiling point of the metal. In a numerical model such curve is searched approximately. The front wall is founded iteratively as cubic spline or by least-squares method. It is searched in the outer loop of the whole system of nested loops of iterations.

Relationship (4) and the assumptions made are still insufficient for finding the shape of rear wall. At the second stage of the estimations a straight-line segment is proposed as some approximation of rear wall shape. This segment is suggested to touch the mentioned circle at one end, another end coinciding with the boiling isotherm of the surface  $z = 0$ . Here we omit some minor details related to the fact that at the second stage one could define the position of keyhole walls somewhat more precisely. Note merely that variation of their position effects the results of calculation only in their close vicinity, with the beam vicinity being the governing element of the whole calculation. And the slope of the front wall at beam axis and in its vicinity controls the main part of the keyhole depth.

In the calculations, condition (4) can be met precisely enough at the front wall in the beam vicinity. As the numerical solution of the problem with the



absence of plasma keyhole converges on the grid sequence with the first order, the solution of the problem with the keyhole is required to have the same order of convergence. This leads to accuracy requirements for satisfying heat balance.

Additional details of the wall construction are presented in relation with its correction at the third stage of the solution.

Conditions on the internal free boundaries are used for correcting their positions in the course of iterations starting with the second stage. They are met with the accuracy of approximation order when iterations will converge. Conditions on the internal boundaries were realized rather simply in this study (these details are omitted).

It is pertinent to note that this set of the first and second stages presents some complete approximate numerical model of laser welding of metal plates.

Temperature value calculated at the end of the second stage is taken as an initial one for the third stage.

To correct the shape of the keyhole at the third stage, together with heat balance (5) the additional condition of dynamic equilibrium on its surface is suggested. It is written as

$$P(T) = \sigma K_r + g\rho_3 z. \quad (11)$$

That is, at the keyhole walls the pressure is balanced by surface tension and hydrostatic pressure. In (11),  $\sigma$  is the surface tension factor of liquid metal;  $g$  is the gravitational acceleration;  $K_r$  is the surface curvature which is defined by relation

$$K_r = \operatorname{div} \left( \frac{\nabla Z_c}{\sqrt{1 + |\nabla Z_c|^2}} \right). \quad (12)$$

Vapour overpressure  $P$  is the sum of static pressure  $P_s$  at surface evaporation and recoil pressure  $P_r$ , i.e.  $P = P_s + P_r$ . We assume linear dependence of  $P_r$  with  $P_s$ , namely  $P_r = bP_s$ . Saturation pressure of mixture of evaporated alloy components is determined by formula

$$P_s = \sum_{j=0}^1 0.001 C_j \frac{P_{0j}}{T} e^{A_j - B_j/T}, \quad (13)$$

where  $C_j$  is the molar concentration of  $j$ -th alloy component;  $P_{0j}$ ,  $A_j$ ,  $B_j$  are the some empirical constants.

Formula (11) points to the fact that shape of keyhole walls depends on temperature. That is, complex problem arises: it is necessary to solve heat conduction equations (1), (2) with nonlinear heat balance conditions together with second order partial differential equation (12) on unknown keyhole boundary. To avoid this, we propose a simplified method for correcting the shape of keyhole walls.

At the third stage the shape of rear wall and temperature distribution are corrected. Front keyhole

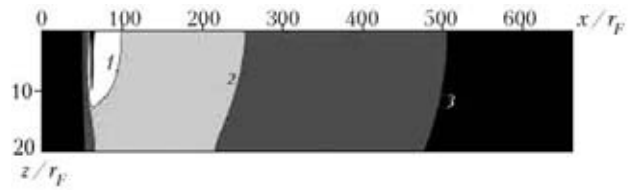


**Figure 2.** Temperature field in the domain: 1 – isotherm  $T = 1207$  K; 2 – liquidus ( $T = 862$  K); 3 – isotherm  $T = 517$  K

wall which was constructed from requirement of satisfying condition (4) is not corrected anymore. We assume that its shape is affected mainly by evaporation under laser radiation.

The greatest curvature is related to maximal pressure at the keyhole bottom. Due to the great surface tension there the keyhole surface is approximately bottom part of a sphere with radius comparable to laser beam radius  $r_F$ . At the second stage the rear wall was taken as straight line which connects the end of boiling isotherm at  $z = 0$  found at first stage and touches right side of sphere part on the keyhole bottom mentioned above. At the third stage in the external iteration loop the curvature of rear wall is determined from (11) and at the next iteration the boundary-value problem is solved with condition (4) on the rear wall with taking into account only reflected radiation.

**Numerical experiments.** Numerical experiments were performed on sequence of grids with decreasing steps. The behavior of parameters calculated such as temperature distribution, positions of isotherms, inter-phase boundaries and keyhole walls was controlled and first order of convergence was established.

We carried out calculation for butt welding of two plates of aluminum alloy AL2 (Al + 10 wt.% Si) which is used in aircraft industry. Welding speeds were taken corresponding to those in real welding process. In the calculations we determine temperature field in the object, location of internal boundaries between the phases, form and depth of the vapour keyhole. Based on the calculations, one can predict size of the zones occupied by the different phases in the welding process, characteristic size of the crystal grain, and determine which speed of the laser movement along the weld at a given laser power can ensure appearance of a sufficiently large liquid-phase zone in absence of the through keyhole (i.e. without breaching the object by the laser beam). Figure 2 shows the isotherm distribution in the domain for one of computations. The radius of laser beam in focal plane is taken as length unit. For the purpose of demonstration clearness there are different scales in  $x$ - and  $z$ -directions. More dark hue of gray corresponds to lower temperature. The keyhole is marked as narrow black area wedged into high temperature region.

1. Borisov, V.T. (1987) *Theory of two-phase zone of metal ingot*. Moscow: Metallurgiya.
2. Zinoviev, V.E. (1989) *Thermophysical properties of metals at high temperatures*: Refer. Book. Moscow: Metallurgiya.

# PREDICTION OF MICROSTRUCTURE AND MECHANICAL PROPERTIES OF WELD METAL WITH CONSIDERATION FOR REAL WELD GEOMETRY

V.A. KARKHIN<sup>1</sup>, P.N. KHOMICH<sup>1</sup> and V.G. MICHAILOV<sup>2</sup>

<sup>1</sup>St.-Petersburg State Polytechnic University, Russia

<sup>2</sup>Cottbus University of Technology, Germany

Technique of reconstructing the welding temperature field from the measured real weld geometry is proposed. It is based on the solution of the 3D direct heat conduction problem by using Green's function method and numerical solution of the inverse problem for unknown parameters of a moving volumetric heat source. A welding time-temperature transformation diagram is used to determine microstructure distribution taking the local temperature cycle into consideration. The final mechanical properties of the weld metal are determined as a function of a local cooling time/rate. The distributions of calculated and measured hardness in TIG-welded heat-resistant steel joint are compared.

In welding technologies the following problem often arises. Given: the welding conditions, welding consumables and base metal (its chemical composition and properties). Required: the distribution of microstructure and mechanical properties. How can estimates of the distributions be made? The phenomenological and statistical models allow one to determine microstructural phases and mechanical properties (hardness, yield strength, ultimate tensile strength, elongation, reduction in area, etc.) are known [1–4]. For such calculations the temperature characteristics (peak temperature, cooling rate, cooling time, etc.) are required as input data.

The well-known solutions [5, 6] give quite accurate thermal history in the zones of the workpiece where temperature is less than about 30 % of the melting point, but they are subject to serious errors for temperatures in or near the fusion and heat-affected zones (HAZ). The main difficulties are caused by the complexity of the physical phenomena (interaction of a heat source with a weld pool, convection and evaporation of a molten metal, etc.). Sophisticated mathematical models and computer codes are used to determine the weld geometry and temperature cycles in the HAZ. They require prescription of a large number of input parameters (effective thermal conductivity, effective viscosity, surface tension, etc.), which, in turn, are dependent on the problem solution [7]. Such calculation requires highly trained personnel, much time and expenses.

A choice of method for solving the heat conduction problem is governed by an accuracy required (by further use of the results). When one needs to predict the metal microstructure and properties after welding only the temperature profiles in a solid part of the weldment are of interest. Therefore the temperature problem formulation can be simplified. In this case the boundary conditions for a solid part including the solidus face of the molten pool (which carries the

resulting information on all physical processes in the weld pool) should be available. Such approach allows determining the temperature field in the surroundings of the molten pool and is used in the «equivalent heat source» conception [8]. The weld interface can be determined experimentally. It is simple matter in welding of a thin plate. This calculation technique was used for the first time to evaluate the thermal processes near moving weld pool [9, 10]. In welding of a thick plate only incomplete information on 3D solidus face is usually available.

The aim of the study is to develop a calculation technique in order to reconstruct the 3D temperature field and predict the microstructure and mechanical properties. The technique is based on the solution of the direct 3D temperature problem by a functional-analytical method, the numerical solution of the inverse problem for unknown parameters of a volume heat source, the employment of the known models for prediction of the microstructure and mechanical properties by welding thermal cycle. Some experimental data (weld crater or ripples visible on the weld surface, weld interface in cross section, thermal cycles at some points, etc.) are used.

## Formulation of direct heat conduction problem.

The following assumptions are made:

- plate is homogeneous and infinitely long and wide;
- thermophysical properties (thermal diffusivity  $a$  and volume-specific heat capacity  $cp$ ) are temperature-independent;
- heat source centre and attached reference frame  $x, y, z$  move uniformly and linearly with constant velocity  $v$  along  $x$ -axis during time  $t$ ;
- plate surface is heat-impermeable;
- initial temperature  $T_\infty$  is constant.

Then the equation for the conservation of energy takes the form:

$$\frac{\partial T}{\partial t} = a \left( \frac{\partial^2 T}{\partial x^2} + \frac{\partial^2 T}{\partial y^2} + \frac{\partial^2 T}{\partial z^2} \right) + v \frac{\partial T}{\partial x} + \frac{q_3}{c\rho}, \quad (1)$$

$$q_3 = q_{3net} + q_{3c} + q_{3L}, \quad (2)$$

where  $q_3$  is the apparent power density (per volume);  $q_{3net}$ ,  $q_{3c}$ ,  $q_{3L}$  are the power densities of the real source (arc, beam, etc.), of the convection, and of the latent heat, respectively (Figure 1).

Equation (1) with the corresponding boundary conditions represents the formulation of a direct heat conduction problem.

**Model for heat source.** The apparent source [2] represents simultaneous influence of the real source (arc, beam, etc.), of the convection, and of the latent heat. Note that the dimensionality of function  $q_3$  is equal to the dimensionality of the temperature field even though the dimensionality of the real source  $q_{3net}$  is less. For example, if a thick plate is heated by a real 2D surface heat source the temperature field and, consequently, the apparent source are 3D. Function  $q_3(x, y, z)$  can be approximated by prescribing the form of distribution beforehand. For instance, the power density distribution unbounded in extent along all axes can be described by the Gaussian normal distribution, such source is called ellipsoid heat source [11]. In reality the domain of a volume source distribution along  $z$ -axis is bounded by the weld pool interface and does not have a physical meaning outside the pool.

Let us consider bounded normally distributed front ( $x > 0$ , subscript  $f$ ) and rear ( $x < 0$ , subscript  $r$ ) halves of the source:

$$q_{3i}(x, y, z) = \frac{4q_i}{\pi^{3/2} x_{ei} \Phi(x_{cf}/x_{ef}) y_{ei} \Phi(y_{ci}/y_{ei}) z_{ei} \Phi(z_{ci}/z_{ei})} \times \exp \left( - \left( \frac{x}{x_{ei}} \right)^2 - \left( \frac{y}{y_{ei}} \right)^2 - \left( \frac{z}{z_{ei}} \right)^2 \right), \quad i = f, r, \quad (3)$$

where  $q_i$  is the power of the  $i$ -th source;  $x_{ci}$ ,  $y_{ci}$  and  $z_{ci}$  are the coordinates of source boundary;  $x_{ei}$ ,  $y_{ei}$  and  $z_{ei}$  are the power distribution parameters (the coordinates of the points on the axes where the density is  $e$  times smaller than in the centre);  $\Phi$  is the error integral. If function  $q_3(x, y, z)$  is continuous (that is,  $q_{3f}(0, 0, 0) = q_{3r}(0, 0, 0)$ ,  $y_{cf} = y_{cr} = y_c$ ,  $y_{ef} = y_{er} = y_e$ ,  $z_{cf} = z_{cr} = z_c$ ,  $z_{ef} = z_{er} = z_e$ ) (Figure 2), then

$$q_{3i}(x, y, z) = \frac{4q}{\pi^{3/2} [x_{ef} \Phi(x_{cf}/x_{ef}) x_{er} \Phi(x_{cr}/x_{er})] y_e \Phi(y_c/y_e) z_e \Phi(z_c/z_e)} \times \exp \left( - \left( \frac{x}{x_{ei}} \right)^2 - \left( \frac{y}{y_{ei}} \right)^2 - \left( \frac{z}{z_{ei}} \right)^2 \right), \quad i = f, r, \quad (4)$$

where  $q = q_f + q_r$  is the total apparent power.

Note that the convection and the latent heat do not violate the balance of energy [12]:

$$q = q_{net} = \eta q_{gross},$$

where  $q_{net}$  is the net power of the real heat source;  $\eta$  is the heat efficiency; that is, the fraction of the total power  $q_{gross}$  absorbed by the solid.

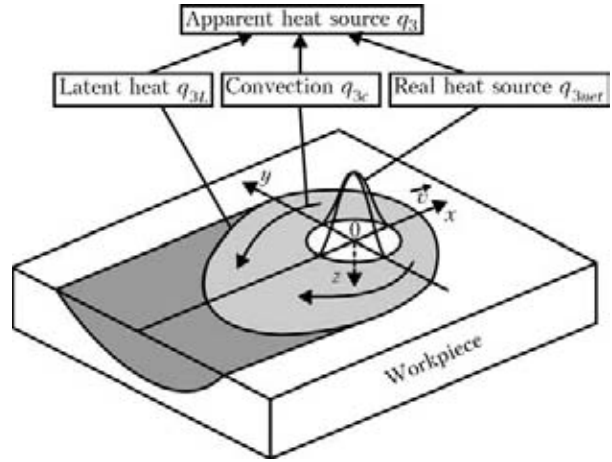


Figure 1. Schematic diagram for moving reference frame and apparent heat source

On physical grounds, the apparent heat source can be represented by several sources, for example, by surface and submerged sources. The power density of a surface source  $q_{2i}(x, y)$ ,  $W \cdot m^{-2}$ , results from integration of  $q_3(x, y, z)$  over the plate thickness:

$$q_{2i}(x, y) = \frac{2q}{\pi [x_{ef} \Phi(x_{cf}/x_{ef}) + x_{er} \Phi(x_{cr}/x_{er})] y_e \Phi(y_c/y_e)} \times \exp \left( - \left( \frac{x}{x_{ei}} \right)^2 - \left( \frac{y}{y_{ei}} \right)^2 \right), \quad i = f, r.$$

#### Solution of direct heat conduction problem.

Under the assumptions made above the equations (1), (3) and (4) can be solved using the Green's function method [6]. The temperature increment at any point  $x, y, z$  at any moment  $t$  is the sum of the temperature increments due to the front and rear sources:

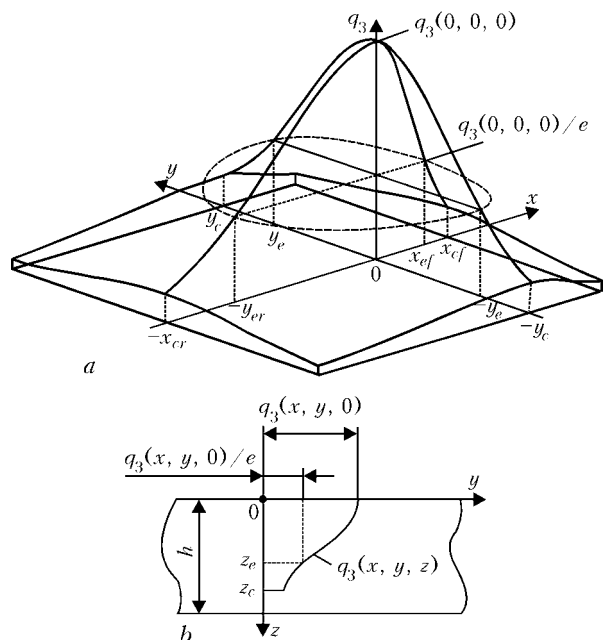


Figure 2. Volumetric power density distribution of apparent heat source in the plane (a) and through the thick plate thickness (b)

$$T(x, y, z, t) - T_\infty = \sum_{i=f,r} \frac{q_i}{c\rho h^3} \int_0^t f_{xi}(x, \tau) f_{yi}(y, \tau) f_{zi}(z, \tau) d\tau, \quad (5)$$

where

$$f_{xi}(x, \tau) = \frac{h}{\Phi(x_{ci}/x_{ei})\sqrt{\pi(4a\tau + x_{ei}^2)}} \exp\left(-\frac{(x + v\tau)^2}{4a\tau + x_{ei}^2}\right) \times$$

$$\times \left[ \Phi\left(\frac{-k(x + v\tau)x_{ei}}{\sqrt{4a\tau(4a\tau + x_{ei}^2)}} + \frac{x_{ci}}{x_{ei}}\sqrt{1 + \frac{x_{ei}^2}{4a\tau}}\right) + \Phi\left(\frac{k(x + v\tau)x_{ei}}{\sqrt{4a\tau(4a\tau + x_{ei}^2)}}\right); \right.$$

$$f_{yi}(y, \tau) = \frac{h}{2\Phi(y_{ci}/y_{ei})\sqrt{\pi(4a\tau + y_{ei}^2)}} \exp\left(-\frac{y^2}{4a\tau + y_{ei}^2}\right) \sum_{j=-1,1} \Phi\left(j \frac{y y_{ei}}{\sqrt{4a\tau(4a\tau + y_{ei}^2)}} + \frac{y_{ci}}{y_{ei}}\sqrt{1 + \frac{y_{ei}^2}{4a\tau}}\right);$$

$$f_{zi}(z, \tau) = \frac{h}{\Phi(z_{ci}/z_{ei})\sqrt{\pi(4a\tau + z_{ei}^2)}} \sum_{n=-\infty}^{\infty} \exp\left(-\frac{(z - 2nh)^2}{4a\tau + z_{ei}^2}\right) \sum_{j=-1,1} \Phi\left(\frac{z_{ci}}{z_{ei}}\sqrt{1 + \frac{z_{ei}^2}{4a\tau}} + j \frac{(z - 2nh)z_{ei}}{\sqrt{4a\tau(4a\tau + z_{ei}^2)}}\right).$$

Here  $k = 1$ , if  $i = f$ ;  $k = -1$ , if  $i = r$ ;  $h$  is the plate thickness.

If function  $q_3(x, y, z)$  is continuous (see Figure 2), then

$$T(x, y, z, t) - T_\infty = \frac{q_i}{c\rho h^3} \times \int_0^t f_x(x, \tau) f_y(y, \tau) f_z(z, \tau) d\tau, \quad (6)$$

where

$$f_x(x, \tau) = \frac{x_{ef}\Phi(x_{cf}/x_{ef})f_{xf}(x, \tau) + x_{er}\Phi(x_{cr}/x_{er})f_{xr}(x, \tau)}{x_{ef}\Phi(x_{cf}/x_{ef}) + x_{er}\Phi(x_{cr}/x_{er})};$$

$$f_y(y, \tau) = f_{yf}(y, \tau) = f_{yr}(y, \tau);$$

$$f_z(z, \tau) = f_{zf}(z, \tau) = f_{zr}(z, \tau).$$

If power  $q$  varies with time, it should be taken inside the integral sign. The integrals are expressed as the known functions in very rare cases, therefore they are calculated by numerical methods. It is evident from the equations that the temperature field depends on the plate thickness ( $h$ ), material properties ( $c\rho$  and  $a$ ), source power ( $q_i$ ), its distribution ( $x_{ei}$ ,  $y_{ei}$ ,  $z_{ei}$ ), boundedness ( $x_{ci}$ ,  $y_{ci}$ ,  $z_{ci}$ ), velocity ( $v$ ) and time of action ( $t$ ). When  $t \rightarrow \infty$  the field is quasi-stationary. If the source is unbounded along  $x$ ,  $y$  or  $z$  ( $x_{ci}$ ,  $y_{ci}$  or  $z_{ci}$  equal infinity) then the form of corresponding equations  $f_{xi}$ ,  $f_{yi}$  or  $f_{zi}$  is simplified. If necessary, the distribution of apparent power over the thickness  $q_{3i}(z)$  can be represented by several curves with different values of  $z_{ci}$  and  $z_{ei}$ , that is, it can be represented with desired accuracy by a continuous piecewise normal function. The influence of finite width and finite length of the solid with its heat-impermeable edges can be easily taken into consideration by using the method of images [6]. The effect of the latent heat can be more accurately considered separately [13].

#### Solution of inverse heat conduction problem.

Each  $i$ -th source is described by 7 parameters (vector  $\mathbf{p} = \{\eta_i, x_{ei}, x_{ci}, y_{ei}, y_{ci}, z_{ei}, z_{ci}\}$ , totally 14 parameters),

in the case of a continuous source it is described by 9 parameters (vector  $\mathbf{p} = \{\eta, x_{ef}, x_{cf}, x_{er}, x_{cr}, y_e, y_c, z_e, z_c\}$ ). The unknown parameters, that is a vector of design variables, are determined from the best fit to the experimental data. The corresponding optimisation problem (minimisation of the objective function  $F$ ) with the set of inequality constraints of physical nature is presented in the following form [12, 13]:

$$F(\mathbf{p}) = \sum_{n=1}^N \omega_n^f [f_n^m - f_n(\mathbf{p})]^2 + \sum_{k=1}^K \omega_k^p (p_k^0 - p_k)^2 \rightarrow \min,$$

$$\sum_{i=f,r} \eta_i \leq 1; \quad 0 \leq x_{ei} \leq x_{ei \max} \text{ etc.},$$

where  $N$  is the number of observations;  $K$  is the number of unknown parameters;  $f_n$  and  $f_n^m$  are the respective calculated and measured (prescribed) values of temperature field characteristic at point  $n$  (weld pool length, temperature, peak temperature, etc.);  $p_k$  is the  $k$ -th unknown parameter;  $p_k^0$  is the  $k$ -th parameter known from prior information;  $\omega_n^f$  and  $\omega_k^p$  are the weighting factors for the  $n$ -th measurement and parameter  $p_k$ , respectively (they are prescribed depending on dimensions and measurement error);  $x_{ei \max}$  is the peak allowable value of parameter  $x_{ei}$ . The constraints have a physical meaning (for example, the heat source efficiency can not be more than 1, the depth of the source can not exceed the depth of the weld).

The objective function  $F$  is a non-linear function of the parameter vector  $\mathbf{p}$  and may have many local minima in the feasible design space. Therefore, at first the global minimum region of the objective function has to be found by comparison of its values at the prescribed finite set of feasible points. Then the global minimum (true optimum) can be found using numerical optimisation [13, 14].

It is worth noting that many dozens of 3D direct problems have to be solved in order to solve one inverse problem. Therefore the CPU time for a direct problem is of the utmost importance. The time needed

to obtain the results by a functional-analytical method is less by many orders of magnitude than that by a numerical method.

**Prediction of microstructure and mechanical properties.** All parameters of the apparent heat source result from the solution of inverse problem. Formulae (5) and (6) make it possible to calculate the temperature field and its characteristics, for instance, the peak temperature  $T_{max}$  and cooling time  $t_{850/500}$  from 1123 K (850 °C) to 773 K (500 °C).

The welding time-temperature transformation diagrams allows the phase composition to be found at any point of HAZ when cooled [3]. The cooling stage can be identified by one index, for example, by cooling time  $t_{850/500}$ . Figure 3 shows the mechanical properties of 12CrMo4.3 heat-resistant steel versus cooling time  $t_{850/500}$ . The diagram has been obtained from the corresponding  $T-t$  plot [3].

*Example.* The TIG welding of 12Kh1MF heat-resistant steel 7 mm thick is performed under the following conditions: current 250 A, voltage 12 V, speed  $v = 5 \text{ mm/s}$ , temperature  $T_{\infty} = 288 \text{ K}$ . The chemical composition of 12Kh1MF steel (%: 0.11–0.15C, 0.9–1.2Cr, 0.25–0.35Mo, 0.15–0.3V) [15] is similar to that of 12CrMo4.3 steel (%: 0.11C, 1.02Cr, 0.29Mo, 0.19V) [3]. The following properties are taken:  $a = 9.40 \text{ mm}^2/\text{s}$ ,  $cp = 0.0035 \text{ J}/(\text{mm}^3 \cdot \text{K})$ , melting temperature  $T_{melt} = 1773 \text{ K}$ ,  $A_{c_3} = 1173 \text{ K}$  [15]. As the input data, the coordinates of HAZ boundaries, where  $T_{max} = T_{melt}$  and  $T_{max} = A_{c_3}$  (Figure 4, left side), and tail part of the weld pool (ripples, Figure 5), where  $T = T_m$  are taken.

Comparison of the calculated and experimental weld pools shows good agreement (see Figures 4 and 5, solid line). The following heat source parameters are obtained:

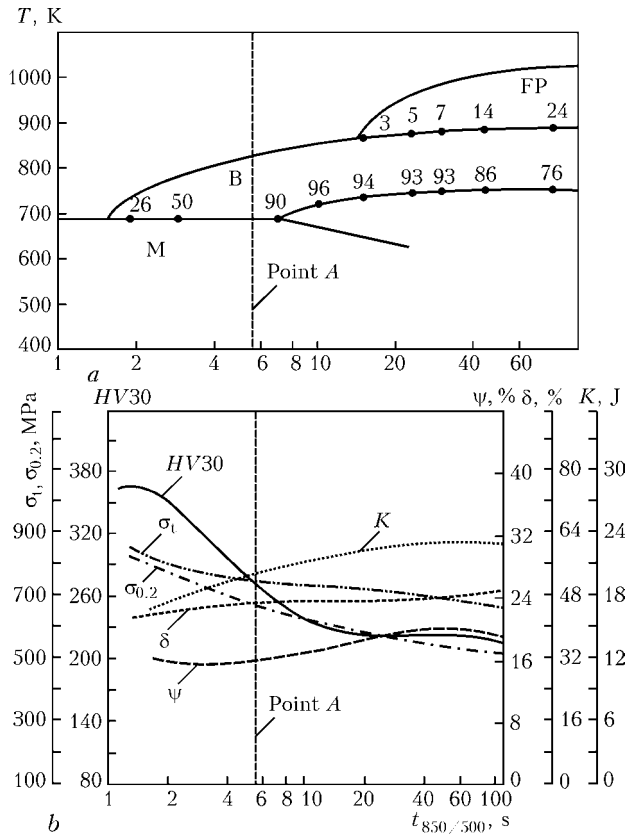


**Figure 3.** Welding cooling time-temperature transformation diagram (a) and 12CrMo4.3 welded steel properties (b) at peak temperature of 1623 K [3] (point A is shown in Figure 4)

- $\eta = 0.37$ ,  $x_{ef} = x_{er} = y_e = 4 \text{ mm}$  for a surface source (mainly imitating the arc);
- $\eta = 0.23$ ,  $x_{ef} = x_{er} = y_e = 4 \text{ mm}$ ,  $x_{cf} = x_{cr} = y_c = 1 \text{ mm}$ ,  $z_c = 4 \text{ mm}$ ,  $z_c = 3.5 \text{ mm}$  (mainly imitating the convection);
- $\eta = 0.30$ ,  $x_{er} = 100 \text{ mm}$ ,  $x_{cr} = 9 \text{ mm}$ ,  $y_e = 4 \text{ mm}$ ,  $y_c = 0.8 \text{ mm}$ ,  $z_e = 100 \text{ mm}$ ,  $z_c = 0.7 \text{ mm}$  (imitating

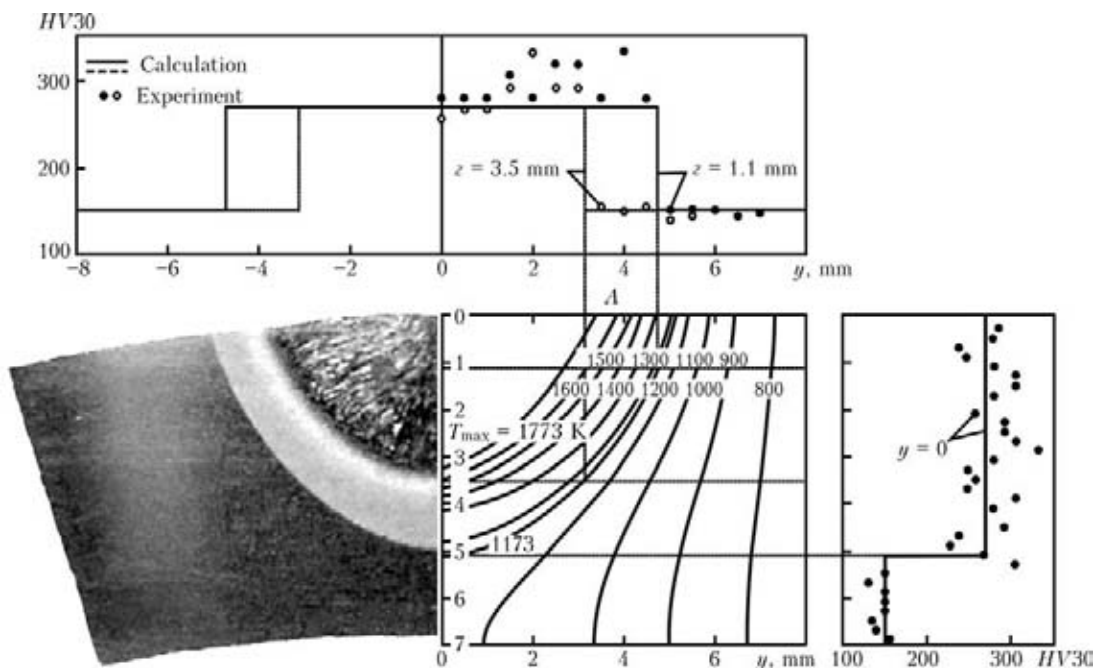


**Figure 4.** Peak temperature field and hardness distribution in TIG-welded 12CrMo4.3 steel cross-section at  $I_w = 250 \text{ A}$ ,  $U_a = 12 \text{ V}$  and  $v = 5 \text{ mm/s}$

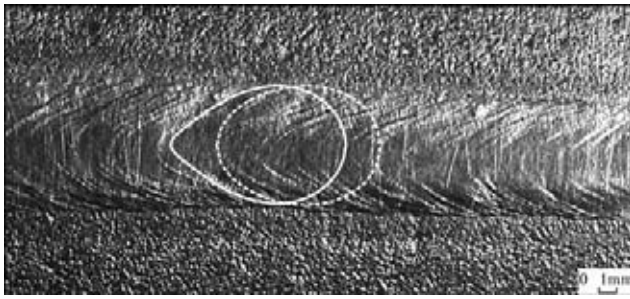


**Figure 5.** 12CrMo4.3 steel welded joint and calculated geometry of molten pool in TIG welding

the convection and latent heat), total heat source efficiency  $\eta = 0.90$ .

The metal heated above  $A_{c3}$  is cooled down at 1123–773 K (850–500 °C) during 5.6 s (Figure 6). It corresponds to residual microstructure consisting of 76 % of bainite and 24 % of martensite and to the following mechanical properties: hardness  $HV_{30-270}$ ,  $\sigma_{0.2} = 670$  MPa,  $\sigma_t = 750$  MPa,  $\psi = 16$  %,  $\delta = 46.7$  % and impact toughness  $K = 20.3$  J (see Figure 3, *b*). The mechanical properties of the base metal are as follows:  $HV_{30-150}$ ,  $\sigma_{0.2} = 450$  MPa,  $\sigma_t = 580$  MPa,  $\psi = 6$  %,  $\delta = 38$  %,  $K = 32$  J [3]. The experimental hardness distributions agree with the calculated ones (see Figure 4). The measured hardness of weld and HAZ metal is an average of  $HV_{30-287}$ , the calculated hardness is  $HV_{30-270}$ .

Note that one surface circular source with normal distribution of heat source density  $q_2$  does not allow reproduce satisfactorily the experimental size of pool and weld (the calculated weld pool is shown by a broken white line in Figure 5).

If the rapidly moving point source on the semi-infinite solid [6] is taken, then the cooling time is

$$t_{850/500} = \frac{1}{2\pi a} \frac{q/v}{c\rho} \left( \frac{1}{773 - T_\infty} - \frac{1}{1123 - T_\infty} \right).$$

For the current example  $t_{850/500} = 1.3$ – $1.8$  s at  $\eta = 0.5$ – $0.6$  [3], and hardness is  $HV_{30-370}$ – $360$  which is a very overestimated value.

If the rapidly moving line source in the infinite plate [6] is taken, then the cooling time is

$$t_{850/500} = \frac{1}{4\pi a} \left[ \frac{q/(vs)}{c\rho} \right]^2 \left[ \frac{1}{(773 - T_\infty)^2} - \frac{1}{(1123 - T_\infty)^2} \right].$$

For the current example  $t_{850/500} = 3.7$ – $5.3$  s and hardness is  $HV_{30-300}$ – $270$ .

## CONCLUSIONS

1. The proposed technique based on function-analytical solution of the 3D direct heat conduction problem and on numerical solution of the inverse problem makes it possible to reconstruct the temperature field in the solid part of weldment using some measured characteristics of this field.

2. The bounded heat source with normal distribution of volumetric heat density can be used for calculation of the temperature field during TIG welding.

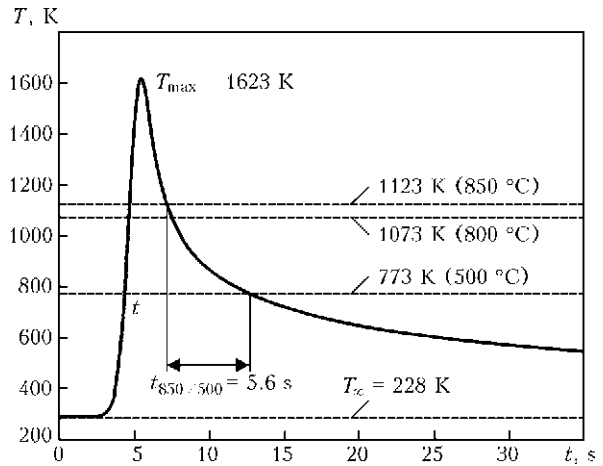


**Figure 6.** Temperature cycles at points A (see Figure 4)

3. The proposed technique allows the distribution of microstructural phases and mechanical properties to be predicted taking the real weld geometry into consideration.

4. Comparison of the calculated and measured hardness distributions in heat-resistant steel weld shows good agreement.

- Kasatkin, O.G., Mikhoduj, L.I. (1992) Choice of alloying system in welding of high-strength low-alloy steels. *Avtomatich. Svarka*, **5**, p. 19–25.
- Buchmayr, B. (1991) *Computer in der Werkstoff- und Schweisstechnik: Anwendung von mathematischen Modellen*. Duesseldorf: DVS.
- Seyffarth, P., Meyer, B., Scharff, A. (1992) *Grosser Atlas Schweiss-ZTU-Schaubilder*. Duesseldorf: DVS.
- Stadtaus, M., Michailov, V., Wohlfahrt, H. (2002) Simulation of weld shape, microstructure, distortion and residual stresses for laser beam welding. In: *Mathematical modelling of weld phenomena 6*. Ed. by H. Cerjak. London: Maney Publ.
- Rosenthal, D. (1941) Mathematical theory of heat distribution during welding and cutting. *Welding J.*, **20**(5), p. 220–234.
- Rykalin, N.N. (1951) *Calculation of heat flow in welding*. Moscow: Mashgiz.
- Kumar, A., Zhang, W., Kim, C.-H. et al. (2005) A smart bi-directional model of heat transfer and free surface flow in gas metal arc fillet welding for practicing engineers. In: *Mathematical modelling of weld phenomena 7*. Ed. by H. Cerjak, H.K.D.H. Bhadeshia, E. Kozeschnik. Graz: Graz University of Technology.
- Radaj, D. (2002) *Welding residual stresses and distortion. Calculation and measurement*. Duesseldorf: DVS.
- Pavelic, V., Tanbakuchi, R., Ueyhara, O.A. et al. (1969) Experimental and computed temperature histories in gas tungsten-arc welding of thin plates. *Welding J.*, **48**(7), p. 295–305.
- Makhnenko, V.I., Petun, L.A., Prilutsky, V.P. et al. (1964) Estimation of thermal processes near moving weld pool. *Avtomatich. Svarka*, **11**, p. 1–6.
- Goldak, J., Chakravarti, A., Bibby, M. (1984) A new finite element model for welding heat sources. *Metallurg. Transact. B*, **15**, p. 229–305.
- Karkhin, V.A., Plochikhine, V.V., Ilyin, A.S. et al. (2002) Inverse modelling of fusion welding processes. In: *Mathematical modelling of weld phenomena 6*. Ed. by H. Cerjak. London: Maney Publ.
- Karkhin, V.A., Pesch, H.J., Ilyin, A.S. et al. (2005) Effect of latent heat of fusion on thermal processes during welding. In: *Mathematical modelling of weld phenomena 7*. Ed. by H. Cerjak, H.K.D.H. Bhadeshia, E. Kozeschnik. Graz: Graz University of Technology.
- Vanderplaats, G.N. (1984) *Numerical optimization techniques for engineering design*. New York: McGraw-Hill Publ.
- (1989) *Steels and alloys: Handbook*. Ed. by V.G. Sorokin. Moscow: Mashinostroenie.

# COMPUTER-AIDED EXPRESS DETERMINATION OF DIFFUSIBLE HYDROGEN IN DEPOSITED WELD METAL

V.A. KARKHIN<sup>1</sup>, A.M. LEVCHENKO<sup>1</sup>, P.N. KHOMICH<sup>1</sup> and V.G. MICHAÏLOV<sup>2</sup>

<sup>1</sup>St.-Petersburg State Polytechnic University, Russia

<sup>2</sup>Cottbus University of Technology, Germany

A calculation method to reduce the time of determination of diffusible hydrogen in deposited weld metal is proposed. It uses measurements at the beginning of the hydrogen effusion. The functional-analytical solution of direct 3D hydrogen diffusion problem for a parallelepiped-shaped solid is found. The inverse problem for unknown initial concentration of hydrogen introduced through a deposited metal is stated and solved numerically. It is demonstrated that as much as a quarter of total diffusible hydrogen can effuse prior to its measurement according to the standard procedure. The proposed method allows the time of determination of diffusible hydrogen to be reduced by several factors.

Hydrogen is a major factor in cold cracking problem. The principal sources of hydrogen in welding are moisture contained in and picked up by electrode coatings and fluxes, other hydrogenous materials which may break down in the heat of the arc, oil, dirt and grease in the plate surface or trapped in the surface layers of welding wires, and atmospheric moisture during welding [1].

The most commonly used methods of determination of the hydrogen content in the weld metal are the following:

- diffusible hydrogen evolves from the test piece and collects in the capillary tube over the liquid (spirit, glycerin, oil, mercury and so on) [2];
- diffusible hydrogen collects in the preliminarily evacuated space of a known volume and its content is determined by measuring the pressure (as in the vacuum method) or by analysis the gas composition (as in the chromatographic method) [3].

A practical disadvantage of the first method (when spirit, glycerin or oil are used) is the underestimation and the wide scatter of experimental data as a result of high hydrogen solubility in the liquid and the sensitivity of the method to physical properties of the liquid. The evolution takes place at room temperature and consequently the collection time is typically about 14 days [2]. The mercury method gives a reliable result, but mercury is a hazardous substance.

The vacuum method was developed at the St.-Petersburg Polytechnic University, Russia [4], and was used as the basis for the standard [3]. It is rather simple and reliable in operation. The experimental results obtained by vacuum and mercury methods are in good agreement [4]. The chief drawback of the method is the hydrogen collection time (5 days) [3].

A common disadvantage of all methods is omission of the hydrogen evolved before measurement. This part of hydrogen is not fixed, it depends on the welding conditions, materials and postweld preparation

of the sample. The estimation of this part is of practical interest. For instance, when solving a boundary-value problem of hydrogen diffusion in a real weldment the amount of hydrogen introduced in a weld pool is to be given. For this reason the following question arises in the welding practice: can the total volume of diffusible hydrogen be predicted on the basis of the initial part of the hydrogen effusion curve? A positive answer would allow reducing the test time and evaluating the total hydrogen introduced in the weld.

The aim of the study is to develop a calculation technique of determining the hydrogen content in the deposited metal using short-term experiment. The technique is based on solving the inverse problem which, in turn, uses the solution of the direct hydrogen effusion problem.

**Solution of direct diffusion problem.** The proposed technique is based on the functional analysis solution of mass transfer problem for the solid with the weld bead (centre test piece) (Figure 1, *a*).

The following assumptions are made:

- solid is homogeneous and parallelepiped-shaped,  $L$  long,  $W$  wide and  $H$  thick (Figure 1, *c*);
- weld cross-section is known (it is measured on the ends of the test piece). For example, if the weld surface is described by parabola  $S$  in length and the weld interface is described by sinusoid, then the weld is specified by three parameters: width  $w$ , height of the deposited metal (weld reinforcement)  $h_{\text{rein}}$  and depth of the fused metal (penetration)  $h_{\text{pen}}$  (Figure 1, *b*);
- in calculation the weld is positioned along the specimen centreline and has a plane surface, its surface area is equal to that of the real weld (Figure 1, *c*);
- weld cross-section is presented to sufficient accuracy as a set of  $M$  rectangles (Figure 1, *c*);
- weld is divided into  $K$  short intervals of length  $l'_k - l''_k$ ,  $1 \leq k \leq K$  (Figure 1, *c*). The interval length can be associated with the droplet transfer frequency.

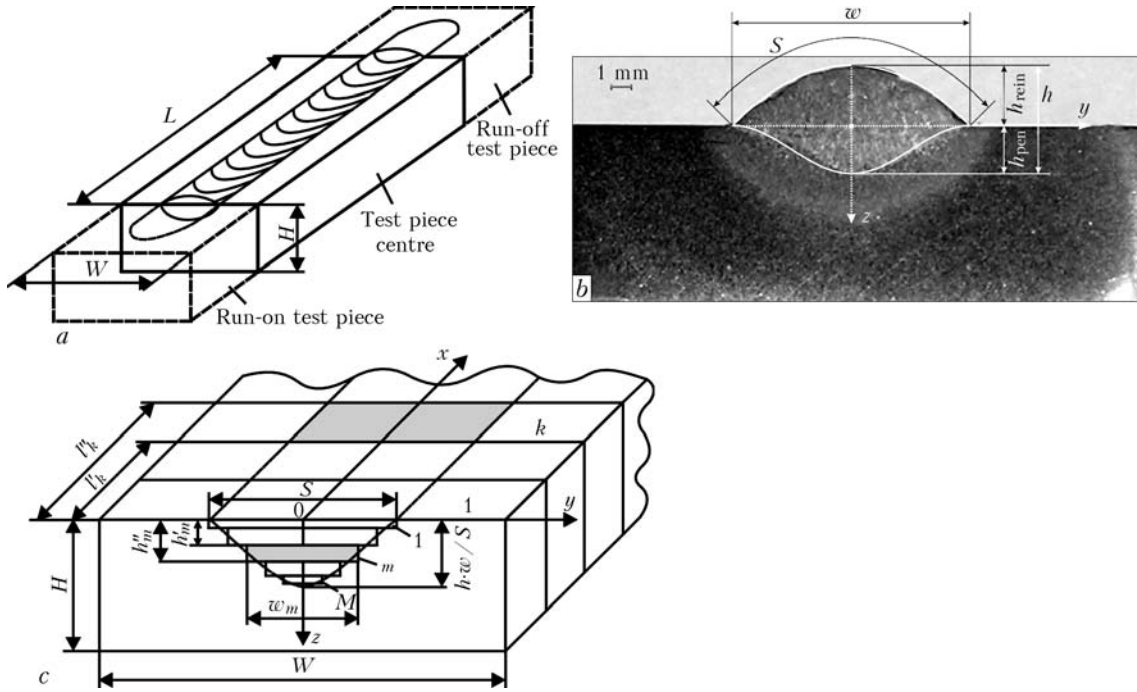


**Figure 1.** Weld test assembly (a), macrosection of weld (b) and representation of weld as longitudinal and transverse layers (c) (for designations see the text)

The instant of completion of the  $k$ -th interval  $t_k$  is determined by its location at the  $x$ -axis;

- hydrogen is introduced in the solid by means of the liquid metal and distributed immediately over the weld cross-section  $A_w$ . As this takes place, the hydrogen concentration in the cross section increases by  $C_0$ ;
- hydrogen content  $Q_{int}$  increases linearly at steady welding conditions (Figure 2);
- prior to welding the hydrogen concentration  $C$  equals zero;
- hydrogen concentration at the solid surfaces is equal to zero (according to Sieverts' law at low solubility of hydrogen in the solid and low partial pressure of the hydrogen in the gaseous environment);
- hydrogen diffusivity coefficient for a hot specimen (before force-cooling)  $D_h$  and for a cold specimen (after force-cooling)  $D$  are constant, that is, they are averaged (apparent) ones.

In parallel with the real time scale  $\Delta t$  (where the initial fixed point of hydrogen effusion is taken as

zero) the equivalent time scale  $t$  is introduced (where the start of welding of the centre test piece is taken as zero) (see Figure 2). The equivalent time allows switching from diffusion at different temperature to diffusion at constant (room) temperature. Under the assumptions made the relation between the equivalent time  $t$  and the real time  $\Delta t$  takes the form:

$$t = \begin{cases} (\Delta t_h + \Delta t_p + \Delta t)D_h/D, & \text{if } \Delta t < -\Delta t_p, \\ \Delta t_h D_h/D + \Delta t_p + \Delta t, & \text{if } \Delta t \geq -\Delta t_p; \end{cases}$$

$$t_0 = t_h + t_p; \quad t_h = \Delta t_h D_h/D; \quad t_p = \Delta t_p; \quad t_w = \Delta t_w D_h/D,$$

where  $\Delta t_w$ ,  $\Delta t_h$  and  $\Delta t_p$  are the real times of welding of test piece, the duration in a hot state (before cooling) and the preparation time of cold specimen for hydrogen measurement (after cooling), respectively. The diffusivity is  $D_h$  during real time  $\Delta t_h$  and is  $D$  through the rest of the time (see Figure 2).

Under the stated assumptions the formulation of the direct problem is as follows.

*Diffusion equation:*

$$\frac{\partial C}{\partial t} = D \left( \frac{\partial^2 C}{\partial x^2} + \frac{\partial^2 C}{\partial y^2} + \frac{\partial^2 C}{\partial z^2} \right) + f(x, y, z, t),$$

where term  $f$  accounts for the hydrogen input through the weld pool.

*The initial conditions (at  $t = 0$ ):*

$$C(x, y, z, 0) = 0.$$

*The boundary conditions:*

$$C(0, y, z, t) = C(L, y, z, t) = C(x, -W/2, z, t) = C(x, W/2, z, t) = C(x, y, 0, t) = C(x, y, H, t) = 0.$$

The direct problem is solved by using the Green's function method:

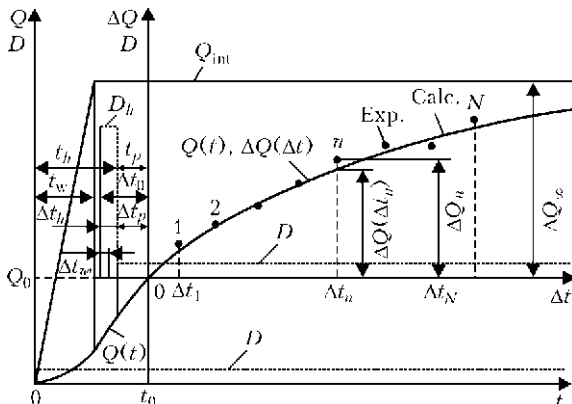


**Figure 2.** Schematic diagram for hydrogen evolved from the test piece (for designations see the text)



$$\begin{aligned}
C(x, y, z, t) = & \frac{C_0}{8} \sum_{k=1}^K \sum_{i=-\infty}^{\infty} \sum_{r=-1, 1} \times \\
& \times r \sum_{s=-1, 1} S\Phi \left( \frac{x - E_{kirs}}{\sqrt{4D(t-t_k)}} \right) \times \\
& \times \sum_{m=1}^M \sum_{i=-\infty}^{\infty} (-1)^{|i|} \sum_{r=-1, 1} r \Phi \left( \frac{y - G_{mir}}{\sqrt{4D(t-t_k)}} \right) \times \\
& \times \sum_{i=-\infty}^{\infty} \sum_{r=-1, 1} r \sum_{s=-1, 1} S\Phi \left( \frac{z - P_{mirs}}{\sqrt{4D(t-t_k)}} \right); \\
E_{kirs} = & 2iL - (r+1)(l'_k + l''_k)/2 - \\
& - (S+1)(l'_k - l''_k)/2 + l'_k; \\
G_{mir} = & iW - r\omega_m/2; \\
P_{mirs} = & 2iH - (r+1)(h'_m + h''_m)/2 - (S+1) \times \\
& \times (h'_m - h''_m)/2 + h'_m,
\end{aligned}$$

where  $\Phi$  is the error integral;  $l'_k, l''_k, \omega_m, h'_m, h''_m$  are the geometric parameters of the weld layers (see Figure 1, c);  $t_k < t$  is the time of completion of the  $k$ -th weld interval.

Using the above formula the rate of flow of hydrogen per unit time (effusion rate) across any specimen surface at any moment  $t$  can be derived:

$$\begin{aligned}
q_x(x, t) = & -2 \int_0^{W/2} \int_0^H D \frac{\partial C(x, y, z, t)}{\partial x} dy dz; \\
q_y(y, t) = & - \int_0^L \int_0^{W/2} D \frac{\partial C(x, y, z, t)}{\partial y} dx dz; \\
q_z(z, t) = & -2 \int_0^L \int_0^{W/2} D \frac{\partial C(x, y, z, t)}{\partial z} dx dy.
\end{aligned}$$

The volume of hydrogen evolved from all specimen surfaces over time  $t$  is the difference of the introduced hydrogen  $Q_{\text{int}}$  and the hydrogen presented in the specimen:

$$\begin{aligned}
Q(t) = Q_{\text{int}}(t) - & 2 \int_0^L \int_0^{W/2} \int_0^H C(x, y, z, t) x dy dz = \\
Q_{\text{int}}(t) = & \frac{C_0}{4} \sum_{k=1}^K \sum_{i=-\infty}^{\infty} \sum_{r=-1, 1} r \sum_{s=-1, 1} \times \\
& \times S \int_0^L \Phi \left( \frac{x - E_{kirs}}{\sqrt{4D(t-t_k)}} \right) dx \times \\
& \times \sum_{m=1}^M \sum_{i=-\infty}^{\infty} (-1)^{|i|} \sum_{r=-1, 1} r \int_0^{W/2} \Phi \left( \frac{y - G_{mir}}{\sqrt{4D(t-t_k)}} \right) dy \times \\
& \times \sum_{i=-\infty}^{\infty} \sum_{r=-1, 1} r \sum_{s=-1, 1} S \int_0^H \Phi \left( \frac{z - P_{mirs}}{\sqrt{4D(t-t_k)}} \right) dz; \\
Q_{\text{int}}(t) = & \begin{cases} C_0 A_w v t D / D_h & \text{if } t < t_w, \\ C_0 A_w L & \text{if } t \geq t_w. \end{cases}
\end{aligned} \quad (1)$$

All above integrals and derivatives are expressed by the known functions:

$$\begin{aligned}
\int_0^A \Phi \left( \frac{U-B}{\sqrt{4D(t-t_k)}} \right) dU = & (A-B) \Phi \left( \frac{A-B}{\sqrt{4D(t-t_k)}} \right) - \\
& - B \Phi \left( \frac{B}{\sqrt{4D(t-t_k)}} \right) + \sqrt{\frac{4D(t-t_k)}{\pi}} \times \\
& \times \left[ \exp \left( -\frac{(A-B)^2}{4D(t-t_k)} \right) - \exp \left( -\frac{B^2}{4D(t-t_k)} \right) \right]; \\
\frac{\partial}{\partial U} \Phi \left( \frac{U-B}{\sqrt{4D(t-t_k)}} \right) = & \frac{1}{\sqrt{\pi D(t-t_k)}} \exp \left( -\frac{(U-B)^2}{4D(t-t_k)} \right).
\end{aligned}$$

The volume of hydrogen evolved from any specimen surface can be found by integration of corresponding flux:

$$Q_i(t) = \int_0^t q_i(t) dt, \quad i = x, y, z.$$

The total volume of effused hydrogen is

$$\begin{aligned}
Q(t) = \int_0^t [ & -q_x(0, t) + q_x(L, t) + 2q_y(W/2, t) - \\
& - q_z(0, t) + q_z(H, t) ] dt.
\end{aligned}$$

This expression is identical to formula (1) and it can be used for additional check upon accuracy of the solutions.

Hence the above formulae allow one to calculate the distribution of hydrogen concentration in the specimen, hydrogen flux across each surface and the volume of effused hydrogen at any moment. All series are fast converging.

It is worth noting that a consideration of complex specimen geometry (reinforcement), micro- and macrotraps and hydrides, non-uniformity of the distributions of temperature, hydrogen solubility and diffusivity across the solid makes the problem formulation more complicated. Then the problem can be solved only by numerical methods [5-8]. In this case to find the required input data is a real challenge.

**Method of calculating the hydrogen concentration in the deposited metal (solution of inverse problem).** It was supposed in the direct problem that initial concentration  $C_0$  and diffusivity coefficients  $D$  and  $D_h$  are known. Actually the concentration  $C_0$  is sought. The hydrogen diffusivity depends to a large extent on the chemical composition, the steel microstructure and varies over a wide range (three orders of magnitude). Therefore the diffusivity is practically unknown. Let us find  $C_0, D$  and  $D_h$  by using experimental data solving the following inverse problem.

Let the volume of effused hydrogen  $\Delta Q_n$  at some time  $\Delta t_n$  ( $n = 1, \dots, N$ ) be known (see Figure 2). Let us find such values of  $C_0, D$  and  $D_h$  which correspond to the best position of a calculated curve  $Q(t)$  with respect to the experimental points. In other words, let us solve the following optimisation problem with the set of inequality constraints of physical nature:

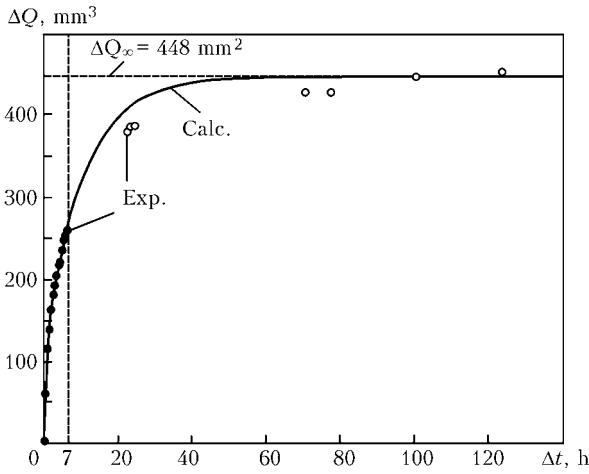


Figure 3. Volume of hydrogen evolved from the test piece

$$F(C_0, D, D_h) = \sum_{n=1}^N w_n [\Delta Q_n - \Delta Q(C_0, D, D_h, \Delta t_n)]^2 \rightarrow \min;$$

$$C_0 > 0; \quad D > 0; \quad D_h > 0; \quad D_h > D.$$

Here  $w_n$  is the weighting factor of the  $n$ -th measurement (it is the greater, the smaller is the measurement error). If the measurement error is the same, then  $w_n = 1$ .

The minimum of the objective function  $F$ , depending on the design variables  $C_0$ ,  $D$  and  $D_h$ , can be found by using one of the optimisation methods [9]. The corresponding values of  $C_0$ ,  $D$  and  $D_h$  determine the sought values  $Q_{\text{int}}$ ,  $\Delta Q_{\infty}$  and  $Q_0$  (see Figure 2).

Note that functions  $Q(C_0)$  and  $\Delta Q(C_0)$  are linear, therefore the optimum value of  $C_0(D, D_h)$  for any pair of  $D$  and  $D_h$  can be explicitly deduced from the condition for minimum,  $\partial F(C_0, D, D_h) / \partial C_0 = 0$ . The values of  $D$  and  $D_h$  are simply found by the search methods. Such approach considerably reduces the time of solving the inverse problem.

The solution of the inverse problem can be based not only on presented functional-analytical solution, but also on a numerical method of solution of the direct 3D problem. However in the latter case the total solution time increases by many orders of magnitude. This fact is of practical importance because all algorithms of nonlinear problem solution usually come to successive solution of many dozens of direct problem (number of direct problems depends on number of the parameters sought, method of inverse problem solution and first approximation which, in turn, is taken as the result of analysis of objective function behaviour in the feasible design space).

**Example.** According to the standard [3] a single weld bead is deposited on the centre test piece ( $L \times W \times H = 100 \times 25 \times 8$  mm) prepared from a plain carbon non-rimming St3sp steel (0.15 % C, 0.02 % S). The welding conditions are the following: 150 A current, 24 V voltage, 2.5  $\text{mms}^{-1}$  welding speed, 4 mm diameter UONI 13/45 basic coated electrode, welding time  $\Delta t_w = 40$  s, hot state time  $\Delta t_h = 50$  s, rapid quenching in stirred iced water, preparation time  $\Delta t_p = 250$  s at room (ambient) temperature of 20 °C,

10–12  $\text{gm}^{-3}$  humidity. It is assumed that the reinforcement is a parabola and the weld interface is a sinusoid.

The weld dimensions are as follows (see Figure 1, b): reinforcement  $h_{\text{rein}} = 2.5$  mm, penetration  $h_{\text{pen}} = 2.0$  mm, weld width  $w = 10$  mm, weld cross-sectional area  $A_w = 26.7$   $\text{mm}^2$ , deposited metal cross-sectional area of 16.7  $\text{mm}^2$  (it corresponds to 13.1 g). The value of  $h_{\text{pen}}$  is determined from the mass of deposited metal on the centre test piece  $G$ :  $h_{\text{pen}} = 3G / 2\rho wL$ , where  $\rho = 0.00785$   $\text{g}\cdot\text{mm}^{-3}$  is the density.

The volume of diffusible hydrogen is measured during 5 days (Figure 3). The measurements (number of experimental points  $N = 14$ ) at first 7 h (see solid circles Figure 3) are taken as the input data for the inverse problem. It is assumed that  $w_n = 1$ ,  $M = 10$ ,  $K = 100$ .

The solution of the problem is the following: concentration  $C_0 = 0.2033$  (of units of the effused hydrogen per unit weld volume), diffusion coefficients  $D = 1.625 \cdot 10^{-4}$   $\text{mm}^2 \cdot \text{s}^{-1}$  and  $D_h = 3.335 \cdot 10^{-3}$   $\text{mm}^2 \cdot \text{s}^{-1}$ . Averaged (apparent) diffusivity  $D$  falls in between ferrite and martensite diffusivity [10]; the latter can form as a consequence of force-cooling. The solution results in hydrogen content  $Q_{\text{int}} = 542$   $\text{mm}^3$ , or 4.14 ml per 100 g of deposited metal or 2.59 ml per 100 g of fused weld metal (corrected to STP) or 2.33 ppm by mass. The hydrogen is evolved from the test piece before measurement ( $Q_0 = 94$   $\text{mm}^3$  or 17 % of the total volume) and after the start of the measurement ( $\Delta Q_{\infty} = Q_{\text{int}} - Q_0 = 448$   $\text{mm}^3$ ).

Data treatment of other similar samples shows that the part of hydrogen effused prior to measurement can be as much as a quarter of the total diffusible hydrogen. The calculation time is about 1 s for a direct problem (calculation of objective function  $F$ ) and approximately 1 min for the whole (inverse) problem if a conventional personal computer is used.

Half of hydrogen total amount is effused during first 7 h (see solid circles in Figure 3). After 3 days the hydrogen hardly evolves from the test piece and the measurement can be stopped (a change, over 24 h, is no more than 1 % of the total volume collected according to [2]). From the comparison between the calculation curve and the experimental evidence it follows that the developed technique, using the experimental data obtained only during 24 h, allows for predicting the hydrogen evolution with an acceptable accuracy.

The time dependences of hydrogen fluxes (rates of flow per unit time) across all surfaces of the specimen are shown in Figure 4, a. The start of welding of the centre test piece is taken as zero. The maximum total flux  $q$  falls on the end of welding. Prior to measurement most of the hydrogen evolves from the face surface, small quantities evolve from the front surface, and practically nothing evolves from the back and side surfaces. The back flux  $q_z$  ( $z = 8$  mm) is maximal at about of 10 h, the time increases as the

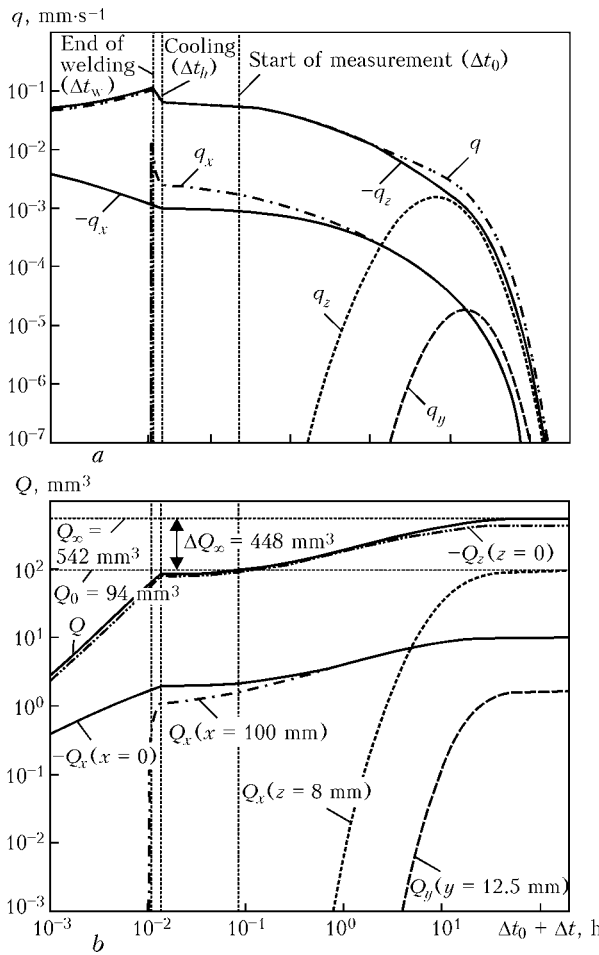


**Figure 4.** Rates of hydrogen evolution from all surfaces,  $q$ , from front  $-q_x$  ( $x = 0$ ), rear  $q_x$  ( $x = 100$  mm), side  $q_y$  ( $y = 12.5$  mm), face  $-q_z$  ( $z = 0$ ) and back  $q_z$  ( $z = 8$  mm) surfaces (a), and volume of hydrogen,  $Q$ , evolved from the same surfaces after start of welding centre test piece (b)

specimen thickness increases [1]. The curve inflections at 50 s (0.014 h) result from a sharp change in the hydrogen diffusivity at force-cooling. It follows from Figure 4, b that the hydrogen has mainly crossed the face and back surfaces (79 and 17 % of the total amount, respectively), the remainder has crossed front and rear surfaces (about 4 %) and side surfaces (less than 1 %). Notice that such information about hydrogen evolution enables us to optimise the test piece dimensions.

As an example Figure 5 shows the hydrogen concentration field in  $yz$ -plane at  $x = 50$  mm and  $\Delta t = 2$  h, when  $\Delta Q \approx 0.2\Delta Q_\infty$ . The dimension of the concentration is the unit of hydrogen volume (at STP)

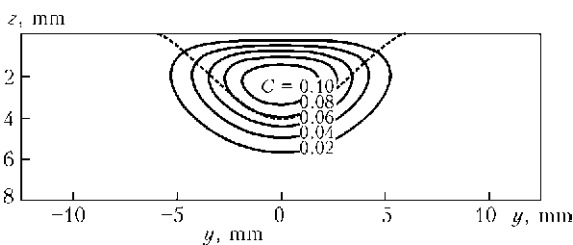


**Figure 5.** Hydrogen concentration field at central cross section of the test piece ( $x = 50$  mm) at  $\Delta t = 2$  h

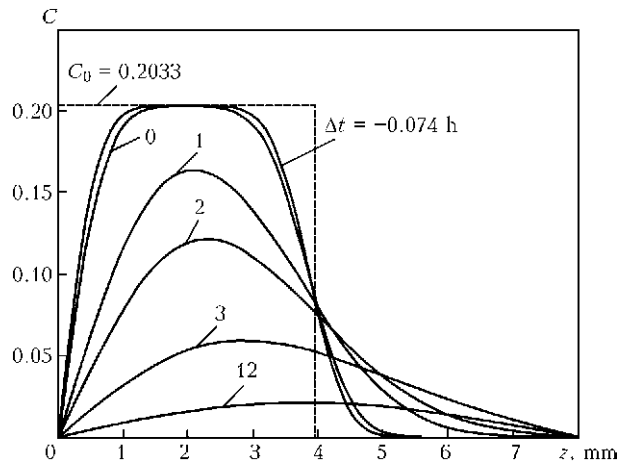


**Figure 6.** Distribution of hydrogen across the specimen thickness ( $x = 50$  mm,  $y = 0$ ) at different time (for explanation see the text)

per unit of weld volume. The broken line shows the calculated weld interface.

The distribution of the hydrogen concentration at the central cross-section ( $x = 50$  mm,  $y = 0$ ) along  $z$ -axis at different time  $\Delta t$  are given in Figure 6. We notice that the zone where the concentration is maximal changes its position during the time. Such curves make it possible to analyse HAZ in cold cracking problems. The hydrogen distribution along the weld is non-uniform as the weld is not performed instantly along its full length (Figure 7). Even at the end of the welding ( $\Delta t = -\Delta t_p = -250$  s = -0.07 h) and the start of the measurement ( $\Delta t = 0$ ) the hydrogen concentration at a depth of 1 mm is remarkably below the initial concentration  $C_0$ . Such a profound effect of the welding time is caused by high diffusivity at high temperature ( $D_h \gg D$ ). Later the concentration falls and the distribution along the weld becomes symmetric about the central cross-section of the specimen. Post welding non-uniform hydrogen distribution was observed experimentally [11].

Note that the measurement time  $\Delta t_N$  can be decreased with increase in the  $\Delta Q_n$  measurement accuracy. The preparation time  $\Delta t_p$  can be increased, which will allow the specimen to be better prepared for testing (to remove all surface sources of hydrogen).

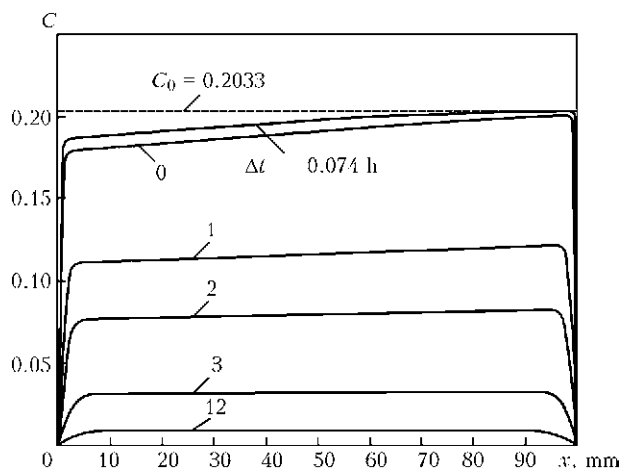


**Figure 7.** Hydrogen distributions along weld axis ( $y = 0$ ) at depth of 1 mm at different time

The proposed technique can be used also for other fusion welding processes and other methods of determination of the hydrogen content in weld metal.

It should be emphasised that the assumption of uniformity of the test piece and the deposited metal with respect to the hydrogen diffusivity and solubility is essential. A strong non-uniformity can significantly influence the concentration distribution and hydrogen evolution from the solid [10].

## CONCLUSIONS

1. The functional-analytical solution of 3D hydrogen diffusion problem for a parallelepiped-shaped solid is found. The solution allows calculating the concentration distribution, volume and rate of hydrogen effusion at any time.

2. The inverse problem for the unknown hydrogen content in the weld metal is stated and solved numerically. It enables the boundary conditions of the direct problem to be reconstructed using some measurements of the hydrogen evolved from the test piece.

3. The developed computer-aided technique makes it possible to determine the hydrogen content in the deposited weld metal from the measurement of effused hydrogen at the beginning of effusion (when approx-

imately half its volume is effused). It allows the measurement time to be drastically reduced.

1. Pokhodnya, I.K., Yavdoshchin, I.R., Paltsevich, A.P. et al. (2004) *Metallurgy of arc welding. Interaction of metal with gases*. Kiev: Naukova Dumka.
2. *ISO 3690:2000*: Determination of hydrogen content in ferritic steel arc weld metal.
3. *GOST 23338-91*: Welding of metals. Methods for determination of diffusible hydrogen in deposited weld metal and fused metal.
4. Petrov, G.L., Levchenko, A.M. (1979) Determination of diffusible hydrogen in welded joints by vacuum method without mercury. *IIV Doc. II-901-79*.
5. Karkhin, V.A., Michailov, V.G. (1985) Distribution of hydrogen in the single-pass welding of steel. *Avtomatich. Svarka*, **6**, p. 32-35.
6. Yurioka, N. (1989) A review of numerical analyses on the hydrogen diffusion in welding of steel. *IIV Doc. IX-1553-89*.
7. Michailov, V.G., Thomas, K., Wohlfahrt, H. (1996) Numerische Simulation der Wasserstoffverteilung in mehrlagigen Schweissverbindungen. *Schweissen und Schneiden*, **48(1)**, p. 47-54.
8. Makhnenko, V.I., Korolova, T.V., Lavrynets, I.G. (2002) Numerical study on the effect of microstructural transformation on hydrogen redistribution in fusion welding of structural steels. In: *Mathematical modelling of weld phenomena 6*. Ed. by H. Cerjak. London: Maney Publ.
9. Gill, P.E., Murray, W., Wright, M.H. (1984) *Practical optimization*. London: Academic Press.
10. Karkhin, V.A., Marx, O.Y. (1994) Analysis of influence of welded joint heterogeneity on hydrogen concentration in heat-affected zone. *Avtomatich. Svarka*, **2**, p. 9-14.
11. Christensen, N., Gjermundsen, K., Rose, R. (1958) Hydrogen in mild-steel weld deposits. *British Welding J.*, **5(6)**, p. 272-281.

# NUMERICAL STUDY OF INFLUENCE OF EDGE PREPARATION ANGLE OF BUTT, TEE AND CORNER JOINTS ON MICROSTRUCTURE AND MECHANICAL PROPERTIES IN FZ AND HAZ ON LOW-ALLOY STEELS OF GENERAL DESIGNATION

T.V. KOROLYOVA<sup>1</sup>, V.A. STARODUBTSEV<sup>2</sup>, B.V. STEPANOV<sup>2</sup> and V.A. YAROCKIN<sup>2</sup>

<sup>1</sup>E.O. Paton Electric Welding Institute, NASU, Kiev, Ukraine

<sup>2</sup>Uralmashzavod, Ekaterinburg, Russia

Developed at the E.O. Paton EWI computer system ArcWeldSys allows mathematical simulation of processes of heat and mass transfer in fusion zones (FZ) and heat-affected zones (HAZ) in arc welding of structural steels of various groups, and predict on this basis parameters of thermal cycles, chemical composition of metal in FZ, microstructural changes and mechanical properties in the welded joint area. Use of this system allows replacing a significant volume of experimental studies on specimens, when selecting filler materials and conditions of welding, with numerical studies, which make it possible to significantly reduce material expenses. In this work system ArcWeldSys is used for substantiating possibility of using reduced angles of preparation of various welded joints in comparison with those regulated by GOST 14771-76. It is shown that for the whole number of steels of the types 09G2S, 17G1S, 10KhSND, 12GN2MFAYu and corresponding to these steels welding wires of the types SV-08G2S, OK Autrod 13.26, OK Autrod 13.29, etc. 1.2–1.6 mm in diameter, increase of  $\Delta t_{8/5}$  during welding in the mixture of shielding gas (Ar + 20 % CO<sub>2</sub>) because of reduction of the groove angle from 60° to 30° in butt joints B17 and B25, corner joints C6 and C8, and from 40° to 30° in tee joints T6 and T8 does not cause significant change of microstructure and mechanical properties under the same conditions of welding. At the same time significant reduction of the volume of built-up metal and reduction of angular deformations and cross shrinkage takes place. It is shown that efficiency of such change reduces when the steel to be welded is rather sensitive to thermal cycle of welding.

In manufacturing various welded structures, it is expedient to apply in the first place such technological processes, which provide a required quality of products at minimum funds and time expenditures. Substantial economy of such expenditures can be obtained thanks to the reduction of welded joint edge preparation angles, which obviously leads to the reduction of volumes of deposited metal and reduces the time of production. The experts on the basis of many years experience of preparing quality welded joints developed recommendations of GOST 14771-76. It is however known that application of modern arc welding techniques in many cases provides for the quality formation of welds at reduced welded joint edge preparation angles.

But evident benefit in the reduction of expenditures is not enough. Of importance is also the effect of the change in geometric parameters of the joint on the microstructure and mechanical properties of the weld and near-weld zone metal, as it is accompanied by heat impact on the metal in the weld zone. Clarification of the significance of such an effect is the subject of this investigation.

**Investigation method.** Calculations were made for butt B17 and B25, corner C6 and C8 and tee T6 and T8 joints (in compliance with GOST 14771-76). For the above types of welded joints was conducted com-

parative study of influence of edge preparation angle on thermal processes, including the size of penetration zone, chemical composition of that zone and time  $\Delta t_{8/5}$ ; microstructural changes in the metal of penetration zone and HAZ; and mechanical properties of the weld and HAZ metal in welded joint.

Calculation methods developed by the E.O. Paton Electric Welding Institute, Ukraine, and implemented in the computer system ArcWeldSys, were applied. In accordance with such methods, it is required, in the first place, to provide a specific description of the base and filler material, specimen geometry, modes and conditions of welding.

Used in this study structural carbon and low-alloy steels can be categorized in groups according to the classification accepted in a number of countries:

- group 1: carbon structural steels (VSt3, VSt5, St20);
- group 2: low-alloy structural general-purpose steels (St20GS, 09G2S, 17G1S, 17GS, 10KhSND).

Besides, calculations were made for hardened-tempered steel 12GN2MFAYu.

The filler material was represented by one brand of indigenous welding wire Sv08G2S and 4 brands of the ESAB welding wire, namely OK Autrod 12.51, Autrod 12.64, Autrod 13.26 and Autrod 13.29, having diameter of 1.2–1.6 mm.

Группа 1 Углеродистые стали (C<0.3%)													
Примеры химического состава (в %):													
Марка стали	C	Si	Mn	Cr	Ni	Cu	S	P	V	Mo	Nb	N	
ВСт2п (ГОСТ 380-71)	0.14-0.22	<0.07	0.3-0.6	<0.3	<0.3	<0.3	<0.05	<0.05					
A575 (ASTM)	0.23-0.38	0.15-0.40	0.6-1.8										
A-105 (ASTM)	0.25-0.30	0.1	0.25-0.96										
Тяжелые металлы и химический состав стали:													
C	0.2	Mo	0.5	Si	0.2	Ni	0.2	W		Al		Co	0.2
Ti		W		P	0.03	S	0.03	As	0.06	Zr		N	0.2
										O <sub>2</sub>		N <sub>2</sub>	
Термофизические характеристики и критические температуры													
Коэффициент температурного расширения, 1/град													
T, °C	20	100	200	300	400	500	600	700	800	900	1000	1100	1200
λ	0.55	0.51	0.48	0.44	0.43	0.39	0.36	0.32	0.28	0.26	0.28	0.28	0.30
Объемная теплоемкость, джоуль/град													
T, °C	20	100	200	300	400	500	600	700	800	900	1000	1100	1200
c <sub>v</sub>	3.7	3.7	3.8	3.95	4.1	4.4	4.5	4.9	5.85	5.51	5.42	5.40	5.37
Особенности технологии и условий дуговой сварки													
Способность к образованию холодных (водородных) трещин определяется значением $SE=C+(Mn/80) \cdot 4$ , %. Чувствительность к холодным трещинам равно нулю при $SE < 0.4\%$ и предварительный подогрев не требуется. При $SE > 0.4$ $T_{под} = 1000 \cdot (SE - 0.4)$ , °C. При $SE > 0.65$ заливочные стали не соответствуют конструктивным стандартам и в этом случае система не имеет соответствующих рекомендаций.													

Figure 1. Basic characteristics of steel St20 entered using computer system

Geometrical dimensions of weldments corresponding to joints B17, B25, C6, C8, T6 and T8 with regard for the variation of angle  $\alpha$ , were the same as for the specimens during experimental development of welding technologies, i.e. transverse dimensions were selected depending on the thicknesses to be welded  $(15-20)\delta$ , where  $\delta$  is the thickness of specimens, while their lengths are 300-500 mm. Mode of MAG

welding in shielding gas mixture of Ar + 20 % CO<sub>2</sub> using electrode 3 mm in diameter, was as follows:  $I_w = 225$  A,  $U_a = 37$  V,  $v_w = 0.4$  cm/s. The deposition coefficient was selected using the ArcWeldSys computer system containing all required experimental dependences, and was found to be  $\alpha_d = 14.7$  g/(A·h). The number of passes and arrangement of beads of «stitch» welds, the system determines itself, in accordance with the preset welding mode.

Using this system, the data on average chemical composition, thermo-physical characteristics, peculiarities of the technology and MIG welding conditions were determined for the base metal (for instance, as for St20 in Figure 1).

**Chemical composition.** An important factor in predicting the quality of the welded joint in multipass welding, is the evaluation of the average chemical composition of the melted during the given pass metal, with account of filler material. To do this, it is necessary to know not only the quantity of the filler material during the given pass, but also the quantity of the melted base material and the material of successive passes. For each pass average chemical composition of fusion zone is determined on the basis of

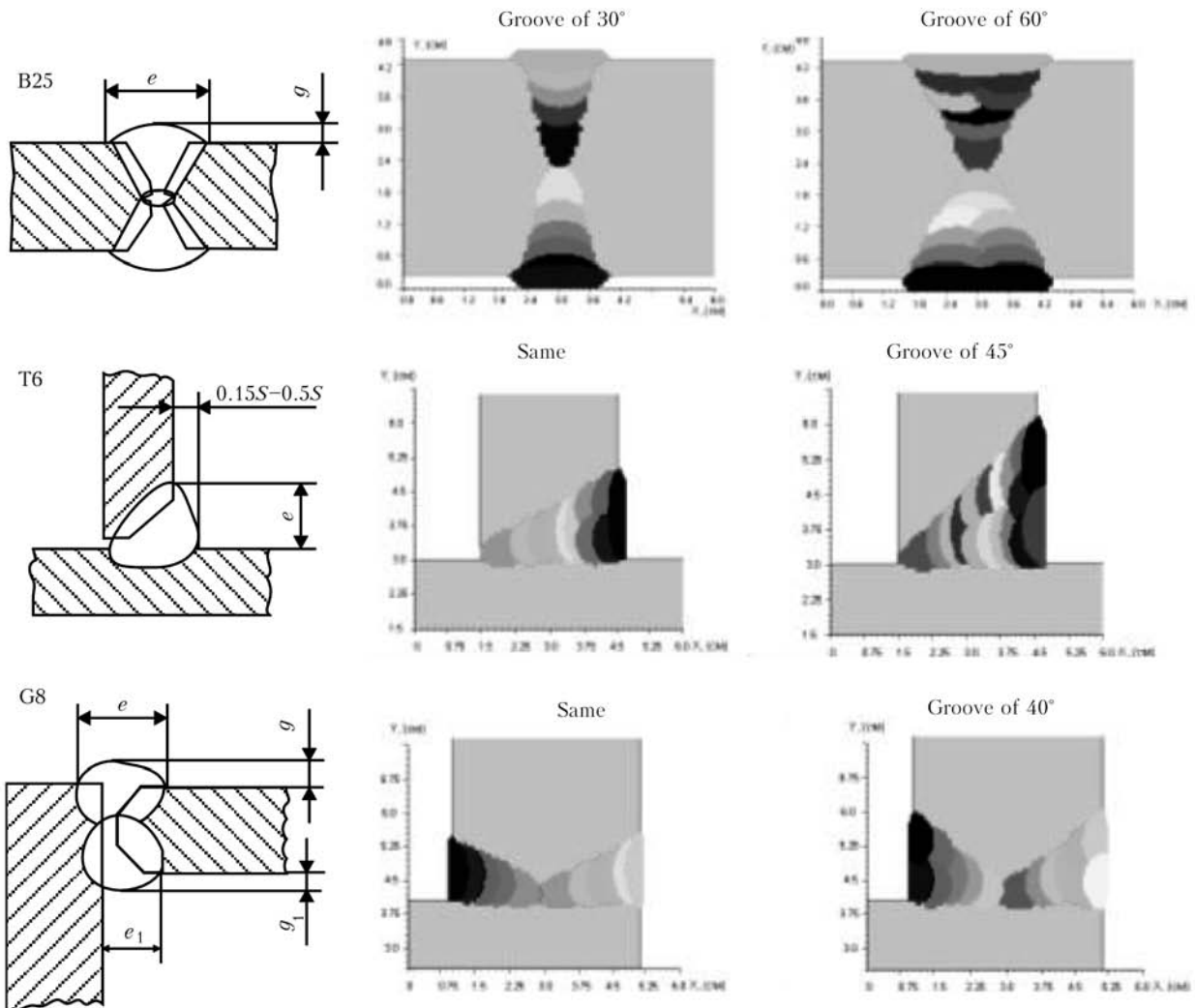


Figure 2. Sketches of welded joints and fusion zones formed in filling the groove

knowledge of the dimensions and chemical composition of the melted areas, as well as quantity and composition of the filler material being deposited.

**Microstructure.** On the basis of the knowledge of chemical composition in each specific section point of the joint in performing a concrete pass, as well as of the  $\Delta t_{8/5}$  values, microstructure of weld zone metal, after completion of the given pass, is calculated.

Application of the known approximate dependences for calculation of microstructure and mechanical properties of the metal, is most expedient in comparative studies, as it allows one to significantly reduce the scope of the experimental works, having obtained the idea of the influence of any parameter.

**Account of repeated heating.** In considered variants of butt, corner and tee joints, made using mul-

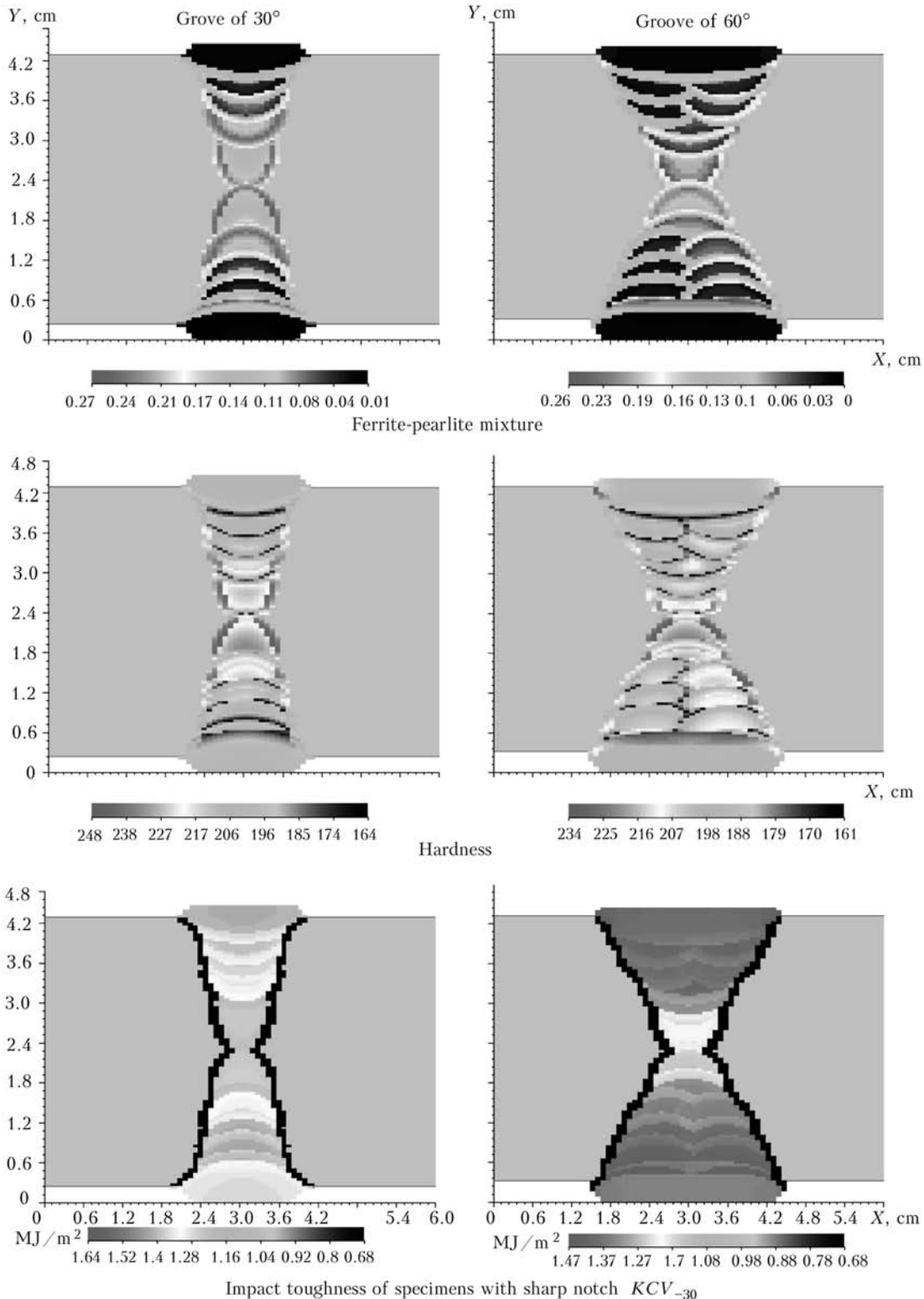


Figure 3. Some calculated characteristics of weld metal for two-sided butt joint at different edge preparation angles

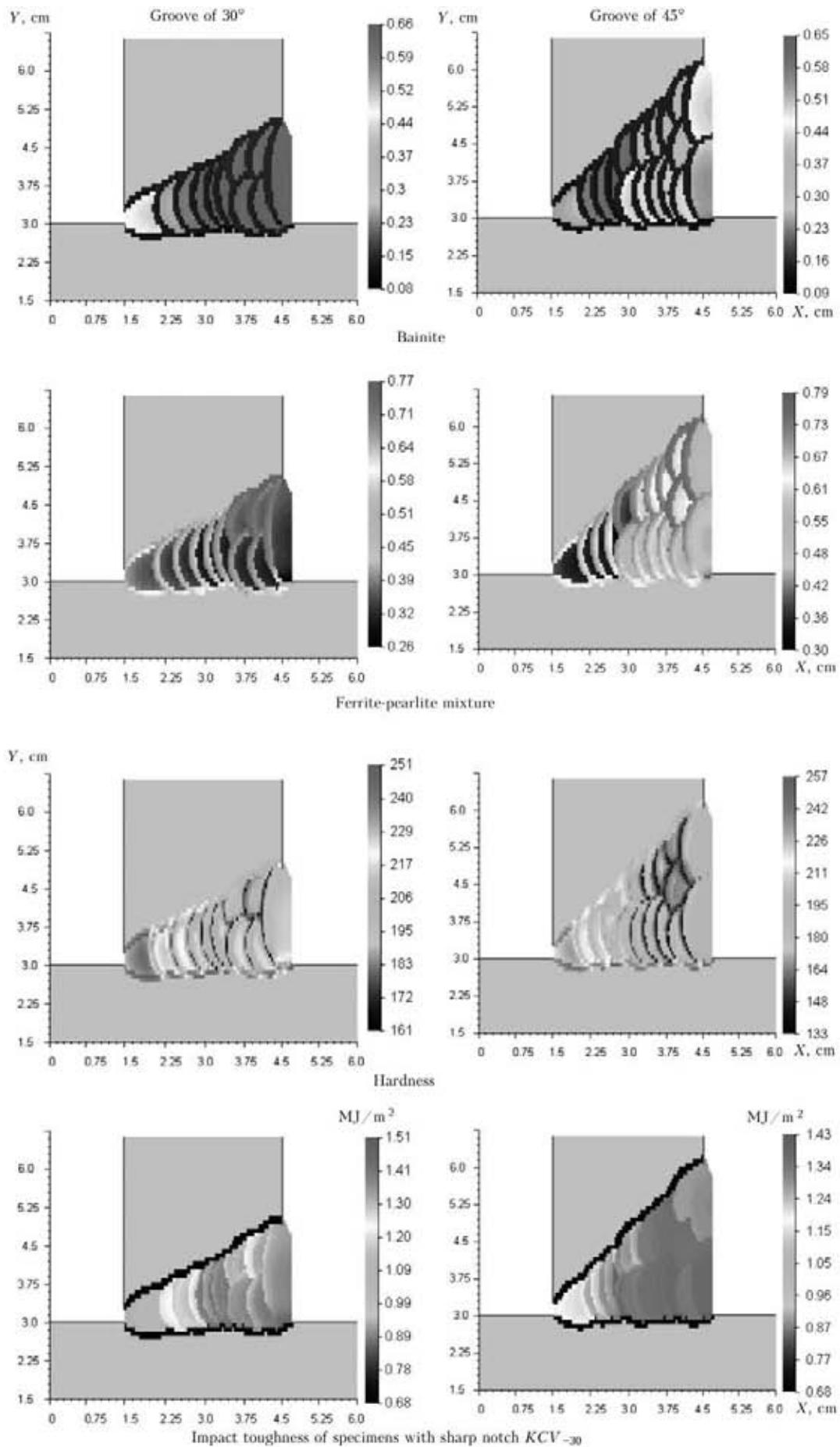
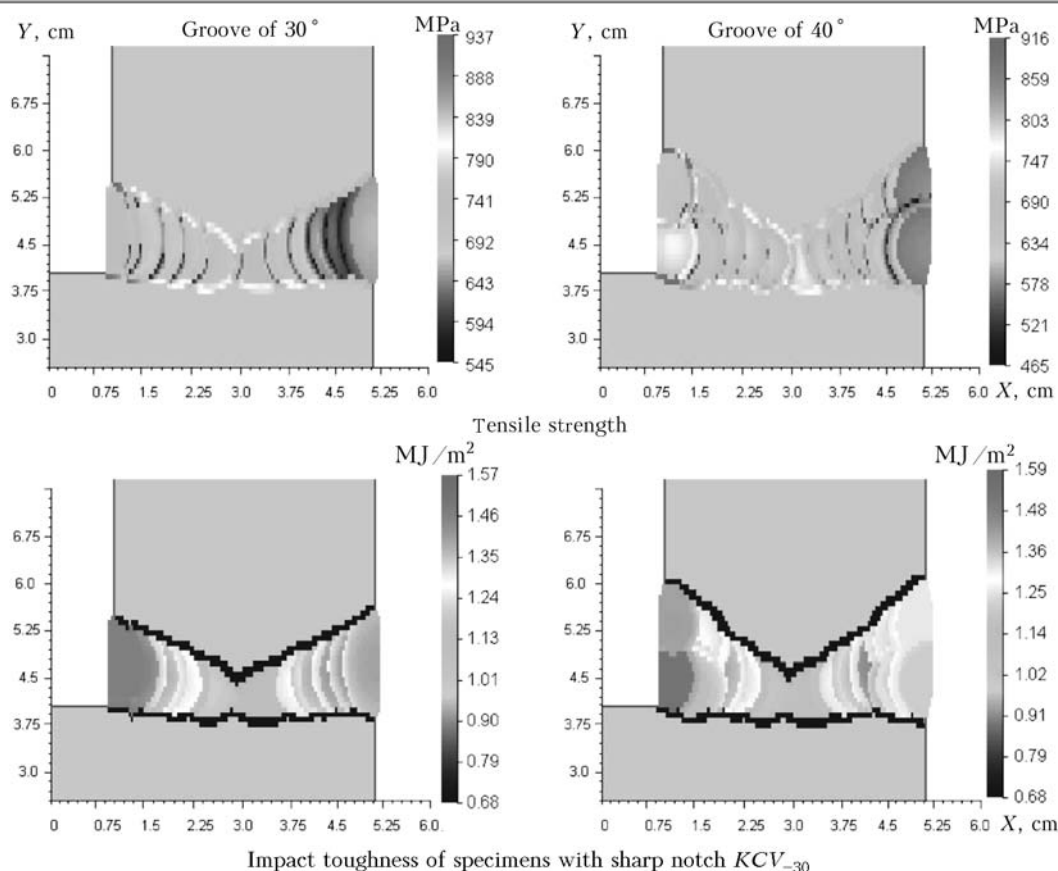


Figure 4. Some calculated characteristics of weld metal for tee joint at different edge preparation angles



Impact toughness of specimens with sharp notch  $KCV_{-30}$ 

**Figure 5.** Some calculated characteristics of weld metal for corner joint with two-sided groove at different edge preparation angles

tipass welding, a certain change in microstructure and mechanical properties takes place due to previous passes, which is found in the weld and HAZ metal and is accounted for in calculations by ArcWeldSys system. It is assumed that repeated heating to above  $A_{c3}$  assists in formation of a new microstructure, based of the new chemical composition and new thermal cycle parameters. Repeated heating to below  $A_{c3}$  does not affect the microstructure, but promotes changing of mechanical properties by a respective short-term tempering mechanism.

#### Some results of numerical studies

*Butt joint B25 (Figure 2) 40 mm thick for specimens of St20 welded with OK Autrod 12.51 wire.* Analysis of calculation data presented in Figure 3, shows that changing of edge preparation angle from  $60^\circ$  to  $30^\circ$ , at constant welding mode, does not lead to noticeable change of the microstructure and of the mechanical properties, which is due to relatively small change of  $\Delta t_{8/5}$  depending on the preparation angle and relatively low sensitivity of the base and filler metal to such variations of  $\Delta t_{8/5}$ . A small increase of impact toughness  $KCV$  with decreasing edge preparation angle of within 5 % range, and significant reduction of the number of passes, are observed.

*Tee joint T6* in compliance with GOST 14771–76 (see Figure 2) has a standard angle of wall bevel of  $\alpha = 45^\circ$ . Correlation of the results of calculation of weld formation, microstructure and mechanical properties for  $\alpha = 45^\circ$  and  $30^\circ$  for the same thicknesses of the wall and the web of 30 mm, was conducted.

Method and mode of welding are the same as for the butt joints.

Figure 4 shows the results of calculation of quantitative characteristics of the weld metal for this joint. Reduction of the wall bevel angle from  $45^\circ$  to  $30^\circ$ , enables to reduce the number of passes from 17 at  $45^\circ$  to 11 at  $30^\circ$ . The microstructure of the weld metal is characterized by predominance of bainite and pearlite-ferrite mixture. Martensite content does not exceed 20 % neither at  $\alpha = 45^\circ$  nor at  $\alpha = 30^\circ$ . The observed higher weld metal and near-weld zone hardness for  $\alpha = 30^\circ$ , is however not exceeding 5–10 %. Impact toughness  $KCV$  for HAZ is at a level of  $0.7 \text{ MJ/m}^2$ , while for the weld metal it varies from about  $1.0$  to  $1.4 \text{ MJ/m}^2$  at  $\alpha = 30^\circ$ , and from  $1.1$  to  $1.4 \text{ MJ/m}^2$  at  $\alpha = 45^\circ$ .

It can be considered that in this case the influence of the edge preparation angle on the microstructure and mechanical properties of the weld metal and near-weld zone, is insignificant.

*Corner joint C8.* Results of calculation of weld formation, microstructure and mechanical properties for C8 joint  $40 + 40$  mm thick from St20 and filler wire Sv08G2S show that reduction of costs involved with the reduction of the number of passes from 15 at  $\alpha = 40^\circ$  to 11 at  $\alpha = 30^\circ$ , adds-up with retention of quantitative characteristics of the microstructure and mechanical properties of the joints.

## CONCLUSIONS

On the basis of numerical studies conducted using ArcWeldSys system, of the influence of edge prepara-

ration angles of welded members of butt, tee and corner joints of the types B17 and B25, T6 and T8, C6 and C8 in compliance with GOST 14771-76, from steels VSt3, VSt5, St20, St20GS, 09G2S, 17GS, 17G1S, 10KhSND, 12GN2MFAYu 10–40 mm thick in arc welding in argon-based gas mixture with welding wires Sv08G2S, OK Autrod 12.51, OK Autrod 12.64, OK Autrod 13.26 and OK Autrod 13.29, having diameter of 1.2–1.6 mm, in varying edge preparation angles within 60–30° range, the following can be stated.

1. For butt joints B17 and B25 reduction of edge preparation angles from 60° to 30° leads to the reduction of volumes of the deposited material approximately two-fold. However, at similar arc welding modes, reduction of edge preparation angles leads to a certain increase in the cooling rate. It is shown that for the structural steels considered, said reduction of edge preparation angles somewhat reduces  $\Delta t_{8/5}$  values and, depending on the sensitivity of the steel in the HAZ and FZ to  $\Delta t_{8/5}$  value, the content of hardening microstructures somewhat increases, hardness, strength limit and yield point of the material grow, due to a small reduction in area and relative elongation. A small change of impact toughness, depending on the edge preparation angle, at –30 °C and lower, can occur both ways: towards its increase or decrease. Most markedly said change of microstructure is ob-

served among the steels considered, for carbon steel VSt5, as well as for the HSLA steels 17G1S and, especially, 12GN2MFAYu. Characteristically, that increasing volume of hardening microstructures (martensite and bainite) in HAZ of sparsely-alloyed hardened-tempered high-strength steel 12GN2MFAYu in multipass welding, due to diminishing size of the austenite grains by non-dissolved disperse carbonitrides and respective diminishing size of the hardening products («packets» of martensite and lower bainite), leads to high strength- and ductility properties, including impact toughness  $KCV$  at low temperatures.

2. For simpler steels, sensitive to  $\Delta t_{8/5}$  value (type VSt5 and to some extent 17G1S), reduction of edge preparation angles, with otherwise unchanged conditions and welding modes, leads to increased number of hardening structures and increasing risk of cold crack formation, for which reduction, an increased number of technological procedures is required (for instance, preheating).

3. For the tee joints T6 and T8, as well as for the corner joints C6 and C8, change of the bevel angle of the wall adjoining the web, in the context of microstructural transformation, mechanical properties in HAZ and FZ, produces the same effect as in the case of change of the edge preparation angles of butt joints of similar thickness.

# NUMERICAL SIMULATION OF SHS LASER WELDING OF METALS\*

O.B. KOVALEV and K.A. MANAJCHEV

Institute of Theoretical and Applied Mechanics, RAS SB, Novosibirsk, Russia

A mathematical model is proposed for calculating self-propagating high-temperature synthesis (SHS) laser welding of materials. The method of SHS laser welding suggested is based on a local dynamic laser heating and initiation of a synthesis reaction of powder mixture caused heat generation immediately between the plates. The SHS laser welding is especially useful in case of joining thick materials, as it allows one to decrease a radiation power and exclude a formation of the vapor cavity leading to arising of some defects in the joint region. Mathematical formulation reduces to a two-phase Stefan problem taking into account a heat release at the expense of metal-chemical reactions. An equation of kinetics of Arrhenius type is additionally considered. Numerical simulations yield the spatial distribution of the temperature field in a chemically active zone and in the metal, the position of the inner fusion boundary, and the shape of the fused zone. The optimal physical parameters that ensure stable fusion of the welded joints, are chosen by solving the problem numerically. The computations allow predicting the necessary power of laser radiation, the amount and physical-chemical properties of the powder mixture reacting in the SHS regime, a fused zone of sufficient size for welding of materials is obtained.

There exists a SHS welding of refractory materials based on exothermic interaction of components of a reacting mixture placed in a gap between the materials being joined. Welding is realized in the mode of electrothermal explosion, when the mixture is heated up to the temperature necessary for interaction of reagents. Simultaneously, a synthesis of heat-proof materials is performed, and the welded joint is formed. Strength of a welded joint corresponds to the strength of the materials to be joined. A disadvantage of the electrothermal SHS welding is that the joint parts have to be pre-heated up to the temperature necessary for beginning of the reaction, which surely leads to arising of a residual deformation of the whole structure after its cooling.

SHS is used for welding refractory and dissimilar materials. The mechanism involves exothermic interaction of the components of the reacting mixture located in a gap between the materials being joined [1–3]. The reacting mixture contains powders of metals and non-metals forming carbides, borides, silicides, intermetallic compounds, and other refractory materials. Welding is performed in an electric thermal explosion mode where the reacting mixture is heated up to a temperature at which the reagents start interacting. A high specific heat-release power ( $\sim 100$  kW/g) developed during the reaction supports the high heating rate ( $\sim 10^5$  K/s) [2]. This allows one to substantially reduce the welding period and to prevent recrystallization of refractory materials in the seam zone. The SHS product formed during the reaction is responsible for fusion of material surfaces to be joined. SHS welding is simultaneously accompanied by synthesis of refractory materials and welded joint formation. SHS welding based on the electric ther-

mal explosion allowed obtaining permanent joints of various refractory and dissimilar materials, such as graphite, tungsten, molybdenum, hard alloy, etc. The welded joint strength for these materials is approximately equal to that of materials to be joined [2, 3]. A drawback of electric thermal SHS welding is the necessity of preheating of articles to be joined to a temperature of reaction beginning, which inevitably leads to emergence of residual deformations of the entire structure after its cooling.

The method of SHS laser welding considered is based on local dynamic laser heating and on initiating SHS reactions directly in the gap between the sheets. The reactions are initiated on the joint surface in the region where the laser beam is incident. Fusion stability in the joint zone and high quality of welding are achieved by an appropriate thermal balance including the radiative heat flux (before the moment of reaction initiation), heat release directly in the reacting mixture, and heat output due to thermal conductivity of the material joined. The heat balance is achieved by conformity between the velocity of propagation of the SHS reaction and the welding speed. Practical implementation of SHS welding is complicated by the absence of stable initiation and propagation of SHS chemical reactions in a powder mixture in a narrow gap between heat-conducting sheets. Mathematical modeling of the combination of the above-indicated processes allows one to calculate optimal conditions of fusion and welding of the sheets. The problem of dynamic laser heating and initiation of SHS reactions in a powder mixture located between aluminum sheets is discussed below in accordance with Merzhanov's thermal theory [4, 5].

**Problem formulation.** The problem of laser-radiation interaction with metals is complicated by a variety of physical processes whose detailed description is currently impossible. This problem formulation is based on the following assumptions:

\* This work was supported by Russian Foundation for Basic Research (Grant No. 05-01-00311).

1. The energy of radiation absorbed is used only for material heating and fusion. Evaporation and interaction of radiation with metal vapors are neglected.

2. The convective motion of the fused metal induced by laser radiation is not considered.

3. Heat losses due to radiation and heat exchange with the ambient medium are neglected.

4. The material of the joined sheets and the powder mixture are isotropic media with homogeneous thermophysical properties in solid and liquid states.

Figure 1 shows the fusion welding scheme where a mixture of reacting powders is placed between the sheets to be joined. The arrows show the direction of radiation that locally heats the material and initiates the SHS reactions. By virtue of symmetry of the problem, we consider only one half of the domain shown in Figure 1 and denote the area of the domain occupied by the powder mixture by  $\Omega_1$  and the area occupied by the metal by  $\Omega_2$ :

$$\Omega_1 = \{x, y, z: -L_x \leq x \leq L_x, 0 \leq y \leq \delta, 0 \leq z \leq d\},$$

$$\Omega_2 = \{x, y, z: -L_x \leq x \leq L_x, \delta \leq y \leq L_y, 0 \leq z \leq d\},$$

where  $L_x$  and  $L_y$  are the sheet lengths in the  $x$  and  $y$  directions, respectively;  $\delta$  is the half-width of the gap filled by the combustible mixture;  $d$  is the thickness of the metal sheet (it is assumed that  $\delta \ll d$ ).

The mathematical formulation reduces to considering a conjugate problem that involves ignition and combustion of the powder mixture in the gap with simultaneous heating and fusion of the metal of the sheet. Let us consider a moving coordinate system fitted to the laser beam moving along the axis  $OX$  with a velocity  $v_w$  (see Figure 1).

To describe the combustion of the reacting mixture in the domain  $\Omega_1$ , we use the SHS thermal theory based on a formally kinetic approach [4]:

$$c_1 \rho_1 \left( \frac{\partial T_1}{\partial t} - v_w \frac{\partial T_1}{\partial x} \right) = - \frac{\partial}{\partial x} \lambda_1 \frac{\partial T_1}{\partial x} + \frac{\partial}{\partial y} \lambda_1 \frac{\partial T_1}{\partial y} + \frac{\partial}{\partial z} \lambda_1 \frac{\partial T_1}{\partial z} + Q_c \frac{\partial \eta_1}{\partial t}, \quad (1)$$

$$\frac{\partial \eta_1}{\partial t} - v_w \frac{\partial \eta_1}{\partial x} = k_p (1 - \eta_1)^p \exp \left( - \frac{E_a}{RT_1} \right), \quad (2)$$

where  $t$  is the time;  $x, y, z$  are the coordinates;  $T_1(t, x, y, z)$  is the temperature in the domain  $\Omega_1$ ;  $\eta_1(t, x,$

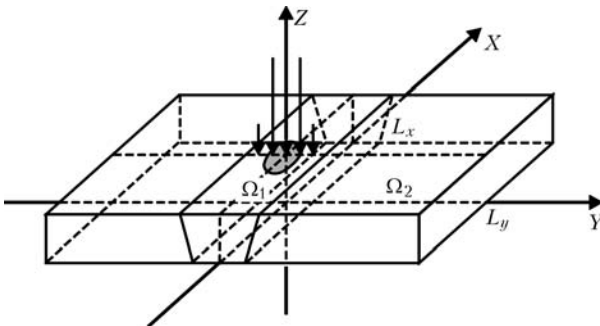


**Figure 1.** Scheme of using the powder mixture reacting in the SHS mode in laser welding of metal

$y, z)$  is the degree of conversion of the material in  $\Omega_1$ ;  $\rho_1, \lambda_1, c_1$  are the density, thermal conductivity, and specific heat of the powder mixture;  $v_w$  is the velocity of beam motion (or the welding speed);  $Q_c$  is the thermal effect of the SHS reactions;  $k_p$  is the pre-exponent;  $p$  is the order of the reaction;  $E_a$  is the activation energy; and  $R$  is the gas constant.

Heat propagation in the metal and metal heating and melting in the domain  $\Omega_2$  are described by the two-phase Stefan problem:

$$c_2 \rho_2 \left( \frac{\partial T_2}{\partial t} - v_w \frac{\partial T_2}{\partial x} \right) = \frac{\partial}{\partial x} \lambda_2 \frac{\partial T_2}{\partial x} + \frac{\partial}{\partial y} \lambda_2 \frac{\partial T_2}{\partial y} + \frac{\partial}{\partial z} \lambda_2 \frac{\partial T_2}{\partial z}, \quad (3)$$

$$\rho_2 H_m \left( \frac{\partial f_m}{\partial t} - v_w \frac{\partial f_m}{\partial x} \right) = \lambda_{2s} \frac{\partial T_2}{\partial n} \Big|_{z=f_m(t, x, y) - 0} - \lambda_{2m} \frac{\partial T_2}{\partial n} \Big|_{z=f_m(t, x, y) + 0}, \quad (4)$$

$$T_2(t, x, y, f_m(t, x, y) - 0) = T_2(t, x, y, f_m(t, x, y) + 0) = T_m, \quad (5)$$

where  $T_2(t, x, y, z)$  is the temperature in  $\Omega_2$ ;  $z = f_m(t, x, y)$  is the phase-transition surface;  $\vec{n}$  is the normal to this surface;  $\rho_2, \lambda_2, c_2$  are the density, thermal conductivity, and specific heat of the metal; and  $H_m$  is the latent heat of the phase transition.

*Initial conditions at  $t = 0$ .* The powder mixture and the metal sheet are assumed to have a constant temperature before the beginning of irradiation, i.e. the conditions at the initial time are

$$T_1(0, x, y, z) = T_2(0, x, y, z) = T_0, \quad (6)$$

$$\eta_1(0, x, y, z) = 0.$$

*Boundary conditions at  $t > 0$ .* The following conditions are satisfied at the domain boundaries at an arbitrary time:

$$x = \pm L_x, 0 \leq y \leq \delta, 0 \leq z \leq d: \frac{\partial T_1}{\partial x} = 0, \quad (7)$$

$$x = \pm L_x, \delta \leq y \leq L_y, 0 \leq z \leq d: \frac{\partial T_2}{\partial x} = 0, \quad (8)$$

$$y = 0, -L_x \leq x \leq L_x, 0 \leq z \leq d: \frac{\partial T_1}{\partial y} = 0, \quad (9)$$

$$y = \delta, -L_x \leq x \leq L_x, 0 \leq z \leq d: \lambda_1 \frac{\partial T_1}{\partial y} = 0 = \lambda_2 \frac{\partial T_2}{\partial y}, \quad (10)$$

$$y = L_y, -L_x \leq x \leq L_x, 0 \leq z \leq d: \frac{\partial T_2}{\partial y} = 0, \quad (11)$$

$$z = 0, -L_x \leq x \leq L_x, 0 \leq y \leq \delta, \frac{\partial T_1}{\partial z} = 0, \quad (12)$$

$$z = 0, -L_x \leq x \leq L_x, \delta \leq y \leq L_y, \frac{\partial T_2}{\partial z} = 0, \quad (13)$$

$$z = d, -L_x \leq x \leq L_x, 0 \leq y \leq \delta, \\ \lambda_1 \frac{\partial T_1}{\partial z} = A(\gamma)I(x, y) \cos \gamma, \quad (14)$$

$$z = d, -L_x \leq x \leq L_x, \delta \leq y \leq L_y, \\ \lambda_2 \frac{\partial T_2}{\partial z} = A(\gamma)I(x, y) \cos \gamma, \quad (15)$$

where  $I(x, y)$  is the radiation intensity;  $A(\gamma)$  is the absorption coefficient; and  $\gamma$  is the angle of incidence.

The boundary conditions take into account radiation absorption by the combustible mixture (14) and by the metal (15). Correlations (7)–(9) and (11)–(13) describe the absence of the heat exchange with the ambient medium. The conjugation condition (10) describes the heat-exchange between the powder and the metal at their contact boundary; the validity of this condition is based on the assumption that the physical properties of the contacting media are homogeneous.

We consider continuous radiation of a CO<sub>2</sub> laser, whose intensity is described by the Gaussian distribution:

$$I(x, y) = \frac{2W}{\pi\omega_0^2} \exp\left\{-\frac{2(x^2 + y^2)}{\omega_0^2}\right\}, \quad (16)$$

where  $W$  is the radiation power; and  $\omega_0$  is the beam radius in the focal plane.

The temperature-dependent behavior of heat capacity, density and thermal conductivity is taken into account in the phase-transition region. It is assumed that the density and thermal conductivity experience a jump at the phase-transition boundary at  $T_2(t, x, y, z) = T_m$ , and the heat capacity is described by the Dirac  $\delta$ -function [6].

**Method of solution.** The existing effective algorithms of the numerical solution of the two-phase Stefan problem are based on the method of smoothing of the enthalpy jump [6] or transport coefficients [7] in the heat-conduction equation at the fusion point. This smoothing technique allows computations in the entire domain, i.e. computations without explicit identification of the fusion front. Taking into account the differences in thermophysical properties of the contacting media (powder and metal), let us consider an additional problem in the domain  $\Omega_1 \cup \Omega_2$  with variable coefficients in the heat-conduction equation:

$$cp \left( \frac{\partial T}{\partial t} - v_w \frac{\partial T}{\partial x} \right) = \\ = \frac{\partial}{\partial x} \lambda \frac{\partial T}{\partial x} + \frac{\partial}{\partial y} \lambda \frac{\partial T}{\partial y} + \frac{\partial T}{\partial z} \lambda \frac{\partial T}{\partial z} + Q_c \frac{\partial \eta}{\partial t}, \quad (17)$$

$$\frac{\partial \eta}{\partial t} = k_p(1 - \eta)^p \exp\left(-\frac{E}{RT}\right). \quad (18)$$

Here the unknown functions and transport coefficients are defined in the entire domain  $\Omega_1 \cup \Omega_2$ :

$$T(t, x, y, z) = \begin{cases} T_1(t, x, y, z), & x, y, z \in \Omega_1 \\ T_2(t, x, y, z), & x, y, z \in \Omega_2 \end{cases}, \\ \eta(t, x, y, z) = \begin{cases} \eta_1(t, x, y, z), & x, y, z \in \Omega_1 \\ 1, & x, y, z \in \Omega_2 \end{cases}, \\ c(t, x, y, z) = \begin{cases} c_1, & x, y, z \in \Omega_1 \\ c_2, & x, y, z \in \Omega_2 \end{cases}, \\ \rho(t, x, y, z) = \begin{cases} \rho_1, & x, y, z \in \Omega_1 \\ \rho_2, & x, y, z \in \Omega_2 \end{cases}, \\ \lambda(t, x, y, z) = \begin{cases} \lambda_1, & x, y, z \in \Omega_1 \\ \lambda_2, & x, y, z \in \Omega_2 \end{cases}.$$

The boundary conditions are

$$x = \pm L_x, 0 \leq y \leq L_y, 0 \leq z \leq d: \frac{\partial T}{\partial x} = 0, \quad (19)$$

$$y = 0, -L_x \leq x \leq L_x, 0 \leq z \leq d: \frac{\partial T}{\partial y} = 0, \quad (20)$$

$$y = L_y, -L_x \leq x \leq L_x, 0 \leq z \leq d: \frac{\partial T}{\partial y} = 0, \quad (21)$$

$$z = 0, -L_x \leq x \leq L_x, 0 \leq y \leq L_x: \frac{\partial T}{\partial z} = 0, \quad (22)$$

$$z = d, -L_x \leq x \leq L_x, 0 \leq y \leq L_x, \\ \lambda \frac{\partial T}{\partial z} = A(\gamma)I(x, y) \cos \gamma. \quad (23)$$

Equations (17) and (18) with the initial (6) and boundary conditions (19)–(23) were solved numerically with the use of an integro-interpolation explicit difference scheme of the second order on a uniform grid. The coefficients were smoothed in accordance with the method described in [7]:

$$b_{i,j,k}^n \frac{\theta_{i,j,k}^{n+1} - \theta_{i,j,k}^n}{\Delta t} - v_w b_{i,j,k}^n \frac{\theta_{i+1,j,k}^n - \theta_{i,j,k}^n}{\Delta x} + \frac{1}{\Delta x} \times \\ \times \left( a_{i+0.5,j,k}^n \frac{\theta_{i+1,j,k}^n - \theta_{i,j,k}^n}{\Delta x} - a_{i-0.5,j,k}^n \frac{\theta_{i,j,k}^n - \theta_{i-1,j,k}^n}{\Delta x} \right) + \\ + \frac{1}{\Delta y} \left( a_{i,j+0.5,k}^n \frac{\theta_{i,j+1,k}^n - \theta_{i,j,k}^n}{\Delta y} - a_{i,j-0.5,k}^n \frac{\theta_{i,j,k}^n - \theta_{i,j-1,k}^n}{\Delta y} \right) + \\ + \frac{1}{\Delta z} \left( a_{i,j,k+0.5}^n \frac{\theta_{i,j,k+1}^n - \theta_{i,j,k}^n}{\Delta z} - a_{i,j,k-0.5}^n \frac{\theta_{i,j,k}^n - \theta_{i,j,k-1}^n}{\Delta z} \right) + \\ + Q_c k_p (1 - h_{i,j,k}^n)^p \exp\left(-\frac{E_a}{R\theta_{i,j,k}^n}\right), \quad (24)$$

$$h_{i,j,k}^{n+1} - h_{i,j,k}^n - v_w \frac{h_{i+1,j,k}^n - h_{i,j,k}^n}{\Delta x} = \\ = k_p (1 - h_{i,j,k}^n)^p \exp\left(-\frac{E_a}{R\theta_{i,j,k}^n}\right), \\ a_{i+0.5,j,k} = 0.5(\lambda_{i+1,j,k} + \lambda_{i,j,k}), \\ \lambda_{i,j,k} = \begin{cases} \lambda_{2s}, & \theta_{i,j,k} < T_m - \Delta \\ 0.5(\lambda_{2s} + \lambda_{2m}), & |\theta_{i,j,k} - T_m| < 2\Delta, \\ \lambda_{2m}, & \theta_{i,j,k} \geq T_m + \Delta \end{cases}, \quad (25)$$

$$b_{i,j,k} = \begin{cases} c_{2s} \rho_{2s}, & \theta_{i,j,k} < T_m - \Delta \\ 0.25(\rho_{2s} + \rho_{2m})(H_m/\Delta + c_{2s} + c_{2m}), & |\theta_{i,j,k} - T_m| < 2\Delta, \\ c_{2m} \rho_{2m}, & \theta_{i,j,k} \geq T_m + \Delta \end{cases}$$

In Eqs. (24) and (25), the grid analogs  $\theta_{i,j,k}$  and  $h_{i,j,k}$  are assigned to the functions  $T(t, x_i, y_j, z_k)$  and

$\eta(t, x_i, y_j, z_k)$ . The problem is solved by a time-dependent method in which the numerical solution should converge to the precise one ( $\theta \rightarrow T, h \rightarrow \eta$ ) as the time increases unlimitedly ( $t \rightarrow \infty$ ).

**Numerical results and their discussion.** The mathematical model described above and the method of the solution are aimed at conducting numerical experiments and optimizing the physical parameters of the problem. For a given thickness of the metal sheet and beam velocity, it is necessary to obtain stable combustion modes of the reacting mixture and, thus, provide a fusion zone of a sufficient size, which forms the weld after cooling down.

The laws of SHS initiation and combustion-front propagation were considered in some papers [4]. SHS is assumed to refer to combustion processes difficult to initiate. For a given power of the heat flux supplied locally to the end surface of a cylindrical specimen, there is a certain delay and an ignition temperature above which gasless combustion begins. A certain condition of combustion is established after initiation. This combustion mode is characterized by the linear velocity of combustion-front motion, maximum burning temperature, and degree of conversion of matter. For cylindrical specimens, a steady mode with a constant burning rate is observed in most cases. The burning rate, however, it known to depend on a number of physical parameters (initial temperature of the specimen, its diameter, porosity, and composition, and fineness of the powder mixture); hence, unsteady unstable modes can arise at the combustion limit as long as the combustion lasts [4, 5]. Mathematical modeling of SHS initiation and propagation in a one-dimensional formulation was performed in [8].

The objective of the present computations is to obtain steady stable combustion modes of the reacting mixture in the gap under the condition of complete fusion of the welded aluminum sheets at the interface with the combustible mixture. The following initial reference data were used:

1. Linear sizes of the region:  $L_x = 2$  cm,  $L_y = 3$  cm,  $d = 1$  cm, and  $\delta = 1$  mm.
2. The thermophysical properties of the powder mixture in the solid state and in the liquid phase are

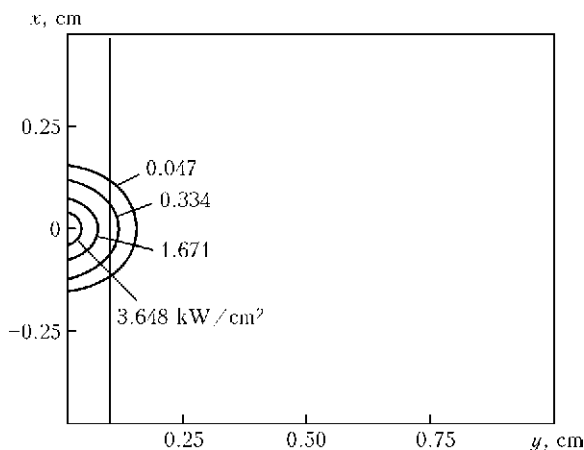


**Figure 2.** Distribution of intensity of absorbed power in a radiation spot

assumed to be constant and independent of temperature:  $\rho_{1s} = \rho_{1m} = 1.25$  g/cm<sup>3</sup>,  $c_{1s} = c_{1m} = 454$  J/(kg·K),  $\lambda_{1s} = \lambda_{1m} = 16$  J/(m·s·K).

3. Thermophysical properties of aluminum:

- in the solid state:  $\rho_{2s} = 2.7$  g/cm<sup>3</sup>,  $c_{2s} = 910$  J/(kg·K), and  $\lambda_{2s} = 233$  J/(m·s·K);
- in the liquid phase:  $\rho_{2m} = 2.6$  g/cm<sup>3</sup>,  $c_{2m} = 960$  J/(kg·K),  $\lambda_{2m} = 62$  J/(m·s·K),  $T_m = 933$  K, and  $H_m = 167$  kJ/kg.

4. Constants of the kinetics of SHS chemical reactions of the powder mixture:  $Q_c = 5.25 \cdot 10^9$  J/m<sup>3</sup>,  $k_p = 1.51 \cdot 10^6$  kg/(s·m<sup>3</sup>), and  $p = 0.8$ ,  $E_a = 34$  kJ/mol.

5. Other parameters:  $W = 600$  W,  $\omega_0 = 850$   $\mu$ m,  $A(\gamma) = 0.14$ ,  $T_0 = 300$  K, and  $v_w = 0.12$  m/s.

The kinetics of chemical reactions of high-temperature synthesis of the powder mixture is chosen by analyzing the experimental results reviewed in [4, 5].

Numerical investigations were performed with the physical parameters of the problem varied within wide ranges, e.g. the width  $\delta$  of the gap where the reacting mixture is located, the thermophysical properties of the mixture, the beam velocity, the beam diameter, etc.

Figure 2 shows the distribution of the intensity of radiation absorbed by the material. As the primary role of radiation is the initiation of SHS reactions, the laser beam parameters were chosen so that that the maximum part of the energy entered the domain  $\Omega_1$  between the sheets. Radiation whose power is lower approximately by an order of magnitude is incident onto the metal, domain  $\Omega_2$ .

Figures 3–5 show the computed results demonstrating steady combustion of the mixture in a coordinate system fitted to the laser beam, as well as heating and fusion of the metal. The radiation power of 600 W affecting the joint surface is only sufficient to initiate chemical reactions in its upper part. The emerging combustion wave penetrates throughout the entire depth of the joint already in a self-propagating mode.

The isolines in Figure 3 show the degree of conversion of the material in the combustion wave; the width of the zone of chemical reactions is 2–3 mm. The combustion-wave velocity practically coincides with the beam velocity  $v_w = 0.12$  m/s. The slope of the combustion front in the  $xz$  plane characterizes a certain delay of the combustion wave at the lower part of the joint.

The isolines of the temperature field in a chemically active zone and in the metal are plotted in Figures 4 and 5 in two mutually perpendicular planes. The combustion-wave structure has a typical «plateau» with a high gradient of temperature in the front. Intense heat removal into the metal sheet occurs. Owing to high thermal conductivity of aluminum, the thermal wave in the metal propagates faster and is able to heat the lower part of the joint. The maximum temperature in the combustion wave is 4643 K. Such a high temperature is obtained because the problem is solved without allowance for heat exchange with the ambient medium. Note that the experimental SHS reactions described in the literature define the range of combustion temperature reached (1500–4000 K) [4, 5, 9].

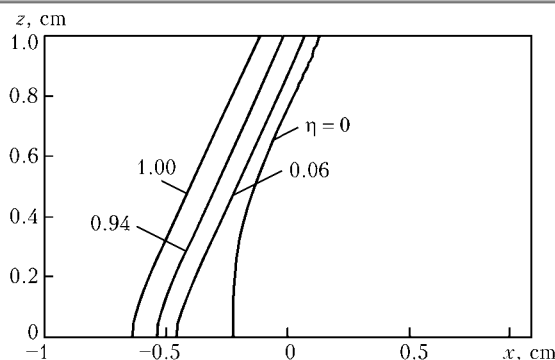


Figure 3. Conversion depth isolines at the axis of symmetry  $y = 0$

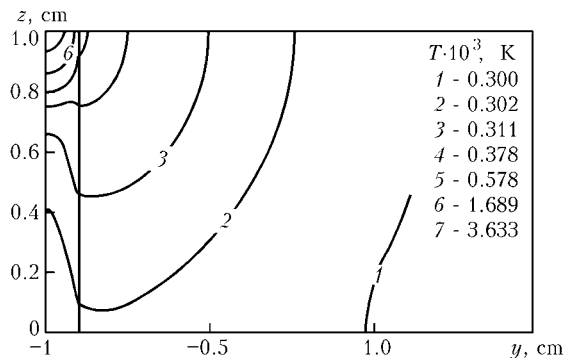


Figure 5. Temperature isolines in the  $zy$  plane,  $x = 0$

Figure 6 shows that the combustion wave propagating in the powder heats the contact surfaces of the aluminum sheets throughout their thickness to a temperature above the melting point (933 K), which leads to formation of a welded joint after cooling. The maximum temperature (1256 K) in the aluminum melt is significantly lower than its boiling point (2723 K). This indicates that welding occurs in the deep fusion mode without formation of a vapor-gas zone.

## CONCLUSION

A mathematical model for in-depth fusion of metal sheets joined by laser welding is described in the paper. The model is based on a physical-chemical mechanism of fusion of the welded joints with the use of the energy of chemical interaction of SHS powder systems. The reacting mixture placed in a narrow gap between two heat-conducting sheets is initiated by a focused laser beam moving continuously along the boundary between the sheets. The power of the laser radiation and physical-chemical properties of the reacting powder necessary to ensure a sufficient magnitude of welding speed and fusion depth are determined. The computational experiments performed made it possible to theoretically justify the possibility of SHS laser welding of aluminum sheets in a stable mode with the velocity of the gasless combustion front in the powder mixture not exceeding the welding speed.

It was calculated a SHS laser welding of aluminum applied in aircraft industry and other fields of mechanics. A fine mixture of powders was used as a SHS reacting material. The calculations have been made

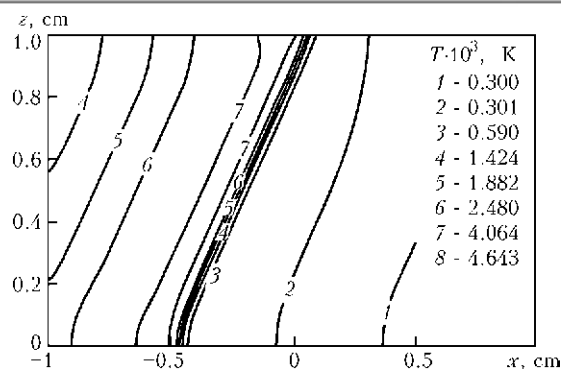


Figure 4. Temperature isolines at the axis of symmetry  $y = 0$

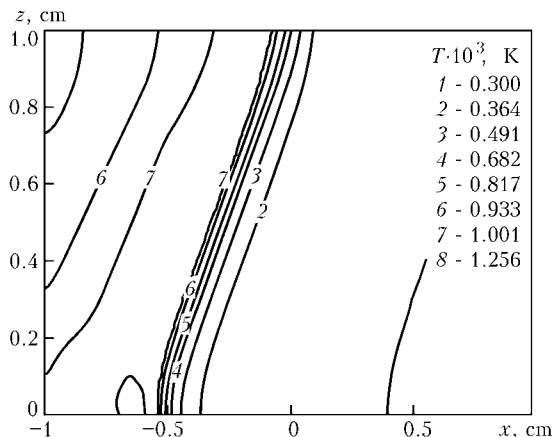


Figure 6. Temperature isolines at the contact boundary between the metal and combustible mixture

for determining the temperature fields in the welding zone, a position of an inner melting boundary, and a form of the molten pool. In accordance with the calculation results one can determine a necessary laser power, quantity and composition of the chemically reacted powder and to make a prediction. These actions are necessary for obtaining a sufficient in size fusion zone and providing a stable welding of sheet materials without formation of a vapor channel.

1. Merzhanov, A.G., Borovinskaya, I.P., Shtejnberg, A.S. et al. (1980) *Method of material joining*. USSR authors' cert. 747661.
2. Shcherbakov, V.A., Shtejnberg, A.S. (1993) Welding of refractory materials. *J. Self-Propagating High-Temp. Synthesis*, 2(4), p. 357-369.
3. Shcherbakov, V.A. (2001) Exothermal electric welding of steel-containing hard alloy. In: *Self-propagating high-temperature synthesis: Theory and practice*. Chernogolovka, p. 255-270.
4. Merzhanov, A.G. (1983) Self-propagating high-temperature synthesis. In: *Physical chemistry. Modern problems*. Moscow: Khimiya, p. 6-45.
5. Merzhanov, A.G. (1990) Self-propagating high-temperature synthesis: Twenty years of research and findings. In: *Combustion and plasma synthesis of high-temperature materials*. New York: VCH Publ., p. 1-53.
6. Samarsky, A.A., Moiseenko, B.D. (1965) Efficient scheme of through computations for a multidimensional Stefan problem. *Zhurnal Vyssh. Mat. Mat. Fiz.*, 5(5), p. 816-827.
7. Budak, B.M., Soloviova, E.N., Uspensky, A.B. (1965) Differential method with smoothing of coefficients for solving the Stefan problems. *Ibid.*, 5(5), p. 828-840.
8. Kovalev, O.B., Fomin, V.M. (1997) The problem of propagation of a gasless combustion wave over a mixture of reacting metal powders. *Comb., Expl., Shock Waves*, 33(2), p. 183-188.
9. Odawara, O. (1998) Combustion mechanisms in combustion synthesis. In: *Chemistry of combustion synthesis*. Moscow: Mir, p. 27-39.

# MODEL OF EVAPORATION-CONDENSATION PROCESSES IN WELDING AND MATERIAL TREATMENT

I.V. KRIVTSUN, V.F. DEMCHENKO and A.B. LESNOJ  
E.O. Paton Electric Welding Institute, NASU, Kiev, Ukraine

A simplified model of the physical phenomena occurring in the Knudsen layer of vapor, which is formed near the metal surface during its convective evaporation or condensation of the vapor phase on this surface is proposed. The model allows one to calculate the rate of condensation/evaporation, as well as mass, momentum and energy fluxes to/from the condensed phase surface, depending on the temperature and concentration of ambient vapor/gas, temperature of the surface and value of the condensation coefficient. With the help of the proposed model the numerical analysis of evaporation and condensation processes on the plane metal surface having uniform temperature has been made.

In various technologies of joining and treatment of metallic materials (laser and electron beam welding, vacuum arc and electron beam remelting, PVD processes etc.) the technological process course, operating characteristics and quality of a finished product are substantially affected by heat and mass transfer caused by metal evaporation and its condensation from the vapor phase. The most in-depth analysis of the evaporation-condensation processes is based on a kinetic description of the vapor phase within the frames of either Boltzmann equation [1], or kinetic equation with the model integral of collisions [2, 3], which solution requires using complex numerical methods and powerful computers.

An example of a simpler description of these processes is the approach based on consideration of the Knudsen layer (forming in the vapor phase near the condensed matter boundary) as a gas dynamic discontinuity, taking certain assumptions concerning the explicit form of distribution functions of vapor particles at the boundaries of this layer and using balance conditions expressing conservation of mass, momentum and energy of the evaporated material particles. Earlier, a similar approach was realized to describe the convective mode of surface evaporation of metals both into vacuum [4], and into a medium with back pressure [5], provided the condensation coefficient  $\alpha$  equals one.

In this paper, such an approach is generalized to describe the process of vapor condensation on a flat uniformly heated surface. The latter means that the curvature of the condensed phase surface and the scale of the temperature change along this surface are essentially larger than the Knudsen layer thickness  $L_K$  equal to a few mean free paths of the vapor particles. Moreover, this generalization provides for taking into account the influence of the condensation coefficient  $\alpha$  (defined as ratio of the number of particles absorbed by the surface of condensed matter to the total number of particles incident on this surface) on the rates of vaporization and condensation.

Further we restrict our consideration to the stationary processes of evaporation of a single-component

material and condensation of vapor on the surface of this material. It should be noted here that such a consideration still stands for the vapor condensation on the surface of another material, provided this surface has already been covered with a thick enough layer of the condensing material.

For mathematical description of the evaporation-condensation processes, a system of coordinates with axis  $OZ$  directed along the outer normal to the surface of the condensed phase was chosen, and this surface was taken as plane  $z = 0$ . The vapor is assumed to be a monatomic perfect gas which in the gas dynamic region (outside the Knudsen layer) is in local thermodynamic equilibrium at temperature  $T$  and has concentration  $n$ . Let normal to the surface directional velocity of the vapor be denoted as  $u$  ( $u > 0$  in case of evaporation,  $u < 0$  in case of vapor condensation). Then the distribution function of the vapor particles at the Knudsen layer outer boundary may be represented as

$$f(\mathbf{v})|_{z=L_K} = n \left( \frac{m}{2\pi kT} \right)^{3/2} \exp \left\{ -\frac{m}{2kT} [v_{\parallel}^2 + (v_z - u)^2] \right\}, \quad (1)$$

where  $m$  is the vapor atom mass;  $k$  is the Boltzmann constant;  $v_{\parallel}^2 = v_x^2 + v_y^2$ .

The distribution function of the particles emitted by the surface can be written assuming that at  $z = 0$  these particles are in thermal equilibrium with the condensed phase surface:

$$f(\mathbf{v})|_{z=0} = \alpha n_s \left( \frac{m}{2\pi kT_s} \right)^{3/2} \exp \left\{ -\frac{m}{2kT_s} [v_{\parallel}^2 + v_z^2] \right\}, \quad (2)$$

$$v_z > 0,$$

where  $T_s$  is the surface temperature;  $n_s$  is the correspondent concentration of saturated vapor which can be defined by means of the well-known relation [4]

$$n_s = \left( \frac{2\pi m c_0^{*2}}{kT_s} \right)^{3/2} \exp \left( -\frac{\lambda}{kT_s} - 1 \right). \quad (3)$$



Here  $v_0$  is the Debay frequency of atomic oscillation in the condensed matter;  $\lambda$  is the work function of an atom.

It was assumed in the evaporation process description [5] that as a result of collisions of the particles emitted by the surface, back-scattered particles appeared in the vapor flow, the distribution function of which at the phase interface was chosen proportional to  $f(\mathbf{v})|_{z=L_K}$ :

$$f(\mathbf{v})|_{z=0} = \beta f(\mathbf{v})|_{z=L_K}, \quad v_z < 0, \quad (4)$$

where  $\beta$  is the proportional coefficient determining, in fact, the concentration of the vapor particles returning to the surface.

It is assumed when considering the condensation process that within the Knudsen layer due to collisions of the condensing vapor particles with evaporating particles changes take place not only in concentration, but also in mean velocity of the particles moving towards the surface. This fact may be taken into account by writing the distribution function of the particles approaching the phase interface as follows [6]:

$$f(\mathbf{v})|_{z=0} = \beta n \left( \frac{m}{2\pi kT} \right)^{3/2} \exp \left\{ -\frac{m}{2kT} [v_x^2 + (v_z - u_0)^2] \right\}, \quad (5)$$

$$v_z < 0,$$

where  $u_0$  is the mean velocity of condensing particles at  $z = 0$ .

Having set the explicit form of the distribution functions, one can calculate: mass flux

$$q_m = \int v_z m f(\mathbf{v}) d\mathbf{v}, \quad (6)$$

momentum flux

$$q_p = \int v_z m v_z f(\mathbf{v}) d\mathbf{v}, \quad (7)$$

and translational energy flux

$$q_e = \int v_z \frac{m(v_x^2 + v_y^2 + v_z^2)}{2} f(\mathbf{v}) d\mathbf{v}. \quad (8)$$

Comparing the corresponding fluxes at the Knudsen layer boundaries and taking into consideration the fact that not all the particles incoming the condensed phase surface are absorbed by it, one can obtain:

$$2\bar{u}\bar{\pi} + \alpha\beta \{ \exp(-\bar{u}_0^2) - \bar{u}_0\bar{\pi} \operatorname{erfc}(\bar{u}_0) \} = \frac{\alpha}{\bar{n}\bar{T}^{1/2}};$$

$$2(2\bar{u} + 1) + \frac{2 - \alpha}{\sqrt{\pi}} \beta \times$$

$$\times \{ 2\bar{u}_0 \exp(-\bar{u}_0^2) - (2\bar{u}_0^2 + 1)\sqrt{\pi} \operatorname{erfc}(\bar{u}_0) \} = \frac{\alpha}{\bar{n}\bar{T}}; \quad (9)$$

$$\bar{u}\bar{\pi} \left( \bar{u}^2 + \frac{5}{2} \right) + \alpha\beta \times$$

$$\times \left\{ \left( \frac{\bar{u}_0^2}{2} + 1 \right) \exp(-\bar{u}_0^2) + \frac{\bar{u}_0}{2} \left( \bar{u}_0^2 + \frac{5}{2} \right) \sqrt{\pi} \operatorname{erfc}(\bar{u}_0) \right\} = \frac{\alpha}{\bar{n}\bar{T}^{3/2}}.$$

Here

$$\bar{u} = u \left( \frac{m}{2kT} \right)^{1/2}; \quad \bar{u}_0 = u_0 \left( \frac{m}{2kT} \right)^{1/2}; \quad \bar{n} = \frac{n}{n_s};$$

$$\bar{T} = \frac{T}{T_s}; \quad \operatorname{erfc}(x) = \frac{2}{\sqrt{\pi}} \int_x^\infty \exp(-\xi^2) d\xi. \quad (10)$$

The balance relations (9) describing the condensation process represent a system of three algebraic equations as regards the unknown  $u$ ,  $u_0$  and  $\beta$ , which allows having the set values of the temperature  $T$  and the vapor phase concentration  $n$ , the surface temperature  $T_s$  (and the corresponding saturated vapor concentration  $n_s$ ), as well as of the condensation coefficient  $\alpha$ , to define the velocity  $u$  of condensing vapor at the Knudsen layer outer boundary. It should be noted here that the values  $n$  and  $T$  included into these relations may not be interrelated by the saturated vapor adiabatic equation, i.e. this vapor may be both superheated, and supercooled (supersaturated). Possible in the latter case, volumetric condensation of the vapor phase in gas dynamic region and formation of microdrops will be neglected.

When  $u$  substitutes for  $u_0$  in (9), this system of equations may be used to analyze the evaporation process, as well. In this case, the unknown values are  $n$ ,  $T$  and  $\beta$ , and the velocity  $u$  is an external parameter which is defined by the state of vapor flow in the gas dynamic region [5]. Thus, the system of equations (9) generalizes the known results [5] obtained to describe the rapid surface evaporation process for the case of an arbitrary value of  $\alpha$ .

Since the system of balance relations under consideration describes both the condensation process and convective evaporation process, its solution allows analyzing all the states of vapor near the condensed phase surface. In particular, the solid curve in Figure 1 shows the edge of the region of vapor phase states at which condensation of this phase on the surface with a set temperature ( $\alpha = 1$ ) is possible. The dashed curve represents the saturated vapor adiabatic curve  $\bar{n} = \frac{1}{T^{3/2}} \exp \left[ -\bar{\lambda} \left( \frac{1}{T} - 1 \right) \right]$  at  $\bar{\lambda} \equiv \frac{\lambda}{kT_s} = 20$  dividing these states into the regions of superheated and supercooled vapor. The vapor phase states near the condensed medium surface that are characterized by the values  $\bar{n}$  and  $\bar{T}$  under the boundary curve cannot be stationary, since this vapor will be driven back from the surface by the expanding vapor flow, for which according to [5] concentration and temperature values lying on the evaporation curve will be found (dotted curve in Figure 1).

Let us consider in detail the process of convective metal evaporation into the surrounding gas having the temperature  $T_0$  and pressure  $p_0$ . Such process characteristics, important from the point of view of technological applications, as the mass flux  $q_m$ , the total energy flux  $q_E$  (taking into account the latent heat of evaporation) from the evaporating surface, as well

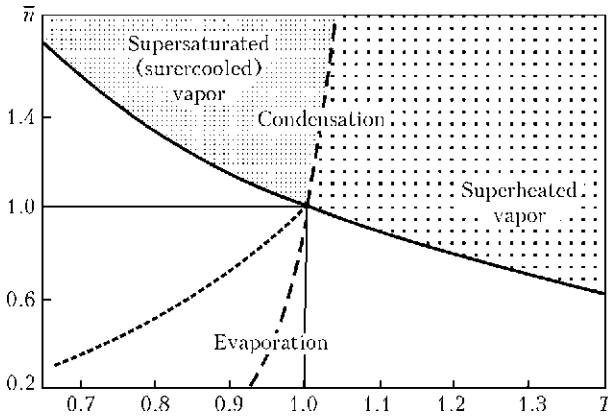


Figure 1. Vapor state diagram

as the total vapor pressure  $p$  (including the reactive component) on this surface may be defined by means of the expressions (6)–(8), which give

$$\begin{aligned} q_m &= mn u; & q_E &= nu \left( \frac{5}{2} kT + \frac{\mu^2}{2} \right) + \frac{q_m}{m} \lambda; \\ p &= n(kT + mu^2), \end{aligned} \quad (11)$$

where the vapor concentration  $n$  and temperature  $T$  are calculated by solving the system (9), and the vapor velocity  $u$  at the Knudsen layer outer boundary is found by the flow pattern in the gas dynamic region. In case when the vapor flow just outside the Knudsen layer is subsonic, to find this value one can use a known relation [5]:

$$u = s_0 \left( \frac{nkT}{p_0} - 1 \right)^{1/2} / \gamma_0 \sqrt{1 + \frac{\gamma_0 + 1}{2\gamma_0} \left( \frac{nkT}{p_0} - 1 \right)}. \quad (12)$$

Here,  $s_0$  is the speed of sound in the ambient gas;  $\gamma_0$  is its specific heat ratio. It should be noted here that expression (12) is right provided the ambient gas is at rest, and the Knudsen layer is stationary and adjoins the evaporating metal surface  $z = 0$  moving (due to mass losses) with the velocity  $v = q_m / \rho \ll u$ , where  $\rho$  is the metal density.

Calculated in this way, the vapor expansion relative velocity dependencies (the Mach number  $M =$

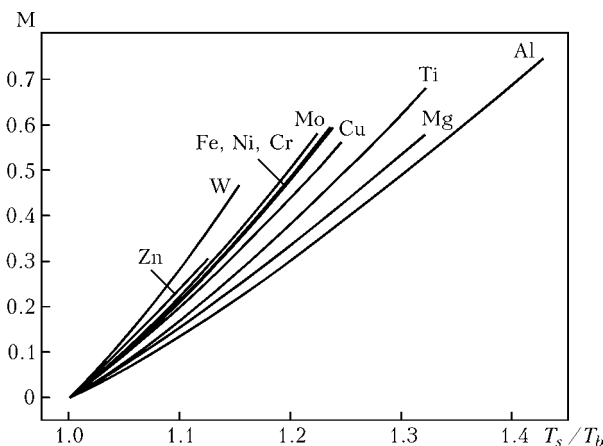


Figure 2. Mach number of vapor flow at the Knudsen layer outer boundary versus dimensionless temperature of evaporating metal surface ( $\alpha = 1$ )

$= u/s$ , where  $s = \sqrt{\frac{5kT}{3m}}$  is the local speed of sound)

at the Knudsen layer outer boundary for various metals on the dimensionless temperature of the metal surface  $T_s/T_b$ , where  $T_b$  is the boiling temperature (temperature at which the saturated vapor pressure is equal to the atmospheric one), are presented in Figure 2. Figure 3 shows the calculation dependencies of the mass and energy fluxes, as well as of the vapor pressure on the liquid aluminum surface on the temperature of this surface at convective evaporation into the argon medium of atmospheric pressure having the temperature 300 K.

The results of calculation of the vapor condensation process on a flat uniformly heated surface are presented in Figures 4 and 5. In particular, Figure 4 shows the influence of the concentration and temperature of the vapor phase on its condensation rate at  $\alpha = 1$ . It follows from the curves presented in this Figure that the condensing vapor flow velocity at the Knudsen layer outer boundary essentially depends on the degree of the vapor superheating or supersaturation with respect to the saturated vapor corresponding to the given value of  $T_s$ . Besides, since the vapor is assumed to be a monatomic perfect gas, based on (10) one has  $|\bar{u}| = \sqrt{\frac{5}{6}} M$ . Thus, at some values of  $\bar{n}$  and  $\bar{T}$  the condensing vapor flow velocity may significantly exceed the local speed of sound.

In Figure 5 illustrated is the influence of the condensation coefficient  $\alpha$  on the vapor phase condensation rate. The calculation data presented are evidence of the fact that at low values of  $\alpha$  a smooth enough variation of  $u(\alpha)$  is observed, whereas at  $\alpha > 0.5$  the condensing vapor flow velocity essentially depends on the condensation coefficient value. This circumstance should be taken into account when analyzing the metal vapor condensation process, since for most metals the condensation coefficient value is within  $0.8 < \alpha < 0.9$  [6], and the use of approximation  $\alpha = 1$  may produce nearly twice as high condensation rate (see Figure 5).

Knowing the condensing vapor velocity in the gas dynamic region, by means of expressions (11) one can calculate the mass and total energy fluxes, as well as the vapor pressure on the condensed phase surface. For instance, in case of condensation of saturated aluminum vapor having the temperature  $T = 2720$  K, on the liquid aluminum surface at  $T_s = 2620$  K the condensing vapor velocity is  $248.2$  m/s,  $q_m = 34.2$  kg/(m<sup>2</sup>·s),  $q_E = 4.68 \cdot 10^8$  W/m<sup>2</sup> and  $p = 0.11$  MPa. These calculation data are evidence of the necessity of taking into account the heat and mass transfer processes caused by metal evaporation, expansion and condensation of the metal vapor, e.g. in the keyhole which is formed in the melt in laser and electron beam welding.

In conclusion, it should be noted that the simplified model considered allows one to calculate the evaporation and condensation process characteristics without involving powerful computers and with accu-

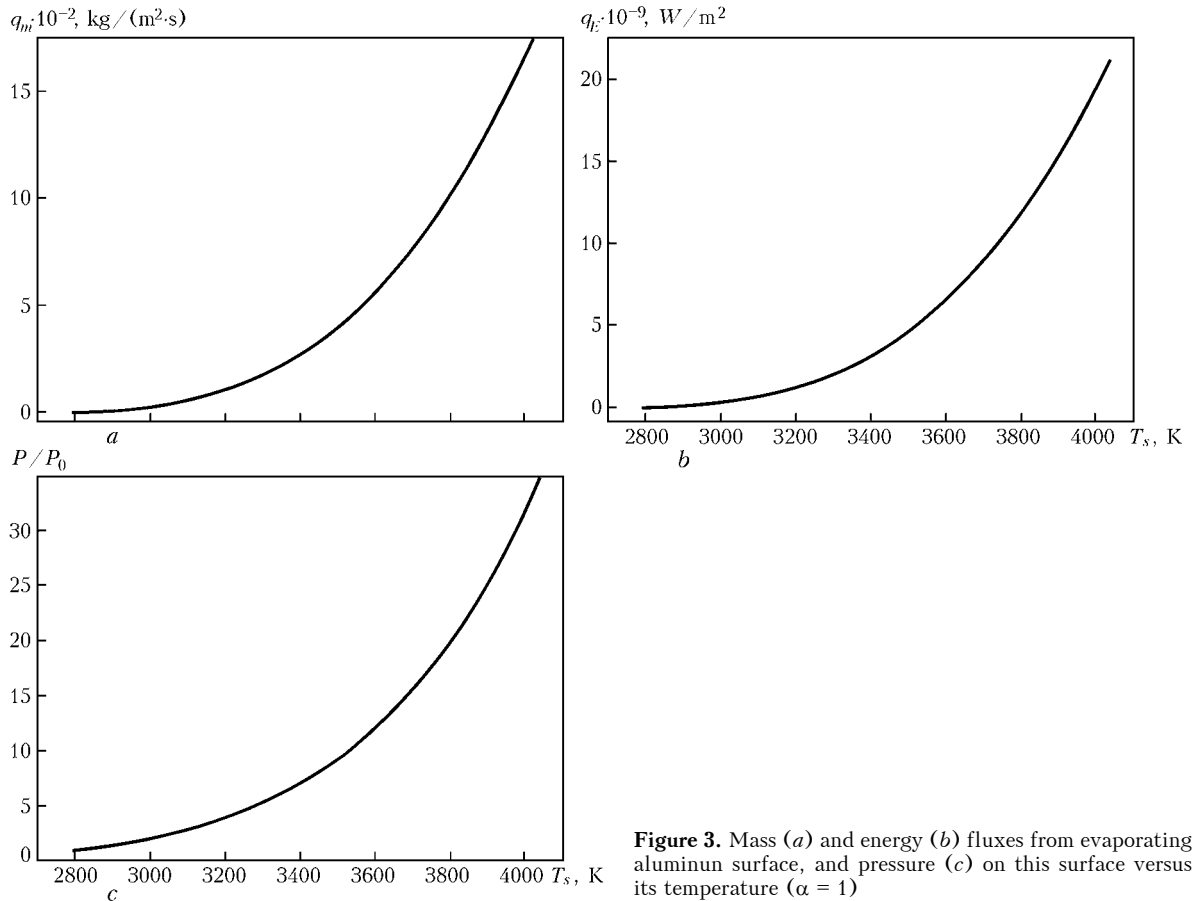


**Figure 3.** Mass (a) and energy (b) fluxes from evaporating aluminum surface, and pressure (c) on this surface versus its temperature ( $\alpha = 1$ )

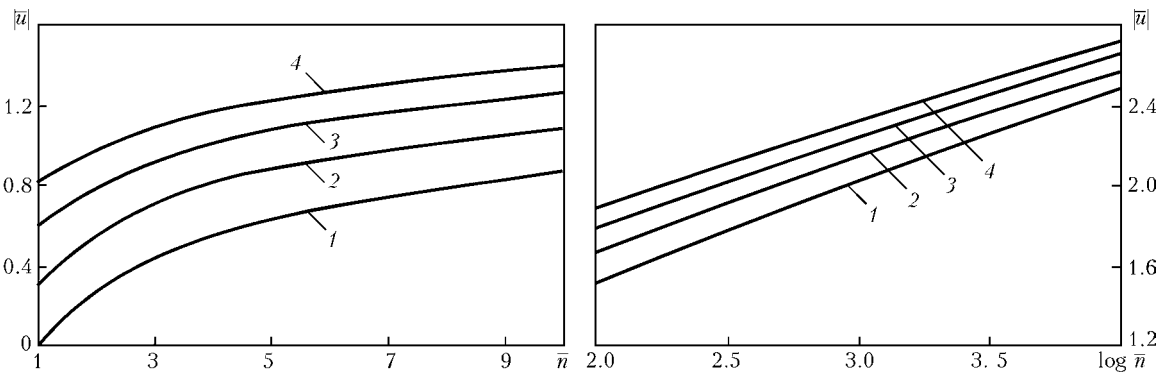


**Figure 4.** Dimensionless velocity of condensing vapor flow at the Knudsen layer outer boundary versus dimensionless vapor concentration: 1 -  $T/T_s = 1$ ; 2 - 2; 3 - 4; 4 - 8

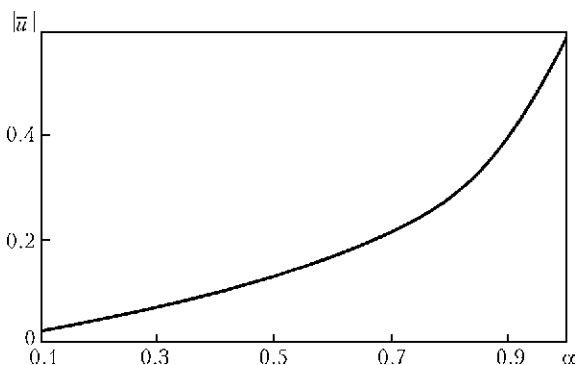


**Figure 5.** Influence of condensation coefficient on dimensionless velocity of condensing vapor ( $\bar{n} = 2$ ;  $\bar{T} = 2$ )

uniformly heated surfaces, as well as for analysis of evaporation and condensation of multicomponent substances. Similar conditions are realized in many technological processes of welding and material treatment based on using high concentration heat sources.

1. Cheremisin, F.G. (1972) Motion of rarefied gas between plane emitted and absorbed surfaces. *Doklady AN SSSR. Mekhanika Zhidkosti i Gaza*, **6**, p. 176-178.
2. Sone, Y., Onishi, Y. (1973) Kinetic theory of evaporation and condensation. *J. Phys. Soc. of Japan*, **35(6)**, p. 1773-1776.
3. Bishaev, A.M., Rykov, V.A. (1978) Intercondensation of monatomic gas at the small Knudsen number. *Zhurnal Vych. Matematiki i Mat. Fiziki*, **18(3)**, p. 709-717.
4. Anisimov, S.I., Imas, Ya.A., Romanov, G.S. at al. (1970) *Effects of high power radiation on metals*. Moscow: Nauka.
5. Knight, Ch.J. (1979) Theoretical modeling of rapid surface vaporization with back pressure. *AIAA J.*, **17(5)**, p. 519-523.
6. Demchenko, V.F., Krivtsun, I.V., Nesterenkov, V.M. (2004) Model of evaporation-condensation processes on the plane surface. *Dopovidi NANU*, **1**, p. 90-94.

racy sufficient for practical applications. It makes this model promising for investigation of heat and mass exchange phenomena due to the vapor phase for non-

# NUMERICAL MODELLING OF THERMAL CYCLES IN STEEL DURING SURFACING AND WELDING WITHOUT PREHEATING AND THEIR COMPARISON WITH EXPERIMENTAL DATA

M. LOMOZIK

Instytut Spawalnictwa, Gliwice, Poland

By means of the ANSYS 5.6 programme thermal fields in the HAZ of overlay-welded and welded steel without preheating have been modelled and multiple thermal cycles numerically calculated. The designed geometric models are of the 2D type with 3D characteristics. The number of overlay-welded and welded layers was varied from 1 to 6. After numerical calculations for the individual overlay-welded and welded layers, the course of thermal cycles was analyzed for the 1st, 3rd and 6th layer. Such a procedure followed from practical utilization of the computation results. ASME regulations recommend welding of minimum 6 layers to get the desired tempering effect of hardened microstructures in the HAZ, which are characterized by unfavourable toughness. Parameters of thermal cycles in the HAZ of overlay-welded and welded steel, calculated numerically and measured experimentally, were compared. Moreover the effect of temperature field asymmetry was raised, which is caused by the heat flow from successive layers of the overlay weld.

The postweld heat treatment (PWHT) is an important problem, as is the case in welding of components in the power industry. The objective of PWHT is the maximum reduction of welding residual stresses and the improvement of heat-affected zone (HAZ) and weld metal toughness. However, in the case of repair welding of big objects PWHT may cause serious difficulties. In those situations an effective means of ensuring proper high HAZ toughness is the application of so-called temper bead welding (TBW). The method consists in such a means and sequence of laying individual weld beads, to temper the martensitic microstructure in the HAZ of previously welded beads, by the controlled welding thermal cycle. The TBW technique enables lowering of hardness of martensitic and upper bainitic microstructures, which occur in the coarse grain region of the HAZ, and in consequence, toughness improvement of these welded joint zones.

To replace effectively the traditional PWHT by the TBW technique it is essential to gain knowledge on the temperature distribution at individual weld beads (layers) and on the influence of welding thermal cycles on structure transformations in the coarse grain HAZ regions.

**Mathematical modelling of temperature fields at various HAZ regions by means of the ANSYS program.** Results of numerical computations, performed by the application of the ANSYS program with a partition ability of the identified area into 32 thousands nodes and elements, are presented in this paper. Modelling of thermal fields in the HAZ region of steel has been performed under the influence of multiple welding thermal cycles with different parameters (maximum temperatures  $T_{\max}$  and cooling times  $t_{8/5}$ ).

The designed 2D models with 3D attributes have mapped multilayer welding and surfacing without preheating. The number of weld layers has been changed from 1 to 6. The technological input data (welding method; welding current  $I$ , A; arc voltage  $U$ , V; welding speed, cm/s; time passed between welding of successive layers; initial and interpass temperature, °C; and the joint thickness, mm) have been taken from the results of research projects [1, 2]. The physical properties of modeled steels, such as mass density  $DENS$  ( $\gamma$ ), kg/mm<sup>3</sup>; thermal conductivity  $KXX$  ( $\lambda$ ), cal/(mm·s·°C); and specific heat  $c$ , cal/(kg·°C), were taken from the literature ( $DENS$ ,  $KXX$  are the designations used in the ANSYS program) [3–5].

Thermal cycles measured during overlay TIG welding under argon shielding are presented in the research report [1]. The course of the experiment was as follows: on the SM400A steel plate 6 layers have been successively overlay-welded, one after another. The first layer consisted of 6 runs, and every next layer of 1 run less. The scheme of the overlay process is shown in Figure 1.

For numerical calculations a geometrical model has been used (Figures 2 and 3). The model has represented the experimental conditions.

The following general input data were used for numerical computations:

- base metal: unalloyed steel;
- welding filler metal: alloyed;
- overlay welding method: TIG without preheating, 6 layers;
- plate thickness:  $\delta = 20$  mm.

For technological data and physical properties see Tables 1–3.

Numerical computations have been performed for the overlay-welded layers 1–6 (see Figure 3), general

**Table 1.** Experimental conditions for TIG surfacing and welding at average welding speed  $v_{av} = 15$  cm/min and initial temperature  $T_{in} = 20$  °C [1]

Heat input $Q$ , kJ/cm	$I$ , A	$U$ , V
5.5	100	9.2
9.4	150	10.5
14.8	200	12.3

**Table 2.** Data at room temperature of 20 °C [4, 5, 7]

Physical value	Material 1 (base unalloyed steel)	Material 2 (alloyed steel melted weld metal)	Material 3 (alloyed steel solidified weld metal)
DENS ( $\gamma$ ), kg/mm <sup>3</sup>	$0.79 \cdot 10^{-5}$	$0.7 \cdot 10^{-5}$	$0.7 \cdot 10^{-5}$
KXX ( $\lambda$ ), cal/(mm·s·°C)	$0.96 \cdot 10^{-2}$	$0.2 \cdot 10^{-3}$	$0.4 \cdot 10^{-2}$
$c$ , cal/(kg·°C)	174	160	160

**Table 3.** Thermal conductivity at various temperatures for the base and weld metals [4, 5, 7]

Welded joint zone	KXX ( $\lambda$ ), cal/(mm·s·°C), at $T$ , °C			
	20	600	1200	1500
Material 1	0.0096	0.0075	0.0054	0.0005
Material 3 (layers 1–5 acc. to Figure 1)	0.0040	0.0032	0.0024	0.0002

view of the models and calculated thermal fields for the individual weld layers contains Table 4.

#### Numerical modelling results for overlay welding.

After numerical computations have been performed for the individual overlay-welded layers, the course of thermal cycles has been analysed for the first, third and sixth layer. The reason was the necessity of practical utilization of the calculated results. The ASME regulations [8] recommend a minimum of 6 welded (overlay-welded) layers to get the desired tempering effect of hardened microstructures, which occur in the HAZ and are characterized by unfavourable toughness.

Results of numerical calculations for the overlay-welded layers 1, 3 and 6 are presented in Figures 4–6, 7 and 8, and 9 and 10, respectively.

**Development of geometrical model concept and generation of computation mesh for welding process modelling.** One of the most important stages of the modelling process was the adoption of an optimal, from the practical point of view, geometrical model of the welded joint. The final shape of the geometrical model was decided by the welding practice and repair regulations of welded joints by means of the TBW technique. The following course of reasoning was approved. In a hypothetical structure part under service (e.g. power plant structure) a crack has been detected, which causes a risk for the farther safe operation. The defect has to be repaired by welding (Figure 11).

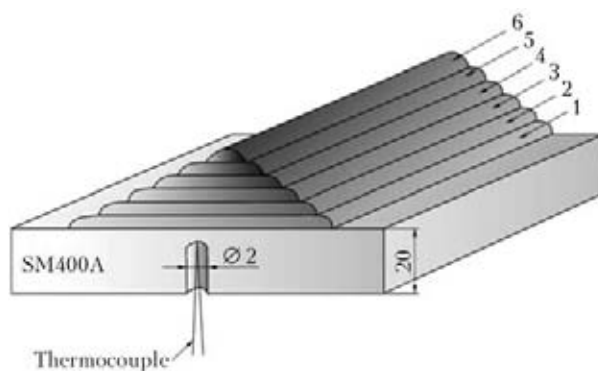


**Figure 1.** Scheme of overlay welding [1]

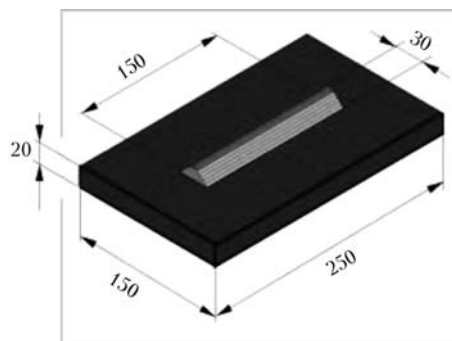


**Figure 2.** General view of the model of 3D version [6]

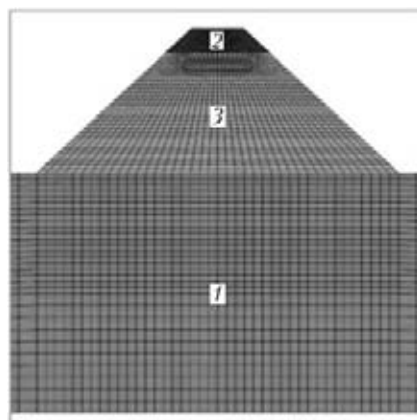


**Figure 3.** Model for overlay-welded zone numerical calculations with a finite element mesh [6]: 1 – base metal; 2 – melted weld metal; 3 – solidified weld metal

For numerical calculations the geometrical model shown in Figures 12 and 13 was applied.

**Modelling of thermal fields in the HAZ for welding conditions.** The following general input data have been taken for numerical calculations.











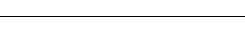

- base metal: unalloyed steel;
- filler metal: alloyed steel;
- welding method: TIG, without preheating, 6 welded layers;
- plate thickness:  $\delta = 40$  mm.

For technological data see Table 1, physical properties at room and elevated temperatures were the same as in Tables 2 and 3.

Results of numerical calculations for the welded layers 1, 3, 6 are presented in Figures 14–16, 17 and 18, and 19–22, respectively.

**Discussion of results.** In Table 5 thermal cycle parameters ( $T_{max}$  and  $t_{8/5}$ ) in the HAZ region, obta-

**Table 4.** General view of models and calculated thermal fields for the individual weld layers [6]

Overlay-welded layer No.	Model general view	Numerically calculated thermal field
1		
2		
3		
4		
5		
6		

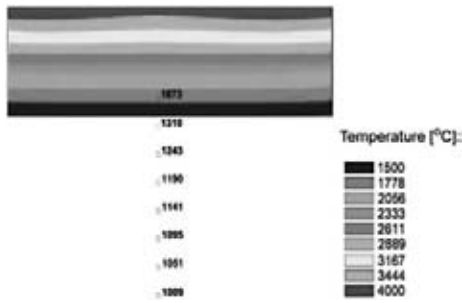


Figure 4. Welded layer 1: temperature distribution in nodes and fragment of temperature field

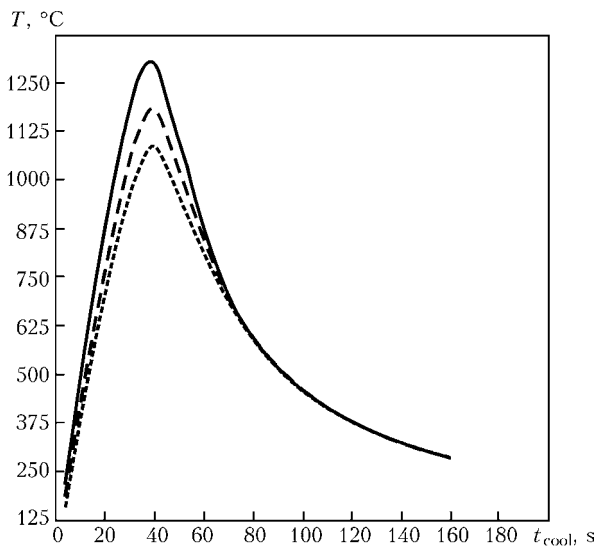


Figure 5. Welded layer 1: thermal cycles in nodes acc. to Figure 4 with  $T_{max} = 1310, 1190$  and  $1095$  °C

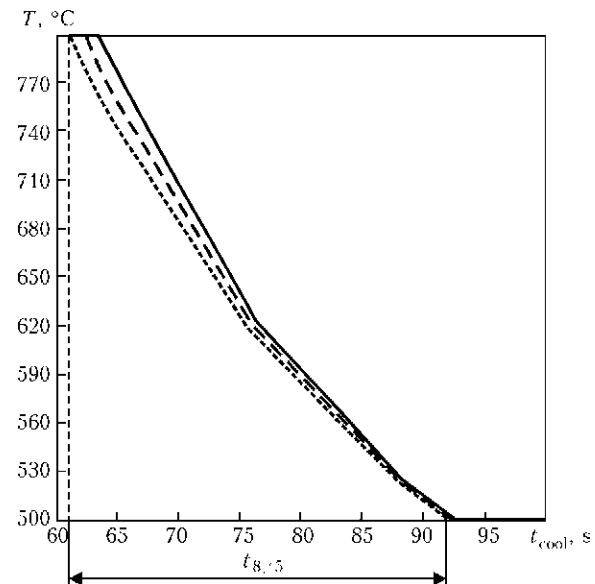


Figure 6. Welded layer 1: example of determination of  $t_{8/5}$  for thermal cycles acc. to Figure 5

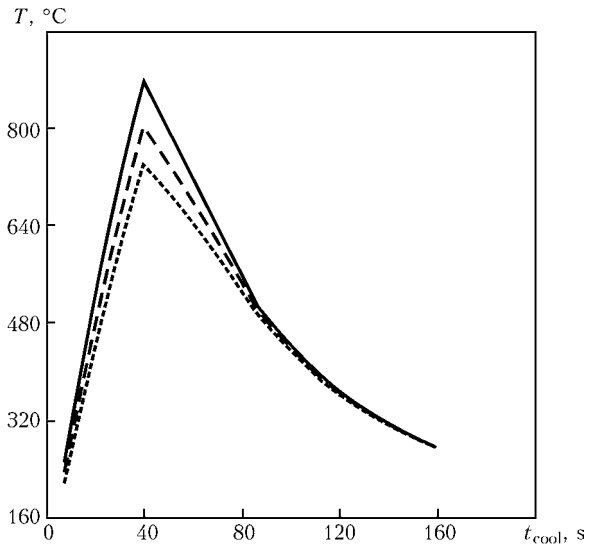


Figure 7. Welded layer 3: thermal cycles in nodes with  $T_{max} = 875, 804$  and  $740$  °C

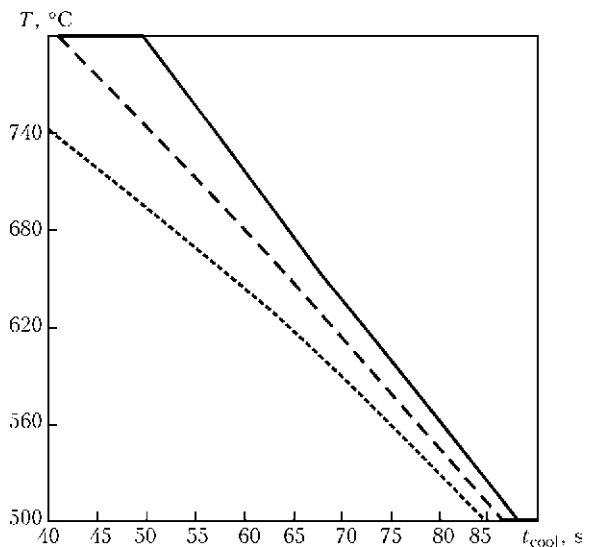


Figure 8. Welded layer 3: determination of  $t_{8/5}$  for thermal cycles acc. to Figure 7

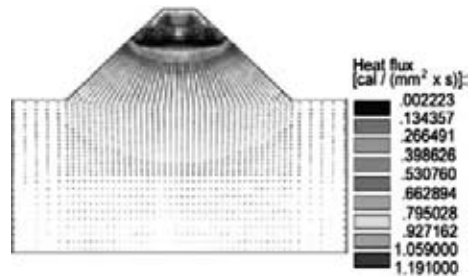


Figure 9. Welded layer 6: heat flux propagation [9] after welding termination

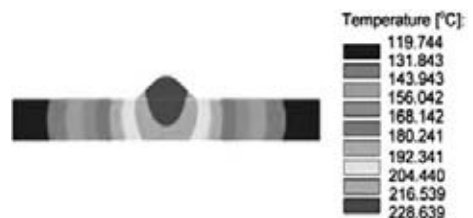


Figure 10. Welded layer 6: thermal field numerically calculated after 120 s of cooling stage

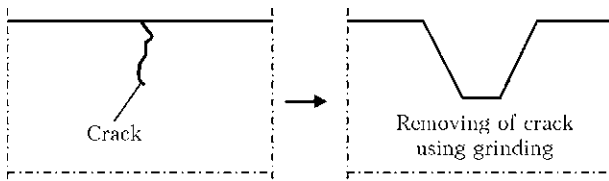


Figure 11. Example of crack in hypothetical structure part and its removal by machining [6]

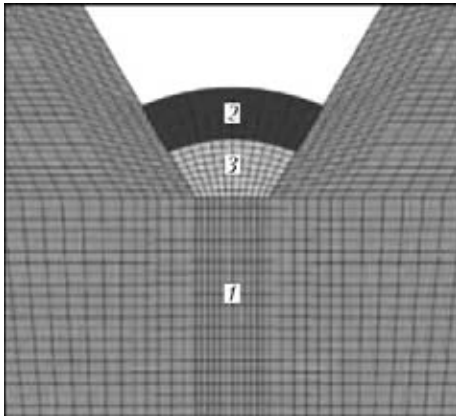


Figure 12. General view of geometrical model with finite element mesh divided into base (1), melted (2) and solidified (3) weld metals

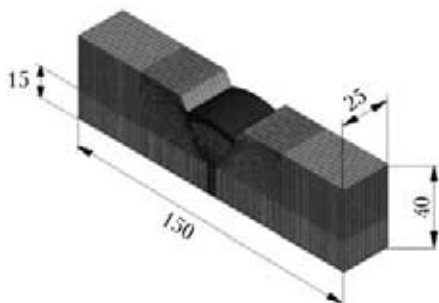


Figure 13. 3D model as in Figure 12 with finite element mesh

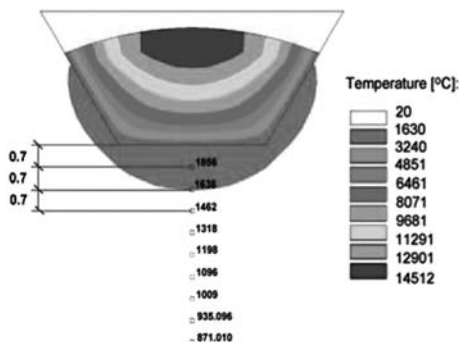


Figure 14. Welded layer 1: temperature distribution in nodes and temperature field

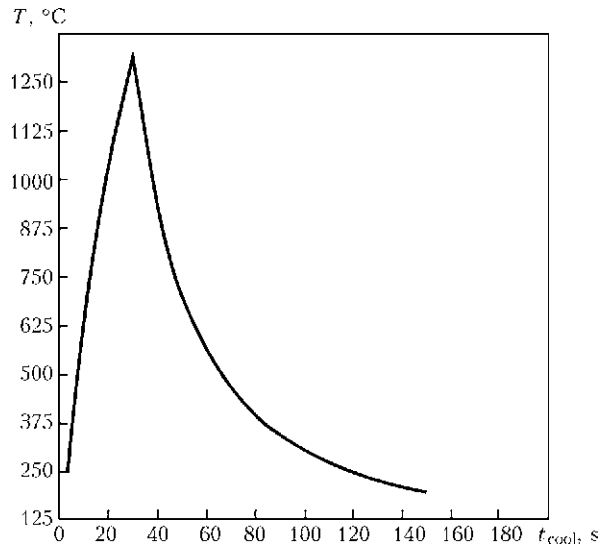


Figure 15. Welded layer 1: thermal cycle in node at distance of 2.8 mm from groove bottom with temperature of 1318 °C

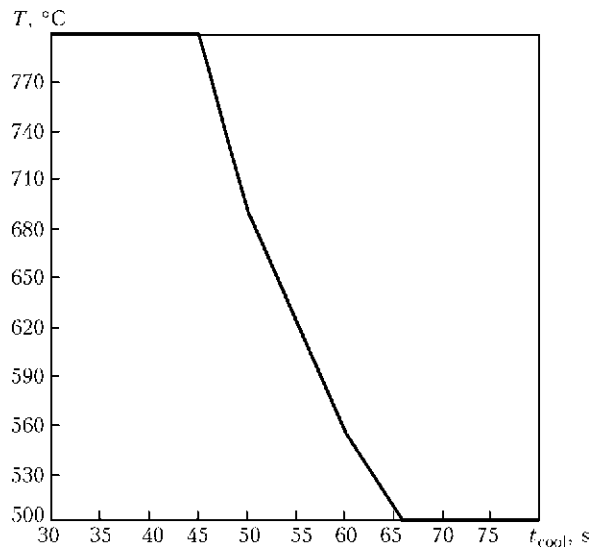


Figure 16. Welded layer 1: determination of  $t_{8/5}$  for thermal cycle acc. to Figure 15

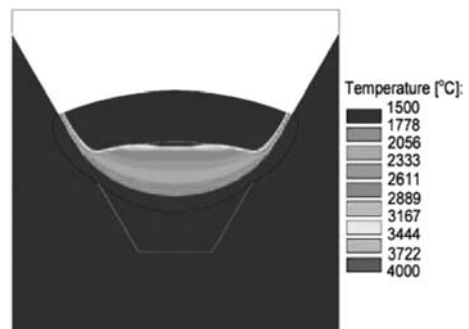


Figure 17. Welded layer 3: depth of penetration into base metal determined by the 1500 °C isotherm



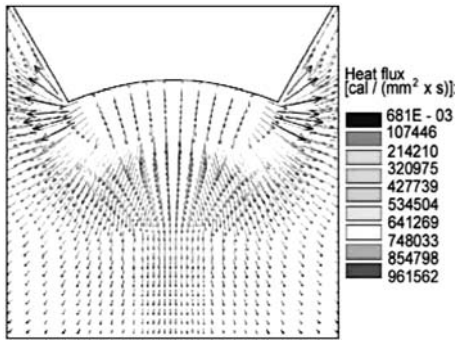


Figure 18. Welded layer 3: heat flux propagation after 30 s of welding termination

ined by numerical calculations for overlay welding and welding, are compared with those determined experimentally.

The data obtained by numerical modelling and presented in Table 5, enable anticipation of thermal process development in welded joints. From these data it is evident that beginning from the 4th layer up to the 6th layer, in the HAZ under the weld the maximum temperatures of the thermal cycles are lower than 800 °C, and the analysis of the increasing cooling time is not justified from the point of view of metals science.

In real welding conditions the thermal field shows asymmetry, which is caused by heat transfer during welding of consecutive beads in the layer. An attempt was made in numerical calculations to find how does the thermal field asymmetry influence the thermal conditions, which accompany the heating and cooling process of an overlay-welded specimen. An example of thermal field asymmetry in overlay-welded layer is shown in Figures 23 and 24.

Figure 23 shows that just after finishing the overlay-welding of 6 beads in the first layer a differentiation of temperatures occurs, the highest temperature is recorded in the last bead (on the right), and the lowest – in the first one (on the left). After 120 s of the cooling process the temperature level out in the hot specimen, and the asymmetry in the temperature field distribution decays (see Figure 24). It results that the analysis of thermal processes in the central part of the overlay-welded specimen can be

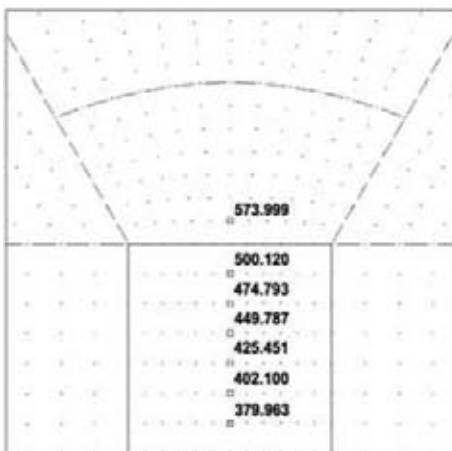


Figure 19. Welded layer 6: temperature distribution in nodes

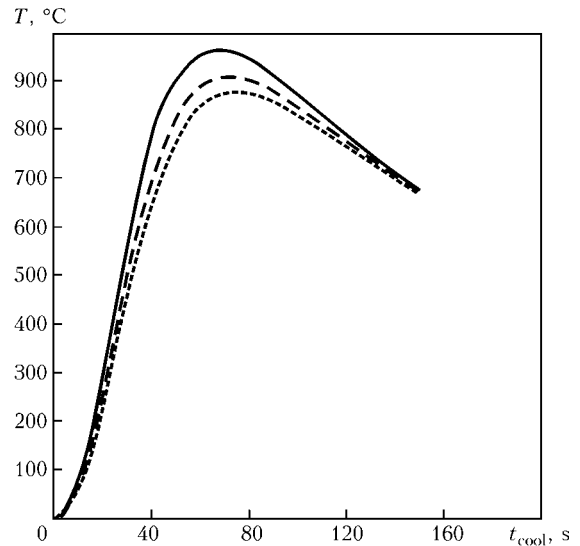


Figure 20. Welded layer 6: thermal cycles in nodes with  $T_{max} = 573, 500$  and  $449$  °C

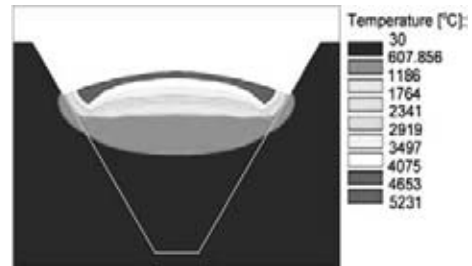


Figure 21. Welded layer 6: temperature field after 30 s from start of welding

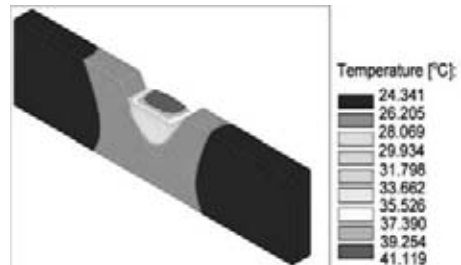


Figure 22. Welded layer 6: sector of the 3D model, calculated thermal field after 125 s of cooling phase

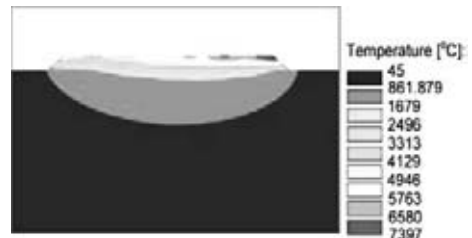


Figure 23. Numerically calculated temperature distribution illustrated the thermal field asymmetry as result of heating in welding of consecutive beads in layer 1 after 40 s

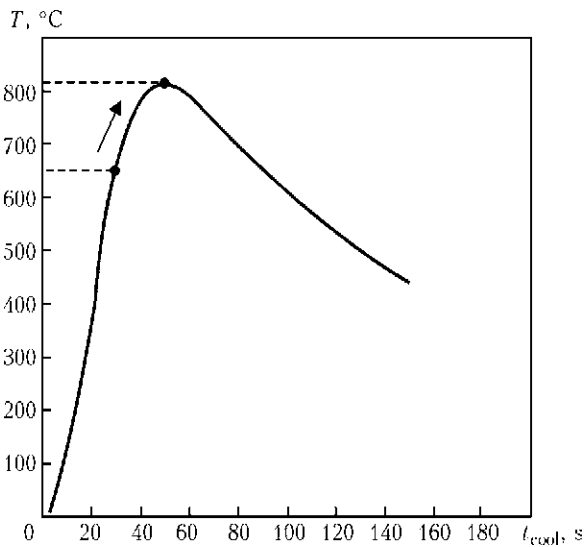


Figure 24. Numerically calculated temperature distribution in layer 1 after 120 s of cooling phase

**Table 5.** Overlay welding and welding thermal cycle parameters for HAZ

Overlay welded layer No.	Welding thermal cycle parameters								
	Numerical						Experimental for overlay welding		
	Overlay welding			Welding					
	$T_{max}, ^\circ C$	$t_{8/5}/CT, s$	$d, mm$	$T_{max}, ^\circ C$	$t_{8/5}/CT, s$	$d, mm$	$T_{max}, ^\circ C$	$t_{8/5}/CT, s$	$d_1, mm$
1	1310	30	0.5	1318	22	2.8	1336	20	1.2
	1190	31	1.5						
	1095	32	2.5						
2	1052	37	1.0	1031	26	1.4	1008	30	1.9
	1009	37	1.5						
	968	38	2.0						
3	875	39	1.0	808	48	2.1	783	60	2.8
	804	46	2.0						
	740	58	3.0						
4	685	61	1.0	674/728*	91	0.7	684	66	3.5
5	522	117	1.0	649/810*	72	0.7	628	69	4.2
6	440	–	2.0	449/880*	–	2.1	442	73	5.0

Notes.  $d$  – distance from weld groove bottom to HAZ;  $d_1$  – distance from thermocouple tip to fusion line; CT – cooling time for thermal cycles with  $T_{max}$  lower than 800 °C determined for temperature range of  $T_{max} - 500$  °C; \* –  $T_{max}$  of thermal cycle after taking into consideration the thermal inertia.



**Figure 25.** Welded layer 5: thermal cycle in node with  $T_{max} = 649$  °C and effect of thermal inertia

done without taking into consideration the influence of the temperature field asymmetry (the reading of temperature values and thermal cycles is done along the vertical symmetry axis of the overlay-welded specimen).

Beginning with the layer 4, the effect of thermal inertia was observed. For example, at the thermal cycle selected in a node with  $T_{max} = 649$  °C (Figure 25) the temperature still rises and reaches the maximum value of 815 °C. The effect of thermal inertia can be explained by changes of the thermal conductivity  $KXX (\lambda)$  with temperature, as shown in Figure 26.

It follows from Figure 26, *a* that for materials characterized by great thermal conductivity values ( $\lambda \gg 1$ ) the effect of thermal inertia does not occur. But the effect can be observed for materials with thermal conductivity values  $\lambda$  much lower than 1 at 20 °C (Figure 26, *b*) and its further decrease with increasing temperature [10].

From comparison of numerically calculated overlay welding data with those determined experimen-

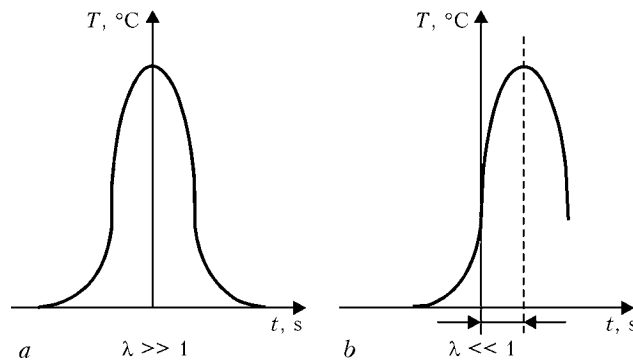


**Figure 26.** Occurrence of effect of thermal inertia in dependence on the  $\lambda$  value of material [10]

tally for the individual layers (see Table 5) it is apparent that the thermal cycle parameters ( $T_{\max}$  and  $t_{8/5}/CT$ ) show nearly similar values.

From the results of numerical calculations performed for the welding process it can be seen that the cooling time increases for the consecutive welded layers.

## CONCLUSIONS

1. The upper part of the HAZ cooling curve is characterized by the highest heat abstraction, that is the greatest temperature gradient, which slows down with time and has an effect on the temporary conditions of allotropic structure transformations and precipitations which occur at high, medium and lower temperatures.

2. When welding low-carbon steel, the available  $\gamma \rightarrow \alpha$  transformation time is shorter than that available for the bainite transformation, which occurs at lower temperatures. That is why the fraction of hardening microstructures, especially bainite, can increase, which may deteriorate the HAZ metal toughness.

3. By numerical modelling, values of thermal cycle parameters (maximum temperatures and cooling times) comparable with the experimental ones have been obtained. It can be concluded therefore that on the basis of numerical modelling results, the develop-

ment and course of thermal processes in real welded joints can be anticipated.

1. Lomozik, M. (2002) *Badanie cykli cieplnych spawania podczas układania sciegów odpuszczających dla poprawy własności plastycznych stref wpływu ciepła*: Praca badawcza Instytutu Spawalnictwa nr Da-96. Gliwice.
2. Lomozik, M. (2003) *Badanie zmian własności SWC stali pod wpływem wielokrotnych cykli cieplnych w oparciu o techniki symulacji*: Ibid., nr Id-115. Gliwice.
3. <http://gepard.cyf-kr.edu.pl/APLIKACJE/FLUENT/flu ent.html>
4. Kazimirov, A.A., Nedoseka, A.Ya., Lobanov, A.I. et al. (1968) *Calculation of temperature fields for plates in fusion welding*: Refer. Book. Kiev: Naukova Dumka.
5. Havalda, A. (1963) *Procesy cieplne przy spawaniu elektrycznym*. Warszawa: WNT.
6. Lomozik, M. (2004) *Modelowanie pol temperatur w obszarach strefy wpływu ciepła złączy spawanych stali przy pomocy programu ANSYS*: Praca badawcza Instytutu Spawalnictwa nr Da-99. Gliwice.
7. Jezewski, M., Kalisz, J. (1957) *Tablice wielkości fizycznych*. Warszawa: Państwowe Wydawnictwo Naukowe.
8. (1998) *ASME Boiler & Pressure Vessel Code*. Section XI: Rules for inservice inspection of nuclear power plant components.
9. Szargut, J. et al. (1992) *Modelowanie numeryczne pol temperatury*. Warszawa: WNT.
10. Kubiszyn, I. (1996) *Analiza numeryczna cykli cieplnych przy wielowarstwowym spawaniu elementów płaskich*: Praca badawcza Instytutu Spawalnictwa nr Id-106. Gliwice.
11. Haze, T., Aihara, S. (1986) Metallurgical factors controlling HAZ toughness in HT50 steels. *IIW Doc. IX-1423-86*.

# NUMERICAL SUBSTANTIATION OF MAXIMUM PRESSURE IN PNEUMATIC-AQUARIUM METHOD OF TESTING THE TIGHTNESS OF HEAT EXCHANGE TUBES AND THEIR WELDED JOINTS OF THE PGV-1000M STEAM GENERATOR

O.V. MAKHNENKO

E.O. Paton Electric Welding Institute, NASU, Kiev, Ukraine

State-of-the-art detection of air-tightness failure (leakages) in heat-exchange tubes and welded joints, by which they are welded to the tube plate (a header body) of steam generators of big power plants, is urgent task of state-of-the-art nuclear power engineering, in which high-power steam generators are used with respectively high number of heat-exchange tubes. For example, PGV-1000M generator contains 11 ths tubes and, respectively, 22 ths welded joints. Pneumatic-aquarium method for detecting leakages by means of air pressure in the steam generator body and registration of air bubbles in the header filled with water up to a respective level is sufficiently efficient method, whereby by means of the test air pressure increase, efficiency of the method significantly increases. However, risk of failure of welded joints, by which welded tubes are attached to the header body, also increases. These are slit-type connections with a weld located in the apex of a slit. Test pressure in contrast to the working pressure opens such slits thus, naturally, enabling efficient detection of defects (leakages) in a welded joint. However, this causes risk of integrity violation of, in general, rather serviceable joints. Numerical study carried out on order of NAEC of Ukraine allowed establishing upper limit of the test pressure on the basis of state-of-the-art approaches of destruction mechanics allowing for residual weld stresses and variation of geometric sizes of welds because of operation wear.

Pneumatic-hydraulic aquarium method of testing of the OF PGV-1000M steam generator tightness [1] is presently the most efficient method of detecting leaks in heat exchange tubes (HET) and welded joints between HET butt ends and the collector. In such a method of testing of second loop tightness of PGV-1000M (Figure 1, *a*), an overpressure is formed in the steam generator body (second loop) while the collector is filled with water to a certain level (first loop).

In the presence of tightness defects «leaks» in tubes or welded joints (Figure 1, *b*), air bubbles are escaping into the water of the first loop in the area of the respective tubes of the «hot» or «cold» collector, which is registered by respective observation means. The frequency of air bubbles escaping in the area of the given tube, depending on the air pressure during the tests, enables to determine the leakage extent  $Q_{100}$ , l/h (Figure 2), where  $Q_{100}$  is the extent of the heat exchanger (feed water) leakage, in the area of the given tube at overpressure between loops I and II of 100 kgf/cm<sup>2</sup>  $\approx$  10 MPa. The quantity of  $[Q_{100}] = 2$  l/h is acceptable.

The diagram of Figure 2 clearly shows that increase of the test pressure significantly decreases testing time, since the time  $\tau$  between successive bubbles shortens. Thus at  $Q_{100} = 2$  l/h,  $\tau$  decreases from 500 s at air pressure  $P = 1$  kgf/cm<sup>2</sup> down to 7 s at  $P = 20$  kgf/cm<sup>2</sup>. Taking into account that about 11000

tubes in each PGV-1000M generator are subject to examination, such a reduction is of great benefit.

Increase of the overpressure on the loop II side in the steam generator leads to the growth of the gap between the HET and the collector wall (see Figure 1, *b*), which produces at the tip of such a gap (weld root) additional stresses, which under certain conditions (residual stresses in the weld, embrittlement of the weld material, insufficient penetration  $c$  as in Figure 1, *b*), may contribute to loss of integrity by crack-like structural defect incipience mechanism.

Evaluation of the risk of such incipience at growing overpressure  $P$  is the subject of this study.

**Task setting.** With a certain degree of conservatism it can be accepted for the diagram of Figure 1, *b*, that the gap is a circumferential crack, where a uniform overpressure  $P$  is created, while at the butt end there is an annular connecting strip  $c$  thick. In the connecting strip there exist non-relaxed radial residual stresses  $\sigma_{rr}^{res}$ , contributing to the integrity loss (if  $\sigma_{rr}^{res} > 0$ ).

To obtain a sufficient quantitative evidence on the potential of integrity loss, depending on  $P$  value and non-relaxed residual welding stresses  $\sigma_{rr}^{res}$ , the criterion of brittle-viscous failure [2] is assumed (procedure R6), whose applicability for welded joint materials (austenitic steels) is shown in Figure 3 [2], where curve  $D$  corresponds to experimental data for austenitic steels, curve  $E$  is a generalized dependence  $K_r = f(L_r)$ :

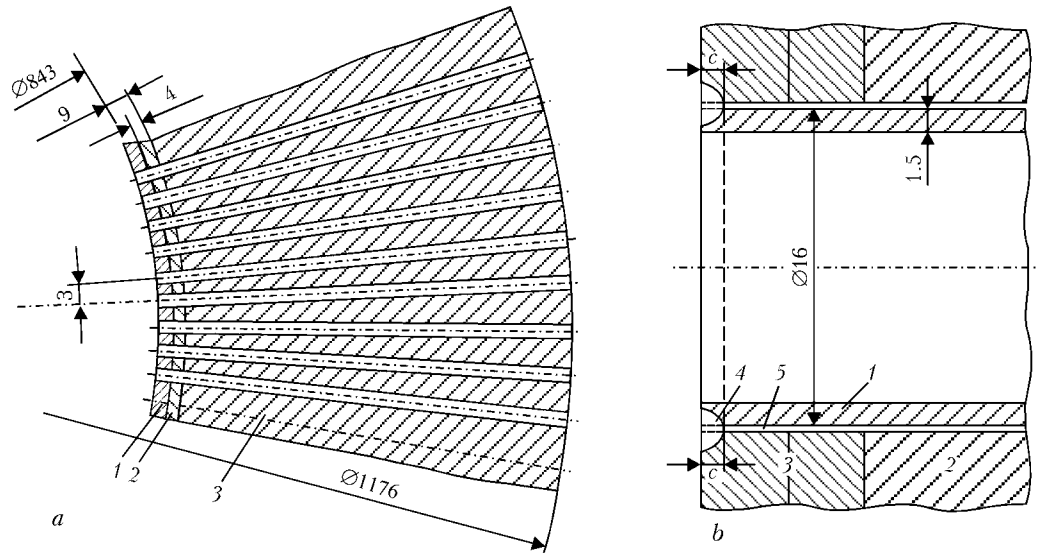


**Figure 1.** Diagram of mounting HET in PGV-1000M collector body (a): 1 – 04Kh20N10 steel deposited layer; 2 – 07Kh25N10 steel first deposit; 3 – 10GN2MFA base steel, and diagram of welded joints on HET with collector and in HET end piece (b): 1 – HET; 2 – collector wall; 3 – austenitic deposit; 4 – weld; 5 – gap between HET and collector

$$K_r = (1 - 0.14L_r^2)[0.3 + 0.75 \exp(-0.65L_r^6)]$$

$$\text{at } L_r < L_r^{\max} = \frac{\sigma_y + \sigma_t}{2\sigma_y}; \quad (1)$$

$$K_r(L_r) = 0 \text{ at } L_r > L_r^{\max},$$

where  $K_r = K_I/K_{Ic}$ ;  $L_r = \sigma_{\text{ref}}/\sigma_y$ ;  $K_I$  is the stress intensity factor for the normal tear-off crack considered, determining with regard for critical value for the given material  $K_{Ic}$ , the risk of brittle fracture;  $\sigma_{\text{ref}}$  is the stress caused by the action of pressure  $P$  in the gap, capable to cause plastic instability in connecting strip  $c$ , determines purely ductile fracture of the connecting strip from the action of pressure  $P$ ;  $\sigma_y$  and  $\sigma_t$

are respectively the yield point and tensile strength of the  $c$  material.

To calculate  $K_I$  in the connecting strip (weld), having  $c$  value, the model of semi-restricted crack in an elastic semi-space ([3], p. 133) was used, where the connecting strip is loaded with a bending moment  $M$  and force  $Q$ :

$$K_I = 3.975 \frac{M}{c\sqrt{c}} + 7.044 \left( \frac{Z_Q}{c} - 0.368 \right) \frac{Q}{\sqrt{\pi c}}, \quad (2)$$

where  $Z_Q$  is the distance from the connecting strip edge to the line of force  $Q$  action.

Values  $Q$  and  $M$  can be represented as

$$M = M_p + M_{\text{res}}, \quad Q = Q_p + Q_{\text{res}}, \quad (3)$$

where subscript  $p$  relates the value to the load from excessive pressure  $P$  in the space between the tube wall and the collector wall, whereas subscript  $\text{res}$  denotes such values dependent on the unrelaxed residual stresses.

Values of  $M_p$  and  $Q_p$  can be defined as reactions in a fixed edge of a long cylindrical shell having

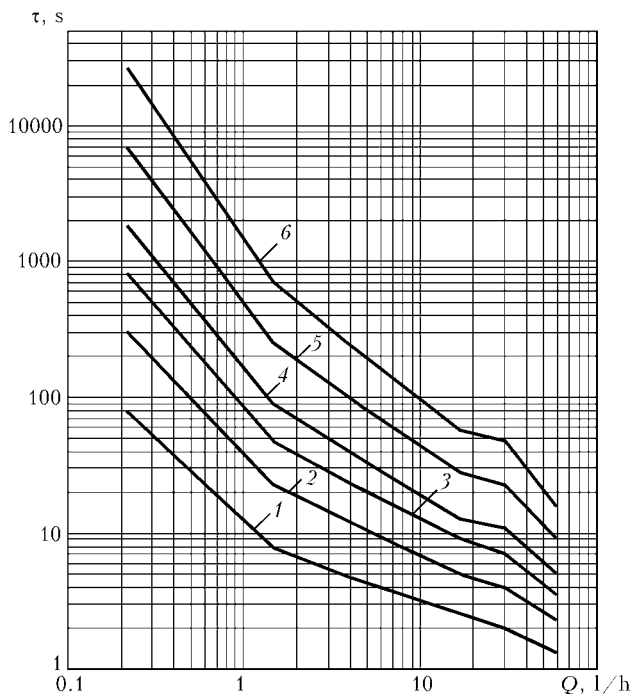


**Figure 2.** Working diagram showing duration  $\tau$  of steam generator holding under air test pressure depending on leakage magnitude  $Q_{100}$ , l/h [1]: test air overpressure  $P = 20$  (1), 10 (2), 6 (3), 4 (4), 2 (5) and 1 (6) kgf/cm<sup>2</sup>

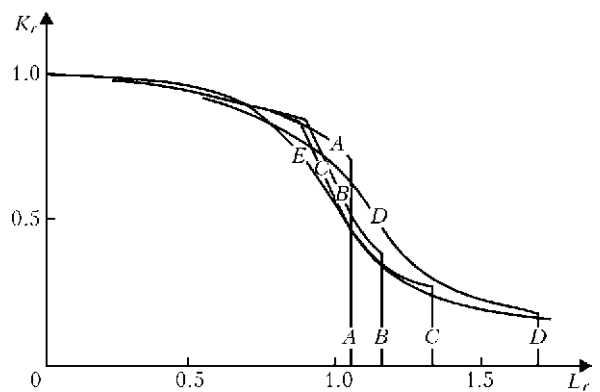


**Figure 3.** Diagram of limiting state  $K_r = f(L_r)$  for different types of structural steels [2]: A – high-strength steel EN408; B – pressure vessel steel A553B; C – low-carbon steel with manganese; D – austenitic steel; E – calculated curve by [2]

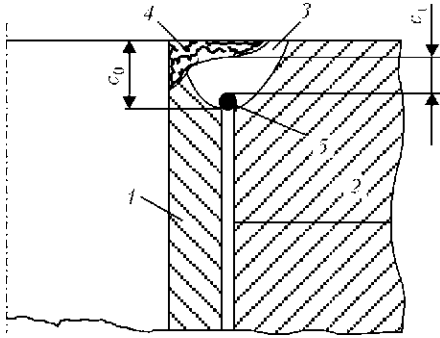


**Figure 4.** Diagram of in-service decreasing in  $c$  size from  $c_0$  to  $c_i$ : 1 – tube; 2 – collector wall; 3 – weld; 4 – corrosion-erosion damage zone; 5 – zone of stress intercrystalline crack propagation

diameter  $2R$  and wall thickness  $h$  under external pressure  $P$  [4].

In this case at  $Z/c = 1.0$ , by [4]

$$Q_p = \frac{(2 - \nu)P}{2\sqrt{3(1 - \nu^2)}} \sqrt{Rh}, \quad M_p = \frac{(2 - \nu)P}{2\sqrt{3(1 - \nu^2)}} Rh \quad (4)$$

or at  $\nu = 0.3$

$$Q_p = 0.52\sqrt{Rh}, \quad M_p = 0.26PRh. \quad (5)$$

For stresses  $\sigma_{ref}$  the following dependence can be used:

$$\sigma_{ref} = \frac{Q_p}{c} + \frac{4(M_p + Q_p c/2)}{c^2} = \frac{0.52p}{c} \left( 3\sqrt{Rh} + \frac{2Rh}{c} \right). \quad (6)$$

Residual stresses in are not accounted for  $\sigma_{ref}$ , since in ductile fracture they have time to get fully relaxed.

The size of connecting strip  $c$  according to technical specifications of welding HET for the case considered, should be of the order of 1.5–1.0 mm. However after a certain period of service life its thinning, due to corrosion, is possible. Thus at least two mechanisms of corrosion-related reduction of the  $c$  size can be stated (Figure 4), namely due to corrosive-erosive damage on the side of the first loop, or due to development of transcrystalline (intercrystalline) corrosion on the side of the second loop.

Objective conditions for the former type damage are present along the whole length of tubes, including the butt ends, which is especially true for horizontal-type steam generators [5]. Damage of the latter type is possible, if  $K_I$  values by (2) with regard that in operational conditions the pressure differential between loops II and I is  $\Delta P < 0 \approx -10$  MPa, will be significantly above zero value, which is possible only at a certain magnitude of unrelaxed residual stresses.

Thus, knowledge of the magnitudes of residual stresses in the zone of tube welded joints is very important for the solution of this problem.

**Residual stresses.** Small welding zone dimensions in the case of welding tubes to the collector wall (see Figure 1,  $b$ ), makes experimental determination of residual stresses difficult. This circumstance explains a rather limited scope of available published information on this subject [6, et al.]. Among sector-specific

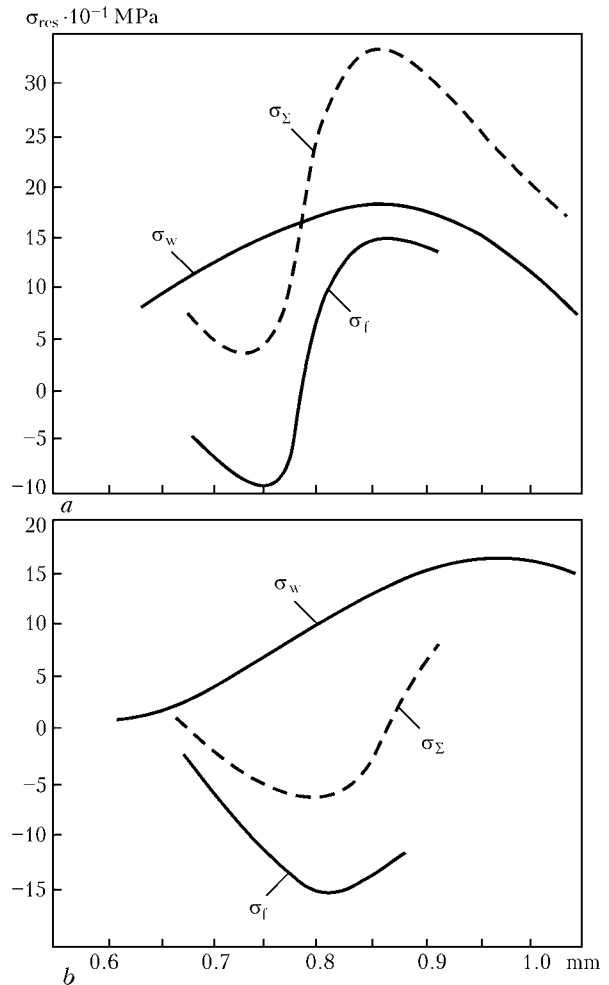
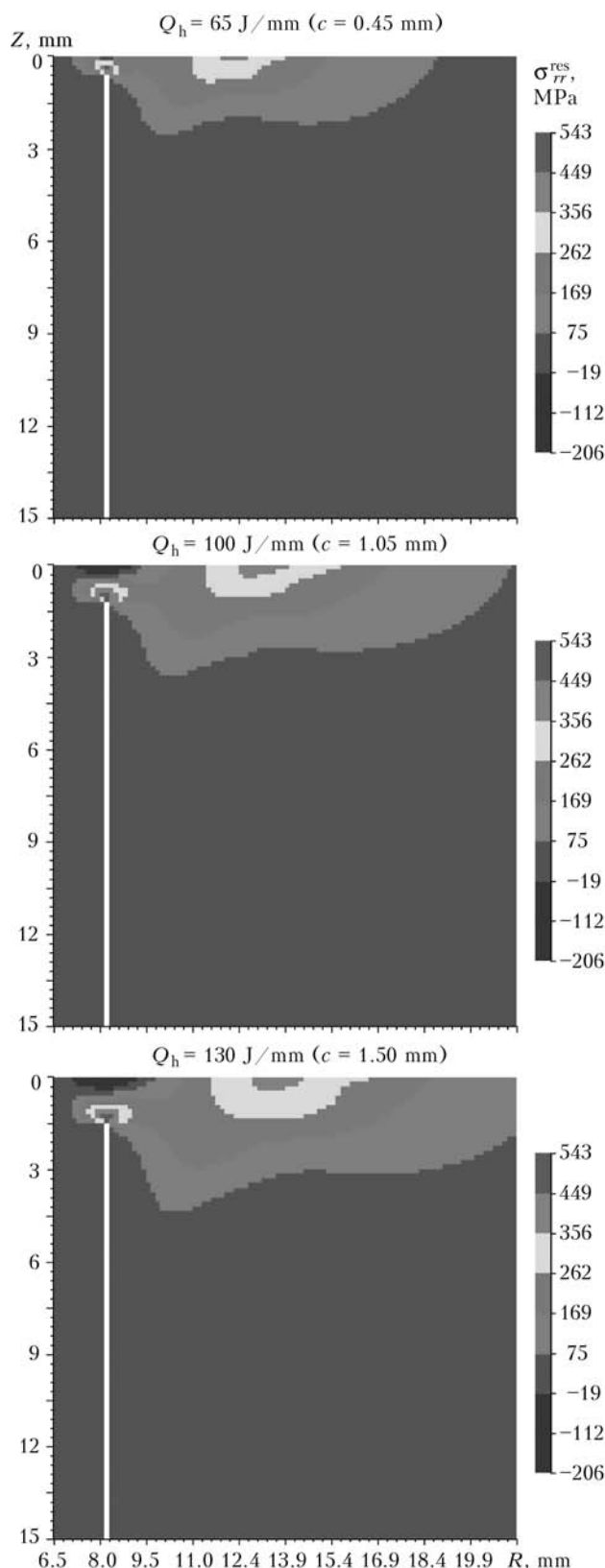


**Figure 5.** Experimental measured data [7] on residual stresses in HET wall due to butt end welding and flaring:  $a$  – tangential (circumferential) stresses;  $b$  – radial stresses in as-weld (index  $w$ ) and post-flaring ( $f$ ) conditions; index  $\Sigma$  – total stresses

official documents should be mentioned the report [7] containing experimental evaluation of residual stresses in HET wall, depending on the method of welding and flaring of the butt end. Figure 5 shows respective results from [7], whose plausibility on the above reason is low.

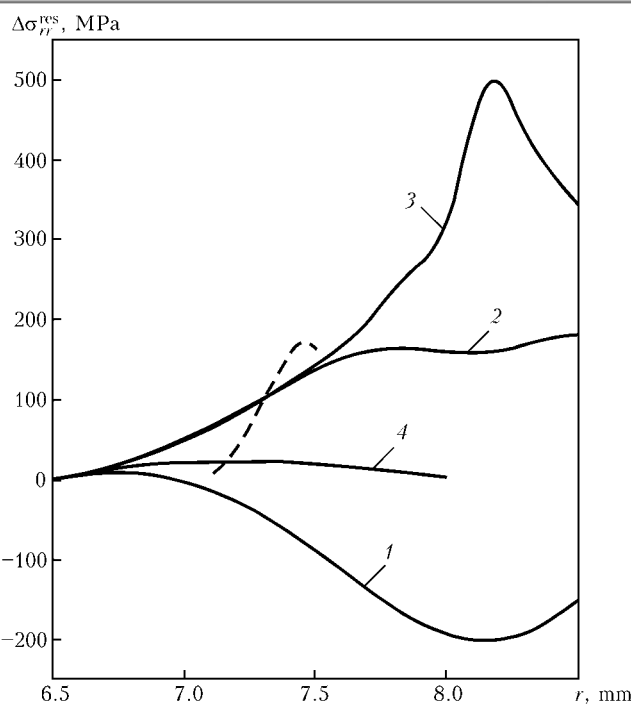
In 2000, the E.O. Paton Electric Welding Institute, on the order of the Infacor GmbH, has worked out a calculation procedure for stressed state determination, involved with welding HETs to tube plates. This procedure has been adapted to different HET and tube plate materials, welded joint configurations, etc. [6]. The method is based on mathematical simulation of the kinetics of thermomechanical processes taking place in zones of welding tubes to tube plates. This study uses the above method of obtaining data on residual stresses for the case shown in Figure 1,  $b$ .

Figure 6 shows distribution of residual stresses  $\sigma_{rr}^{res}$  in the welded joint zone at various welding conditions, providing  $c$  value within 0.45 to 1.50 mm range. Under such conditions post-welding distribution of residual stresses has a rather complicate pattern, since availability of free surfaces (inner tube surfaces, gap between tube and collector, butt end surface), markedly affects the distribution of residual



**Figure 6.** Calculated distribution of radial residual stresses  $\sigma_{rr}^{\text{res}}$  in the welded joint zone at different welding conditions providing penetration depth  $c$  of 0.45–1.50 mm

stresses. In sections  $z = \text{const}$  (i.e. in planes at different distances from butt end) distribution of  $\sigma_{rr}^{\text{res}}$  along the radius  $r$  has two extreme zones: one at  $r = 8$  mm (tube surface) and another at  $r = 12$ – $13$  mm (approximately midway between neighboring tubes).



**Figure 7.** Distribution of residual welding stresses  $\sigma_{rr}^{\text{res}}$  through tube wall thickness of  $6.5 \leq r \leq 8$  mm and tube plate of  $r > 8$  mm for welding condition providing connecting strip size of  $c = 1.05$  mm: solid lines — calculated results in different sections  $z = \text{const}$ , i.e. in planes at different distances from tube butt end; dashed line — experimental data [7];  $z/c = 0$  (1), 0.5 (2), 1.0 (3), 1.5 (4)

With increasing  $z$  the stressed state diminishes quite abruptly, and at  $z = 4$ – $5$  mm the residual stresses level in collector walls becomes insignificant.

Figure 7 shows for variant at  $c = 1.05$  mm, calculated data on distribution of residual stresses  $\sigma_{rr}^{\text{res}}$  in planes  $z = \text{const}$  in the tube wall and the collector wall, depending on  $r$  coordinate. There too are shown data of Figure 5, reported in [7]. Such a comparison shows experimental data are close to calculated in the middle part of the tube at  $z/c \approx 0.5$  and  $7.0 < r < 8.0$  mm. Data of Figure show that welding conditions produce a certain effect on the residual stresses in the weld.

Figure 8 shows in more detail (compared to Figure 6) such data for surface  $r = 8.0$  mm (HET diameter was 16 mm) at different welding conditions, clearly demonstrating influence of the latter.

These data were approximated by linear distribution within  $0 < z < c$  (see dashed line in Figure 8), and respectively  $M_{\text{res}}$  and  $Q_{\text{res}}$  were calculated for  $ZQ/c = 0.5$  (Table 1).

Data of Table 1 show that increase of  $c$  from 0.45 to 1.50 mm, contributes to increasing of  $K_I^{\text{res}}$  by (2) from 224 to  $409 \text{ MPa} \cdot \text{mm}^{1/2}$ .

Table 2 shows calculated by (2) and (6) loading characteristics for various excessive pressures  $P$ .

These data show that contribution of residual stresses produced during welding, increases in the  $K_I^P + K_I^{\text{res}}$  amount with increasing size of  $c$  and reduction of pressure  $P$ . At  $P < 4$  MPa, proportion of residual stresses in said amount makes over 66 % at

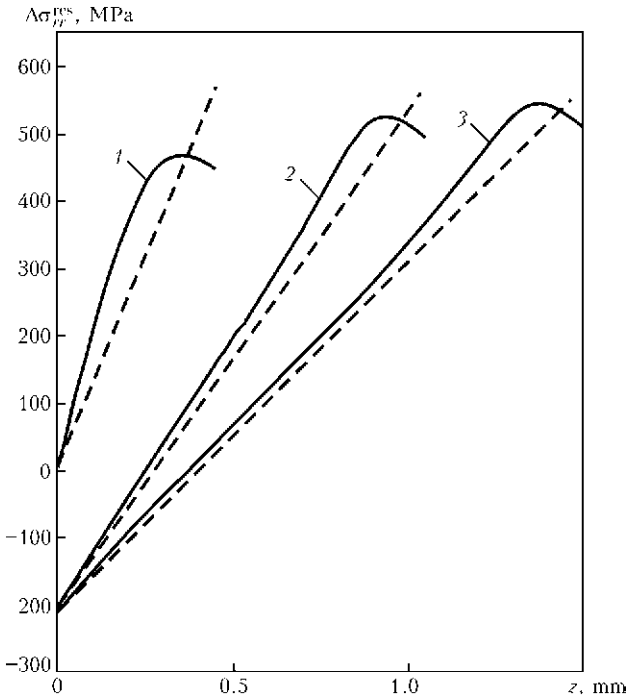


**Figure 8.** Distribution of residual stresses  $\sigma_{rr}^{res}$  through connecting strip thickness in section  $r > 8$  mm for different welding conditions providing connecting strip size of  $c = 0.45$  (1), 1.05 (2) and 1.50 (3) mm: solid lines – results of visco-plastic stress analysis; dashed – approximations

$c = 0.45$  mm, 85 % at  $c = 1.05$  mm and 91 % at  $c = 1.50$  mm.

**Material properties governing the welded joint integrity.** To obtain quantitative evidence on the integrity of welded joints by the dependence (1), data on calculated resistance of the weld material to brittle

**Table 1.** Results of processing data of Figure 8 at  $Z_O/c = 0.5$

Variant No.	Heat input $q_h$ , J/mm	$c$ , mm	$Q_{res}$ , MPa·mm	$M_{res}$ , MPa·mm <sup>2</sup>	$K_{I_1}^{res}$ , MPa·mm <sup>1/2</sup>
1	65	0.45	129	9.4	224
2	100	1.05	191	65.1	338
3	130	1.50	268	144.7	409

fracture  $K_{Ic}$  and plastic instability  $\sigma_y$  and  $\sigma_t$ , are necessary. Since the welding is performed using a non-consumable electrode, so the weld metal has intermediate properties, including those of the tube and the upper deposited layer in the collector, at testing temperature, i.e. at  $T = 15-30$  °C.

Tensile strength values  $\sigma_t$  for tube material (HET) and the deposited layer are in the range 640–700 MPa [5]. Yield point  $\sigma_y$  depends on deformational hardening (cold deformation) and, according to calculated data for the weld metal, it is close to  $\sigma_y = 350-380$  MPa. We assume as normative values  $\sigma_t = 640$  MPa,  $\sigma_y = 350$  MPa. Respectively, calculated values  $\sigma_y$  and  $\sigma_t$  should be diminished  $n$  times, where  $n$  is the safety factor. For hydrotesting conditions as in [8]  $n = 2.0$  is assumed, i.e. calculated values are  $\sigma_t = 320$  MPa,  $\sigma_y = 175$  MPa.

For  $K_c$ , data on critical value of  $J$ -integral of steel type 08Kh18N10T can be used. Respective tests have been run many times. For one, reported in [9], test values are  $K_c = 65$  MPa·mm<sup>1/2</sup> = 2050 MPa·mm<sup>1/2</sup>, which are quite conservative. Should this value be assumed as a normative one, so the calculations will give  $K_c = 2050/n = 1025$  MPa·mm<sup>1/2</sup>.

**Table 2.** Characteristics of loading of welded joints as a function of overpressure  $P$  and residual stresses  $\sigma_{rr}^{res}$

$c$ , mm	$P$ , MPa	$\sigma_{ref}$ , MPa	$K_{I_1}^P$ , MPa·mm <sup>1/2</sup>	$K_{I_1}^P + K_{I_1}^{res}$ , MPa·mm <sup>1/2</sup>	$L_r$	$K_r$
0.45	0.2	15.2	9.6	233.6	0.087	0.228
	1.0	75.6	47.83	271.8	0.43	0.265
	2.0	151.2	95.7	319.7	0.86	0.312
	3.0	226.8	143.5	367.5	1.296	0.358
	4.0	302.4	191.4	415.4	1.73	0.405
1.05	0.2	3.3	3.2	337.2	0.029	0.329
	1.0	16.5	15.94	349.9	0.094	0.341
	2.0	33.0	31.9	365.9	0.188	0.357
	4.0	66.0	63.8	397.8	0.377	0.388
	10.0	165.0	159.4	493.4	0.94	0.481
	15.0	247.5	239.1	573.1	1.41	0.559
1.50	0.2	1.83	2.1	411.1	0.01	0.401
	1.0	9.15	10.44	419.4	0.052	0.409
	2.0	18.3	20.9	429.9	0.104	0.119
	4.0	36.6	41.8	450.8	0.203	0.440
	10.0	91.5	104.4	513.4	0.523	0.500
	15.0	137.2	156.6	565.6	0.784	0.552
	20.0	183.0	208.8	617.8	1.045	0.603
	25.0	228.7	261.0	670.0	1.30	0.653



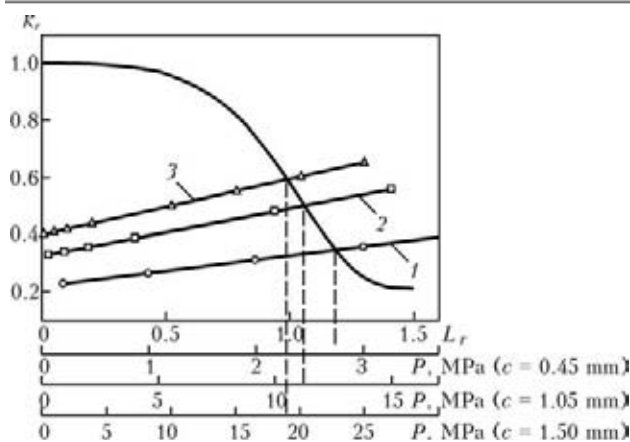


**Figure 9.** Results of overlaying onto the limiting state diagram  $K_r = f(L_r)$  by (1) of calculated points  $K_r(P)$  and  $L(P)$  for different  $c$  values, mm: 1 – 0.45; 2 – 1.05; 3 – 1.50

**Allowable values of test air overpressure.** With a view of the above, i.e. at  $n = 2.0$ , calculated values of  $\sigma_y$ ,  $\sigma_t$  and  $K_c$  are:  $\sigma_y = \sigma_y^{\text{nor}}/n = 175$  MPa and  $\sigma_t = \sigma_t^{\text{nor}}/n = 320$  MPa,  $K_c = K_c^{\text{nor}}/n = 1025$  MPa·mm<sup>1/2</sup>,

$$L_r^{\text{max}} = \frac{\sigma_y + \sigma_t}{2\sigma_y} = 1.41, \text{ and, using dependences (1)}$$

and data of Table 2, we obtain for different overpressures  $P$ , coordinates  $K_r$  and  $L_r$  (see Table 2) on the diagram controlled by the dependence (1), as shown in Figure 9. Values of these coordinates for a fixed  $c$  value are proportionate to  $P$  value, i.e. these points can be connected with a straight line. Intersections of these direct lines with curve by (1), control critical test overpressure  $P_{cr}$ . Thus we obtain that at  $c = 0.45, 1.05$  and  $1.50$  mm,  $P_{cr} = 2.7, 11.2$  and  $19.0$  MPa, respectively.

From the data presented it follows that with dimensions  $c > 0.5$  mm, test overpressure up till  $2.7$  MPa  $\approx 27$  kgf/cm<sup>2</sup> provides integrity of welded joints between the tubes and the collector.

Unfortunately,  $c$  size is difficult to control by non-destructive methods. The initial size provided by the welding technique used, is usually not below  $1.0$  mm. However after a lengthy service period it can get reduced, due to corrosion. This process can proceed can be very intense at quite high  $K_I = K_I^P + K_I^{\text{res}}$ , where  $K_I^{\text{res}}$  is the  $K_I$  value at working pressure of about  $-10$  MPa. For original  $c$  and  $K_I^{\text{res}}$  values, from Table 1, at  $P_p = -10$  MPa and  $c = 0.45, 1.05$  and  $1.50$  mm we obtain, respectively,  $K_I = K_I^P + K_I^{\text{res}} = -254$  and  $-8.03, +179$  and  $+5.66, +305$  and  $+9.6$  MPa·mm<sup>1/2</sup>.

Using the data of Figure 10 [10], we see that at the  $K_I$  values above mentioned, corrosion crack growth rate under stress is not exceeding  $5 \cdot 10^{-5}$  mm/h for  $c = 1.5$  mm,  $10^{-5}$  mm/h for  $c = 1.0$  mm and is distinctly below  $10^{-6}$  mm/h =  $0.00876$  mm per year at  $c = 0.45$  mm. With a certain degree of conservatism it can be assumed that this law of reduction of corrosion crack growth rate remains in force in the process of  $c$  thinning, due to corrosion from  $c = 1.50$  to  $c =$

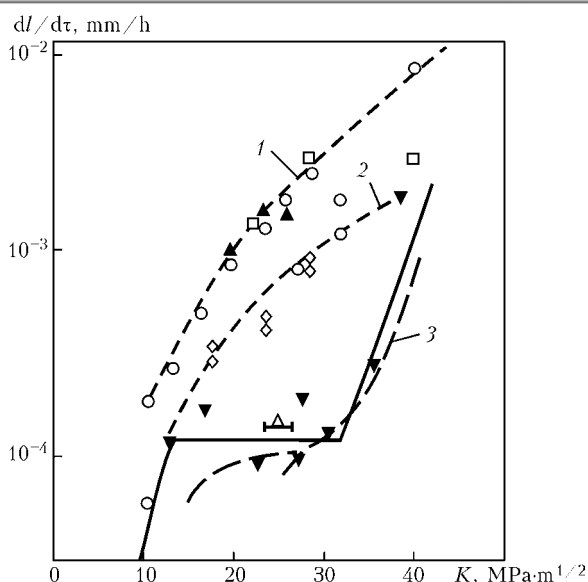


**Figure 10.** Kinetics of stress intercrystalline corrosion crack growth at long-term static loading in Cr-Ni steels: 1 – upper sensitization level; 2 – mean sensitization; 3 – insignificant sensitization; ▼ – sensitization at 650 °C for 2 h,  $O_2 \approx 0.2$  mg/l; ▲ – sensitization at 650 °C for 2 h,  $O_2 \approx 0.2$  mg/l (another melt); ◆ – different sensitization,  $O_2 \approx 0.2$  mg/l; ○ – sensitization at 650 °C for 24 h,  $O_2 \approx 8$  mg/l; ■ – sensitization for 24 h,  $O_2 \approx 0.2$  mg/l

$= 0.45$  mm. At  $c \approx 0.5$ – $0.6$  mm the «crack» is closed due to negative pressure  $P^p$ , and corrosive damage is insignificant.

## CONCLUSION

For a 15–20 year service life of the steam generator, there is no ground to consider that calculated dimensions of  $c$  for tube welded joints will diminish to below  $0.45$  mm, therefore it is quite possible to apply the test overpressure of up to  $2.7$  MPa  $\approx 27$  kgf/cm<sup>2</sup>, in the context of preserving the integrity of welded joints considered.

1. *PGV-1000M steam generator: pneumatic-aquarium method of tightness testing*: Test method 320.585.00.00.000. Hidroress.
2. Harrison, R.P., Loosemore, K., Milne, J. et al. (1980) Assessment of the integrity of structures containing defects. *Report R/H-CEGB R6*. Rev. 2.
3. (1988) *Fracture mechanics and material strength*: Handbook. Vol. 2: Intensity stress factors for bodies with crack. Ed by V.V. Panasyuk. Kiev: Naukova Dumka.
4. (1968) *Strength, stability, fluctuations*: Handbook. Vol. 1. Moscow: Mashinostroenie.
5. Melekhon, R.K., Pokhmursky, V.I. (2003) *Structural materials for power equipment*. Kiev: Naukova Dumka.
6. Makhnenko, V.I., Velikoivanenko, E.A., Makhnenko, O.V. et al. (2002) Computer program «Welding of tubes to tube sheets of heat exchangers». *The Paton Welding J.*, 8, p. 2–9.
7. (1994) *Material state testing*: Report on PGV-100M steam generator state of the KNPP block 1. Hidroress.
8. (1989) *PNAE G-7-002-86*: Design standards for strength of the NPP equipment and pipings. Moscow: Energoatomizdat.
9. Krasovsky, A.Ya., Orynyak, I.V. (2000) Assessment of residual life of welds in piping of the first loop of nuclear power stations damaged by intercrystalline corrosion. *The Paton Welding J.*, 9/10, p. 54–62.
10. Horn, R.M., Kass, J.N., Rangantath, K. (1984) Evaluation of growth and stability of stress corrosion cracking in sensitized austenitic pipings. *Transact. of ASME*, 106(2), p. 201–208.

# FORECASTING OF DURABILITY OF WELDED ARCH PYLON OF BRIDGE OVER THE RIVER MOSKVA

O.V. MAKHNENKO and V.I. MAKHNENKO

E.O. Paton Electric Welding Institute, NASU, Kiev, Ukraine

This work is dedicated to the study of durability of welded joints of the weldment AUv0-06 of arch pylon on the basis of the information presented on the loading spectrum and nominal stresses due to such loading in the zone of welded joints to be calculated.

Figure 1 shows a schematic illustration of a weldment of arch pylon made from low-alloyed steel 10KhSND (GOST 6713-75) 32 mm thick, having a configuration of a shaped box-type beam. To the wall of that beam along the lines (axes) 1 and 2, with tee joints 3 (Table 1) (GOST 14771-76) through their entire lengths, excluding sections between nodal points 82-213 and 597-433, are welded longitudinal brackets of plates 20 mm thick. Between nodal points 82-213 and 597-433 are welded joints 2 and 22. Along the axes 3 and 4 are welded transverse brackets with joints 21 and 20. Inert-gas shielded welding was used throughout.

It was necessary to evaluate durability of welded joints at postulated initiation of fatigue failure in hot spots *A* and *B* of Table 1, on the basis of the knowledge of respective normal nominal membrane stresses.

Tables 2 and 3 contain selective results of numerical analysis of nominal stressed state in the most representative points along axes 1-4 in the direction promoting formation of longitudinal fatigue cracks in points *A* and *B* of Table 1. Values of  $\sigma_c^d$  correspond to the distribution of stresses from constant design loads, stresses  $\sigma_{tI}$  and  $\sigma_{tII}$  are the same from additional temporary design loads. Based on such data, three

typical cycles of alternating loading with terminal points of the cycle by the stresses can be singled out:

$$\begin{aligned} 1: & \sigma_c^d + \sigma_{tI}^d - \sigma_c^d, \quad \Delta\sigma_1 = |\sigma_{tI}^d|; \\ 2: & \sigma_c^d + \sigma_{tII}^d - \sigma_c^d, \quad \Delta\sigma_2 = |\sigma_{tII}^d|; \\ 3: & \sigma_c^d + \sigma_{tI}^d - \sigma_c^d + \sigma_{tII}^d, \quad \Delta\sigma_3 = |\sigma_{tI}^d - \sigma_{tII}^d|, \end{aligned} \quad (1)$$

where maximum and minimum values  $\sigma_{max}^i$  and  $\sigma_{min}^i$  are determined by said terminal points depending on  $\sigma_c^d$ ,  $\sigma_{tI}$  and  $\sigma_{tII}$  (Figure 2). Longitudinal normal nominal stresses along the axes 1 and 2 according to data of numerical analysis are characterized by values  $\sigma_c^d = -134.9$  MPa and  $\Delta\sigma = 20.8$  MPa, varying little along the axes 1 and 2 of welded joints. It was intended to evaluate durability of the welded joints considered, first proceeding from the most conservative variant 1 of cyclical loading of Tables 2 and 3, and then calculate durability based on the loading spectrum (1) at various proportions of  $\alpha_j$  of the *j*-th spectrum constituent (1).

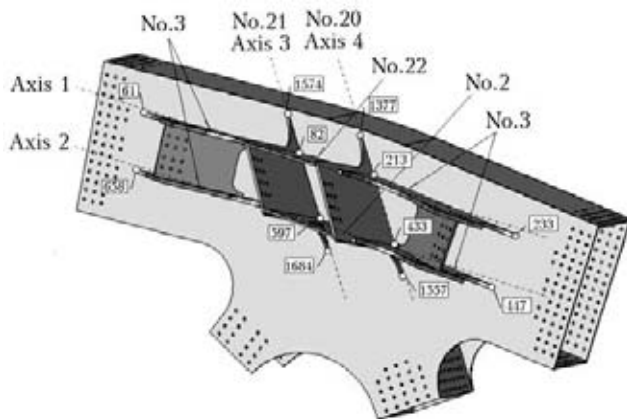
**Calculation method.** To carry out the above work involving determination of durability of the welded joints (see Table 1), for which crack-like defects due to lack of fusion are unacceptable, method of [1] was used to evaluate durability of such a welded joint type on the basis of the fatigue crack formation in the transition zone from the weld metal to the base one (see Table 1, «hot spots» *A* or *B*).

This IIW-developed method generalizes a multitude of experimental studies for standard welded joints, which enabled to formulate for each of them recommendations with regard to allowable amplitude of nominal stresses at recurrent loading as

$$[\Delta\sigma] = \frac{FAT f_1(R) f_2(N) f_3(\partial) f_4(T)}{\gamma_m}, \quad (2)$$

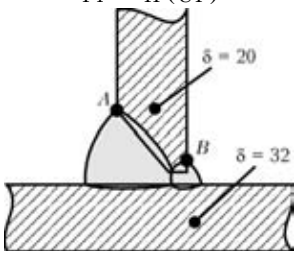
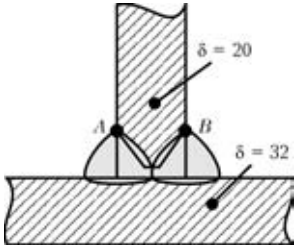
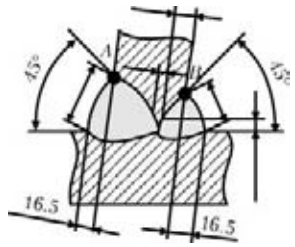
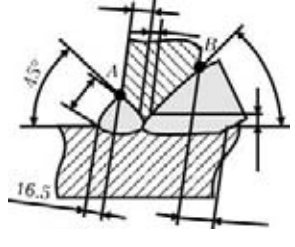
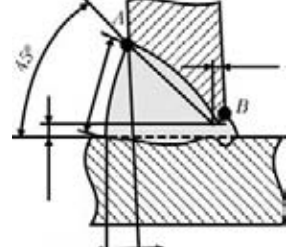
where FAT is the joint class or allowable amplitude for the joint on the basis of  $2 \cdot 10^6$  cycles of recurrent loading (constant loading cycle parameters) at  $f_1 = f_2 = f_3 = f_4 = \gamma_m = 1$ ;  $\gamma_m$  is the safety factor.

In [1] is found a Table of FAT values for different standard welded joints. The joints considered (see Table 1) in the absence of lacks of fusion and down-



**Figure 1.** Schematic illustration of weldment of arch pylon with indication of axes 1-4 along which is to be evaluated durability of the welded joints Nos. 2, 3, 20, 21 and 22, and control points (weldments)

**Table 1.** Welded joints to be calculated for their strength

Weld No.	Standard designation	Designation of welded joint	Data required for calculation	Location on the weldment sketch
<i>Standard</i>				
2	GOST 23518-79	T4 – IP(UP) 	Two-sided tee welded joint with single bevel  Full penetration	Along axis 2 between weldments 597 and 433
3	GOST 23518-79	T7 – IP(UP) 	Two-sided tee welded joint with double bevel  Full penetration	Along axis 1 between weldments 61 and 82, 213 and 233  Along axis 2 between weldments 658 and 597, 433 and 447
<i>Non-standard</i>				
20	Inert gas shielded arc welding  Welding method acc. to GOST 14771-76*		Full penetration	Along axis 4 between weldments 1377 and 1557
21	Same		Same	Along axis 3 between weldments 1574 and 1684
22	Same		Same	Along axis 1 between weldments 82 and 213
* Base material – structural steel 10KhSND, GOST 6713-75.				

**Table 2.** Initial data on nominal stress values across the weld for different points along axes 1–4

Axis 1				Axis 2			
Weldment No.	$\sigma_c^d$ , MPa	$\sigma_{II}$ , MPa	$\sigma_{III}$ , MPa	Weldment No.	$\sigma_c^d$ , MPa	$\sigma_{II}$ , MPa	$\sigma_{III}$ , MPa
61	3.4	1.5	1.0	658	3.0	1.2	1.0
82	8.4	-12.7	0.5	5220	-53.7	-26.6	-2.5
76	-40.0	-25.1	-1.6	672	-53.5	-29.2	-2.8
7130	-35.6	-29.4	-1.9	5217	-52.9	-32.2	-3.1
77	-39.9	-32.2	-2.9	673	-51.7	-39.3	-3.3
7126	-30.5	-34.5	-2.2	5214	-49.8	-35.1	-3.4
78	-24.6	33.4	-1.9	674	-47.2	-34.0	-3.3
7124	-13.7	-28.1	-1.3	5211	-43.0	-30.7	-3.0
79	-6.4	-2.34	-0.7	597	21.4	0.4	0.2
213	24.9	4.5	2.7	433	-25.5	-2.6	-1.0
233	1.6	0	0	447	5.5	0.5	1.0

**Table 2 (cont.)**

Axis 3				Axis 4			
Weldment No.	$\sigma_c^d$ , MPa	$\sigma_{II}$ , MPa	$\sigma_{III}$ , MPa	Weldment No.	$\sigma_c^d$ , MPa	$\sigma_{II}$ , MPa	$\sigma_{III}$ , MPa
1574	1.0	0	0	1377	0.7	0.1	0.1
1578	11.2	3.5	1.7	1404	43.7	5.3	2.7
1657	41.6	1.6	1.5	6773	34.4	4.7	2.7
2549	43.6	1.4	1.1	3214	48.2	6.6	2.7
2552	43.2	1.6	0.9	3207	49.8	6.7	2.5
2555	41.3	1.9	0.7	1403	49.4	6.4	2.6
1656	43.3	1.4	1.3	1402	49.7	6.9	2.5
1654	42.4	1.7	0.8	1401	48.1	7.1	2.3
1653	39.6	2.1	0.8	1399	40.2	7.2	1.6
1652	33.3	2.7	5.5	433	-25.5	2.6	-1.0
1684	1.8	0	0	1557	1.7	0.3	0.1

hand welding correspond to No.411 and have FAT = 80 MPa. If the welding is other than downhand, then the welded joints are of No.412 type and have FAT = 71 MPa. It can be with a certain degree of conservatism assumed for the welded joints from Table 1 that FAT = 71 MPa.

In (3) multiplier  $f_1(R)$  takes account of the asymmetry of the loading cycle:

$$R = 1 - \frac{\Delta\sigma}{\sigma_{max}^d}, \quad (3)$$

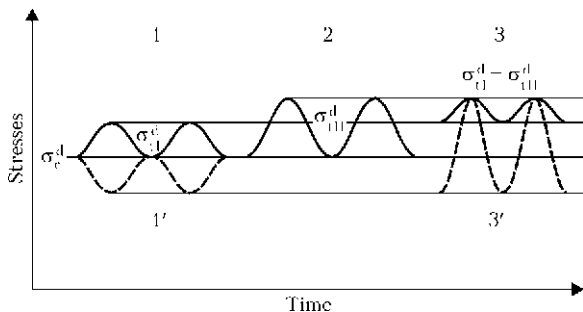


**Figure 2.** Graphic interpretation of variants 1–3 of loading cycles (1) with the same (solid line) and different (dashed) signs of  $\sigma_c^d$

as well as the level of residual stresses in the joint zone. In the case when residual stresses do not exceed  $0.2\sigma_y$ , where  $\sigma_y$  is the yield point of the material (for steel 10KhSND  $\sigma_y \approx 400$  MPa), then after [1]

$$\begin{aligned} f_1(R) &= 1.6 \text{ for } R < -1.0, \\ f_1(R) &= 0.4R + 1.2 \text{ for } -1.0 \leq R \leq 0.5, \\ f_1(R) &= 1.0 \text{ for } R > 0.5. \end{aligned} \quad (4)$$

In the case when residual stresses either exceed  $0.2\sigma_y$  (approximately 80 MPa for the case considered), or joining of 2D or 3D elements, then  $f_1(R) = 1.0$ , i.e. minimum value of multiplier  $f_1(R)$  for dependence (3). For the case considered  $f_1(R) = 1.0$  can be assumed.

Multiplier  $f_2(N)$  takes account of limited fatigue. Within the range of  $10^4 < N < 5 \cdot 10^6$  cycles, according to [1] (Figures 3 and 4) it is determined by the dependence:

$$f_2(N) = \left(\frac{C}{N}\right)^{1/m}, \quad (5)$$

**Table 3.** Calculated durability for different points along axes 1 and 2 acc. to Table 2

Axis 1			Axis 2		
$N_1$ , cycle	$N_2$ , cycle	$N_3$ , cycle	$N_1$ , cycle	$N_2$ , cycle	$N_3$ , cycle
$> 10^8$	$> 10^8$	$> 10^8$	$> 10^8$	$> 10^8$	$> 10^8$
$> 10^8$	$> 10^8$	$> 10^8$	$6.8 \cdot 10^7$	$> 10^8$	$7.4 \cdot 10^7$
$9.1 \cdot 10^7$	$> 10^8$	$9.7 \cdot 10^7$	$4.3 \cdot 10^7$	$8.4 \cdot 10^7$	$4.6 \cdot 10^7$
$4.1 \cdot 10^7$	$7.3 \cdot 10^7$	$4.4 \cdot 10^7$	$2.6 \cdot 10^7$	$5.0 \cdot 10^7$	$2.8 \cdot 10^7$
$2.6 \cdot 10^7$	$4.7 \cdot 10^7$	$2.8 \cdot 10^7$	$1.9 \cdot 10^7$	$3.6 \cdot 10^7$	$2.1 \cdot 10^7$
$1.9 \cdot 10^7$	$3.3 \cdot 10^7$	$2.0 \cdot 10^7$	$1.7 \cdot 10^7$	$3.2 \cdot 10^7$	$1.8 \cdot 10^7$
$2.2 \cdot 10^7$	$3.8 \cdot 10^7$	$2.3 \cdot 10^7$	$2.0 \cdot 10^7$	$3.8 \cdot 10^7$	$2.2 \cdot 10^7$
$5.2 \cdot 10^7$	$8.8 \cdot 10^7$	$5.6 \cdot 10^7$	$3.3 \cdot 10^7$	$6.3 \cdot 10^7$	$3.6 \cdot 10^7$
$> 10^8$	$> 10^8$	$> 10^8$	$> 10^8$	$> 10^8$	$> 10^8$
$> 10^8$	$> 10^8$	$> 10^8$	$> 10^8$	$> 10^8$	$> 10^8$
$> 10^8$	$> 10^8$	$> 10^8$	$> 10^8$	$> 10^8$	$> 10^8$

Notes. 1. Calculated durability along axes 3 and 4 are  $N_1 > 10^8$ ,  $N_2 > 10^8$  and  $N_3 > 10^8$  cycles. 2.  $N_1$  – minimal durability for 3-cycle loading (1);  $N_2$  – durability for variant 2;  $N_3$  – same for variant 3.

where  $N$  is the durability of the welded joint;  $C = 2 \cdot 10^6$ ,  $m = 3$  at  $10^4 < N < 5 \cdot 10^6$  cycles, and  $C = 2.54 \cdot 10^6$ ,  $m = 5$  at  $5 \cdot 10^6 < N < 10^8$  cycles.

Correction for the thickness of the adjoining element, where a fatigue crack is originated,  $f_3(\delta) = 1.0$ , if thickness is  $\delta < 25$  mm. At greater thicknesses

$$f_3(\delta) = \left(\frac{25}{\delta}\right)^{0.3} \tag{6}$$

For joints considered  $f_3(\delta) = 1.0$ .

Multiplier  $f_4(T)$  takes account of operating temperature  $T$  of the joint. According to [1] at  $T < 100$  °C,  $f_4(T) = 1.0$  can be assumed.

With account of the above, for the welded joints considered, dependence (2) can be presented as

$$[\Delta\sigma] = \frac{\text{FAT}}{\gamma_m} \left(\frac{C}{N}\right)^{1/m} \tag{7}$$

Respectively, limiting durability  $N_j$  at recurrent loading with amplitude  $\Delta\sigma_j$  from (7) is expressed as

$$N_j = C \left(\frac{\text{FAT}}{\Delta\sigma_j \gamma_m}\right)^m \tag{8}$$

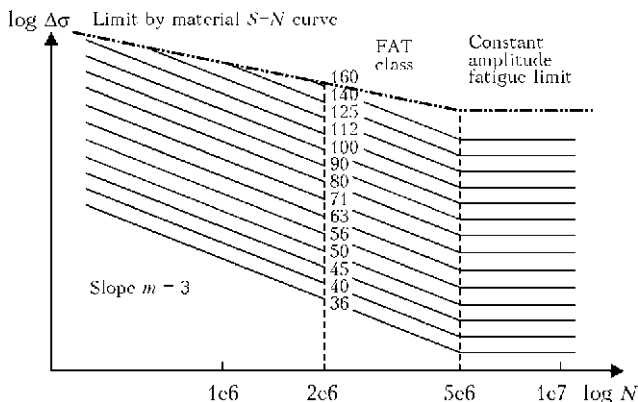


**Figure 3.** Generalized Woehler curves [1] for different FAT (steel) at  $m = 3$  under normal nominal stresses at  $N < 5 \cdot 10^6$  cycles

In adopting safety factor  $\gamma_m$ , it has to be remembered that FAT in [1] is recommend based on 0.95 of non-failure probability according experimental data. That is why in [1] it is recommended to select  $\gamma_m$  from within 1.0–1.4. Here safety factor value  $\gamma_m = 1.4$  is for the case of imminent danger to human life.

Respectively, assuming  $\gamma_m = 1.4$  and  $\text{FAT} = 71$  MPa = 724 kgf/cm<sup>2</sup>, we obtain from (8):

$$N_j = C \left(\frac{514}{\Delta\sigma_j}\right)^m \tag{9}$$

where  $C = 2 \cdot 10^6$ ,  $m = 3$  at  $10^4 < N_j < 5 \cdot 10^6$  cycles, and  $C = 2.54 \cdot 10^6$ ,  $m = 5$  at  $5 \cdot 10^6 < N_j < 10^8$  cycles.

Dependence (9) can be used to evaluate durability after the most conservative variant of recurrent cyclical loading (2) using data of Table 2.

In the case of account taking of the loading spectrum consisting of three recurrent cycles, determined by dependences (1), durability  $N_{sp}$  by [1] is determined by linear summation of the damage instances (Palmgren–Mainer method):

$$\sum_{j=1}^m \frac{n_j}{N_j} = 1, \tag{10}$$

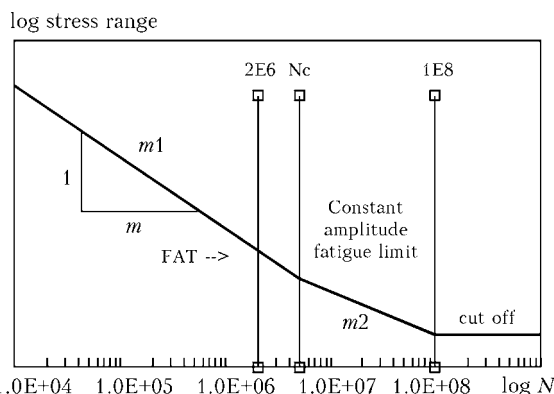


**Figure 4.** Woehler curves [1] for some FAT at  $N < 10^8$  cycles

where  $n_j$  is the number of  $j$ -cycles with amplitude  $\Delta\sigma_j$ ; and  $N_j$  is the same as in (9).

If  $n_j = \alpha_j N_{sp}$ , where  $\alpha_j$  is the fraction of the  $j$ -th loading in total loading on the basis of  $N_{sp}$  cycles, then from (10) it follows that

$$N_{sp} = \frac{1}{\sum_{j=1}^m \frac{\alpha_j}{C_j \left(\frac{514}{\Delta\sigma_j}\right)^{m_j}}} \quad (11)$$

What concerns the methodological issues of evaluation of cyclical strength of the joints considered along axes 1 and 2 (see Figure 1), so in accordance with the initial data, in the wall of the pylon 32 mm thick, to which with welds 2, 3 and 22 the adjoining elements are welded, act the following nominal stresses along said axes.

These are design constant stresses  $\sigma_{zz}^d = -134.9$  MPa at amplitude  $\Delta\sigma^d = 20.8$  MPa. Under the action of such a loading, transverse fatigue cracks may appear. In [1] the potential of such cracks is also evaluated on the basis of FAT for such type of joints. Away from the ends of the weldment, the joints considered correspond to No.323 and have the value  $FAT = 90$  MPa. At the end of the welded adjoining element having a smooth transition with radius  $r > 150$  mm (Figure 5), welded joints correspond to No.522 and also have a value  $FAT = 90$  MPa. Here it is worth noting that high negative stresses  $\sigma_{zz}^d$  are no hindrance

for fatigue damage initiation, since in that zone act high tensile residual longitudinal stresses (similar to  $\sigma_y$  of the base material, i.e. of about 350–400 MPa), therefore real loading cycle will be within a tensile zone at  $R > 0.5$ . Therefore in dependence (3) for the assumed  $[\Delta\sigma]$ ,  $f_1(R) = 1.0$ .

Similar situation is also observed at transverse loading of considered welded joints, where after Table 2, design constant stresses in the negative zone are as high as  $-53$  MPa. Although transverse residual stresses during welding rarely exceed  $0.5\sigma_y$ , i.e. of about 170 MPa, nevertheless at said  $\sigma_c^d$ , cyclic loading occurs in the tensile zone.

**Results of calculation of durability of welded joints of AUv0-06 weldment.** Table 3 shows the results of calculation of minimal durability  $N$  by dependence (9) for variants (1), initial data on which are also entered in Table 2. It is the most conservative variant of recurrent cyclic loading giving durability  $N$  exceeding  $10^7$  ( $1.7 \cdot 10^7$ ) cycles in all considered points of the welded joints 2, 3, 20, 21 and 22 along the axes 1–4 (see Figure 1).

For comparison, there also is presented durability  $N_{sp}$  by dependence (10) for cyclic loading spectrum (1) in each weldment. Values  $\alpha_j$  (proportion of the  $j$ -th loading in the total loading on the basis of  $N_{sp}$  cycles) was assumed within the following limits:

- variant 2:  $\alpha_j = 0.9$  for  $\Delta\sigma_{max}$ , for the rest  $\alpha_j = 0.05$ ;
- variant 3:  $\alpha_j = 1/3$  for all  $j = 1, 2, 3$ .

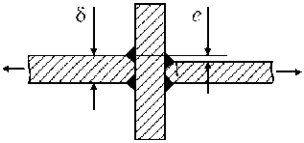
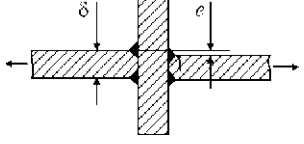
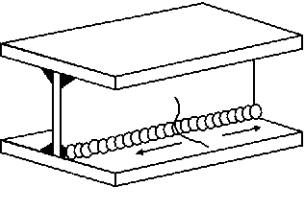
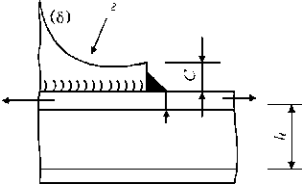
Weldment No.	Structural detail (structural steel)	Description	FAT
411		Cruciform joint or T-joint, K-butt welds, full penetration, no lamellar tearing, misalignment $e < 0.15\delta$ , weld toe ground, toe crack	80
412		Cruciform joint or T-joint, K-butt welds, full penetration, no lamellar tearing, misalignment $e < 0.15\delta$ , toe crack	71
323		Continuous manual longitudinal fillet or butt weld (based on stress range in flange)	90
522		Longitudinal fillet welded gusset with radius transition, end of fillet weld reinforced and ground, $c < 2\delta$ , max 25 mm, $r > 150$ mm	90

Figure 5. Types of welded joints and FAT values [1] corresponding to considered welded joints of arch pylon weldment

It is seen that loading spectrum schemes used give less conservative results on calculated durability compared with the extreme variant of recurrent cyclic loading (1).

For welded joints 2, 3 and 22 along axes 1 and 2 (see Figure 1), durability, by the condition of formation of transverse fatigue cracks, is determined following (8) as

$$N = C \left( \frac{\text{FAT} f_3(\delta)}{\Delta \sigma \gamma_m} \right)^m, \quad (12)$$

where  $C = 2 \cdot 10^6$ ,  $m = 3$  at  $10^4 < N < 5 \cdot 10^6$  cycles, or  $C = 2.54 \cdot 10^6$ ,  $m = 5$  at  $5 \cdot 10^6 < N < 10^8$  cycles;  $\text{FAT} = 90 \text{ MPa} = 918 \text{ kgf/cm}^2$ ;  $f_3(\delta)$  is determined by (6), i.e.  $f_3(\delta) = (25/32)^{0.3} = 0.93$ ;  $\Delta \sigma = 208 \text{ kgf/cm}^2$ ;  $\gamma_m = 1.4$ .

Respectively, by (12), we obtain durability

$$N = C \left( \frac{918 \cdot 0.93}{208 \cdot 1.4} \right)^m = 5.5 \cdot 10^8 \text{ cycles.}$$

## CONCLUSION

Results of calculation of durability of the welded joints Nos. 2, 3, 20, 21, 22 along the axes 1–4 of weldment AUv0-06 of arch pylon on the basis of preset loading and recommendations of IIW [1], based on rather conservative generalization of the experimental data, obtained for standard welded joints, show that

- fatigue strength of said welded joints under the action of transverse nominal stresses is not below  $1.7 \cdot 10^7$  cycles;

- durability of the welded joints along the axes 1 and 2 under the action of longitudinal nominal stresses is not below  $10^8$  cycles.

1. (2002) Recommendations for fatigue design of welded joints and components. *IIW Doc. XII-1539-96, XV-845-96.*

# MATHEMATICAL SIMULATION OF THERMAL STRAIGHTENING OF CYLINDRICAL SHELLS AND SHAFTS WITH GENERAL DISTORTION OF LONGITUDINAL AXIS

O.V. MAKHNENKO and A.F. MUZHICHENKO

E.O. Paton Electric Welding Institute, NASU, Kiev, Ukraine

As a result of welding during manufacturing or under various actions in the course of operation, long cylindrical shells may acquire inadmissible general longitudinal axis distortion. These distortions may be caused either by local action, for example, bending of the shell axis as a result of welding of a circumferential weld, or by distributed over the length of the shell action, which causes its uniform bending over the length. One of the ways of reducing these distortions down to acceptable level may be thermal straightening, which is poorly studied and not used in practice in relation to the cylindrical shell structures. Numerical study of a distorted state (residual plastic deformations and general change of the form) of cylindrical shells in case of local heating was carried out using thermo-elastic-plastic analysis and FEM for the purpose of studying possibility of using straightening for cylindrical structures and determining optimum parameters of heating. The results obtained made it possible to successfully perform a real thermal straightening of long cylindrical shells with general distortion of longitudinal axis caused by butt welding of circumferential welds, and straightening of long auger shafts with longitudinal deflection deformations.

As a result of welding process in manufacturing or under the action of different effects in operation, long cylindrical shells can assume unacceptable general distortions due to longitudinal axis bending. Such deformations can be caused either by a local effect, for instance bending of shell axis due to application of the girth weld, or by a distributed along the shell action, which leads to uniform bend along the entire length. One of the ways of reducing such distortions to an acceptable level can be thermal straightening, which, in the context of cylindrical shell-like structures, is poorly studied and is not used in practice.

In order to study the possibility of applying thermal straightening for cylindrical structures, as well as determine optimal parameters of heating, numerical investigation of distorted state (residual plastic strains and general shape change) of cylindrical shells by local heating, using thermo-elastic-plastic and FEM analyses, were conducted. The results obtained enabled to successfully perform real thermal straightening of long cylindrical shells having general distortions like bending of the longitudinal axis caused by applying butt girth welds, as well as straightening of long auger shafts with longitudinal deflections.

Forecasting general bending distortions of a long cylindrical thin-wall shell in welding non-closed girth welds on the basis of the general approach of thermo-elastic-plastic theory and FEM analysis is at present a rather complicated task, requiring elaboration of a 3D mathematical model and considerable computational resources in looking for the solution. Inasmuch as during thermal straightening decision on the selection of thermal effect parameters must be obtained promptly, in real time, it was decided to work

out a calculation algorithm of determining parameters of thermal straightening on the basis of the approximated method of shrinkage function (inherent strain method).

Objective of the study was development of thermal straightening techniques of general bending distortions of the cylindrical shell axis.

Tasks of the study were as follows:

- carry out numerical investigation of the distorted state of cylindrical shells at local heating using thermo-elastic-plastic and FEM analyses;
- perform theoretical substantiation and work out a calculation algorithm to control the straightening process on the basis of the approximated method of shrinkage function;
- approbate the developed straightening method by experimental straightening of a long cylindrical shell and auger shaft;
- make a conclusion on the workability of the developed straightening method.

**Theoretical substantiation.** Figure 1 shows a schematic of a non-closed girth heating of a long cylindrical thin-wall shell. Heat of  $AB$  strip provides transverse shrinkage from heating the strip in a free state, dashed line encircles a zone  $D$  wide, where transverse shrinkage tensile forces are active:

$$N_{xx} = \int_{-\delta/2}^{\delta/2} \sigma_{xx} dz, \quad (1)$$

$$N_{xx} = \frac{E}{1 + \nu} [\epsilon_{xx} + \nu \epsilon_{\beta\beta} - \epsilon_{xx}^p],$$



where  $\epsilon_{xx}$  and  $\epsilon_{\beta\beta}$  are the distortions along  $X$  axis and circumference on the median surface  $z = 0$ ;

$$\epsilon_{xx}^P \approx -\frac{\Delta_{tr}}{b} \quad (2)$$

is the free shrinkage distortion on the basis of plastic deformation zone  $b$  wide.

Neglecting the  $\nu\epsilon_{\beta\beta}$  value and using the plane sections hypothesis, i.e.

$$\epsilon_{xx} = \epsilon_{xx}^0 + \chi R \cos \alpha, \quad (3)$$

where  $\chi = -\frac{\partial^2 W}{\partial x^2}$  is the shell axis curvature, then the equilibrium equation for section  $x = \text{const}$  is

$$\int_0^{2\pi} N_{xx} d\alpha = \frac{E}{1+\nu} [2\pi\epsilon_{xx}^0 - 2\alpha\epsilon_{xx}^P] = 0;$$

$$\int_0^{2\pi} N_{xx} R \cos \alpha d\alpha = 2 \frac{E}{1+\nu} \left[ \chi R^2 \frac{\pi}{2} - \epsilon_{xx}^P R \sin \alpha \right] = 0.$$

Wherefrom we obtain

$$\epsilon_{xx}^0 = \epsilon_{xx}^P \frac{\alpha}{\pi}; \quad \chi = \frac{2\epsilon_{xx}^P \sin \alpha}{\pi R}. \quad (4)$$

Curvature value  $\chi$  of the shell axis is the function of  $x$  coordinate. Respectively,

$$\chi = \chi(x) = -\frac{\partial^2 W}{\partial x^2}. \quad (5)$$

Searched for angle  $\beta$  of curvature of the shell axis is

$$\beta = \frac{\partial W}{\partial x} = -\int_{-D}^D \chi(x) dx = \frac{-2\epsilon_{xx}^P \sin \alpha}{\pi R} 2D. \quad (6)$$

Using for  $\epsilon_{xx}^P$  dependence (2) and assuming that  $b = \delta K_1$  and  $D = \delta K_2$ , we obtain

$$\beta = \frac{2\Delta_{tr} \sin \alpha}{\delta K_1 \pi R} 2\delta K_2 = \frac{4\Delta_{tr} \sin \alpha}{\pi R} K_3. \quad (9)$$

**Algorithm of heating parameters selection.** If the cylindrical shell has a longitudinal bend caused by some local action (Figure 2), for instance non-linearity of the shell axis from application of a girth weld, so straightening must be performed by heating of strip in the site of axis non-linearity. Location of such a heating is chosen such that the angle coordinate of

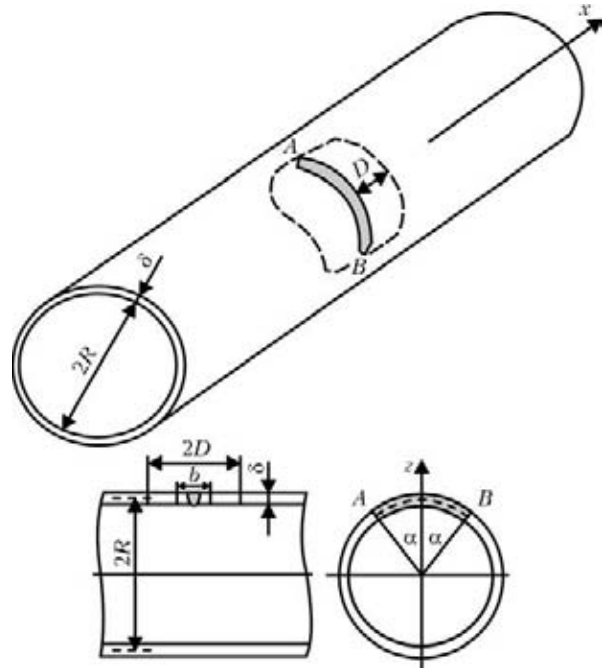


Figure 1. Schematic of circumferential heating of long cylindrical thin-wall shell (for designations see the text)

the heating median point is equal to the coordinate of maximum shaft outward bend of the axis ( $-W_{\max}$ ). In so doing the length of the heating strip is determined through the  $\alpha$  angle by the following dependence:

$$\sin \alpha = \frac{\pi R}{4\Delta_{tr} K_3} \beta,$$

where  $R$  is the shell radius;  $\Delta_{tr}$  is the transverse shrinkage from heating strip;  $K_3 \approx (1-2)$  is the calculation-experimental factor;  $\beta = \frac{W_{\max}}{L}$  is the angle of deviation of the shell axis.

If the cylindrical shell has a uniform along-the-axis curvature (Figure 3), then straightening should be performed by a series of  $N$  heating strips, uniformly distributed along the shell. In so doing the length of the heating strips is determined through angle  $\alpha$  by the following dependence:

$$\sin \alpha = \frac{\pi R}{4\Delta_{tr} K_3} \frac{4W_{\max}}{L(1+(N-1)N)}.$$

**Straightening of cylindrical shells.** On the basis of EBW and the developed calculation algorithm, were conducted experiments of thermal straightening of axis curving distortions of the long cylindrical shell from titanium alloy VT-1, consisting of three 2 m

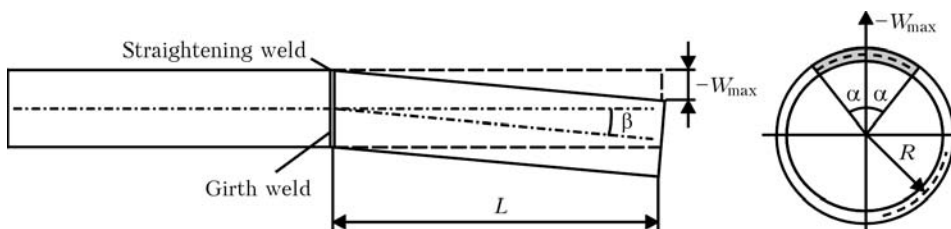


Figure 2. Straightening calculation algorithm for cylindrical shell with longitudinal bend

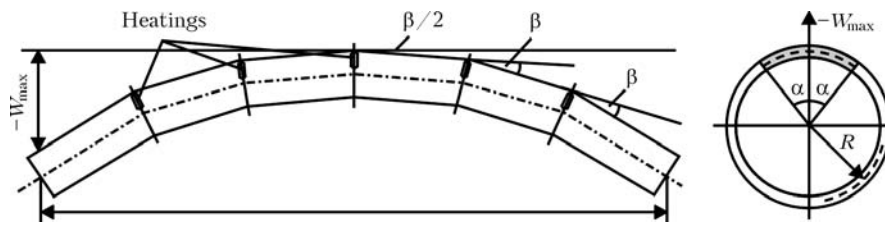


Figure 3. Straightening calculation algorithm for cylindrical shell with uniform along-the-axis curvature

long sections, having diameter 350 mm and wall thickness 6 mm (Figure 4). As curving distortions can develop during applying of butt girth welds, it was therefore decided to straighten the shell by applying non-closed beads over the existing girth welds. First, it does not introduce into the shell any new fusion zones nor HAZ, due to the use of the existing girth weld zones. Second, as was shown in experimental measurement of distortions in EBW of plates, repeated beads have close values of transverse shrinkage compared to the first bead, i.e. repeated heating does not practically reduce efficiency of thermal straightening.

The objective of the experiment was to carry out approbation of the new method of thermal straightening of general curving distortions of the long cylindrical shell, as well as to experimentally precise the value of factor  $K_3$  in the worked out calculation algorithm, as applied to said cylindrical shell and EBW conditions.

Therefore, in the sites of the butt girth welds, were applied non-closed welds of different lengths. Half of the length of the weld in straightening was performed at  $\alpha$  angle. Location of such welds was chosen on the basis of the results of measurement of curving distortions of the shell axis: angular coordinate of the median part of the bead was equal to the coordinate of maximum shell deviation, but with a minus sign. EBW conditions for these welds were preset a bit less powerful than for standard conditions of applying a butt girth weld, so that dimensions of the HAZ would not exceed the already existing HAZ of the butt girth weld. The selected EBW conditions of thermal straightening based on the results of measurements on plane specimens, produce a transverse shrinkage at a level of  $\Delta_{tr} = 0.15$  mm.



Figure 4. Thermal straightening of the VT-1 titanium alloy shell 6 m length, 350 mm diameter and 6 mm wall thickness having longitudinal axis bend distortions

To control the accuracy of straightening of the welded cylindrical shell, a system, enabling to measure the axis bending distortions right in a vacuum chamber was worked out. Visualization of the distortion measurements as well as of the thermal straightening can be monitored on the operator display. Deviation of the shell shape from straightness  $W$ , was measured at  $L = 1800$  mm from the girth weld. Measurements were conducted both before applying the straightening weld and after the shell was fully cooled. The results are presented in Table 1.

Experimental results have demonstrated high efficiency of the new method of thermal straightening of curvature of the axis of the long cylindrical shell, as well as confirmed validity of the assumption that magnitude of factor  $K_3$  is within  $K_3 \approx (1-2)$  range, as it was used in the developed calculation algorithm. Table 1 shows experimental data on  $K_3$  value obtained at different weld lengths in straightening. It is seen that for such a shell and welding conditions chosen for straightening, value of the factor can be quite accurately assumed at  $K_3 = 1.5$ . Thus, to determine the required weld length for straightening of the shell axis distortion, the developed calculation algorithm can be efficiently used.

Experimental results are characterized by repetitiveness with quite a satisfactory accuracy. The new method of thermal straightening enables to reduce to the acceptable value significant axis bending distortions, and in so doing in just one attempt. However, if after the first attempt bending distortions were not reduced to the required value, and then with subsequent beads, whose length must take into account variation of the distortion value, the straightening process can be successfully accomplished.

**Numerical study of the distorted state of cylindrical shells at local heating.** In order to study the possibility of application of thermal straightening to cylindrical structures and determine optimum heating

Table 1. Results of measurements

$\alpha$ , deg	$W_{\text{before}}$ , mm	$W_{\text{after}}$ , mm	$W$ , mm	$K_3$
15	1.26	0.50	0.76	1.49
15	2.04	1.16	0.88	1.72
30	3.16	1.90	1.26	1.28
30	2.36	0.79	1.57	1.60
60	3.21	0.55	2.66	1.56
60	0.75	-2.20	2.95	1.72
75	4.14	1.0	3.14	1.65
85	4.85	2.04	2.81	1.45

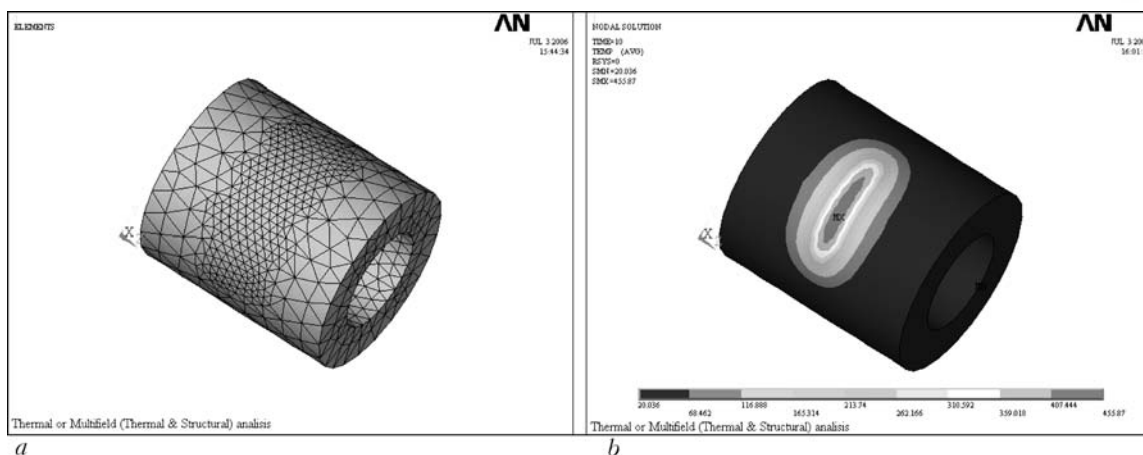


**Figure 5.** Model of cylindrical shell with finite element grid marked (a) and temperature distribution on the outer shell surface by the end of strip heating (b)

**Table 2.** Results of calculation

$\alpha$ , deg	$L$ , mm	$P_q$ , W	$T_q$ , s	$T_{max}$ , °C	$f_{max}$ , mm	$\beta$ , deg
25	40	3.2-400	30	650	0.00016	
38	62	3.9-600	10	649	0.00015 (0.00021)	
38	62	2.5-600	30	667	0.00045	
38	62	2.5-600	60	642	0.00067	
56	90	2.8-900	30	640	0.00035?	

parameters, numerical study of the distorted state (residual plastic strains and general shape change) of cylindrical shells at local heating using a thermo-elastic-plastic and FEM analyses, was conducted.

Investigation was conducted as applied to thermal straightening of long auger shafts having longitudinal deflection distortions. Since the shafts considered are hollow, so for the mathematical model (Figure 5) was chosen a cylindrical shell having the internal diameter  $D_{in} = 50$  mm corresponding to the shaft internal diameter, while the external shell diameter  $D_{ex} = 92$  mm was assumed to be equal to the mean diameter of the auger profile. Length of the cylindrical shell was limited to 100 mm. The material assumed was stainless steel 20Kh13. Heating of the heating strip was imi-

tated by the heat flux distributed along the strip. Maximum heating temperature was limited to 650 °C. A series of calculation experiments was run, aimed at determining residual value of angle  $\beta$  (see Figure 1) of the cylindrical shell bend, depending on the length of the heating strip and heating time to maximum temperature or heating power. Results of the calculations are shown in Table 2.

The results obtained enabled to successfully carry out thermal straightening of long auger shafts having bend longitudinal distortions.

**Straightening of long shafts.** General deflection distortions of long (2000 mm) auger shafts (Figure 6), caused by non-uniform heating as a result of emergency interruption of a technological process, can be reduced to an acceptable value (1 mm) by thermal straightening. Thermal straightening is implemented by applying a certain number of non-closed circumferential heatings (600–650 °C) having a certain length, uniformly distributed along the shaft (Figure 7). Locations of such heatings is chosen on the basis of measurement of deflection distortions of the auger axis, such that angular coordinate of the median part of the heating is equal to the coordinate of maximum shaft outward bend ( $-f_{max}$ ). Heating length can be rather efficient at  $L_h \approx (0.1-0.2)2\pi R$ , but not

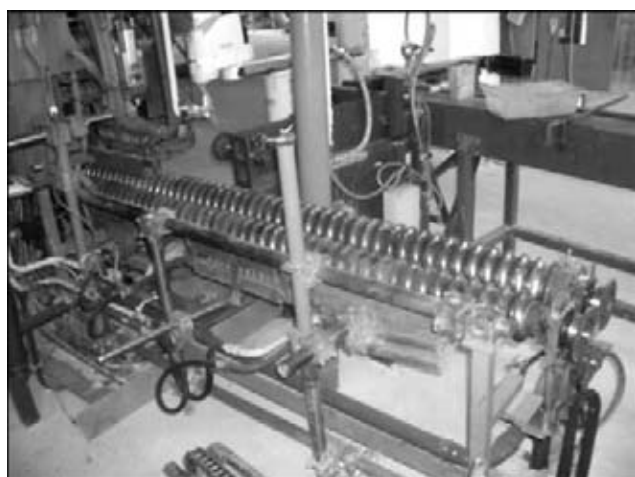


**Figure 6.** General view of the stainless steel auger shafts 2000 mm length

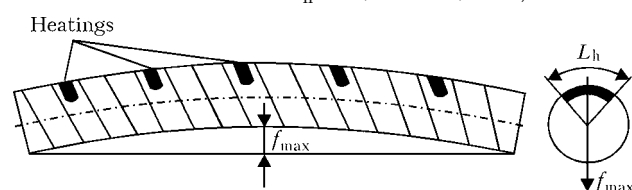


**Figure 7.** Heating sketch

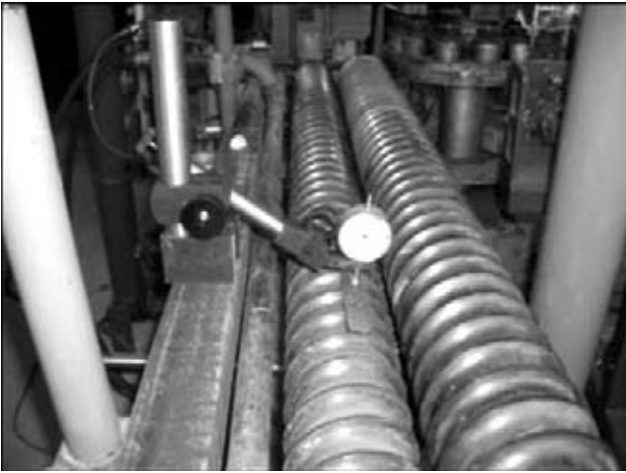


Figure 8. Measuring shaft deflections



Figure 9. Performing circumferential non-closed heating

exceeding half of the length of the shaft circumference ( $L_h < \pi R$ ).

After a series of heatings, shaft deflection measurement (Figure 8) must be performed only after its full cooling. If as a result of the first attempt of thermal straightening, shaft axis deflections were not reduced to the required value, then by progressive approximation method, with subsequent heatings the process can be successfully accomplished.

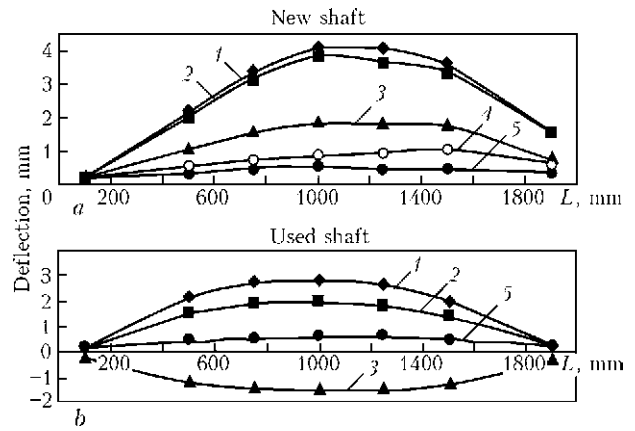


Figure 10. Results of measurements of deflections along shaft before (a) and after (b) thermal straightening: 1 – before straightening; 2 – after 1st run of heating (5 h); 3 – after 2nd run of heating (10 h); 4 – after 3rd run of heating (8 h); 5 – after 4th run of heating (5 h)

Thermal straightening (Figure 9) of two auger shafts (2000 mm long), with maximum deflection values of 4 and 2.8 mm, respectively, was carried out. Results of the measurements of deflections along the axis before and after the straightening are entered in Figure 10. After thermal straightening, deflection values were reduced to 0.5 and 0.7 mm, respectively, which satisfies the requirement to tolerance value (1 mm) for auger shaft deflection.

## CONCLUSIONS

1. Calculation algorithm for determining optimal parameters of thermal straightening on the basis of the approximate method of shrinkage function (inherent strain method) is worked out, which enables in thermal straightening of bending distortions of cylindrical shell axis, to obtain a solution on the choice of parameters of thermal effect promptly in real time.

2. Experimental approbation in thermal straightening of general bending distortions of a long cylindrical shell axis and long auger shafts has demonstrated a high efficiency of the developed method of thermal straightening.

# NUMERICAL STUDY OF FORMATION OF LAMELLAR CRACKS IN WELDING OF SHELLS OF MANHOLES INTO BODY OF RESERVOIR RVS 75,000 m<sup>3</sup> IN TOWN OF BRODY

O.V. MAKHNENKO, E.A. VELIKOIVANENKO and N.I. PIVTORAK  
E.O. Paton Electric Welding Institute, NASU, Kiev, Ukraine

Lamellar failures in state-of-the-art welded structures is rather rare phenomenon, although as far back as 40–50 years ago such defects in thick-wall structures in the area of tee, and especially cruciform joints occurred rather frequently. Substantial studies carried out in 1970–1980s of the previous century enabled establishment of more strict requirements to thick-wall steel rolled stock in regard to the content of impurities (in particular sulfur) and ductility of the material in  $z$ -direction, which enabled successful overcoming of the problem of lamellar failures in structures made of these materials. Nevertheless, it is difficult to completely exclude occurrence of lamellar defects, that's why it is necessary to take this threat into account. It should be mentioned that in a number of cases an attempt is made to place responsibility for technological or design miscalculations on insufficiently high resistance of the material to formation of mentioned defects. From this viewpoint the considered case of welding of shells of manholes from steel 09G2S 16 mm thick into body of the reservoir RVS 75,000 m<sup>3</sup> in town of Brody is rather indicative. This steel, the content of sulfur in which is ~0.045 %, has reduced resistance to lamellar failure ( $KCV = 28 \text{ J/cm}^2$  and  $\delta_c = 0.02 \text{ cm}$  in  $Z$ -direction at  $KCV = 134 \text{ J/cm}^2$  and  $\delta_c = 0.024 \text{ cm}$  in plain of the sheet), that's why observed during hydrostatic tests of the reservoir leakiness of welded joints, by which the shells of the manholes were welded to the reservoir wall using cover plates, was connected with lamellar defects in the shell. Carried out numerical study of stressed state (residual welding stresses, and total stresses allowing for stresses from the test pressure) showed that at considered thicknesses and radii of curvature in structures of protection manholes risk of occurrence of lamellar failures is very low. Change of the welded joint design made it possible to avoid leakiness in welded joints during hydraulic tests and confirmed results of numerical estimations, which showed rather low risk of lamellar failure occurrence in the considered welded assembly.

Lamellar failures in modern welded steel structures are quite a rare phenomenon, although yet 40–50 years ago such defects in thick-walled structures in the area of tee and especially cruciform joints were encountered quite often. Studies conducted in the 1970–1980s of the last century stimulated tightening of the requirements to heavy gage steel rolled stock in respect of impurities content (particularly sulfur) and material viscosity in  $z$ -direction, which promoted successful prevention of lamellar failures in structures made of such materials. Nevertheless, to fully exclude ap-

pearance of lamellar defects is evidently difficult, therefore such a danger must be taken account of. In a number of cases purely technological or design errors are attributed to insufficiently high stability of the material to the formation of said defects.

In this connection quite illustrative is the considered below a quite typical case with welding of shells of manholes into body of reservoir RVS 75,000 m<sup>3</sup> in town of Brody.

Figure 1, *a* shows a schematic diagram of cross-section of the welded joint across the weld, connecting

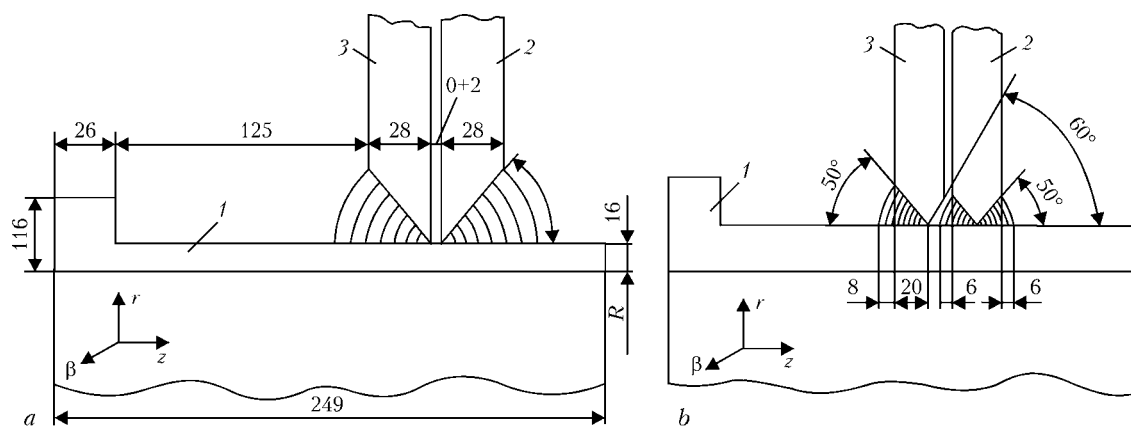


**Figure 1.** Schematic diagram of welded joint cross-section of branch pipe 1 with wall 2 and overlay sheet 3 of cleaning manhole of reservoir of the Brody LVDS, made using variant 1 (a) and 2 (b)

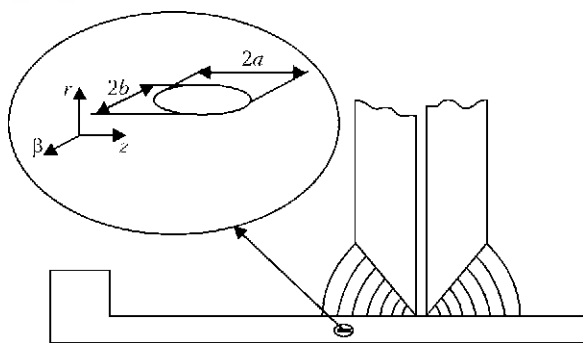


Figure 2. Scheme of lamellar crack in the welded joint zone

the branch pipe 1 with the reservoir wall 2 and the overlay sheet 3. This diagram corresponds to the conservative conditions of welding the branch pipe by one-sided welds to the wall and the overlay sheet. Along the manhole contour the curvature radius varies. In hydraulic tests variant of Figure 1, *a* provided poor tightness of the joint, which was attributed to appearance of lamellar cracks, as shown in Figure 2.

Figure 1, *b* shows a variant of a later developed welding technology of the branch pipe 1, where the shell wall 2 is first welded to the branch pipe 1 with a two-sided multipass weld, and then the overlay sheet 3 is mounted in place and welded to the branch pipe 1 with a one-sided multilayer weld. Before mounting of the overlay sheet, the weld between the branch pipe and the wall is checked for tightness. Such a variant of joint has successfully passed hydrostatic testing.

Below is considered the zone of minimal radius *R*, as this zone has the highest normal stresses  $\sigma_{rr}$ , responsible for eventual occurrence of lamellar cracks (see Figure 2).

The material of branch pipes of Figure 1 is low-alloyed steel 09G2S in compliance with GOST 19281–89, and low-alloyed steel 06G2B according to TU 14-16-150–99. Some branch pipes (approximately 25) were made from steel 09G2S, while others (approximately 70) were made, as well as the reservoir wall, from steel 06G2B. Chemical composition of the ma-

terial revealed by the spectral analysis, is shown in Table 1.

Here not shown is an important, in the context of resistance to formation of lamellar cracks, material characteristic — sulfur content. Steel 06G2B has a good isotropy of mechanical properties in all directions, therefore for branch pipes from that steel, there are no problems with lamellar failure. Steel 09G2S in compliance with GOST, may contain sulfur up to 0.045 % and possesses a quite noticeable anisotropy of mechanical properties. Below are shown respective data on mechanical properties of steel 09G2S [1] obtained during a number of works conducted by the E.O. Paton Electric Welding Institute, Kiev, Ukraine (Table 2).

From Table 2 it is seen that for steel 09G2S anisotropy of properties is quite noticeable, which requires a definite caution in its application in structures involving heavy gages and loads across the rolling direction (in *r*-direction by Figure 1). Thickness of branch pipes of 16 mm are not considered great, but this is the limit, at and beyond which lamellar cracks at higher loads may occur (see Figure 2).

Lamellar cracks, as it follows from [2], belong to the type of defects in the welded joint zone, which can occur when during welding the HAZ experiences action of loading force aimed towards sheet thickness (*r*-direction). Such a loading can occur during the welding process itself (welding stresses), or due external loading during testing or operation of the welded joint.

The principal factor affecting plastic properties of the steel sheet throughout its thickness is the concentration of non-metallic inclusions. These inclusions of sulfide or oxide type, during sheet manufacture (rolling) get elongated, whereby films or aggregates (strips) parallel to the rolling direction are formed. Under the action of high normal stresses in the plane of such a film, depending on the properties of the base material, brittle or viscous-brittle lamellar fractures (lamellar cracks) may occur.

Table 1. Chemical composition of the material of branch pipes 600 × 900 and 900 × 1500 mm

Steel	Element content, %									
	C	Si	Mn	Cr	Ni	Cu	Nb	Mo	Al	Ti
09G2S	0.08–0.12	0.50–0.74	1.25–1.70	0.002–0.092	0.05–0.12	0.011–0.310	0.001–0.012	–	–	–
06G2B	0.04–0.08	0.27–0.32	1.28–1.36	0.004–0.110	0.04–0.07	0.21–0.23	0.028–0.031	0.062–0.078	0.027–0.037	0.011–0.017

Table 2. Mechanical properties of steel 09G2S 35 mm thick containing, %: 0.05C, 0.67Si, 1.3Mn, 0.1Cr, 0.02Ni, 0.02V, 0.05Cu, 0.017P, 0.045S

Sample positioning	Tensile test at $T = 20\text{ }^{\circ}\text{C}$				Impact bending $KCV$ , $\text{J}/\text{cm}^2$ , at $T$ , $^{\circ}\text{C}$				$\delta_c$ , mm
	$\sigma_y$ , MPa	$\sigma_t$ , MPa	$\delta$ , %	$\psi$ , %	–70	–40	0	+20	
Standard position	405	493.6	31.75	76.3	54.5	72.5	174.0	134	0.24
<i>r</i> -position (across rolling direction acc. to GOST 28870–90)	349	476.3	27.45	32.0	8.5	12.0	27.5	28	0.02

Note. Here  $\sigma_y$  — yield point,  $\sigma_t$  — tensile strength,  $\delta$  — relative elongation,  $\psi$  — reduction in area,  $\delta_c$  — critical opening.

Thus, resistance to lamellar failure of steel sheets is controlled by the quantity of sulfide or oxide inclusions, i.e. by the sulfur content in steel, as well as by the properties of the matrix to resist both origination and propagation of lamellar cracks. It is natural that with the same quantity of sulfide films, resistance to origination of lamellar cracks is higher with a more plastic matrix, therefore the value of reduction in area in testing the samples cut-out across the sample thickness, is to a certain degree a characteristic of said resistance.

Based on the results of multiple tests of structural steels by the Japanese researchers [2], it is suggested to refer them, by their resistance to lamellar cracks, to one of the 3 classes.

1. Class A: high-resistant steels with  $S < 0.007\%$  and  $\psi_r \geq 25\%$ .

2. Class B: resistant steels with  $S < 0.01\%$  and  $\psi_r \geq 15\%$ .

3. Class C: low-resistant steels with  $S \geq 0.02\%$  and  $\psi_r \geq 8\%$ .

Said classification provides for the quite stringent conditions in respect of stressed state, i.e. corresponds to welding of rather highly loaded weldments of very thick elements.

Steel 09G2S under conditions of Table 1, is difficult to refer to a concrete class (A, B or C). It can however be stated that with regard for sulfur content, it is susceptible to lamellar cracks formation, in the presence of significant enough stresses applied in  $r$ -direction (see Figure 2).

**Stressed state in branch pipes in welded joint zone.** Stressed state in branch pipes in welded joint zone is controlled by the effect of the welding thermal deformation cycle, as well as by external load (for instance, by hydrostatic pressure). To determine welding stresses, a method of consecutive monitoring of temperature fields, stress and deformation development in performing welding joints, was used. A computer FEM-based software package WELDPREDIC-

**Table 3.** Calculated values of  $q_h$  for variant 2 in Figure 1, *b*

Pass No.	$q_h$ , J/cm
1	15937.5
2	15937.5
3	23906.25
4	23906.25
5	15937.5
6	15937.5
7	23906.25
8	23906.25
9	15937.5
10	15937.5
11	23906.25
12	23906.25
13	23906.25
14	23906.25
15	23906.25
16	23906.25
17	23906.25

TIONS, developed by the E.O. Paton Electric Welding Institute, was used.

Manual arc welding was simulated in filling the groove by 10–12 passes, both in welding to the wall and welding to the overlay sheet (see Figure 1). Accordingly were chosen welding modes and arc heat input, i.e.  $I_w = 170\text{--}300$  A,  $U_a = 25\text{--}26$  V,  $v_w \approx 0.15\text{--}0.20$  cm/s for variant 1 in Figure 1, *a*, and  $I_w = 170$  A,  $U_a = 25$  V at various  $v_w$  values corresponding to  $q_h$  values of Table 3 for the variant 2 of Figure 1, *b*.

Necessary for the calculation thermophysical properties, viscosity characteristics depending on the temperature for low-alloyed steels of the type considered are available in the database of the package

**Table 4.** Mechanical and thermophysical properties of steel 09G2S used in the calculations

$T$ , °C	$E$ , MPa	$\sigma_y$ , MPa	$\alpha$ , $1/^\circ\text{C}$	$\lambda$ , J/(cm-s·°C)	$c_T$ , J/(cm <sup>3</sup> ·°C)
20	208000	400	0.0000120	0.520	3.76
100	203000	367	0.0000120	0.508	3.80
200	199000	347	0.0000130	0.479	3.88
300	195000	335	0.0000137	0.442	4.01
400	188000	310	0.0000142	0.425	4.15
500	172000	282	0.0000147	0.400	4.33
600	153000	220	0.0000150	0.360	4.55
700	143000	114	0.0000152	0.325	4.96
800	130000	53	0.0000153	0.280	5.48
900	108000	37	0.0000190	0.260	5.48
1000	82000	25	0.0000194	0.270	5.42
1100	32000	16	0.0000194	0.290	5.38
1200	7000	8	0.0000195	0.300	5.36

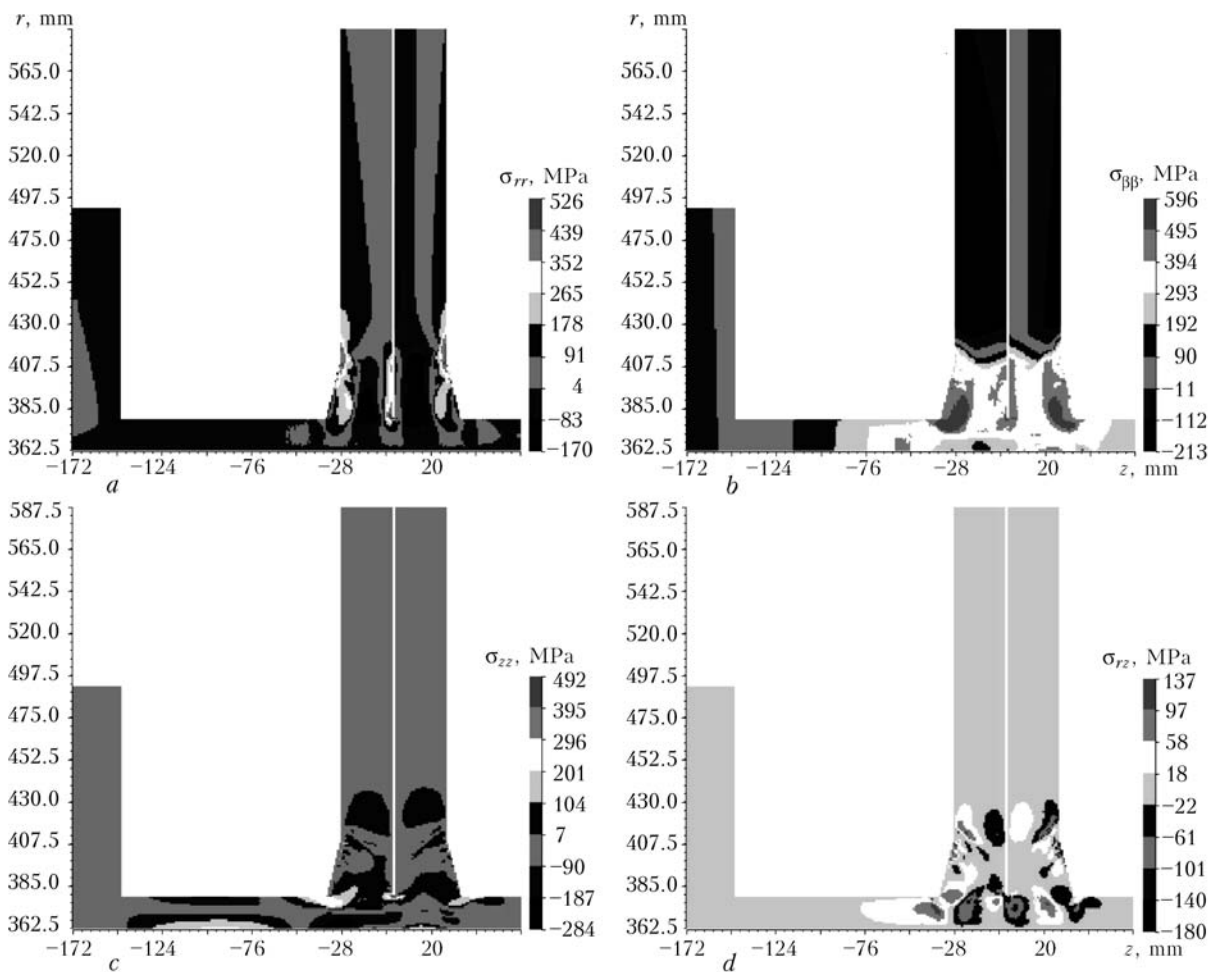


Figure 3. Distribution of residual stresses  $\sigma_{rr}$  (a),  $\sigma_{\beta\beta}$  (b),  $\sigma_{zz}$  (c) and  $\sigma_{rz}$  (d) across weld axis in cross-section at  $R = 362.5$  mm

used. The printout of these data for steel 09G2S, used in our calculations, is shown in Table 4.

Below are presented the results of calculation for cross-sections with respect to weld axis ( $z = 0$ ) of Figure 1 for normal stresses  $\sigma_{\beta\beta}$  along the axis of the weld, acting in the plane of branch pipe generatrix transverse stresses  $\sigma_{zz}$ , through-thickness stresses  $\sigma_{rr}$  and tangential stresses  $\sigma_{rz}$ .

Data of Figure 3, *a-d* demonstrate the general picture of distribution of residual welding stresses over the cross-section, after completing the welding procedure by variant 1 of Figure 1, *a* for  $R = 362.5$  mm. It is seen that the largest area of high tensile residual stresses is connected with the longitudinal stresses  $\sigma_{\beta\beta}$ , while the smallest — with through-thickness stresses  $\sigma_{rr}$ .

As for our further considerations are important numerical values of stresses  $\sigma_{rr}$ , so in Figures 4 and 5 are shown in more detail distributions of such stresses in the branch pipe weld zone of  $-38 < z < 38$  mm for variant 1, where the solid line marks penetration and re-crystallization zone ( $T > 1300$  °C), where lamellar cracks are not formed because typical lamellar structure produced in rolling steel 09G2S, is not present there. Higher residual stresses  $\sigma_{rr}$  below the mentioned line are observed at  $R = 362.5$  mm, however

these values do not exceed 203 MPa (see Figure 4, *a*), and for  $R = 503.5$  mm — 192 MPa (see Figure 5, *a*).

Application of the method of continued monitoring of stressed state development, enables to take account of loading of the considered zone with hydrostatic pressure in testing the reservoir by water filling, as one of the stages of monitoring, after obtaining data on residual stresses. Figures 4, *b* and 5, *b* show such results for stresses  $\sigma_{rr}$ . It is seen that such a loading partially changes the distribution pattern and magnitudes of  $\sigma_{rr}$ . Characteristically, that maximum values of  $\sigma_{rr}$  markedly grow only in the concentrator zone, between the wall and the overlay leaf (zone  $z = 0$ ), where their magnitudes reach about 216 (see Figure 4, *b*) and 206 MPa (see Figure 5, *b*).

Similar picture is observed for other  $R$  too; thus the above regularity remains in force, i.e. increasing  $R$  reduces  $\sigma_{rr}$ .

Considered also was a variant 2 of a welded joint of Figure 1, *b*. Respective calculations data have shown that at lower welding heat inputs, for this case stresses  $\sigma_{rr}$  somewhat increase in the near-weld zone below fusion line, however such stresses do not exceed 250 MPa.

**Risk of lamellar cracks formation in the steel 09G2S branch pipes.** Since the steel in question features a reduction in area of beyond 25 % ( $\psi = 32$  %



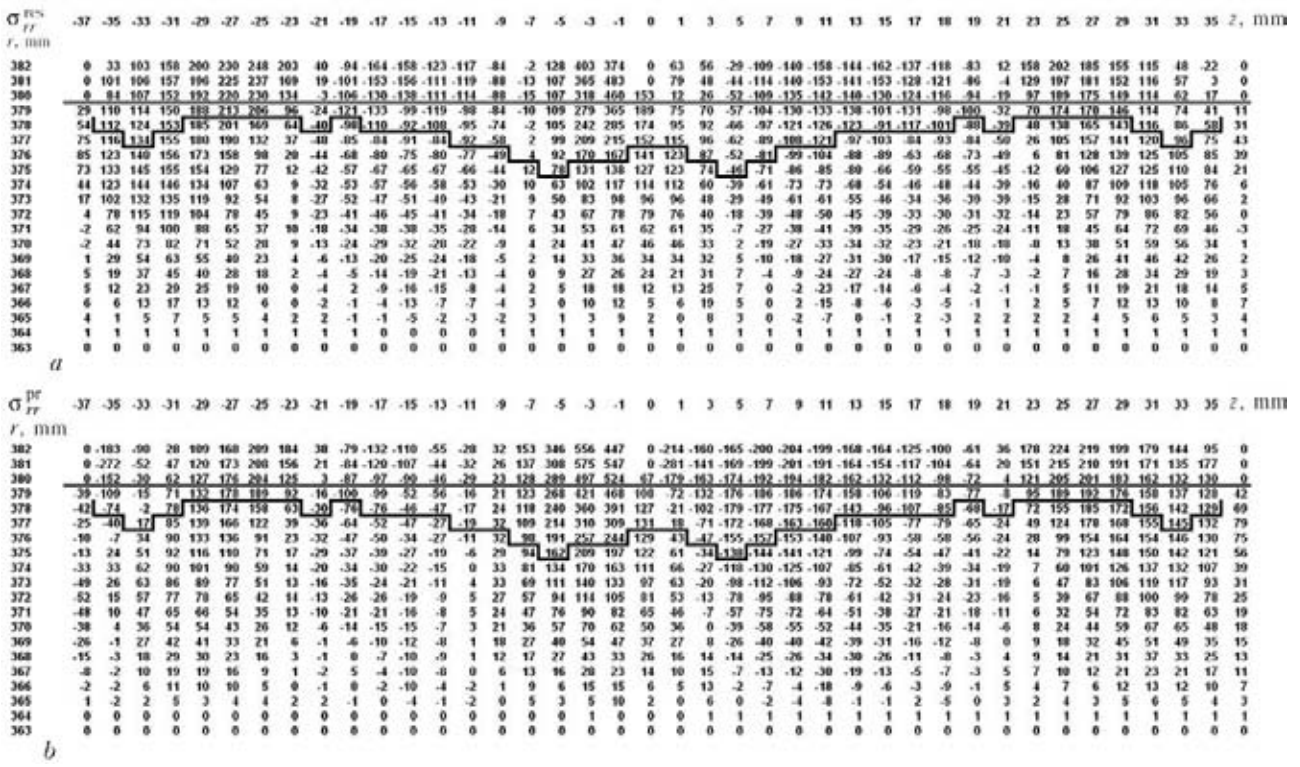


Figure 4. Residual stresses  $\sigma_{rr}$  across weld axis (a) and total stresses  $\sigma_{rr}$  in hydrostatic pressure testing the reservoir (b) for  $R = 362.5$  mm (solid line shows dividing the weld zone and the base metal by fusion line)

by Table 2) at  $r$ -direction tensile, the process of origination of lamellar type cracks involves tensile normal stresses  $\sigma_{rr}$  at the level exceeding the yield point of the material at respective testing. Judging from the data of Table 1, this level is  $> 350$  MPa. This is an average level corresponding to specimen section in

such testing. True local stresses of incipience will evidently be higher, nearing the value of  $\frac{\sigma_t}{1 - \psi/100} = 726$  MPa.

Hence, the condition of non-incipience of lamellar cracks, if normal stresses  $\sigma_{rr}$  are below 350 MPa, can

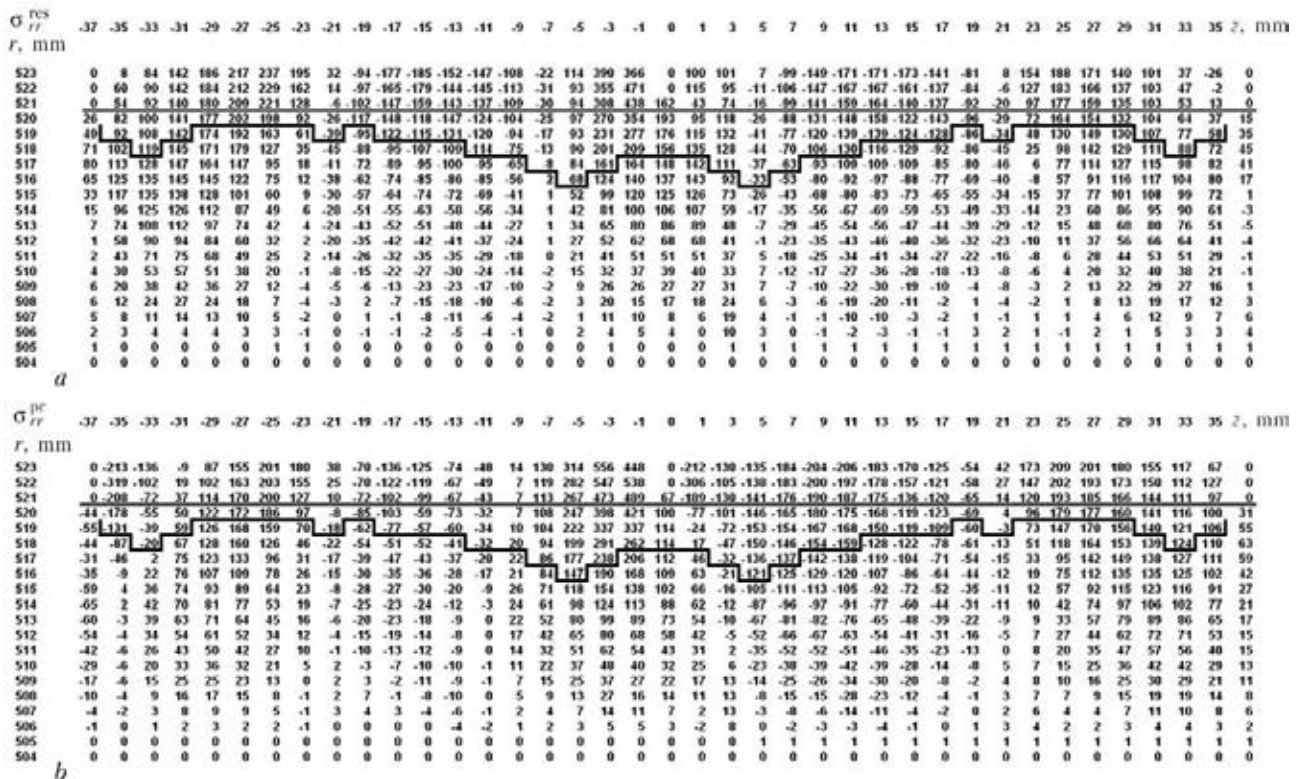


Figure 5. Residual stresses  $\sigma_{rr}$  across weld axis (a) and total stresses  $\sigma_{rr}$  in hydrostatic pressure testing the reservoir (b) for  $R = 503.5$  mm (solid line shows dividing the weld zone and the base metal by fusion line)

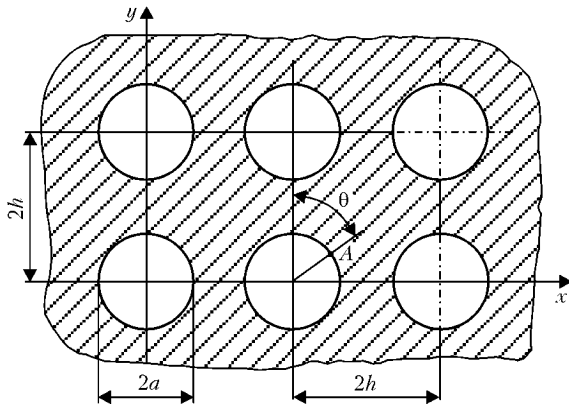


Figure 6. Section of infinite body with double-periodic system of disc-like cracks in plane  $r = 0$ .

be easily considered as a quite conservative condition, which fully matches the stressed state in Figures 3–5.

However this is not sufficient, since crack nuclei on one or other reason can already exist in the branch pipe material of the considered joint zone, irrespective of residual and total stresses  $\sigma_{rr}$ . It is necessary to evaluate the potential of such defects growth in the  $\sigma_{rr}$  stress fields, discussed before.

As a pre-condition of such a growth, it is possible with a certain degree of conservatism, to apply the condition of brittle initiation of a plane crack with a normal  $r$  and dimensions  $2a \times 2b$  (see Figure 2).

The condition can be written as  $\bar{\sigma}_{rr} \sqrt{\pi a} f_r = K_c$ , where  $\bar{\sigma}_{rr}$  is the mean stress in the area  $z \pm a$  of Figures 4 and 5, and  $f_r$  is the factor depending on  $a/b$  relation and distance between neighboring cracks.

In a specific case, for a system of disc-like cracks, having a period of  $2h$  (Figure 6), under tensile stresses  $\sigma$  normal to  $x, y$  plane,  $f_r$  in point  $A$  is determined after [3] by the dependence

$$f_r = \frac{2}{\pi} [1 + 0.2393\varepsilon^3 + 0.0810\varepsilon^5 + 0.0574\varepsilon^6 + \varepsilon^7 \times \\ \times (0.0035 + 0.0537(\cos^4 \theta + \sin^4 \theta) + \\ + 0.0147 \cos^2 \theta \sin^2 \theta)]; \\ \varepsilon = a/h.$$

At  $a/h = 0.8$  and  $0.9$ ,  $f_r = 0.744$  and is about 1.162, respectively. With a certain degree of conservatism, it can be accepted that in reality  $f_r < 1.4$ .

Fracture toughness of material in  $r$ -direction,  $K_c$ , can be determined through values of  $\delta_c$ ,  $\sigma_y$  and modulus of elasticity  $E = 2 \cdot 10^5$  MPa:

Table 5. Calculation of  $a_{cr}$  depending on  $\bar{\sigma}_{rr}$

$\bar{\sigma}_{rr}$ , MPa	300	250	200	150
$2a_{cr}$ , mm	10.0	14.4	22.6	40.2
$2a_{real}$ , mm, acc. to Figure 4	0	0	~ 3.0	~ 10.0

$$K_c \approx \sqrt{2\delta_c E \sigma_y} = \sqrt{2 \cdot 0.02 \cdot 2 \cdot 10^5 \cdot 350} = 1673 \text{ MPa} \cdot \text{mm}^{1/2}.$$

Accordingly we find that critical dimension  $2a_{cr}$  depending on stresses  $\bar{\sigma}_{rr}$ , is determined as

$$2a_{cr} = 2 \left( \frac{1673}{\bar{\sigma}_{rr}} \right)^2 \frac{1}{\pi f_r} = 0.324 \left( \frac{1673}{\bar{\sigma}_{rr}} \right)^2.$$

Table 5 shows the results of such a calculation for different  $\bar{\sigma}_{rr}$ . There too are entered values of  $a_{real}$  after Figure 4, within which range the level is not below  $\bar{\sigma}_{rr}$ . It is seen that  $a_{real}$  is significantly lower then value of  $a_{cr}$ , i.e. the possibility for growth of hardly possible hypothetical discontinuities having  $a_{cr}$  dimensions in the stress field  $\sigma_{rr}$  obtained, shown in Figure 4, is rather limited. Similar phenomenon is observed for the data of Figure 5, as well as for other manhole sizes of  $R > 362.5$  mm.

## CONCLUSIONS

1. On the basis of the conducted analysis of stressed state in the welded joint zones of oval-shaped manholes of reservoir RVS 75,000 m<sup>3</sup> and resistivity of the material of the steel 09G2S branch pipe to origination and propagation of lamellar cracks, it follows that the possibility of through defects of lamellar crack type in branch pipes is very small. It can be explained by relatively small thickness of branch pipe walls (16 mm) and rather high (over 25 %) values of reduction in area of material in the direction normal to the rolling plane.

2. It can be considered that application of steel 09G2S for branch pipes of oval-shaped manholes of reservoir RVS 75,000 m<sup>3</sup>, is quite acceptable.

3. Observed in hydrostatic tests of the reservoir leakiness of welded joints in Figure 1,  $a$ , is involved with poor design and technological solution of the welded joint.

- Bernadsky, A.V. (2000) Influence of anisotropy of the rolled stock mechanical properties on initiation and development of tough and lamellar-tough fractures. *The Paton Welding J.*, **7**, p. 31–37.
- Hrivnyak, I. (1984) *Weldability of steels*. Moscow: Mashinostroenie.
- (1988) *Fracture mechanics and strength of materials: Handbook. Vol. 2: Stress intensity factors for bodies with cracks*. Ed by V.V. Panasyuk. Kiev: Naukova Dumka.

# ASPECTS OF PREDICTING SAFE OPERATION PERIOD OF WELDED JOINTS WITH THE ESTABLISHED DEFECTS

V.I. MAKHNENKO

E.O. Paton Electric Welding Institute, NASU, Kiev, Ukraine

In approximately 70 % of fixed infringements of conditions of safe operation (refusals) of modern welded structures it is connected with welded joints and the defects arising at various stages of operation in their zone. In this connection perfection of methods of forecasting of a resource of safe operation of welded joints of responsible long period of operation structures is enough an actual problem to which a lot of works in the different countries is devoted. At the E.O. Paton Electric Welding Institute also closely concern to the decision of various questions of this problem, thus importance of the system approach based on corresponding monitoring loading of welded joints (units), their conditions given to technical diagnostics during the moment of an estimation of a resource of safe operation, use of authoritative settlement codes for the forecast, objective decision-making (for example, on the basis of risk-analysis) is emphasized. Four sections of this system approach are considered in the report on separate concrete examples of an estimation of a resource of safe operation of welded joints of various structures.

Safe operation of the critical welded structures involves recurrent technical diagnostics of the condition of such structures, on whose basis different shape defects, discontinuities, degree of degradation of the «hot spots» material to resist different types of failure, and then prediction of safe operation period until the next examination is made.

As the welded joints, in the overwhelming number of cases, are «hot spots» of modern critical welded structures, so the methodological aspects of predicting safe operation period of the welded joints with the established defects are quite urgent. Much attention is paid to these aspects, by IIW [1, 2] and other organizations, for instance API [3, 4], PWI [5, 6], etc.

In a general case the approaches developed require knowledge of the loading of the joint zone; diagnostics of the state (geometry of the defects, degradation of the properties, residual stress); estimation codes (mathematical models of the behavior of the defects in the given conditions and the risk of integrity loss).

Detected during the diagnostics geometric defects, depending on the estimation codes applied, are subdivided into the shape defects (Figure 1) and discontinuity defects. Discontinuity defects, in their turn, are subdivided into the volumetric defects and fissure defects (Figures 2 and 3, *d*) and crack-like defects (Figures 4, *a* and 5, *b*). By origin the shape defects and discontinuities can be both technological (Figures 1, 2, 5) and operational ones (Figures 3, 4).

There are certain rules of defects schematization, used for their mathematical description [1, 3, 7 etc.]. Such a schematization to a certain degree is necessitated by the approach applied for evaluation of acceptability of the defect considered. The size of this work does not allow us to discuss in detail all representative variants of such an approach. Below are discussed two concrete typical examples, connected with practice.

*Example 1* involves the estimation of the defect acceptability in the place of local thinning of the pipe (see Figure 3, *b*). As a result of technical diagnostics, by changing real thickness in the zone of the thinning, the contour record of the thinning site in the longitudinal and lateral directions is plotted (Figure 6), on its basis the minimal measured thickness  $\delta_{\text{meas}}^{\text{min}}$  in the defect zone is determined. The basis of rather popular method of calculation of acceptability of the defects of such type [3, 8 etc.], is grounded on comparing of the value of  $\delta_{\text{meas}}^{\text{min}}$  with permissible  $\delta^{\text{min}}$  for the given section in the absence of thinning. The  $\delta^{\text{min}}$  values are usually known as they can be determined through strength calculations for the pipeline of specific designation.

Usually

$$\delta^{\text{min}} = \delta - c, \quad (1)$$

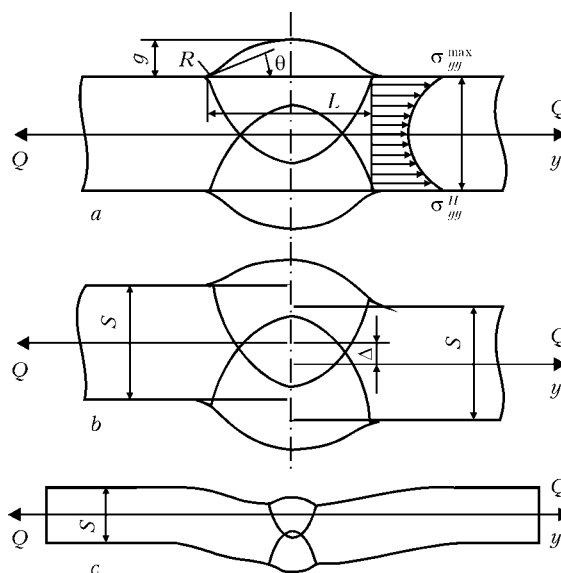


**Figure 1.** Geometric parameters, determining in butt joint concentration of stresses conditioned by weld shape (*a*), displacement of edges (*b*) and angular distortions (*c*)

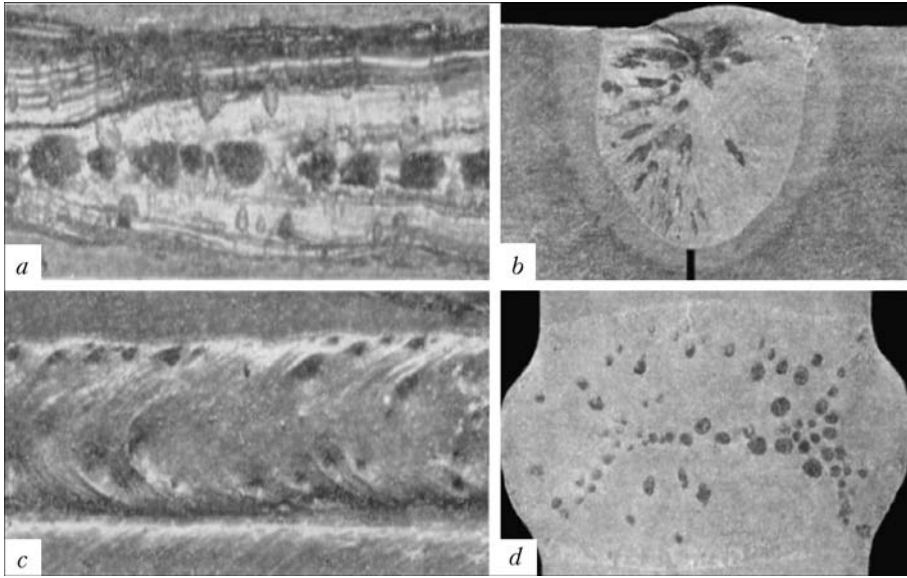


**Figure 2.** Pores in weld metal: emerging (a), not emerging (b) at weld surface, group location (c) and location of pores in electroslag welding (d)

where  $\delta$  is the nominal wall thickness,  $c$  is the total added thickness.

$$c = c_{11} + c_{12} + c_2, \quad (2)$$

where  $c_{11}$  is the addition to the wall thickness equal to the negative tolerance;  $c_{12}$  is the addition to the wall thickness, which compensates possible thinning of the semi-finished product in manufacturing;  $c_2$  is the addition to the wall thickness, which accounts the wall thinning, resulting from all types of corrosion during item service life.

Estimated thinning defect dimensions by Figure 3,  $b$  along the pipe  $s$  and circumferentially  $c$ , are determined as shown in Figure 6,  $b$  and  $c$ , in terms of their acceptability according to [3], from dependence

$$R_8^{(j)} \leq \frac{\delta_{\text{meas}}^{\text{min}} - v_{\text{cor}} t_{\text{exp}}}{\delta_{\text{min}}} \quad (j = s, c), \quad (3)$$

where  $t_{\text{exp}}$  is the expected time of safe operation (time to next examination);  $v_{\text{cor}}$  is the corrosion thinning speed;  $R_8^{(j)}$  are the geometric characteristics, relating defect dimensions  $s$  and to pipe dimensions  $c$ :

$$R_8^{(c)} = \frac{-0.736 + 10.51(c/D)^2}{1.0 + 13.84(c/D)^2} \text{ at } c/D > 0.348, \quad (4)$$

$$\text{at } c/D \leq 0.348 \quad R_8^{(c)} = 0.2;$$

$$R_8^{(s)} = 0.9(M_t - 1)/(M_t - 0.9), \quad (5)$$

$$M_t = (1 + 0.48\lambda^2)^{0.5} \text{ from [3] at } \lambda > 0.3475.$$

Such quite simple dependences based on knowledge of  $\delta_{\text{min}}$  obtained by other researchers, for instance [8], imply that in the thinning zone too, the mechanism of limiting state onset remains the same as in the absence of thinning.

In the case of detection of discontinuities in the form of cracks, such an approach is unfortunately unacceptable. Here the most accepted are approaches

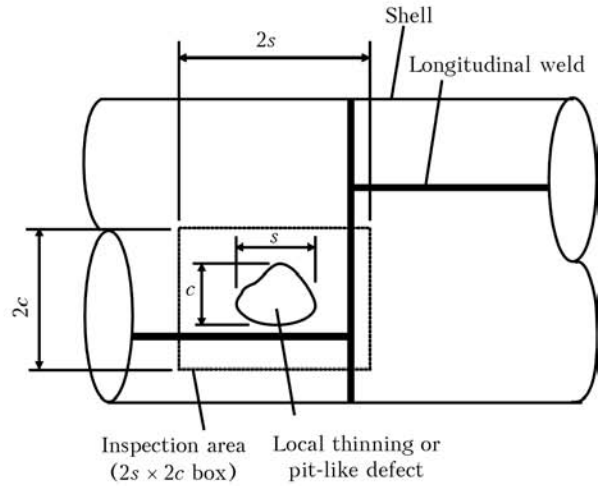
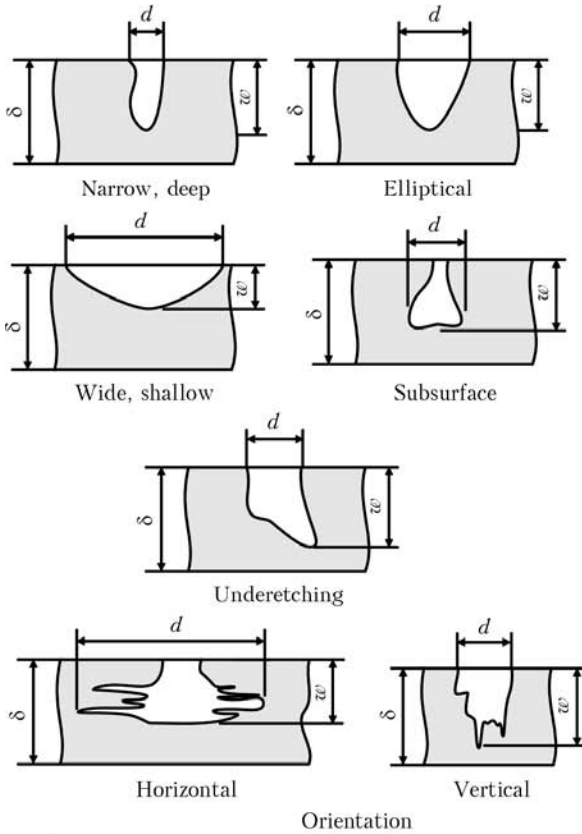
based on the premises of mechanics of failure of bodies with cracks.

Within the framework of such an approach, a crack-like defect is schematized by a crack of canonic shape of appropriate size [1, 2, 7] (Figure 7). Acceptability of a respective crack is evaluated, in the first turn, in the context of the risk of spontaneous development of such a crack in specific loading conditions. Of special attention is application for this purpose of a well-known approach R6, i.e. of the diagram of the type shown in Figure 8,  $a$ , where crack equilibrium is determined by parameters  $K_r = K_I/K_{IC}$  and  $L_r = \sigma_{\text{ref}}/\sigma_y$ , where  $K_I$  is the stress intensity factor along the contour of the considered crack, depending upon external load and residual stresses;  $K_{IC}$  is the  $K_I$  critical value from conditions of brittle and ductile failure of the material along the crack contour;  $\sigma_{\text{ref}}$  are the stresses in the crack zone proceeding from the given external load, capable at proportional growth of loading, to cause plastic collapse in the crack zone;  $\sigma_y$  is the material yield point.

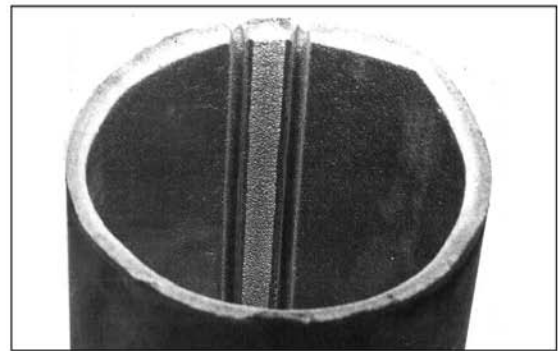
It is clear that in predicting safe operation period  $t$  of welded joints, it is necessary to take into account that detected cracks may grow, i.e.  $K_I$  and  $\sigma_{\text{ref}}$  are determined for crack dimensions with account of such growth.

Several crack growth mechanisms are distinguished, of which the main are fatigue, corrosion and creep, also combinations of these three mechanisms are possible.

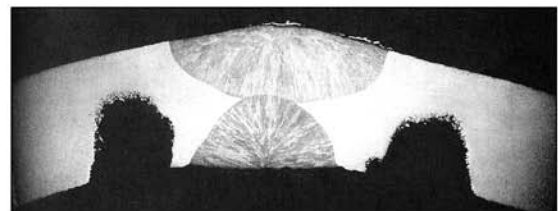
Experimental diagrams of eventual crack growth are used, those being of the type schematically shown in Figure 8,  $b$  for corrosion crack growth at static loading. In the same coordinates  $\left(\lg \frac{dv}{dt}, K_I\right)$  are plotted graphs for crack growth in conditions of static creep. At repeated loading the graph is constructed in coordinates  $\lg \frac{\Delta l}{\Delta N}, \Delta K_I$ , where  $\Delta l/\Delta N$  is the rate of growth during one cycle of varying loading;  $\Delta K_I$  is the  $K_I$  change range during one cycle.



b

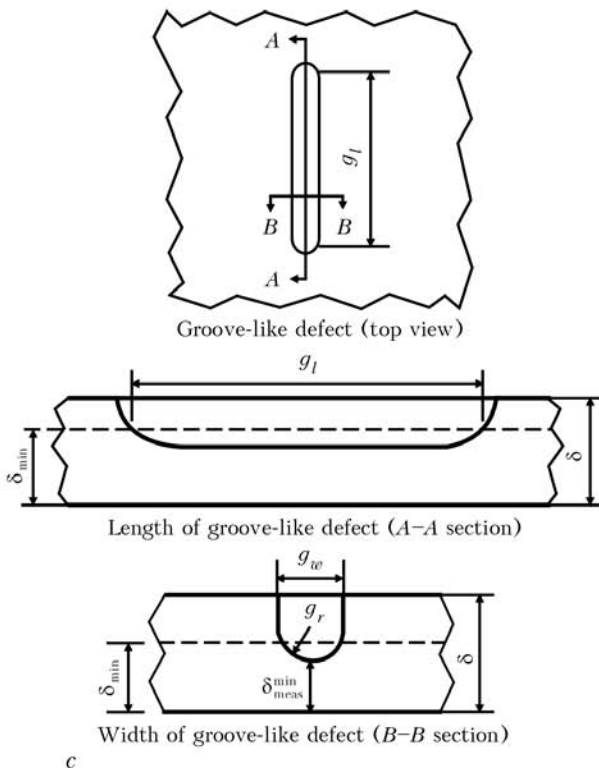


Fragment of pipe with intercrystalline corrosion in HAZ



Cross section of longitudinal pipe weld showing corrosion extent

d



c

**Figure 3.** Bulk discontinuity defects of material in form of separate pittings (a), local thinning of pipe (b), elongated bulk defects in form of groove-like flow (c) and intercrystalline corrosion in pipe of stainless steel type 304 (d):  $s$  – longitudinal size of defect;  $c$  – transverse one (for the rest designations see the text)

Such diagrams have three quite typical sections (see Figure 8, b), namely section I accounts for quite small growth rates, section II – for intense crack growth, and section III is the zone of imminent spontaneous failure.

Conditional border between I and II sections for purely corrosive cracks is  $K_{ICSS}$ , where the principal

electrochemical growth mechanism changes to hydrogen embrittlement.

For creep cracks, as well as for fatigue cracks, section I is separated from section II by threshold values, respectively  $K_{th}$  and  $\Delta K_{th}$ .

Sections II and III are separated in approximately all cases by  $K_{IC}$  value, depending on temperature,

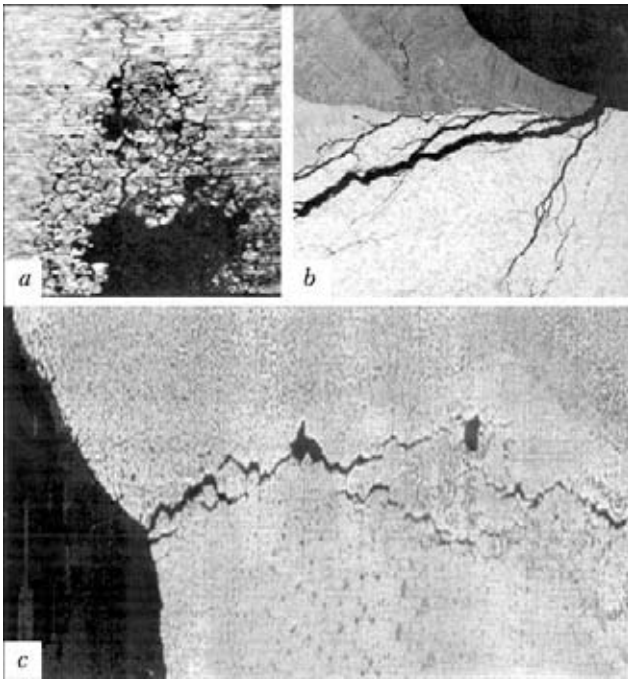


**Figure 4.** Corrosion of austenitic stainless steel showing its inter-grain nature (a), transcrystalline stress corrosion initializing in fillet weld zone (b), and stress corrosion cracking (c), initiated in fusion line near the weld root

microstructure, etc. of the structural material of the given chemical composition.

Consider a concrete example.

*Example 2.* During planned maintenance works'2005, conducted in January 2006, on steam generator 3 of power unit 4 of the Zaporozhie NPP in the zone of weld 111, a discontinuity was detected by ultrasonic control method, which in accordance with the existing Rules has features of surface crack-like defect of  $a = 40$  mm deep and  $2c = 90$  mm long (Figure 9, b). Stresses in the zone of that defect (residual post-weld and high annealing, and caused by

pressure in steam generator  $P = 6.4$  MPa) are shown in Tables 1 and 2 for section  $\beta = \text{const}$ , that is in  $r, z$  system of coordinates. The crack considered is oriented in plane  $z = \text{const}$  and emerges on the free surface of the «pocket», from where it initiates now by stress corrosion mechanism. The crack is schematized by semi-elliptic crack with semi-axes  $a \times c$  in the near-weld zone (at the root of weld 111).

Wall thickness in crack zone is  $\delta = 72.5$  mm. Summary normal stresses  $\sigma_{zz} = \sigma_{zz}^{\text{res}} + \sigma_{zz}^{\text{norm}}$ , equal to  $\sigma_{zz}^{\text{res}}$  residual ones plus  $\sigma_{zz}^{\text{nom}}$  nominal ones due to pressure  $P$ , in the branch pipe wall in crack plane by data of Table 1, are shown in Figure 10. Along the circumference of the branch pipe (coordinate  $\beta$ ), stressed state is not changing. Data of Table 1 were obtained by calculations using the WELDPREDICTIONS software package developed at the PWI. It was assumed that with crack corrosion growth, distribution of stresses  $\sigma_{zz}$  in Figure 10 is not changing.

Values of  $K_I G$  and  $K_I D$  in representative contour points (see Figure 9, b) were calculated based on  $\sigma_{zz}$  curve in Figure 10, using dependences of [7], i.e.

$$K_I(j) = s_j J_j \sqrt{a/1000}, \text{ MPa}\cdot\text{m}^{1/2},$$

$$j = G, D \tag{6}$$

$$\text{at } a/c \leq 1.0; \quad a/\delta \leq 0.7,$$

where

$$J(j) = \frac{\sqrt{\pi} \gamma(j)}{\left[ 1 - \left( 0.89 - 0.57 \sqrt{\frac{a}{c}} \right)^3 \left( \frac{a}{\delta} \right)^{1.57} \right]^{3.25} \left[ 1 + 1.464 \left( \frac{a}{c} \right)^{1.656} \right]^{70.5}};$$

$$J_j = \gamma(D) = \left[ 1 + 0.32 \left( \frac{a}{\delta} \right)^2 \right] \left[ 1.23 - 0.09 \frac{a}{c} \right] \sqrt{\frac{a}{c}};$$

$$\gamma(G) = 1.12 - 0.08 \frac{a}{c}; \tag{7}$$

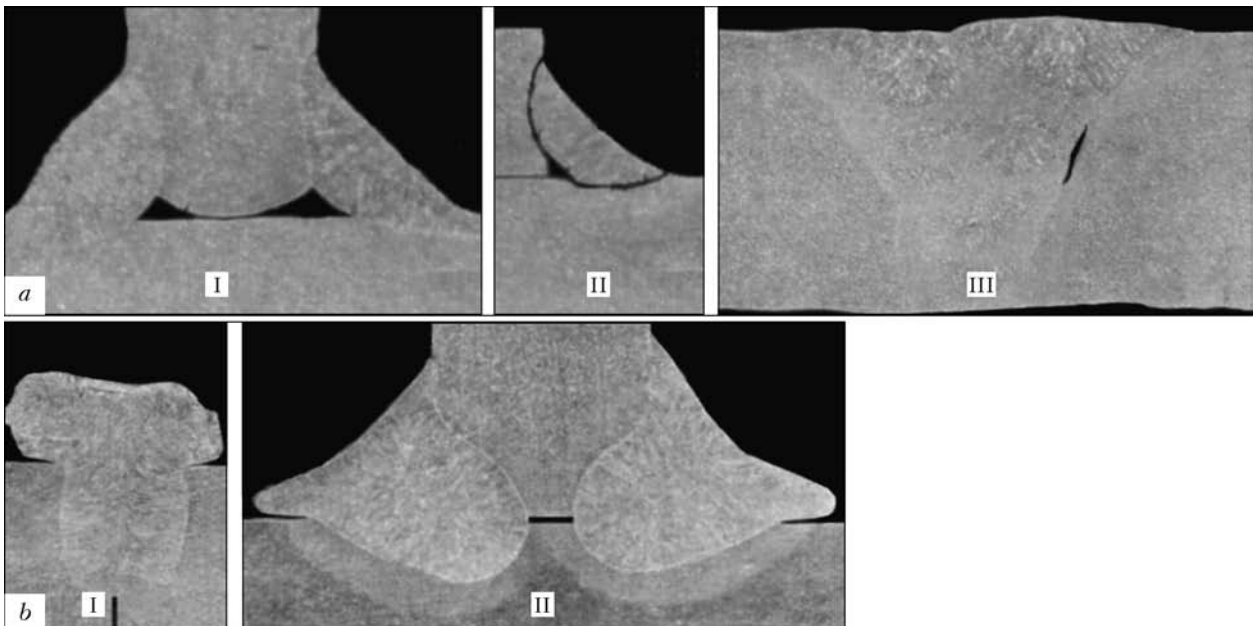


**Figure 5.** Lacks of fusion in heel (I, II) and along the edge (III) (a), overlap in welding of butt (I) and fillet (II) welds (b)

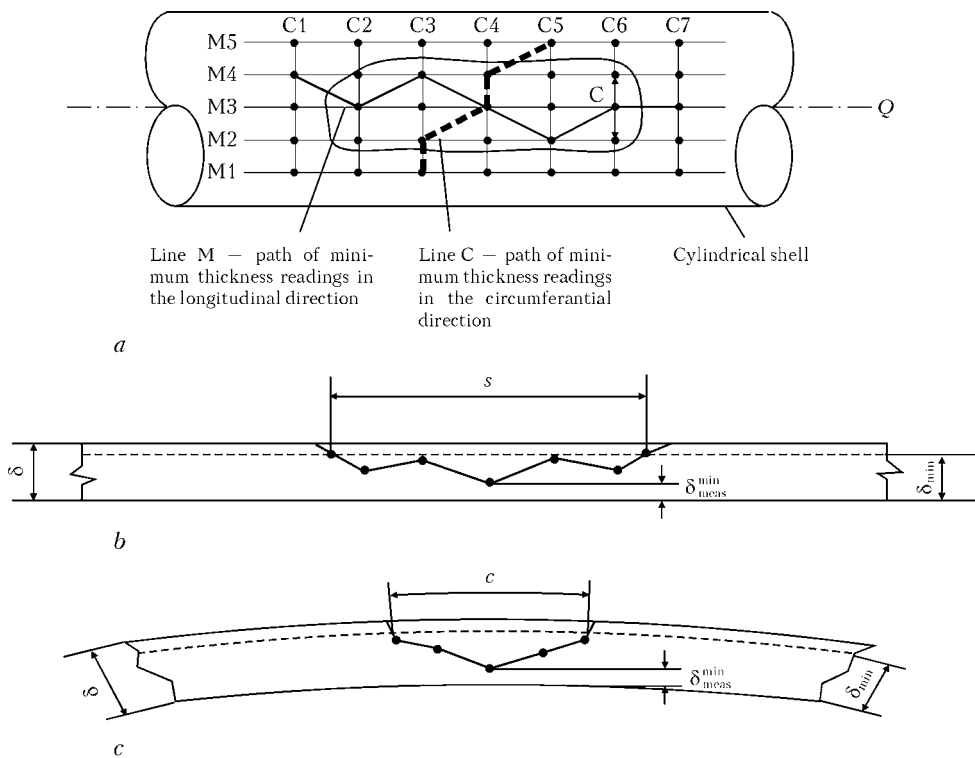


**Figure 6.** Surface defects of «local thinning» type in pipelines: *a* – inspection planes and critical thickness profile; *b* – critical thickness profile – longitudinal plane (projection of line M); *c* – critical thickness profile – circumferential plane (projection of line C)

$s_j$  is the equivalent stresses, defined by the formulae [7] as

$$s_G = \sum_{i=0}^{20} \left[ C_i + \frac{a}{c} D_i + \lambda E_i \right] \sigma_{zz}(i),$$

$$s_D = \sum_{i=0}^{20} F_i \sigma_{zz}(i).$$

Here,  $\sigma_{zz}(i)$  are the summary  $\sigma_{zz}$  stresses based on curve in Figure 10 at depth  $(a/20)i$  ( $i = 0, 1, 2, \dots, 20$ ) from the surface;  $C_i, D_i, E_i, F_i$  are the tabulated weight functions of [7];

$$(8) \quad \lambda = \frac{a}{\delta} \left[ 1.0 - 1.9 \left( \frac{a}{c} \right)^{1.75} + 0.9 \left( \frac{a}{c} \right)^{1.5} \right]. \quad (9)$$

For deep cracks, where  $a/\delta > 0.7$  and  $0.2 \leq a/c \leq 1.0$  according to [7], dependence (6) was used:

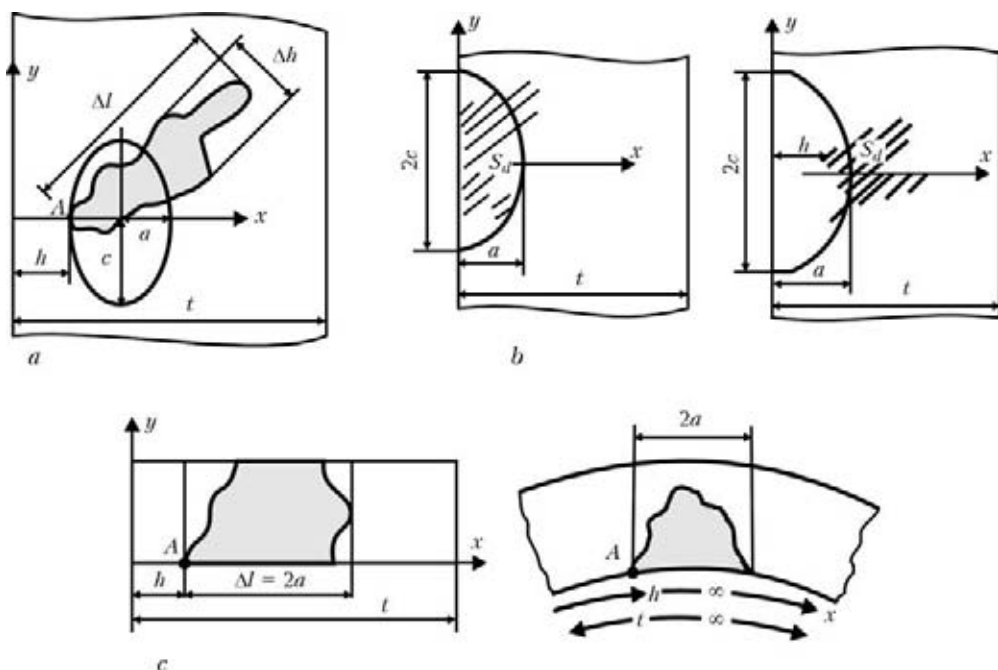


**Figure 7.** Schematization of crack-like defects: subsurface (*a*), surface (*b*) and through defects (*c*)

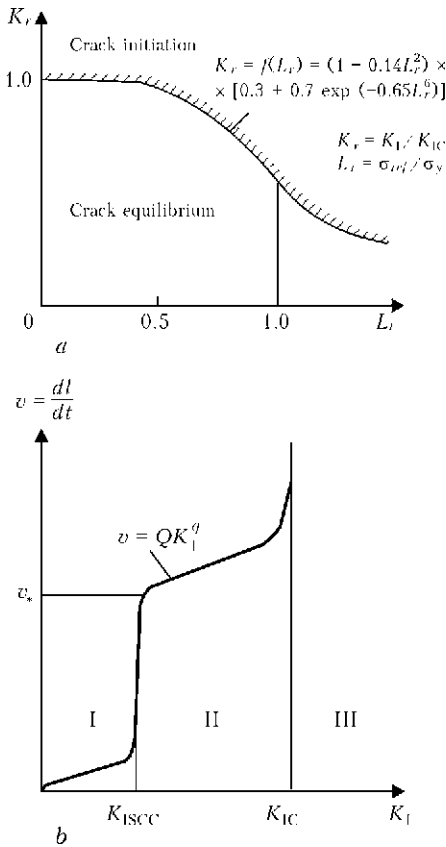


Figure 8. Criteria of acceptability of crack-like defects (static loads): DOR-diagram (a) and diagram of corrosion crack growth at static loading (b)

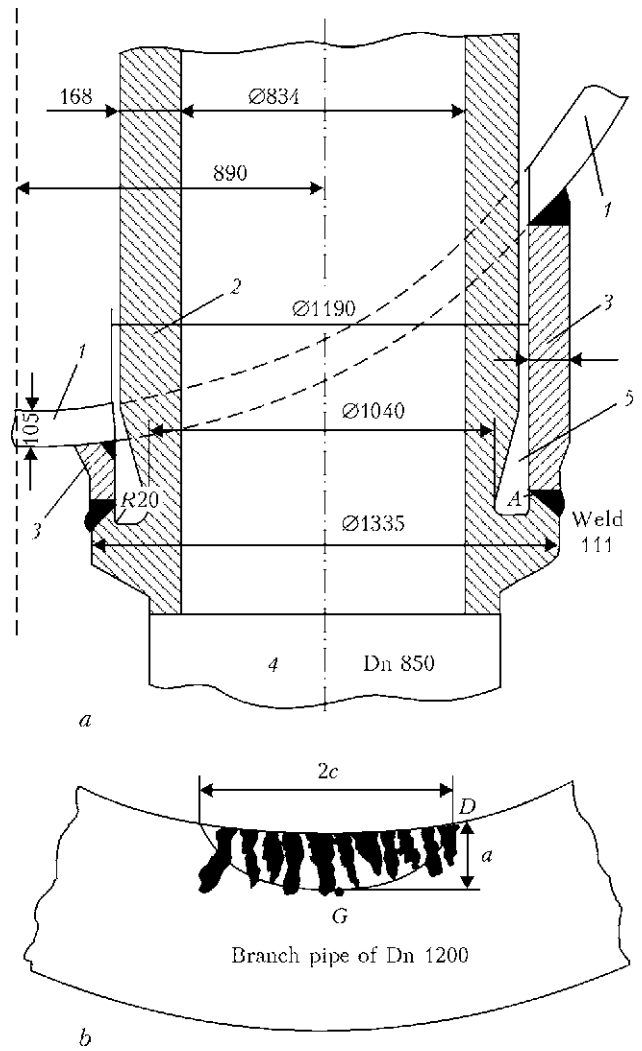


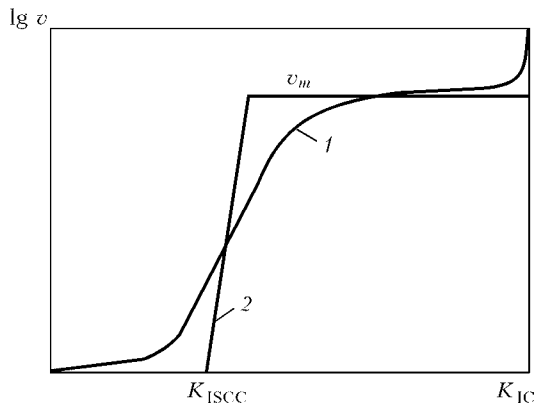
Figure 9. Diagram of weld 111 location (a) and schematization of considered discontinuity A in section  $z = \text{const}$  (b): 1 – steam generator body; 2 – collector; 3 – branch pipe; 4 – pipeline; 5 – pocket; A – discontinuity-like defect; G and D – representative points of semi-elliptical crack

Table 1. Residual stresses in zone of welded joint 111

$z, \text{mm}$	$\sigma_{pp}, \text{MPa}$								$r_1, \text{mm}$	$\sigma_{zz}, \text{MPa}$								$r_1, \text{mm}$		
	597.00	607.00	617.00	627.00	637.00	647.00	657.00	667.00		597.00	607.00	617.00	627.00	637.00	647.00	657.00	667.00			
5.000	86.85	86.16	79.91	69.22	56.83	45.29	36.04	29.33	0.00	0.00	0.00	0.00	0.00	0.00	0.00	0.00	0.00	0.00	0.00	0.00
15.000	78.68	73.50	67.96	61.79	55.16	48.58	42.70	38.36	0.00	0.00	0.00	0.00	0.00	0.00	0.00	0.00	0.00	0.00	0.00	0.00
25.000	68.66	64.57	62.28	60.81	58.88	55.92	52.38	49.80	-1.95	-2.22	-1.82	-1.44	-1.13	-0.94	-0.74	-0.74	1.08	-0.74	1.08	0.45
35.000	60.43	59.21	60.62	62.98	64.64	64.71	63.52	62.49	-4.00	-4.55	-3.61	-2.82	-2.36	-2.13	-1.65	0.45	-1.65	0.45	-2.53	-8.01
45.000	54.47	56.44	61.17	66.49	70.96	73.82	75.29	76.35	-5.28	-5.54	-4.11	-3.38	-3.36	-3.60	-3.51	-2.53	-3.51	-2.53	-8.01	-15.72
55.000	50.49	55.20	62.84	70.49	77.27	82.77	87.32	91.32	-4.79	-4.29	-2.67	-2.92	-4.16	-5.59	-6.68	-6.68	-8.01	-6.68	-8.01	-15.72
65.000	48.13	54.79	65.22	74.84	83.40	91.44	99.35	107.16	-0.98	0.10	0.79	-1.75	-5.09	-8.22	-11.22	-11.22	-15.72	-11.22	-15.72	-25.03
75.000	47.85	55.10	68.98	79.36	89.29	99.99	111.13	123.36	9.25	8.48	5.54	-0.74	-6.46	-11.37	-17.05	-17.05	-25.03	-17.05	-25.03	-35.33
85.000	49.83	65.62	74.51	84.07	95.50	108.96	122.86	138.84	32.00	20.30	9.06	-0.62	-8.14	-14.73	-23.57	-23.57	-35.33	-23.57	-35.33	-46.46
95.000	130.20	99.19	86.20	91.58	103.41	119.35	135.39	151.88	77.13	25.73	10.57	-0.15	-9.62	-17.85	-29.56	-29.56	-46.46	-29.56	-46.46	-60.02
105.000	149.72	130.69	126.18	123.01	128.53	134.43	140.64	168.11	77.15	38.92	16.74	2.45	-10.54	-14.90	-23.85	-23.85	-46.46	-23.85	-46.46	-60.02
115.000	186.77	180.50	171.04	165.63	160.97	161.56	170.41	185.63	72.34	55.81	24.51	6.80	-14.09	-30.21	-42.14	-42.14	-60.02	-42.14	-60.02	-70.82
125.000	220.88	218.10	212.87	209.39	202.81	197.88	197.18	209.39	75.02	58.04	31.26	7.83	-12.88	-30.98	-44.28	-44.28	-60.02	-44.28	-60.02	-78.54
135.000	225.84	224.91	222.37	214.19	210.04	204.41	200.93	214.19	71.89	59.03	39.01	12.81	-8.29	-30.50	-50.93	-50.93	-60.02	-50.93	-60.02	-78.54
145.000	168.50	156.43	149.18	163.81	160.58	174.71	182.66	163.81	71.18	62.12	34.81	10.29	-4.80	-29.46	-67.14	-67.14	-80.64	-67.14	-80.64	-111
155.000	157.85	145.07	145.82	154.03	164.00	175.81	191.44	154.03	73.07	55.38	37.69	19.15	-3.37	-30.38	-56.17	-56.17	-80.64	-56.17	-80.64	-111
165.000	149.33	139.96	139.98	145.89	158.92	178.75	197.80	212.97	70.90	51.62	37.78	20.00	-2.80	-28.33	-56.96	-56.96	-77.92	-56.96	-77.92	-111
175.000	140.76	132.79	132.63	141.22	157.36	179.27	203.90	220.17	70.13	47.18	31.88	17.42	0.28	-24.37	-53.05	-53.05	-75.94	-53.05	-75.94	-111
185.000	129.27	121.76	123.57	132.08	148.67	173.68	206.78	229.28	64.36	41.92	28.38	15.90	2.36	-18.87	-48.92	-48.92	-73.00	-48.92	-73.00	-111
195.000	115.26	108.45	107.98	113.02	126.15	151.31	198.05	249.03	54.66	37.11	24.34	13.21	3.03	-10.10	-36.41	-36.41	-64.85	-36.41	-64.85	-111
205.000	100.87	93.09	87.86	85.61	86.63	89.35	86.97	47.65	45.79	31.68	19.44	8.44	-0.92	-7.59	-27.82	-27.82	-54.85	-27.82	-54.85	-111
215.000	86.60	77.67	69.44	61.95	53.59	40.48	14.86	-48.71	38.92	26.40	16.02	7.04	-0.66	-10.18	-32.65	-32.65	-54.85	-32.65	-54.85	-111
225.000	73.60	63.97	53.83	42.38	28.19	8.36	-24.61	-63.10	31.55	20.91	11.88	3.72	-4.71	-15.71	-29.52	-29.52	-54.85	-29.52	-54.85	-111
235.000	62.82	52.91	41.57	28.06	11.29	-10.67	-37.26	-68.46	23.90	14.94	7.02	-0.47	-8.05	-15.34	-14.46	-14.46	-32.65	-14.46	-32.65	-111
245.000	55.26	45.35	33.47	19.13	1.78	-18.47	-41.81	-69.35	16.37	9.09	2.42	-3.70	-8.89	-10.27	-4.54	-4.54	-11.11	-4.54	-11.11	-111
255.000	51.64	41.86	29.84	15.47	-1.39	-20.33	-41.67	-66.95	9.65	4.00	1.48	-5.41	-7.62	-5.51	-1.66	10.60	-1.66	10.60	-1.66	10.60
265.000	52.50	42.84	30.93	16.66	0.27	-17.83	-38.00	-61.50	4.36	0.13	-3.49	-5.86	-5.00	-2.12	5.10	12.71	-2.12	5.10	12.71	-111
275.000	57.95	48.35	36.39	22.10	5.83	-12.13	-31.81	-54.00	0.80	-0.26	-4.58	-5.58	-4.41	-0.18	6.75	13.79	-0.18	6.75	13.79	-111
285.000	68.16	58.42	46.21	31.63	14.85	-3.83	-23.83	-45.07	-0.86	-3.35	-4.65	-4.79	-3.33	0.42	6.62	13.80	-3.33	6.62	13.80	-111
295.000	83.11	73.00	60.38	45.24	27.06	6.80	-14.46	-35.42	-0.97	-3.38	-3.77	-3.57	-2.58	0.04	4.96	12.00	-2.58	4.96	12.00	-111
305.000	102.56	92.08	79.19	62.15	42.36	20.35	-2.92	-25.70	-0.25	-2.56	-2.11	-2.30	-1.91	-0.85	2.49	8.50	-1.91	2.49	8.50	-111
315.000	126.93	116.79	103.69	87.15	67.68	46.29	24.70	3.41	0.30	-0.76	-1.01	-1.10	-1.00	-0.35	1.30	-0.35	1.30	-0.35	1.30	-111







**Figure 11.** Schematic diagram of static corrosion crack resistance of structural material: 1 –  $\lg v - K_I$  diagram based on experimental data; 2 – idealized diagram  
 $a, c, \text{ mm}$

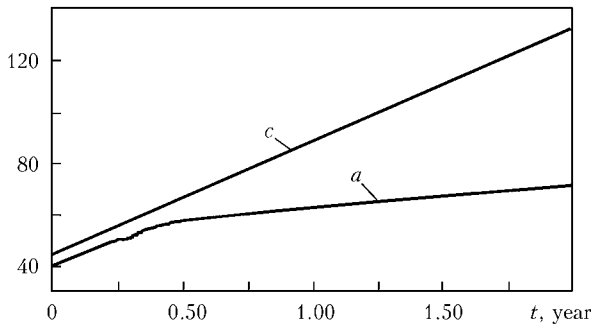


**Figure 12.** Prediction of growth kinetics in time  $t$  of original crack of  $a_0 = 40 \text{ mm}$ ,  $c_0 = 45 \text{ mm}$  for 4th steam generator of the Zaporozhie NPP at  $K_{ISCC} = 10 \text{ MPa}\cdot\text{m}^{0.5}$  and  $v_m = 44 \text{ mm/year}$

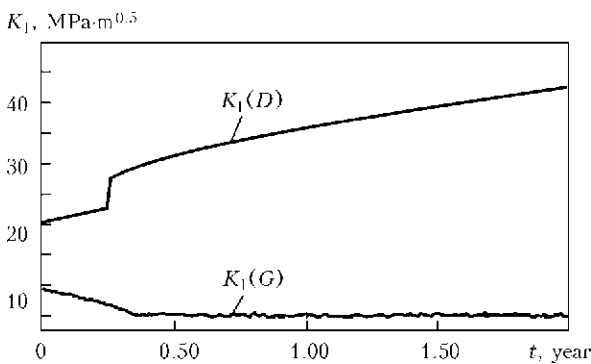


**Figure 13.** Prediction of variation in time  $t$  of SIF  $K_I(D)$  and  $K_I(G)$  for original crack of  $a_0 = 40 \text{ mm}$ ,  $c_0 = 45 \text{ mm}$  in welded joint zone 111 of 4th steam generator of the Zaporozhie NPP

Knowing magnitudes of  $K$  and  $\sigma_{\text{ref}}$ , it is possible to evaluate the reserve factor  $n$  to spontaneous failure at any moment of crack growth  $t$ , if  $a(t)$  and  $c(t)$  are also known. For that purpose we use analytical description (DOR) in Figure 8 of [3], i.e.

$$K_r n = [1 - 0.14(L_r n)^2][0.3 + 0.7 \exp(-0.65L_r^6 n^6)];$$

$$K_r = 0 \text{ at } L_r = L_r^{\text{max}} = \frac{\sigma_y + \sigma_t}{2\sigma_y}.$$

Substituting  $K_r(t)$  and  $L_r = \sigma_{\text{ref}}(t)/\sigma$ , it is possible to find  $n(t)$  from this equation. Clear, that to do this, knowledge of variation of  $a(t)$  and  $c(t)$  is necessary.

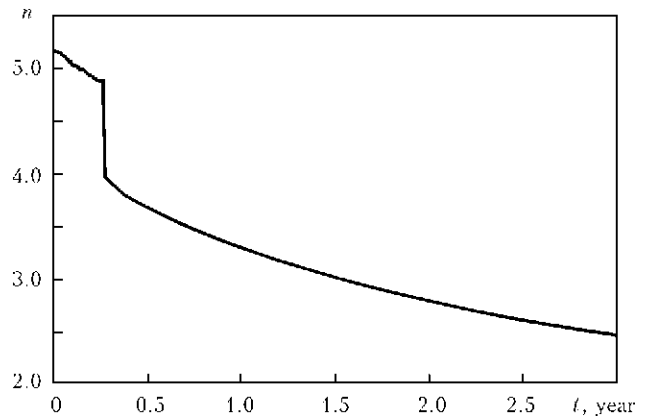


**Figure 14.** Kinetics of reduction of reserve factor against spontaneous crack growth of  $a_0 = 40 \text{ mm}$ ,  $c_0 = 45 \text{ mm}$  in time at  $K_{ISCC} = 10 \text{ MPa}\cdot\text{m}^{0.5}$

For steel 10G2NMFA, from which branch pipe of the steam generator was manufactured, on the basis of experimental data of [2], were obtained parameters  $K_{ISCC}$  and  $v_m$  (Figure 11) of simplified diagram of corrosion crack growth in the feeding water medium of the Yuzhno-Ukrainskaya NPP, which can quite conservatively be applied for the considered case of the Zaporozhie NPP.

Figure 12 shows estimated growth kinetics of  $a(t)$  and  $c(t)$  at  $K_{ISCC} = 10 \text{ MPa}\cdot\text{m}^{1/2}$ ,  $v_m = 44 \text{ mm/year}$  and  $K_{IC} = 138 \text{ MPa}\cdot\text{m}^{1/2}$ , corresponding to such growth,  $K_I(D)$  and  $K_I(G)$  values are shown in Figure 13, while  $n$  values – in Figure 14.

It seen from these data that until the next planned maintenance works'2006, that is in one year of operation, the crack depth  $a$  will increase from 40 to 62 mm, when wall thickness is 72.5 mm. In doing so the crack length will almost double, i.e. from  $2c = 90$  to  $2c = 180 \text{ mm}$ . Reserve factor  $n$  will decrease from 5.4 to 3.6. These data appeared quite sufficient for substantiation of the acceptability of the detected defect, at least for one-year service.

On insistence of the Administration of Nuclear Regulation of Ukraine, in about 5 months of service control measurement of the defect in question, was conducted. These measurements confirmed rather high conservatism of the estimation of Figure 12.

1. (1990) IIW Guidance on assessment of the fitness for purpose of weld structures. *IIW/IIS-SST-1157-90*.
2. (2002) Recommendations for fatigue design of welded joints and components. *IIW Doc. XIII-1539-96, XV-845-96*.
3. (2000) *Fitness-for-service*: Recom. practice 579. 1st ed. API.
4. (1999) *API Standard 1104*: Welding of pipelines and related facilities. Appx. 13: Service welding. API.
5. Makhnenko, V.I., Makhnenko, O.V. (2000) Development of calculation procedures for assessment of allowable defects in welded joints of critical structures. *The Paton Welding J.*, **9/10**, p. 79-87.
6. Makhnenko, V.I. (2003) Improvement of methods for estimation of residual life of welded joints in durable structures. *Ibid.*, **10/11**, p. 107-116.
7. (1990) *MR-125-01-90*: Calculation of stress intensity factors and section weakening for defects in welded joints. Kiev.
8. Garf, E.T., Netrebky, M.A. (2000) Assessment of the strength and residual life of pipelines with erosion-corrosion damage. *The Paton Welding J.*, **9/10**, p. 13-18.

# CURRENT PROBLEMS OF MATHEMATICAL MODELLING IN WELDING AND RELATED TECHNOLOGIES

V.I. MAKHNENKO

E.O. Paton Electric Welding Institute, NASU, Kiev, Ukraine

Conferences, whose main focus are problems of mathematical modelling of welding processes (related technologies), are regularly held all over the world. Here, in the first place, are to be noted those well known to the welding community:

- Computer Technology in Welding and Manufacturing (principal organizer is The Welding Institute, by now the 16-th conference, started in 1986);
- Numerical Analysis of Weldability (principal organizer is Austrian university in Graz-Seggau, the 8-th conference in 2006, held once in two years);
- Mathematical Modelling and Computer Simulation of Metal Technologies (organizer is Israeli College of Judea, Samaria, the 4-th conference in 2006, held once in two years);
- Mathematical Modelling and Information Technologies in Welding and Related Processes (organizer is the E.O. Paton Electric Welding Institute, NASU, Kiev, Ukraine, in 2006 held the 3-rd conference, started in 2000).

Despite the above coincidence in time, these conferences gather quite many participants and reports, involved with mathematical modelling in welding and related technologies, which is indicative of great interest to this field among the experts busy with studying and developing respective technologies, as well as in predicting the behavior of a product of such technologies in operational conditions. Such an interest conditions, on the one hand, ever growing requirements to efficiency and quality of products of welding technologies, and, on the other hand, promising applications evolving from the progress of computer engineering, mathematics and PC.

It is natural that main current problems of mathematical modelling in welding and related technologies are the problems of growth (expansion) of efficient application of such approaches in studying new (poorly studied) phenomena accompanying welding and related processes (deposition, coating, special electrometallurgy, etc.).

It is self-evident, that the author of this report does not endeavor to make an exhausting review of all the problems, especially with regard for quite recently published reviews [1–3]. Below are considered only some of problem issues, being, in the opinion of the author, quite topical.

In the field of mathematical modelling of typical for welding and related technologies phenomena, in

recent years of special interest are the phenomena, occurring in liquid metal as a weld pool, as well as of some other adjacent technologies.

**Evaporation and condensation.** These substantially well studied in physics and well-known in practice phenomena, attract experts in connection with description of conditions of deep penetration in electron beam welding methods [4–6 etc.], as well as in the production of materials and deposition of coatings in vacuum using electron-beam physical vapor deposition (EB-PVD) [7]. A number of reports at this conference are dedicated to this topic. Here it is worth noting that the process of liquid evaporation (especially in the form of bubble- or film boiling) refers to the 1st kind phase transitions, and is accompanied by considerable energy absorption at a given boiling temperature  $T_b$ , whose magnitude is determined by chemical composition of the liquid being heated and pressure in the vapor phase over the liquid.

In accordance with Clapeyron–Klausius equation, variation of pressure  $P$  in the forming vapor phase with variation in its temperature, is defined as

$$\frac{dP}{dT} = \frac{L}{T(V_2 - V_1)}, \quad (1)$$

where  $L$  is the latent evaporation (condensation) energy;  $T$  is the evaporation (boiling) temperature;  $V_2 - V_1$  is the variation of vapor volume in transition of the substance from liquid to the vaporous state.

Although the equation (1) holds strictly true only for equilibrium conditions, however it follows from that equation that temperature higher than boiling temperature  $T_b$ , promotes increase of pressure  $P$  in the given zone of the liquid surface. Shown in Figure 1 [6] temperature and pressure distribution diagram in EBW with deep penetration shows that in the presence of metal evaporation from the weld pool walls, a pressure drop takes place, promoting expelling the liquid metal and deeper penetration of the electron beam.

To initiate evaporation, quite a high density  $q$  of heat energy input into the given area of the liquid surface is required, i.e.

$$q \geq W_{h,f} + L \frac{dW_1}{dt}, \quad (2)$$

where  $W_{h,f}$  is the heat flux density,  $W/cm^2$ , to satisfy the condition  $T \geq T_{ev}$ ;  $dV_1/dt$  is the liquid metal

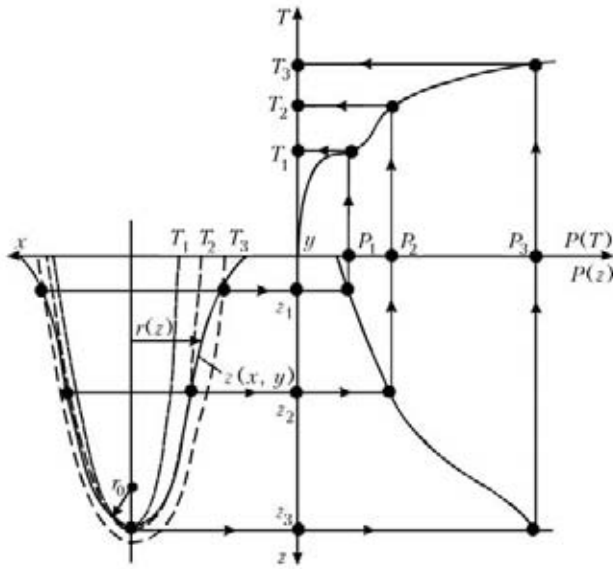


Figure 1. Diagram of pressure distribution in evaporating material from keyhole walls in EBW with deep penetration [6]

volumetric evaporation rate of the liquid metal from a unit of area,  $\text{cm}^3/(\text{s}\cdot\text{cm}^2)$ .

The Table shows data on values  $q - W_{h,f}$  at  $dV_1/dt = 1 \text{ cm}^3/(\text{s}\cdot\text{cm}^2)$  and  $T_b$  for some representative metals, from which it is seen that density of energy inputted into a unit of area of the evaporated liquid, in boiling conditions (at  $dV_1/dt > 0.2 \text{ cm}^3/(\text{s}\cdot\text{cm}^2)$ ) with regard for  $W_{h,f}$  should exceed  $10^4 \text{ W/cm}^2$ , which is usually the case with beam methods of deep penetration welding heating.

With arc methods of welding, heat flux values are usually lower. Thus, for TIG welding, distinguished for its highest concentration of heat energy, heat flux density does not exceed  $(0.2-0.3)\cdot 10^4 \text{ W/cm}^2$ .

However even with A-TIG welding (Figure 2), when due to shielding with flux of the weld zone, dimensions of the effective heating spot are decreasing, one can obtain close to  $10^4 \text{ W/cm}^2$  heat flux density, with 2-3 times decreasing effective spot diameter, which is quite feasible and, respectively, effective evaporation from the surface (in boiling con-

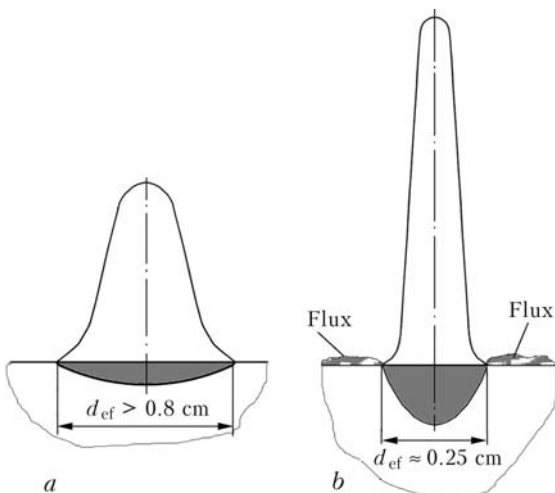


Figure 2. Diagram of inputted heat energy distribution for TIG (a) and A-TIG (b) welding

Values of  $T_b$  and  $q - W_{h,f}$  for some metals at  $dV_1/dt = 1 \text{ cm}^3/(\text{cm}^2\cdot\text{s})$

Material	Fe	Al	Ti	Cu
Parameter				
$q - W_{h,f}, \text{ W/cm}^2$	$0.477\cdot 10^5$	$0.2475\cdot 10^5$	$0.44\cdot 10^5$	$0.39\cdot 10^5$
$T_b, \text{ K}$	3023	2658	3535	2813

ditions) can be assumed being one of the possible factors of increasing penetration in A-TIG welding.

It is clear that all this requires more exhaustive investigations, where methods of mathematical modelling based on solution of the equation of mass conservation, pulse and energy for a respective vapor flux [8], will promote finding an adequate solution of the A-TIG welding problem.

Phenomenon of liquid metal vapor condensation, efficiently used in EB-PVD technology, etc., 1st kind phase transition, but only with heat emission according to equation (1), exerts some influence on heat- and mass transfer in the keyhole at heat source movement, which has not yet found a respective reflection in existing models of beam welding with deep penetration [6].

It has also to be noted that detailed mathematical description of the above well-known EB-PVD technologies is yet unavailable, though it is certain that with them many bottlenecks of those technologies could be solved with lower material and time expenses.

**Surface tension.** Surface tension in a liquid material (metal of weld pool, etc.) objectively manifests itself in almost all fusion welding technologies (Figure 3), as well as in related processes involved with liquid metal.

On the basis of knowledge of surface tension, mathematical models of welded joint formation, heat- and mass transfer in a liquid pool with regard for free surface presence, Marangoni forces, etc. [5], are constructed. Models on the basis of surface tension forces in molten metal are successfully applied in related technologies too.

Let me elaborate on one of such technologies, involving obtaining tungsten carbide spherical particles used as a component of filler material in surfacing of drill bits, etc. Tungsten carbide melting temperature is  $2780 \text{ }^\circ\text{C}$ , which substantially complicates the pro-

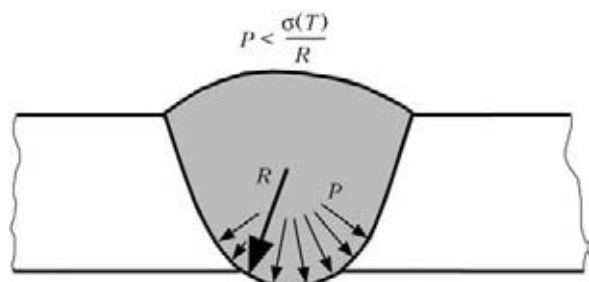


Figure 3. Diagram of one-sided butt weld formation with full penetration with regard for surface tension forces

cesses of producing tungsten carbide pellets of a given particle-size distribution. The E.O. Paton Electric Welding Institute of the NASU (Kiev, Ukraine) has developed a unique technology for tungsten carbide pellet production by melting of the tip of the rotating stick of tungsten carbide (Figure 4).

The task of mathematical modelling was construction of mathematical dependences, linking main process parameters (geometric dimensions, thermal response of heating source, rotation speed) with the process output (speed of axial feeding of the melted stick  $V_f$  as in Figure 4) and mean size of the produced tungsten carbide particles. Solution of this problem is described in detail in [9].

A closed model has been constructed, including the process of heating the tip of the stick, formation, growth and separation of the drop (Figure 5). Normal law of particle size distribution (breaking off tungsten carbide drops) was used, which parameters depend on stick rotation speed at constant power of the plasma heating source.

The process of drop formation (see Figure 5) is conditioned by the developing excessive pressure  $P$  in the melted layer on the stick tip under the influence of centrifugal forces. The  $P(r)$  values distribution depending on the stick rotation speed comes from Navier–Stokes equation. At some specific temperature of surface layer heating and respective pressure  $P(r)$ , liquid metal flat surface shape becomes less rational. This condition is defined as

$$P > \sigma(T) \frac{F_d}{V_d}, \quad (3)$$

where  $\sigma(T)$  is the surface tension of the material at  $T$ ;  $F_d$  is the surface area of the forming drop;  $V_d$  is its volume.

It was shown that the time for formation, growth and detaching of the drop in a given point of the liquid layer  $\Delta t_d$  constitutes about 30 % of time  $\Delta t_i$  spent on incubation period, connected with rehabilitation of the given area for the next formation, growth and detaching of the drop. Thus obtained time characteristics enabled us to generalize in [9], based on original parameters (Figure 6) and obtain fairly well agreeing data on process productivity and size of tungsten carbide grains.

One of the fundamental issues concerning the liquid metal, is the issue of interaction of the metal with gases and slag, involved in the welding (related) process.

In this field a number of publications on application of mathematical modelling for describing the processes of gas absorption by the liquid metal [8, 10] have appeared, using quite effective approaches for describing the process of evaporation and absorption, based on Knudsen theory and Navier–Stokes equations for evaporation and movement of metallic vapor molecules, as well as for diffusion equations for expansion of the absorbed element in the liquid metal. Compared with classic approaches based on empirics

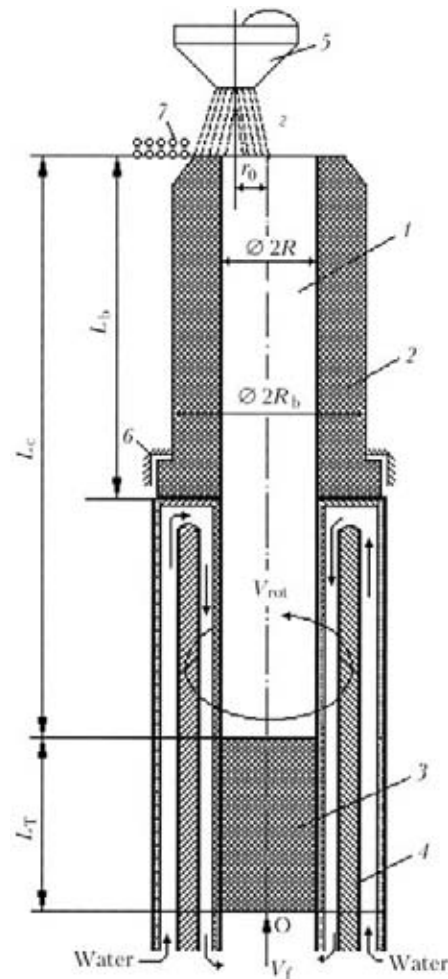


Figure 4. Diagram of tungsten carbide pellet production: 1 – tungsten carbide stick; 2 – graphite bushing; 3 – graphite pusher; 4 – water-cooled spindle axle; 5 – plasma torch; 6 – spindle support; 7 – tungsten carbide drops

of transition factors [11, etc.], mathematical models of the types developed in [8, 10] are, undoubtedly, more promising.

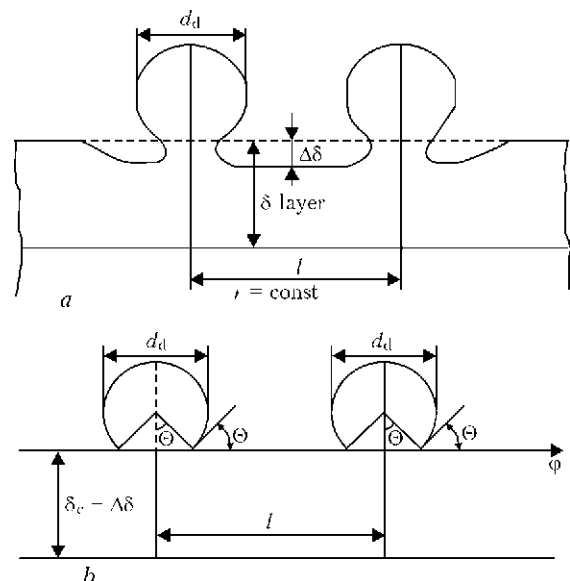


Figure 5. Diagram of drop formation in circumferential section  $r = \text{const}$  (a), and corresponding to it estimated implementation (b)

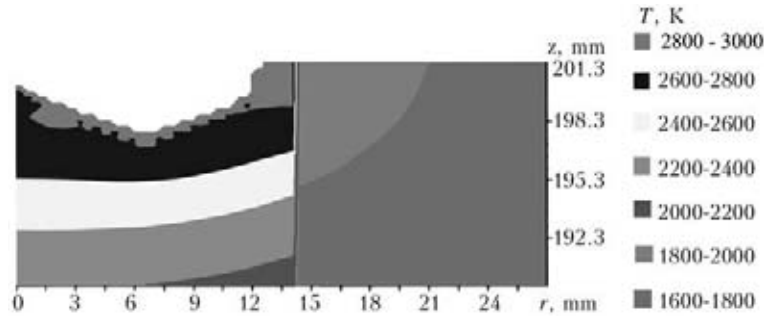


Figure 6. Results of calculation of temperature fields and tip surface profile in stick and bushing for steady state at  $\eta_1^d = 0.45$  and  $\eta_1 = 0.31$  [9]

**Processes in two-phase zone of  $T_S < T < T_L$ .**

In that zone there takes place primary crystallization of the liquid metal, determining primary microstructure, local chemical inhomogeneity etc., i.e. phenomena, in many cases substantially controlling quality of the crystallized metal. Naturally, the interest to that zone (including that of experts on mathematical modelling) is rather keen [1, 2 etc.]. However complexity of real processes in the temperature range of  $T_S < T < T_L$ , mechanisms of their realization depending on the rate of cooling, temperature gradients etc. essentially restricts the capabilities of classical determined approaches. More promising, in that respect evidently are stochastic models, as that of [12 etc.]. However their construction and realization involves considerable difficulties.

*Formation of intermetallides.* Intermetallides are most often formed in the process of welding of dissimilar materials, which is now quite an issue in aviation-, ship-building and instrument-making, chemical industries, etc. Intermetallides are unwanted formations, as they very adversely affect mechanical properties of welded joints [13]. To prevent formation of intermetallides in welding-brazing of dissimilar alloys having essentially different melting temperatures (for instance, Ti + Al, Fe + Al), it is necessary to provide temperature conditions, at which the period of contact of the solid metal with the liquid one is below  $\tau_{cr}(T)$ , as is shown in Figure 7 for TiAl<sub>3</sub> intermetallide [13].

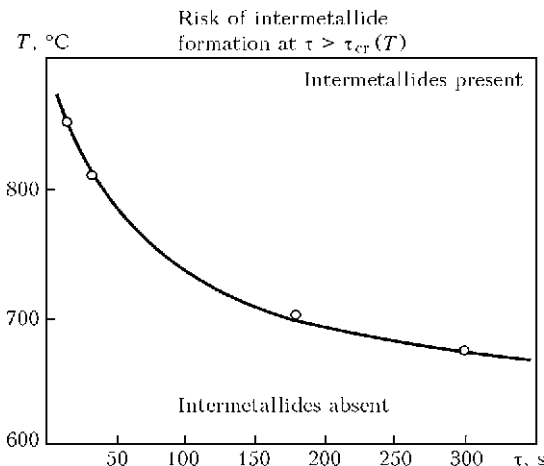


Figure 7. Temperature dependence of duration of latent period of TiAl<sub>3</sub> formation at boundary of surface contact of solid titanium with liquid aluminum

Under conditions of varying in time temperature, the criterion of non-formation of an intermetallide  $\tau_{cr}(T)$ , can be substituted by condition

$$\chi = \int_0^{\tau} \frac{dt}{\tau_{cr}(T)} \leq 1.0. \quad (4)$$

It is seen that at contact temperature below  $T_L \approx 660$  °C for aluminum, formation of TiAl<sub>3</sub> is actually impossible.

*Hot (crystallization) cracks.* These cracks are usually formed almost in a two-phase zone of the crystallizing metal (Figure 8), and are due to insufficient capability of plastic deformation of metal because of the presence in limited quantity of liquid interlayers along the grain boundaries.

Hot cracks are brittle fractures (within brittleness temperature range, BTR), therefore availability of quite plausible diagrams of the type shown in Figure 8 [14], enables to formulate the criterion of emergence of hot (crystallization) cracks in the form

$$T_S > T > T_S - BTR; \quad (5)$$

$$\varepsilon_{ii}(T) \geq \delta_{cr}^{(i)}(T) \text{ at } \sigma_{ii}(T) > 0,$$

where  $\varepsilon_{ii}(T)$  is the normal strain accumulated in BTR between  $T_S$  and  $T$ .

Direction  $-i = x, y, z$  is quite logical to choose along or across the weld, since most often the quantity  $\delta_{cr}^{(i)}$  possesses a certain anisotropy, conditioned by liquation phenomena at crystallization.

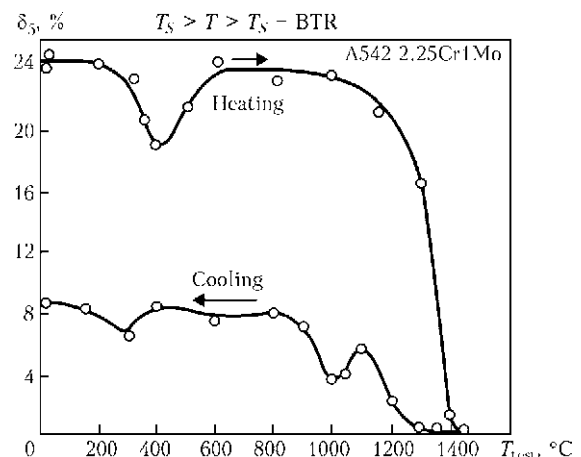
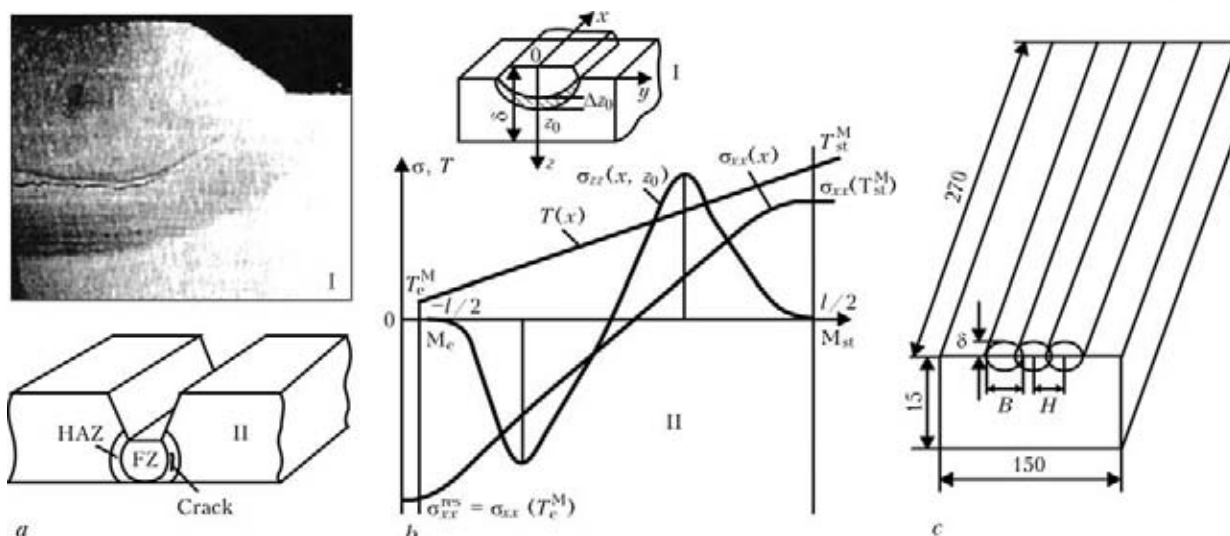


Figure 8. Variation of relative elongation of low-alloyed improved steel at heating to high temperature and cooling down from temperature 1430 °C



**Figure 9.** Longitudinal cold cracks on surface (I) and in root of weld (II): *a* – fusion zone (FZ); *b* – sketch of zone of martensite transformation (cross section I) and curves of temperature distribution  $T(x)$  and stresses  $\sigma_{xx}(x)$  and  $\sigma_{zz}(x, y)$  in transformation zone  $-l/2 \leq x < l/2$  (II); *c* – sketch of longitudinal specimen with bead width  $B = 20$  mm and distance between bead centers  $H = 18$  mm for variant 4, and  $B = 12$  mm and  $H = 10$  mm for other variants

**Processes in solid phase.** Most typical solid-phase processes are those, defining microstructure and properties of the weld metal and the near-weld zone, stress-strain state, cold (hydrogen) crack formation. They are fairly well described, however here too, there are some gaps.

Let us consider one typical phenomenon connected with formation of underbead cold cracks at welding heating (surfacing) of hardening-susceptible steels (Figure 9).

In such steels, cold (hydrogen) cracks are usually formed at temperatures below  $150^\circ\text{C}$  under the following conditions:

- presence of at least 50 % of microstructure with martensite or lower bainite component;
- presence of diffusive hydrogen in quantities of at least  $1 \text{ cm}^3/100 \text{ g}$ ;
- presence of rather high tensile normal stresses in the respective direction.

The latter condition for underbead cracks of Figure 9, *a*, judging by the residual stresses, obtained either by experimental measurements or by computational methods within the framework of the model of plane stressed state, is evidently not observed, although presence of underbead cracks is an objective reality. A more detailed analysis of stress kinetics connected with martensite formation in the near-weld zone, when longitudinal stresses  $\sigma_{zz}(T)$  and  $\sigma_{yy}(T)$  having tensile and compression peaks of magnitudes [15], revealed by 3D analysis. In [15] it is shown that at about 90 % of martensite content, tensile peak of 110 MPa is quite sufficient for the formation of the underbead crack for steel 65G, i.e. the third of the above conditions, is fully implementable in the temperature zone of martensite transformation of  $T_e^M < T < T_{st}^M$ .

**Creation of complex problem-oriented systems for engineering applications (CPOSEA).** This is the field of developments, whose potential is underlined

in reviews [1, 2], as well as in [16–20 etc.], it is in demand by the engineering practice of today, conditioned by the progress of information technologies and increased computer literacy of present generation of engineers. Such systems must be maximally problem-informative, convenient in their use, and available at an affordable price. The requirement to combine these three features substantially complicates the development of such systems, however it is a stimulus for many developments, involved with mathematical description of physical-chemical processes accompanying welding (related technologies), since generation of respective knowledge on the basis of such mathematical models in specific engineering developments allows substantial funds and time saving.

It should also be noted here that development of CPOSEA is not an alternative to available commercial systems and software packages types SYSWELD and WELDPREDICTIONS, designed for solving representative fundamental problems (modelling of temperature fields, thermal cycles, microstructure variations, stresses and strains at welding heating) for rather common geometric shapes and dimensions of objects, initial and boundary conditions, whose rendering concrete is by far not a simple work for the user.

When using CPOSEA an engineering users is freed from extrinsic to them work of selecting mathematical models, describing initial and boundary conditions, selecting rational dimensions of finite elements, time between monitoring procedures, etc. In conjunction with information support, necessary for solving only a specific representative problem, CPOSEA is very convenient for engineering use.

Among those developed at the E.O. Paton Electric Welding Institute CPOSEAs [16–19], quite popular (used at a number of industrial enterprises of Ukraine), is the ArcWeldSys system [20] (Figure 10), designed for reducing the scope of experiments on specimens in selecting alternative welding consumab-

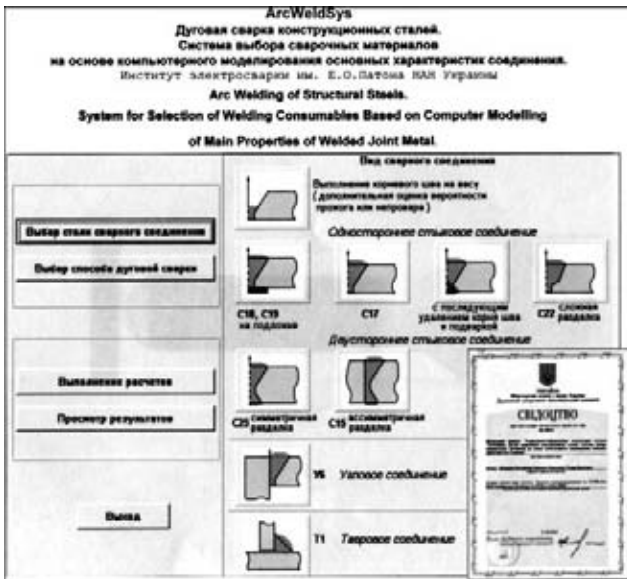


Figure 10. ArcWeldSys system for selection of welding consumables for arc welding of structural steels, based on computer modelling of main properties of welded joints

les for specific welded joints in arc welding of structural steels [21].

ArcWeldSys system [21] enables to select for different methods of arc welding and different structural steels (low-carbon, general purpose low-alloy, high-strength low-alloy carbonitride-strengthened, sparsely alloyed hardened-tempered, heat hardenable, heat-resistant chromium-molybdenum, weather-resistant low-alloy, cold-resistant low-alloy, cold-resistant nickel, martensitic stainless (high-temperature), stainless ferritic class, stainless austenitic class), alternative welding consumables of various companies all over the world, rational welding modes, and subsequently obtain information on:

- weld formation (butt, corner, tee) (see Figure 10);

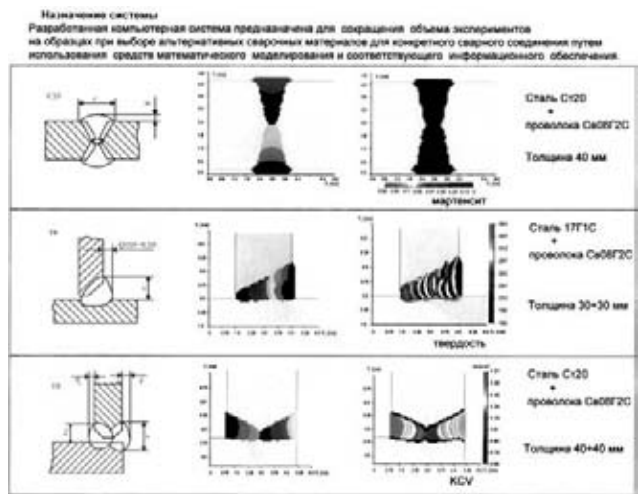


Figure 11. Example of information, provided by ArcWeldSys system for various joints, on multilayer weld formation, martensite content, hardness *HV* and impact toughness *KCV*

- chemical composition of fusion zone (in single- and multi-pass welding);
- microstructure and mechanical (functional) properties;
- risk of hot and cold crack formation (Figure 11).

**Production tooling and welded joints.** Issues of interaction of production tooling and welded joints in different weldments of structures in recent years attract much attention in connection with the development of new highly efficient technological manufacturing processes, requiring high accuracy of positioning welded members. Thus, in single-pass welding without tacks of large steel plates (butt weld length of about 16 m) in modern shipbuilding, it is very important in the process of welding to preserve along the whole butt the original gap width with preset tolerance, which requires using appropriate production tooling.

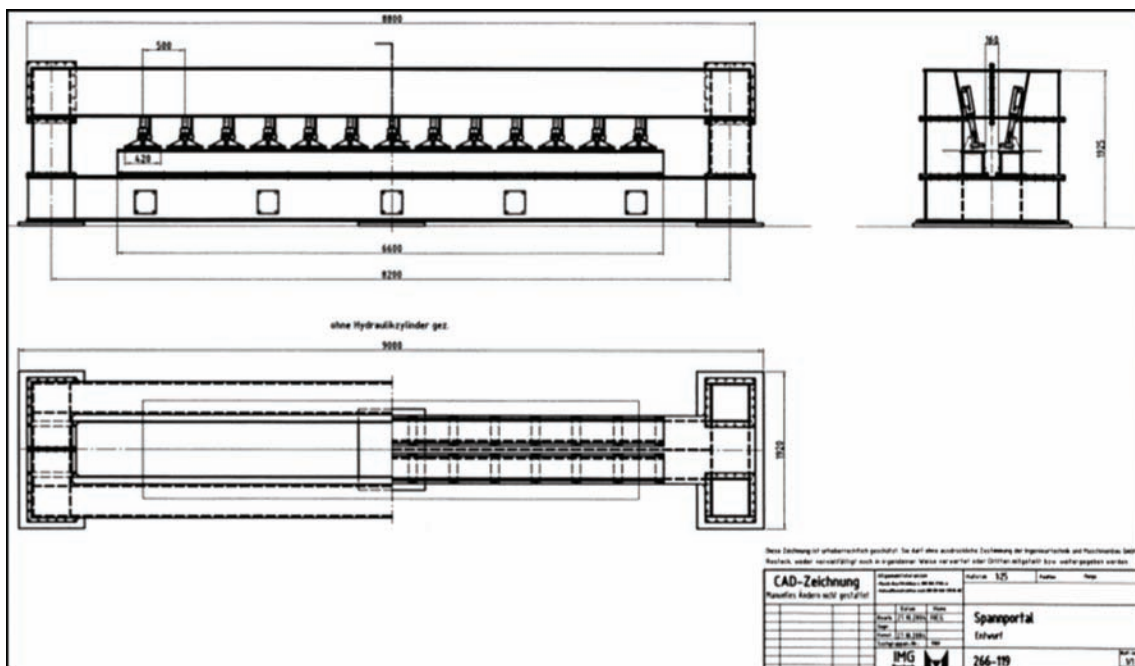


Figure 12. Schematic of the JMG device



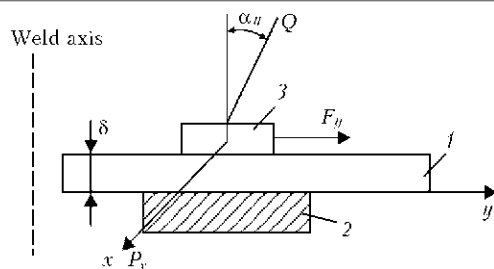


Figure 13. Schematic diagram of edge fixing with clamp: 1 – welded plate; 2 – base; 3 – clamp

Figure 12 shows a schematic diagram of the device, developed by German company JMG, for containment the gap width at single pass butt welding of steel plates 3–19 mm thick.

Containment is provided by clamps, pressing welded plate edges to the base of the production tooling (Figure 13). Clamping force is provided by the hydraulic system and respective rigidity of the device portal (see Figure 12). Friction forces  $F$ , preventing edge dislocation, are proportional to normal clamping force (Figure 14) up to a certain magnitude, above which sliding occurs without increasing of friction force  $F$ . Clearly, substantiation of the design of such a device necessitated the knowledge of clamping forces  $Q$  for large plates, different thicknesses and welding modes. Results of successful solution of this problem, using mathematical modeling, are described in the work of Prof. P. Seyffarth, discussed at the Conference and included into the Proceedings Book.

## CONCLUSION

All over the world interest to mathematical modelling of complex phenomena, taking place in welding and related technologies, is aimed at reducing the scope of purely experimental investigations, funds and time saving. Objective conditions of such growing interest are permanently growing requirements to new technologies and high rates of computer technologies growth. The role of mathematical modelling in solving problems, involving selection of rational technological solutions both with regard for parameters and production tooling, is growing.

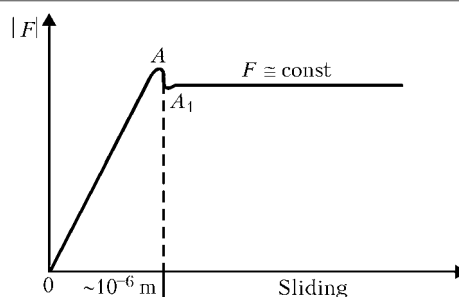


Figure 14. Friction force value as a function of relative displacement of friction bodies in shear, turning to sliding, at  $Q_z = \text{const}$

- Makhnenko, V.I. (2002) Prospects of mathematical modeling and information technologies in welding and allied processes. In: *Proc. of Int. Conf. on Mathematical Modelling and Information Technologies in Welding and Related Processes* (Katsiveli, Crimea, Ukraine, Sept. 16–20, 2002). Kiev: PWI, p. 3–11.
- Makhnenko, V.I. (2004) Advances in mathematical modeling and information technologies for welding and related technologies. In: *Ibid.* (Katsiveli, Crimea, Ukraine, Sept. 13–17, 2004). Kiev: PWI, p. 11–23.
- Boitout, F., Bergheau, J.-M. (2003) Numerical simulation of welding in Europe: Present capabilities and future trends. *Transact. of JWRI*, 32(1), p. 197–206.
- Fuhrich, T., Berger, P., Hugel, H. (2003) Numerical calculation of the weld pool in deep penetration laser welding. In: *Mathematical modeling of welding phenomena 6*. Ed. by H. Cerjak. London, p. 93–120.
- Ehlen, G., Ludwig, A., Sahm, P.R. (2003) Influence of welding power and welding duration on the shape of the weld pool: Transient effects. *Ibid.*, p. 161–191.
- Sudnik, V.A., Erofeev, V.A., Richter, K.-H. et al. Numerical modelling of the electron beam welding process. In: *Proc. of 16th Int. Conf. on Computer Technology in Welding and Manufacturing and 3rd Int. Conf. on Mathematical Modelling and Information Technologies in Welding and Related Processes* (Katsiveli, Crimea, Ukraine, June 6–8, 2006). Kiev: PWI, p. 295–300.
- Movchan, B.A. (1998) PV-deposited non-organic materials. In: *Modern materials science of the 21st century*. Kiev: Naukova Dumka, p. 318–332.
- Pokhodnya, I.K., Portnov, O.M. (2003) Mathematical modelling of absorption of gases by electrode metal drop. *The Paton Welding J.*, 6, p. 2–5.
- Makhnenko, V.I., Zhudra, A.P., Velikoivanenko, E.A. et al. (2004) Mathematical modeling of the process of manufacture of spherical fused tungsten carbide granules. *Ibid.*, 2, p. 2–8.
- Pokhodnya, I.K., Shvachko, V.I., Portnov, O.M. (2000) Mathematical modelling of absorption of gases by metal during welding. *Ibid.*, 7, p. 11–16.
- Erokhin, A.A. (1964) *Kinetics of arc welding metallurgical processes*. Moscow: Mashinostroenie.
- Nastac, L., Sandarraj, S., Yu, K.-O. et al. (1998) Stochastic modeling of solidification structures in alloy 718 remelt ingots. *JOM*, March, p. 30–35.
- (1986) *Metallurgy and methods of welding titanium and its alloys*. Ed. by V.N. Zamkov. Kiev: Naukova Dumka.
- Hryvnyak, I. (1984) *Weldability of steels*. Moscow: Mashinostroenie.
- Makhnenko, V.I., Gajvoronsky, A.A., Sarzhevsky, V.A. et al. (2004) Stresses in surfacing of parts made from high-carbon steels of the 65G type and risk of cold cracking. *The Paton Welding J.*, 7, p. 2–6.
- Makhnenko, V.I., Korolyova, T.V., Lavrinets, I.G. (2003) Computer system for selection of welding consumables for arc welding of structural steels. *Ibid.*, 2, p. 12–17.
- Makhnenko, V.I., Velikoivanenko, E.A., Seyffarth, P. et al. (2002) Mathematical modelling of the process of tube-to-tube plate welding. In: *Proc. of Int. Conf. on Mathematical Modelling and Information Technologies in Welding and Related Processes* (Katsiveli, Crimea, Ukraine, Sept. 16–20, 2002). Kiev: PWI, p. 229–230.
- Lobanov, L.M., Pivtorak, V.A., Savitsky, V.V. (2002) Mathematical model for processing holographic interferograms in non-destructive control of structure elements. In: *Ibid.*, p. 239–242.
- Makhnenko, V.I., Velikoivanenko, E.A., Rozyinka, G.F. et al. (2002) Mathematical modelling of multipass circumferential arc welding of thick-walled shells. In: *Ibid.*, p. 231–234.
- Korolyova, T.V. (2004) Development of the ArcWeldSys system in terms of mathematical modelling and information filling. In: *Ibid.* (Katsiveli, Crimea, Ukraine, Sept. 13–17, 2004). Kiev: PWI, p. 127–133.
- Lavrinets, I.G., Korolyova, T.V. (2002) Computation system for prediction of properties of different zones of welded joints in arc welding of structural steels. In: *Ibid.* (Katsiveli, Crimea, Ukraine, Sept. 16–20, 2002). Kiev: PWI, p. 210–221.

# MATHEMATICAL MODELING OF THERMODEFORMATIONAL AND PHYSICOCHEMICAL PROCESSES DURING WELDING OF LAP AND BUTT DISSIMILAR TITANIUM-ALUMINUM JOINTS

V.I. MAKHNENKO, A.S. MILENIN and A.P. SEMYONOV  
E.O. Paton Electric Welding Institute, NASU, Kiev, Ukraine

The process of welding of the dissimilar joints is a complex of complicated and interrelated physical processes, those to a certain extent have an influence on the quality of the welded joints. To calculate the thermodeformational processes, those are taking place during the welding of the dissimilar joints of the type titanium-aluminum, the complex of computer programs, which gives an opportunity to simulate the temperature fields, and also the fields of current and residual stresses and strains, has been developed. Moreover these mathematical models make it possible to estimate the risk of the formation of intermetallic compounds and the thickness of intermetallic layer in the region of the contact of the dissimilar metals. An adequacy of the results, those have been obtained with the developed programs, was verified during the working out of the technological cycle of the welding of the samples for Airbus project.

At present the use of welding to obtain permanent links of metal components is widely adopted, including such conservative from point of view of application of welding technologies fields as aircraft construction [1]. In spite of the fact that the use of welded assemblies and structures is limited to a sufficient extent to noncritical parts, the high emphasis is placed on the quality of welded joints.

The most commonly used structural materials in aircraft building are titanium, aluminum and their alloys [2], at that some constructional units imply the presence of permanent joints of details made from these materials. Therefore the dissimilar welded joints of titanium with aluminum are of certain interest.

Welding of dissimilar joints is often the complex of complicated interrelated physicochemical, thermal and metallurgical processes, those finally determine

the quality of obtained welded joint. This fact, in turn, makes difficult to optimize the corresponding welding technology [3, 4]. Experimental researches in this field are complicated and expensive enough, so that the use of the mathematical modeling of the kinetics of the processes, those take place during the welding of dissimilar joints, on basis of corresponding numerical methods, is appropriate [5].

Quality and working capacity of dissimilar titanium-aluminum welded joints is determined both with processes of reaction diffusion (those can lead to the formation of brittle intermetallic layers), and with formation of the fields of strains (those cause the change of the shape of sample) and stresses (those can diminish the working capacity of the unit, lead to hot cracking in the region of welded joint and also stimulate the process of stress-corrosion).

To describe the processes of reaction diffusion and thermodeformational processes during the welding of dissimilar titanium-aluminum joints by the example of lap and butt welded joints, corresponding mathematical model has been developed.

**Characteristic features of processes during the welding of titanium to aluminum.** The processes mentioned above, those are typical for the welding of dissimilar structures, in case of joining of titanium with aluminum have some specific features.

As it can be seen from the equilibrium diagram of the titanium-aluminum system (Figure 1), there are four stable intermetallic compounds in this system:  $Ti_3Al$ ,  $TiAl$ ,  $TiAl_2$ , and  $TiAl_3$  (stoichiometric phase). However the experimental researches have shown that in case of surface contact of aluminum and titanium the processes of their interdiffusion lead to the for-

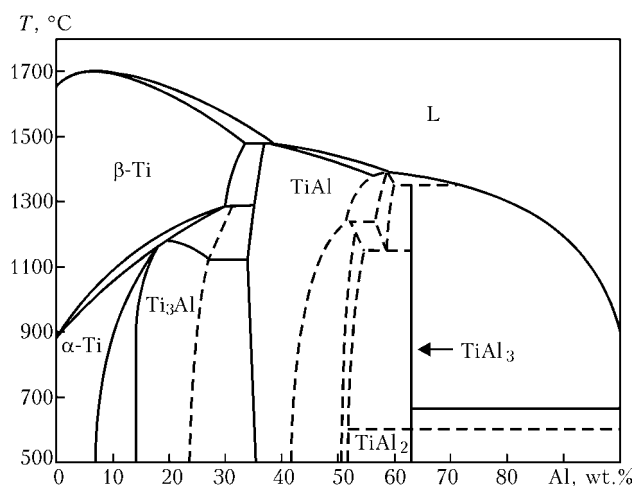


Figure 1. Equilibrium diagram of the binary Ti-Al system [1]

mation of single intermetallic layer  $\text{TiAl}_3$ , whereas the amount of other intermetallic phases either vanishingly small or absolutely absent [6]. Intermetallic compound  $\text{TiAl}_3$  has low processing characteristics that make its presence in the region of welded joint inadmissible.

However the fact that the melting points of titanium ( $T_{\text{liq}}^{\text{Ti}} = 1668^\circ\text{C}$  [7]) and aluminum ( $T_{\text{liq}}^{\text{Al}} = 660^\circ\text{C}$  [8]) are sufficiently different makes it possible to use so called brazing-welding, to obtain the welded joints of these metals. In this case technological parameters of the welding process are selected in that way to melt only aluminum part of the joint whereas the titanium one remains in the solid state.

This approach is implemented for example for laser beam welding of butt joints of titanium alloy Ti6Al4V and aluminum alloy AA6056 [1], and also for the argon-arc welding of aluminum and titanium plates with the use of aluminum filler wire (Figure 2) [3].

But such approach doesn't exclude the appearance of the brittle  $\text{TiAl}_3$  layers in the region of the surface contact of the liquid aluminum and solid titanium. But in this case so called latent period of the intermetallic layer formation is present. In course of this period of time from the physical contact of the liquid aluminum and solid titanium the intermetallic layer of sufficient thickness doesn't form [3, 4, 9]. Experimental dependence of the latent period duration on the temperature of the welded joint region during the welding process is shown in Figure 3. Thus with the use of certain optimization it is possible to obtain the welding cycle when the kinetics of the temperature fields exclude the long-duration staying of the contact region under the high temperatures and consequently to receive the titanium-aluminum welded joint practically without brittle intermetallic layer in the region of the contact surface of parts being welded.

To estimate numerically the  $\text{TiAl}_3$  layer formation risk under the variable temperature field the calculated value of the intermetallic compounds formation risk coefficient can be used. This coefficient in turn can be expressed as follows [3]:

$$\chi = \int_0^{t_0} \frac{dt'}{\tau(T)}, \quad (1)$$

where  $t_0$  is the observable time of staying of the given point of the contact of solid titanium with liquid aluminum;  $T = T(t')$  is the time dependence of the temperature at the given point on the moment of time  $t'$ ;  $0 \leq t' \leq t_0$ ;  $\tau(T)$  is the duration of latent period according to Figure 3. In this case the fulfilling a condition  $\chi < 1$  along the contact surface guarantees the absence of the intermetallic layers of sufficient thickness.

**Mathematical modeling of diffusion processes by the example of brazing-welding of lap aluminum-titanium joints.** The process of the intermetallic  $\text{TiAl}_3$  layer formation and propagation at the border of the surface contact of aluminum and titanium can be ten-

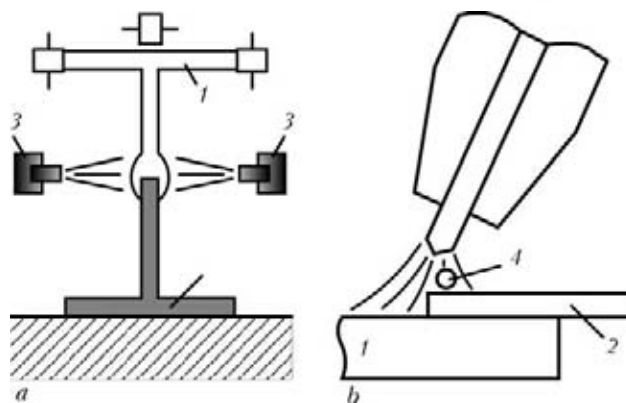


**Figure 2.** Examples of scheme of welding of lap (a) and butt (b) dissimilar aluminum-titanium joints: 1 – aluminum part; 2 – titanium part; 3 – laser welding heat source; 4 – aluminum filler wire

tatively divided into three successive steps, namely relaxation of the energy peak at the phase boundary «liquid aluminum–solid titanium»; formation of new phase islets in the region of surface defects, growth of these islets along the contact region and their joining in the continuous intermetallic layer; and normal growth of intermetallic layer in the direction from contact region as a result of reaction diffusion of elements.

Processes, those take place within first and second stages, are complicated and ambiguous, but the amount of appeared intermetallic phase is rather little (the thickness of the layer doesn't exceed 2–5  $\mu\text{m}$  [1, 9]). Therefore from point of view of the working capacity of welded joint the summarized duration of these stages, that in turn depends on the temperature conditions in the investigated area and can be estimated with the duration of the latent period, is important. Third stage corresponds to the diffusion growth of the intermetallic phase layer. The kinetics of this process can be estimated with the use of second Fick's law that in 2D case and taking into account the chemical reaction of intermetallic compound formation takes on following form:

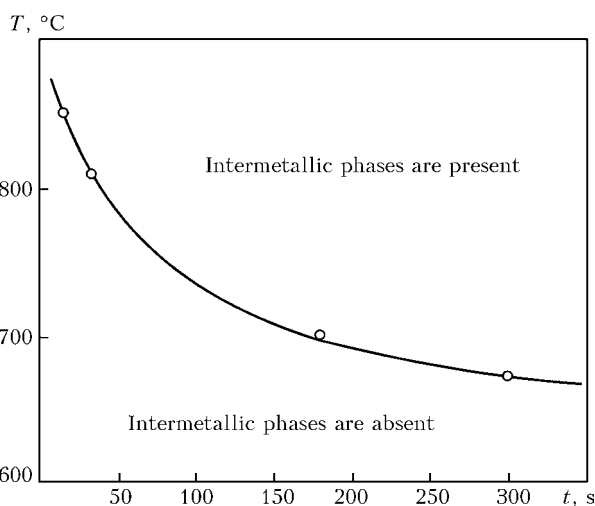


**Figure 3.** Temperature dependence of retardation period of  $\text{TiAl}_3$  formation in surface contact area of solid titanium and liquid aluminum

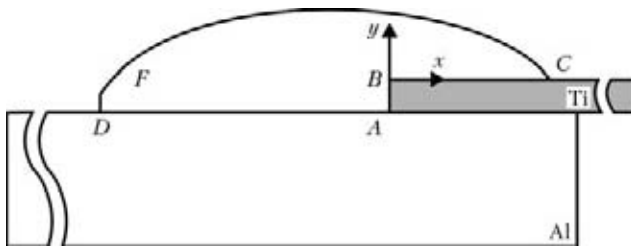


Figure 4. Scheme of lap dissimilar welded joint [1, 5]

$$\frac{\partial c_i}{\partial t} = \frac{\partial}{\partial x} \left( D_i(x, y, T, c_i) \frac{\partial c_i}{\partial x} \right) + \frac{\partial}{\partial y} \left( D_i(x, y, T, c_i) \frac{\partial c_i}{\partial y} \right) - V_i(c_i, c_{TiAl_3}), \quad (2)$$

where  $c_i$  is the concentration of  $i$ -th element ( $i = Al, Ti$ ) at the moment of time  $t$ ;  $D_i$  is the diffusion coefficient of  $i$ -th element,  $mm^2/s$ ;  $T$  is the temperature of the point of the welded joint under consideration with the coordinates  $(x, y)$ ;  $V_i(c_i, c_{TiAl_3})$  is the function of volume source of  $i$ -th material,  $1/c$ , i.e. if the aluminum and titanium ratio in the solution is such that the excess of one of them is present, the decrease of the concentration of excess element with the simultaneous increase of the corresponding amount of intermetallic takes place.

Diffusion coefficients  $D_i$  in general case are the functions both of the temperature and the composition at the given point of material. As for the interdiffusion of titanium and aluminum these dependencies are given for example in [10]. As for the initial conditions for solution of the equation (2) the distribution of concentrations of diffusing elements in the corresponding parts of the welded joint has been accepted. With taking into account of the fact that diffusion processes during the welding are local enough, the boundary conditions of this problem are to be assumed

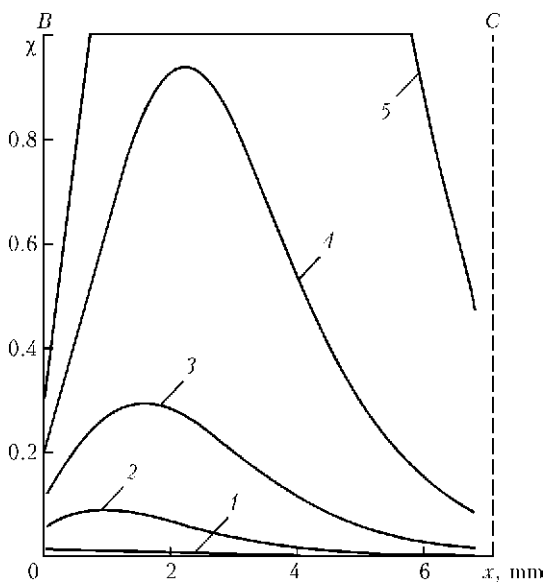


Figure 5. Coefficient of risk of  $TiAl_3$  formation as a function of the contact surface point coordinates at the different positions of welding heat source: 1 –  $x_0 = -2.7$ ; 2 –  $x_0 = 0$ ; 3 –  $x_0 = 1$ ; 4 –  $x_0 = 2$ ; 5 –  $x_0 = 3$  mm

Table 1. Technological parameters of lap joint welding process

Motion rate of surface arc heat source along welded joint, mm/s	4
Heat source power, kW	4.4
Heat efficiency coefficient, %	50
Welding spot diameter, mm	3

Table 2. Properties of aluminum and titanium [3]

Property	Ti	Al
Atomic weight	47.90	26.98
Density, $g/cm^3$	4.51	2.70
Melting point, $^{\circ}C$	1668	660
Boiling point, $^{\circ}C$	3260	2327
Latent melting heat, J/g	435.5	393.7
Heat capacity, $J/(cm^3 \cdot ^{\circ}C)$ , at $T, ^{\circ}C$ :		
20	2.44	2.43
500	2.97	2.94
Heat conductivity, $W/(cm \cdot ^{\circ}C)$ , at $T, ^{\circ}C$ :		
20	0.19	2.26
500	0.21	2.19

the zero value of concentration gradient at the boundary of sample.

The kinetics of the changing of temperature field in course of welding process can be obtained with the numerical solution of the heat conduction equation. Such calculation has been carried out to describe the diffusion processes from the point of view of the existent technology of the argon-arc welding of the lap joint of titanium and aluminum plates with the use of aluminum filler wire, the technological parameters of which are shown in Table 1. The scheme of the welded joint is shown in Figure 4. The sufficient motion rate of the welding heat source and simple geometry of the welded joint give an opportunity to use corresponding 2D models of kinetic processes for the calculation.

Some properties of titanium and aluminum are given in Table 2.

To verify the adequacy of the developed mathematical model of diffusion processes the characteristic features of the process of heat and mass transfer were determined depending on the different positions of welding heat source centre relatively to the edge of titanium part of the welded assembly.

The results of the calculation of intermetallic compounds formation risk coefficient at the different positions of the welding heat source for the process (see Table 1) are shown in Figure 5 (values  $\chi$  aren't shown). As it can be seen in this Figure, from point of view of the ensuring of the intermetallic formation absence (with taking into account possible fluctuation arc deflections) the position of the welding source either near the titanium edge or towards the aluminum part is acceptable, that is proved to be true with the

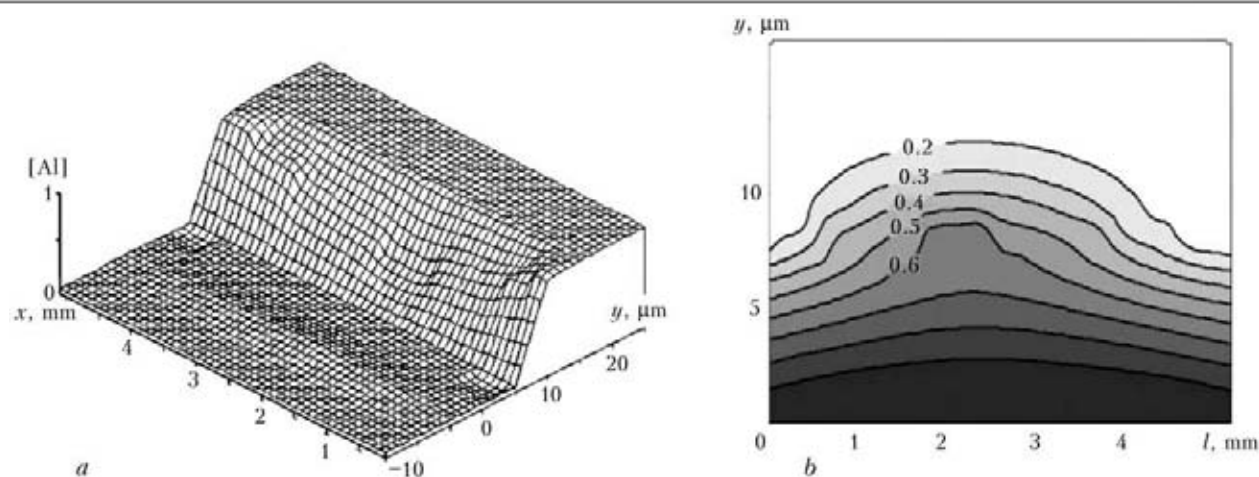


**Figure 6.** Weight concentration of aluminum (a) and intermetallic compound  $\text{TiAl}_3$  (b) in the contact area at location of heat source in distance  $x_0 = 3$  mm from the edge of welded joint titanium part

**Table 3.** Chemical composition of aluminum alloy AA6056, wt.% [11]

Si	Fe	Cu	Mn	Mg	Cr	Zn
0.7–1.3	0.5	0.5–1.1	0.4–1.0	0.6–1.2	0.25	0.1–0.7

**Table 4.** Chemical composition of titanium alloy Ti6Al4V, wt.% [3]

Al	V	N	C	H	Fe	O
5.3–6.8	3.5–5.3	0.05	0.1	0.0125	0.3	0.2

**Table 5.** Physical and mechanical properties of aluminum alloy AA6056 and titanium alloy Ti6Al4V

Alloy	$\sigma_t$ , MPa, at $T$ , °C		$E \cdot 10^{-5}$ , MPa, at $T$ , °C		$\lambda$ , W/(mm $\cdot$ °C), at $T$ , °C		$c_p \cdot 10^2$ , J/(mm $^3 \cdot$ °C), at $T$ , °C	
	20	500	20	500	20	500	20	500
AA6056	220	100	0.98	0.60	0.110	0.200	0.250	0.295
Ti6Al4V	1060	460	1.19	0.91	0.0059	0.0128	0.248	0.301

recommended modes, those have been obtained with the processing of experimental data [3].

At the position of the heat welding source at a distance of 3 mm from the edge of titanium part of the welded structure unit (see curve 5 in Figure 5) the intermetallic layer of the length  $\sim 5$  mm forms. Mass concentration of intermetallic compound  $\text{TiAl}_3$  in the region of the welded joint as well as distribution of the aluminum in the same region is shown in Figure 6. Maximum thickness of intermetallic layer is evidently observed in the region of the welding heat source location, that is accounted for the sufficient heating of this region.

#### Mathematical modeling of thermoderformational processes by the example of brazing-welding of butt

**Table 6.** Technological parameters of butt joint welding process

Motion rate of laser beam along welded joint, mm/s	4.33
Heat source power, kW	1.75
Heat efficiency coefficient, %, for:	
aluminum surface	35
titanium surface	20
Welding spot diameter, mm	5

**joints of details made from titanium alloy Ti6Al4V and aluminum alloy AA6056.** Form changing of the sample in course of the welding processes can have sufficient importance in case of the welding of stretched details. Particularly, the problem of estimation of the welding distortions has been appeared during the optimization of the process of commercial produc-

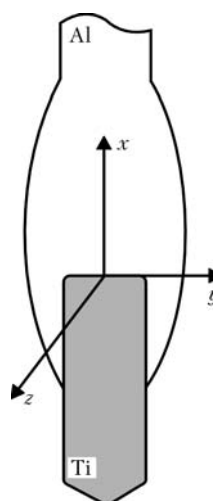


**Figure 7.** Scheme of weld on lap dissimilar joint

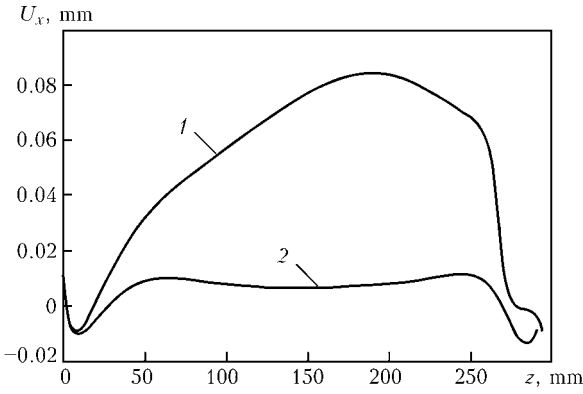


Figure 8. Distribution of maximal current (1) and residual (2) weld displacements  $U_x$

tion of the dissimilar welded beams (seat tracks of the airliner Airbus) developed in BIAS (Germany) [1].

The chemical composition and some properties of this sample are given in Tables 3–5. Physical configuration of the welded structure and the technological parameters of this process are shown in Table 6 and Figure 7.

The welding is carried out from the both sides of the sample by two laser beams with the synchronous moving of them along the seam.

The technique of the numerical determination of the stresses and strains during the welding process, is based on the numerical solution of the corresponding problem of the nonstationary thermoplasticity by means of the successive tracing of the development of the elastic-plastic deformations starting with the primary state before the welding and finishing with the final state after the absolute cooling of the sample [12].

To model the deformation of the axis of the beam and correspondently the changing of the geometry of the welded seam because of the nonuniform heating 2D model of the state of strain and stress kinetics (i.e. actually of the plane  $y = 0$ ) can be used. The analysis of the kinetics of the temperature field from the point of view of the intermetallic layers formation risk, the method of which has been mentioned above, showed that such geometry of welded joint practically excludes the possibility of the intermetallic phases formation in this region (maximum value of  $\chi$  doesn't exceed 0.1). Highest values of the displacement of

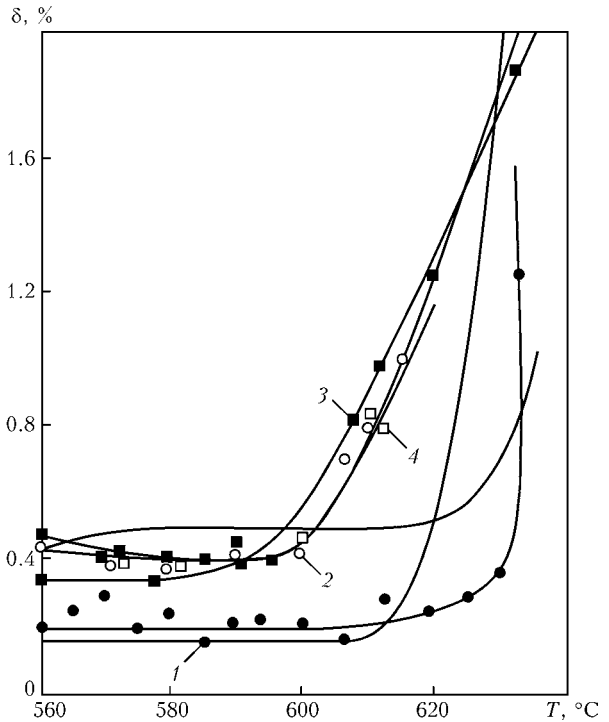


Figure 9. Al + 0.5 % Cu alloy elongation at destruction in the brittleness temperature range: 1 – columnar crystallization structure; 2 – equilibrium crystallization structure; 3 – 10 °C/min cooling rate; 4 – 100 °C/min cooling rate [13]

the axial line within the scope of this calculation don't exceed 0.1 mm, and the residual state of the welded joint corresponds to the maximum displacements along the  $x$ -axis those value aren't exceed 0.02 mm (Figure 8).

One of the characteristic features of this technological scheme of the dissimilar joints welding is the possibility of spalling over the temperature interval of brittleness [13]. The risk of crack formation can be estimated on the basis of experimental data according to the deformations under which the destruction of similar alloy takes place (Figure 9). However in this case the distribution of stresses in the cross section of the sample is of importance because in the region of the dissimilar contact the values of the local stresses and strains are highest.

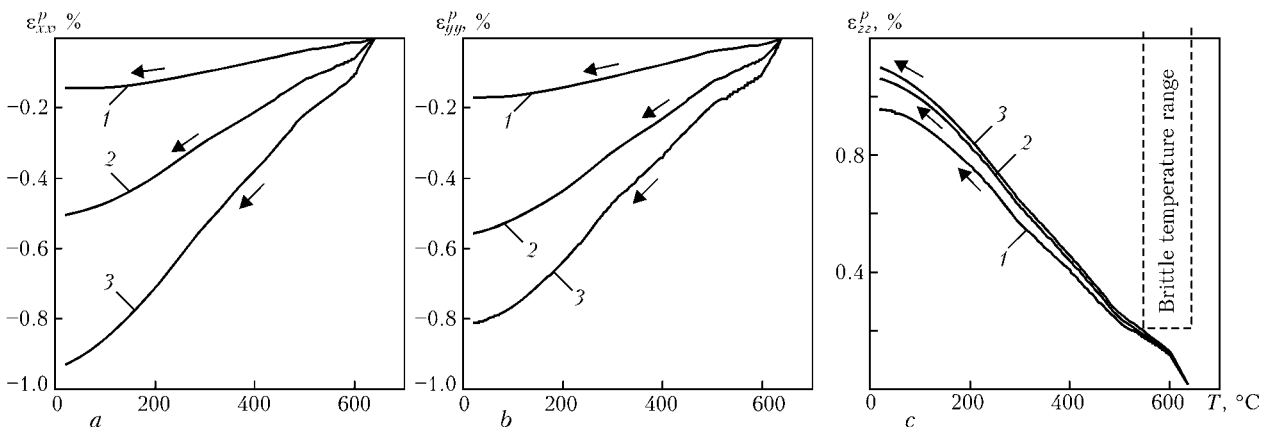


Figure 10. Kinetics of the  $\epsilon_{xx}^p$  (a),  $\epsilon_{yy}^p$  (b),  $\epsilon_{zz}^p$  (c) elastic deformation growth during cooling

To estimate the risk of crack formation during the welding of such welded joint the following conservative criterion: hot cracks will be undoubtedly absent if the plastic deformation, those have been accumulated in the aluminum part of the welded sample in temperature interval of brittleness during the cooling of the sample, don't exceed the values higher then critical ones, shown in Figure 9. Another necessary condition for the spalling of aluminum alloy is positiveness of the normal components of the stress tensor on the region under study.

Figure 10 shows the growth kinetics of elastic deformations  $\varepsilon_{xx}^p$ ,  $\varepsilon_{yy}^p$ ,  $\varepsilon_{zz}^p$  during the cooling in some characteristic points where the normal components of corresponding normal components of the stress tensor are positive. It can be seen that  $\varepsilon_{xx}^p$ ,  $\varepsilon_{yy}^p$  are negative and can't cause the crack formation. As for the value of  $\varepsilon_{zz}^p$  it is positive and moreover this value is large enough, so the risk of hot cracking in the region of the dissimilar contact is rather high. Nevertheless the region where this situation occurs is too small ( $0.2 \div 0.4$ ) to cause the hot crack formation.

## CONCLUSIONS

1. The analysis of diffusion processes during the welding of dissimilar titanium-aluminum joints by the example of the production of lap argon-arc welding has been carried out; both the brittle intermetallic layers formation risk and distribution of the elements in the region of the welded contact were estimated.

2. The modeling of thermodeformational processes by the examples of butt laser welding of the joints from titanium alloy Ti6Al4V and AA6056 has shown insufficient level of form changing of the sample.

3. The analysis of the plastic strains accumulated during the cooling over the temperature interval of brittleness, from point of view of hot cracking risk

has shown the low possibility of generation of such defects as for technological cycle under study.

**Acknowledgements.** *The authors of this research appreciate the contribution to the obtaining of the calculation results made by the PWI Group of Modeling of Physical-Mechanical Processes in Welding (head of the Group – Dr. E.A. Velikoivanenko). The correct validation of some calculation data was made due to the fruitful collaboration with Dr. Thomas Pretorius and his colleagues from BIAS (Germany).*

1. Kreimer, M., Vollertsen, F. (2005) Processing titanium-aluminum hybrid joints for aircraft applications. In: *Proc. of 3rd Int. WLT Conf. on Lasers in Manufacturing* (Munich, June, 2005).
2. (1966) *Theory and practice of passenger aircraft*. Moscow: Nauka, p. 314.
3. (1986) *Metallurgy and technology of welding of titanium and its alloys*. Ed. by V.N. Zamkov. Kiev: Naukova Dumka, p. 173.
4. Rabkin, D.M., Ryabov, V.R., Gurevich, S.M. (1975) *Welding of dissimilar joints*. Kiev: Tekhnika, p. 10.
5. Ryabov, V.R. (1983) *Welding of aluminum and its alloys to other metals*. Kiev: Naukova Dumka, p. 63.
6. Dybkov, V.I. (2002) *Reaction diffusion and solid state chemical kinetics*. Kiev: IPMS, p. 144.
7. Eryomenko, V.N. (1960) *Titanium and its alloys*. Kiev: AN USSR, p. 108.
8. (1989) *Aluminum: properties and metallurgy*. Ed. by J.E. Hatch. Moscow, p. 24.
9. Lankina, L.V., Korniyuk, Yu.M. (1974) Processes at the boundary of the bimetal titanium-aluminum joints during heating. *Svarochn. Proizvodstvo*, 4.
10. Zwickler, U. (1979) *Titanium and its alloys*. Moscow: Metallurgiya, p. 56.
11. (2004) *Int. alloy designation and chemical composition limits for wrought aluminum and wrought aluminum alloys*. Aluminum Assoc. Inc., p. 9.
12. Makhnenko, V.I., Velikoivanenko, E.A., Pochynok, V.E. et al. (1999) Numerical methods of the predictions of welding stresses and distortions. In: *Welding and Surf. Rev.*, Vol. 13, Part 1. Ed. by B.E. Paton. Harwood A.P., p. 147.
13. Prokhorov, N.N. (1976) *Physical processes in metals and alloys during welding*. Vol. 2. Moscow: Metallurgiya, p. 332.

# NUMERICAL INVESTIGATION OF CAUSES OF FAILURE OF WELDED PILLARS OF CASTING STAND CROSSHEAD

V.I. MAKHNENKO, E.A. VELIKOIVANENKO, G.F. ROZYNKA and N.I. PIVTORAK

E.O. Paton Electric Welding Institute, NASU, Kiev, Ukraine

This work presents analysis of photographic materials on failed pillars of crosshead of casting stand, provided by the customer, a hypothesis of failure reasons has been chosen, and numerical calculations of load-carrying capacity of failed fillet welds in static and cyclical loading with regard for detected lacks of fusion. The results are checked with load-carrying capacity of the bolted joint at its different states. Expert opinion on prime cause of the failure has been concluded.

One of the efficient ways of using described approaches for determining duration of safe operation of welded joints (assemblies) is analysis of the causes of different failures of welded structures by modelling the situation preceding the failure, and finding the weakest links which could potentially cause the failure observed.

The case of failed pillars of crosshead of casting stand described below, is a quite typical object of expert investigations, when serious consequences (death of two workers of the bay and big material losses), require finding true cause and those guilty of the wrecking.

Casting stand MNLZ-2 at Nizhny Tagil Metallurgical Works (NTMK) was manufactured in 1996, assembled and put into operation at NTMK in March 1998.

Main technical features of the stand are listed in Table 1.

Photograph of tilted stand crosshead after wrecking is shown in Figure 1.

Such a position of the crosshead is due to failure of supporting pillars (Figure 2) in whose journals horizontal shaft of the crosshead is located. Figure 3,  $a$  and  $b$  shows photographs of failure of the right and left pillar (made of steel 3sp), welded joints were completed by CO<sub>2</sub> arc welding with Sv08G2S wire.



Figure 1. Tilted stand crosshead after wrecking

Characteristically, they failed very differently. The left pillar failed along the bolted joint (bolt material is steel 40Kh), with which the pillar flange is fastened to the base plate. The welds here, however, are almost fully intact. The right pillar failed along the welds connecting walls and pillar ribs with bearing flange. The bolted joint is fully intact.

To find out the causes of said failure of pillars, a number of experts from different organizations, including from the E.O. Paton Electric Welding Institute, NASU, Kiev, Ukraine, were engaged.

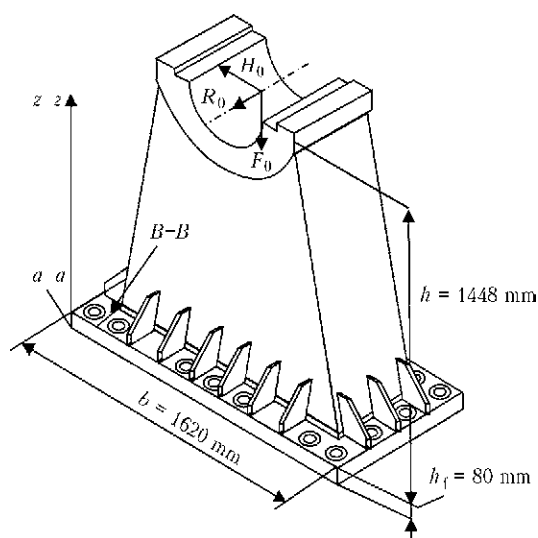


Figure 2. Pillar loading diagram

Table 1. Main technical features of the stand

Features	Value (rated)
Mass of casting ladle with metal, t	230
Height of ladle lifting, mm	800
Rate of ladle lifting (lowering), mm/s	32
Speed (working/emergency) of stand rotation, rpm	1.0/0.5
Stand turning angle, deg	290



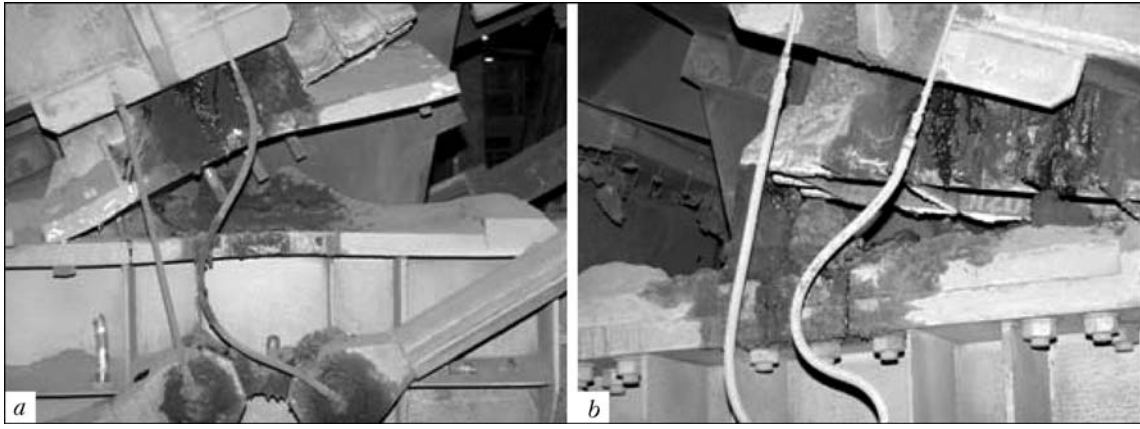


Figure 3. Left (a) and right (b) pillar failure

The evidence gathered in respect of factors conducive to failure of welded joints of the right pillar and the bolted joint of the left pillar can be summarized in the following form: each pillar experiences forces shown in Figure 2. Magnitudes of these forces are conditioned by the weight of the ladle with liquid metal, crosshead, as well as inertial forces occurring while the crosshead moves. With production capacity of the stand of 1.1 mln t per year, the number of loading cycles for the design life of stand operation of 15 years, will amount to 51,563 cycles, with production capacity of the stand of 1.5 mln t per year, i.e. 70,313 cycles.

Table 2 shows, based on the data of the examination, values of maximum loading  $F_0$ ,  $H_0$  and  $R_0$ , depending on the ladle with metal mass  $m$ .

Said forces  $F_0$ ,  $H_0$  and  $R_0$ , cause respective stresses in the right pillar welds failure plane (see Figure 3, b). Figure 4 shows schematic representation of the estimated A-A section of the pillar base, in which joints T3 and T6 (Figure 5) connect respectively ribs (T3), longitudinal and cross walls (T6) with the base flange (plate) of the pillar 80 mm thick.

Table 2. Highest loads on the crosshead depending on mass of ladle with molten metal  $m$

$m$ , t	Normally loaded	Maximum load	Loaded at failure
Maximum load, kN	215	230	245
$F_0$	1321.5	1362.7	1403.6
$H_0$	2026.2	2167.5	2308.9
$R_0$	43.0	46.0	49.0

In A-A section, rated normal stresses  $\sigma_{zz}$  are determined by the action of force  $F_0 - (\sigma_{zz}^{(2)})$  and moments of forces  $H_0 - (\sigma_{zz}^{(1)})$  and  $R_0 - (\sigma_{zz}^{(3)})$ . Besides, forces  $H_0$  and  $R_0$  cause tangent components of stress tensor of a certain magnitude:  $\sigma_{zz}$  of force  $H_0$  and  $\sigma_{zy}$  of force  $R_0$ .

Table 3 shows for representative points Nos. 1–4 of Figure 4, estimated values of rated stresses at extremes of the loading cycle, but at ladle mass of 230 t (including metal mass in it of 175 t, mass of slag of 5.5 t, empty ladle mass is 45 t).

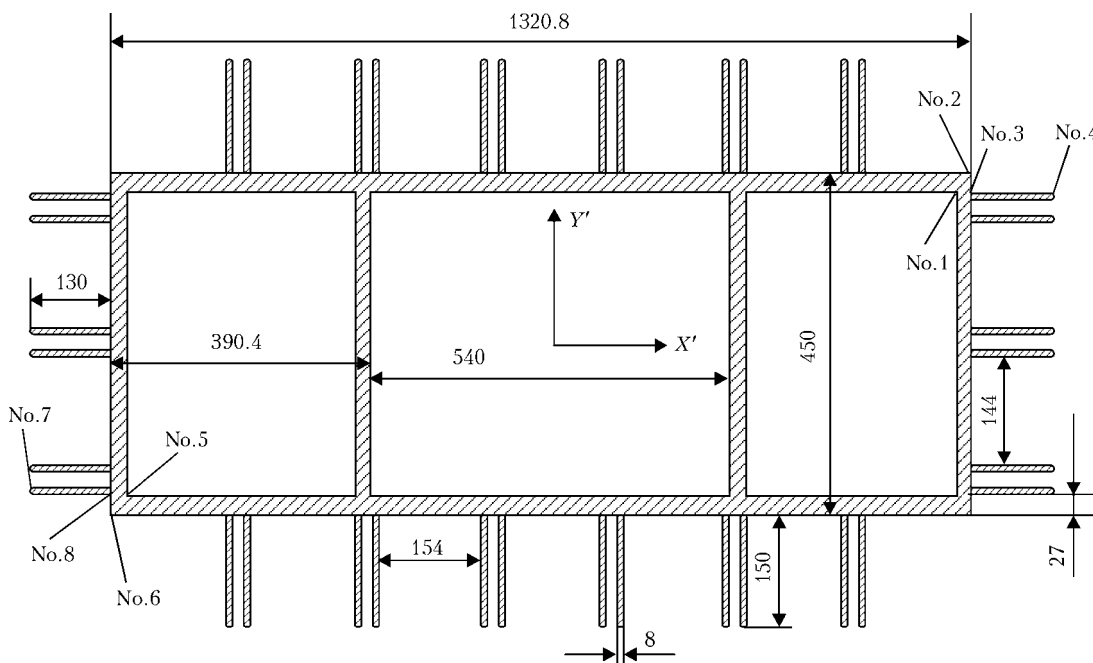


Figure 4. Estimated A-A section of the pillar base

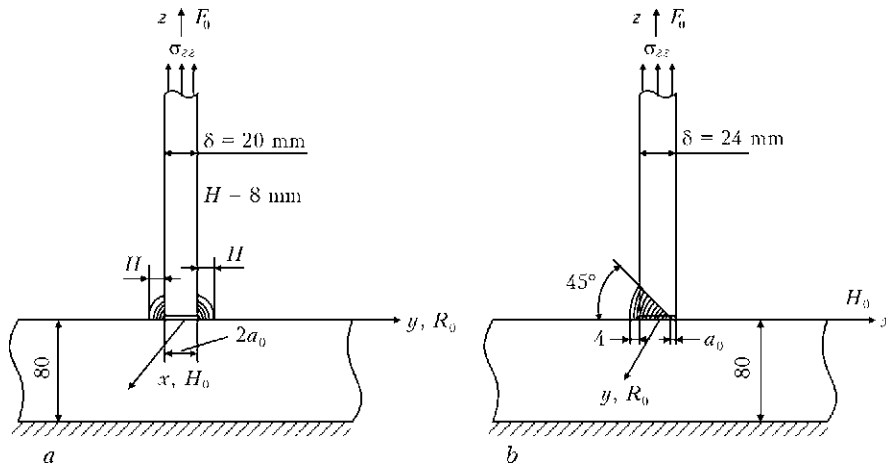


Figure 5. T-joints with fillet welds considered: a – T3; b – T6

Table 3. Estimated values of rated stresses in representative section points A-A (acc. to Figure 4) for extremes of loading cycle

Loaded state	Point No.	Rated stresses, MPa					
		$\sigma_{zz}^{(1)}$	$\sigma_{zz}^{(2)}$	$\sigma_{zz}^{(3)}$	$\sigma_{zz}$	$\sigma_{zx}$	$\sigma_{zy}$
Maximum loading	1	70.0	-9.5	2.1	62.6	29.5	0.7
	2	72.6	-9.5	2.4	65.5	0	0
	3	72.6	-9.5	2.1	65.2	29.5	0.7
	4	86.9	-9.5	2.1	79.5	0	0
Minimum loading	1	-70.0	-9.5	-2.1	-81.6	29.5	0.7
	2	-72.6	-9.5	-2.4	-84.5	0	0
	3	-72.6	-9.5	-2.1	-84.2	29.5	0.7
	4	-86.9	-9.5	-2.1	-88.5	0	0

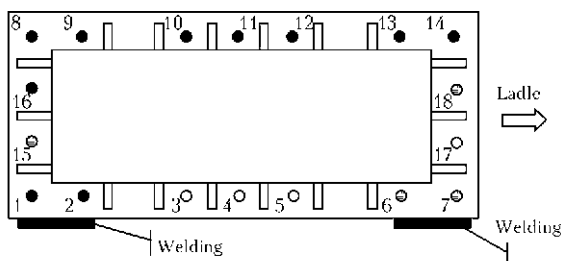
It is evident from Table 3 that principal loading of the zones considered in plane A-A is connected with normal variable stresses  $\sigma_{zz}$ . Here for points 2 and 4 (of T3 joint) this is the only loading. For points 1 and 3 along with variable  $\sigma_{zz}$ , loading is caused also by tangential permanent stresses  $\sigma_{zx}$  and  $\sigma_{zy}$ . Value of  $\sigma_{zy}$  can obviously be neglected, since it is of the order of 1 % of  $\sigma_{zz}^{max}$ . As to  $\sigma_{zx}$ , their presence has to be accounted for.

With a certain degree of conservatism it can be assumed that welded joint T3 in Figure 5 works at rated stresses of points 3 near the wall and 4 near the rib end, namely variable stresses  $\sigma_{zz}$  are acting, MPa:  $\sigma_{zz}^{max} = 79.5$ ,  $\sigma_{zz}^{min} = -88.5$  near the rib end, and  $\sigma_{zz}^{max} = 65.5$  and  $\sigma_{zz}^{min} = -84.5$  near the cross wall, i.e. ranges of rated stresses are 168 and 150 MPa, respectively,

or based on the data of [1], and joint 414 has a limited lifetime (FAT = 45 MPa).

For a welded joint T6, connecting the cross wall with the plate, also with a certain degree of conservatism it can be assumed that along the whole weld length there act rated stresses  $\sigma_{zz}$ , MPa:  $\sigma_{zz}^{max} = 65.2$ ,  $\sigma_{zz}^{min} = -84.2$ ,  $\Delta\sigma = 149.4$  and permanent tangential rated stresses  $\sigma_{zx} = 29.5$ , i.e. as follows from [1], this joint also belongs to the joints with limited lifetime as their longevity is much below  $2 \cdot 10^6$  cycles. However, by technical specification on stand operation, its longevity, as indicated above, should be not less than 51,560 cycles at productivity of 1.1 mln t a year, or 70,310 cycles at productivity 1.5 mln t a year, and with regard that failure occurred after about  $2.3 \cdot 10^4$  cycles, so without additional investigations it is difficult to consider the prime cause of stand failure being fatigue failure of welds of the right pillar, although aggravating factors discovered were lacks of fusion  $a$  up to 10 mm deep in joint T6 (see Figure 5).

Analysis of bolted joint of the left pillar (Figure 6) conducted in the process of the examination revealed that in the presence of all 18 bolts and their uniform tightening, distribution of loads on bolts at maximum cycle loading for the left pillar, mass of the maximum loaded ladle being 210 t, is determined by the data of Figure 7.



● Bolt without washer ● Bolt with washer ⊙ Bolt present ○ Bolt absent  
 Figure 6. Condition of bolted joint of left pillar flange before failure: 1–18 – bolt numbers

With original bolt section area of 1380 mm<sup>2</sup>, maximum stresses in bolts reaches 311.2 MPa, which for the bolts material (high-strength steel 40Kh) and at base of  $2.4 \cdot 10^4$  cycles, is quite acceptable for fault-free operation. However the experts have uncovered a whole range of aggravating factors: insufficient bolt tightening, which is evidenced by the presence of the gap between pillar flange and the base plate, where rust and lubricant have been found, absence of some bolts (see Figure 6) and an attempt to compensate their absence with welding, obvious overloading of some bolts, which after  $2.4 \cdot 10^4$  loading cycles has led to that fatigue failure accounted for about 75 % of the overall fracture section (Figure 8).

The reason for such an unsatisfactory state of the bolted joint of the left pillar lies in the absence of adequate monitoring of the bolted joint condition on the part of the NTMK respective services.

In the light of the above, two possible scenarios of casting stand failure have been formulated:

- due to the erroneous design of welded joints of the right pillar and lacks of fusion, there took place fatigue failure of the welded joints T3 and T6 connecting ribs and walls of the pillar, which caused a noticeable overloading of the left pillar, failure of its bolted joint and stand wrecking;

- because of the poor technical maintenance of the bolted joint of the left pillar and excessive overloading of some bolts, there took place fatigue failure of the left pillar, which lead to overloading of the right pillar, failure of the welded joint of that pillar and stand wrecking.

As coincidence of occurrence of the two scenarios is out of the question, then the immediate party in fault of the failure can be only one of the parties: either the party, responsible for stand manufacturing, or the party responsible for its operation.

Below follows the estimational analysis of the carrying capacity of the failed fillet welds and the bolted joint at static and repeated loading with account of the detected lacks of fusion in the welds and imperfections of the bolted joint; on that basis the conclusion on prime cause of the failure is made.

*Carrying capacity of welded joints of the right pillar.* Consider first joints T3, connecting outer ribs of the pillar (see Figure 5) with the flange.

The 20 mm thick rib is welded to the flange with a two-sided fillet weld having the leg  $h = 8$  mm. Filler material is Sv-08G2S wire. «Hot spots», as indicated above, are points 3 and 4 (see Table 3).

T3 joints were designed with incomplete penetration, with  $2a_0 \approx 20$  mm (see Figure 5). In repeated loading this value may grow, respectively critical failure loading should diminish.

With a certain degree of conservatism this loading  $\sigma_{zz}^{cr}$  can be determined from brit-

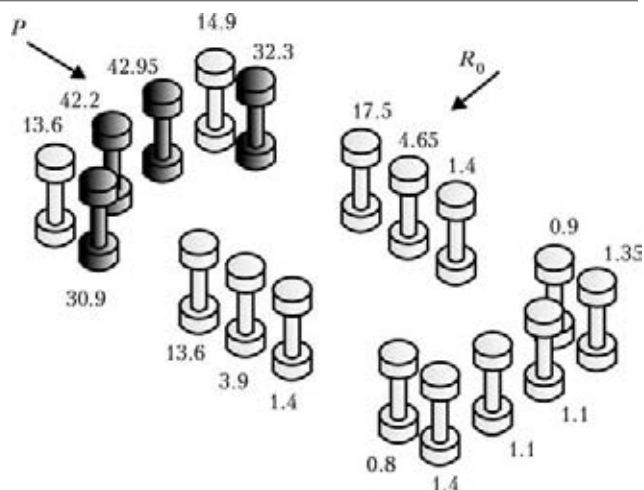


Figure 7. Distribution of loads on bolts

tle-ductile failure conditions [2, 3], depending on  $2a$  value, modelling lack of fusion with a crack of great length running along the weld. Following recommendations of [1], value of stress intensity factor (SIF)  $K_I$  can be determined as

$$K_I = \frac{\sigma_{zz}(A_1 + A_2 a/w) \sqrt{\pi a \sec \frac{\pi a}{2w}}}{1 + 2h/\delta}, \quad (1)$$

where  $w = h + \delta/2$ ;

$$A_1 = 0.528 + 3.287 \frac{h}{\delta} - 4.361 \left(\frac{h}{\delta}\right)^2 + 3.696 \left(\frac{h}{\delta}\right)^3 - 1.875 \left(\frac{h}{\delta}\right)^4 + 0.415 \left(\frac{h}{\delta}\right)^5; \quad (2)$$

$$A_2 = 0.218 + 2.717 \frac{h}{\delta} - 10.171 \left(\frac{h}{\delta}\right)^2 + 13.122 \left(\frac{h}{\delta}\right)^3 - 7.755 \left(\frac{h}{\delta}\right)^4 + 1.783 \left(\frac{h}{\delta}\right)^5.$$

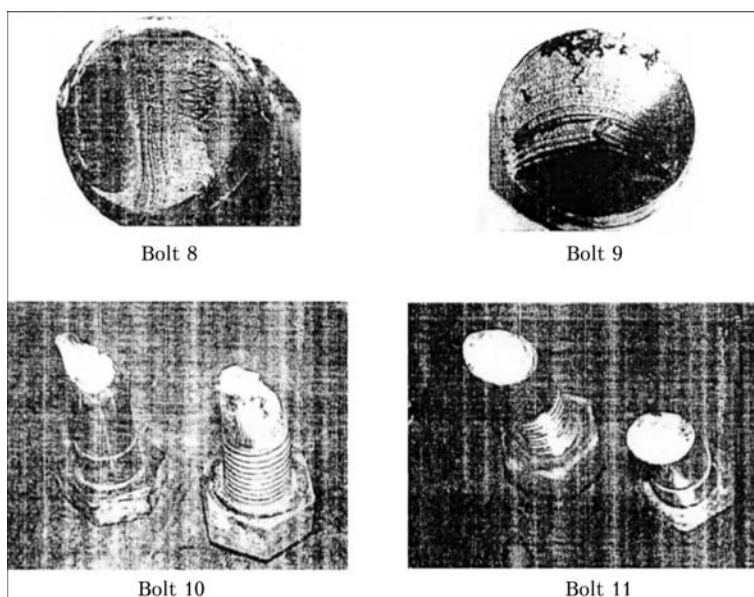


Figure 8. Bolts fractured by fatigue mechanism (8, 9), by shear (10) and by tear (11)

Since  $a$  value in repeted loading does not remain constant, it is calculated by the known Paris' relation. In [1, p. 121] it is recommended to use for this purpose dependence

$$\frac{da}{dN} = \frac{C_0 \Delta K_I^m}{(1-R) - \frac{\Delta K}{K_C}} \text{ at } \Delta K > \Delta K_{th};$$

$$\frac{da}{dN} = 0 \text{ at } \Delta K < \Delta K_{th},$$
(3)

**Table 4.** Results of calculation of  $2a$  and  $\sigma_{zz}^{cr}$  values depending on  $N$  for T3 joint at  $K_C = 3000 \text{ MPa}\cdot\text{mm}^{1/2}$ ,  $C_0 = 2 \cdot 10^{-13}$  and  $2a_0 = 20 \text{ mm}$

N, cycle	2a, mm	$\sigma_{zz}^{cr}, \text{MPa}$	2a, mm	$\sigma_{zz}^{cr}, \text{MPa}$
	Point 4		Point 3	
20000	21.1	202.1	20.6	209.1
22000	21.2	200.4	20.6	208.2
24000	21.3	198.8	20.7	207.4
26000	21.5	197.1	20.7	206.6
28000	21.6	195.4	20.8	205.8
30000	21.7	193.6	20.9	205.0
32000	21.9	191.8	20.9	204.1
34000	22.0	189.9	21.0	203.3
36000	22.2	188.0	21.1	202.4
38000	22.3	186.0	21.1	201.6
40000	22.5	184.0	21.2	200.8
42000	22.6	181.9	21.3	199.9
44000	22.8	179.8	21.3	198.9
46000	23.0	177.5	21.4	198.1
48000	23.1	175.2	21.5	197.1
50000	23.3	172.8	21.5	196.2
52000	23.5	170.4	21.6	195.3
54000	23.7	167.8	21.7	194.4
56000	23.9	165.1	21.8	193.4
58000	24.1	162.2	21.8	192.4
60000	24.4	159.3	21.9	191.4
62000	24.6	156.2	22.0	190.4
64000	24.9	152.9	22.1	189.4
66000	25.1	149.5	22.1	188.4
68000	25.4	145.9	22.2	187.3
70000	25.7	141.9	22.3	186.2
72000	26.0	137.7	22.4	185.1
74000	26.4	133.1	22.5	184.1
76000	26.8	128.1	22.6	182.9
78000	27.2	122.6	22.6	181.8
80000	27.7	116.3	22.7	180.6
82000	28.2	109.1	22.8	179.4
84000	28.9	100.4	22.9	178.3
86000	29.7	89.4	23.0	177.1
88000	30.9	73.7	23.1	175.8
90000	34.1	29.7	23.2	174.6

where  $\Delta K_I = K_I^{\max} - K_I^{\min}$ ;  $K_I^{\max}$  and  $K_I^{\min}$  are calculated according to (1) depending on  $a$  at  $\sigma_{zz}^{\min}$  and  $\sigma_{zz}^{\max}$ . Here,  $K_I^{\min} \geq 0$ ,  $R = K_I^{\min}/K_I^{\max}$ ,  $C_0$  and  $m$  are the experimental data on the material;  $\Delta K_{th}$  is the threshold value of amplitude  $\Delta K_I$ . In [1] the following dependence for  $\Delta K_{th}(R)$  is recommended:

$$\Delta K_{th}(R) = 190 - 144R, \text{ MPa}\cdot\text{mm}^{1/2};$$

$$\Delta K_{th}(R) \geq 62, \text{ MPa}\cdot\text{mm}^{1/2}.$$
(4)

Integration over  $N$  (3) with regard for (1) and (4) and preset  $a_0$ , enables to obtain kinetics of  $a$  growth depending on loading cycles  $N$ .

For materials type steel 3sp quite a number of experiments on fatigue crack growth [4, 5 etc.], and processing of such data to determine  $m$  and  $C_0$ , have been conducted.

Calculations for joint T3 at  $m = 3$  gave

$$C_0 = 2 \cdot 10^{-13} \frac{\text{mm}/\text{cycle}}{\text{MPa}\cdot\text{mm}^{1/2}} \text{ and } 2a_0 = 20 \text{ mm}.$$

Simultaneously, from condition of brittle-ductile failure [2, 3] with regard for (1),  $\sigma_{zz}^{cr}(N)$  critical stresses, in whose presence the risk of spontaneous growth of «crack» appears, were determined.

Required value  $L_r$ , was calculated from the dependence

$$L_r = \frac{\sigma_{zz}^{cr}}{\sigma_y}; \quad \sigma_{ref} = \frac{\sigma_{zz}^{cr} \delta}{(w - 2a)}.$$
(5)

Here restriction [2, 3] was applied:

$$L_r \leq L_r^{\max} = \frac{\sigma_t + \sigma_y}{2\sigma_y}$$
(6)

and at  $L_R = L_r^{\max}$ ,  $K_r = 0$ .

Results of calculation of  $2a$  and  $\sigma_{zz}^{cr}$  for the zone of point 4, i.e. for the cycle of variation of rated stresses  $\sigma_{zz}^{\max} = 79.5$  and  $\sigma_{zz}^{\min} = -88.5$  MPa, as well as for the zone of point 3, i.e. at  $\sigma_{zz}^{\max} = 65.5$  and  $\sigma_{zz}^{\min} = -84.5$  MPa, are entered in Table 4.

It is seen that the joints considered react to such repeated loading with growth of  $2a$  actually from the start of operational loading, since amplitude of SIF  $\Delta K_I$  is greater than  $\Delta K_{th}$  as follows from (4). However growth rates are rather slow, i.e. in  $N = 3 \cdot 10^4 - 4 \cdot 10^4$  cycles, they grow by 2–3 mm. Nevertheless, such traces of fatigue «failure» can be detected in a weld, though, judging from  $\sigma_{zz}^{cr}$  in comparison with  $\sigma_{zz}^{\max}$ , exhaustion of carrying capacity does not occur yet.

Judging from  $\sigma_{zz}^{cr} \gamma_M$  the in comparison with  $\sigma_{zz}^{\max}$ , the joint is not under threat of spontaneous failure up to  $N = 75,000$  cycles at  $\gamma_M \approx 1.6$ .

However with failure of the left pillar the loading had to increase almost twice. Respectively, even  $N = 2400$  cycles is critical for welded joint T3 of the right pillar at the above assumption, that bolted joint of that pillar is in a good working condition.

**Table 5.** Estimated kinetics of variation of  $a$ ,  $\sigma_{zz}^{cr} \gamma_M$  depending on  $N$  for different  $a_0$  values in welded joint T6

$N$ , cycle	$a_0 = 2$ mm		$a_0 = 4$ mm		$a_0 = 5$ mm		$a_0 = 6$ mm	
	$a$ , mm	$\sigma_{zz}^{cr} \gamma_M$ , MPa	$a$ , mm	$\sigma_{zz}^{cr} \gamma_M$ , MPa	$a$ , mm	$\sigma_{zz}^{cr} \gamma_M$ , MPa	$a$ , mm	$\sigma_{zz}^{cr} \gamma_M$ , MPa
20000	2.1	315	4.2	266	5.4	246	6.6	227
22000	2.1	315	4.3	266	5.4	245	6.7	226
24000	2.1	315	4.3	265	5.5	245	6.8	225
26000	2.1	315	4.3	265	5.5	244	6.8	224
28000	2.1	315	4.3	264	5.6	243	6.9	222
30000	2.1	314	4.4	264	5.6	242	7.0	221
32000	2.1	314	4.4	263	5.7	242	7.1	220
34000	2.1	314	4.4	263	5.7	241	7.2	219
36000	2.1	314	4.4	262	5.8	240	7.3	218
38000	2.1	314	4.5	262	5.8	239	7.3	216
40000	2.1	314	4.5	261	5.9	239	7.4	215
42000	2.1	313	4.5	261	5.9	238	7.5	214
44000	2.1	313	4.6	260	6.0	237	7.6	212
46000	2.1	313	4.6	260	6.0	236	7.7	211
48000	2.1	313	4.6	259	6.1	235	7.8	209
50000	2.2	313	4.6	259	6.1	234	8.0	208
52000	2.2	313	4.7	258	6.2	233	8.1	206
54000	2.2	312	4.7	258	6.2	232	8.2	204
56000	2.2	312	4.7	257	6.3	232	8.3	203
58000	2.2	312	4.8	257	6.4	231	8.5	201
60000	2.2	312	4.8	256	6.4	230	8.6	199
62000	2.2	312	4.8	256	6.5	229	8.7	197
64000	2.2	311	4.9	255	6.6	228	8.9	195
66000	2.2	311	4.9	254	6.6	227	9.1	193
68000	2.2	311	4.9	254	6.7	225	9.2	191
80000	2.3	310	5.1	250	7.2	218	10.6	174
90000	2.3	309	5.3	247	7.7	212	12.4	152
100000	2.3	308	5.6	243	8.2	204		
110000	2.4	307	5.8	239	9.0	194		
118000	2.4	306	6.0	236	9.7	185		

Consider load-carrying capacity of welded joint T6 (see Figure 5, *b*) as applied to the cross wall and provided that bolted joint is a quality one (right pillar). According to Table 3, the joint in this case experiences effect of rated variable stresses  $\sigma_{zz}^{\max} = 62.6$  and  $\sigma_{zz}^{\min} = -81.6$  MPa in point 1 (see Figure 4), and  $\sigma_{zz}^{\max} = 65.6$  and  $\sigma_{zz}^{\min} = -84.2$  MPa in point 2. Besides, active also are rated constant tangential stresses  $\sigma_{zx} = 29.5$  MPa.

Under conditions of two-axis loading, [1] recommends to consider propagation of fatigue crack resulting from lack of fusion in the plane of action of the main stress  $\sigma_1$ , determined by condition

$$\sigma_1 = \sigma_{zz}^{\max} + \sqrt{(\sigma_{zz}^{\max})^2 + 4\sigma_{zx}^2}. \quad (7)$$

Respectively, the angle of crack propagation plane  $\omega$  from axis  $x$  is determined by dependence

$$\operatorname{tg} 2\omega = \frac{2\sigma_{xz}}{\sigma_{zz}^{\max}}. \quad (8)$$

With above-specified values of  $\sigma_{zz}^{\max}$  and  $\sigma_{xz}$ ,  $\omega = 21^\circ 06'$  and  $21^\circ 36'$ , respectively, these are points 2 and 1. Stesses on the site  $\omega$  under consideration, when  $\sigma_{zz} = \sigma_{zz}^{\min}$  and  $\sigma_{zx}$  are preset, while other stress tensor components are zero, can be found from the equation

$$\sigma_{\omega\omega}^{\min} = \sigma_{zz}^{\min} \cos^2 \omega + \sigma_{zx} \sin 2\omega. \quad (9)$$

Accordingly, we obtain, using Table 3:

- for  $\omega = 21^\circ 06'$ ,  $\sigma_1 = \sigma_{\omega\omega}^{\max} = 76.2$  MPa,  $\sigma_{\omega\omega}^{\min} = -58.63$  MPa;

- for  $\omega = 21^\circ 36'$ ,  $\sigma_1 = \sigma_{\omega\omega}^{\max} = 73.7$  MPa, and  $\sigma_{\omega\omega}^{\min} = -55.46$  MPa.

For the plane considered, calculation of SIF according to [1] is made by the dependence

Table 5 (cont.)

N, cycle	a <sub>0</sub> = 7 mm		a <sub>0</sub> = 8 mm		a <sub>0</sub> = 9 mm		a <sub>0</sub> = 10 mm	
	a, mm	σ <sub>zz</sub> <sup>cr</sup> /M, MPa	a, mm	σ <sub>zz</sub> <sup>cr</sup> /M, MPa	a, mm	σ <sub>zz</sub> <sup>cr</sup> /M, MPa	a, mm	σ <sub>zz</sub> <sup>cr</sup> /M, MPa
20000	8.0	208	9.5	187	11.4	164	14.4	131
22000	8.1	206	9.7	185	11.8	160	15.6	118
24000	8.2	204	9.9	182	12.2	154	18.1	93
26000	8.3	203	10.1	179	12.8	149		
28000	8.5	201	10.4	176	13.4	141		
30000	8.6	199	10.7	173	14.2	133		
32000	8.8	197	11.0	169	15.4	120		
34000	8.9	195	11.3	165	17.5	98		
36000	9.1	193	11.7	161				
38000	9.3	190	12.1	156				
40000	9.4	188	12.6	150				
42000	9.6	186	13.2	143				
44000	9.8	183	14.0	135				
46000	10.1	180	15.1	124				
48000	10.3	177	16.8	105				
50000	10.6	174						
52000	10.9	170						
54000	11.2	166						
56000	11.6	162						
58000	12.0	157						
60000	12.5	152						
62000	13.0	145						
64000	13.7	138						
66000	14.7	128						
68000	16.1	113						

$$\begin{aligned}
 K_I &= \sigma_{\omega\omega} \sqrt{\pi a} \left[ 1.13 - 0.718 \left( \frac{a}{W} \right)^2 + 0.432 \left( \frac{a}{W} \right)^4 \right] \times \\
 &\times \sec \pi/2 \sqrt{\frac{a}{W}}, \quad W = \delta + h; \\
 \Delta K_I &= K_I^{\max} - K_I^{\min}, \\
 \sigma_{\text{ref}} &= \sigma_{\omega\omega} \frac{\delta}{W - 2a} \text{ at } \sigma_t = 0.
 \end{aligned}
 \tag{10}$$

K<sub>I</sub><sup>max</sup> is determined at σ<sub>ωω</sub><sup>max</sup>, while K<sub>I</sub><sup>min</sup> at σ<sub>ωω</sub><sup>min</sup> with account that K<sub>I</sub><sup>min</sup> ≥ 0. Since for ω considered, difference in loading is small, below is considered the utmost loading variant, i.e. σ<sub>ωω</sub><sup>max</sup> = 76.2 and σ<sub>ωω</sub><sup>min</sup> = -58.63 MPa, and ω = 21°06'. Original values a<sub>0</sub> of lack of fusion were varied within the range of 2–10 mm.

The results of respective calculations of a(N) and σ<sub>zz</sub><sup>cr</sup>(N) by the same method, as for the weld T3, but with account of (12) are shown in Table 5.

It is clearly seen that joint T6 in «hot spots» 1 and 2 is quite susceptible for fatigue failure in the presence of lack of fusion.

Design lifetime (5.2·10<sup>4</sup> cycles) at γ<sub>M</sub> = 1.2 is provided only at a<sub>0</sub> < 8 mm. Nevertheless, at N = 2.4·10<sup>4</sup> cycles, i.e. by the moment of the wrecking, even at a<sub>0</sub> = 10 mm, stress amplitude magnitude margin was γ<sub>M</sub> = 1.22, or in terms of lifetime – 1.82. However, even a relatively small overloading (by 25 %) related to, for instance, failure of the left pillar, may cause failure in the considered «hot spot» of the weld T6, connecting cross wall of the pillar with the flange.

- Hobacher, A. (2002) Recommendations for fatigue design of welded joints and components. *IIW Doc. XIII-1339-96, XV-849-96*.
- Harrison, R.P., Loosmore, K., Milne, J. et al. (1980) Assessment of the integrity of structures containing defects. In: *Report P/H R6*. Rev. 2. CEBG.
- Milne, L., Ainsworth, R.A., Dowling, A.R. et al. (1986) *Assessment of the integrity of structures containing defects*. Rev.3. CEBG.
- Rosmary, P., Tot, L., Nad, D. (1980) Analysis of regularity of fatigue crack propagation in metals. *Problemy Prochnosti*, **12**, p. 18–28.
- Ohta, A., Sasaki, E., Kasuge, M. et al. (1987) *Fatigue crack growth and threshold stresses intensity factor for welded joints*. *Current research of fatigue cracks*. Elsevier Sci. Publ., p. 181–200.

# AMORPHOUS BRAZING FILLER ALLOYS, RESEARCH AND MODELLING OF THEIR STRUCTURAL STATE

S.V. MAKSYMOVA<sup>1</sup>, V.F. KHORUNOV<sup>1</sup> and G.M. ZELINSKAYA<sup>2</sup>

<sup>1</sup>E.O. Paton Electric Welding Institute, NASU, Kiev, Ukraine

<sup>2</sup>G.V. Kurdyumov Institute of Metal Physics, NASU, Kiev, Ukraine

Structure of rapid-quenched Ti-Cu, Ti-Cu-Zr-Ni and Ti-Cu-Zr-Ni-V-Be system based alloys was studied by X-ray diffraction and metallography analysis. Structural factors were calculated, and atom radial distribution functions (ARDF) were determined using special software. Structural state of amorphous brazing filler alloy Ti<sub>50</sub>Cu<sub>50</sub> was modeled on the basis of resulting curves of the structural factor, ARDF and their parameters, and using quasi-crystalline model. Structural components were identified, and phase composition of the brazing filler alloy after isothermal annealing was studied.

Amorphous brazing filler alloys (BFA) are perspective for application in many branches of industry. They are characterized by a number of unique properties, in particular, small thickness (30–50 μm), high degree of plasticity and homogeneity of their chemical composition, which is especially important for brazing of thin-walled structures, when simultaneous melting of the BFA over the entire volume of the structure being brazed is necessary for preventing erosion of the base metal. Amorphous BFA can be used as inserts of complex configurations, which enables to dose the amount of the used braze. It is necessary to note that the method of ultrarapid quenching has enabled to obtain plastic homogeneous foils from brittle alloys, which could previously be used only in a powder form. Application of amorphous BFA provides good wetting of the surfaces being brazed, uniform distribution of the components of the braze in a zone of brazing, which reduces probability of formation of brittle phases in the brazed seam and, finally, provides optimum durability of brazed joints.

In this work are presented the results of X-ray diffraction analysis and metallography investigations of BFA on the basis of system Ti-Cu, Ti-Cu-Zr-Ni, Ti-Cu-Zr-Ni-V-Be, obtained with the help of a method of ultrarapid quenching of the melt. On the example of

BFA Ti<sub>50</sub>Cu<sub>50</sub> (hereinafter in wt.%), was carried out modeling of the structural state, and phase composition after isothermal annealing was also determined.

Microstructural investigations of the amorphous braze Ti<sub>50</sub>Cu<sub>50</sub> show that typical pattern of the surface of the amorphous tape contacting the air, is characterized by smooth mirror (glass-like) surface, absence of any pits or roughness (Figure 1, *a*). Reverse side of the tape, contacting with the surface of the drum, has irregularities (Figure 1, *b*) caused by the roughness of the material of the drum, speed of its rotation, etc.

Chemical elements of the braze are distributed over the surface of the tape uniformly, only on its edges the tendency to insignificant change of concentration of alloying elements is observed. This phenomenon requires further investigations.

Radiographic investigation of the structure of samples of amorphous BFA was carried out on diffractometer DRON-3 in MoK<sub>α</sub>-radiation in point scanning mode. The time of exposure had been selected such that statistical error of measuring the intensity at the big angles of scattering did not exceed 1 %.

Graphite monochromator was stationed on the primary beam. Modes of recording equipment for each sample were selected in such a manner that the noise, fluorescent scattering from the sample, as well as

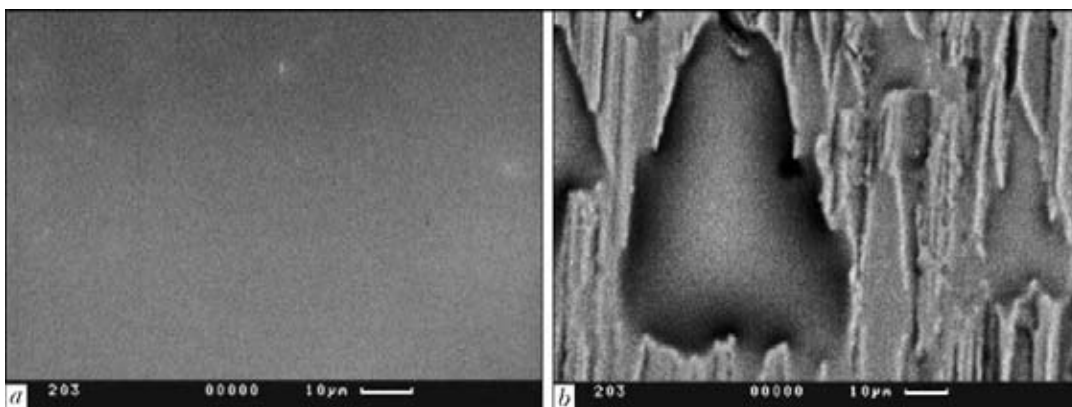


Figure 1. Surface of tape contacting air (*a*) and drum (*b*)

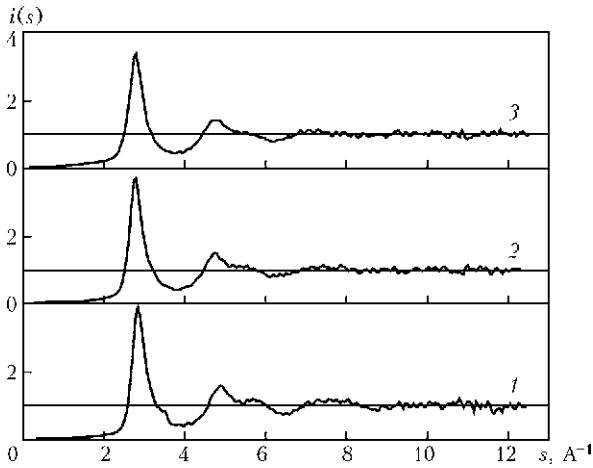


Figure 2. Structural factors of amorphous tapes: 1 – Ti<sub>50</sub>Cu<sub>50</sub>; 2 – Ti<sub>33</sub>Cu<sub>23</sub>Zr<sub>12</sub>Ni<sub>12</sub>; 3 – Ti<sub>33</sub>Cu<sub>23</sub>Zr<sub>12</sub>Ni<sub>12</sub>V<sub>0.8</sub>Be<sub>1.5</sub>

radiation from the continuous spectrum at wavelength of  $\lambda/2$ , which is transmitted by the monochromator crystal, were excluded.

An important point in the research of amorphous tapes for reflectivity is the fulfillment of the requirements of the theory regarding an infinitely absorbing sample. For this purpose the studied samples were prepared in packs made of 4–7 layers of amorphous tape.

The technique of making corrections for non-coherent scattering, polarization, absorption, fluorescent scattering by the sample, as well as diffraction curves normalization, were common in [1, 2]. Using the software package developed by A.G. Iliinsky, structural factors were calculated:

$$i(s) = \frac{I_{\text{incoh}}}{F^2},$$

where  $I_{ke} = k \frac{I_{\text{exp}}}{AP} - I_{\text{incoh}}$ ;  $s = 4\pi \sin \theta / \lambda$ . Here  $\theta$  is the half of the scattering angle;  $\lambda = 0.71\text{A}$  is the molybdenum radiation wavelength;  $1/A$  is the factor of absorption which for the method of  $\theta \times \theta$  diffractometer is not dependant on the scattering angle;  $1/P$

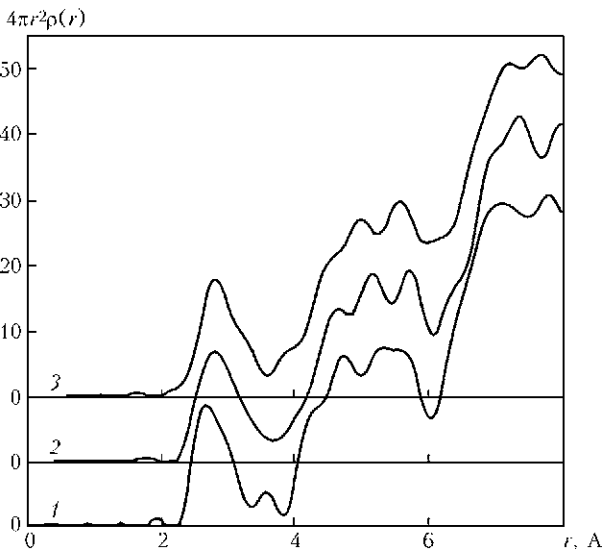


Figure 3. ARDFs for amorphous tapes of Ti<sub>50</sub>Cu<sub>50</sub> (1), Ti<sub>33</sub>Cu<sub>23</sub>Zr<sub>12</sub>Ni<sub>12</sub> (2) and Ti<sub>33</sub>Cu<sub>23</sub>Zr<sub>12</sub>Ni<sub>12</sub>V<sub>0.8</sub>Be<sub>1.5</sub> (3)

is the polarization factor;  $I_{\text{incoh}}$  is the intensity of incoherent scattering in electronic units, calculated by reference points, pre-assigned for each alloy atom;  $k$  is the normalization factor;

$$F^2 = n_1 f_1^2 + n_2 f_2^2$$

for a two-component alloy with scattering characteristics of components  $f_1, f_2$  and atomic concentration  $n_1, n_2$ ; and correlation functions (ARDF)

$$4\pi r^2 \rho(r) = 4\pi r^2 \rho_0 + \frac{2r}{\pi} \int_0^\infty [i(s) - 1] s \sin s r ds,$$

where  $\rho(r)$  is the function atomic density;  $\rho_0$  is the mean atomic density.

Different scattering characteristics of the components  $k_i^2 = f_i^2 / \sum n_i f_i^2$  are taken into account. Here  $\rho(r) = \sum \sum n_i k_i \rho_{ij}(r)$ ;  $n_i$  is the atomic concentration;  $f_i$  is the atomic component factor.

From functions  $i(s)$  and ARDF, basic structural characteristics were determined, namely position  $s_1$  and height  $i(s_1)$  of the structural factor, the first ARDF maximum position  $r_1$  and area  $A$ , defined symmetrically  $A_c$  and by the first minimum  $A_{\text{min}}$ . The shape of the obtained curves  $i(s)$ , ARDF and their parameters were used for modeling the structure [3, 4].

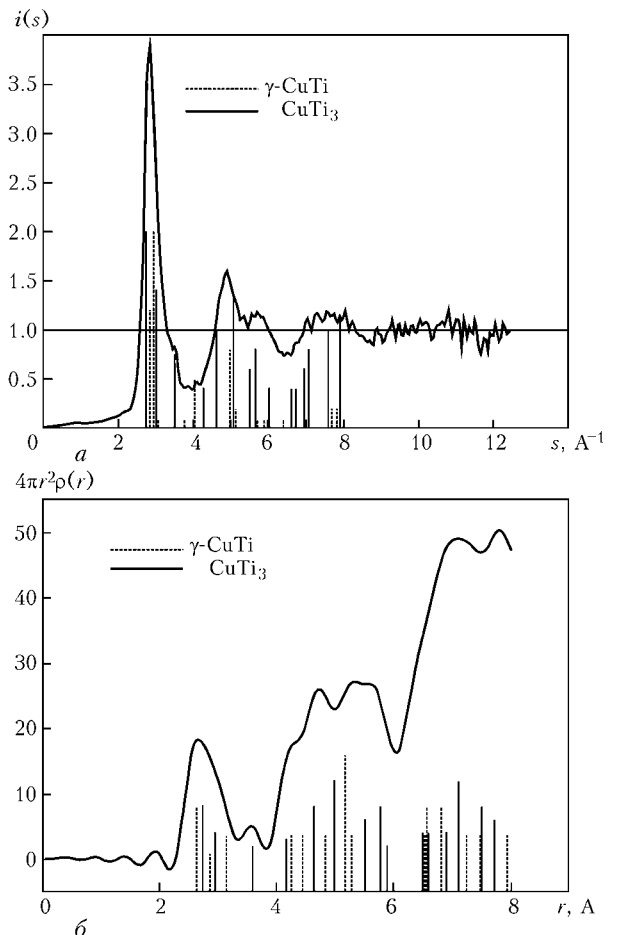


Figure 4. Structural factor (a) and ARDF (b) of amorphous tape Ti<sub>50</sub>Cu<sub>50</sub>



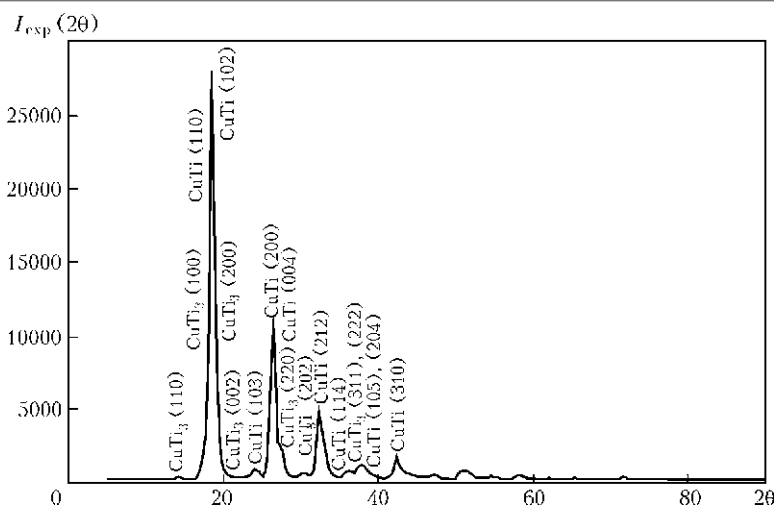


Figure 5. X-ray pattern of the  $Ti_{50}Cu_{50}$  sample after isothermal annealing

Research of the structure of amorphous BFA on the basis of systems Ti–Cu, Ti–Cu–Zr–Ni, Ti–Cu–Zr–Ni–V–Be with the help of X-ray diffraction analysis shows that they feature a diffraction pattern similar to that of metal liquids (Figure 2).

They feature a typical diffraction pattern containing diffuse maxima with a clearly pronounced effect of splitting of the second maximum (see Figure 2), which is typical of alloys in an amorphous state [5]. It has to be noted that on the right branch of the first maximum of structural factor  $i(s)$  for alloy  $Ti_{50}Cu_{50}$  the overlap at  $s \approx 35 \text{ \AA}^{-1}$  is observed, while the ARDF curve for this alloy features asymmetry of the first maximum and an additional maximum in the vicinity of  $r \approx 3.6 \text{ \AA}$  (Figure 3). These facts may testify to that the first diffraction maximum and the ARDF first maximum, as is also the case with melts, can be regarded as a superposition of several maxima, caused by the existence of several types of atomic groupings [2].

For the amorphous alloy  $Ti_{50}Cu_{50}$  obtained from the eutectic melt, modeling and testing of the types of structures, corresponding to the state diagram of system Ti–Cu, were conducted. Using respective software, from the point of view of quasi-crystalline model [2], were computed positions of diffraction reflections  $s_i$  and the arrangement of coordination spheres  $r_i$  for such structures. It was found that their height corresponds to the intensity of reflections for  $i(s)$  and to the quantity of atoms for ARDF (Figure 4).

The most probable appeared microgroupings of the type  $\gamma$ -CuTi with tetragonal packing of atoms ( $a = 3.108 \text{ \AA}$ ,  $c = 5.887 \text{ \AA}$  [6]), and  $CuTi_3$  ( $a = 4.158 \text{ \AA}$  and  $c = 3.594 \text{ \AA}$  [6]), which represent well all the peculiarities on the interference curves  $i(s)$  and ARDF curves, as well as their basic structural parameters ( $s_1 = 2.84 \text{ \AA}^{-1}$ ,  $i(s_1) = 3.9$ ,  $r_1 = 2.66 \text{ \AA}$ ,  $A_c = 8.3$ ,  $A_{\min} = 11.9$  at  $r_{\min} = 3.34 \text{ \AA}$ ) for modeling the structure of the given alloy after [4].

It is necessary to note that the parameter of high magnitude of the structural factor  $i(s_1)$ , connected with density of packing of atoms, is a very sensitive characteristic testifying to the presence in the amor-

phous tape of some fraction of the crystalline phase. It is connected with a number of technological factors at quenching, in particular, conditions of obtaining amorphous tapes from the liquid-state metal, i.e. temperature of the melt and the duration of soaking before quenching [1, 7, 8].

X-ray diffraction study of the alloy  $Ti_{50}Cu_{50}$ , carried out after annealing in vacuum at  $510 \text{ }^\circ\text{C}$  for 1 h [9], has revealed the presence of packings of  $\gamma$ -CuTi and  $CuTi_3$  types (Figure 5).

## CONCLUSIONS

- Rapid-quenched BFA on the basis of systems Ti–Cu, Ti–Cu–Zr–Ni, Ti–Cu–Zr–Ni–V–Be are X-ray amorphous.

- The structure of amorphous  $Ti_{50}Cu_{50}$  alloy, from the point of view quasi-crystalline model, can be represented as quasi-eutectic microareas of the type  $\gamma$ -CuTi and  $CuTi_3$ .

3. After annealing of the amorphous BFA  $Ti_{50}Cu_{50}$ , with the help X-ray diffraction analysis, crystalline structures  $\gamma$ -CuTi and  $CuTi_3$  were identified.

1. Nemoshkalenko, V.V., Romanova, A.V., Illinsky, A.G. et al. (1987) *Amorphous metal alloys*. Kiev: Naukova Dumka.
2. Romanova, A.V. (1995) Some historical facts and memoirs on development of conception of the liquid and metallic glass atomic structure. *Metallofizich. Nov. Tekhnologii*, **8**, p. 3–29.
3. Romanova, A.V., Kuchak, G.M. (1964) X-ray study of the molten intermetallic compounds of indium-bismuth system. *UFZh*, **9(4)**, p. 428–440.
4. Romanova, A.V., Illinsky, A.G. (1974) On method of the experimental data interpretation at X-ray study of two-component melts. *Ibid.*, **19(9)**, p. 564–566.
5. Golder, Yu.G. (1978) Metallic glasses. *Tekhnologiya Lyog. Splavov*, **6**, p. 74–93.
6. Karlsson, N. (1951) An X-ray study of the phases in the copper-titanium system. *J. Inst. Met.*, **79**, p. 391–405.
7. Zelinskaya, G.M., Romanova, A.V., Nemoshkalenko, V.V. et al. (1983) Influence of production conditions of the iron-boron hypereutectic alloy amorphous metal films on their structure. *UFZh*, **28(9)**, p. 1393–1397.
8. Illinsky, A.G., Zelinskaya, G.M., Maslov, V.V. et al. (2004) Structural transformations of the amorphous  $Fe_{80}Si_6B_{14}$  tapes at long-term air soaking. *Metallofizich. Nov. Tekhnologii*, **26(11)**, p. 1501–1507.
9. Maksymova, S.V., Khorunov, V.F., Zelinskaya, G.M. (2006) Titanium-based amorphous brazing filler alloy. In: *Proc. of 7th Int. Conf. on Equipment and Technology for Heat Treatment of Metals and Alloys*. Kharkov: KhFTI, p. 150–153.

# ANALYSIS OF THERMO-ELECTRICAL PROCESSES AND ELECTRODE METAL TRANSFER DURING GAS-METAL-ARC WELDING WITH THE AID OF NUMERICAL MODELLING

O. MOKROV, V. PAVLYK and U. DILTHEY

ISF – Welding and Joining Institute, Aachen University, Germany

This paper presents a transient numerical model and a computational module for analysis of electrical and thermal characteristics of electrode melting and metal transfer during gas-metal-arc welding (GMAW) processes. The model considers following phenomena and factors: contact resistance, ohmic heating, heat flux at the anode layer into drop, heat diffusion, evaporation heat loss, temperature dependencies of thermal and electrical material properties, electromagnetic and surface tension forces, dependencies of voltage drops at cathode, anode and in arc column, as well as dependence of anode spot radius from welding current and plasma composition. In addition, the regulation algorithms of power source are considered. The sub-models of different parts of the process are assembled into a whole model, which couples electrical, thermal and mass transfer phenomena and thus allows the process to be simulated as a whole. Analysis of mean voltage, current and power for pulse processes with  $U/I$  and  $I/I$ -modulation modes which was carried out with the model and compared with the experiments demonstrates a high accuracy of the model predictions. The model is used in the simulation package SimWeld for calculation of magnitude and distribution of cathode, anode and arc column heat sources at the weld pool surface.

Thermo-electrical processes in the «equipment–wire–arc–workpiece» system determine the thermal characteristics of the welding arc and process stability and thus directly influence the welding results during GMAW process. The system is strongly coupled which complicates or makes in many cases impossible to clarify the influence of each phenomenon separately, either experimentally or theoretically. Therefore, a fully coupled theoretical analysis by means of mathematical modelling is needed to study the process.

Leskov [1] has reviewed and carried out a comprehensive analysis of thermo-electrical processes in welding arcs for both non-consumable and consumable electrodes. He suggested a simplified channel model of arc with separate anode, arc column and cathode regions. Based on the analysis of thermal balance in the electrode-sheath areas, formulas were derived for effective voltage drops in anode, cathode and arc column. Leskov has pointed out in 1970 that more deep and detailed analysis of arc phenomena will be possible with computer modelling when the computer power will increase.

Sudnik [2] has considered thermo-electrical processes in the whole circuit for the case of equilibrium between the mean wire feed rate and the melting rate in a normal process with constant voltage. The voltage drop in the wire extension and the ohmic heating were taken into account, without consideration of heat conduction in the wire. The current was calculated from equality between the thermal energy released in the wire and in the anode layer, and the experimentally determined droplet enthalpy. The process in pure  $\text{CO}_2$  and in mixtures with argon was considered. The ther-

mal process efficiency was defined by relation of sum of cathode and anode voltage drops to the total voltage drop in arc, including the arc column. This heat source model was used for modelling of weld formation in butt joint in a steady-state formulation with fast moving heat source. This model was extended later for pulse  $U/I$  modulation process [3] and MIG welding of aluminium [4].

Zhu [5] has developed a dynamic model which combines three components, each simulating an aspect of the process: system electrical circuit, consumable anode and welding arc. He performed a process simulation by unification of these sub-models in a coupled loop. The sum of voltages at the anode and cathode was assumed to be constant and equal to 15 V. The arc voltage was calculated from the simulations with the arc model of Lowke et al. [6] for TIG arc. 1D heat conduction equation was solved in the wire to determine the temperature and voltage distribution, with account for translational advective term, ohmic heating and anode heat flux. The anode heat flux was expressed through the convective flux from the plasma, work function and kinetic energy of electrons. Thus the heat flux at the anode and the anode voltage drop was considered to be independent of each other. Zhu applied the model for a non-pulse process and has shown a good agreement with experiments.

There is no commonly accepted interpretation of the anode voltage drop for welding arcs. Tanaka and Ushio [7] have theoretically analysed the anode processes for a TIG arc with account for the ambipolar diffusion. They have shown that the voltage drop in the anode layer can be either positive (for high currents) or negative (for low currents). Leskov [1] and

Sudnik [2] consider the anode voltage drop  $U_a$  as a Volt-equivalent of the Joule-heating at the anode, without additional detailed elaboration about its distribution across the anode layer etc.

A rigorous analytical analysis of temperature and voltage distribution along the wire extension in continuous and pulse GTAW has been presented by Karshin et al. [8]. The authors considered the heating at the contact tube-wire surface due to contact resistance, Joule (ohmic) heating by the transiting current, 1D heat diffusion and advection along the wire axis, and heating by the liquid-solid interface at the molten electrode end. The anode heat flux and consequently the temperature of the molten droplet were not considered. Besides, the length of the wire extension was assumed to be constant with time. Thus, the model gives detailed information about the temperature and voltage distribution in the wire, but does not allow for the analysis of the total circuit and the process dynamics, including the process energy characteristics and arc length.

Several comprehensive numerical models of droplet dynamics in GMAW with the application of computational fluid dynamics have been presented recently, for example in [9–11]. The space resolved numerical models provide a deep inside information about the fluid motion, temperature distribution, shape dynamics and droplet detachment and, without any doubt, will become linked to the real process conditions in a near future. However, we found no publication yet, where such models are closely involved in the analysis of the whole process circuit equipment–wire–arc–workpiece.

In this paper we present a dynamic thermo-electric-mechanical model of the whole process circuit which is based on the following fundamentals: description of the voltage drops at anode, cathode and arc column based on ideas of arc channel model of Leskov [1]; consideration of the anode voltage drop as a Volt-equivalent of heat; a 2D axi-symmetric non-linear equation of heat diffusion with advection, ohmic and contact heating in the wire and droplet; a geometric 2D axi-symmetric model of the droplet shape and mechanical model of the droplet dynamic under influence of capillary, electromagnetic and gravitational forces; supplementation of the physical modelling with the regulation algorithms of modern digital power sources.

### Description of the model

**Governing equations of electrical and thermal phenomena.** Instant electric power in the circuit of a welding arc can be represented by the product of current on the sum of voltage drops in different sections this circuit. If we consider the power source with its controlling algorithms as a «black box», then the power on the circuit section between the clips of the source will be written as follows:

$$P(t) = I(t)U_{\text{source}}(t) \quad (1)$$

with

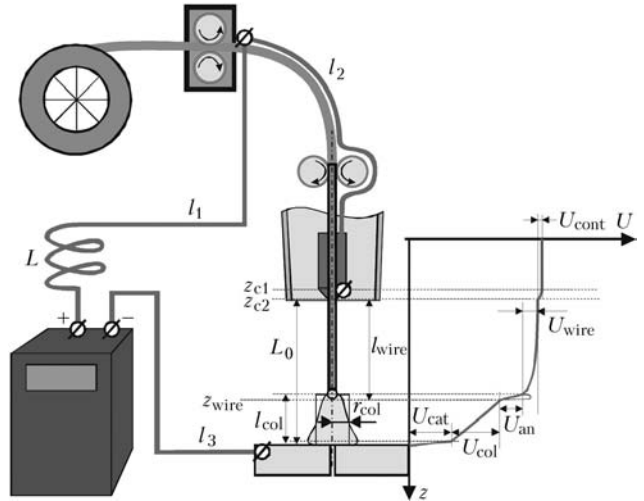


Figure 1. GMAW process diagram (for designations see the text)

$$U_{\text{source}}(t) = U_{\text{cable}}(t) + U_{\text{cont}}(t) + U_{\text{wire}}(t) + U_{\text{an}}(t) + U_{\text{col}}(t) + U_{\text{cat}}(t) + L \frac{dI}{dt}, \quad (2)$$

where  $t$  is the time;  $I$  is the current;  $U_{\text{cable}}$ ,  $U_{\text{cont}}$ ,  $U_{\text{wire}}$ ,  $U_{\text{an}}$ ,  $U_{\text{col}}$ ,  $U_{\text{cat}}$  are the voltage drops in cables, contact tube, wire extension, anode layer, arc column and cathode layer, respectively;  $L$  is the inductance of the circuit (Figure 1). The wire extension is defined as the distance between the end of the wire feed nozzle and the end of electrode including droplet.

Voltage drop in cables is expressed as

$$U_{\text{cable}} = I\rho_c(T_0) \left( \frac{l_1}{S_1} + \frac{l_2}{S_2} + \frac{l_3}{S_3} \right), \quad (3)$$

where  $\rho_c(T_0)$  is the specific electric resistance of the cable material at room temperature;  $l_1$ ,  $l_2$  and  $l_3$  are the lengths of hose assembly, cable to wire feeder and cable to the workpiece, respectively;  $S_1$ ,  $S_2$  and  $S_3$  are their effective cross-section areas.

Voltage drop due to contact resistance between wire and contact nozzle is

$$U_{\text{cont}}(t) = I(t)R_{\text{cont}}(t, T_c), \quad (4)$$

where  $R_{\text{cont}}(t, T_c)$  is the contact resistance (defined empirically);  $T_c$  is the nozzle temperature.

Voltage drop in the wire extension is described by the integral

$$U_{\text{wire}} = \int_{z_{c2}}^{z_{\text{wire}}} j(t)\rho_w(\bar{T}(z))dz, \quad (5)$$

where  $\rho_w(\bar{T}(z))$  is the specific electric resistance of wire;  $\bar{T}(z)$  is the wire average temperature in the cross-sections with axial co-ordinate  $z$ ;  $z_{c2}$  is the bottom co-ordinate of the contact place;  $z_{\text{wire}}$  is the co-ordinate of the wire stick-out;  $j(t)$  is the current density.  $U_{\text{wire}}$  can be calculated if the temperature distribution along the wire extension is known.

The temperature distribution is found from the solution of the 2D axi-symmetric differential heat

transfer equation, taking into account translation (feeding) of the wire and ohmic heating by the transiting current:

$$\rho \left( \frac{\partial H(T)}{\partial t} + v_f \frac{\partial H(T)}{\partial z} \right) = \frac{\partial}{\partial z} \left( \lambda(T) \frac{\partial T}{\partial z} \right) + \frac{1}{r} \frac{\partial}{\partial r} \left( r \lambda(T) \frac{\partial T}{\partial r} \right) + j^2(t) \rho_w(T), \quad (6)$$

where  $\rho$  is the density;  $H$  is the enthalpy of wire material;  $v_f$  is the wire feed speed;  $\lambda(T)$  is the thermal conductivity.

The following boundary conditions are set at the wire boundaries:

$$-\lambda(T) \frac{\partial T}{\partial r} = \begin{cases} 0 & \text{(within the contact tube,} \\ & \text{except for the contact area)} \\ \frac{I^2(t) R_{\text{cont}}(t, T)}{S_{\text{cont}}} & , z_{c1} \leq z < z_{c2} \\ \alpha(T)(T - T_0) + \varepsilon(T) \sigma_0 (T^4 - T_0^4) & \text{(at the contact area)} \\ \alpha(T)(T - T_0) + \varepsilon(T) \sigma_0 (T^4 - T_0^4) & \text{(otherwise)} \end{cases} \quad (7)$$

where  $z_{c1}$  is the top co-ordinate of the contact place;  $\varepsilon$  is the emissivity;  $\alpha$  is the convection coefficient;  $S_{\text{cont}}$  is the effective contact area.

At the boundary between the droplet and anode layer, the normal heat flux is described by

$$-\lambda(T) \frac{\partial T}{\partial n} = j(t) U_{\text{an}}(t) - P_e(T), \quad (8)$$

where  $P_e$  is the power loss due to evaporation.

The evaporation is taken into account by limiting the droplet temperature to the boiling point. Thus, the fraction of the droplet enthalpy, which exceeds the enthalpy at the boiling point, is simply subtracted. The anode voltage drop  $U_{\text{an}}$  is considered here as the Volt-equivalent of the heat generated at the anode. The 2D consideration is required in order to take into account the distribution of heat flux at the droplet surface and the different radiuses of droplet and wire. For numerical solution of Eqs. (6)–(8) a finite difference scheme is used.

The description of anode, arc and cathode is based on the channel model of Leskov [1], similar to the works of Sudnik et al. [2–4]. Leskov's model distinguishes between anode and cathode layers and the arc column with an effective radius. According to this model, the energy of anode and cathode layers contributes to the heat exchange with the wire metal and the workpiece, respectively. The arc column loses its energy only by radiation from the outer surface.

According to Leskov [1], the effective voltage drop in the anode layer is described as

$$U_{\text{an}} = 6.8 \cdot 10^4 \frac{\bar{T}_a^{1/5} \Delta T^{3/5} I^{2/15} g_e^{7/15}}{U_i^{19/15} a^{4/15} g^{3/5} m}, \quad (9)$$

where  $\bar{T}_a$  is the mean temperature in the anode layer;  $\Delta T$  is the temperature difference between the arc co-

lumn and the anode layer;  $g_e$  and  $g$  is the effective cross-sections of collisions of atoms with electrons and with each other, respectively;  $U_i$  is the ionisation potential of anode vapour;  $a = 2(g_i/g)$  with  $g_i$  being the effective cross-section of ion collisions;  $m$  is the atomic weight of anode vapour.

Thus, for the heat balance of wire-droplet we can calculate inflow of heat from the anode layer, heat flow due to thermal conduction and ohmic heating in the wire (6) and evaporative heat loss from the droplet surface. From this balance, dynamic values of the enthalpy and dynamically average temperature of the droplet is calculated.

The voltage drop in arc column is presented by

$$U_{\text{col}} = E_{\text{ef}} l_{\text{col}}, \quad (10)$$

where  $E_{\text{ef}}$  is the effective electric field intensity;  $l_{\text{col}}$  is the arc column length.

$$E_{\text{ef}} = 4.2 \cdot 10^7 \frac{U_{\text{ef}}^{29/12} p^{1/6} g_e^{1/3} \beta^{2/3}}{a^{1/3} I^{1/3}}, \quad (11)$$

where  $U_{\text{ef}}$  is the effective ionization potential;  $p$  is the arc column pressure;  $\beta$  is the arc plasma emissivity.  $U_{\text{ef}}$  is defined after Saha ionization equation, assuming a local thermodynamic equilibrium:

$$U_{\text{ef}} = \frac{T}{5800} \ln \sum_{i=1}^k \left( \frac{n_i}{n} \right)^{1/2} \exp \left( - \frac{5800 U_i}{T} \right), \quad (12)$$

where  $n_i/n$  is the concentration fraction of each plasma constituent;  $T$  is the mean temperature of plasma column.

The column length  $l_{\text{col}}$  is defined by difference between the given contact nozzle distance and the momentary wire extension  $l_w$ . The latter is defined by the wire feed rate and the amount of metal leaving the electrode with droplets  $m_{\text{dr}}$  and with vapour  $m_{\text{vap}}$ :

$$l_w(t) = l_{w0} + v_f t - \frac{\rho(T)}{\pi r_w^2} (m_{\text{dr}}(t) + m_{\text{vap}}(t)); \quad (13)$$

$$L_{\text{col}}(t) = L_0 - l_w(t),$$

where  $l_{w0}$  is the initial wire extension;  $L_0$  is the contact nozzle distance;  $r_w$  is the wire radius.

Effective voltage drop in the cathode layer is described by

$$U_{\text{cat}} = U_{c0} + a I^b, \quad (14)$$

where  $U_{c0}$ ,  $a$  and  $b$  are the empirical coefficients, which depend on cathode material.

In case of a process with preset current values (for instance, pulsed  $I/I$ -modulation), the current is given by the power source, so we can calculate the voltage drops and powers at each chain of the circuit, according to the above equations. For non-pulse process with given total voltage  $U_{\text{source}}$  and for the peak phase of pulsed process with  $U/I$ -modulation, the current is calculated from the formulas:

$$dU_{\text{source}}(t) = U_{\text{source}}(t) - (U_{\text{cable}}(t-dt) + U_{\text{cont}}(t-dt) + U_{\text{wire}}(t-dt) + U_{\text{an}}(t-dt) + U_{\text{co}}(t-dt) + U_{\text{cat}}(t-dt)); \quad (15)$$

$$dI(t) = \frac{dU_{\text{source}}(t)}{L} dt, \quad (16)$$

where  $(t - dt)$  is the previous time step in an incremental procedure.

The system of Eqs. (1)–(16) describes the dynamics of the welding circuit and the electrode extension, including the critical cases of short circuit and «burning-out» to the contact nozzle.

#### Sub-model of droplet formation and detachment.

An important chain of the total model is the sub-model of droplet formation and detachment, since it determines the droplet temperature and mass. Thus, it regulates the mass and energy balance in the total model.

Droplet formation and detachment is modelled on the basis of following assumptions and considerations. The droplet shape is considered to be an axi-symmetric body, consisting of two parts, a hemisphere and a conic frustum which bounds with solid metal of the electrode wire as shown in Figure 2. One of diameters of the conic frustum is equal to the wire diameter, while the second is equal to the diameter of the hemisphere. The height of the conic frustum  $h$  is equal to the radius of the hemisphere  $r_d$ . The total volume of the hemisphere and the conic frustum is equal to the volume of molten metal on the end of the electrode.

The integral balance of forces  $F$  acting on the droplet consists of the surface-tension force  $F_s$ , the electromagnetic force  $F_e$ , and the gravitational force  $F_g$ :

$$F = F_s + F_e + F_g. \quad (17)$$

The response force of evaporating metal is not considered, since its calculation requires a complex modelling of temperature at the anode and the interaction with the arc plasma.

The capillary force due to the surface tension, which reacts against the droplet detachment, is calculated from the Laplace pressure:

$$F_s = \frac{2\sigma}{r_d} \pi r_w^2, \quad (18)$$

where  $\sigma$  is the surface tension;  $r_d$  is the radius of the hemisphere (droplet radius).

The electromagnetic force is expressed [1] by

$$F_e = \frac{\mu I^2}{4\pi} \ln \frac{r_c}{r_w}, \quad (19)$$

where  $\mu$  is the magnetic permeability of molten metal;  $r_c$  is the radius of the arc column near the anode. The arc column radius is calculated with assumption of a uniform current distribution in the arc column cross-section adjoining the droplet [1]:

$$r_c = \frac{I^{2/3} g_e^{1/3}}{(5.5 \cdot 10^{-8} \pi)^{1/2} U_1^{19/12} a^{1/3}}. \quad (20)$$

If the resulting force  $F$  is directed opposite to the wire feed speed, it is compensated by the reacting force from the solid wire, thus no droplet movement is considered. Otherwise, i.e. if  $F > 0$ , the spherical droplet of radius  $r_d$  obtains acceleration and starts to move. Thereafter, the droplet movement is considered in a simple mechanical approximation, which is not related to the wire melting. Thus, the real processes taking place at the droplet detachment are not considered in details. Instead, the mass and volume of the droplet are fixed, while the acceleration determines the droplet velocity and the way, which the droplet passes. The resulting force is still considered to be dependent on current, according to Eqs. (19) and (20). If the droplet centre passes the way which is equal to its radius  $r_d$ , the droplet is supposed to detach from the wire. If the droplet was not yet detached, but the acting force has changed its direction due to changing the current in a pulsed process ((19), (20)), the droplet may slow down and even come back to the initial position, with account for the inertia.

A differential consideration of the droplet detachment demands more detailed description of the processes in the anode layer and is planned to be realised in the future.

#### Process modulation modes and their features.

There are three different types of process, which must be considered with different approaches: normal process, pulse process with  $U/I$ -modulation and pulse process with  $I/I$ -modulation. In normal process, the voltage is kept constant and the current results from the physics of the wire heating and melting, arc phenomena, droplet detachment and circuit inductance. In pulse process with the  $U/I$ -modulation, the voltage in the pulse period  $U_p$  is assigned and the current in the base period  $I_b$  is kept constant. In the pulse process with the  $I/I$ -modulation, both currents in the pulse  $I_p$  and in the base  $I_b$  period are controlled. One of the advantages of pulse processes is the better control of the material transfer. The pulses can have

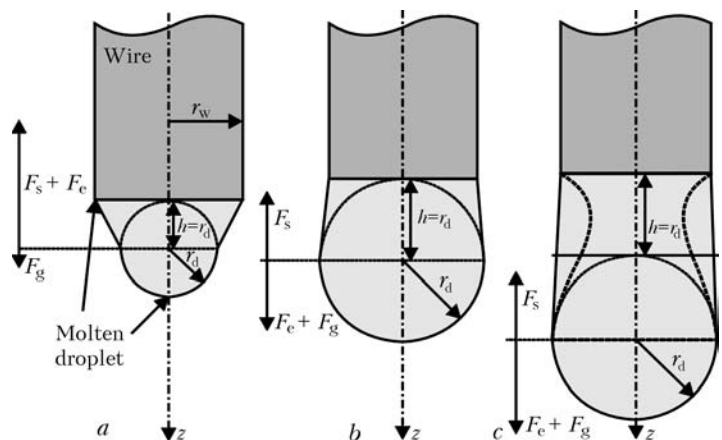


Figure 2. Geometrical approximation of droplet and forces at the end of melting wire: a – initial stage; b – intermediate stage; c – droplet detachment condition

either simple or more complex shapes in order to improve the process stability and the material transfer.

*I/I-modulation.* In case of *I/I*-modulation, the model equations, which describe the voltage drops in contact place, in anode layer, in arc and in cathode layer ((4), (9)–(12), (14)) are solved explicitly, since the current is known.  $U_{wire}$  is solved from the thermal wire model ((5–8)).

At the *I/I*-modulation for a given wire feed speed, there exists a narrow process parameter window, in which a self-regulation of the free wire extension length takes place. This window depends also on wire diameter and on specific resistance of the wire material  $\rho_w(T)$ . In general case, an external regulator is required, which controls the arc power by changing the pulse characteristics and/or frequency. The algorithms of external regulators permanently modify the pulse parameters in order to keep the arc length constant. Thus, they must be also considered when ap-

plying the model for simulation of welding processes with the particular power sources.

*U/I-modulation.* The *U/I*-modulation has a wider self-regulation window, since the given voltage in the peak phase regulates the arc length automatically. An additional regulation is required only for short circuits. When, however, the process parameter set lies outside of the self-regulation for a given wire feed speed, the model reproduces either permanent short circuits or «burn-out» of the electrode to the contact nozzle.

*Non-pulse process.* At normal process, the voltage  $U_{source}$  is set and the instantaneous current is calculated from Eqs. (15, 16).

**Process power.** In all cases, the mean integral electric power  $\bar{P}_{el}$  which is released between the welding torch and the workpiece during an interval between  $t_1$  and  $t_2$ , can be expressed from the given or calculated currents and voltages:

$$\bar{P}_{el} = \frac{1}{t_2 - t_1} \int_{t_1}^{t_2} \times \quad (21)$$

$$\times [U_{wire}(t) + U_{an}(t) + U_{cat}(t) + U_{co}(t)]I(t)dt.$$

The thermal power which represents the heat source acting on the workpiece is expressed taking into account the heat losses due to evaporation and heat losses from the arc column:

$$\bar{P}_{HS} = \frac{1}{t_2 - t_1} \times \quad (22)$$

$$\times \left[ \sum_{n=1}^N H(T)_n m_n + \int_{t_1}^{t_2} [U_{cat}(t) + \eta U_{co}(t)]I(t)dt \right],$$

where  $N$  is the number of droplets detached between  $t_1$  and  $t_2$ ;  $H(T)$  is the droplet enthalpy;  $m$  is the droplet mass;  $\eta$  is the thermal efficiency of the arc column, which depends on the joint preparation geometry and arc length.

The calculated powers in wire, at the anode, at the cathode and in the arc column are used in the model of heat transfer and weld formation as described elsewhere [12, 13].

**Computer code Arc-Solver**

The model described above has been implemented in computer code Arc-Solver which is a part of software package SimWeld [12, 13]. Supplemented with a simple user interface, databases of material properties and controlling and regulation algorithms of power sources, it becomes a suitable tool for process study. Besides, SimWeld uses the heat and arc pressure distributions calculated by Arc-Solver as boundary conditions when simulating the temperature distribution in the workpiece and the weld bead formation.

Figure 3, *a* shows a screenshot of Arc-Solver with the equipments specification (left), dynamic graphical representation of the torch-wire-droplet (middle), currently simulated wave shapes of current (lower graph) and voltage (upper graph) and integral

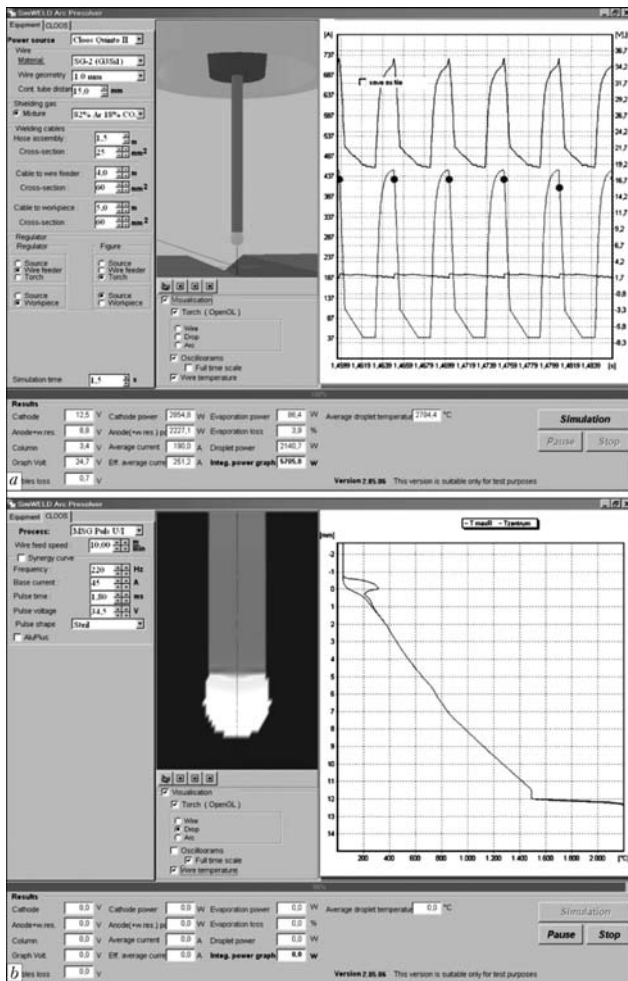


**Figure 3.** Module Arc-Solver in the stand-alone mode: *a* – example of simulation of pulse characteristics with use of power source Cloos Quinto II for *U/I*-modulation (the pre-set by the power source current in base and voltage in peak periods and the calculated arc length, base voltage and pulse current are shown on the graphs; the droplet detachment is indicated with circles at the current curve; in the result window the integrated mean parameters are presented for cathode power of 2854.8 W, droplet power of 2140.7 W, mean current of 190 A, mean-square current of 251.2 A, mean voltage of 24.7 V); *b* – process parameters, temperature distribution in wire and droplet and temperature profiles along the wire extension

results for mean electrical and thermal characteristics (bottom).

The pulse parameters for  $U/I$ -modulation and power source CLOOS Quinto II are shown in Figure 3, *b* (left). In the middle of the screenshot, the temperature map in the wire and droplet is presented. The graphs show the axial temperature distribution along the wire centre and outer wire surface. The temperature peak at the surface near the contact nozzle is caused by the contact heating.

#### Analysis of processes and discussion

**Voltage and current pulse shapes.** Figure 4 shows comparison between simulated and experimental voltage and current waves during pulsed process with  $U/I$  modulation. Simulated voltage and current are in a close agreement with the experimental data. The peak voltage in Figure 4, *a* reaches 35 V, while the set peak voltage of the process was 36 V. The 1 V was lost in cables, because the measurements were carried out at the torch. For the verification in a wide range of process parameter sets, a series of experiments were conducted, the results of which are presented in Figures 5–7.

**Mean pulse frequency for  $I/I$ -modulation.** The simulated versus experimental mean pulse frequency for welding with power source CLOOS Quinto II in  $I/I$ -modulation is presented in Figure 5. A good correlation between both frequencies was obtained, after implementation of regulation algorithm of the power source into the model. As was already mentioned, there exist no mechanism of arc length self-regulation for  $I/I$ -modulation mode. The power source analyses the pulse voltage and permanently changes the pulse frequency in order to stabilize the mean voltage and consequently the arc length. Variations of pulse shape would influence the droplet detachment and thus the process stability. Therefore, the regulation in CLOOS Quinto II is realized by changing the pulse frequency, by so-called pulse-frequency modulation.

**Mean voltage, current and power for  $U/I$ -modulation.** *Influence of wire feed rate.* Figure 6 shows comparison of mean values of voltage (measured on the torch), current, mean-square current and power obtained in experiments and in simulations for pulse  $U/I$ -modulation mode as functions of wire feed rate. The latter was varied from 3 to 13 m/min. The pulse parameters were set in accordance of the synergy curves of the power source. All monitored mean values increase with increasing wire feed rate. The simulation results reproduce the absolute values and the tendency of changes very good.

*Influence of distance from contact nozzle to work-piece surface.* The next experimental series has been conducted with the aim to investigate the influence of spacing between the wire feed nozzle and the work-piece (cathode) on the mean voltage, current, mean-square current and power. Welding was performed in  $U/I$ -modulation mode, and the wire feed rate of 8 m/min, pulse shape and frequency were kept constant. The variation of contact nozzle distance from

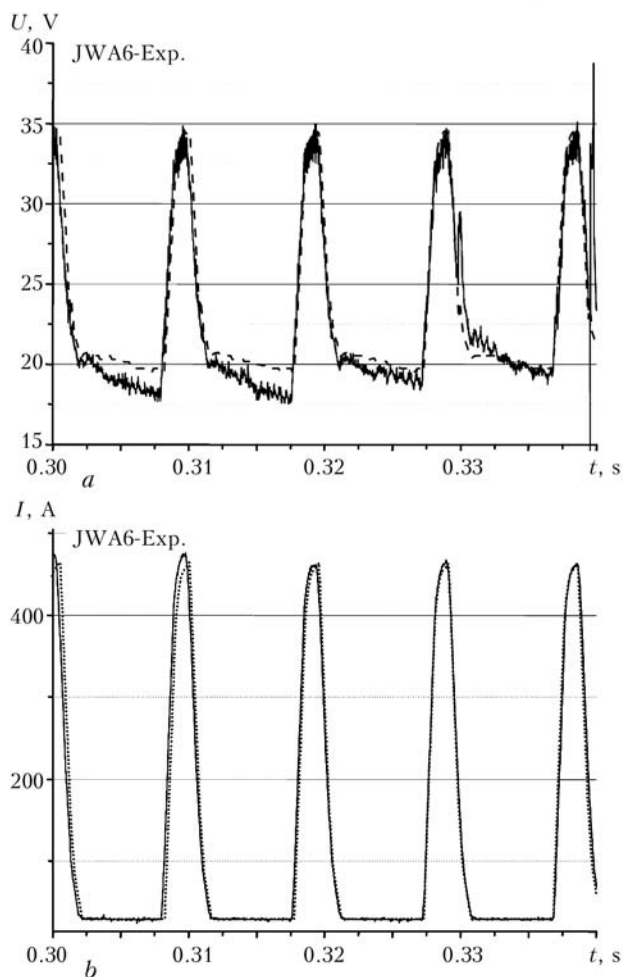


**Figure 4.** Experimental (solid curves) and simulated (dashed) oscillograms of voltage (*a*) and current (*b*) for welding with power source CLOOS Quinto II in  $U/I$ -modulation mode at base current  $I_b = 30$  A, pulse voltage  $U_p = 36$  V, pulse duration  $t_p = 1.8$  ms, frequency  $f = 108$  Hz, using pulse shape according to CLOOS Quinto II definition «very flat», wire G2Si1 with diameter  $d_w = 1$  mm, wire feed speed  $v_f = 6$  m/min, contact tube distance of 15 mm, in Corgon18 ( $\text{CO}_2 + 82\% \text{ Ar}$ ) shielding gas

10 to 18 mm results in decrease of mean currents (Figure 7, *b*) and power (Figure 7, *c*) and to a small increase of mean voltage (Figure 7, *a*). The electric

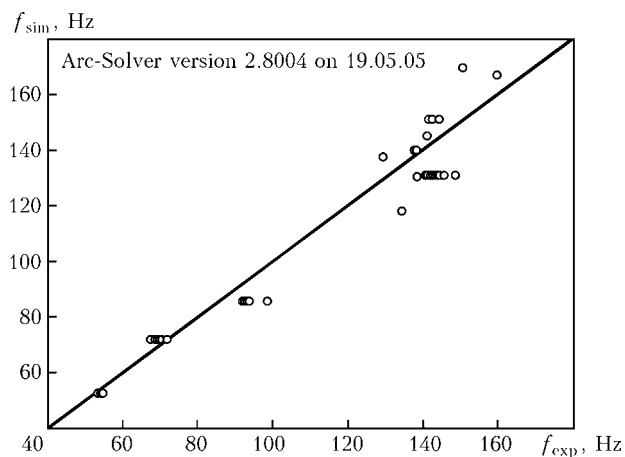


**Figure 5.** Experimental (solid curve) and simulated (O) frequency for welding with power source CLOOS Quinto II in  $I/I$ -modulation mode using wire G2Si1 with  $d_w = 1$  mm at  $v_f = 3$ –14 m/min, contact tube distance of 15 mm, Corgon18 ( $\text{CO}_2 + 82\% \text{ Ar}$ ) shielding gas

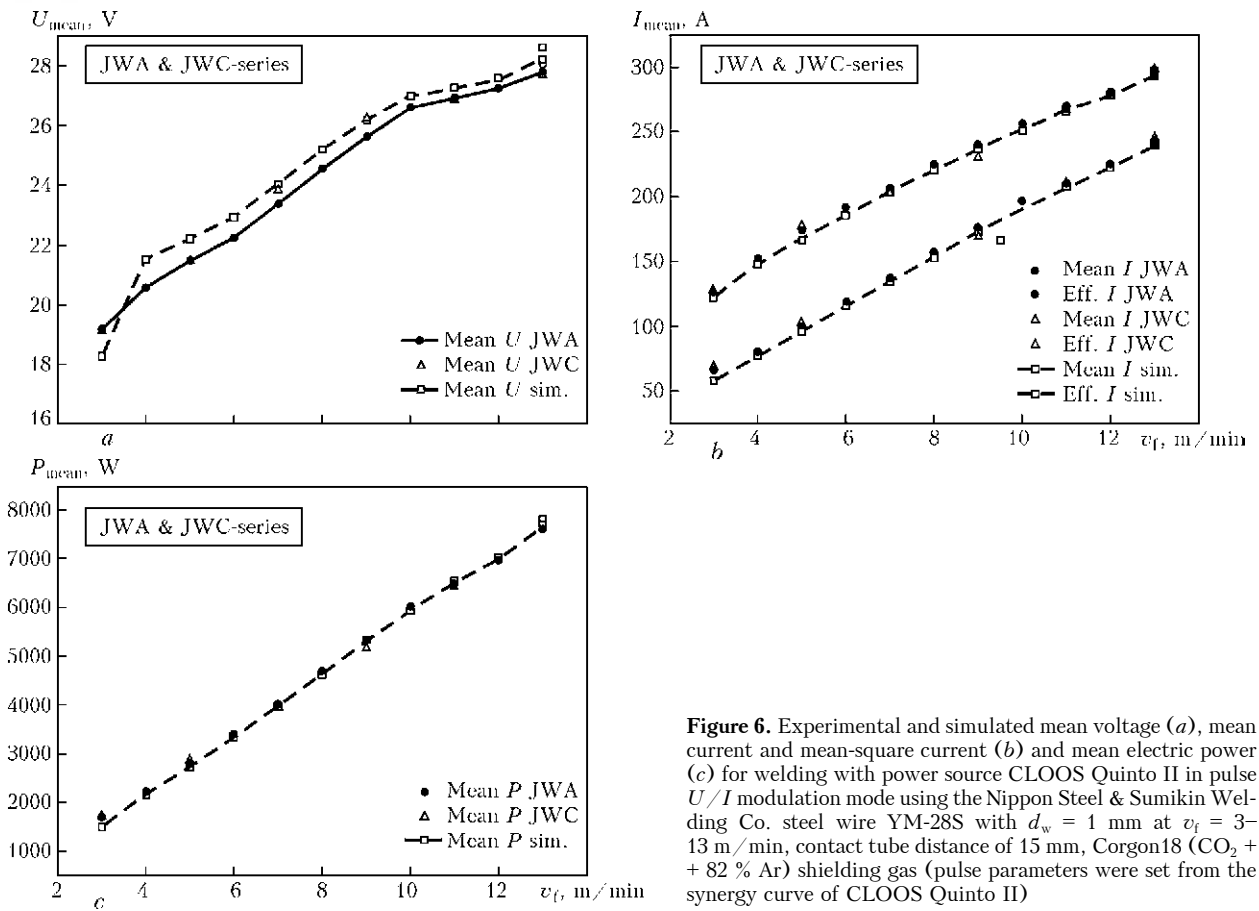


**Figure 6.** Experimental and simulated mean voltage (a), mean current and mean-square current (b) and mean electric power (c) for welding with power source CLOOS Quinto II in pulse  $U/I$  modulation mode using the Nippon Steel & Sumikin Welding Co. steel wire YM-28S with  $d_w = 1$  mm at  $v_t = 3$ – $13$  m/min, contact tube distance of 15 mm, Corgon18 ( $CO_2 + 82\%$  Ar) shielding gas (pulse parameters were set from the synergy curve of CLOOS Quinto II)

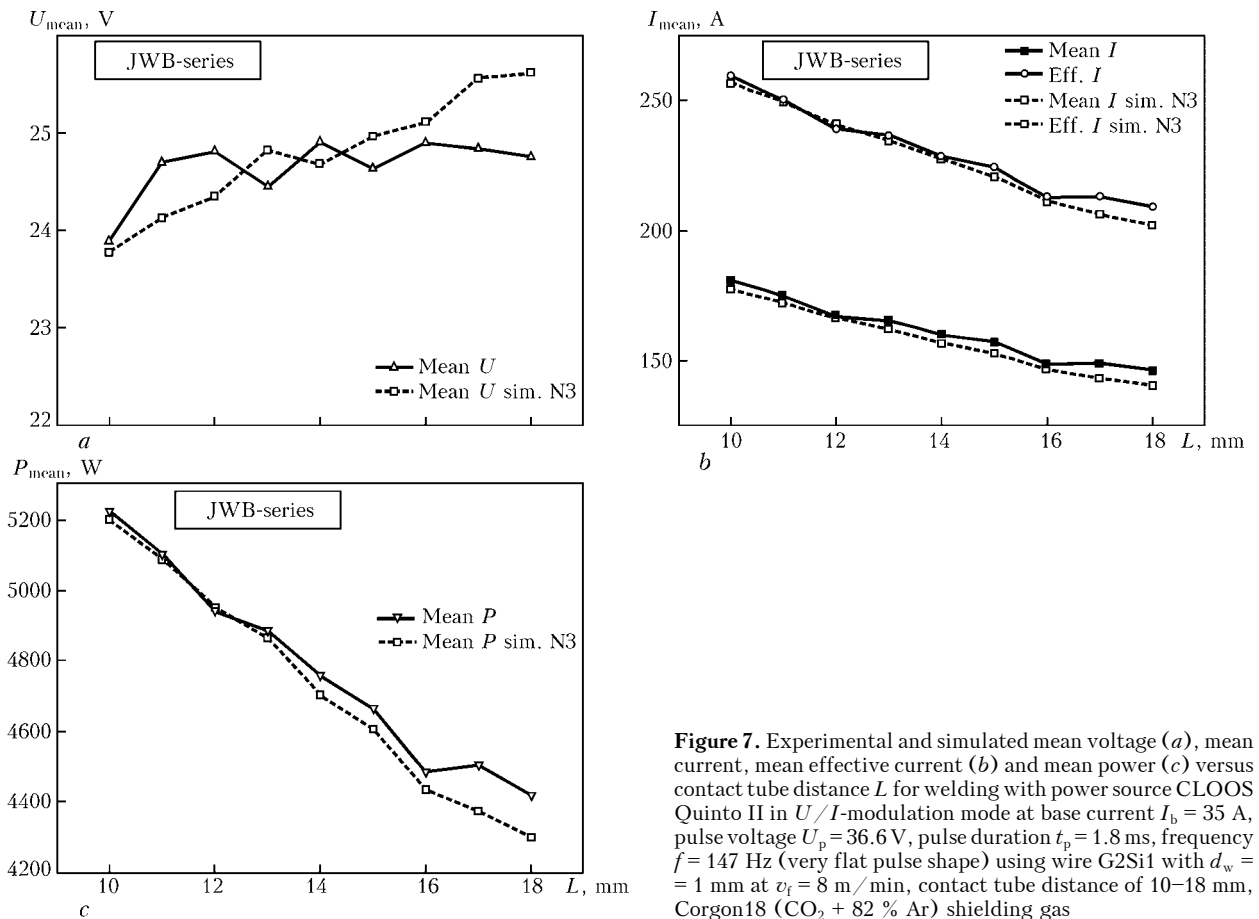


**Figure 7.** Experimental and simulated mean voltage (a), mean current, mean effective current (b) and mean power (c) versus contact tube distance  $L$  for welding with power source CLOOS Quinto II in  $U/I$ -modulation mode at base current  $I_b = 35$  A, pulse voltage  $U_p = 36.6$  V, pulse duration  $t_p = 1.8$  ms, frequency  $f = 147$  Hz (very flat pulse shape) using wire G2Si1 with  $d_w = 1$  mm at  $v_t = 8$  m/min, contact tube distance of 10–18 mm, Corgon18 ( $CO_2 + 82\%$  Ar) shielding gas



power on the torch has decreased from ~5200 to ~4400 kW, i.e. on ~23 %. It demonstrates that the contact nozzle distance is an important technological parameter, which influences the energy input. It is worth to point out that, as far as we know, the synergy data of power sources do not take this parameter into account, i.e. they are usually obtained for a fixed contact distance. The modelling reproduces the experimental tendencies, the deviations of absolute values being within 3 % of tolerance, which is almost perfect result taking into account the measurement errors.

## CONCLUSIONS

The model described by the system of equations (1)–(16) has been developed as a non-stationary realization of the Leskov's arc channel model which is complemented with a heat transfer model of the electrode wire. In order to apply the model for the simulation of welding processes in different modulation modes and using modern welding equipment, the computer code also integrates the models of the power sources. An adequate representation of the process dynamics with the use of a particular digital power source is only possible with involving of its controlling algorithms. This requires a close cooperation with the power source manufactures.

The presented comparisons of simulation examples with the experiments demonstrate that the developed computer code based on the model can simulate the welding processes with real equipment and to calculate the process power. The program represents a tool for a fast finding of stable process parameter sets and even generating of synergic curves in a wide wire feed rate range. At the same time, the program represents a framework for investigation and improvement of the models of individual physical phenomena. Separate model units can be modified, refined or modified relatively independently of each other.

**Acknowledgments.** *This work was carried out within the SIMPRO-Project, financed by Federal Ministry of Education and Research (bmb + f), Germany) and the companies DaimlerChrysler AG,*

*CLOOS Schweissttechnik, Fronius International GmbH, BoehlerThyssen Welding and Linde AG. Authors wish to record their grateful acknowledgement for this funding. Our thanks are also expressed to company CLOOS Innovations GmbH for providing the power source and its regulation algorithms, and for company OTC Daihen Corp. for providing the welding wires.*

1. Leskov, G.I. (1970) *Electric welding arc*. Moscow: Mashinostroenie.
2. Sudnik, V. (1997) Modelling of the MAG process for pre-welding planning. In: *Mathematical modelling of weld phenomena 3*. London: Inst. of Materials, p. 791–816.
3. Sudnik, W., Iwanow, A., Mokrov, O. et al. (2001) Simulation des MAG-Schweissens. In: *Moderne Trends beim MAG-Schweissen*. Graz: Graz, TU, p. 85–102.
4. Sudnik, W., Rybakow, A., Radaj, D. et al. (2001) Simulation of pulsed MIG-welding of aluminium alloys. In: *Proc. of 7th Int. Aachen Welding Conf. on High Productivity Joining Processes: Fundamentals, Applications, Equipment*. Ed. by U. Dilthey. Aachen: Shaker, p. 431–446.
5. Zhu, P. (1999) Computer simulation of gas metal welding arcs. In: *Proc. of 5th Int. Conf. on Trends in Welding Research* (Pine Mountain, USA, June 1–5, 1998). Ed. by J.M. Vitek et al. ASM Int., p. 283–288.
6. Lowke, J.J., Kovitya, P., Schmidt, H.P. (1992) Theory of free-burning arc columns including the influence of the cathode. *J. Phys. D: Appl. Phys.*, **25**, p. 1600–1606.
7. Tanaka, M., Ushio, M. (1999) Plasma temperature of anode boundary layer in gas-tungsten-arc and its modelling. In: *Proc. of 5th Int. Conf. on Trends in Welding Research* (Pine Mountain, USA, June 1–5, 1998). Ed. by J.M. Vitek et al. ASM Int., p. 388–393.
8. Karkhin, V.A., Fedotov, B.V., Babkin, I.N. et al. (2002) Analysis of temperature and voltage drop distributions in the wire extension in continuous and pulsed arc welding. In: *Mathematical modelling of weld phenomena 6*. Ed. by H. Cerjak and H.K.D.H. Bhadeshia. London: Inst. of Materials, p. 121–141.
9. Fan, H.G., Kovacevic, R. (1999) Droplet formation, detachment, and impingement on the molten pool in gas metal arc welding. *Metal. Mater. Transact. B*, **30**, p. 791–801.
10. Wang, G., Huang, P.G., Zhang, Y.M. (2003) Numerical analysis of metal transfer in gas metal arc welding. *Ibid.*, **34**, p. 345–353.
11. (2004) <http://www.choparc.de/haupt.html>
12. Dilthey, U., Pavlyk, V., Mokrov, O. et al. (2005) Software package SimWeld for simulation of gas-metal-arc-welding processes of steels and aluminium alloys. In: *Mathematical modelling of weld phenomena 7*. Ed. by H. Cerjak, H.K.D.H. Bhadeshia, E. Kozeschnik. Graz: Graz TU, p. 1057–1079.
13. Dilthey, U., Mokrov, O., Pavlyk, V. (2005) Modelling of consumable electrode gas-shielded multi-pass welding of carbon steel with preheating. *The Paton Welding J.*, **4**, p. 2–6.

# ROLE OF QUASI-KEYHOLE AND MARANGONI CONVECTION IN FORMATION OF DEEP PENETRATION IN A-TIG WELDING OF STAINLESS STEEL (Phenomenological model of A-TIG process)

B.E. PATON, K.A. YUSHCHENKO, D.V. KOVALENKO, I.V. KRIVTSUN, V.F. DEMCHENKO,  
I.V. KOVALENKO and A.B. LESNOJ  
E.O. Paton Electric Welding Institute, NASU, Kiev, Ukraine

Peculiarities of thermal, mass exchange, electromagnetic and hydro (gas) dynamic processes occurring in the arc column and weld pool in A-TIG welding are considered on the basis of analysis of available experimental and theoretical data. It is shown that factors leading to increase in the penetrating capacity of A-TIG welding include formation of the quasi-keyhole, concentration-capillary Marangoni convection and intensification of the downward flow of the melt to the bottom of the weld pool caused by increase in the centripetal component of Lorentz force.

A-TIG welding is a modification of TIG welding. It is characterised by the fact that welding is performed with a surface arc over a layer of activating flux deposited on the surface of a workpiece in a layer 5–20 mm wide and 10–100  $\mu\text{m}$  thick. Such an insignificant, on the face of it, modification of TIG welding leads, at the same time, to striking changes in shape of the weld, which show up as decrease in the weld width and substantial increase in the penetration depth (more than 3 times), compared with conventional TIG welding. Within a certain range of thicknesses of workpieces, A-TIG welding can serve as a very simple alternative to TIG welding, as well as to plasma, laser and electron beam welding. The A-TIG process allows square-groove welding of different metals in one pass using no filler wire, e.g. butt joints in steels of small and medium thickness (from 1 to 12 mm) can be made by one-sided welding, butt joints in steels from 6 to 25 mm thick can be made by two-sided welding, and root welds can be made by welding in groove with increased root face (4–6 mm). Furthermore, A-TIG welding provides welds of the consistent size and quality on steels of the same grades independently of cast to cast variations, and allows deformation and shrinkage of welded joints to be decreased [1–4].

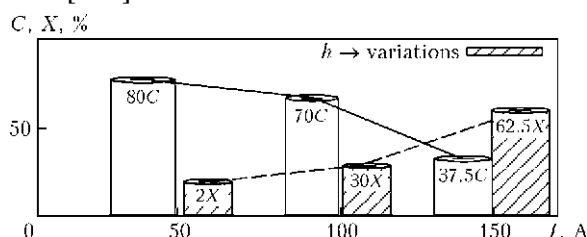


**Figure 1.** Comparative analysis of distribution of balance of the impact by different components ( $C$  – contraction;  $X$  – total of others) of TIG and A-TIG welding processes at the identical reduced thermodynamic effect of arc current  $I$  on penetration depth  $h$  of stainless steel 304H 7 mm thick

To further develop the technology for welding over the layer of activating flux, it is necessary to give a physical interpretation of the phenomenon of the increased penetrating capacity of the A-TIG welding process. Different hypotheses have been put forward recently concerning causes and mechanisms of an increased penetration depth in A-TIG welding, compared with the TIG process. The hypotheses offered include:

- change in character and structure of hydrodynamic flows in the weld pool caused by a change in direction of the Marangoni flow [5, 6], and growth of the role of ponderomotive (Lorentz) forces in formation of the flow of molten metal [7, 8];
- contraction of the arc due to electronegative elements present in an activating flux and associated increase in the concentration of the thermal effect of the arc on the weld pool surface [2, 9–11].

These hypotheses require a deeper and more detailed investigation, especially in view of emergence of the new experimental data [12, 13] on formation of the quasi-keyhole in A-TIG welding.

As shown by our earlier studies [14] of TIG and A-TIG welding of stainless steel 304H (using aerosol oxide activator PATIG S-A), increase in the arc current is accompanied by re-distribution of the effect of mechanisms of deep penetration (the first and second hypotheses) on the penetrating capacity of A-TIG welding. In particular, contraction of the arc turns out to be the most important factor in welding at low (100 A and below) currents. As the current is increased from 100 to 150 A, the effect of the arc contraction on the penetration depth and weld formation is mitigated more than twice in the total balance of mechanisms causing deep penetration in A-TIG welding (Figure 1).

The paper gives comparative analysis of experimental data on configuration of the weld pool in TIG

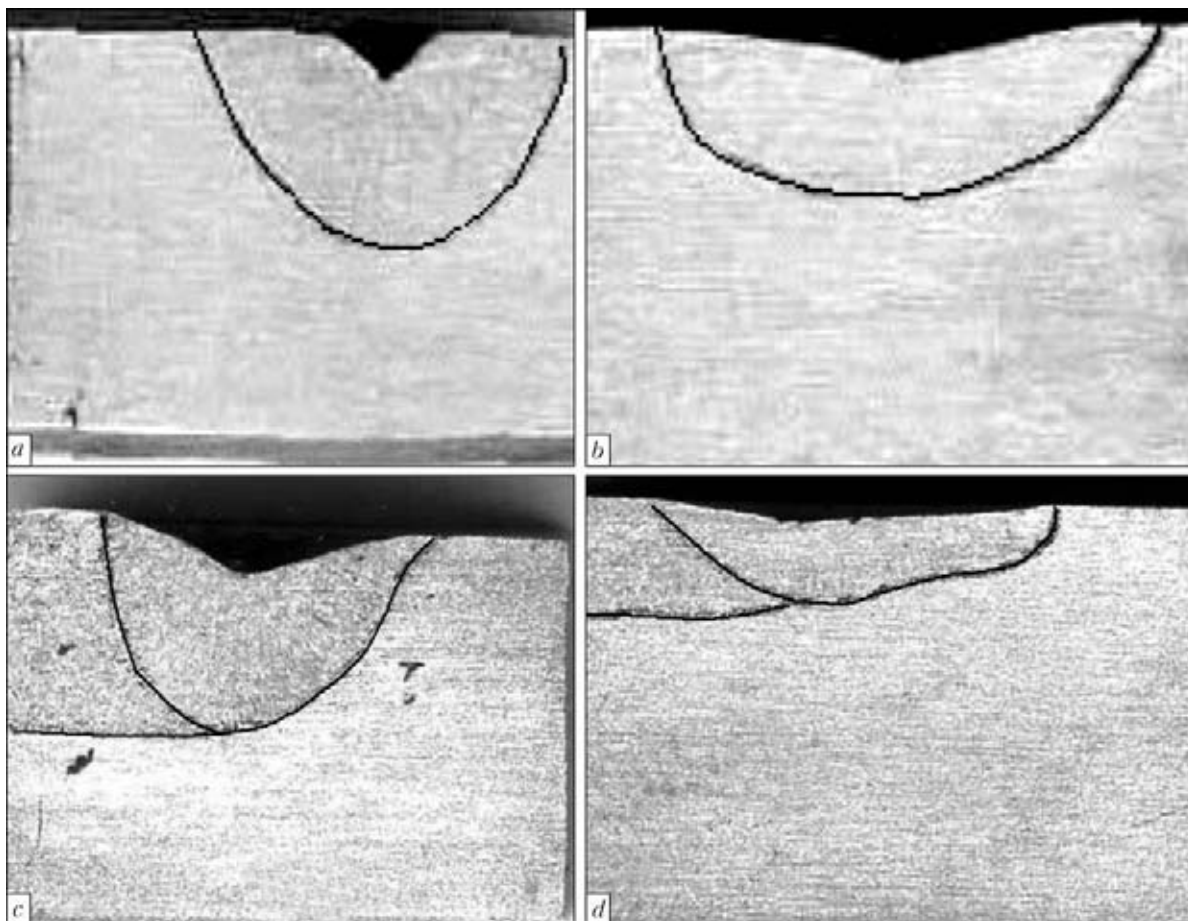


**Figure 2.** Configuration of the weld pool in transverse (*a, b*) and longitudinal (*c, d*) sections of solidified weld pools in TIG (*a, c*) and A-TIG (*b, d*) welding at  $I = 150$  A using  $\text{TiO}_2$  activator deposited on the steel 304H surface in a layer 5 mm width and 50  $\mu\text{m}$  thick (for the rest parameters see the text)

and A-TIG welding of stainless steel 304H with incomplete penetration, and analyses of different physical factors, which are capable of intensifying the processes of heat transfer from the anode region towards the weld pool bottom, occurring in A-TIG welding, thus providing an increased penetration depth.

**Formation of quasi-keyhole.** Consider results of experimental studies of configurations of the weld pools in TIG and A-TIG welding. The experiments were conducted on stainless steel 304H (0.006 % S, 0.006 % O) plates measuring  $150 \times 50 \times 9$  mm. A controlled uniform activator layer 5 mm wide and 20  $\mu\text{m}$  thick was deposited on the plate surface prior to A-TIG welding. Thickness of the activator layer was controlled using the special thickness gauge TP-34 based on an eddy current converter. The following monoxide compounds (chemically pure and pure grades) were used as activators:  $\text{Al}_2\text{O}_3$ ,  $\text{MgO}$ ,  $\text{CaO}$ ,  $\text{SrO}$ ,  $\text{Cr}_2\text{O}_3$ ,  $\text{MnO}$ ,  $\text{CoO}$ ,  $\text{Fe}_2\text{O}_3$ ,  $\text{Ga}_2\text{O}_3$ ,  $\text{In}_2\text{O}_3$ ,  $\text{GeO}_2$ ,  $\text{SnO}_2$ ,  $\text{V}_2\text{O}_5$ ,  $\text{MoO}_3$ ,  $\text{TiO}_2$ , and  $\text{SiO}_2$ . The experiments were conducted using the TIG welding machine OB-2279 equipped with a thyristorised power unit VSVU-315 for the following welding parameters:  $I = 100, 150$  and  $200$  A,  $v_w = 100$  mm/min, arc length of 1.5 mm, shielding gas is argon, tungsten electrode with a 3.2 mm diameter,  $30^\circ$  pointing angle and 0.5 mm tip.

As it is difficult to control profile and measure size of the liquid pool during the welding process, the

experiments were conducted using the following procedure. The arc was instantaneously extinguished during welding by switching off the power unit and stopping movement of a workpiece relative to the tungsten electrode. The shape of the weld pool in longitudinal and transverse sections of the weld at the moment of interruption of TIG and A-TIG welding can be evaluated from macrosections of the weld pool shown in Figure 2. Substantial differences in configuration of the pool in TIG and A-TIG welding are indicative of different penetration mechanisms of these welding processes. Characteristic feature of the shape of the metal pool in A-TIG welding is a pronounced deformation of its free surface (see Figure 2). With this experimental procedure, the depth of the formed crater can serve as an approximate criterion for estimation of the true sag of the pool, as after instantaneous switching off of the power unit the melt start spreading, partially filling up the crater, during solidification of the weld pool.

To begin with, consider the first of the two factors causing deformation of the free surface of the weld pool, i.e. gas-dynamic pressure of the arc column and pressure of recoil of vapours. Movement of the arc column plasma occurs under the effect of electromagnetic force  $\vec{F} = \vec{j} \times \vec{B} = \mu_0 \mu \vec{j} \times \vec{H}$ , where  $\mu$  is the magnetic permeability. In approximation of the axisymmetric electromagnetic field, current density vector  $\vec{j}$  has a

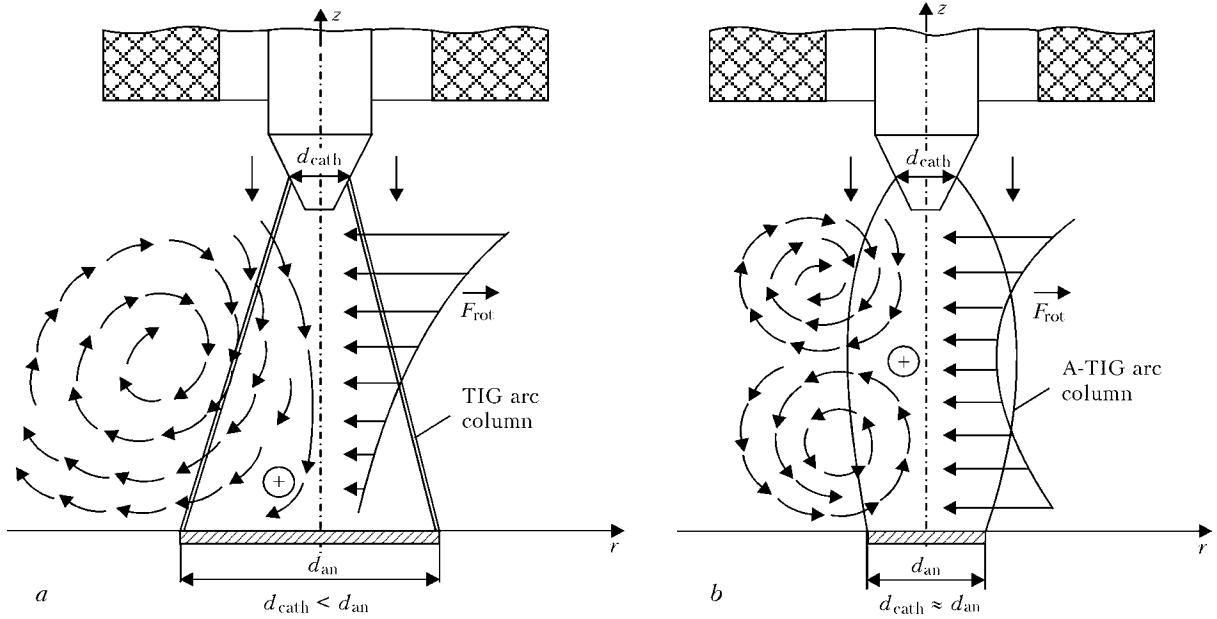


**Figure 3.** Distribution of vortex component of Lorentz force (to the right) and flow of plasma of the TIG (*a*) and A-TIG (*b*) arc column (to the left)

non-zero radial and axial components, while the magnetic field intensity vector  $\vec{H}$  has one azimuthal component  $H_\phi$ , which is other than zero. Given that  $\vec{j} = \text{rot}\vec{H}$ , for Lorentz force it can be written as follows:

$$\vec{F} = -\mu_0\mu \left( 0.5 \text{ grad } H_\phi^2 + \frac{H_\phi^2}{r} \vec{e}_r \right), \quad (1)$$

where  $\vec{e}_r$  is the unit ort in the radial direction.

According to the Helmholtz theorem, any vector field  $\vec{F}$  can be represented as a sum of the potential and vortex fields:  $\vec{F} = \vec{F}_{\text{pot}} + \vec{F}_{\text{rot}}$ . It follows from (1)

that  $\vec{F}_{\text{pot}} = -0.5\mu_0\mu \text{ grad } H_\phi^2$  and  $\vec{F}_{\text{rot}} = -\mu_0\mu \frac{H_\phi^2}{r} \vec{e}_r$ .

Impact of the potential component of the force is known to be limited to formation (in liquid, gas or plasma) of magnetostatic pressure  $P_{\text{mag}} = 0.5\mu_0\mu H_\phi^2$ , which does not prevent movement of a medium under the effect of other body force. Therefore, movement of the welding arc column is caused by an axial gradient of centripetal rotation component  $\vec{F}_{\text{rot}}$  of the Lorentz force. Under the TIG welding conditions, the anode spot diameter  $d_{\text{an}}$  is much larger than the cathode spot diameter  $d_{\text{cath}}$ . That is by the diagram of distribution of resultant force  $\vec{F}_{\text{rot}}$  in height of the arc column has a maximum (Figure 3, *a*) near the cathode, where the current density is maximal. Thus, a flow of plasma in the axial direction (from cathode to anode) is formed in the arc column. While interacting with the weld pool surface, this flow spreads to form a characteristic bell-shaped arc column (see Figure 3, *a*), and the near-anode region of the arc column has maximum of the gas-dynamic pressure. The situation is different in A-TIG welding (Figure 3, *b*). In welding over the layer of activating flux, the arc contraction shows up in decrease of the anode spot to a size comparable with that of the cathode region. Accordingly, distribution of the current density in height

of the arc column has two maxima located near the cathode and anode. Distribution of the rotation component of the Lorentz force is of a similar character, thus causing two opposite plasma flows (see Figure 3, *b*) directed from the cathode and anode to the middle part (in height) of the arc column.

Their interaction results in formation of a barrel-shaped arc column with a pressure maximum at the point of collision of the plasma flows. It follows from this analysis that the gas-dynamic pressure of the arc column is not a dominant factor that causes deformation of the weld pool free surface in A-TIG welding.

As found by experimental studies [15], decrease in size of the anode spot in A-TIG welding at a welding current of 200 A results in the heat flow density equal to  $10^4 \text{ W/cm}^2$  or higher. It is a known fact that to provide intensive evaporation of metal its surface should be heated with a source having a heat flow density of about  $10^5\text{--}10^6 \text{ W/cm}^2$  within the heat spot [16]. Although the heat flow densities in the anode spot during A-TIG welding are lower than those achieved with beam welding methods (arc power is distributed over the free surface of the weld pool in a spot of a much smaller size than the typical focal spot), in our opinion, they may be sufficient to provide overheating of the melt surface to temperatures close to a boiling point or higher. Study [17] presents calculations of evaporation and gas-dynamic scatter of vapour of different metallic materials in overheating of melts to above their boiling temperatures. Figure 4 shows temperature dependence of relative pressure  $P_{\text{reac}}$  of recoil of iron vapours at  $P_{\text{atm}} = 1$ .

Figure 5 shows deformation of the free surface of the weld pool calculated with allowance for hydrostatic pressure of the melt, vapour recoil pressure of metal evaporating from the surface of the weld pool, and surface tension force. Deformation of the free surface of the weld pool was calculated using a mathematical model similar to [18]. Geometry of an ex-

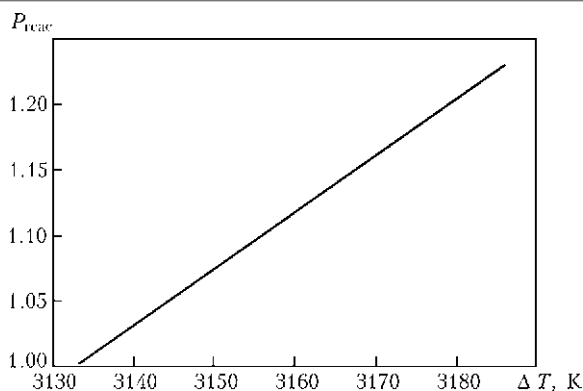


**Figure 4.** Temperature dependence of relative vapour recoil reaction pressure in evaporation of iron at  $P_{\text{atm}} = 1$

perimentally measured shape of the weld pool and calculated vapour recoil reaction pressure varied depending upon the overheating temperature were used as the input data. It was assumed that  $P_{\text{reac}}$  was distributed over the pool surface following the normal law in a spot 2 mm in diameter.

As follows from Figure 5, it is sufficient to overheat the surface of the weld pool in the anode spot by 30 K to form the quasi-keyhole 0.8 cm deep. Specific mass flow of vapour from the melt surface at the overheating temperature is equal to  $0.22 \text{ g}/(\text{cm}^2 \cdot \text{s})$ , while the specific heat losses for evaporation corresponding to this flow are equal to  $1658 \text{ W}/\text{cm}^2$  [17]. At the anode spot diameter  $d_{\text{an}} = 2 \text{ mm}$ , heat losses for evaporation are equal to 52 W, and radiation losses are not greater than 17 W. Thus, at  $I = 100 \text{ A}$  and  $U = 9 \text{ V}$  (allowing for efficiency  $\eta = 0.8$ ) the power of the welding heat source consumed in item heating in A-TIG welding is equal to 651 W, thus providing the density of the heat flow in the anode spot of about  $2 \cdot 10^4 \text{ W}/\text{cm}^2$ . As follows from these estimates, at a diameter of the anode spot less than 5 mm the heat flow density is sufficient to heat the melt to a boiling temperature and compensate for the evaporation and radiation losses of heat, and consumption of heat for heating of a weldment in the balance of heat on the surface of the anode spot.

Consider experimental data on penetration depth  $H_{\text{pen}}$  and maximal value of the crater in the solidified weld pool,  $H_{\text{crat}}$ , in A-TIG welding depending upon the activating flux used (Figure 6). Formation of the quasi-keyhole in A-TIG welding is a factor that promotes increase in the penetration depth, as it makes it possible to move (similar to immersed-arc welding) the heat source deep into a piece welded. However, unlike immersed-arc welding, in A-TIG welding the set distance between the tungsten electrode and surface of a piece welded remains unchanged, and the anode spot is localised in the upper part of the surface of a formed crater. This is indirectly evidenced by the fact that the welding current being the same, A-TIG welding is performed at a voltage only about 10–12 % higher than in TIG welding. Thus, because of the principle of the local effect, deep penetration in A-TIG welding cannot be explained only by the heat effect of immersion of the arc deep into the weld pool. The-

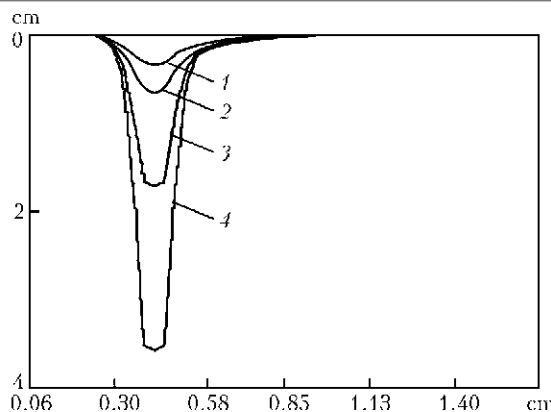


**Figure 5.** Shape of the weld pool free surface (longitudinal section) depending upon temperature  $\Delta T$  of overheating of the melt above the boiling temperature: 1 –  $\Delta T = 18$ ; 2 – 24; 3 – 29; 4 – 35 K

efore, there are also other factors that provide this penetration, analysis of which is given below.

**Hydrodynamics of weld pool in TIG and A-TIG welding.** For further analysis of the penetrating capacity of A-TIG welding, consider peculiarities of hydrodynamics of the weld pool under the effect of capillary and ponderomotive forces. Marangoni convection is known to form under the effect of tangential stress  $\tau_{\sigma} = +\text{grad } \sigma$ , which results from the gradient of the surface tension coefficient,  $\sigma$ , on the surface of the weld pool, and is in equilibrium with viscous friction stress. Given that in a general case  $\sigma$  depends upon temperature  $T$  and concentration  $C$  of an element dissolved in metal, e.g. oxygen, it yields that  $\tau_{\sigma} = +(\tau_{\sigma}^{(T)} + \tau_{\sigma}^{(C)})$ , where  $\tau_{\sigma}^{(T)} = \beta_T \text{ grad } T$ ;  $\tau_{\sigma}^{(C)} = \beta_C \text{ grad } C$ ;  $\beta_T = \frac{d\sigma}{dT}$ ;  $\beta_C = \frac{d\sigma}{dC}$ ; and gradients of temperature and concentration are calculated along the curvilinear free surface. Movements of the melt formed under the effect of stresses  $\tau_{\sigma}^{(T)}$  and  $\tau_{\sigma}^{(C)}$  are called thermal-capillary and concentration-capillary convection (Marangoni convection), respectively.

In TIG welding of steel with a low oxygen content, the Marangoni convection is initiated by tangential stress  $\tau_{\sigma}^{(T)}$  in the surface layer of the melt, caused by variations in the surface tension coefficient depending upon the temperature (diagram of distribution of the surface tension coefficient along the free surface is

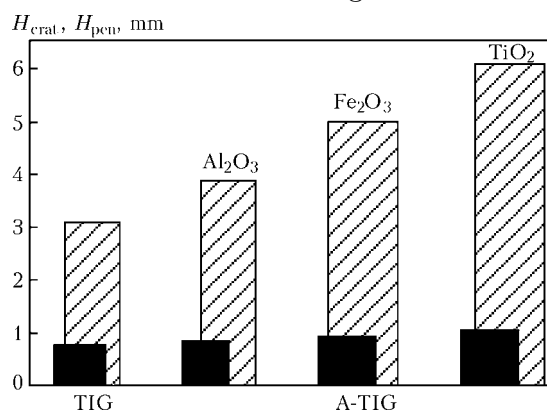


**Figure 6.** Effect of the TIG and A-TIG welding process using different oxides on the depth of crater  $H_{\text{crat}}$  (black region) and penetration  $H_{\text{pen}}$  (dashed region) in weld pools at  $I = 200 \text{ A}$

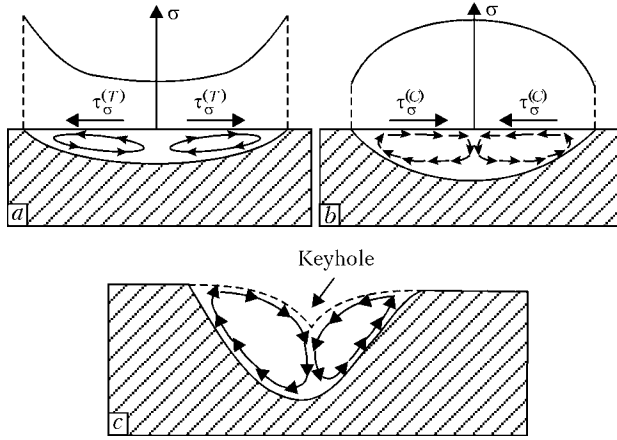


**Figure 7.** Diagram of Marangoni convection in TIG welding of steel with low (a) and high (b) oxygen content and in A-TIG welding of steel with both low and high oxygen content (c)

shown in Figure 7, a). The thermal-capillary convection formed in this case is directed from the centre of the anode spot to the periphery of the weld pool. It is a known fact [19] that the surface tension coefficient decreases with increase in the oxygen concentration of steel. Oxygen concentration  $C$  is much lower at the centre of the anode spot because of intensive evaporation than on the periphery of the weld pool. This results in formation of the gradient of surface tension, which initiates the concentration-capillary convection (Figure 7, b). Flows of the melt moving to the centre of the anode spot turn around, transporting overheated metal to the pool bottom. As experimentally found, in TIG welding of steel with an increased oxygen content ( $C \approx 100$  ppm), the penetration depth grows (compared with steel with a low oxygen content ( $C \approx 10$  ppm)), although not that significantly as in the A-TIG process. The concentration-capillary convection in A-TIG welding develops following a similar scheme, the only difference being that the sub-surface volumes of the melt are enriched with oxygen through absorption from molten flux after dissociation of oxide. It might be expected that in this case  $\text{grad } C$  will be markedly higher than in TIG welding of steel with a high oxygen content. Hence, the Marangoni flow will also be more intensive.

The deformed free surface of the weld pool, acting as a geometric activator of the Marangoni flow, has a substantial effect in A-TIG welding on intensification of the downward flow of the melt transporting the overheated melt from the anode region to the weld pool bottom. With a flat shape of the free surface of the weld pool, the opposite melt flows moving to the centre of the weld pool towards each other (see Figure 7, b) lose their momentum at collision. Therefore, the downward melt flow has low intensity, and the resulting vortex flow localised in the upper part of the weld pool exerts just a limited effect on the penetration depth. Hydrodynamic situation in the weld pool initiated by the concentration-capillary Marangoni convection will change greatly, if a crater (quasi-keyhole) forms as a result of the vapour recoil reaction on the weld pool surface. In this case, the

melt flows moving along an inclined surface of the keyhole meet at some angle  $\alpha$  ( $\alpha \approx 45^\circ$  or more). As a result of interaction of these flows, their momenta sum up to form an intensive downward jet flow (Figure 7, c), which becomes capable of transporting overheated metal to the pool bottom, thus providing a substantial increase in the penetration depth, compared with the situations considered in Figure 7, a and b. Therefore, the quasi-keyhole can be regarded as a sort of a hydrodynamic activator of the Marangoni convection initiating the downward flow of the overheated melt to the weld pool bottom.

To estimate the effect of the Lorentz force on convection of the weld pool in the A-TIG process, assume in the first approximation that the electromagnetic field in the melt has an axial symmetry. Then, in analogy with (1), the force leading to electromagnetic stirring of the melt is a rotation component of the Lorentz force,  $\bar{F}_{\text{rot}}$ . Estimate distribution of  $F_{\text{rot}}$  in the anode spot, assuming that the current density in the anode spot having the form of a circle is distributed uniformly. Designate radius of the anode spot as  $R$ , then

$$\bar{F}_{\text{rot}}(r, 0) = -\mu_0 \mu \frac{I^2}{4\pi R^3} \frac{R}{r} \bar{e}, \quad 0 < r < R, \quad (2)$$

i.e. the rotation component of the Lorentz force in the anode spot is directly proportional to square of the welding current, and inversely proportional to cube of the anode spot radius (in surface points with the same relative radius  $\bar{r} = r/R$ ) and directly proportional to the square of welding current. In the weld pool volume the density of the rotary component of the Lorentz force depends on the anode spot radius in a similar manner. For evaluation of bulk distribution  $\bar{F}_{\text{rot}}$  we assume that the electromagnetic field is axially symmetric in the weld pool. Let us integrate the equation for the magnetic field intensity by the finite difference method:

$$\text{rot rot } \bar{H} = 0; \quad 0 < r < R^*, \quad 0 < z < L \quad (3)$$

at the following boundary conditions:

$$H_\varepsilon(r, 0) = \begin{cases} \frac{I}{2\pi R} \bar{r}, & 0 < r < R, \\ \frac{I}{2\pi r}, & r > R; \end{cases}$$

$$H_\varepsilon(0, z) = 0;$$

$$\left. \frac{\partial H_\varepsilon}{\partial r} \right|_{z=L} = 0;$$

$$H_\varepsilon(R^*, z) = 0.$$

Figure 8 shows the change of  $\bar{F}_{\text{rot}}(R, z)$ , depending on coordinate  $z$  calculated from the weld pool surface for three anode spot radii. At  $R = 1$  mm (assumed to be identical to spot radius in A-TIG welding) compared to  $R = 3$  mm (in TIG welding) the rotary component of the Lorentz force is significantly higher. The velocity of the melt flow moving from the anode

spot to the weld pool bottom under the impact of the centripetal bulk force  $\bar{F}_{rot}$ , is the higher, the larger  $|\bar{F}_{rot}|$  and the greater its change in the axial direction. Therefore, decrease in size of the anode spot characteristic of A-TIG welding leads to intensification of the downward flow of the melt, and is a factor that is responsible (along with the concentration-capillary Marangoni convection) for the penetrating capacity of the A-TIG process.

## CONCLUSION

In A-TIG welding of stainless steel the activating action of the flux is manifested in the following:

- processes of heat-mass and electric transfer developing in the near-anode plasma of the welding arc due to the electronegative elements of the activating fluxes (oxygen, fluorine, chloride), reduce the anode spot size;
- gradient of the element concentration develops on the weld pool surface, which initiates the concentration-capillary convection of the melt, directed from the pool periphery to its center and further on to the pool bottom.

Small dimensions of the anode spot result in an increased density of the welding thermal flow, so that conditions are in place for overheating of the weld pool surface above the boiling temperature, formation of a quasi-keyhole and arc immersion into the melt. In A-TIG welding the small dimensions of the anode spot lead to an essential increase of the centripetal component of the Lorentz force which, together with the concentration-capillary Marangoni convection, transports the overheated metal from the anode spot to the weld pool bottom.

The following physical factors can be given which ensure an increased penetrability of A-TIG welding:

- thermal impact of the arc immersed into the quasi-keyhole;
- transport of the overheated melt from the anode spot to the weld pool bottom due to concentration-capillary Marangoni convection and magnetohydrodynamic flow of the melt, which is due to the eddy component of the Lorentz force.

In order to reply to the question on the dominant factor (depending on A-TIG welding conditions), further experimental studies are required, which are aimed at precise determination of the weld pool free surface, recording the actual keyhole, dimensions of the anode spot and current density distribution in it.

Mathematical simulation of the processes of heat mass transfer and hydrodynamics of the weld pool, allowing for the interaction of the mass and capillary forces, deformation of the free surface of the weld pool, evaporation and condensation of the substance and features of arcing under the conditions of A-TIG welding, is definitely interesting.

1. Yushchenko, K.A., Kovalenko, D.V., Kovalenko, I.V. (2001) Application of activators for TIG welding of steels and alloys. *The Paton Welding J.*, **7**, p. 37–43.

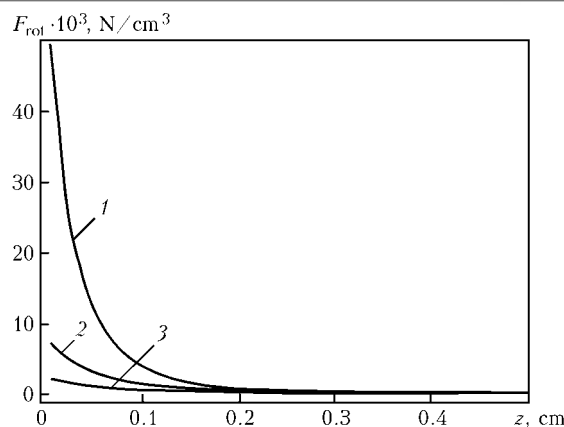


Figure 8. Distribution of centripetal component of the Lorentz force across the pool depth at different dimensions of the anode spot: 1 –  $R = 1$ ; 2 – 2; 3 – 3 mm

2. Savitsky, M.M., Kushnirenko, V.N., Olejnik, O.I. (1999) Peculiarities of TIG welding with activating fluxes. *Automatich. Svarka*, **12**, p. 20–26.
3. Lucas, W., Howse, D. (1996) Activating flux – increasing the performance and productivity of the TIG and plasma processes. *Welding and Metal Fabr.*, **1**, p. 11–15.
4. Lucas, W. (2000) Activating flux – improving the performance of the TIG process. *Ibid.*, **2**, p. 7–10.
5. Heiple, C.R., Roper, J.R., Stagner, R.T. et al. (1983) Surface active element effects on the shape of GTA, laser and electron beam welds. *Welding J.*, **62**(3), p. 72–77.
6. Tanaka, M., Shimizu, T., Terasaki, H. et al. (2000) Effects of activating flux on arc phenomena in GTAW. *Sci. and Techn. of Welding and Joining*, **5**(6), p. 397–402.
7. Ostrovsky, O.E., Kryukovsky, V.N., Buk, B.B. et al. (1977) Effect of activating fluxes on penetrability of welding arc and power concentration in anode spot. *Svarochn. Proizvodstvo*, **3**, p. 3–4.
8. Zamkov, V.N., Prilutsky, V.P. (2004) Theory and practice of TIG-F (A-TIG) welding (Review). *The Paton Welding J.*, **9**, p. 11–14.
9. Paton, B.E., Zamkov, V.N., Prilutsky, V.P. et al. (2000) Contraction of the welding arc caused by the flux in tungsten-electrode argon-arc welding. *Ibid.*, **1**, p. 5–11.
10. Lucas, W., Howse, D., Savitsky, M.M. et al. (1996) A-TIG – increasing the performance and productivity of the TIG process. *IIW Doc. XII-1448-96*.
11. Lowke, J., Tanaka, M., Ushio, M. (2004) Insulation effects of flux layer in producing greater weld depth. *IIW Doc. 212-1053-04*.
12. Paton, B.E., Yushchenko, K.A., Kovalenko, D.V. et al. (2005) Formation of quasi keyhole is a cause of deep penetration in A-TIG welding of stainless steel. *IIW Doc. 212-1085-05*.
13. Paton, B.E., Yushchenko, K.A., Kovalenko, D.V. et al. (2006) Role of keyhole in formation of deep penetration in A-TIG welding of stainless steel. *The Paton Welding J.*, **6**, p. 3–8.
14. Yushchenko, K.A., Kovalenko, D.V., Kovalenko, I.V. (2005) Comparative analysis of TIG and A-TIG welding of stainless steel. *IIW Doc. 212-1088-05*.
15. Yushchenko, K.A., Kovalenko, D.V., Kovalenko, I.V. (2003) Investigation of peculiarities of A-TIG welding of stainless steels. *IIW Doc. 212-1047-03*.
16. Arutyunyan, R.V., Baranov, V.Yu., Bolshov, L.A. et al. (1989) *Effect of laser radiation on materials*. Moscow: Nauka.
17. Krivtsun, I.V., Demchenko, V.F., Lesnoj, A.B. (2006) Model of evaporation-condensation processes in welding and material treatment. In: *Proc. of Joint 16th Int. Conf. on Computer Technology in Welding and Manufacturing and 3rd Int. Conf. on Mathematical Modelling and Information Technologies in Welding and Related Processes* (Kiev, Ukraine, June, 2006). Kiev: PWI, 184–187.
18. Zhang, W., DeBroy, T. (2002) Modelling of solidified free surface profile during GMA welding. In: *Proc. of Int. Conf. on Mathematical Modelling and Information Technologies in Welding and Related Processes* (Katsiveli, Crimea, Ukraine, September, 2002). Kiev: PWI, p. 24–30.
19. Lancaster, J.F., Mills, K.C. (1991) Recommendations for the avoidance of variable penetration in gas tungsten arc welding. *IIW Doc. 212-796-91*.

# INTEGRATIVE WELDING SIMULATION: EXAMPLE OF GMA WELDING

V. PAVLYK, O. MOKROV and U. DILTHEY

ISF – Welding and Joining Institute, Aachen University, Germany

From the practical engineering point of view, the mechanical properties, residual stresses and distortions are the most important characteristics of weld joint, which determine technological and operation properties. Their prognostication with the aid of computer simulations using finite element methods (FEM) can assist in optimisation of welding procedure and cost reduction. Usually the heat source for the thermo-mechanical analysis has to be determined experimentally. It is a time-consuming procedure, which deteriorates the acceptance of FEM-analysis in practice. From other side, several mathematical models and simulation tools have been developed, which allow simulating the heat source and the weld seam shape based on technological parameters of the process. To such tools belongs program package SimWeld developed by authors. In this paper, the simulation of gas-metal-arc welding (GMAW) using this tool is described. The simulation takes into account thermo-physical and electrical properties of materials and shielding gases, joint type, technological welding conditions, and also specific controlling algorithms of modern digitally controlled welding power sources. Based upon the calculated heat input into the workpiece and the weld pool dimensions an equivalent volumetric heat source is generated which can be applied for analysis of thermal influence of welding over residual stresses and distortions using commercial FEM-programs like, for instance, SYSWELD. Combination of process modelling and modelling of consequences of thermal effects results in an integrative approach to modelling of welding as a whole. In this presentation, a concept of the integrative modelling of welding is discussed, which also must include predictions of microstructure, mechanical properties and possible defects.

Fast growth of computer performance and rapid developments in numerical methods and geometric modelling have facilitated the use of computational welding mechanics for solution of an increasing number of practical and industrially relevant problems, as pointed out by Goldak and Akhlaghi [1]. Computational welding mechanics focuses on calculation the thermal cycle and elastoplastic stress-strain state, which result from the action of a welding heat source. The fast heating, melting, solidification and cooling cause also changes of microstructure and properties of welded materials. Most often, the practically important purpose of a simulation is prediction of heat effects of welding, i.e. residual stresses, distortions as well as microstructure and mechanical-technological properties, with the goal of their optimisation or improvement (Figure 1). Importance of the integra-

tive welding simulation was emphasised in the works of Radaaj [2–4]. According to Radaaj, the welding process simulation, which predicts heat input, temperature field and weld geometry is one of the three integral parts of a total welding simulation. The two others are the structure simulation (stress-strain and strength) and the material simulation (microstructure and mechanical-technological properties).

A practical realisation of a coupled integrative welding simulation has appeared recently, which demonstrates the development of welding simulation tool in Germany [5]. The structural analysis with ANSYS was extended to modelling of material transformations, and a link to a laser welding simulation tool which generates the heat source was developed.

This paper describes the GMAW process simulation. For this purpose, a software package SimWeld was developed [6–8], which predicts the heat input, temperature field, molten zone and weld geometry from the technological input parameters (see Figure 1). The process simulation provides also an equivalent heat source, which is used to perform mechanical stress-strain simulation with software package SYSWELD.

**GMAW process modelling and computer program SimWeld**

**GMAW process sub-models and their coupling.**

The modelling of GMAW process itself consists of several parts: heat source modelling, modelling of heat transfer in the workpiece, and modelling of free surface formation, as shown in Figure 2. The sub-model of heat source considers thermo-electrical process in wire extension, droplet formation and detachment and also includes regulation algorithms of power sources as described in [9]. This sub-model delivers the heat source for the thermal model in the workpiece

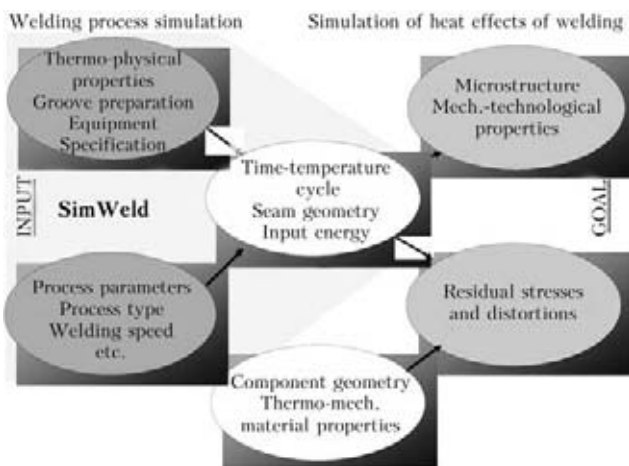


Figure 1. Flowchart of integrative welding simulation



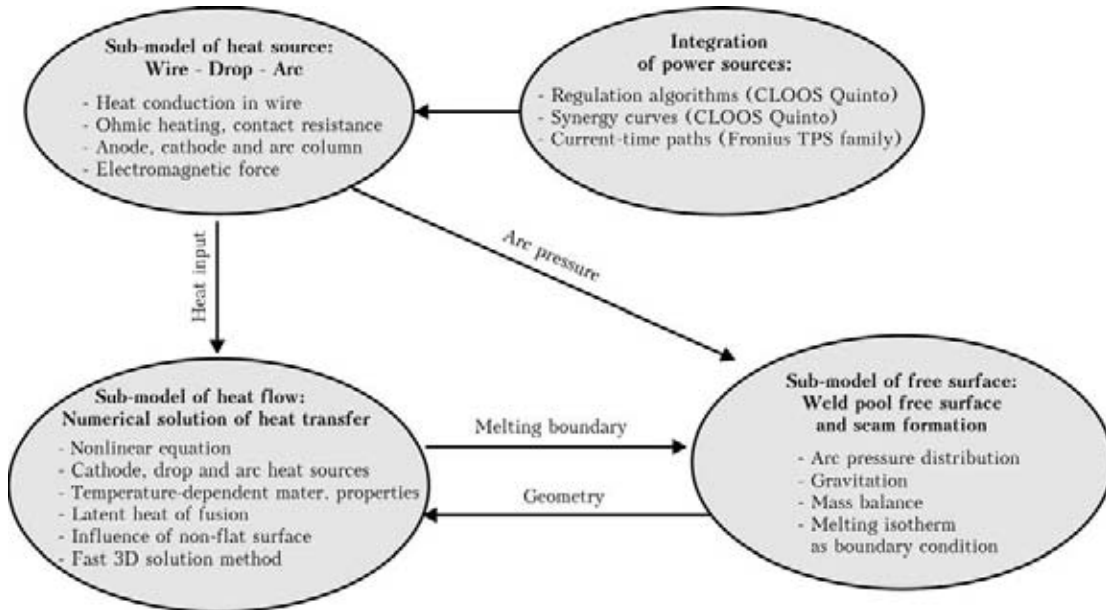


Figure 2. SimWeld process sub-models and their coupling

and the arc pressure distribution for the model of free surface. The thermal model is based on a numerical solution of non-linear heat diffusion equation with advective term which results from the heat source movement. The melting boundary obtained with this sub-model is used as boundary condition for the calculation of weld seam geometry in the sub-model of free surface. The weld pool surface deformation changes the geometry for the heat diffusion, thus it must be taken into account when calculating the heat flow in the workpiece. Thus, all three sub-models are coupled to each other (see Figure 2) and must be solved iteratively.

**Modelling of heat source.** The input parameters for the heat source calculations are the primary technological parameters of the process such as wire feed speed, diameter and material, shielding gas composition, contact nozzle distance, voltage, pulse volt-

age or pulse current, base current, frequency, cable diameters and lengths, regulations of welding equipment etc. (altogether 20 or more parameters). The outputs are the mean electrical and thermal characteristics of the process, arc pressure and arc length. A detailed description of the heat source modelling, which was realized in the software module Arc-Solver of SimWeld, is presented in other paper of these proceedings [9].

Currently, three types of GMAW processes are realized: non-pulse (continuous), pulse process with  $U/I$ -modulation and pulse process with  $I/I$ -modulation (Figure 3). The characteristics and regulations of power sources of companies CLOOS and Fronius are also considered in the module Arc-Solver.

Several experimental series were carried out with the aim of verifications of the Arc-Solver. Results of the predicted versus experimental electrical power for a wire feed rates from 3 to 16 m/min are shown in

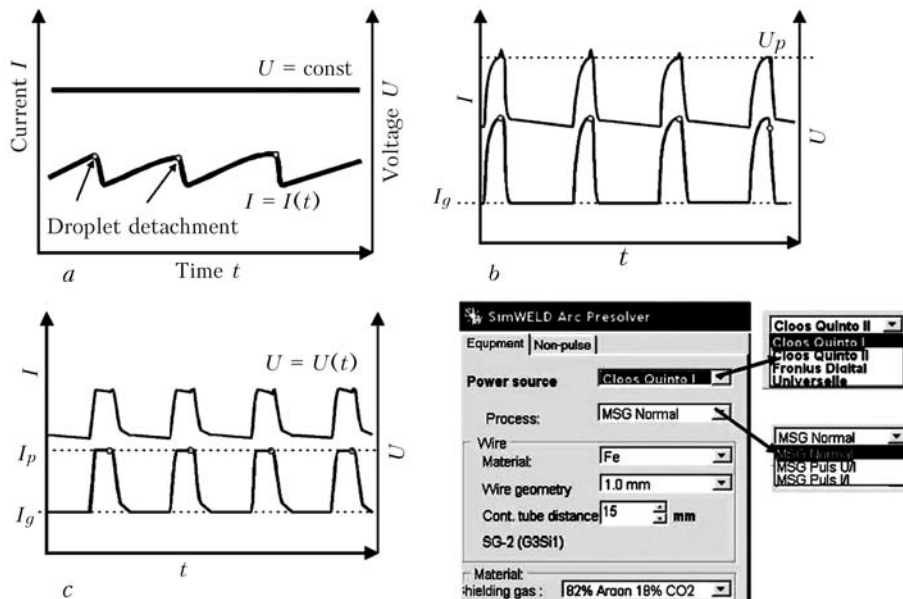


Figure 3. SimWeld module Arc-Solver: implemented normal (a), pulse with  $U/I$  (b) and  $I/I$  (c) modulation processes of GMAW, and power sources

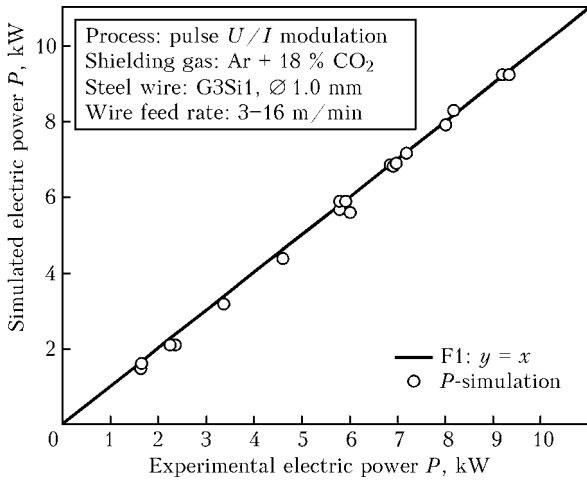


Figure 4. Arc-Solver: model verification for pulse process with  $U/I$  modulation using power source CLOOS Quinto II

Figure 4. It was proved that the Arc Solver, which simulates the heat input, calculates the electric power of the process with an accuracy of at least 10%. Hence, the heat input into the workpiece can be predicted with a sufficient accuracy for engineering applications in many cases.

**Program code SimWeld.** The program package SimWeld was developed for the managing of the entire simulation chain of the GMAW process, from the heat source to the temperature distribution in the workpiece and the weld pool dimensions. The preprocessor (Figure 5) includes all parameters for Arc-Solver and the welding speed (Equipment and Parameters), thermo-physical properties of base and wire materials which are stored in a database (Materials), joint specification (Joint) and geometrical orientations of the torch and the welded plates (Orientation). The input data are processed consecutively by the Arc-Solver and then by the temperature and free surface solver.

The results of simulations are presented and can be explored with the module Postprocessor, which is shown in Figure 6. In the right window, the cross-section of a lap joint with the geometrical dimensions is shown. A

3D view of the weld result with the temperature field map is shown in the left-bottom window.

The total SimWeld process modelling was verified for different welding conditions. Results of a series of experiments with varying welding speed are presented in Figure 7. Steel plates of 1.5 mm thickness were welded with power source CLOOS Quinto II in pulse  $I/I$ -modulation mode. When welding speed was increasing from 80 to 180 cm/min, the full weld penetrations gave place to the partially one. Hence, the both weld width at the top side and at the bottom side of the plate were analysed. The upper graph in Figure 7 demonstrates a good correlation of calculated top width with the experimental measurements. A correct tendency of the weld width at the bottom side of plate is demonstrated by the lower graph. However, the model overestimates the absolute value of the bottom weld width. A possible reason of this is believed to be associated with the influence of the convective heat transfer on the weld formation in case of full penetration weld. Indeed, the fusion line in a cross-section of fully penetrated weld has a concave shape, as shown in the metallographic image in Figure 7. Such shape can not be obtained in frame of a solely conductive heat transfer model.

**Integration with FEM-simulation: equivalent heat source**

After Goldak et al. have presented in 1984 the volumetrically distributed double ellipsoid heat source [10], their model became widely popular for the stress-strain FEM-analysis of welded structures. The Goldak’s heat source is represented by two half-ellipsoids, with in general different distributions parameters for front and rear ellipsoids. Generally, six independent parameters describe the characteristic of the source: heat intensity generation in front and rear parts,  $Q_f$  and  $Q_r$ , half-length of the front and rear parts,  $a_f$  and  $a_r$ , half-width  $b$  and half-depth  $c$ . Using one additional constraint of heat flux continuity at the boundary of two ellipsoids, the number of inde-

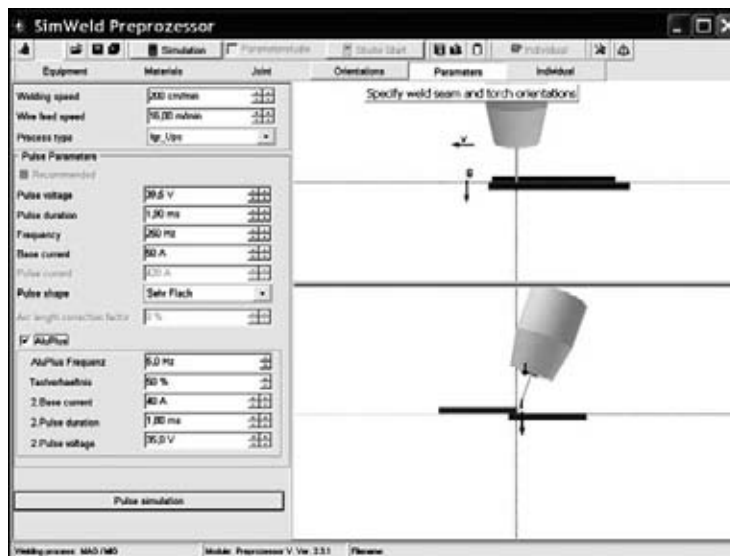


Figure 5. SimWeld Preprocessor: process parameters and joint type 2D view

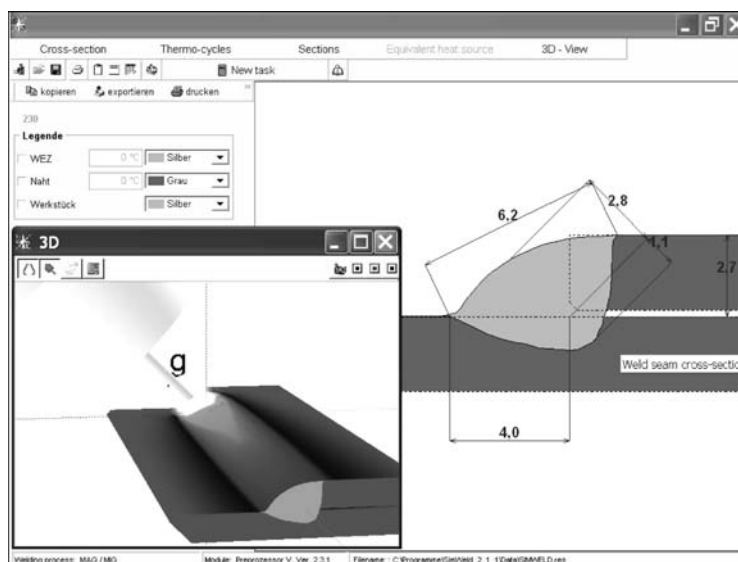


Figure 6. SimWeld Postprocessor: weld seam shape and sizes

pendent parameters reduces to five. The geometrical parameters can be good approximated with the corresponding dimensions of the weld pool. Therefore, a standard procedure of the heat source calibration requires measurements of experimental weld pool sizes and temperature course near the weld pool. The sizes are used for  $a_f$ ,  $a_r$ ,  $b$  and  $c$ , while the temperature measurement is used for calibration of process efficiency. A fine turning of heat source model parameters is made by means of comparison of calculated weld pool sizes and temperature history with experimentally measured. Thus, the calibration procedure demands experiment, from one side, and a number of simulation trials, from the other. It complicates the use of FEM-analysis for optimisation of welding parameters, for example, the study of the influence of welding speed on the stress-strain state of a weld. An effective alternative for definition of heat source in such case is utilization of the results of process simulation.

Indeed, the process simulation tool provides the data on heat input, weld geometry and temperature field. Thus, the weld pool dimensions are also available. Parameter  $b$  corresponds to the maximum weld

pool width, parameter  $c$  – to the weld pool depth at the cross-section of the maximum width, and parameters  $a_f$  and  $a_r$  are the distances from the centre of this cross-section to the fusion lines in front and in the tail of the weld pool, respectively (Figure 8). The fractions of the heat input in the front and in the rear half-ellipsoids,  $Q_f$  and  $Q_r$ , are determined by integration of the cathode and arc column heat distributions over corresponding areas of the weld pool surface, and anode (droplet) heat distribution over corresponding sub-volumes of the pool. These heat distributions are determined in the module Arc-Solver, as described above.

The double ellipsoid volumetric heat source substitutes in such manner the more realistic heat distributions. Therefore it is called «equivalent heat source». The appellation «equivalent» emphasises that the total heat input and weld pool sizes obtained using this source must be equal to the heat input and weld pool sizes, which were obtained in process simulation tool by application of two surfactant heat sources (cathode and arc) and one volumetric (anode/droplet) source.

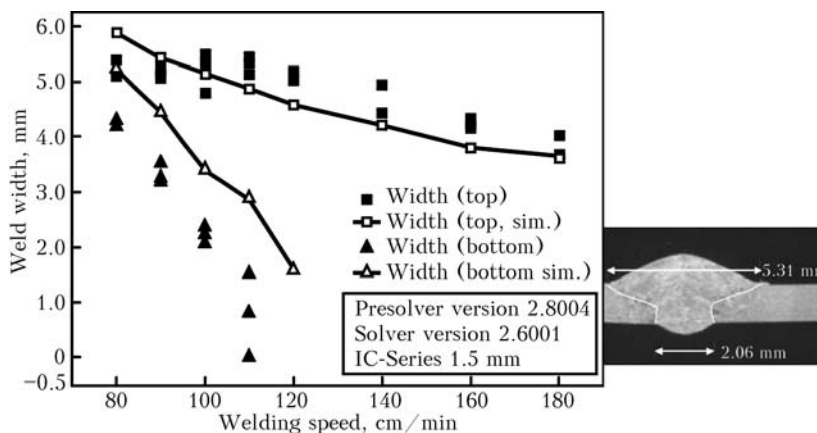


Figure 7. SimWeld model verification for pulse  $I/I$ -modulation with CLOOS Quinto II: simulated weld width (curves and symbols) on top and bottom of the workpiece in comparison with experimental dimensions (symbols) for different speed of welding of steel DCO1 with 1.0 mm wire G3Si1 (SG2) in  $\text{CO}_2 + 18\% \text{ Ar}$  mixture at  $h = 1.5$  mm,  $v_f = 6$  m/min,  $f = 100$  Hz,  $t_p = 1.8$  ms,  $I_b = 30$  A,  $I_p = 460$  A, arc length correction of 66 %

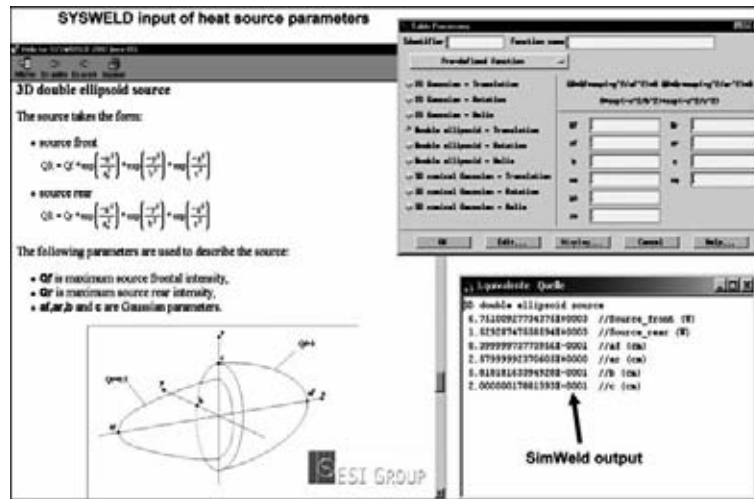


Figure 8. SimWeld link to SYSWELD: parameters of double-ellipsoid equivalent heat source of SYSWELD (left-top, with permission of ESI Group) and the same parameters generated by SimWeld from the process simulation (bottom-right)

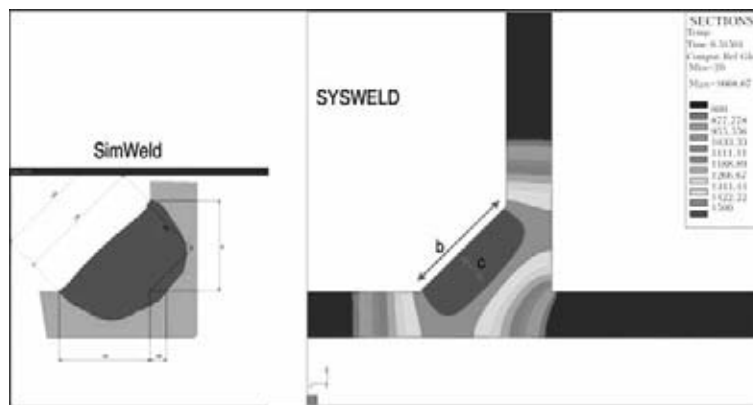


Figure 9. Comparison of weld cross sections simulated by SimWeld (left) and SYSWELD (right, with permission of ESI Group) using the equivalent heat source generated by SimWeld

Currently, heat source link between SimWeld and FEM-package SYSWELD is realised in such way that the parameters of the heat source are first generated by SimWeld and are then input to SYSWELD by means of its user interface (see Figure 8). An example of a cross-section map of simulated temperature field with SYSWELD which uses the equivalent heat source is shown in Figure 9. The corresponding weld seam cross-section from SimWeld simulation is also shown in the Figure, for comparison.

#### Conclusion and outlook

The integrative simulation of welding, which includes welding process, elastoplastic stress-strain state of structure and mechanical-technological properties becomes an essential part of modern engineering. It allows a faster and more effective development of new technologies, products and structures. Further development in this field will go in direction of closer links of different sub-models and extensions including different types of welding processes.

**Acknowledgements.** The authors gratefully acknowledge the financial support of the German Ministry of Education and Research (bmb + f) and following companies DaymalerChrysler, CLOOS Schweisstechnik GmbH, Fronius International, BoehlerThyssen Welding and Linde AG within the National Center of Excellence for Process Simulation

SimPRO (<http://www.rwth-aachen.de/simpro/>). We also express our thanks to Mr. H. Porzner from ESI Group for co-operation and for courtesy to present the simulation results with SYSWELD.

- Goldak, J., Akhlaghi, M. (2005) *Computational welding mechanics*. Springer.
- Radaj, D. (2002) *Eigenstressungen und Verzug beim Schweißen, Rechen- und Messverfahren*. Dusseldorf: DVS.
- Radaj, D. (1999) *Schweißprozesssimulation. Grundlagen und Anwendungen*. Dusseldorf: DVS.
- Radaj, D. (2002) Integrated finite element analysis of welding residual stress and distortion. In: *Mathematical modelling of weld phenomena 6*. Ed. by H. Cerjak and H.K.D.H. Bhadeshia. London: Institute of Material, p. 469–489.
- BMBF-Verbundprojekt: «SST – Schweißsimulationstool» (<http://www.schweissimulation.de>).
- Dilthey, U., Dikshev, I., Mokrov, O. et al. (2002) Process modelling and software tools for MAG/MIG welding. In: *Proc. of Int. Conf. on Mathematical Modelling and Information Technologies in Welding and Related Processes* (Katsiveli, Crimea, Ukraine, Sept. 16–20, 2002). Kiev: PWI, p. 201–209.
- Dilthey, U., Pavlyk, V., Mokrov, O. et al. (2005) Software package SimWeld for simulation of gas-metal-arc-welding processes of steels and aluminium alloys. In: *Mathematical modelling of weld phenomena 7*. Ed. by H. Cerjak, H.K.D.H. Bhadeshia, E. Kozeschnik. Graz: Graz TU, p. 1057–1079.
- Dilthey, U., Mokrov, O., Pavlyk, V. (2005) Modelling of consumable electrode gas-shielded multi-pass welding of carbon steel with preheating. *The Paton Welding J.*, 4, p. 2–6.
- Mokrov, O., Pavlyk, V., Dilthey, U. Analysis of thermo-electrical processes and electrode metal transfer during GMAW with the aid of numerical modelling. In: *This Book*, p. 250–257.
- Goldak, J., Chakravarti, A., Bibbi, M. (1984) A new finite element model for welding heat sources. *Metallurg. Transact. B*, 15, p. 299–305.

# NUMERICAL SIMULATION OF SOLIDIFICATION CRACKING DURING LASER BEAM WELDING OF ALUMINIUM ALLOYS

V. PLOSHIKHIN<sup>1</sup>, A. PRIKHODOVSKY<sup>1</sup>, A. ILIN<sup>1</sup>, M. MAKHUTIN<sup>1</sup>, C. HEIMERDINGER<sup>2</sup> and F. PALM<sup>2</sup>

<sup>1</sup>Neue Materialien Bayreuth GmbH, Germany

<sup>2</sup>European Aeronautic Defence and Space Company Deutschland GmbH, Ottobrunn, Germany

The recent results of the numerical simulation of solidification cracking during laser beam welding of aluminium alloys are presented. The model takes into account the thermo-dynamic properties of material to be welded and the effects of strain accumulation. The results of the numerical simulation are successfully used for development of technological means for elimination of solidification cracking. The crack elimination achieved by the application of multi-beam welding technology is numerically predicted and experimentally approved.

Solidification cracking is one of the most frequent forms of weld defect which is observed during manufacturing. The pioneering experimental research on the solidification cracking in aluminium alloy welds was carried out by Singer et al. [1–3] and later by Pumphrey et al. [4] at the end of the 1940s.

The first approach to modelling of solidification cracking in welds was proposed by Prokhorov at the beginning of 1950s [5–7]. In Prokhorov's theory the mechanical tensile strain is supposed to be the reason for the crack formation. Prokhorov calculates the deformation of the liquid-solid region integrally and compares it with the so called «deformability». The last term is introduced by Prokhorov in order to characterise the ability of material to accumulate deformations without rupture at higher temperatures within the solidification range. It was considered as a material property, which value can be obtained experimentally. When the actual deformation of the two-phase region exceeds the deformability of the material, the hot cracking occurs. Despite some critical

disadvantages, the majority of works on modelling of solidification cracking in welds [8–17] is based on the Prokhorov theory.

There are a few modelling approaches appearing recently, which are based upon the localised consideration of crack formation [18–22]. This works are the further development of the Pellini's theory [23] which was also introduced at the beginning of the 1950s. Based on the number of tensile tests of solidifying samples Pellini suggested his «strain theory of hot cracking». According to this theory the tensile strain developed during solidification is localised in the mechanically weak intergranular film formed at the end of solidification due to the segregation. This film limits the strain transmission and therefore it accumulates the major part of the whole strain. The accumulated tensile strain exceeding some critical value leads to the tearing of the liquid film, i.e. to the formation of the solidification crack. Figure 1 shows the principal difference between Pellini's and Prokhorov's theory.

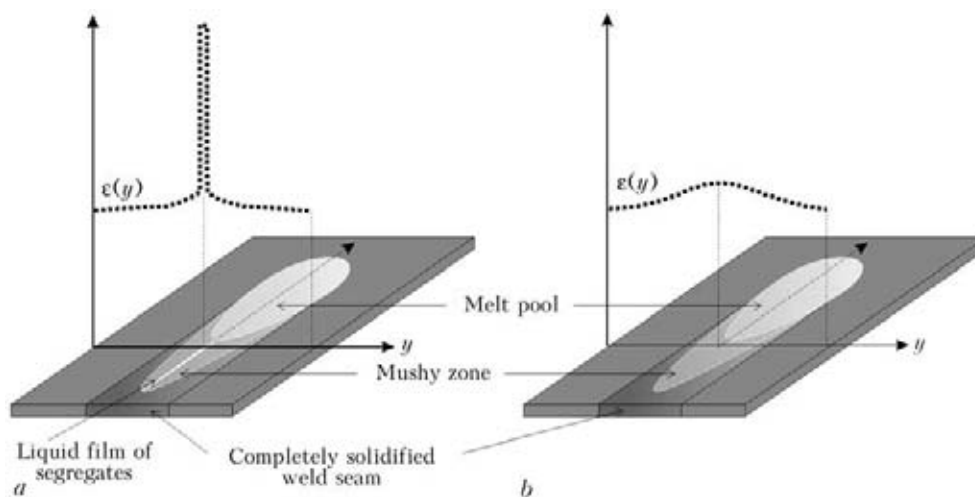


**Figure 1.** Schematic illustration of the difference between the basic theories of the solidification cracking: *a* – Pellini's theory (considering the strain localisation [23]); *b* – Prokhorov's theory (without regard to the strain localisation [5])

**Integrated mechanical-metallurgical approach**

**Modelling approach.** After carried out experimental investigation [24] the following mechanism of the solidification cracking has been proposed (Figure 2). The crack critical region is the intergranular film of the residual liquid in the mushy zone behind the weld pool. This liquid film accumulates the tensile strain transmitted from solid regions by the dendrites of the primary solidified phase. The initiation of the solidification crack (tearing of the intergranular liquid film) occurs when the accumulated displacement value  $\delta_{acc}$  exceeds some critical value  $\delta_{acc}^{cr}$ .

The displacement of the liquid film is accumulated in the region between isotherms of the real liquidus and the real solidus. The real liquidus can be assumed to be represented by the liquidus temperature from the equilibrium phase diagram, if the undercooling of the dendritic tips is neglected. The real solidus represents the lowest temperature of the existence of the mushy state. For a certain alloy, this temperature must be calculated taking into account the effects of micro segregation [25].

General form of the criterion for the crack initiation can be represented as follows:

$$\delta_{acc}^{max} \geq \delta_{acc}^{cr},$$

where  $\delta_{acc}^{max}$  is the maximal displacement accumulated in the intergranular liquid film;  $\delta_{acc}^{cr}$  is the critical displacement, which characterises the ability of the liquid film to accumulate tensile strain without tearing.

The maximal displacement value  $\delta_{acc}^{max}$  depends on the design of the welded joint, the welding parameters (laser beam power and velocity), as well as the properties of the base and the filler material. The left part of the cracking criterion represents the thermo-mechanical aspect of the cracking phenomenon, i.e. the mechanical loading of the intergranular liquid film. The value of the maximal displacement can be calculated only numerically because of the nonlinearity of the material properties and the complexity of the boundary conditions.

The critical displacement  $\delta_{acc}^{cr}$  depends on the material properties and the solidification conditions,

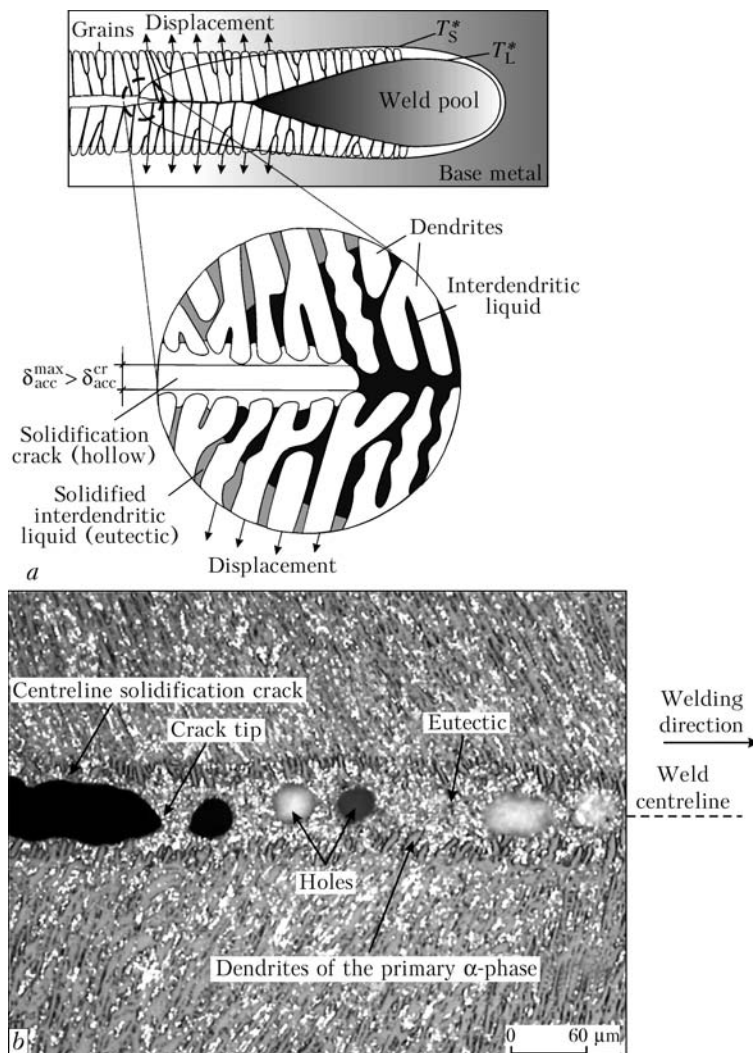


**Figure 2.** Microscopic nature of the solidification cracking mechanism: schematic representation on the macro- and microscopic scale (a) and experimental micrograph of the «frozen» tip of centreline solidification crack (b) (top view of the weld on binary Al-4 % Si alloy)

which determine parameters and morphology of the microstructure as well as the thickness of the intergranular liquid film. The right part of the cracking criterion represents therewith the metallurgical aspect of the cracking phenomenon, i.e. the ability of the intergranular liquid film to accumulate tensile strain without tearing. The value of  $\delta_{acc}^{cr}$  can be considered to be constant for similar materials welded under similar conditions.

**Numerical realisation.** A proper modelling of the solidification cracking mechanism described above implies the solution of the following constituent problems:

- thermo-mechanical problem (evaluation of the maximal displacement of the intergranular liquid film taking into account the effect of the strain localisation);
- metallurgical problem (evaluation of the real solidification range taking into account the effects of segregation; calculation of the phase distribution within the mushy zone; evaluation of the geometrical microstructure parameters).

The thermo-mechanical problem is solved using the finite elements method. The real solidification range for aluminium alloys as well as the liquid phase fraction is calculated on the basis of the Scheil–Gulliver model [25]. For the proper simulation of the strain accumulation, the mechanical properties of the liquid film with relative low yield stress are assigned to the finite elements at the weld centreline (Figure 3). For these elements the value of the accumulated displacement is checked at each time step of calculation. As soon as this value achieves the critical one, the material properties are changed to the properties of air with relative low value of elastic modulus and no heat transfer as well (see Figure 3). Particular attention is given to the proper taking into account of the latent heat release in accordance with the fraction of the liquid phase in the mushy zone.

**Simulation example.** An example of simulation of the crack initiation and growth is shown in Figure 4. The simulation is carried out for the case of the laser beam welding close to the free edge of the 1.5 mm sample from aluminium alloy AlSi3. The influence of the free edge on the solidification cracking formation was deeply investigated in [24]. The Nd:YAG laser power was 1.9 kW and the welding speed was 2.8 m/min.

Two isotherms, the real liquidus and the real solidus, outline the mushy zone. As seen, the crack appears in the inner part of the mushy zone. Once formed the crack creates a thermal barrier, which increases an asymmetry of the temperature field. The position of the crack tip within the mushy zone is not constant; it changes in accordance with the local thermo-mechanical conditions. At the end of the weld seam, close to the right sample edge, the crack is forced out of the mushy zone, i.e. its growth is interrupted. The same behaviour is also observed in all experiments. The reason for the interruption of the crack growth

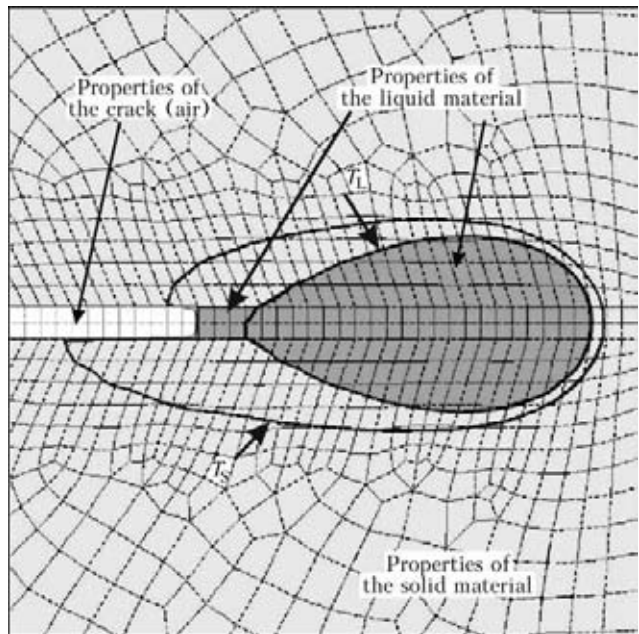


**Figure 3.** Taking into account the effect of strain localization due to proper manipulation of the material properties during numerical simulation

is the decrease of the amount of the accumulated strain occurring due to the overheating and the correspondent decrease of the material strength in the near-edge region of the sample.

#### Application to multi-beam laser welding

The existing welding processes can be analysed with the help of the proposed approach with the purpose of minimising the solidification cracking. There are two possible directions of realisation of the crack-free welding process.

The first one is to change the metallurgical conditions in order to increase the ability of the liquid film to accumulate the tensile strain without tearing, i.e. to maximise the critical displacement  $\delta_{acc}^{cr}$ . It can

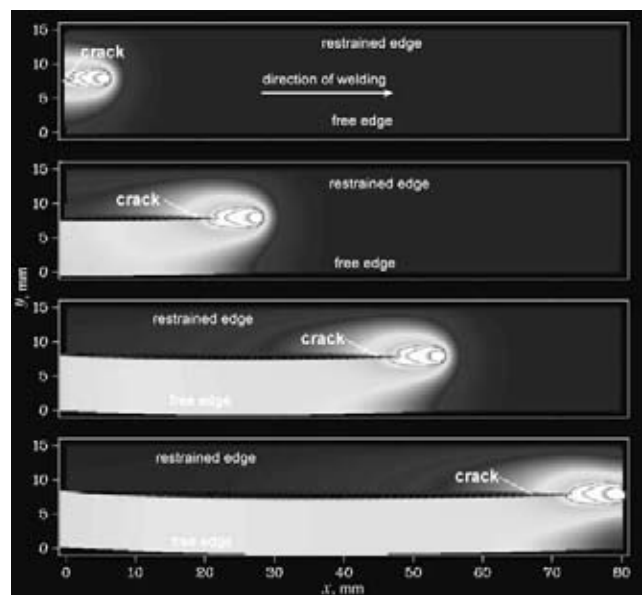


**Figure 4.** Numerical simulation of the crack initiation and growth for the temperature fields at different steps of calculation

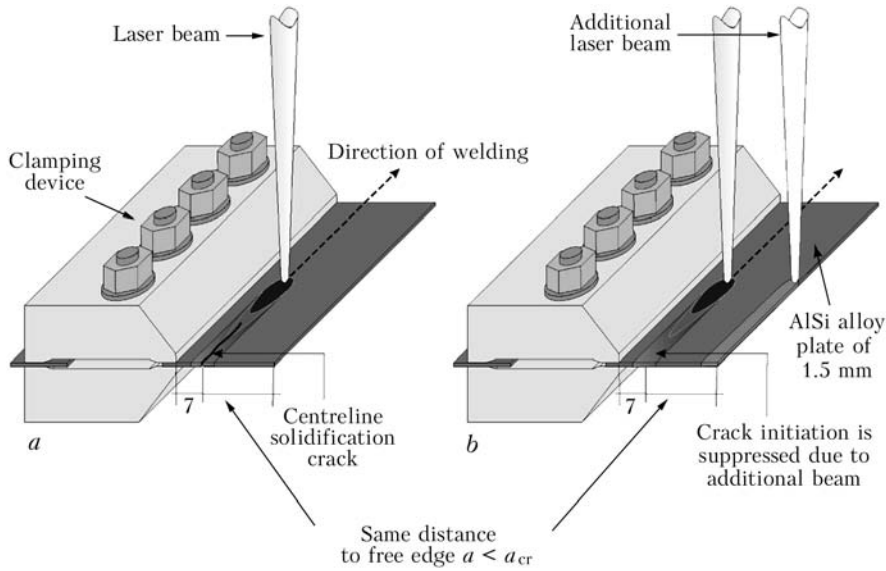


**Figure 5.** Experimental validation of the multi-beam technique: *a* – generation of solidification cracking due to small distance to the free edge; *b* – suppression the solidification cracking under the same conditions due to application of additional laser beam

be achieved, for example, by usage of the appropriate filler material.

The other way is to minimise the tensile strain accumulated in the intergranular liquid film, i.e. to minimise the maximal accumulated displacement  $\delta_{acc}^{max}$ . It can be achieved by the application of the additional heat source, i.e. additional laser beam, which has a proper power and a proper position. The last ones can be determined preliminary by the numerical simulation.

The idea to use additional heat sources as a mean for prevention of solidification cracking in welds was suggested in the 1970s [26, 27]. On the basis of FEM-simulations it was demonstrated [26, 28] that introducing additional heating «in a right place and at the right time [26]» leads to the «beneficial» compressive stress (or strain) in regions, which are critical with respect to the solidification cracking. Despite the apparent simplicity of the suggested idea, the additional heating has still not found the expected industrial application. The determination of «the right place and the right time», i.e. the optimal position, the size and the power of the additional heating spots, seems to be the most important problem hindering the practical application of this technique. As will be shown below, application of the present modelling approach can be very helpful for the industrial realisation of the multi-beam techniques for the crack-free welding.

The experiments on the laser welding close to the free edge described in our previous work [24] have been chosen for the experimental validation of the numerical calculations (Figure 5). The idea was to define the distance to the free edge, which assures the initiation and the stable growth of the solidification crack as shown in Figure 5, *a*. Then, the optimal position and the power of the additional laser beam, that will ensure the suppression of the crack initiation, were found using the numerical simulation (Figure 5, *b*). The experiments were carried out on aluminium alloy AA6056 with the plate thickness of 1.5 mm.

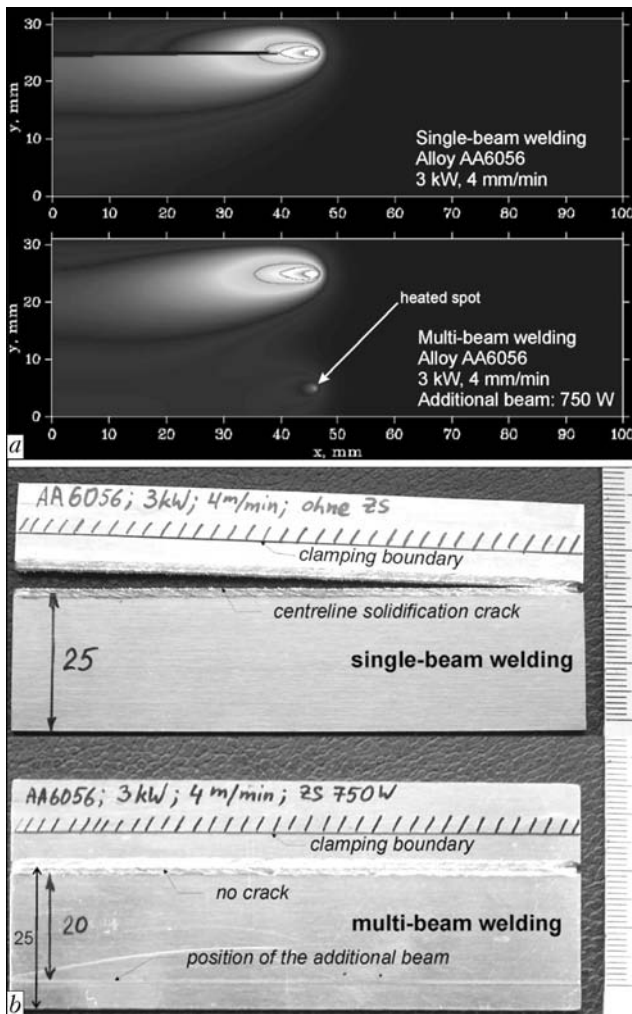


**Figure 6.** Realisation of the multi-beam technique: *a* – preliminary numerical simulation of the temperature fields; *b* – samples produced under the same conditions using the single- (above) and double-beam (below) laser welding



Figure 6 shows the results of the preliminary numerical simulations (temperature fields for the single- and for the double-beam welding) together with the results of the experimental validation. As seen, the application of the additional beam, which moves parallel to the main laser beam at the distance of 20 mm, can be effectively used for the suppression of the crack initiation. The power of the additional beam is significantly less than the power of the main beam. In this special case, the positive effect is achieved at the additional beam power, which value was as high as 25 % of the main beam power.

### Summary

On the basis of the experimental observations an approach for the modelling of solidification cracking in welds is presented. This approach integrates both the thermo-mechanical and the metallurgical aspects of the cracking phenomenon. The modelling implies the solution of the thermo-mechanical problem taking into account the effects of the localisation and the accumulation of displacements in the intergranular liquid film of the segregating alloying elements. The importance of the proper preliminary evaluation of the real solidification range and the phase distribution within the mushy zone is emphasized. The high potential of the presented approach for the development of the industrial crack-free welding techniques is demonstrated on the basis of realisation of the multi-beam laser welding.

**Acknowledgements.** *This work was carried out in the framework of the project «Optimisation of weldability» sponsored by the Bavarian Government, the Foundation of Oberfranken, Allianz-Zentrum für Technik GmbH, AUDI AG, EADS Deutschland GmbH, Linde AG und MTU Aero Engines GmbH. The authors would like to thank all partners for their active support as well as for their very useful discussions. Special thank is addressed to Mr. Dr. C. Heimerdinger (EADS Deutschland GmbH) for his creative co-working by experimental realization of the multi-beam technique.*

- Singer, A.R.E., Jennings, P.H. (1946) Hot-shortness of the aluminium-silicon alloys of commercial purity. *J. Inst. of Metals*, **73**, p. 197–212.
- Singer, A.R.E., Jennings, P.H. (1947) Hot-shortness of some aluminium-iron-silicon alloys of high purity. *Ibid.*, **73**, p. 273–284.
- Jennings, P.H., Singer, A.R.E., Pumphrey, W.I. (1948) Hot-shortness of some high-purity alloys in the systems aluminium-copper-silicon and aluminium-magnesium-silicon. *Ibid.*, **74**, p. 227–248.
- Pumphrey, W.I., Lyons, J.V. (1948) Cracking during the casting and welding of the more common binary aluminium alloys. *Ibid.*, **74**, p. 439–455.
- Prokhorov, N.N. (1952) *Hot cracking during welding*. Moscow: Mashgiz.
- Bochvar, A.A., Rykalin, N.N., Prokhorov, N.N. et al. (1960) On problem of «hot» (crystallisation) cracks. *Svarochn. Proizvodstvo*, **10**, p. 5–7.
- Prokhorov, N.N. (1962) Technological strength of metals in crystallisation during welding. *Ibid.*, **4**, p. 1–8.
- Jonsson, M., Karlsson, L., Lindgren, L.E. (1984) Thermal stresses, plate motion and hot cracking in butt-welding. In: *Mechanical behaviour of materials IV*. New York: Pergamon Press, p. 273–279.
- Dike, J.J., Brooks, J.A., Li, M. (1988) Comparison of failure criteria in weld solidification cracking simulations. In: *Mathematical modelling of weld phenomena 4*. Ed. by H. Cerjak. London: IOM Commun., p. 199–222.
- Feng, Z. (1994) Computational analysis of thermal and mechanical conditions for weld metal solidification cracking. *Welding in the World*, **33(5)**, p. 340–347.
- Zacharia, T. (1994) Dynamic stresses in weld metal hot cracking. *Welding J.*, **73**, p. 164–172.
- Dike, J.J., Brooks, J.A., Krafcik, J.S. (1996) Finite element modelling and verification of thermal-mechanical behaviour in the weld pool region. In: *Trends in welding research*. Ed. by H.B. Smartt et al. ASM Int., p. 159–164.
- Feng, Z., Zaharia, T., David, S.A. (1996) On the thermo-mechanical conditions for weld metal solidification cracking. In: *Mathematical modelling of weld phenomena 3*. Ed. by H. Cerjak. London: IOM Commun., p. 114–147.
- Feng, Z., Zaharia, T., David, S.A. (1997) Thermal stress development in a nickel based superalloy during weldability test. *Welding J.*, **76**, p. 470–483.
- Makhnenko, V.I., Velikoivanenko, E.A., Rozyinka, G.F. et al. (1998) Computer program for prediction the zones with the risk of hot crack formation in welding with deep penetration. *Avtomatich. Svarka*, **10**, p. 57–65.
- Weise, S. (1998) *Heissrissbildung beim Laserstrahlschweissen von Baustählen*. Bremen: BIAS.
- Herold, H., Streitenberger, M., Pchennikov, A. (2001) Modelling of the PRV-test to examine the origin of different hot cracking types. In: *Mathematical modelling of weld phenomena 5*. Ed. by H. Cerjak et al. London: IOM Commun., p. 783–792.
- Shibahara, M., Serizawa, H., Murakawa, H. (2000) Finite element method for hot cracking analysis under welding using temperature dependent interface element. In: *Modelling of casting, welding and advanced solidification processes IX*. Ed. by P.R. Sahn et al. Aachen: Shaker, p. 844–851.
- Shibahara, M., Serizawa, H., Murakawa, H. (2001) Finite element method for hot cracking analysis using temperature dependent interface element. In: *Mathematical modelling of weld phenomena 5*. Ed. by H. Cerjak et al. London: IOM Commun., p. 253–267.
- Bergmann, H.W., Hilbinger, R.M. (1998) Numerical simulation of centreline hot cracks in laser beam welding of aluminium close to the sheet edge. In: *Mathematical modelling of weld phenomena 4*. Ed. by H. Cerjak. London: IOM Commun., p. 658–668.
- Hilbinger, R.M., Bergmann, H.W., Kohler, W. et al. (2001) Considering of dynamic mechanical boundary conditions in the characterisation of a hot cracking test by means of numerical simulation. In: *Mathematical modelling of weld phenomena 5*. Ed. by H. Cerjak et al. London: IOM Commun., p. 847–862.
- Hilbinger, R.M. (2000) *Heissrissbildung beim Schweißen von Aluminium in Blechrandlage*. Bayreuth: Univ. of Bayreuth.
- Pellini, W.S. (1952) *Strain theory of hot tearing foundry*, p. 125–133, 192, 194, 196, 199.
- Plochikhine, V., Prikhodovsky, A., Zoch, H.-W. (2003) Zum Mechanismus der Hei?rissbildung beim Schweißen von Al-Legierungen. *Harterei-Techn. Mitteilungen*, **58(6)**, p. 357–362.
- Saunders, N., Miodownik, A.P. (1998) CALPHAD (Calculation of Phase Diagrams): A comprehensive guide. In: *Pergamon Materials Series*. Vol. 1. Oxford-New York-Tokyo: Elsevier Sci.
- Akesson, B., Karlsson, L. (1976) Prevention of hot cracking of butt welds in steel panels by controlled additional heating of the panels. *Welding Res. Int.*, **6(5)**, p. 35–52.
- Shumilin, V.G., Karkhin, V.A., Rakhman, M.I. et al. *Technique of arc welding*. USSR author's cert. 1109280. Publ. 1980.
- Herold, H., Streitenberger, M., Pchennikov, A. et al. (1999) Modelling of one sided welding to describe hot cracking at the end of longer butt weld seams. *Welding in the World*, **43(2)**, p. 56–64.

# CONDITIONS FOR CHOOSING RATIONAL PARAMETERS OF MODES OF LOCAL HEAT TREATMENT OF WELDED JOINTS

G.Yu. SAPRYKINA

E.O. Paton Electric Welding Institute, NASU, Kiev, Ukraine

In performing field welded joints (in repair welding) of modern critical structures, the problem of choosing rational conditions and modes of local postweld heat treatment (especially in using multi-section heaters) is, as a rule, the problem involving many reference parameters. Its solution, with account of specific geometric dimensions of a treated welded joint, physical properties of the material and its sensitivity to the PWHT thermal cycling, requires much resources and time with traditional experimental approach. Using means of mathematical modelling enables to considerably reduce the expenses. In this work, as applied to local postweld treatment of circumferential joints (high annealing) of pipelines and equipment made of steels type 10GN2MFA, are considered conditions of simultaneous provision of effective reduction of residual stresses and prevention of the risk of annealing crack formation, and noticeable reduction of resistance to growth of stress corrosion cracks.

Welded joints of structural steels of ferrite-pearlite, bainite and martensite classes, especially thicker ones, to reduce residual welding stresses, are subject to local high annealing. It is necessary in the case of operation of the structures at low temperatures, in aggressive media, under cyclic loading, when the role of residual stresses can be substantial. Unfortunately, in a number of cases, local high annealing, due to non-uniform heating, not only removes residual welding stresses, but also produces new ones, whose distribution has no sharp spikes typical for post-welding state, but their level is quite high and significantly influences load-carrying capability. In so doing it is necessary to take into account that high annealing at different temperatures has an ambiguous effect on the microstructure and material properties in the annealing zone.

Consider, for example, data of [1] on the effect of the annealing temperature on the level of residual stresses and hardness in the weld zone (Figure 1), as well as impact toughness  $KCV$  for the near-weld (Figure 2, *a*) and central (Figure 2, *b*) weld zones for structural steel 10GN2MFA. It is seen that for this steel type (widely used in heat-exchange apparatuses, pipelines, pressure vessels, etc.), annealing temperature of the order of 600 °C is conducive to reduction of residual stresses down to 50–70 MPa. Though, for instance, in nuclear power engineering, often 650 °C is applied, which is not bad, as impact toughness of the weld metal increases at moderate holding times (~ 2 h). But 6-hour annealing temperature of 700 °C sharply decreases impact toughness for the base and weld metal, which is connected to degradation processes occurring at high annealing temperatures due to creep flow and diffusion of impurities in the heated zone.

In this respect representative are indices of propensity to annealing crack formation in HAZ of welded joints [1–4, etc.]. This problem was studied in detail in the 1980s. It was shown that propensity to annealing crack formation in HAZ depends on the chemical composition, heating-cooling temperature cycle and the level of the acting stresses. Influence of chemical composition of said steels at maximum chromium content of below 15 % can be evaluated on the basis of parametric equation of [2]:

$$\Delta A = Cr + 3.3Mo + 1.8V + 10C - 2. \quad (1)$$

If  $\Delta A > 0$ , than the steel is susceptible to annealing cracking.

Figure 3 [1] shows the results of testing notched samples on Thermorestor device. The samples were preliminarily subject to imitation of welding thermal cycle  $T_{\max} = 1300$  °C,  $\Delta t_{8/5} = 100$  s ( $T_{\max}$  is the maximum temperature of welding thermal cycle;  $\Delta t_{8/5}$  is the time of cooling from 800 to 500 °C). The material was steel 10GN2MFA at  $\Delta A \approx 0.8$ –1.4, i.e. as follows from (1) it is susceptible to annealing crack-

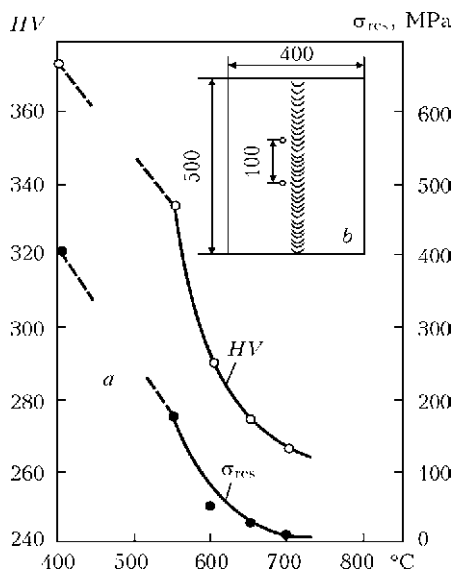
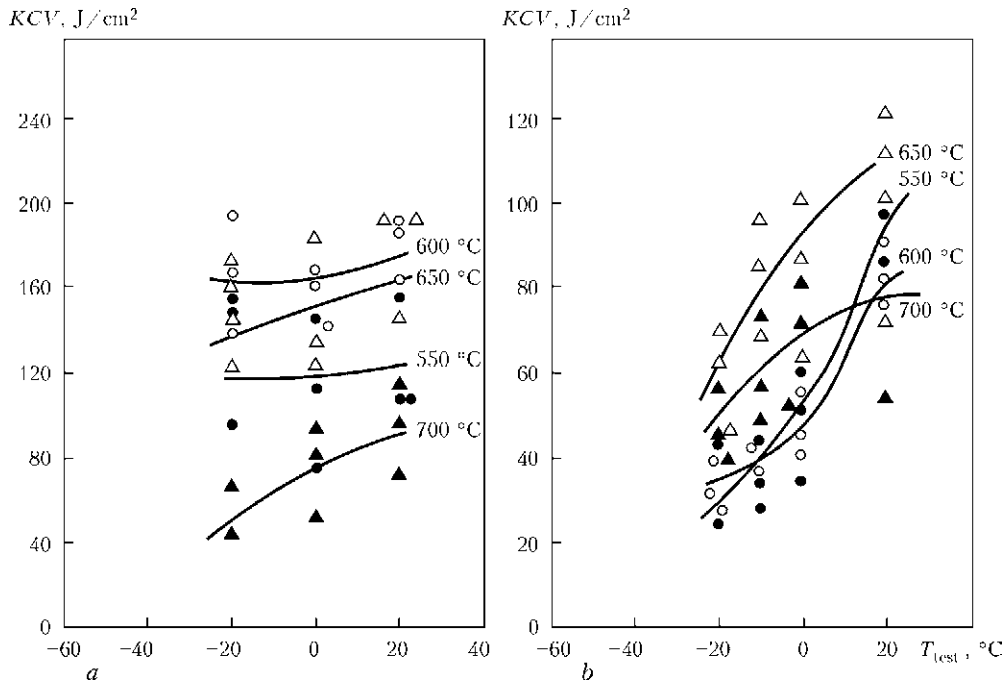


Figure 1. Effect of annealing for 2 h on residual stresses and hardness (*a*) in the weld zone on specimen (*b*) of 10GN2MFA steel



**Figure 2.** Effect of annealing at different temperature for 6 h on impact toughness of near-weld zone (HAZ + 0.5 mm) (a) and central zone of weld (b) of the steel 10GN2MFA welded joint

ing. As is seen from Figure 3, in low-alloy steel 10GN2MFA at about 600 °C sharp decrease of allowable applied stress is observed. Fracture surface of samples tested as in [1], is finecrystalline, which is the result of annealing cracks formation. Based on the results of this study a conclusion is drawn that for this steel heat treatment temperatures of only below 580 °C are not dangerous by the condition of annealing cracks formation in HAZ [1].

These data show that choice of rational temperatures and duration of high annealing of welded joints of modern structural steels, requires accurate observance of the above parameters, whose provision in local annealing, in its turn, involves the necessity to carefully choose energy parameters of heating and cooling conditions. To solve such a problem, in each specific case, it is desirable to apply different estimation methods, since it enables to essentially reduce resources and time for the elaboration of rational local annealing conditions [5, 6, etc.].

Clearly, the experiment is the final stage, necessary for taking the decision. In modelling local annealing process, models and estimational algorithms of welding thermomechanics of respective materials, based on physical model of strain-plasto-elastic medium, for instance in the form of [7], can be used, i.e. total of increments of non-elastic strain tensor of instantaneous plasticity  $\varepsilon_{ij}^p$  and diffusion ductility (creeping)  $\varepsilon_{ij}^c$  are determined on the basis of the flow theory in the following form:

$$d\varepsilon_{ij}^p + d\varepsilon_{ij}^c = (d\lambda + \Omega dt)(\sigma_{ij} - \delta_{ij}\sigma) \quad (2)$$

$(i, j = x, y, z).$

Here scalar factor  $d\lambda$  characterizes development of strains  $d\varepsilon_{ij}^p$  and is determined by yield condition (for instance, that of Mises [7]), while scalar factor  $\Omega$ , i.e. a function of material creeping, is usually assumed

for this purpose on the basis of theory of short-term creeping [8] in the following form:

$$\Omega = \Omega_1(T)\Omega_2(\sigma_i), \quad (3)$$

where  $\Omega_1(T)$  is the temperature function;  $\Omega_2(\sigma_i)$  is the stress intensity function  $\sigma_i$  (equivalent stress):

$$\sigma_i = \frac{1}{\sqrt{2}} \times \sqrt{(\sigma_{xx} - \sigma_{yy})^2 + (\sigma_{xx} - \sigma_{zz})^2 + (\sigma_{yy} - \sigma_{zz})^2 + 6(\sigma_{xy}^2 + \sigma_{xz}^2 + \sigma_{yz}^2)}. \quad (4)$$

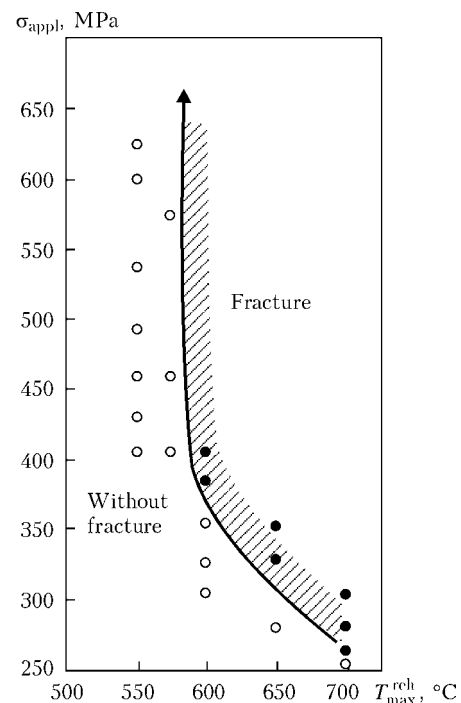


**Figure 3.** Effect of stresses and maximum temperature of re-heating on annealing cracks formation in the steel 10GN2MFA notched samples after thermal cycling simulation at  $T_{\max} = 1300$  °C,  $\Delta t_{8/5} = 100$  s,  $\Delta\lambda \approx 0.8-1.4$  (1)

**Table 1.** Values of  $\Omega_1(T)$  depending on  $T$  for  $n = 5.0$  and  $4.2$  [6]

$T, ^\circ\text{C}$	450	500	600	625
$1.5\Omega_1 (n = 5.0)$	$4.19 \cdot 10^{-22}$	$1.65 \cdot 10^{-18}$	$1.67 \cdot 10^{-16}$	$6.67 \cdot 10^{-16}$
$1.5\Omega_1 (n = 4.2)$	$2.64 \cdot 10^{-21}$	$1.05 \cdot 10^{-17}$	$1.05 \cdot 10^{-15}$	$4.20 \cdot 10^{-15}$

Values of  $\Omega_1(T)$  and  $\Omega_2(\sigma_i)$  are determined experimentally from simple tensile or torsion testing of samples of the given material.

As an example of such an approach to solving the problem of optimizing parameters of local heat treatment of welded joints, the above-mentioned work [6] can be mentioned, where this problem is solved as applied to circumferential pipe butts. In modeling as in [6],  $\Omega_2(\sigma_i) = \sigma_i^n$  was assumed ( $n$  is the index of a power, which selected from within 4.2–5.0 range), while  $\Omega_1(T)$  is as

in Table 1. One of the interesting conclusions of that work is recommendation regarding the width of circumferential heating band from the point of view of rather efficient relaxation of welding stresses and non-appearance of an appreciable field of new residual stresses due to local character of heat treatment. It was shown that for steel pipes, width of circumferential heating band of  $2B = 5\sqrt{R\delta}$  ( $2R$  is the pipe diameter;  $\delta$  is the wall thickness), is quite sufficient for the said purpose at maximum heating temperature of 620 °C, and holding at that temperature for 1 h.

Such a recommendation accords quite well with existing standards [9, 10] and underlines insufficiency of recommendations of [11], where  $2B = 5\delta$  at  $R > \delta$ .

It should be noted that by far not always it is possible to obtain such a simple recommendation regarding the dimensions of the heating zone in local heat treatment of circumferential welded joints.

Figure 4, *a-c* shows data on location of the welded joint 111/1 in steam generators PG-1000M of power reactors WWER-1000. This circumferential one-sided butt weld (Figure 4, *a*) connects steam generator shell with the collector. Thicknesses of materials to be joined are of about 72.5 mm with outer diameter of about 1200 mm. Graphs of intermediate and final high annealing are shown in Figure 4, *b*, while schematic of heating elements installation is shown in Figure 4, *c*. Base material is steel 10GN2MFA.

Regardless of rather lengthy soaking and slow cooling of the heating zone (see Figure 4, *b*), rigidity of the welded joint causes after annealing occurrence of the new field of residual stresses, when the level of circumferential stresses  $\sigma_{\beta\beta}$  of Figure 5 in the weld zone is of the order of 200–230 MPa. These data were obtained by calculations [7]. Creep function in the form of (3) at  $n = 5$  was used.

For  $\Omega_1(T)$  experimental data, obtained in [1] on samples of the steel considered (see Figure 1), are described by the dependence:

$$\Omega_1(T), \text{MPa}^{-6} \cdot \text{h}^{-1} = \begin{matrix} 550 & 600 & 650 & 700 \\ 0.43 \cdot 10^{-17} & 1.13 \cdot 10^{-15} & 1.73 \cdot 10^{-14} & 3.77 \cdot 10^{-12} \end{matrix} \cdot (5)$$

Calculations were conducted using WELDPREDICTIONS software package developed at PWI.

As the working stresses  $\sigma_{\beta\beta}$  in the zone considered do not exceed 50 MPa, so shown in Figure 5 level of residual stresses for steel 10GN2MFA at service temperatures of about 300 °C, raises no concern as to the corrosion crack occurrence, but this is true only in the absence of the defects capable of becoming origins for the development of such cracks. Unfortunately, design of the joint in question substantially complicates access to the inner surface, while industrial plant technology of performing such a joint does not reliably provide a quality formation of the inner surface. Therefore, in such cases the risk of occurrence of stress

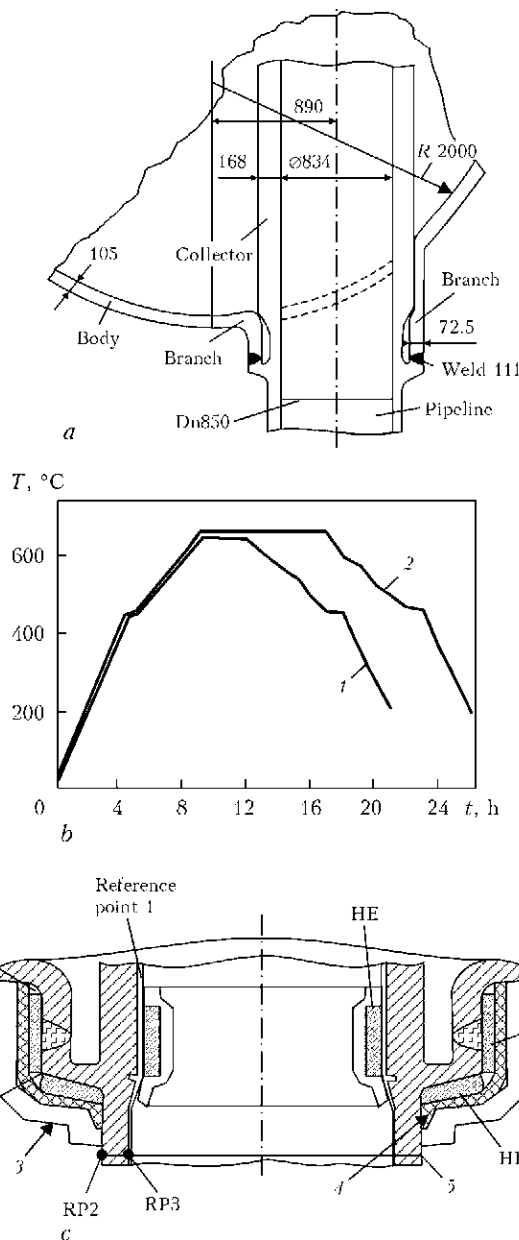


**Figure 4.** Sketch of weld 111/1 location in PG-1000M steam generator (*a*), thermal cycles of intermediate (*1*) and final (*2*) high annealing (*b*), and location of heating elements (*c*): 3 – reinforced basalt sheet; 4 – ceramic mat; 5 – assembly weld Dn 850

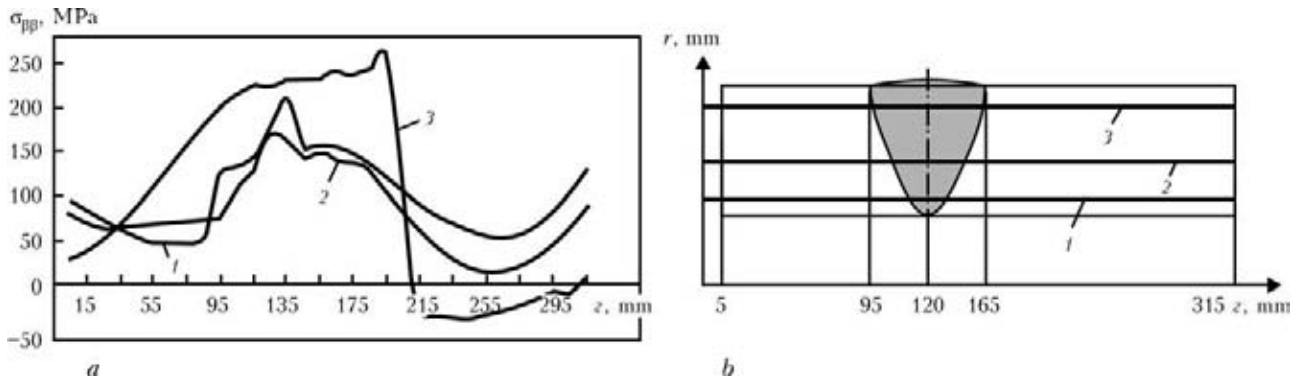


Figure 5. Residual circumferential stresses (a) in the near-weld zone 111/1 (b) for  $r = 597$  (1), 627 (2) and 667 (3) mm

corrosion cracks is quite real, which is demonstrated by the data of Figure 6 on defectograms of transverse cracks in weld 111/1 of steam generator of the Yuzhno-Ukrainskaya NPP.

Characteristically, that NDT of these sections of the welded joint, conducted about 2 years before the discovery of these cracks, had not revealed any noticeable traces of said defects.

These defects, of obviously corrosion type, show that material of welded joint zone during said service period, has substantially lost its capability to withstand the development of such defects. In other words, threshold values of stress intensity factors  $K_{ISCC}$  (Figure 7) for stress corrosion, separating the phase of stress corrosion crack development, when mechanism of electrochemical corrosion prevails, from the second phase, when hydrogen embrittlement mechanism predominates, is sharply reduced as compared to observed along the contour of cracks values of  $K_I$  ( $K_I$  is the SIF for normal tear cracks). Results of  $K_I$  calculation for cracks of Figure 6 with account of acting residual stresses (see Figure 5), and stresses of operational load not exceeding 25 % of the residual stresses, are

entered in Table 2. Procedure of description of a real crack with equivalent semi-elliptical one, with semi-axes  $a$  and  $c$  [12], was used.

It is seen that maximum values of  $K_I(G)$  do not exceed  $75 \text{ MPa}\cdot\text{m}^{1/2}$  for the deepest crack, while for this steel  $K_{ISCC}$  in its initial state is not below  $100 \text{ MPa}\cdot\text{m}^{1/2}$  under conditions considered, i.e. there occurs a substantial degradation of  $K_{ISCC}$  value (by at least a factor of 5).

The latter can be attributed to the inappropriate conditions of high annealing, when lengthy soaking at high temperatures (see Figure 4, b) can cause formation of small defects of the above type, i.e. annealing cracks (Figure 8) located along the grain boundaries, which naturally eases development of inter-crystalline stress corrosion cracks.

This example demonstrates how unsuccessful was the choice of technological parameters of local high annealing both from the point of view of non-relaxed residual stresses, and from the point of view of degradation of material properties.

With decreasing level of non-relaxed residual stresses down to 70–100 MPa,  $K_I$  values in Table 2

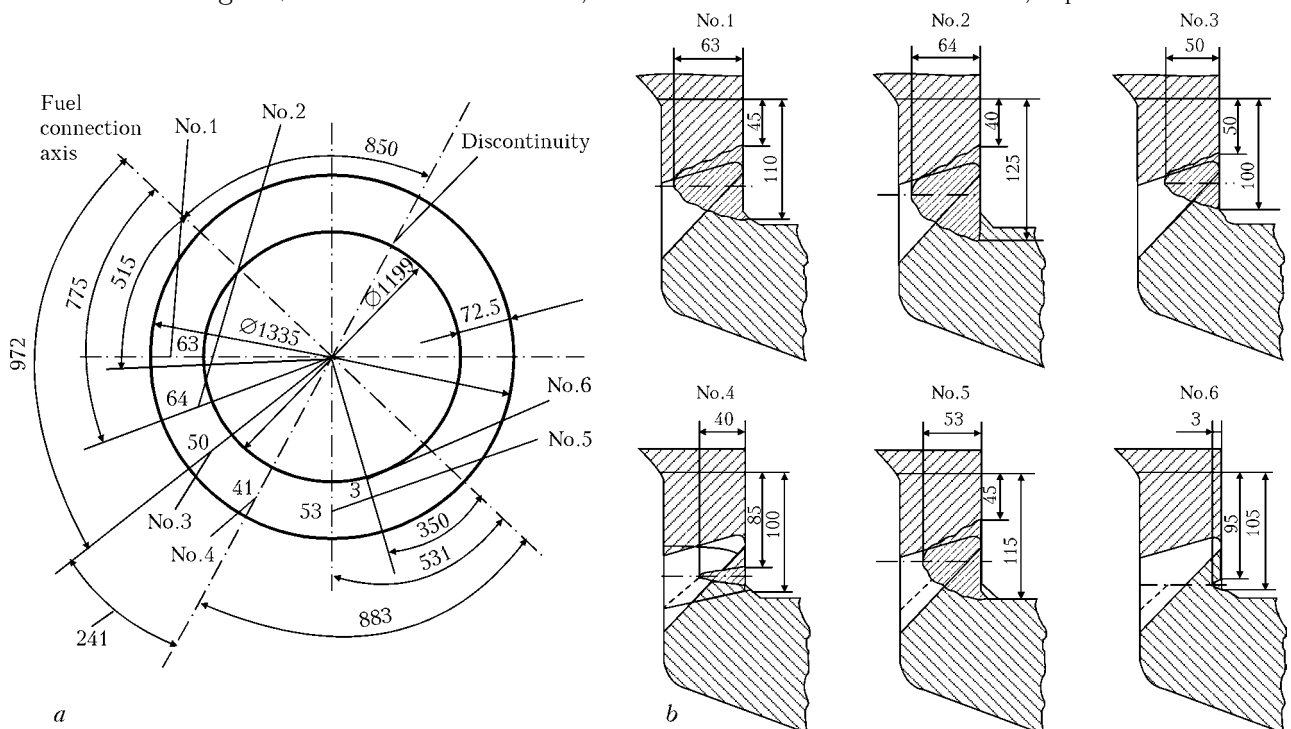


Figure 6. Diagram of defects location on the «hot» PG-1 vapor generator collector in unit 1 along the weld circumference (a), and dimensions and shape of detected defects Nos. 1–6 (b)

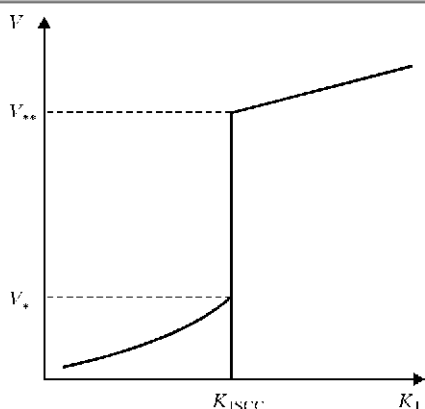


Figure 7. Schematic  $V-K_1$  diagram:  $V_*$ ,  $V_{**}$  – growth rates at  $K_1 = K_{ISCC}$  by electrochemical corrosion and hydrogen embrittlement mechanism

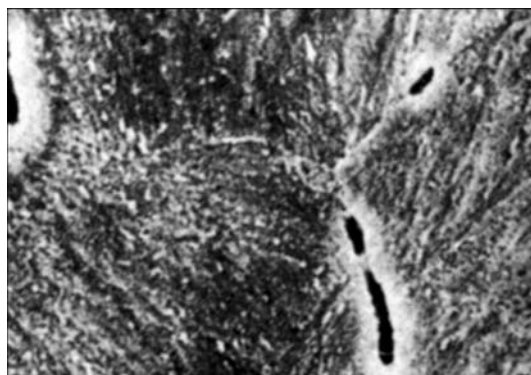


Figure 8. Emergence of cavities at the initial stage of annealing cracks formation in the HAZ on low-alloyed steel

Table 2. Dimensions of defects of equivalent crack, and values of  $K_I(G)$  and  $K_I(D)$

Steam generator	Defect No.	Defect size, mm		Equivalent crack				Semielliptical crack sketch
		Depth $H$	Width $2l$	$a$ , mm	$c$ , mm	$K_I(G)$ , MPa·m <sup>1/2</sup>	$K_I(D)$ , MPa·m <sup>1/2</sup>	
Steam generator 1 (1st unit)	1	63	65	51.2	51.2	59.24	41.18	
	2	64	85	59.0	59.0	70.18	45.20	
	3	50	50	40.0	40.0	45.11	35.50	
	4	40	15	19.6	19.6	26.75	24.34	
	5	53	70	48.7	48.7	55.75	39.90	
	6	3	10	3.0	5.0	10.60	12.15	
Steam generator 2 (2nd unit)	1	8	15	8.8	8.8	17.82	16.34	
	2	50	25	28.3	28.3	33.90	29.40	
	3	40	15	19.6	19.6	26.75	24.34	
	4	35	30	25.9	25.9	31.86	28.07	
	5	10	25	10.0	12.5	19.29	19.63	
	6	48	72	47.0	47.0	53.45	39.04	

will decrease approximately twice, and, respectively, already at crack of  $8 \times 15$  mm,  $K_I$  values of along the contour will be below  $K_{ISCC}$ . Since cracks of such dimensions in NDT are difficult not to notice, such a local annealing could have considerably increase the resistance to defects of the type shown in Figure 6. On the other hand, if parameters of high annealing applied ( $T_{max}$  and duration of staying at  $T_{max}$ ), did not cause reduction of value  $K_{ISCC}$  of the welded joint material, then even at said residual stresses (see Figure 5), such considerable defects would not have appeared (see Figure 6).

This example shows that in a number of cases selection of parameters of local heat treatment of welds requires certain compromise solutions, both from the point of view of relaxation of residual stresses, and of possible degradation of material properties with account of specific conditions of structure service.

**CONCLUSIONS**

1. The process of choosing rational parameters of local heat treatment of welded joints of modern structures, requires applying rather careful solutions as regards dimensions of the heated zone, maximum heating temperature and duration of soaking the material at high-

temperatures, depending on specific conditions of structure service.

2. Application of the means of mathematical modelling enables to considerably ease obtaining rational solutions for specific welded joints and materials.

- Hrivnyak, I. (1984) *Weldability of steels*. Moscow: Mashinostroenie.
- Nakamura, H., Naiki, T., Okabayashi, H. (1969) Stress relief cracking in HAZ. *IIW Doc. IX-548-69, X-531-69*.
- Ito, Y., Nakanishi, M. (1972) Study of stress relief cracking in welded low alloy steels. *IIW Doc. X-668-72*.
- Kameda, Y., Takahashi, H., Suzuki, M. (1976) Residual stress relief and local embrittlement of weld HAZ in reactor pressure vessel steels (SA 533 grade B, Cl. 1). *IIW Doc. IX-1002-76, X-800-76*.
- Wang, J., Lu, H., Murakama, H. (1998) Mechanical behavior in local heat treatment. Part 4: Visco-elasto-plastic FEM analysis in local PWHT. *Transact. of JWRI*, 27(1), p. 83-88.
- Lu, H., Wang, J., Murakama, H. (1999) Mechanical behavior in local heat treatment. Part 1: Influence of residual stress distribution in multi-pass welding. *Ibid.*, 28(1), p. 55-60.
- Makhnenko, V.I. (1976) *Computational methods for investigation of welding stress and strain kinetics*. Kiev: Naukova Dumka.
- Rabotnov, Yu.N., Milejko, S.G. (1970) *Shot-term creeping*. Moscow: Nauka.
- McEnerney, I.W. (1998) Recommended practices of welds in pipe and tubing. *ANSI/AWS D10.10-9X*.
- (1998) *AS 1210*: Australian standard unfired pressure vessels code.
- (1997) *BSS 500*: British standard specification for unfired fusion welded pressure vessel.
- (1990) *MR-125-01-90*: Calculation of stress intensity factors and section weakening for defects in welded joints. Kiev.

# FINITE ELEMENT SIMULATION OF THE CONTINUOUS RF AND THE HF WELDING PROCESS OF INTERNAL HIGH-PRESSURE TUBES

U. SEMMLER<sup>1</sup>, G. von BREITENBACH<sup>2</sup> and A. SEDLMAIER<sup>3</sup>

<sup>1</sup>Chemnitz University of Technology, Germany

<sup>2</sup>Darmstadt University of Technology, Germany

<sup>3</sup>DataM Software GmbH, Valley/Oberlindern, Germany

The paper deals with the continuous roll forming (RF) and high-frequency (HF) welding processes of internal high-pressure (IHP) tubes. Models of the RF process and the induction forced HF welding are presented using the finite element code MSC.MARC/Mentat™. In early works as a rule the tube forming was considered as an isothermal elastic-plastic deformation process. So it was impossible to investigate the influence of the temperature field on tube properties in the weld and heat-affected zone. The HF welding has been considered separately without coupling to the forming process. In so-called V-weld the coil edges are heated by induction. Pressing the hot edges against each other some material is forged into the weld bulges, which must be cut off straight after the welding point. Without the consideration of these forging and cutting processes this material portion must be removed from the simulation models before the coil edges touch each other. In the paper a complete non-isothermal elastic-plastic numerical simulation method is presented including the RF, transient temperature fields during welding, bulge cut-off, temperature behavior in cooling, and tube calibration. The simulations are performed for four different roll geometries and two materials. The results are compared with real process measurements. Using numerical simulation the forming and welding process parameters are modified in order to improve the IHP tube properties by homogenization of the thickness and minimization of the total equivalent plastic strain.

Tube hydroforming (THF) is an established technology among metal tube forming processes. It is the technology used to form closed sections, hollow parts with different cross-sections by applying an internal hydraulic pressure and sometimes additional axial compressive loads to force a tubular blank to conform to the shape of a given die cavity. Material properties have a significant influence on the process stability. Often roll-formed, non-heat-treated tubular materials with longitudinally oriented welding lines are used in THF. Figure 1 shows a scheme of a roll forming line, where the parts of the production line considered here are marked by boxes.

Different production processes involve a change of the material properties from the initial flat sheet to the hydroformable tube. FE analysis of the roll forming (RF) process seeks to improve the hydroformability of tubular semi-finished products. Testing methods, such as tensile tests and conventional forming limit diagrams, do not accurately reflect the state of stress and strain conditions seen in the tubular blank during the hydroforming process.

Material properties significantly influence the stability of forming processes. The prediction of the hydroformability of roll-formed tubes is nowadays often based on estimations using tensile test data. The RF and welding technology influence the material

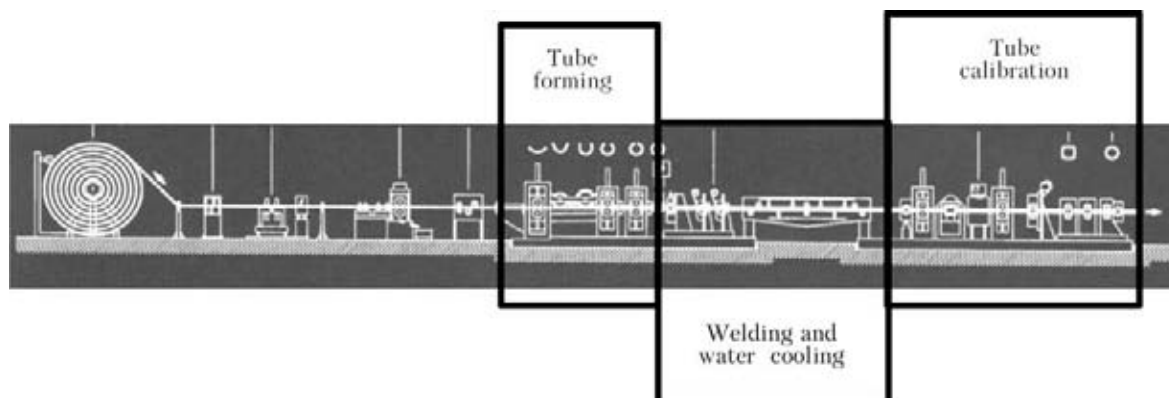


Figure 1. Scheme of roll forming line with the sections in consideration

involving pre-strains and hardening. Therefore, the geometrical and mechanical properties of the tubular semi-finished product differ from the ones of the virgin sheet material.

#### Objectives of the presented work

During the RF process the original sheet material underlies deformations in bending as well as in longitudinal direction. These deformation cause changes in the strip wall thickness and lead to plastic hardening of the sheet material. It is apparent that a varying wall thickness about the tube circumference implies varying hydroforming ability for different angular directions. The accumulated and varying in circumferential direction total equivalent plastic strain (TEPS) reduces tube forming capabilities.

That's why the main goal of the project was to investigate how the materials, geometric and process parameters influence the internal high-pressure (IHP) tube properties. The numerical simulation allows monitoring of the characteristic values during of the forming and welding processes. When known how the rolls geometries and positions influence the TEPS and the wall thickness distribution, one has the possibility to improve and optimize the process by changing the sequence, the size, and the position of the rolls.

Using the finite element programs MSC.MARC/Mentat™ and COPRA® FEA RF 4 real forming strategies of two companies (Benteler Stahl/Rohr GmbH in Paderborn, Germany, and Jansen AG in Oberriet, Switzerland) have been investigated. The produced tubes have been inspected experimentally and compared with the simulation results. The tubes and materials parameters were as follows: final tube diameter of 60 mm (60.5 mm before calibration); tube wall thickness of 2 mm; StW24Ti (DD11) and S500MC high-strength steels for cold forming; welding speed of 50–55 m/min; welding frequency of 304 kHz.

Based on analytical and experimental methods, the subsequent work packages were successfully performed within this project.

In numerical simulation:

- set-up of a simulation model for the tube forming and welding processes including the formation and the cut-off of the welding seam bulges;
- analysis of different tube forming strategies in regard of the resulting tube properties based on FEM;
- inclusion of the welding process into the complete FE simulation of the tube forming process;
- optimization of one tube forming strategy using FE simulation.

In experimental analysis:

- free bulge tests for the characterization of the mechanical tube properties in hydroforming;
- geometric tube and split strip characterization;
- microhardness measurements.

As final result some recommendations for the production of tubes with enhanced properties for hydroforming were given.

#### FE simulation of the RF and HF welding processes

**FE models of RF.** In order to produce tubular semi-products with improved hydroforming properties, it is necessary to analyze the RF process. Experimentally to investigate the development of the tubes properties during the passing through the sequent roll stands is impossible or very difficult. For this purpose, a FE simulation model was developed. In the FEA one can trace the development of the wall thickness and TEPS, representing the materials hardening during RF and welding.

The simulation of the RF process offers the possibility to analyze and understand the phenomena which lead to a property change from the initial blank or coil to the tubular semi-finished product. Single roll geometries can be adapted or new stands can be implemented to improve the forming of tubular semi-finished products for hydroforming.

FE modeling was done using the FE programs MSC.MARC/Mentat™ and COPRA FEA RF™. The last one was developed by the dataM GmbH for the simulation of the RF process. COPRA FEA RF™ contains MSC.MARC™ as an OEM product. The program offers a comfortable GUI for the development of the rolls geometry (rigid contact surfaces), of the strip model (hexahedron elements) and the solution process control with direct coupling to several pre-models (rough assessment of the RF process) and roll geometry measurements.

As a matter of fact, COPRA® FEA RF can be regarded as a «virtual RF mill» that allows the user to try out new roll sets even before the actual manufacturing process. COPRA® FEA can be operated easily and runs on any personal computer. It does not require any time-consuming pre-processing or difficult post-processings. It is tailored to the roll former's needs.

The model illustrated in Figure 2 shows one of the mentioned four real roll lines. The model consists of 24 roll stands including break down stands, fin passes, welding station, calibration stands and side rolls. Because of simplifications considering the welding process calculation and the water bath cooling (see below) the distance between the forming section and the welding station, as well as the distance between the welding station and the calibration stands, were minimized for decreased computation times. The contact between the rolls and the workpiece is modeled as frictionless. Rolls were modeled as segments and represent only the contour of the roll which is in contact with the workpiece. In order to further minimize the computation time, only one half of the tube was simulated (symmetry) and the sheet length of about 1200 mm was limited on a length of 3 to 4 times the distance between the stands. This length guarantees a realistic reproduction of the longitudinal strains typical for RF processes. The mesh is partially refined (Figure 3, left side) in order to reach a high resolution of the geometric and thermo-mechanical



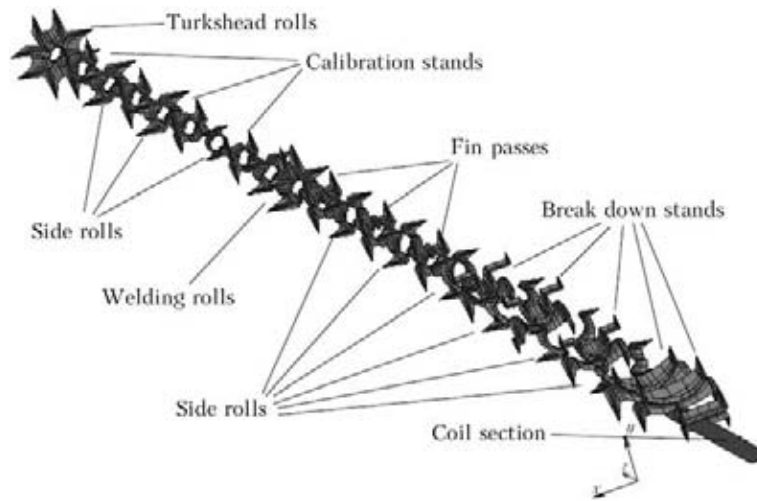


Figure 2. Simulation model for FE analysis

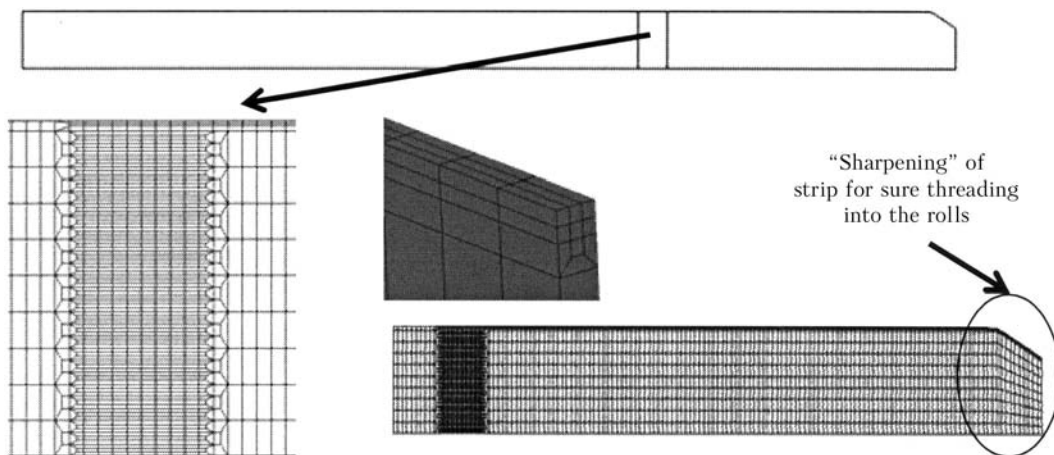


Figure 3. FE model of strip section (details)

values of interest. The total length is about 8400 mm. The number of stands and the length of the modeled coil section are slightly different for the investigated four different forming strategies.

The coil sections consist of 4000–6000 tri-linear hexahedron elements (see Figure 3). The strip section length of about 1200 mm is chosen that the strip has a sure guidance at in 3 stands (the distance of neighbor roll is 350 mm).

The calculation of the refined model over 4800 time amounts 7 days on a well equipped PC (2 GHz CPU).

**FE models of the HF welding process.** In former works as a rule the tube forming was considered as an isothermal elastic-plastic deformation process. So it was impossible to investigate the influence of the temperature field on the tube properties in the weld seam and in the HAZ. That's why one of the main goals of the project was the inclusion of the HF welding process into the over-all simulation of RF and calibration.

In order to avoid program interfaces between several programs with necessary program flow interruptions and loss of accuracy the welding simulation uses the same FE code MSC.MARC/Mentat™ as a unitary FE basic.

From the physical point of view an accurate determination of the temperature distribution requires the solution of the Maxwell equations in the neighborhood of the welding rolls including a detailed geometrical model of the inductor, the impeder, and the strip edges forming the so-called V-weld and touching each other in the welding point between the welding rolls. Figure 4 shows the calculated by FEM in work [1] heat source distribution.

Because of the so-called skin-effect during HF induction the heat generation occurs in a very small region at the surface of the V-weld. The solution of

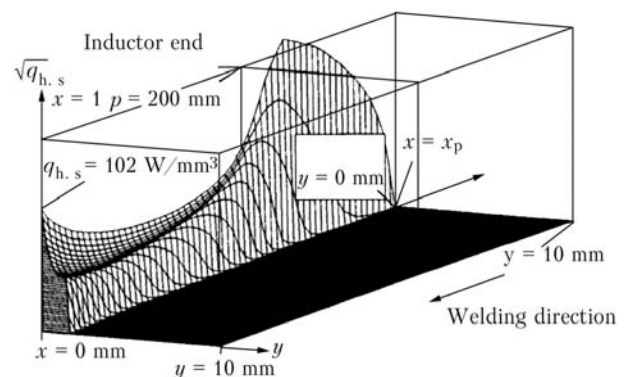


Figure 4. FEM-calculated heat source distribution [1]:  $y$  – depth in the V-edge

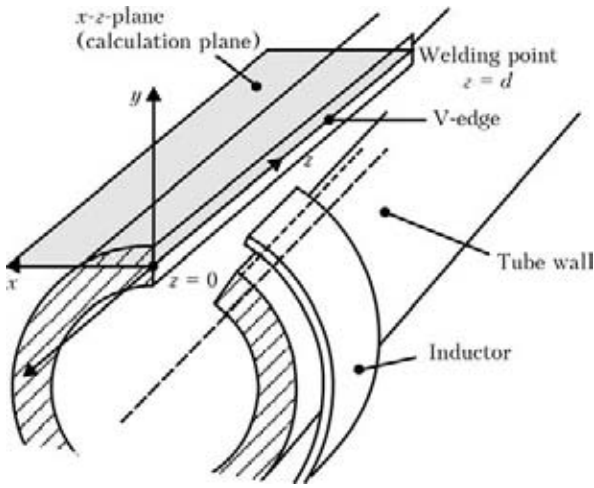


Figure 5. Idealized model for HF heat source calculation

the Maxwell's equations as a part of the over-all RF process simulation would require a very fine mesh in the strip edges. This is impossible by taking into account the high computing times. That's why a compromise with a «3x3+1»-refinement in the strip edges (see Figure 3, middle) was chosen. This relatively coarse mesh requires a simplified model of the HF heat generation [2]. The heat generation is considered in *x-z*-plane shown in Figure 5. The heat conduction in the *y*-direction is neglected and there is no gradient over the wall thickness. By means of these model idealizations it is possible to calculate the needed electrical power  $P_0$  to reach a temperature of  $T = T_0 + \Delta T$ :

$$P_0 = \frac{3\pi\Delta T y_0 d \lambda}{2\xi \left[ \left( \frac{\pi y_0 a}{\xi^2 v_0} + 1 \right)^{3/2 - 1} - \left( \frac{\pi y_0 a}{\xi^2 v_0} \right)^{3/2} - 1 \right]}$$

where  $\lambda$  is the heat conduction coefficient;  $d$  is the strip thickness;  $y_0$  is the distance between inductor and welding point;  $v_0$  is the welding speed;  $a = \frac{\lambda}{\rho c_p}$  is the temperature conductivity;  $\xi = \sqrt{\frac{1}{\pi f \mu \sigma}}$  is the «electrical reference depth»;  $f$  is the frequency;  $\mu = \mu_0 \mu_r$  is the magnetic permeability;  $\sigma$  is the electrical conductivity.

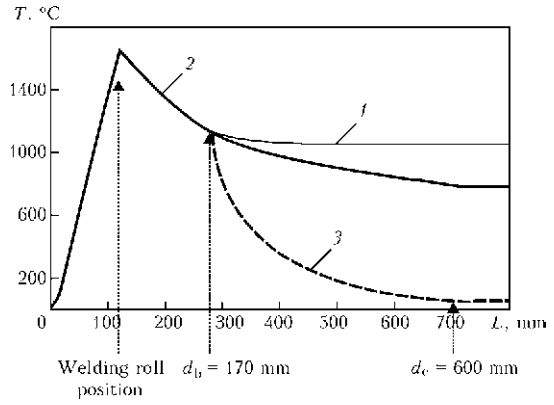


Figure 7. Dependence of the weld seam temperature on heat transfer coefficient: 1 –  $\alpha = 0$ ; 2 – 0.05; 3 – 0.05 W/(K·mm<sup>2</sup>);  $d_b$ ,  $d_c$  – beginning and end of cooling bath, respectively;  $L$  – length direction

The «3x3+1»-refinement compromise (element cross section of about  $0.7 \times 0.7 \text{ mm}^2$ ) cannot sufficiently represent the real temperature gradients in the edges of the V-weld (see Figure 4). That's why the calculated total electric power  $P_0$  has been evenly distributed along the weld V-edges between the end of conductor and the welding point like surface or volume heat sources.

In spite of relatively coarse meshing with element aspect ratios greater than 5, the calculated temperature fields match the real temperature sufficiently good. Figure 6 shows an macrograph of the weld seam cross section in comparison with the calculated 800 °C isoline when the strip edge passes through the welding point.

**FE models of water cooling.** After welding the tubes pass through a water tank positioned between the welding rolls and the first calibration stand (see Figure 1). The real distances between these two stands are in the considered tube production lines 7310–8000 mm. When simulating the cooling with real heat transfer conditions, the coil section with a length of about 1200 mm has to be guided about a distance of some meters by means of auxiliary supports. This complicates the model and consumes a lot of computing time.

So in the simulation the distance was increased to twice of the average stand distance (700 mm). The 10 times artificially shortened water tank length must be compensated by a super elevation of the heat tran-

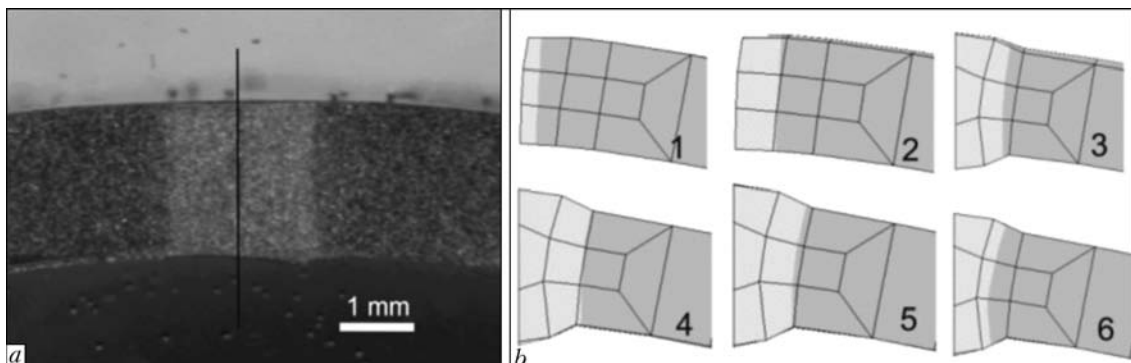


Figure 6. Weld seam macrograph (a), and snapshots of strip edge cross section at positions -60, -30, 0, 30, 60, 90 mm (1–6) relatively to the welding point with the 800 °C isoline (b)

sfer coefficient. In literature one can find quite different values for the heat transfer coefficient between metal surface and circling water. The average value is  $\alpha = 0.005 \text{ W}/(\text{K}\cdot\text{mm}^2)$ . Figure 7 shows how the heat transfer coefficient influences the weld seam temperature about the artificial shortened water tank length.

In spite of the simple modeling of the heat source and of relative coarse mesh in the strip edges good temperature field are computed. Because of the skin effect of the electric current the surface source matches the reality better than volume sources.

Figure 8 shows in temperature calculation considered nodes on outer and inner tube sides, and Figure 9 shows the temperature profiles of the marked in Figure 8 nodes. The two lower diagrams are cut-outs in proximity of beginning and end of cooling. The temperature between 40 and 60 °C reached at the end of water bath is near to reality. The temperature gradients over the wall thickness are too high. Improvement may be achieved by anisotropic heat conduction with artificially increased heat conduction in the radial direction.

In the used FE approximation the assessment of the phase kinetics and of the metal structure behavior is impossible because of smoothed temperature gradients and artificially increased cooling regime (the temperature gradient  $\Delta T$  in a single element may be greater than 400 °C).

**Modeling of the weld bulge cutting-off.** Without consideration of the thermoplastic weld bulge formation of the so-called welding allowance (the part of

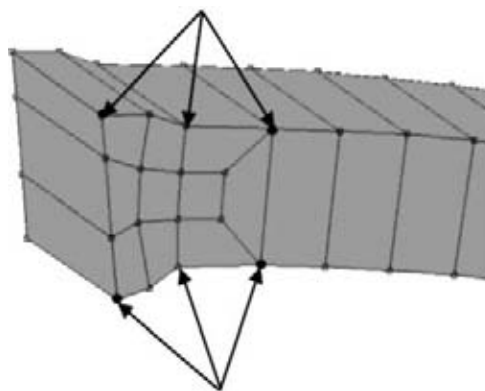


Figure 8. Nodes on outer and inner tube sides

the material which will be forged into the weld bulge) must be omitted from the coil breadth either from the beginning of the simulation process or immediately before the welding rolls. In the simulation process after touching each other the coil edges will stuck together using the «glue contact» facility of the FE programs. In that case one must know the real magnitude of the welding allowance.

If taking into account the real coil breadth and if considering the forming and welding process like coupled thermoplastic models the welding bulges must be cut off during the simulation in analogy to the real tube production process. Unfortunately it is impossible to use of internal program facilities for the simulation of cutting processes (deactivation of elements). Elements may be deactivated only completely, and the size of the deformed elements and the relatively small number of elements in the coil edges

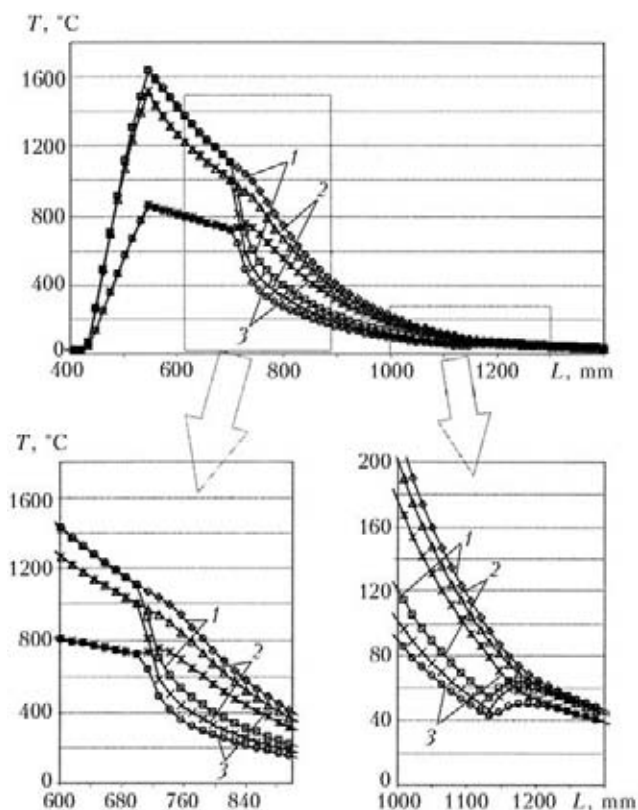
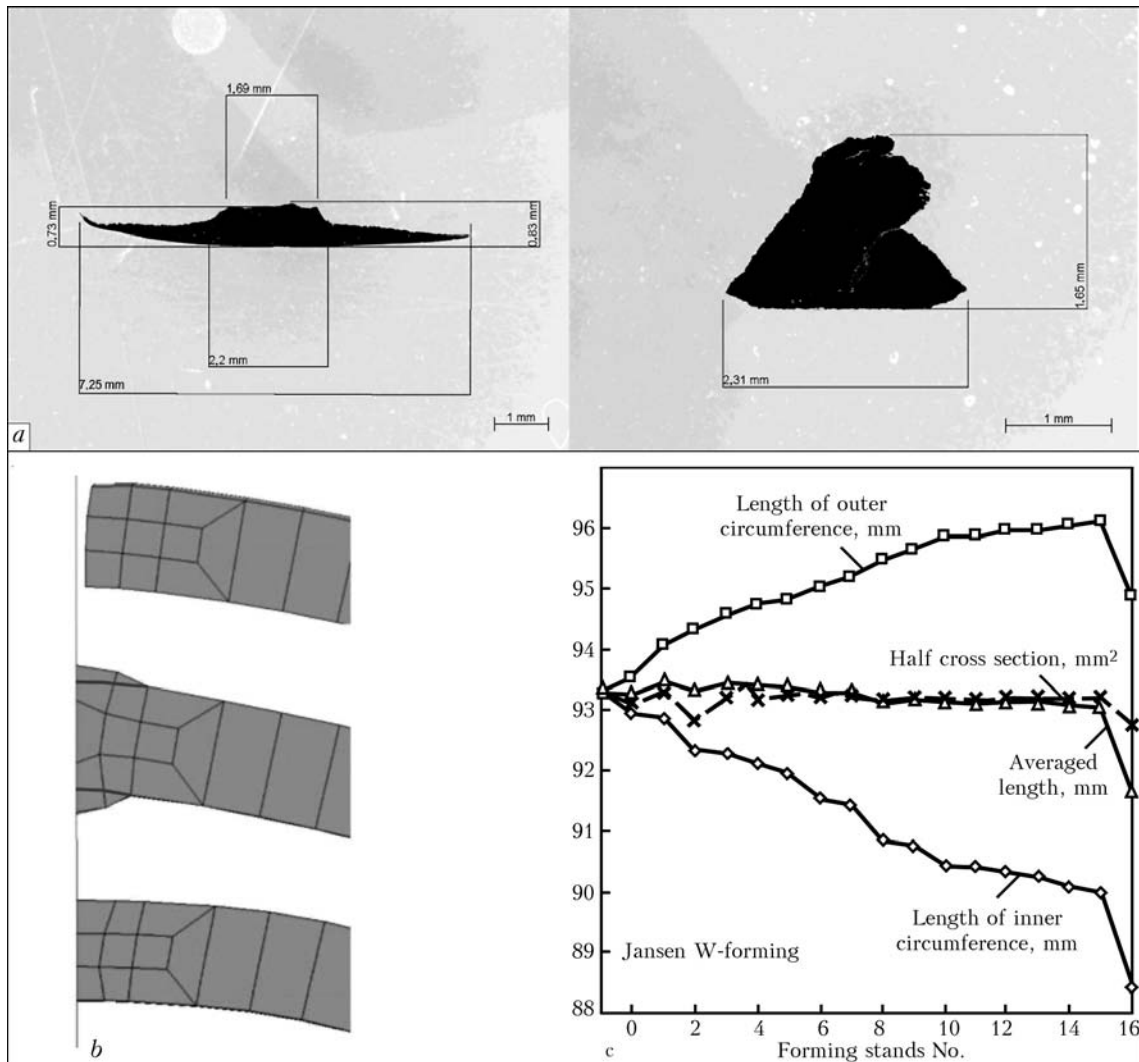


Figure 9. Temperature plot of the marked in Figure 8 nodes during HF heating and subsequent cooling in a depth of 0 (1), 1.5 (2) and 2.5 (3) mm



**Figure 10.** Cross sections of real inner and outer weld bulge chip (a), principle of weld bulge cut-off (b), and development of strip circumference over the forming and welding stands (c)

will produce a «jagged» surface, which is not suitable for further forming in the calibration rolls.

Some different ways have been tested to overcome this problem. As the only feasible way remained the modification of the deformed FE mesh using special adapter programs. In this adapter program the mesh may be deformed on the final tube contour as shown in Figure 10, b.

In order to compare the simulated weld bulge formation with the real process bulges, the inner and outer chips of weld bulge cutting have been measured. The total cross section area is  $5.6 \text{ mm}^2$  (Figure 10, a) resulting in a welding allowance of 2.8 mm (2 mm tube thickness).

An at least qualitatively right reflection of the real bulge sizes in the numerical simulation means: constant tube circumference over all forming stands and reduction in the welding stand by 1.4 mm (half of the welding allowance as only one half tube is modeled); constant tube cross section area as the material is incompressible; and area of the calculated welding bulge must be  $2.8 \text{ mm}^2$ .

Like seen in Figure 10, c, the tube cross section and its circumference are constant in the stands 1–16.

In the stand 15, the welding rolls, the circumferential reduction is the right one (1.4 mm) but simultaneously the cross area reduces perceptibly — a significant violation of the volume constant. The cross section of the calculated bulges amounts only  $0.45 \text{ mm}^2$  in contrast to needed  $2.8 \text{ mm}^2$ .

The significant difference between expected and calculated values means that the coarse elements in the coil edges with a bad aspect ratio (ratio of largest to smallest element edge) greater 5 are unable to reproduce the plastic behavior of the heated coil edges and the resulting stresses and strains. For a near to reality simulation of the thermoplastic weld bulge formation a much higher mesh refinement is necessary.

#### Experimental investigations

In order to measure the geometric and materials properties and to test the hydroformability of tubes, several testing methods were implemented. The geometrical property testing enables a first evaluation of the quality of the tube production process. The free bulge test provides information such as the maximum attainable circumferential expansion and the initial yield pressure of tubes. It can be used to detect variations in semi-finished product charges which lead to

process instability or to analyse the general hydroformability of tubes. Optical strain measurements are used to identify the effect of parameters, such as wall thickness or hardening distribution, onto the tube expansion behavior. Additionally, the bulge test with axial tensile and compression enables the establishment of so-called tube forming limit diagrams (FLD). The tube FLD help to select suitable tubular semi-finished products for hydroforming components. Inhomogeneous distributions of wall thickness and hardening result from specific local loading conditions of the formed sheet during RF.

A big number of tubes formed with all investigated several forming strategies were been tested and the correlation between the simulations and experiments were been carried out. Especially the optical strain analysis showed that the wall thickness distribution and the material hardening along the circumference are the crucial parameters resulting from the RF process.

The simulations of the RF processes assume that the virgin coil material is homogeneous in its mechanical properties and has a constant thickness and that the forming process is completed symmetric. But the measurements showed that the strip thickness varies as over the coil breadth as over the coil length and the resulting tube is unsymmetrical even for symmetrical initial coil geometry. The last fact is an indication that the rolls geometries are partially unsymmetrical.

The experimental methods and results of these experiments are discussed in detail in [3, 4].

## CONCLUSION

Summarizing the carried out simulation and experimental works the mean results are:

- by means of numerical simulations it is possible to calculate the mean properties of the tubes important for the THF process;
- by optimizing one of the four considered forming strategies a reduction of tube wall thickness changes by 53 % and a decrease of the TEPS by 22 % have been reached. At the same time the scattering of these properties reduced significantly;
- simplified models and the «3x3+1» mesh refinement in the strip edges allow a close to reality calculation of the temperature behavior during HF welding; the computation time increases only slightly;

- isothermal FE model for the forming simulation was further developed to a non-isothermal by using a moving Scott's heat source and by modifying the length and the heat transfer parameters during water cooling;

- but this model does not allow calculating the real temperature gradient in the strip edges, the metallurgical transformations, the strains and stresses and the real size and volume of the weld bulges;

- bulge tests showed an asymmetric strain distribution with minima near the weld bead at the 180° position;

- tube FLD show a high potential for the optimization of welded IHP tubes;

- comparison of simulations and experiments shows a symmetric distribution of thickness and plastic strain in all simulations but in the rule asymmetric distributions in the experiments;

- variation of the wall thickness about the tube circumference coincides quite well in simulations and experiments;

- calculated temperature fields in the welding zone and during water bath cooling are satisfying and coincide with the experimental data.

The asymmetry of the measured properties and the partially small correlation between simulation and experiment imply the need of further investigations to measure the real positions and the real profiles of the rolls (in order to locate rolls asymmetry), to investigate the property distribution in the initial coil, and to search for further influences on the tube hydroformability.

**Acknowledgement.** *The presented theoretical and experimental investigations were promoted and supported by the German Federal Ministry of Economics and Technology and by the European Research Association for Sheet Metal Working.*

1. Lessmann, H.-J. (1994) Elektromagnetische und thermische Vorgänge beim induktiven Langsnahtschweißen. Fortschrittsberichte VDI. Reihe 2. *Fertigungstechnik*, **325**.
2. Scott, P.F., Smith, W. (1996) The key parameters of high frequency welding. *Tube Int.*, **15(1)**, p. 147–152.
3. Groche, P., von Breitenbach, G. (2004) Tubular semi-finished product characterisation and optimisation for tube hydroforming. In: *Proc. of Int. Conf. on Innovations in Metal Forming & ERC Reunion* (Brescia, Sept. 23–24, 2004).
4. Groche, P., von Breitenbach, G. (2005) Einfluss des Rohrherstellungsprozesses auf den Innenhochdruck-Umformprozess. In: *4. Int. Konf. Hydroumformung* (Fellbach, Okt. 24–26, 2005). Bd. 4.

# MODELLING LATERAL DEFORMATIONS IN WELDING WITHOUT TACKING OF LARGE PLATES WITH ACCOUNT OF FRICTIONAL FORCES CREATED BY STATIONARY CLAMPS

P. SEYFFARTH<sup>1</sup>, V.I. MAKHNENKO<sup>2</sup> and E.A. VELIKOIVANENKO<sup>2</sup>

<sup>1</sup>Ingenieurtechnik und Maschinenbau GmbH, Rostok, Germany

<sup>2</sup>E.O. Paton Electric Welding Institute, NASU, Kiev, Ukraine

One of actual problems of modern shipbuilding is fusion welding without tacking joints of greater panels. The special stand is developed for keeping of a gap in necessary limits for in special cases welding by Ingenieurtechnik und Maschinenbau GmbH, Germany, with the motionless clips providing at certain pressure of force of friction, capable to keep welded edges from moving above possible. To question of numerical research of deformation of welded steel sheets of thickness up 3 to 19 mm at length of a joint up to 16 m taking into account forces of friction from clips devotes the present report. Influence of thickness of welded panels, modes and ways of welding on necessary sizes of forces of pressure in a clip is shown. In particular, it is shown that application of laser welding of joints at high speeds and low heat input the demanded size of forces of pressure can be essentially lowered in comparison with arc welding. It is shown that in welding panels 19 mm thick and above it is possible to use the stand with the clips, taking into account single-pass welding by two arches of panels of the maximal thickness of 12 mm, for welding without tacking a root pass.

In modern shipbuilding in welding large plates, ever-wider acceptance is gaining one-sided welding at a preset gap, ensuring quality formation of butt weld at preset fusion welding conditions. It is natural that in doing so, quite close tolerances of gap size are preset, and the problem of keeping such a gap in the process of welding with weld length of 16 m and more, arises. Using tacks is not desirable, since it involves an additional inefficient operation and at gaps of about 5 mm distorts the geometry of the butt weld in the tack zone.

Table 1 shows typical conditions of one-sided arc welding of steel plates butts, recommended in shipbuilding by JMG company, from which it is evident that the butt gap sizes during welding must remain, as preset for specific welding conditions, within certain limits. How rigorous are these limits of gap variation, is clearly demonstrated by estimated data of Figures 1–4, showing the results of modelling kinetics of deformational processes in welding 2000 mm wide

and 10000–16000 mm long plates under conditions of Table 1, and in the absence of tacks along the entire butt, but for its beginning and the end. At the ends powerful (through thickness) tacks, 60 mm long, are provided.

WELDPREDICTIONS software package, developed at PWI, was used. Welding was conducted with flux backing. Thermal cycle along the axis of the weld is shown in Figures 1, *b*–4, *b*. From the data of these figures it is evident that tolerance of  $\pm 0.1$  mm for variant 1 (see Table 1), at plate thickness  $\delta = 3$  mm as per line *A* in Figure 1, is not observed already after 1000 mm at total butt length of 16000 mm (by a gap closure mechanism). For variant 2 (see Figure 2) the tolerance of  $\pm 0.5$  mm is transgressed after about of 1500 mm at total butt length of 16000 mm, but now by a gap opening mechanism.

For variant (see Figure 3), tolerance of  $\pm 0.5$  mm is transgressed after 2000 mm by way of opening, but with overall butt length of 10000 mm.

**Table 1.** Considered variants of one-sided butt welding

Variant No.	Variant characteristics	$I_1$ , A	$I_2$ , A	$v_w$ , cm/s	Original gap, mm	Tolerance for edge displacement $\Delta U_y$ , mm
1	$\delta = 3$ mm, CO <sub>2</sub> welding, $U = 23.2$ V	230	–	0.620	1	$\pm 0.1$
2	$\delta = 12$ mm, submerged arc welding, two arcs, $U_1 = U_2 = 38$ V	950	420	0.783	5	$\pm 0.5$
3	$\delta = 12$ mm, submerged arc welding, two arcs, $U_1 = U_2 = 38$ V, additional filler	950	420	0.783	5	$\pm 0.5$
4	$\delta = 8$ mm, submerged arc welding, $U = 35.5$ V, additional filler	785	–	0.762	5	$\pm 0.5$

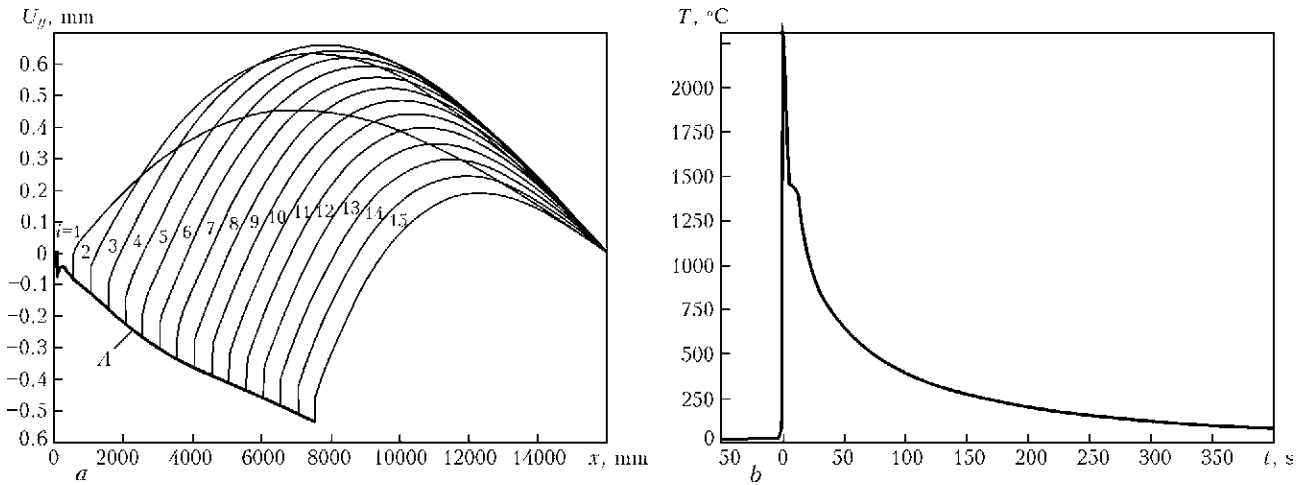


**Figure 1.** Displacement  $U_y$  along edge being welded for variant 1 without tacks (a), and thermal cycle along weld axis in linear portion of butt (b): curve number corresponds to position of welding source center  $x_s = 575 + (i - 1) \cdot 500$  mm, line A – to fixed by welding position of edges

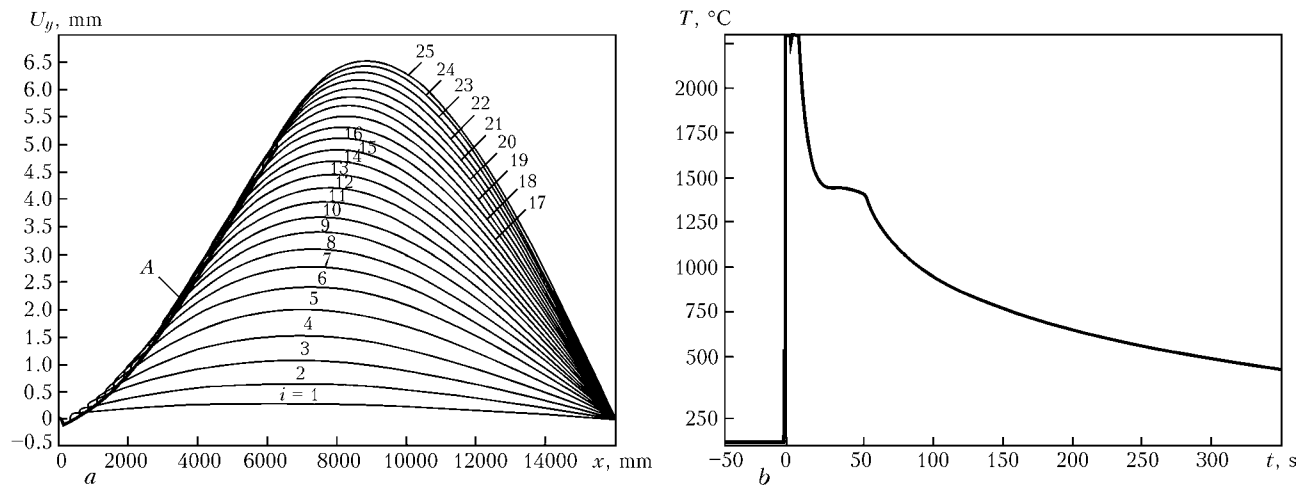


**Figure 2.** Results of calculation of  $U_y$  displacement variation kinetics along edge for variant 2 at  $Q = 0$  (a), and thermal cycle along weld axis (b): number of  $i$ -curve determines position of heating source center  $x_s = 330 + (i - 1) \cdot 250$  mm, curve A corresponds to fixed by welding position of edges

Similarly, for variant 4 (see Figure 4), tolerance of  $\pm 0.5$  mm is transgressed after 1700 mm, with overall butt length of 16000 mm.

Thus, provision of required tolerance for a given gap width for quality formation of one-sided butt welds in the absence of additional technological so-

lutions, equivalent to tacks installation, at quite long butts is not deemed possible.

To solve this problem, JMG company has developed a series of portal-type devices (Figure 5), providing containment of welded edges with special hydraulic clamps (Figure 6), installed on either side of

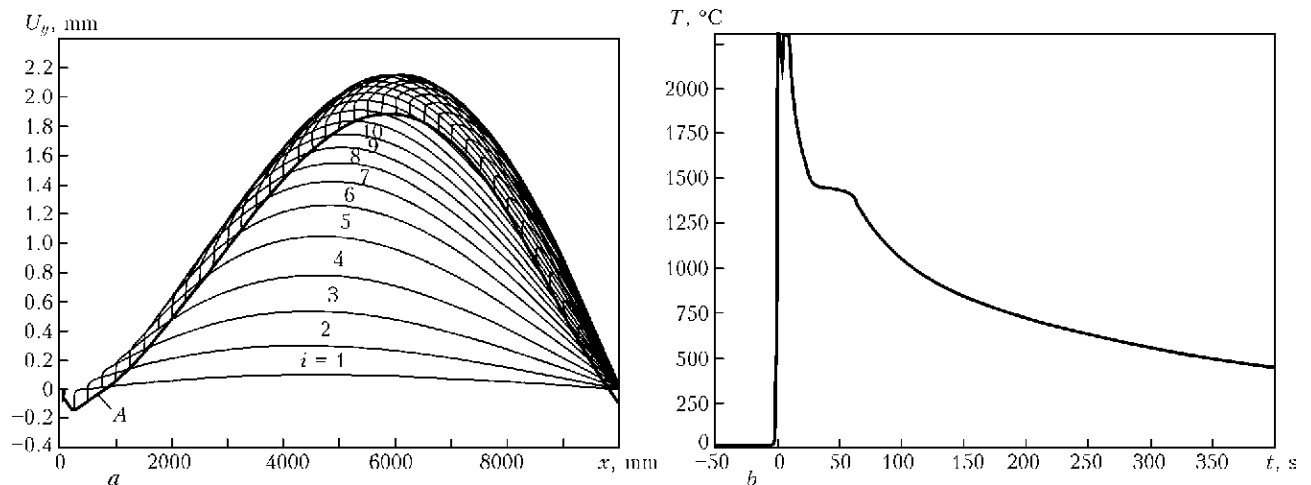


**Figure 3.** Results of calculation of displacement  $U_y$  variation kinetics along edge  $y = 0$  for variant 3 at  $Q = 0$  (a), and thermal cycle along weld axis (b):  $x_s = 255 + (i - 1) \cdot 250$  mm – position of welding source, curve A represents  $1/2$  gap variation in zone  $x_s$

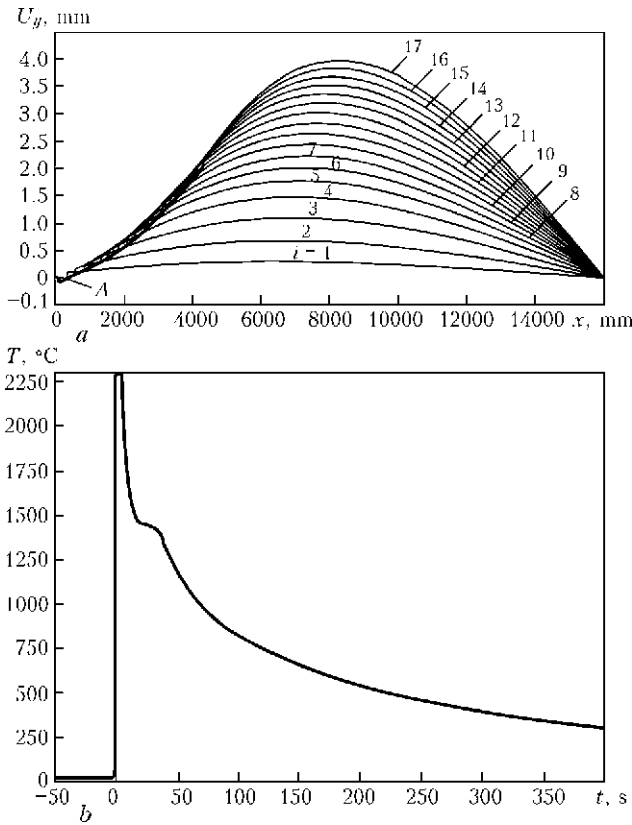


Figure 4. Displacement  $U_y$  along edge being welded for variant 4 at  $Q = 0$  (a), and thermal cycle along weld axis (b): number of  $i$ -curve corresponds to position of welding source center  $x_s = 330 + (i - 1) \cdot 250$  mm, curve A – to fixed by welding position of edges

the butt at  $l = 80$  mm from the butt axis. Dimensions of the clamp foot (see Figure 6) are  $A \times B$ , where  $A$  is the clamp length along the butt, and  $B$  is the total width of contact zone. Distance between clamps along the butt is 500 mm. To each clamp a force  $Q$  at  $\alpha = 10^\circ$  angle to the vertical plane (acting opposite to gap opening forces) is applied. The clamps are all of the same type, and pressure is simultaneously applied (or cut off) to all clamps.

It is necessary to determine force  $Q$ , applied to the clamp for welding variants of Table 1, ensuring containment of gap within tolerance limits of Table 1.

For that purpose the WELDPREDICTIONS software package was used, with addition of a module, accounting for friction forces on the contact surfaces of plates being welded and stationary clamps and the device base plate (Figure 7).

A friction-sliding model was used [1], according to which friction force is zero in the absence of displacements (sliding) and it is proportional to pressure in the presence of sliding (Figure 8).

In system of  $x, y, z$  coordinates (see Figure 7), where plane  $y = 0$  is the plane of symmetry for the welded butt with a longitudinal axis  $x$ , boundary conditions on the surface  $z = 0$  (contact of plate with clamping shoe) and  $z = \delta$  (contact of plate with base plate), can be written as

$$z = \delta \begin{cases} \sigma_{zz} = -q_z, & \frac{\bar{U}_x f_\delta}{U_0}, \\ \sigma_{zx} = q_z \beta_x \frac{\bar{U}_x f_\delta}{U_0}, \\ \sigma_{zy} = q_z \beta_y \frac{\bar{U}_y f_\delta}{U_0} + q_z \frac{\text{tg } \alpha}{2}; \end{cases} \quad (1)$$

$$z = 0 \begin{cases} \sigma_{zz} = -q_z, & \frac{\bar{U}_x f_0}{U_0}, \\ \sigma_{zx} = -q_z \beta_x \frac{\bar{U}_x f_0}{U_0}, \\ \sigma_{zy} = -\left( q_z \beta_y \frac{\bar{U}_y f_0}{U_0} + q_z \frac{\text{tg } \alpha}{2} \right), \end{cases}$$

where  $q_z = \frac{Q}{AB} \cos \alpha$  is the pressure in clamping zone;  $\bar{U}_x$  and  $\bar{U}_y$  are the increments of displacements from the moment when  $U_x = 0$  for  $\bar{U}_x$  and  $\bar{U}_y = 0$  for  $\bar{U}_y$ ;  $f_\delta$  and  $f_0$  are the friction coefficients on surfaces  $z = \delta$  and  $z = 0$ ;  $\beta_x$  and  $\beta_y$  are the parameters determined by condition that friction force grows with increasing

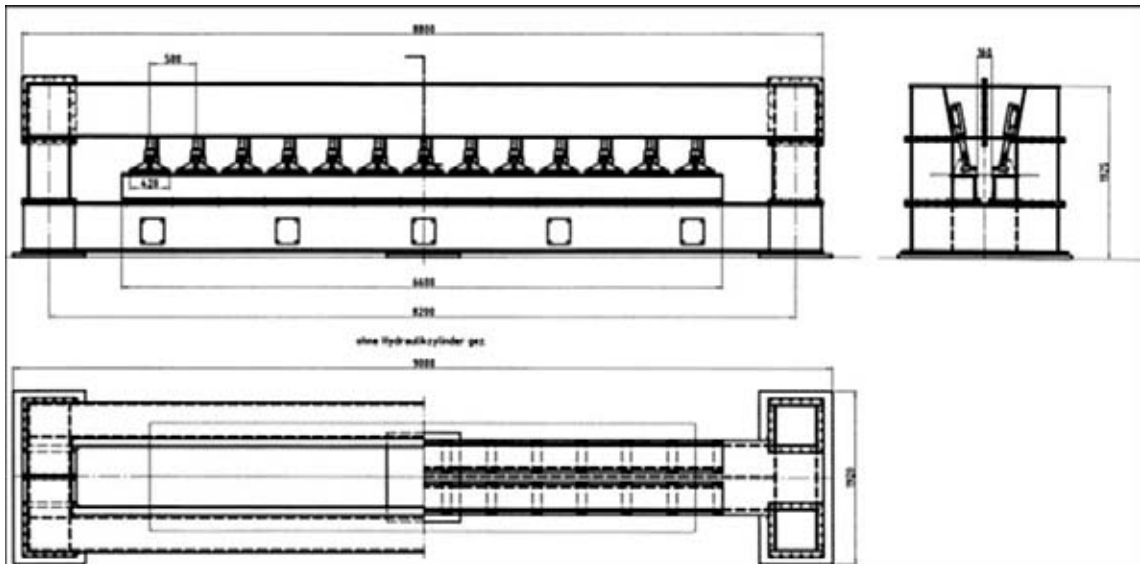


Figure 5. Schematic diagram of device



$\bar{U}_x, \bar{U}_y$  (see Figure 8) up to a certain limit at  $U_0 \approx 10^{-3}$  mm [1].

In numerical simulation of the development of plasto-elastic deformations, implementation of conditions (1) by iteration does not pose any major difficulties, but somewhat increases counting time.

In using the model of plane stressed state (which is quite acceptable for single-pass welding of plates), a 3D equilibrium equations in the clamping zone should be integrated over the thickness ( $z$  coordinate). As a result we obtain, with account of boundary conditions (1)

$$\frac{\partial \sigma_{xx}}{\partial x} + \frac{\partial \sigma_{xy}}{\partial y} + F_x = 0; \quad \frac{\partial \sigma_{xy}}{\partial x} + \frac{\partial \sigma_{yy}}{\partial y} + F_y = 0, \quad (2)$$

where

$$F_x = \frac{1}{\delta} [\sigma_{xz}(\delta) - \sigma_{xz}(0)] = q_z \frac{f_\delta + f_0}{U_0 \delta} \bar{U}_x \beta_x; \quad (3)$$

$$F_y = \frac{1}{\delta} [\sigma_{yz}(\delta) - \sigma_{yz}(0)] = q_z / \delta \left[ \operatorname{tg} \alpha + \frac{f_\delta + f_0}{U_0} \bar{U}_y \beta_y \right].$$

Beyond the contact area, where  $q_z = 0$ ,  $F_x$  and  $F_y \equiv 0$ .

Summary projections of friction force  $P_x$  and  $P_y$  acting on the  $j$ -th clamp with account of (2) and (3)

$$P_x^{(j)} = \delta \int_{x_j}^{x_j+A} \int_{y_j}^{y_j+B} F_x^{(j)} dx dy = - \int_{y_j}^{y_j+B} [\sigma_{xx}(x_j+A) - \sigma_{xx}(x_j)] dy - \int_{x_j}^{x_j+A} [\sigma_{yx}(x_j+B) - \sigma_{yx}(y_j)] dx; \quad (4)$$

$$P_y^{(j)} = \delta \int_{x_j}^{x_j+A} \int_{y_j}^{y_j+B} F_y^{(j)} dx dy = - \int_{x_j}^{x_j+A} [\sigma_{yy}(y_j+A) - \sigma_{yy}(y_j)] dx - \int_{y_j}^{y_j+B} [\sigma_{yx}(x_j+A) - \sigma_{yx}(x_j)] dy.$$

Thus, if stressed state along the shoe contour of  $j$ -th clamp is known, then using dependencies (4), projections  $P_x^{(j)}$  and  $P_y^{(j)}$  of summary forces, acting on the  $j$ -th clamp, can be calculated.

This idea was used in our work at the first stage, to evaluate forces  $P_x^{(j)}$  and  $P_y^{(j)}$  during time  $t$  on condition that  $U_y^{(j)}$  displacements in the  $j$ -th clamp zone, is zero in welding heating.

Accordingly, one can consider that sliding along  $y$  in the  $j$ -th clamp zone will not occur, if

$$P_y^{(j)}(t) < Q^{(j)} \cos \alpha [\operatorname{tg} \alpha + \mu(t)(f_\delta + f_0)], \quad (5)$$

where  $\mu(t) = \pm 1$  depending on the direction of possible increments of displacements  $\bar{U}_y(t)$  at the moment  $t$  in the clamp zone, namely, if  $\bar{U}_y(t) < 0$ , i.e. there is a trend to gap closure, then  $\mu(t) = -1$ ; otherwise  $\mu(t) = 1$ .

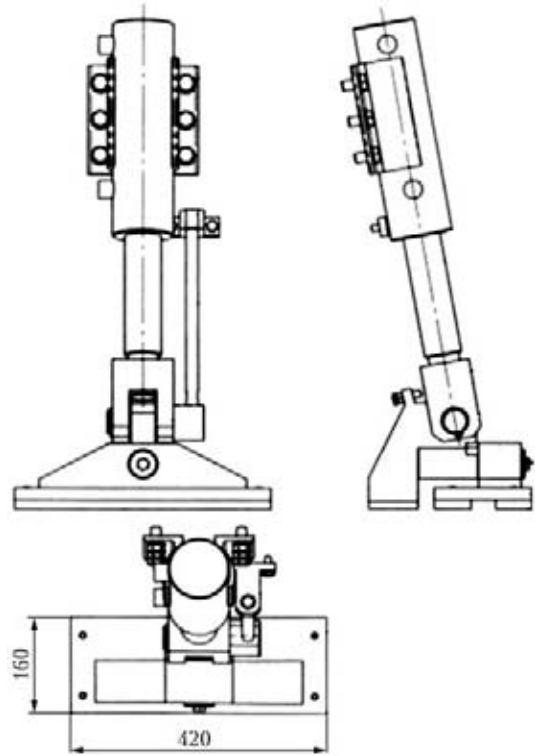


Figure 6. Schematic diagram of clamp

From (5) follows the condition of precluding sliding of plates being welded in the zone of the  $j$ -th clamp in  $y$  direction  $y$ :

$$Q^{(j)}(t) \geq \frac{-P_y^{(j)}(t)}{\sin \alpha + \mu(t)(f_0 + f_\delta) \cos \alpha}. \quad (6)$$

Results of estimated determination of  $P_y^{(j)}(t)$  for variant 3 from Table 1 at  $A = 210$  mm and  $B = 80$  mm are shown in Figure 9, *a*. It is seen that  $P_y$ , contributing to gap opening before respective deposition of the weld section in the  $j$ -th clamp zone, is at its peak,

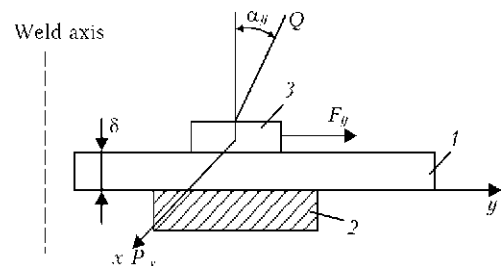


Figure 7. Schematic diagram of edge retention with clamp: 1 – welded plate; 2 – base plate; 3 – clamp

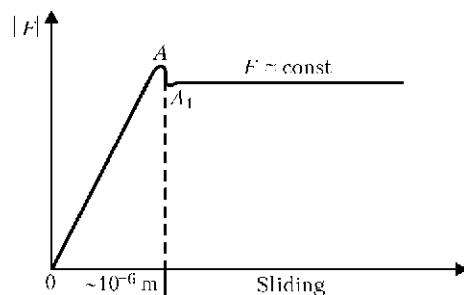
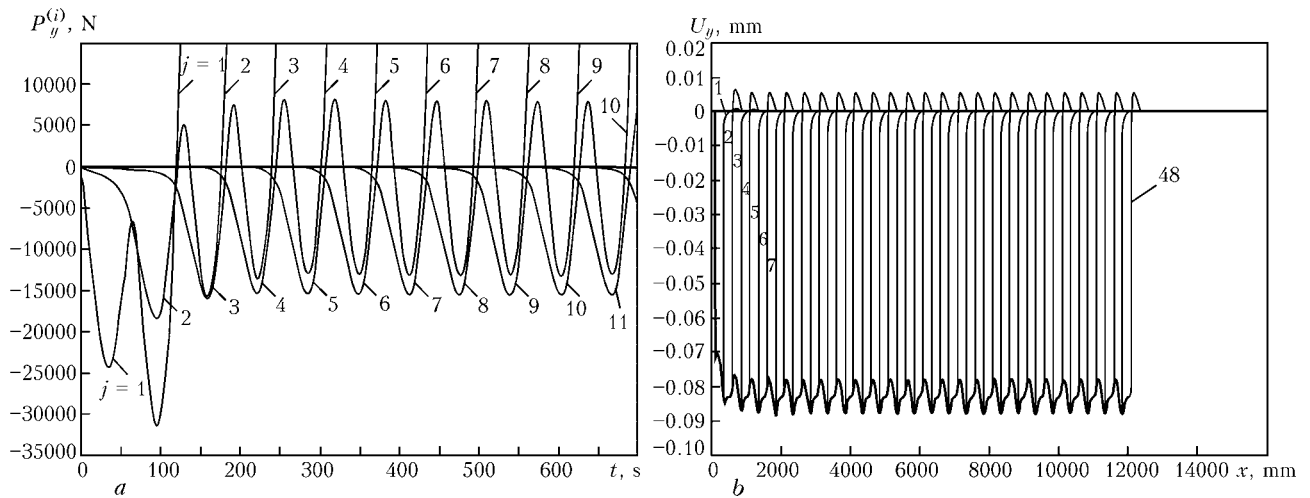
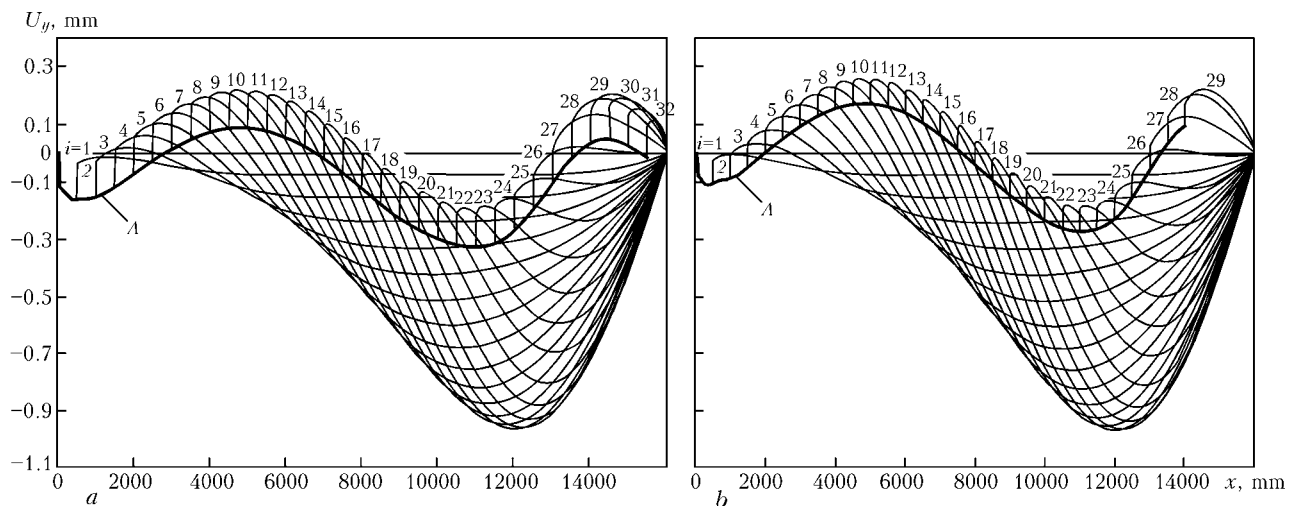


Figure 8. Friction force values versus relative displacement of friction bodies at shearing, turning into sliding at  $Q_z = \text{const}$



**Figure 9.** Results of calculation of forces  $P_y^{(j)}(t)$  for variant 3 at  $A = 210$  mm,  $B = 80$  mm (a), and displacements  $U_y(x)$  in edge welding  $y = 0$ : number of  $i$ -curve corresponds to position of the heating source center  $x_s = 330 + (i - 1) \cdot 250$  mm



**Figure 10.** Kinetics of variation of displacements  $U_y$  along the edge for variant 2 (a) and 3 (b) at  $L = 16000$  mm and  $Q = 15000$  N: number of  $i$ -curve corresponds position of source along the axis  $x_s = 5 + (i - 1) \cdot 500$  mm, curve A –  $1/2$  gap variation in zone  $x_s$

whose value remains the same almost for all  $j$ , but for the terminal ones (at the beginning and end of the weld). Idea on the magnitudes of displacements  $U_y$  of the welded edge (with account of 80 mm free length between the edges of plate and shoe), data of

**Table 2.** Requisite maximum forces for containment of edge from opening in butt welding for variants 1–4 depending on  $A \times B$  dimensions

Variant No.	Force, N	$A \times B$ , mm			
		420 × 160	210 × 80	100 × 80	50 × 80
1	$ P_y^{\max} $	5250	3700	1600	750
	$ Q_j^{\max} $	12800	9020	3900	1830
2	$ P_y^{\max} $	15700	15000	10000	8000
	$ Q_j^{\max} $	38290	36585	24400	19500
3	$ P_y^{\max} $	17200	15100	12200	10000
	$ Q_j^{\max} $	41950	36683	29760	24390
4	$ P_y^{\max} $	11350	11250	8750	6570
	$ Q_j^{\max} $	27683	27439	21341	16024

Figure 9, b give for variant 3. It is seen that these displacements are negligible compared to tolerance of  $\pm 0.5$  mm.

In Table 2 for variants from Table 1 are shown requisite forces  $|P_y^{\max}|$  depending on the  $A \times B$  dimensions of clamp shoe. Characteristically, that reduction of clamp shoe area (especially of its frontal size  $A$ ) contributes to reduction of maximum  $|P_y^{\max}|$ , magnitude of clamping force  $Q_j^{\max}$  as in (6) at  $f_0 = f_\delta = 0.12$ ,  $\alpha_x = 0$ ,  $\alpha_y = 10^\circ$  is also respectively reduced.

The latter is especially manifest at small thicknesses (variant 1).

Attention should be paid to that after the source passes a concrete  $j$ -th clamp,  $P_y^{(j)}(t)$  changes its sign, i.e. at that stage force  $P_y^{(j)}(t)$  precludes lateral shrinkage in the weld zone. It can be very high (welding in constriction on the  $80 \times 2 = 160$  mm base).

It is desirable from that moment on, to apply onto the  $j$ -th clamp a zero clamping force  $Q$ , to avoid the risk of longitudinal cracks in the weld. From the results of Table 2 it follows that for clamp containment, at said conservative approach ( $U_y = 0$  in the

clamps zone), rather high clamping forces  $Q$  are required, i.e. at butt length of 16 m with 32 pairs of clamps, load on the carrying beam of the portal (see Figure 5) will be quite substantial. For example, for variant 3 of Table 2, at  $A \times B = 420 \times 160$  mm, total load is about  $42 \cdot 10^3 \cdot 64 = 2688 \cdot 10^3$  N. In this connection, algorithm of device operation, when all clamps are loaded and unloaded simultaneously with the same force  $Q^{\max}$ , is the simplest for controlling, but it can hardly be considered rational, taking account that in reality only a small group of clamps requires at a specific moment of welding, application of quite substantial forces  $Q$ .

Besides, the data on  $Q_j^{\max}$  in Table 2 are quite conservative, since they provide containment of the edges within  $\pm 0.1$  mm tolerance limits. Such values are acceptable for variant 1 at thicknesses  $\delta = 3$  mm, and will be notably excessive for variants 2–4, where edge displacement tolerance is  $\pm 0.5$  mm.

With the help of the estimation method developed, one can determine rational forces in clamps, depending on welding conditions and edge displacement tolerance.

As an example, in Figure 10 are shown the results of such an estimation for variants 2 and 3 at  $A \times B = 210 \times 80$  mm and constant force  $Q = 15000$  N, ensuring displacement of edges within double margin tolerance limits.

Numerical investigations, conducted for different variants have shown that in welding of steel plates with  $\delta \leq 12$  mm, having yield point of 380–460 MPa, and with the butt weld length of up to 16000 mm, during operation of the bench without individual clamp control, one can recommend at  $A \times B = 210 \times 80$  mm  $Q_j^{\max} = 15000$  N.

1. Kragelsky, I.V., Dobygin, M.N., Kombalov, V.S. (1977) *Fundamentals for friction and wear calculations*. Moscow.

# EXPERIMENTAL DETERMINATION OF RESIDUAL STRESSES BY SEMI-DESTRUCTION METHOD IN CONJUNCTION WITH NUMERICAL SIMULATION OF THEIR DEVELOPMENT

V.M. SHEKERA

E.O. Paton Electric Welding Institute, NASU, Kiev, Ukraine

Results of studies of residual stresses in elements of welded structures, manufactured more than 20 years ago at Chernobyl NPP, are presented. The studies are connected with the need to constantly monitor and estimate safe service life of the structures. A certain complexity of experimental measurements consisted in rather high degree of radioactive contamination of the studied assemblies, which were cut out from a real structure. Object of the study were separate plates 30 and 40 mm thick of steel 10KhSND from the flooring of the power unit of the NPP with such welded elements as stiffening ribs and tubes. The field of residual stresses on the surface of plates was determined by the Matar's method based on drilling of a recess of 3–10 mm diameter at the depth of the diameter and use of foil resistance strain gauges. Rosettes of the sensors consisted of three strain gauges arranged at an angle of  $120^\circ$  to each other around a recess of a respective diameter. Monitoring data on external load of studied and majority of other NPP assemblies in the process of long-term operation are not available. Results of the carried out experiment made it possible to substantiate reliability of calculated data obtained using developed at the E.O. Paton EWI package WELDPREDICTIONS for the curves of distribution of longitudinal (hoop)  $\sigma_{xx}$  ( $\sigma_{\beta\beta}$ ) and lateral (radial)  $\sigma_{yy}$  ( $\sigma_{rr}$ ) residual stresses on the surface of abutting of welded elements and on the reverse surface. Calculated data match experimental data satisfactorily.

Production of critical massive structures and single articles by welding is a common practice. High stresses occurring in welding, require permanent monitoring and evaluating the safe operation period of weldments during many years. Among such structures are, for instance, load-carrying structures of stalled power generating units of Chernobyl Nuclear Power Plant, manufactured over 20 years ago.

Subjects of investigation were two typical welded joints, often encountered in load-carrying structures of power generating units. The first one is T-joint with two-sided welds and K-groove of the adjoining edge (Figure 1), straight linear joint of the two elements being rather long. The second joint, involving welding a pipe to a plate (Figure 2), is also widely used in different structural elements. The material in both cases is steel 10KhSND. Proceeding from the welding technologies applied in the construction of power stations and based on the investigation of the

welded joints, it was determined they were performed by submerged arc method in two passes. Welding conditions of the two passes were, respectively, as follows:  $I = 1000$  A,  $U = 40$  V,  $v_w = 2.87$  mm/s, and  $I = 400$  A,  $U = 35$  V,  $v_w = 2.87$  mm/s.

With a view to obtain a substantial amount of reliable information on stressed state in welded joints considered, a calculational-experimental method of determining residual stresses was chosen. Numerical simulation of the «history» of formation and development of residual stresses has enabled to obtain vast data, requiring, however, reliable experimental confirmation, since monitoring data of external loading are unavailable. For the above-mentioned welded assemblies the most acceptable are experimental methods with partial destruction, enabling to obtain information on elastic strains in specific points of surface layers. On the basis of such information, residual stresses in said points were determined, while subsequent restoration of small volumes of the removed metal does not influence much serviceability of the welded joints. One of semi-destruction methods, many times tested by us, is the Matar's method [1] involving drilling a hole 3–10 mm in diameter to the same depth, measuring elastic strains in the vicinity of the hole, and their referral to residual stresses. Since non-operating power generating units still have high radioactive contamination, the cut-out welded sample assemblies were subject to experimental investigation only after their respective decontamination.

Elastic strains were determined using resistor strain gauges, widely used in experimental investigations of temporary, and especially residual stresses, which,

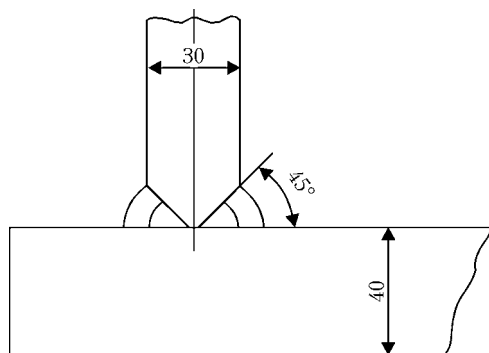


Figure 1. Tee joint

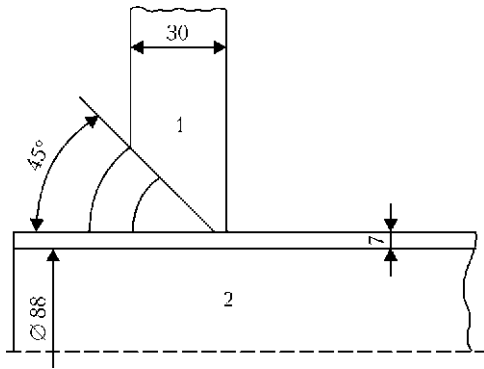


Figure 2. Plate 1 with pipe 2 welded with single-sided weld

on condition of their correct installation, as well as availability of high-quality measuring equipment, enables to obtain reliable results. Foil strain gauges were used, having, compared to wire ones, better metrological characteristics. For the investigation were used strain gauges with sensitive element base of 3, 5 and 10 mm, depending on the magnitude of expected stress gradients on the plate surfaces in conditions of plane stressed state. In a zone (Figure 3) are installed three strain gauges at 120° with respect to each other. Their initial readings are taken, and after drilling a 2a diameter hole, new readings are taken. Thus magnitudes of residual elastic strains in respective directions are determined, and main stresses  $\sigma_1$  and  $\sigma_2$ , as well as angle  $\alpha$  between the main stress  $\sigma_1$  and sensor 1, are calculated:

$$\sigma_1 = -E \{ \mu_1(\lambda)\bar{\varepsilon} + \mu_2(\lambda)\beta \}; \quad \sigma_2 = -E \{ \mu_1(\lambda)\bar{\varepsilon} - \mu_2(\lambda)\beta \};$$

$$\text{tg } 2\alpha = \frac{\delta}{\bar{\varepsilon}_{r1} - \bar{\varepsilon}},$$

where  $\lambda = \frac{r}{a}$ ;  $\mu_1(\lambda) = \frac{\lambda^2}{1 + \nu}$ ;  $\mu_2(\lambda) = \frac{\lambda^4}{4\lambda^2 - 3(1 + \nu)}$ ;  
 $\bar{\varepsilon} = \frac{1}{3} (\bar{\varepsilon}_{r1} + \bar{\varepsilon}_{r2} + \bar{\varepsilon}_{r3})$ ;  $\beta = \sqrt{(\bar{\varepsilon}_{r1} - \bar{\varepsilon})^2 + \delta^2}$ ;  $\delta = \frac{1}{\sqrt{3}} \times$   
 $\times (\bar{\varepsilon}_{r2} - \bar{\varepsilon}_{r3})$ ;  $\bar{\varepsilon}_{r1}$ ,  $\bar{\varepsilon}_{r2}$  and  $\bar{\varepsilon}_{r3}$  are the elastic strains of surface points of strain gauges 1, 2 and 3 (see Figure 3).

Knowing stresses  $\sigma_1$  and  $\sigma_2$  and angle  $\alpha$ , one can determine residual stresses  $\sigma_{xx}$  and  $\sigma_{yy}$  ( $\sigma_{\beta\beta}$ ,  $\sigma_{rr}$ ):

$$\sigma_{xx} = \sigma_1 \cos^2(1, x) + \sigma_2 \cos^2(2, x);$$

$$\sigma_{yy} = \sigma_1 \cos^2(1, y) + \sigma_2 \cos^2(2, y),$$

where (1, x) is the angle between direction 1 and axis x; (2, x) is the same between direction 2 and axis x, etc.

Schematic diagram of placing rosettes of strain gauges in weld zones with indication of their coordinates in the planes is shown in Figure 4. In the first and second joints mean value of weld section leg is 19 and 15 mm, respectively. In a plate with stiffening rib, the first row of rosettes is installed on the weld, while on the reverse side it is shifted onto the projection line of the nearest vertical rib plane. In the second plate the first row of rosettes immediately

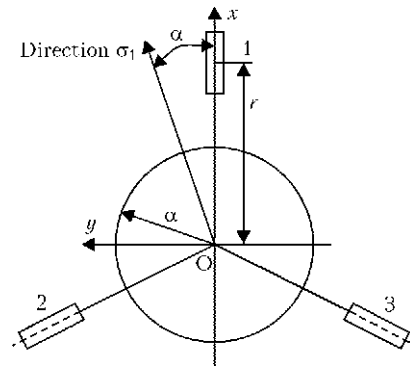


Figure 3. Schematic diagram residual stresses measuring setup: r — distance from center of projected hole O to center of strain gauge grid

adjoins the weld, while on the reverse side, the pipe. Inasmuch as all the four rosettes of each of the four radii are placed uniformly with respect to each other, so all of the rosettes on the reverse side have 7 mm shorter radial coordinates. Radial direction of the rosettes is determined by the crossing point of continuations of pipe radii with edges (2 and 3) of plate (Figure 4, b). The first plate has 20 cemented-on rosettes, the second one — 18.

Comparison of some  $\sigma_{xx}$ ,  $\sigma_{yy}$ ,  $\sigma_{rr}$ ,  $\sigma_{\beta\beta}$  residual stress curves, obtained using the method of [2], applying WELDPREDICTIONS software package, with experimental points in different zones is shown in Fig-

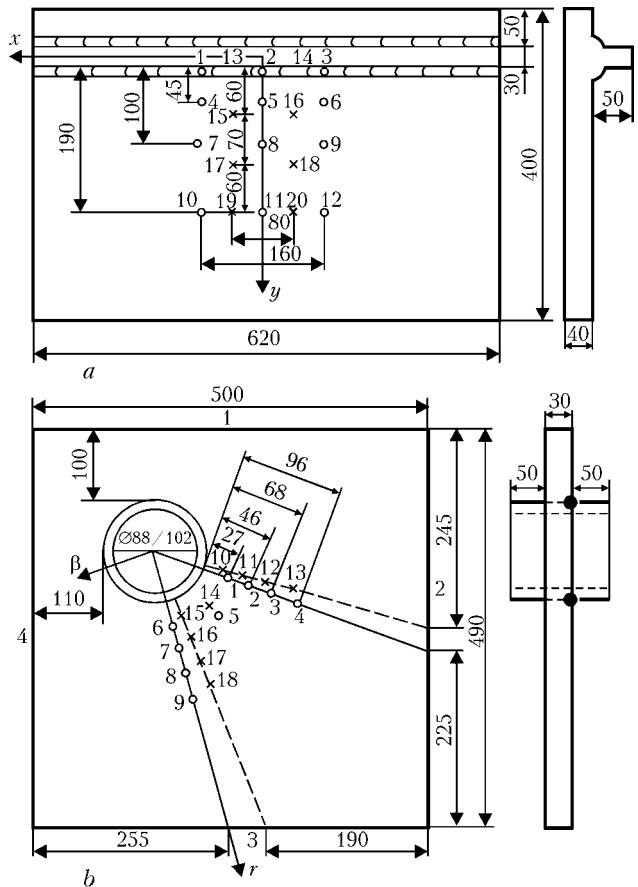


Figure 4. Schematic diagram of placing strain gauge rosettes in weld zone of plate with stiffening rib (a) and with welded-in pipe (b): O — rosettes on surface with weld; X — rosettes on weld-free surface

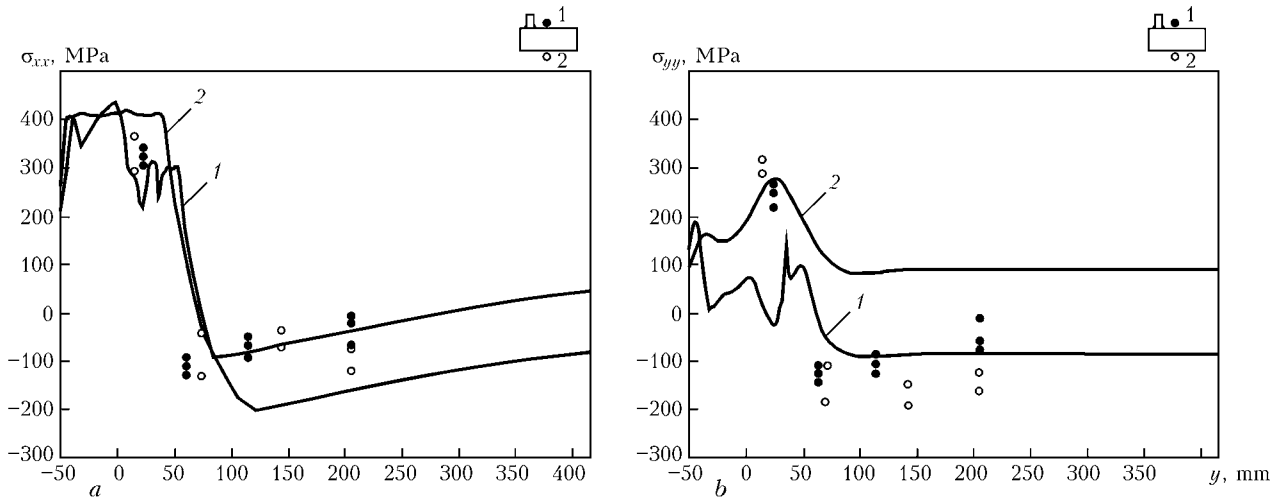


Figure 5. Comparison of estimated  $\sigma_{xx}$  (a),  $\sigma_{yy}$  (b) residual stresses (solid lines) with experimental (●, ○) on surface with (1, ●) and without (2, ○) weld

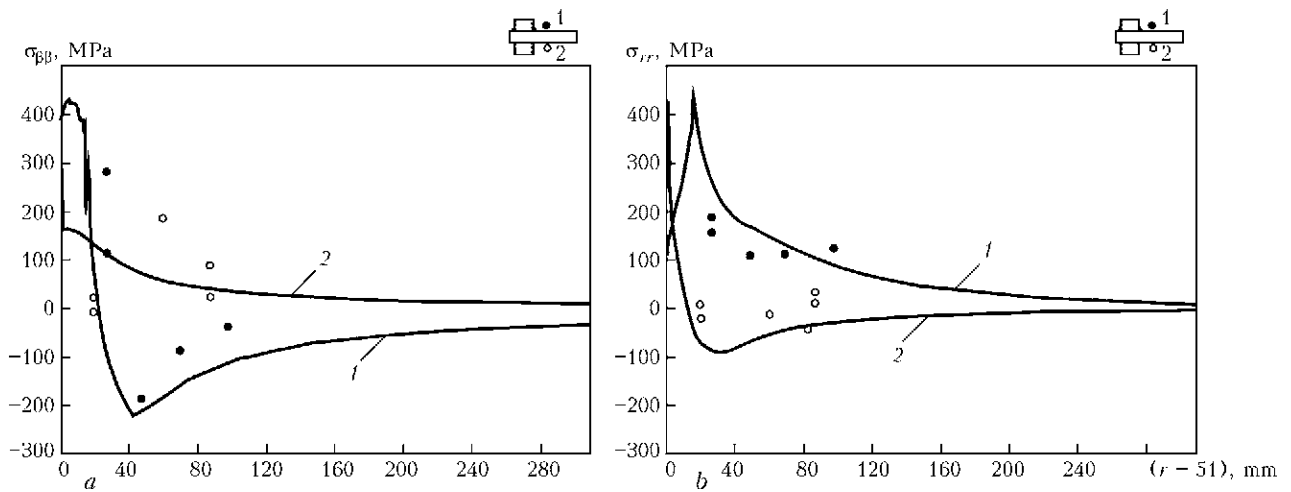


Figure 6. Comparison of estimated  $\sigma_{\beta\beta}$  (a),  $\sigma_{rr}$  (b) residual stresses (solid lines) with experimental (●, ○) on surface with (1, ●) and without (2, ○) weld

ures 5 and 6, where origin of coordinates is shifted in a radial direction by the magnitude of outer pipe surface radius. The Figures show that the curves are satisfactorily agreed with experimental data; in the vicinity of welds residual stresses are commensurable in the main with yield point. It has to be especially noted that complexity of investigation involved some change in the technique of experimental measurements because of the presence of high radioactive emission by one of the assemblies. Change in technique included increasing the time of preparation to carry out measurements, connected with changing wiring diagram of the bridge circuit, in applied matrix of rosettes placing, etc.

### CONCLUSIONS

1. Experience of experimental investigations of residual stresses directly at NPP in the presence of high radioactive emission was gained.
2. Despite long-term operation of load-carrying structures, stress relaxation did not take place; residual stresses were close to yield point in the weld zone.
3. Satisfactory agreement of estimated data with experimental ones proves plausibility of out calculations.

1. Masubuchi, K. (1980) *Analysis of welded structures*. Oxford: Pergamon Press, p. 117-119.
2. Makhnenko, V.I. (1976) *Calculation methods for investigation of welding stress and strain kinetics*. Kiev: Naukova Dumka.

# NUMERICAL MODELLING OF THE EBW PROCESS

V.A. SUDNIK<sup>1</sup>, V.A. EROFEEV<sup>1</sup>, K.-H. RICHTER<sup>2</sup> and K.-U. HEINS<sup>2</sup>

<sup>1</sup>Tula State University, Russia

<sup>2</sup>MTU Aero Engines GmbH, Munich, Germany

A mathematical model for electron beam welding (EBW) on the basis of the differential energy equation, taking into consideration the beam power density has been developed. The surface of the cavity is determined by the isotherm, corresponding to the temperature at which the vapor pressure balances both the capillary and the gravitational pressures in the cavity. The weld pool surface is approximated by the surface equation, accounting for the capillary, gravitational and intrinsic pressures in the melt. The balance between the melted metal volume and the thermal expansion of the melt is also accounted for. A computer program based on the model allows the user to compute temperature distributions in the metal and sizes of the weld pool. The input data for the program are the parameters of the electron beam. A comparison of the calculated and experimental results for the penetration depth, width and height of the weld convexity relate satisfactorily for the welding of titanium and nickel alloys with thickness of 7–20 mm.

The first analytical model, which linked the penetration depth with the parameters of EBW and thermo-physical properties of the material, was created by Hashimoto and Matsuda [1]. Tong and Giedt [2] took additionally into consideration the vapor pressure in the capillary. Erokhin and Reznichenko [3] suggested a model for deep penetration which is a combination of a surface and a line heat sources. A 3D cylindrical heat source was suggested by Miyasaki and Giedt [4]. The energetic characteristics of the electron beam radiation and its elements were analyzed by Schiller et al. [5], Rykalin et al. [6, 7], Bashenko et al. [8] and Kajdalov [9]. The thermo-capillary convection around the capillary was considered in a 2D model by Wei and Giedt [10]. Similarities and distinctions between EBW and laser welding were studied by Bayer et al. [11]. In cooperation between St.-Petersburg Polytechnic University, Russia (Turichin [12]) and Aachen University, Germany (Bohm [13]), there were created models for EBW and on their base the program EBSIM [14] was developed. This software is able to compute the profile and front of the capillary and the weld pool as well as thermal cycles at a certain point. But it doesn't account for the convection in the weld pool and deformative phenomena, influencing the shape of the weld pool and resultant weld.

The numerical model for laser beam welding named LASIM by Sudnik et al. [15] from Tula State University and DaimlerChrysler Corporation is known. It reflects the formation of the capillary and weld pool with accounting for the complex joint geometry [16], gap [17], 2D fluid flow [18] and self-focusing of the laser beam in penetration of aluminum alloys using CO<sub>2</sub> lasers [19]. The numerical simulations for EBW were developed by Rogeon et al. [20] (with the program SYSWELD), Demchenko and Lesnoj [21] (heat transfer and hydrodynamic), and Lundbaeck and Runnemalm [22] (FEM program with use of the program LASIM [15]).

The goal of this work is to summarize theoretical models of different phenomena accompanying EBW, to develop a numerical model of the EBW process on the basis of the model and program LASIM, and to estimate the agreement between the numerical calculations and experiments from MTU Aero Engines GmbH.

**Governing equations. Energy model.** The model of EBW is based on the energy equation computed in the Cartesian coordinates where the beam is static, but welded parts are translated with the welding speed  $v_w$ . The non-stationary thermodynamic condition of the metal is described by the energy conservation equation in the enthalpy formulation  $H(x, y, z, t)$ :

$$\frac{\partial H}{\partial t} - v_w \frac{\partial H}{\partial x} + \rho(T)(\vec{u}, \text{grad } H) = \text{div} [\lambda(T) \text{grad } T], \quad (1)$$

where  $\rho(T)$ ,  $\lambda(T)$  are the density and coefficient of thermal conductivity depending on the temperature  $T$ ;  $\vec{u}$  is the fluid flow velocity. The enthalpy  $H$  is related with the temperature  $T(x, y, z, t)$  by the Kirchhoff equation:

$$H(T) = \int_{T_0}^T c(T) + \psi_L(T)H_L + \psi_V(T)H_V,$$

where  $c(T)$  is the specific heat capacity depending on the temperature  $T$ ;  $\psi_L$  and  $\psi_V$  are the fractions of the molten metal and vapor in the «solid-liquid» and «liquid-vapor» states, respectively;  $\psi = \frac{T - T_S}{T_L - T_S}$ ;  $0 \leq \psi \leq 1$ ;  $H_L$  and  $H_V$  are the heats of melting and vaporization, respectively.

The initial condition at the time  $t = 0$  is

$$H(x, y, z, 0) = H^0(x, y, z).$$

The boundary conditions used here set a heat flow at the capillary surface  $Z_k(x, y)$ :

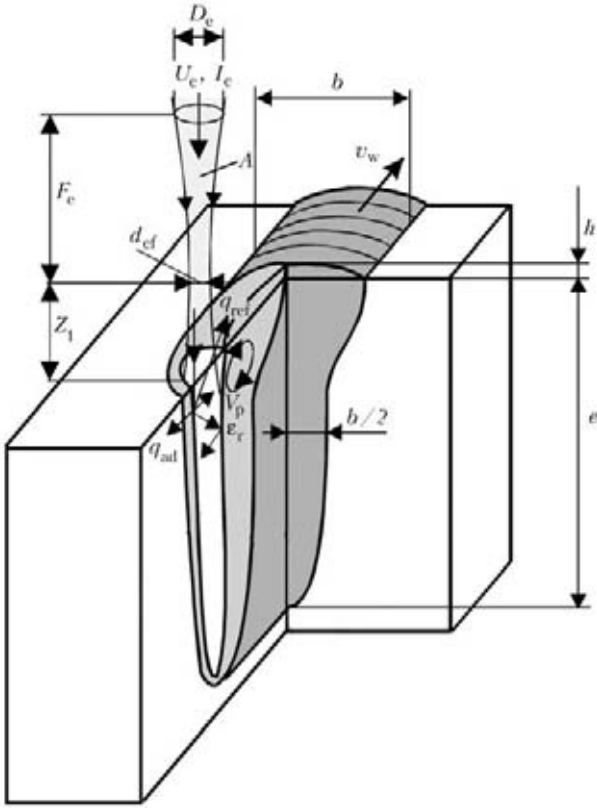


**Figure 1.** Scheme and parameters of the EBW process (for designations see the text)

$$\lambda \frac{\partial T}{\partial z} = q[x, y, Z_k(x, y)],$$

where  $q[x, y, Z_k(x, y)]$  is the specific distribution of the absorbed electron beam intensity at the melt surface.

At the upper  $z = 0$  and lower  $z = -t$  surfaces of the sheet we apply the boundary conditions in the form of the convective heat transfer with the ambient medium at the temperature  $T_0$ :

$$\lambda \frac{\partial T}{\partial z} = \alpha_0(T - T_0),$$

where  $\alpha_0$  is the effective coefficient of the heat exchange that accounts for the heat losses by means of air convection and radiation.

At the side sheet borders

$$T = T_0 \text{ for } x = \pm\infty \text{ or } y = \infty.$$

*Submodel of electron beam.* The electron beam parameters in EBW are the beam current  $I_e$ , the accelerating voltage  $U_e$ , the current of the focusing system  $I_f$ , the work distance  $F_e$ , and focal diameter  $d_{ef}$  (Figure 1). The diameter  $d_{ef}$  depends on both the beam current and the accelerating voltage [6]:

$$d_{ef} = S_0 \left( \frac{I_e}{U_e} \right)^{3/8},$$

where  $S_0$  is the constant for the electro optic system. Since the aberration coefficient of the electromagnetic lenses of the electro optic system is unknown, this constant is calculated on the basis of experimental data. At the distance  $z_f$ , the beam diameter is

$$d_{ez} = \sqrt{d_{ef}^2 + [\text{tg } \gamma(z - z_f)]^2},$$

where  $\gamma$  is the angle of divergence.

The current density distribution in the cross sections of the beam is described by the normal law of distribution:

$$j_e(x, y, z) = \frac{8I_e}{\pi d_{ez}^2} e^{-\frac{8(x^2 + y^2)}{d_{ez}^2}}.$$

When the metal is impinged by the electron beam, some electrons are reflected from the metal surface. The reflection coefficient  $R$  is calculated [7, 8] as

$$R = m(CZ)^{-1/3},$$

where  $m$  is the atom mass;  $Z$  is the atomic number of an element;  $C$  is the constant. Since these data show a strong dependence of the  $R$  on the accelerating voltage, the reflection coefficient was calculated for each metal:

$$R_m = R_{m0} + K_{m1}U_e,$$

where  $R_{m0}$  and  $K_{m1}$  are the coefficients [7, 8].

The electrons absorbed by the metal give completely their energy to the metal, but the reflected ones give their energy partially. Therefore, the absorption coefficient  $\varepsilon_e$  for the beam is  $\varepsilon_e = 1 - k_r R$ , where  $k_r = 0.45-0.50$  is the coefficient accounting for the residual energy of the electrons after the reflection from the capillary surface.

The electrons reflected from the metal surface lose their energy. In the capillary, the most part of the reflected electrons impinge the capillary surface repeatedly and pass their energy completely to the metal. This process is described by the coefficient of the absorption for the reflected electrons:

$$\varepsilon_r = k_r R \left( \frac{Z_k}{Z_k + d_t + d_b} \right),$$

where  $Z_k$  is the capillary depth;  $d_t$  and  $d_b$  are the upper and lower diameters of the capillary, respectively. The distribution of the absorbed beam energy at the capillary surface is determined:

$$q[x, y, Z_k(x, y)] = (\varepsilon_e + \varepsilon_r)U_e j_e - q_v,$$

where  $q_v$  is the energy losses by vaporization. The heat flow because of vaporization is  $q_v = mH_V$ , where the mass velocity of vaporization is  $m = \sqrt{p\rho_v}$  [15] ( $\rho_v$  is the vapor density).

*Submodel of keyhole surface.* The coordinates of the capillary surface  $Z_c(x, y, t)$  are calculated through the temperature distributions  $T(x, y, z, t)$  derived from the solution of the energy equation (1). The equilibrium condition of the capillary surface is reached at the vapor pressure which balances capillary, hydrostatic and inertial pressures.

$$\sigma(T) \left( \frac{1}{r_c + \frac{\partial^2 r_c}{\partial z^2}} \right) = \rho g z + p_v + \rho z \frac{\partial^2 r_c}{\partial t^2}, \quad (2)$$



where  $p_v$  and  $\sigma$  are the dependencies of the vapor pressure and surface tension on the temperature at a certain point of the capillary  $Z_c(x, y, t)$ ;  $\rho$  is the melt density.

The initial conditions are

$$r_c(z, t) = r_c^v, \quad \frac{\partial r_c}{\partial t} = 0,$$

where  $r_c^v$  is the radius of the keyhole base.

The curvature of the capillary surface  $Z_c(x, y)$  is computed by means of numerical approximation of the isotherm corresponding to the temperature, at which the pressures of the capillary are balanced. Here, the following dependence of the pressure on the temperature  $p_m(T_v, v_w)$  is used. It allows us to determine an equilibrium temperature  $T_v$  at a certain capillary point (Figure 2).

**Momentum model. Submodel of convection.** This submodel helps to determine the coordinates of the interfaces between the melt and solid metal as well as the tensions, velocities and depth of the fluid flow. The weld pool sizes are calculated with the help of the location of the solidus surface derived from the solution of the energy equation (Figure 3). This equation takes into consideration the simplified fluid flow resulted from the termocapillary forces and vapor friction forces at the capillary surface. For the calculation of the fluid flow parameters, we applied analytical solutions used in the modeling of laser welding and described in literature [18].

Thermocapillary forces make the melt flow in the radial direction from the capillary to the pool boundaries. Shearing Marangoni stresses  $\tau_\sigma$  produced by the termocapillary forces at the pool surface are determined as follows:

$$\tau_\sigma = \frac{\partial \sigma}{\partial T} \frac{\partial T}{\partial y} = \frac{\sigma_l - \sigma_k}{r_l - r_c},$$

where  $\sigma_l$  and  $\sigma_k$  is the surface tension at the liquidus and solidus temperatures, respectively.

The metal vapour passing through the capillary with high velocities exerts a friction force on the molten metal at the capillary wall, which is connected with the velocity of the flow  $u$  and the ratio of the boundary-layer theory:

$$\tau_v = 0.332 \frac{\sqrt{\rho \mu u^3}}{3},$$

with the dynamic viscosity  $\mu$  of the fluid, and with the coordinate  $r$  in the flow direction.

The thickness  $s$  of the surface layer being subjected to the surface forces [18] is

$$s = \sqrt{\eta t_m} = \sqrt{\frac{\mu}{\rho} t_m},$$

where  $\eta$  is the kinematic viscosity,  $\text{cm}^2/\text{s}$ ;  $t_m$  is the time during which the forces act.

The fluid flow velocity exceeds many times the welding speed. This produces a recirculating motion of the molten metal. Part of the metal taking place in the recirculation motion solidifies and is replaced by the molten

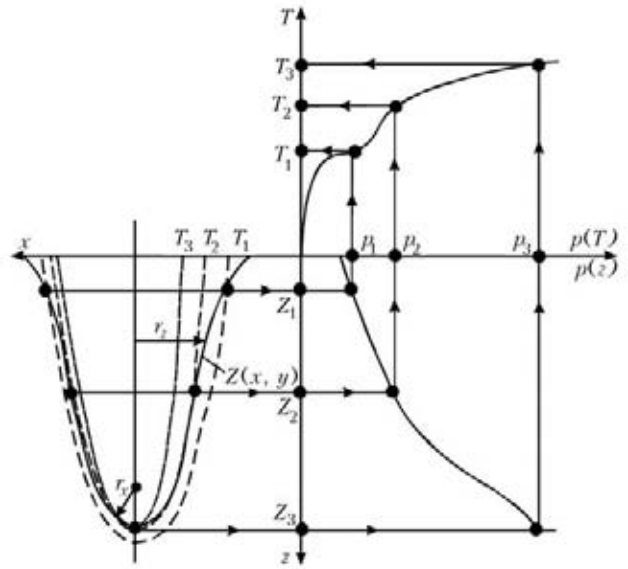


**Figure 2.** Determination of the coordinates of vapour channel surface  $Z(x, y)$  proceeding from the isotherms ( $T_1, T_2, T_3$ ), pressure distribution along the channel axis and dependence of vapour pressure on temperature  $p(T)$

metal. The time of the forces action is equal to that during which the metal exists in the molten state:

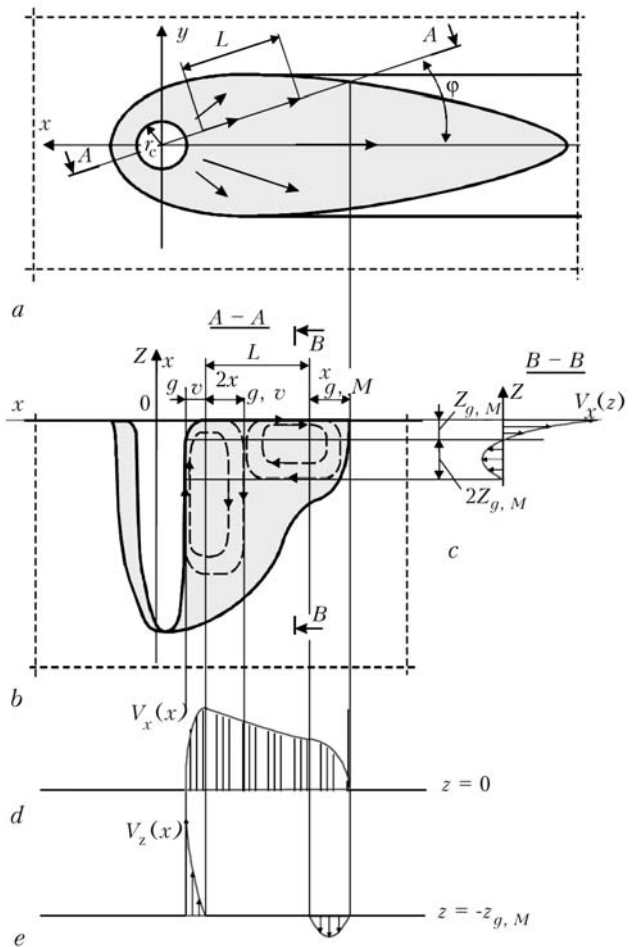


**Figure 3.** Weld pool flow patterns used in the numerical weld pool simulation: thermocapillary flow (a), thermocapillary flow and flow resulting from vapour friction in the capillary (b), and velocity sections (c-e)

$$t \approx \frac{L}{2v_w},$$

where  $v_w$  is the welding speed.

Due to the boundary-layer theory and the fact that the flow in the radial direction is constant, the relevant shear stress  $\tau_v$  and velocity  $u_0$  of the fluid flow at the melt surface are related as [18]

$$u_0 \approx \sqrt[3]{(\tau_\sigma + \tau_v)^2 K},$$

$$K = \left[ \frac{0.332}{r_l - r_c} \sqrt{\rho \mu r_c^3} \left( \frac{1}{r_c - \frac{1}{r_l}} \right)^2 \right]^2 \approx 0.11 \rho \mu \frac{r_c}{r_l}.$$

It's expected that laminar flow takes place with velocities distributed due to the parabolic law

$$u(z) = u_r + k_r(z - z_r)^2,$$

where  $u_r$ ,  $k_r$ ,  $z_r$  are the parameters of the recirculating flow derived from the continuity condition:

$$\int_0^{-s} u(z) dz = \int_{-s}^{-2z_r+s} u(z) dz.$$

Taking into consideration that at the surface  $u(0) = u_0$ , and at the depth  $u(-s) = 0$ , we will obtain:

$$z_r = 2s, \quad u_r = -u_0/3, \quad k_r = u_0/(3s^2).$$

*Submodel of free surface.* The methods usually used for the calculation of the weld pool surface location in arc and laser welding deal with small deformations of this surface in comparison with the weld width [15]. At small deformations of the surface expression for curvature is linear and the differential equation looks like

$$\pm \sigma(T) \left( \frac{\partial^2 Z}{\partial x^2} + \frac{\partial^2 Z}{\partial y^2} \right) = \rho g Z + p_v + \tilde{A}. \quad (2)$$

The constant  $g$  is meaningful internal pressure in the melt, surrounding metal created by thermal expansion. Boundary conditions for equation (2) reflect the coupling of surfaces between the melt and the surface of the solid metal. They look like at the fusion front:

$$Z = 0 \text{ for } T(x, y, 0) = T_L \text{ and } \frac{\partial T}{\partial t} \geq 0.$$

For the description of processes at the crystallization front linear extrapolation is used:

$$\frac{\partial^2 Z}{\partial x^2} = 0 \text{ for } T(x, y, 0) = T_L \text{ and } \frac{\partial T}{\partial t} < 0.$$

For the solution of the equation with boundary conditions it is necessary to determine internal pressure  $g$  in the melt that is determined according to the equation of mass balance.

Thermal expansion of the surrounding metal, phase transformation and local fusion makes the metal move in the direction of the weld pool and the melt pressing-out. Owing to the growth of its volume, a convexity of melt is formed. The form of convexity is fixed at the crystallization front and determines the

form of the weld surface. The subsequent volumetric shrinkage and thermal compression during the cooling of the solid metal reduces the sizes without changing the form of the weld convexity.

In EBW, the form of the weld convexity is close to a circular segment. The diameter of such a circle exceeds sometimes the weld width, i.e. the surface deformation has considerable values. This case will be described later on.

*Weld pool mass model.* The intrinsic pressure  $g$  is calculated on the condition of the pressing-out of the melt pool and volumetric thermal expansion of the metal with accounting for the phase transformation in melting. Since the weld pool is surrounded by the relatively cold and solid metal then we may think that the thermal expansion is directed to the weld pool and presses the melt out of the pool:

$$\iiint_{VM0} \rho_{T_0} dV = \iiint_{VM0} \frac{\rho_{T_0}}{\rho(t)} dV,$$

where  $\rho_{T_0}$  and  $\rho(T)$  are the metal densities at the initial temperature  $T_0$  and at the current temperature  $T(y, z)$  in the section where the weld pool has a maximum width.

**Numerical approximation.** The numerical solution of the energy equation is processed by the control-volume method, splitting up the 3D problem into 1D partial steps within a regular-step grid with equal steps. The problem is also split up according to the different physical processes. The model equations are computed in the following sequence.

- Input of the initial data and thermodynamical properties of the metal to be welded. Here, the grid steps in the  $(x, y)$ -directions and the dimensions of the grid are calculated.

- Then, in an iterative loop, the following parameters are obtained: current density in the beam cross sections; density of the absorbed beam power; enthalpy and temperature at the grid nodes; pressure in the capillary and equilibrium temperature at its surface; configuration of the capillary; and configurations of the weld pool and weld.

This iterative procedure stops when the weld pool sizes are stabilized.

- After the calculation, the program makes the pictures of the weld pool sections and the resultant weld. Additionally, the main process characteristics are also computed.

**Materials properties.** An analysis on the thermo-physical properties of pure nickel, titanium as well as titanium alloy 6242 and nickel alloy Waspaloy was conducted. The thermal conductivities of pure nickel and titanium were taken from literature [23]. Since the data on the thermal conductivity at the boiling point are absent, we took its value at the solidus temperature. The enthalpy was calculated with the use of the thermal dependencies of the heat capacity. The thermal dependence of the density until the solidus temperature was taken from literature [24]. For the temperatures exceeding the solidus temperature we applied an extrapolation.

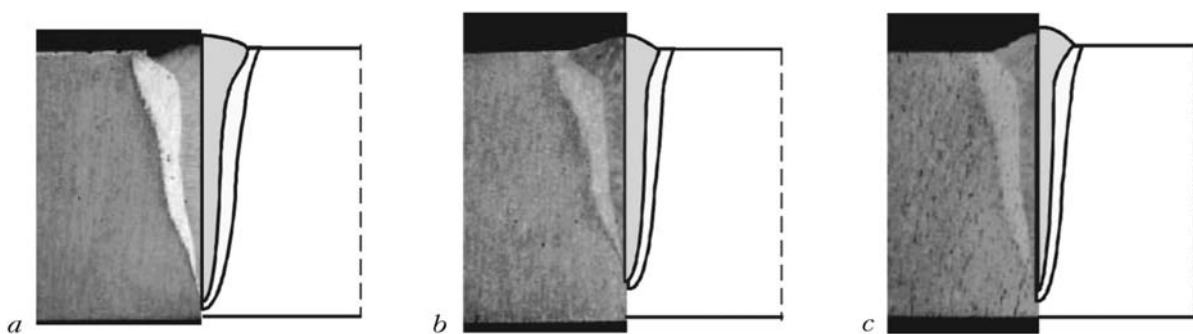


**Figure 4.** Comparison between calculation and experiment for nickel alloy Inconel 718, 7 mm thick at  $U_e = 140$  kV,  $I_e = 9$  mA and  $d_f = 0.58$  mm: *a* –  $F_e = 600$  mm,  $z_f = -16.48$  mm,  $I_f = 2020$  mA; *b* –  $F_e = 800$  mm,  $z_f = 6.99$  mm,  $I_f = 1922$  mA; *c* –  $F_e = 400$  mm,  $z_f = -9.1$  mm,  $I_f = 2170$  mA

tion. The data on the surface tension and the dynamic viscosity at the melting temperature were taken from literature [25]. The surface tension decreases generally linearly as the temperature increases. At the temperature  $T_c = 1.7T_v$  ( $T_v$  is the vaporization temperature) the surface tension is equal to zero [7]:

$$\sigma(T) = \sigma_0 \frac{T_c - T}{T_c - T_0},$$

where  $\sigma_0$  is the surface tension at the temperature  $T_0$ .

The saturation vapor pressure [26] is calculated using the surface temperature  $T$  and the chemical composition [27]:

$$P = \sum_{i=1}^n \gamma_i \text{Me}_i \exp \left( B_i - \frac{A_i}{T} \right),$$

where  $\gamma_i$  is the activity coefficient of a component in the melt;  $\text{Me}_i$  is the atomic fraction of a component in the melt.

**Calibration and verification.** The developed program ELSIM has a few coefficients that can not be defined theoretically, but one can match their values in order to provide a correspondence with the experiment: design coefficient  $S_0$  for the electron beam gun; design coefficient  $K_0$  that relates the focal distance with the focusing current.

The coefficient  $S_0 = 0.07 \text{ mm} \cdot (\text{kV}/\text{mA})^{3/8}$  was calculated on the basis of the measured focal diameter of the beam. The coefficient of the focusing system  $K_0 = 0.00128 (\text{mm} \cdot \text{mA}^2)/\text{kV}$  was determined through the focal distance for the beam current  $I_e$  ranging from 14 to 32 mA and the focusing current  $I_f$  of 2150–2200 mA.

The goal of the verification is to estimate the error of the modeling within the working range of the model parameters and reveal the causes of this error. The results of the modeling for the nickel alloy Inconel 718 (Figure 4) and the titanium alloy 6242 (Figure 5), mode parameters (accelerating voltage of 140 kV, beam current of 8–24 mA and welding speed of 0.6 m/min) were compared with the experimental data. Figure 6 shows the deviation between the calculated and experimental values for the penetration depth when welding titanium alloy 6242. The mean square deviation of this error is 9%. Since the error doesn't have a systematic character,

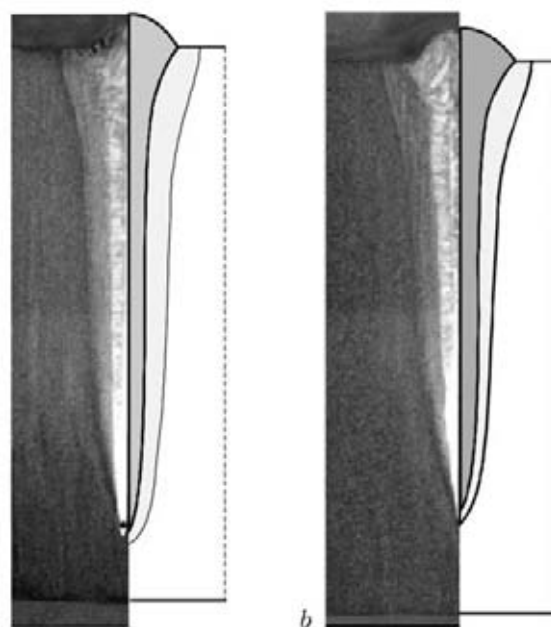


**Figure 5.** Comparison between calculation and experiment for titanium alloy 6242, 20 mm thick at  $U_e = 140$  kV,  $I_e = 24$  mA,  $d_f = 0.98$  mm: *a* –  $F_e = 600$  mm,  $z_f = -1.79$  mm,  $I_f = 2025$  mA; *b* –  $F_e = 800$  mm,  $z_f = 19.9$  mm,  $I_f = 1992$  mA

then the observed deviations could be explained by the errors of the experimental procedure and the initial data in simulation (data on the melt surface tension and viscosity, for example).

## CONCLUSIONS

1. On the basis of the literature data analysis on the models of electron beam and laser welding conducted by the authors, it was established that the model for EBW can be based on the model for laser beam welding. The model is founded on the energy equation that takes into consideration the beam energy absorption, convective and conductive heat propagation in the metal. The submodels for the capillary formation and fluid flow can be left without changing.

2. The model for the electron beam was developed and it accounts for its focal diameter (through its current and voltage), the focusing by the magnetic lens, the focus position and the electron energy absorption by the capillary surface.

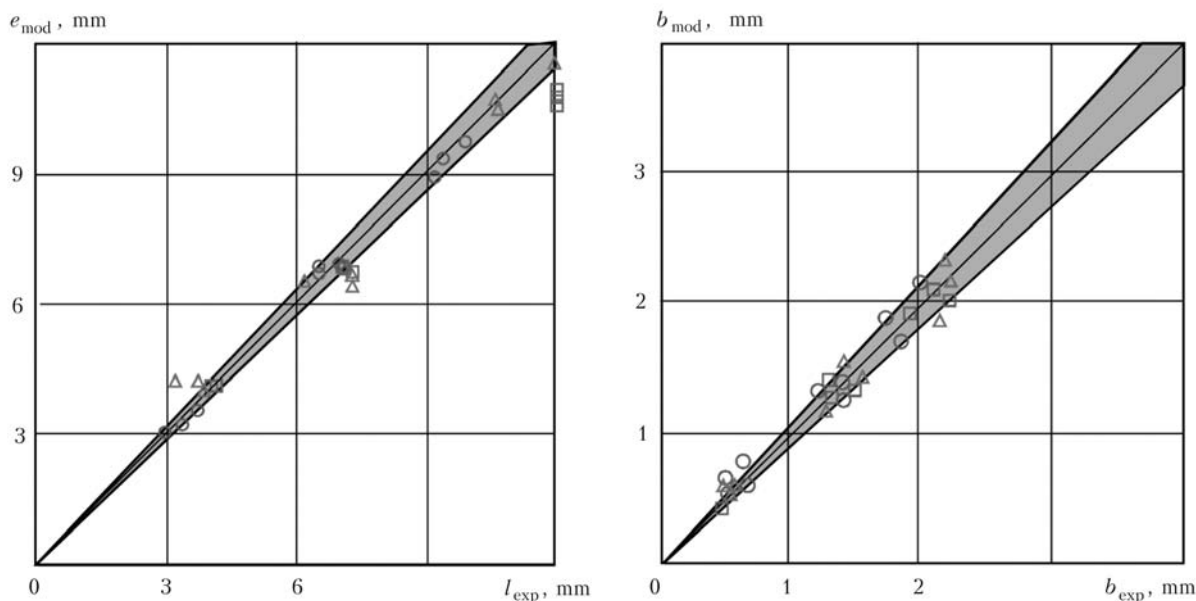


Figure 6. Result of estimation of the model error, mm:  $\square$  – 400;  $\Delta$  – 600;  $\circ$  – 800

3. The model for the weld pool convexity on the basis of the pressure equilibrium equation was created. This equation considers the capillary, gravitational and intrinsic pressures in the melt. The intrinsic pressure is computed through the balance of the melting and crystallizing metal accounting for the thermal shrinkage.

4. After the model calibration, design coefficient of the electron beam gun  $S_0 = 0.07 \text{ mm} \cdot (\text{kV}/\text{mA})^{3/8}$  was determined that relates the beam focal diameter with its current and voltage; and design coefficient of the focusing system  $K_0 = 0.00128 \text{ (mm} \cdot \text{mA}^2)/\text{kV}$  was determined that relates the focal distance with the focusing current and accelerating voltage.

5. The comparison of the computed and experimental data for the titanium alloy 6242 and the Inconel 718 alloy 7–20 mm thick at an accelerating voltage of 140 kV, beam current of 8–24 mA, welding speed of 0.6 m/min showed that the error of the modeling concerning the penetration depth is about 9 %.

1. Hashimoto, T., Matsuda, J. (1965) Effect of welding variables and materials upon bead shape in electron-beam welding. *Transact. of Nat. Res. Inst. for Metals*, 7(3), p. 22–35.
2. Tong, H., Giedt, W.H. (1970) Depth of penetration during electron beam welding. ASME, p. 1–9.
3. Erokhin, A.A., Resnichenko, V.F. (1976) On calculation of penetration depth in electron beam welding. *Svarochm. Proizvodstvo*, 4, p. 4–6.
4. Miyasaki, T., Giedt, W. (1982) Heat transfer from elliptical cylinder moving through an infinite plate applied to electron beam welding. *Int. J. Heat Mass Transfer*, 25(6), p. 807–814.
5. Schiller, S., Heisig, U., Panzer, S. (1976) *Elektronenstrahl-technologie*. Dresden: VEB.
6. Rykalin, N.N., Zuev, I.V., Uglov, A.A. (1978) *Laser and electron beam materials processing*. Moscow: Mashinostroenie.
7. Rykalin, N.N., Zuev, I.V., Uglov, A.A. (1985) *Principles of electron beam materials processing*. Moscow: Mashinostroenie.
8. Bashenko, V.V. (1979) *Feature of the secondary radiations caused by electron beam welding technological process*. Leningrad Polytechnic Univ.
9. Kajdalov, A.A. (1998) *Electron beam welding and related technologies*. Kiev: Incors.
10. Wei, P.S., Giedt, W.H. (1985) Surface tension gradient-driven flow around an electron beam welding cavity. *Welding J.*, 9, p. 251–259.
11. Beyer, E., Herziger, G., Holtt, Ch. et al. (1985) Comparison of laser and electron beam welding. In: *Proc. of 2nd Int. Conf. on Beam Technology*. Vol. 99. Essen: DVS.
12. Turichin, G.A. (1990) *Physical principles of joint formation with deep penetration*: PhD thesis. Leningrad Polytechnic Univ.
13. Boehm, S. (2000) *Modellierung und Simulation des Elektronenstrahl-Schweissprozesses unter Berücksichtigung der Elektronenreflexion und der Elektronenstreuung*. Aachen: Shaker.
14. Boehm, S., Diltthey, U., Welters, T. et al. (1997) *EBSIM – Simulationssoftware fuer das Elektronenstrahlschweissen*. Ber. 186. Duesseldorf: DVS, p. 29–34.
15. Sudnik, W., Radaj, D., Erofeev, W. (1996) Computerized simulation of laser beam welding, modelling and verification. *J. Phys. D: Appl. Phys.*, 29, p. 2811–2817.
16. Radaj, D., Sudnik, W.A., Erofeev, V.A. et al. (1999) Modelling of laser beam welding with complex joint geometry and inhomogeneous material. In: *Mathematical modelling of weld phenomena 5*. IOM Com.
17. Sudnik, W., Radaj, D., Erofeev, W. (1998) Computerized simulation of laser beam weld formation comprising joint gaps. *J. Phys. D: Appl. Phys.*, 31, p. 3475–3480.
18. Sudnik, W., Radaj, D., Breidschwerdt, S. et al. (2000) Numerical simulation of weld pool geometry in laser beam welding. *Ibid.*, 33.
19. Sudnik, V.A., Erofeev, V.A., Radaj, D. et al. (2001) Self-focusing of the laser beam in penetration welding of aluminium alloys using CO<sub>2</sub> lasers. In: *Simulation der Fugetechniken. Potentiale und Grenzen*. Ber. 214. Duesseldorf: DVS, p. 94–99.
20. Rogeon, P., Couedel, D., Carron, D. et al. (1999) Numerical simulation of EBW of metals: sensitivity study of a predictive model. In: *Mathematical modelling of weld phenomena 5*. IOM Com.
21. Demchenko, V.F., Lesnoj, A.B. (2004) Numerical modelling of heat and mass transfer and hydrodynamics in electron beam remelting of titanium alloys. In: *Proc of 2nd Int. Conf. on Mathematical Modelling and Information Technologies in Welding and Related Processes* (Katsiveli, Ukraine). Kiev: PWI, p. 71–76.
22. Lundbaeck, A., Runnemalm, H. (2005) Validation of three-dimensional finite element model for electron beam welding of Inconel 718. *Sci. and Techn. of Welding and Joining*, 10(6), p. 717–724.
23. Zinoviev, V.E. (1989) *Thermophysical properties of metals at high temperatures*. Moscow: Metallurgiya.
24. (1992) *Smithells Metals*: Refer. Book. Oxford: Butterworth-Heinemann.
25. Niszenko, V.I., Floka, L.M. (1981) *Surface tension of hot metals and alloys*. Moscow: Metallurgiya.
26. Dushman, S. (1962) *Scientific foundations of vacuum technology*. New York: Wiley.
27. Yazovskikh, V.M., Utochkhin, V.V. (1977) Thermodynamic estimation of relationship between evaporation temperature and vapor pressure in keyhole in penetration EBW. *Fizika i Khimiya Obrab. Materialov*, 2, p. 73–77.

# NUMERICAL SOLUTION OF INVERSE PROBLEM FOR LASER AND HYBRID WELDING WITH LASERCAD

G. TURICHIN, V. LOPOTA, E. VALDAYTSEVA, P. MALKIN and E. ZEMLYAKOV

Central R&D Institute of Robotics and Technical Cybernetics, St.-Petersburg, Russia

The article devoted to mathematical description of physical processes during laser welding and CAE elaboration for laser welding with LaserCAD. Take into account algorithm of inverse problem solution by means of LaserCAD, which allows defining treatment parameters, guaranteed reception wishful characteristics of weld seam.

High complexity of laser welding processes lead to difficulties in process mode choice by technological experiments. It is impossible to substitute experiments by computer modeling without exact and adequate mathematical model. Such model also necessary for technological equipment design and at last may be assumed as a basis of CAE. For technological application it is necessary not so much be able to solve direct problem — define size and shape of weld pool on adjusted welding mode parameters as inverse — determined treatment parameters, which are guaranteed prescribed characteristics of welding seam. At the same time it's desirable that procedure of solution search admit possibilities of more precise definition and addition of objective characteristic set. For thermal welding problem is exist procedure line of inverse task solutions which are ensure acceptable results from technological point of view [1, 2]. In case of beam welding with deep penetration when for weld pool formation description is insufficiently of heat conduction equation most expedient is not solve inverse problem immediately, but use algorithm of direct task and multidimensional method of nonlinear optimization. For decision direct problem in this instance its necessary quick method and decision algorithm that resolution of inverse problem is taking satisfactory time for technological application.

In connection with mentioned above one can formulate the demands to model:

- calculation exactness must be comparable with accurateness working equipment parameters installation and joining materials properties definition (not worse then 10 %);
- solving time of direct task must be limited by split second;
- program realization of model must be fit to computer technique, which available for technologists and designers;
- solution method of inverse problem must be fixed under technologist work algorithm.

So at first, it's necessary to elaborate quick algorithm of weld pool modeling during welding with deep penetration and then on its base — optimization algorithm of inverse task decision. At the heart of

algorithm is underlying physical model of laser welding [3]. As it is known, under action of radiation flux with density more than  $10^4$ – $10^5$  W/cm<sup>2</sup> in metal forms narrow and deep keyhole [4], besteaded by melt and filled by evaporated metal vapor [5]. Vapor pressure together with recoil pressure under evaporation opposed to surface tension force and so provides existing of a keyhole [6], so that the keyhole is support by mutual influence of heat, hydrodynamic, gas-dynamic, optic and kinetic processes. Evidently that direct numerical solution of such task can not satisfy demands of speed calculation, so one can use approximate numerical-analytic methods of listed tasks resolutions with their subsequent numerical matching [6, 7].

## Mathematical description of physical processes during beam welding

### Laser beam interaction with vapor-plasma phase.

During laser welding the plasma of optic discharge influence on welding process due to absorption and refraction of laser radiation [8]. In this case structure and properties of plasma plume depend on laser radiation parameters [9], composition and shielding gas rate [10]. From gas-dynamic point of view plasma plume is a subsonic submerged hot metal vapor jet [11] in cold shielding gas with volumetric heating owing to laser radiation absorption.

Volume heat generation in plasma plume depends on free electrons density, which is determinate both plasma conduction and value of laser radiation absorption coefficient [12]. In conditions of laser welding the optic discharge plasma is not equilibrium [13], and its description must be based on solution of kinetic equation for electron energy spectrum [14] taking into account chemistry and plasma plume gas-dynamic, which are depend on volume heat generation density defined by plasma ionization degree. The problem of submerged hot metal vapor jet flowing to cold shielding gas (helium) with taking into account compressibility of gas mixture and volume heat generation during laser radiation absorption in plasma was solved for elaboration plasma plume model in axial symmetrical boundary layer approximation. At the same time plasma ionicity was defined from kinetic task resolution in approximation of constant collision rate for helium-iron mixture

without supposition of local thermal equilibrium. For confirmation of received results were held experiments series about interferometry of plasma plume at impulse laser influence on metal targets.

**Radiation absorption and engaged power distribution on keyhole surface.** The problem of incidence radiation power distribution on keyhole surface during laser welding with deep penetration consists of two parts. The first one is connected with determination of absorption coefficient in temperature interval near the boiling temperature and in incidence angle interval of 1–10°. The second one is definition of engaged power distribution on keyhole surface with taking into consideration radiation re-reflection from keyhole surface.

In this context we are suppose following:

- absorption and refraction coefficients are submitted to Hagen–Rubens interrelations, their angle dependence – Fresnel formulates;
- incidence power distribution is calculating separately for parallel (*s*) and perpendicular (*p*) polarization and after that they are summarized.

The existence of local laser beam reflection from keyhole surface leads to output power redistribution on its depth and perimeter. The each point of keyhole surface is absorbs both primary laser radiation and radiation, reflected from remaining keyhole surface. The using of geometric optics approximation allows obtaining recurrent expression for engaged energy distribution of *i*-reflection  $q_{i, II, \perp}(z, \alpha)$  on keyhole surface for both types of polarization (*s* and *p*):

$$q_{i, II, \perp}(z, \alpha) = q_{i-1, II, \perp}(z', \pi - \alpha) \frac{a(z')}{a} \times \left( 1 - R_{II, \perp} \left( \beta(z') - 2 \frac{da}{dz} \right) \theta \left( \beta(z') - \frac{a}{z} \right) \right),$$

where  $i = 1, 2, 3, \dots$  is the reflection number;  $q_{0, II, \perp} = Q_0 \exp \{-k(z)(a^2 + \Delta^2)\} \exp \{2a\Delta k(z) \cos \alpha\}$ ;  $Q_0$  is the radiation power density on beam axis;  $k(z)$  is the laser beam concentration coefficient, dependent on longitudinal coordinate  $z$  and conditioned by focusing;  $\beta$  is the incidence angle of radiation with keyhole surface;  $R_{II, \perp}(\beta)$  is the reflection coefficient accordingly for *s* (*II*) and *p* ( $\perp$ ) polarization;  $z$  is the coordinate admeasured from target surface;  $z'$  is the coordinate of reflection point;  $a$  is the keyhole radius;  $\Delta$  is the beam axis shift from keyhole axis;  $\alpha$  is the polar angle;  $\theta(x)$  is the Heaviside function.

Taking into consideration only three first re-reflections for engaged power distribution one can obtain:

$$q \left( z, \alpha, a(z), \frac{da}{dz} \right) = \sum_{i=0}^3 (a_{iII} + q_{i\perp}).$$

**Heat-mass transfer in weld pool by deep penetration.** Thermal and hydrodynamic processes in work zone during laser welding with deep penetration are characterized by serious interdependence in theoretical description. So, resolution of hydrodynamic problem is determinate coefficients conversion in heat tra-

nsfer expression and solution of thermal task is defined boundary conditions of hydrodynamics problem. From the mathematic point of view the difficulty is available in «physical» nonlinearity because of temperature dependence of such parameters as viscosity, thermal conductivity and thermal diffusivity, and also in geometric nonlinearity, which is nascent because of uncertainty of pending areas boundaries determinate from resolution. At the same time, there are row of factors which make the analytic solution of heat mass transfer problem possible in spite of calculation difficulties. Comparison of characteristic scales allows proceeding from 3D task to 2D one.

At first we examined a hydrodynamic problem. Distribution of melt velocity is described by Navier–Stokes equation:

$$\frac{\partial \vec{V}}{\partial t} + (\vec{V} \nabla) \vec{V} = -\nabla \frac{p}{\rho} + \nu \Delta \vec{V},$$

where  $\vec{V}$  is the flow velocity;  $p$  is the pressure;  $\rho$ ,  $\nu$  is the density and kinematical viscosity, respectively.

Consider a quasi-steady situation, when field velocity is not depending on time evidently. Since Reynolds number at typical parameters values for welding with deep penetration is too much than 1, one can neglect viscosity in first approximation. In this instance melt flow can be examined as a potential with potential  $\varphi$ , satisfied to Laplace equation  $\Delta \varphi = 0$ . On keyhole surface there is condition of boundary impermeability (as evaporation flow is rather small) and on melting front – condition of continuity of normal to surface velocity:

$$\frac{\partial \varphi}{\partial \vec{n}} \Big|_g = 0; \quad \frac{\partial \varphi}{\partial \vec{N}} \Big|_G = -\vec{V}_0 \vec{N},$$

where  $g$  is the keyhole surface;  $\vec{n}$  is the external normal to surface  $g$ ;  $G$  is the melting front;  $\vec{N}$  is the external normal to melting front. The solution of this problem was getting [15] by combination of variables separation and conformal mapping:

$$\varphi = -V_0 \sum_1^{\infty} \frac{b_n \tilde{R}^{2n} - b_{-n}}{\tilde{R}^{2n} - \tilde{a}^{2n}} \left( r^n + \frac{\tilde{a}^{2n}}{r^n} \right) \cos(n\alpha),$$

where  $r$  and  $\alpha$  are the polar coordinates;  $\tilde{R}$ ,  $\tilde{a}$  are the circle radii on surface of conformal mapping, on which are reflected sections of melting front and keyhole, accordingly;  $b_n$  is the coefficient of mapping function

$Z(\tau)$  to Loran’s series expansion  $Z = \sum_{n=-\infty}^{\infty} b_n \tau^n$ .

Heat problem, which is determinate shape of melting front, can be solved by method of iterations. At first, it is calculated melting velocity field without taking into consideration melting boundaries, then determinates temperature field and melting boundary and, at last, the new velocity field with taking into account melt boundaries, and then process repeats.

It is necessary to note that although considerable of melting viscosity is lead to velocity field modification, but on temperature distribution it is not effect practically. As typical spatial scopes are defined in this case by thickness of boundary layers, but it is smaller than typical flow dimensions, so Peclet number for boundary layers is much smaller than that for main flow. Therefore to a first approximation we can neglect their influence to thermal field formation and consider only heat flow which is connected with main melt flow.

The thermal field is determinate by heat transfer equitation with evident boundary conditions:

$$\vec{V}\nabla T = \chi\Delta T; \quad T|_{r \rightarrow \infty} \rightarrow T_0; \quad \left. \frac{\partial T}{\partial n} \right|_g = -\frac{q}{\lambda},$$

where  $\chi$  is the thermal diffusivity;  $\lambda$  is the heat conductivity;  $q$  is the distribution of engaged power radiation on keyhole.

For solving this problem, it is comfortably to proceed from physical plane  $(x, y)$  to complex potential plane  $\Phi = \varphi + i\psi$ , where  $\psi$  is the flow function, and after that use Fourier integral transformation:

$$T(\zeta, \eta) = \frac{a}{\pi\lambda} \exp\{Pe\zeta\} \int_{-1}^1 \frac{q(-\zeta') \exp\{Pe\zeta'\}}{\sqrt{1-\zeta'^2}} \times \\ \times K_0(Pe\sqrt{\eta'^2 + (\zeta - \zeta')^2}) d\zeta', \\ \left\{ \begin{array}{l} \zeta = -\frac{1}{2} \left( \frac{r}{a} + \frac{a}{r} \right) \cos \alpha, \\ \eta = -\frac{1}{2} \left( \frac{r}{a} - \frac{a}{r} \right) \sin \alpha, \end{array} \right.$$

where  $K_0$  is the MacDonald's function.

**Evaporation, condensation and vapor flow in keyhole.** The processes of evaporation, vapor flow and condensation in keyhole are determinate pressure balance supporting keyhole existence. For construction of model evaporation assuming that vapor in keyhole is saturated and submitted to Poisson equation:

$$n = n_0 \exp \left\{ \frac{\lambda_v}{kT_0} - \frac{\lambda_v}{kT} \right\}.$$

Assuming also that vapors removal from external boundary of Knudsen layer is occur not for normal for it, but along its surface, i.e. normal to surface «hydrodynamic» velocity on external boundary of Knudsen layer is equal to zero. Taking into account these theses were received expressions which are contact densities of mass, momentum and energy fluxes with local temperature differences of keyhole surface and streams at surface according to gas dynamic flow velocity.

Quasi 1D approximation was used for description of vapor moving in keyhole. And at the same time, all values, which defined gas dynamic processes (vapor flow velocity  $V$ , its pressure  $p$  and density  $\rho$ ), are the functions of only one coordinate  $z$ , concurred with keyhole axis. For description vapor flow moving were used 1D continuity equations of mass, momentum and energy fluxes along keyhole axis with source-terms connected with evaporation and condensation on its surface.

Boundary conditions were corresponded to adiabatic outflow on keyhole outlet and heat equilibrium in the root. Keyhole radius is defined by balance of atmosphere and capillary pressure, on the one hand, and vapor pressure, on the other hand. For solution this task was developed approximation analytic procedure, which is permissive to consider volumetric and surface condensation influence on vapor flow. For nondimensional density  $s$ , pressure  $\psi$  and velocity  $u$ , the solution is

$$s = \varphi = b - \frac{\sqrt{2\pi}}{l} \frac{\int \mu IdS}{s (k\langle T \rangle + I_e \alpha_e) n_0 \left( \frac{k\langle T \rangle}{m} \right)^{1/2}}, \\ u = \frac{1}{s} \frac{\int_0^z (S\mu IdS) dz}{b(k\langle T \rangle + \alpha_e I_e) n_0 \left( \frac{k\langle T \rangle}{m} \right)^{1/2} - \frac{\sqrt{\pi}}{l} \int S \mu IdS},$$

where  $b = \exp\{y_0 - \langle y \rangle\}$ ;  $y = \frac{\lambda_p}{kT}$ ;  $\langle y \rangle = \frac{\lambda_p}{\langle T \rangle}$ ;  $\sqrt{\alpha_e}$  is the ionicity;  $I_e$  is the ionization potential.

The application criterion of this solution is  $u \ll 1$ .

**Formation of the weld metal microstructure.** In beam processing of steels, when period of material stay at temperatures higher the austenite transformation point makes parts of second, and cooling speeds reach thousand degrees per second, the classical theory of phase transformations in steels predicts a martensite structure in the zone being processed, that does not correspond to experimental data. The reason of such divergence between the theory and reality is an assumption about equilibrium «thermodynamic» character of phase transformations put in the basis of the theory.

Phase transformations in steels occurring at austenite decay (at cooling) or at its formation (at heating) and determining the metal structure as a result consists of two components. The first one is connected to decay (or formation) of carbon solid solution in iron and formation (dissolution) of ferric carbide, and the second one is connected with rebuilding of the face-centered cubic crystal lattice into the volume-centered one in cooling and back in heating.

To calculate parameters of cementite precipitates there was developed the kinetic model of formation and growth of precipitates of the second phase at decay of the solid solutions and kinetic model of rebuilding of the crystal lattice ( $\alpha \leftrightarrow \gamma$  transformation) constructed on the same principles, as the model of origin and growth of precipitates. The role of the kinetic equation in this case is played by the equation of the growth velocity of an area with the volume-centered lattice in austenite matrix (at cooling) or an area with the face-centered lattice in ferrite-pearlite or bainite matrixes (at heating).

Transformation speed here is a difference of speeds of  $\gamma \rightarrow \alpha$  and  $\alpha \rightarrow \gamma$  transformations, besides each of them is proportional to probability of corresponding

fluctuation according to thermofluctuational model of phase transformations.

Since the Gibbs potential of phases at the boundary depends on concentration of the dissolved carbon, so the equilibrium temperature depends on concentration of carbon at the grain surface of a new phase (thus balance is determined by heating and cooling speeds, influencing on diffusion) and the second equation of the model is the equation of non-stationary diffusion in view of temperature dependence of the diffusion factors of carbon for both types of lattices.

As movement speed of the phase border in this case is so that Peclet diffusion number is not small, the diffusion equation, as against a problem about growth of carbides, was solved with considering a convective term. On the other hand, as the sizes of grains in growth stage considerably exceed the diffusion layer thickness, the diffusion problem was considered as 1D. The joint solution of the connected problems about kinetics of a new phase grain growth and about diffusion of carbon before its front allows calculating quantity of the new phase at any moment of the thermal cycle.

Processes of carbide precipitation and rebuilding of the lattice are connected with each other since the difference of Gibbs potential of face-centered and volume-centered phases depends on the dissolved carbon concentration, which, in turn, depends on quantity of carbon fixed in carbides.

Thus, the equations of the model of carbide precipitation and models of rebuilding of the crystal lattice were connected with each other (through factors), and the self-consistent equations system describing both the transformation of the crystal lattice and the decay of the solid solution were obtained, i.e. the new equation system completely describes formation of a material microstructure at high-speed heating and cooling. At the same time, both the initial carbides size and the grains initial

sizes, and density of crystal lattice defects influencing on diffusion factor value are considered as parameters of initial structure of metal. The thermal cycle is in parameter of the model; its features are determined by a technological mode of processing. This solution allows calculating directly evolution of the metal phase combination in the processing zone without attracting empirical dependences, such as the Avrami equation. At the set degree of completeness of the transformation, the model equations change into the ones of connection of temperature and corresponding time after the beginning of transformation, i.e. they describe full TTT diagram of austenite decay. It permits to use existent techniques of quantitative forecasting of phase combination and microstructure on the basis of such diagrams for beam processing.

**Calculation of the weld pool parameters**

A full set of mathematical models of the physical processes, considered above, permits to calculate such characteristics of the melted zone as depth and shape of a keyhole, its surface temperature, weld pool surface shape and other necessary values. Algorithm of the calculations is following: one can substitute value of the absorbed power distribution, taking into account reflections, into an expression for a heat field and suppose  $r = a$ , that corresponds to the keyhole surface. Thus we obtain an equation connecting surface temperature with the keyhole radius  $a$  and an inclination corner of its walls. The second equation of the mathematical model is a forces balance condition, that is equality of vapors pressure in the keyhole and capillary pressure  $p = \sigma/a$  ( $\sigma$  is the surface tension factor), compressing the keyhole. The analysis of evaporation process of at beam acting on metal shows that the vapor condition is close to saturation [16], and we can use an expression for pressure of saturated vapor in order to connect pressure in the keyhole with temperature of its surface  $T$ :

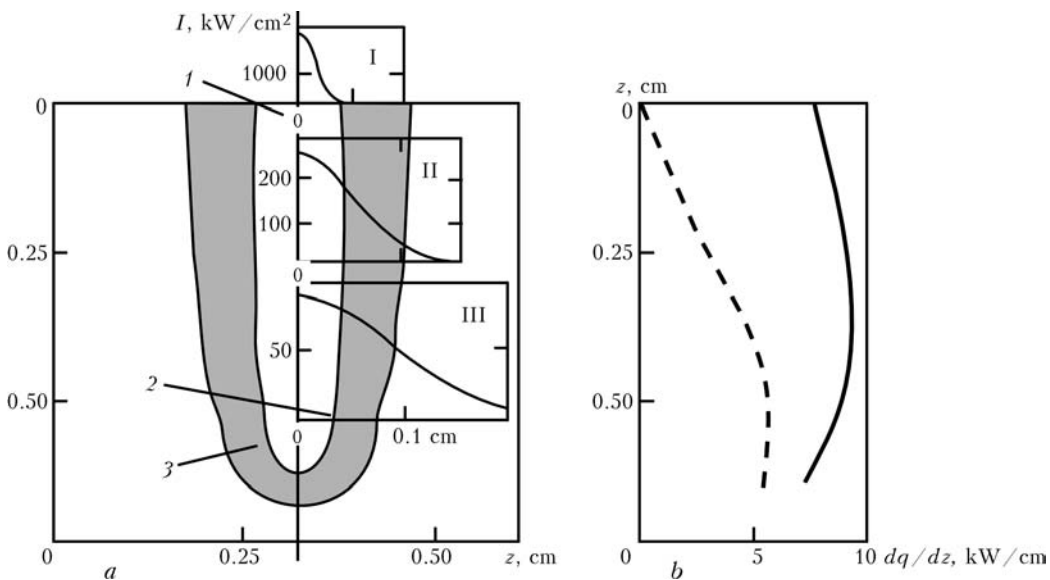


**Figure 1.** Calculation results: *a* – geometry of melt zone in laser welding (front section) and distributions of laser radiation intensity in considering focus on depth of 0 (I), 0.27 (II) and 0.55 (III) cm: 1 – keyhole; 2 – zone of absorption of reflected radiation; 3 – molten pool; *b* – dependence of absorbed energy distribution on *z*-coordinate through the keyhole depth (solid line shows the absorbed energy distribution, dashed – distribution of that part of the absorbed energy which is result of the previous reflections)



$$p = A \exp(-B/T),$$

where  $A$  and  $B$  are the tabulated values.

It is necessary to take an average temperature throughout the keyhole perimeter at the fixed coordinate  $z$ . Excepting temperature from these two equations we get a differential equation for describing cavity surface shape:

$$f\left(a, \frac{da}{dz}\right) = 0.$$

This equation is unsolvable with respect to a derivative and a special algorithm is necessary to solve it. One can take  $\Delta z$  as a step on coordinate  $z$  and number steps by  $k$ ;  $k = 0, 1, 2, \dots$ . It is possible to divide the target thickness into layers with thickness  $\Delta z$  and number them on  $k$ , so that  $k = 0$  meets to the surface layer. Then for  $(k + 1)$ -th layer,  $\frac{da}{dz} =$

$$= \frac{(a_{k+1} - a_k)}{\Delta z}.$$

We take an average value of the keyhole radius on  $(k + 1)$ -th layer, namely  $a = \frac{1}{2}(a_k + a_{k+1})$ . Then on sampling one can obtain  $f(a_k, a_{k+1}) = 0$ .

If  $a_0$  is known, it is possible to construct a cavity profile solving the equation step by step in any way. To determine  $a_0$ , it is necessary to solve the previous equation relative to  $a$  at the certain initial value  $da/dz$  that can be made numerically only. In solving the last equation it should be determined both the cavity radius and the power  $\Delta W_k$  absorbed by  $k$ -th layer with thickness  $\Delta z$  for each step. Calculations stop when a condition  $\Sigma \Delta W_k = W$  is achieved ( $W$  is the full power of falling radiation).

The example of calculations by the model is shown in Figure 1 for welding of the aluminum alloy containing 4 % Zn and 1 % Mg. Here distribution of initial radiation intensity corresponds to mode TEM<sub>00</sub>; welding speed is 5 cm/s, radiation power of 4.9 kW, focus position is 1 mm above the sample surface, focal distance of 15 cm, Fresnel number is 4.7, focal radius (at 86 % of full power inside) is 0.0116 cm.

In Figure 2 there are shown results of comparison of calculations by the model described above with the experiments obtained in Fraunhofer Institute of Laser Technique (Aachen, Germany) for dependence of the melt depth on welding speed. Parameters of the process correspond with ones described above.

#### Methodology of the inverse problem solution.

To choose technological modes of treatment providing the required shape and depth of melting and optimum microstructure of metal in the zone being processed or corresponding to other criteria, which technologist chooses, it is necessary to build a solution of a so-called inverse problem. For this purpose the constructed algorithm of the «direct» problem solution and a method of multivariate nonlinear optimization have been used (a coordinate-wise optimization method). At that the solution of the inverse problem is found by fast fulfilling solutions of the «direct» problem with

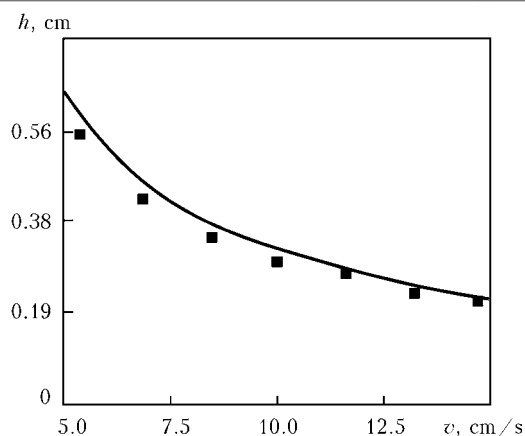


Figure 2. Comparison of model calculations (solid line) with experimental results (points)

various initial conditions. Program realization of the LaserCAD system allows one to execute searching process of the inverse problem solution in three various ways: «manual» optimization when a user can interactively change parameters of a technological mode achieving a desirable result; «manual optimization with tips» when the system specifies direction for changing parameters of a technological mode to achieve desirable result; and «automatic» optimization using a coordinate-wise optimization method. Using such of solutions and the corresponding software to solve the inverse problem it becomes possible to develop technologies of high-speed beam processing of materials providing specified characteristics of welds.

1. Roemer, G.R.B.E. (1999) Modeling and control of laser surface treatment. June 3. University of Twente.
2. Karkhin, V.A., Ploshikhin, V.V., Bergman, H.V. (2002) Simulation of thermal and solidification processes in laser welding of aluminum plates. *The Paton Welding J.*, p. 10–14.
3. Lopota, V.A., Sukhov, Yu.T., Turichin, G.A. (1997) Model of laser welding with deep penetration for using in technology. *Izvestiya AN. Series Physics*, 61(8), p. 1613–1618.
4. Anisimov, S.I., Imas, J.A., Romanov, S.G. et al. (1970) Action of high-power radiation on metals. Moscow: Nauka.
5. Dowden, J., Davis, M., Kapadia, P. (1983) Some aspects of the fluid dynamics of laser welding. *J. Fluid Mech.*, 126, p. 123–146.
6. Beck, M., Berger, P., Hugel, M. (1992) Modelling of keyhole-melt interaction in laser deep penetration welding. *ECLAT*, p. 693–698.
7. Kaplan, A. (1994) Model of deep penetration laser welding based on calculation of the keyhole profile. *J. Phys. D: Appl. Phys.*, 27, p. 1805–1814.
8. Capitelli, M., Casavola, A., Colonna, G. et al. (2004) Laser-induced plasma expansion: theoretical and experimental aspects. *Spectrochimica Acta B*, (59), p. 271.
9. Radziemski, L.J., Cremers, D.A. (1989) *Laser-induced plasmas and applications*. New York: Dekker.
10. Phuoc, T.X. (2005) An experimental and numerical study of laser-induced spark in air. *Optics and Lasers in Engineering*, 43, p. 113.
11. Loiziansky, L.G. (2003) *Mechanics of liquid and gas*. Moscow: Drofa.
12. Koroteev, N.I., Shumaj, I.L. (1991) *Physics of powerful laser radiation*. Moscow: Nauka.
13. Diltey, U., Gumeniuk, A., Lopota, V. et al. (2000) Kinetic description of keyhole plasma in laser welding. *J. Phys. D: Appl. Phys.*, 33(21), p. 2747.
14. Rajzer, Yu.P. (1974) *Laser spark and distribution of optical discharge*. Moscow: Nauka.
15. Turichin, G.A. (1990) *Physical basis of seam formation process in EBW with deep penetration*: PhD thesis. Leningrad: LPI.
16. Pavlyukevich, N.V., Gorelik, G.E., Levdansky, V.V. (1980) *Physical kinetics and transfer processes at phase transformations*. Minsk: Navuka i Tekhnika.

# MODELLING THE INFLUENCE OF RESISTANCE SPOT WELDING ON MATERIAL PROPERTIES

N.J. den UIJL

Corus RD&T, the Netherlands

Currently the majority of joints within the automotive industry is made using resistance spot welding (RSW). An accurate model of the RSW process predicts the resultant material properties. The model enables manufacturers to predict the final characteristics of a workpiece. It also enables the steel producer to identify process windows which can be used for the development of materials. To support these activities research projects have been initiated and carried out at Corus RD&T to simulate RSW and to link chemistry of materials to weldability. Weldability of steels is often summarised as «weldability is reciprocal to hardness». Otherwise put, the maximum hardness after welding is inversely related to the material weldability. Because an RS weld can be subdivided in zones such as the weld nugget, the heat-affected zone (HAZ) and base material, all these zones can be considered in a broader look on weldability. Finite element simulations give first the maximum hardness in the nugget after welding, and second the transition in the HAZ of a fully martensitic weld nugget to the ferritic base material, and third predictions on stress and deformation in the base material. All three effects are considered in this paper while assessing the weldability of a material for automotive applications. In this paper first the RSW process is simulated. The model is then used to investigate the phase composition of the weld nugget and the HAZ. From these thermal analyses stress and deformation due to welding can be predicted. Also the results of thermal calculations can be used to predict maximum hardness levels after welding. This results in a more complete overview of the effects of welding on the material.

RSW was modelled using SYSWELD (Figures 1 and 2) and Sorpas (see Figure 2), commercially available finite element software packages. To verify the results calculated weld nugget sizes at various current intensities were plotted against experimentally collected data of spot-welded steels (see Figure 2). SYSWELD was used to simulate spot-welded DC04 sheets (thickness 1.2 mm) and Sorpas was used to simulate spot-welded mild steel sheets (thickness 1.2 mm). Generally the aim in the automotive industry is to produce resistance spot welds with a weld nugget size of  $5\sqrt{\delta}$ , i.e. 5 times the square root of the material thickness. Smaller welds are to be avoided because they can lead to decreased strength (mechanical performance) of the welds, especially in crash. Larger welds are undesirable because of increased production times.

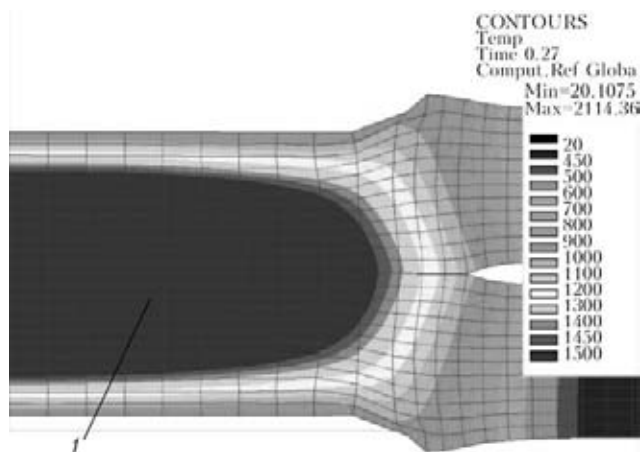


**Figure 1.** SYSWELD simulation of two RS-welded sheets 1.2 mm thick:  $t$  – molten material; other zones – temperatures at the end of welding at  $t = 0.27$  s

In Figure 2 the dotted line represents the  $5\sqrt{\delta}$  weld nugget size (5.48 mm for sheet 1.2 mm thick). At these current densities that are of interest to automotive production processes these simulations agreed very well with experiments.

## Temperature analysis

The RSW model predicts the thermal cycle and resultant thermodynamics and mechanics of welding. Figure 3 depicts the heating and corresponding weld growth of resistance spot welded mild steel (welding schedule of 13 welds 5 holds). In this case the welding current ( $I = 9$  kA) started at  $t = 0.01$  s and lasted for 13 cycles (0.26 s). It can be seen that at first the maximum temperature rises whilst no weld pool is formed as the maximum temperature is still below the melting temperature of the steel.

As soon as melting does occur the weld pool grows very fast, first in diameter (Figure 4) and next in

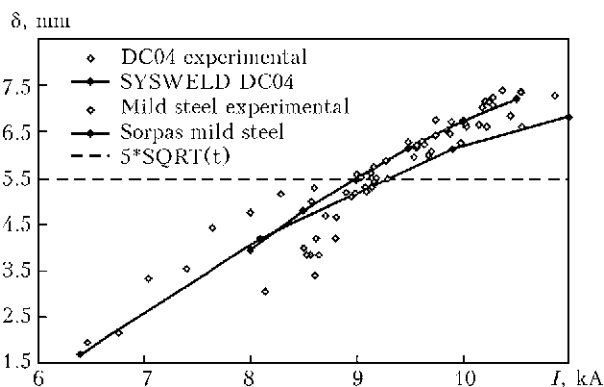


**Figure 2.** Experimental and simulated weld nugget growth curves for uncoated steel sheets 1.2 mm thick

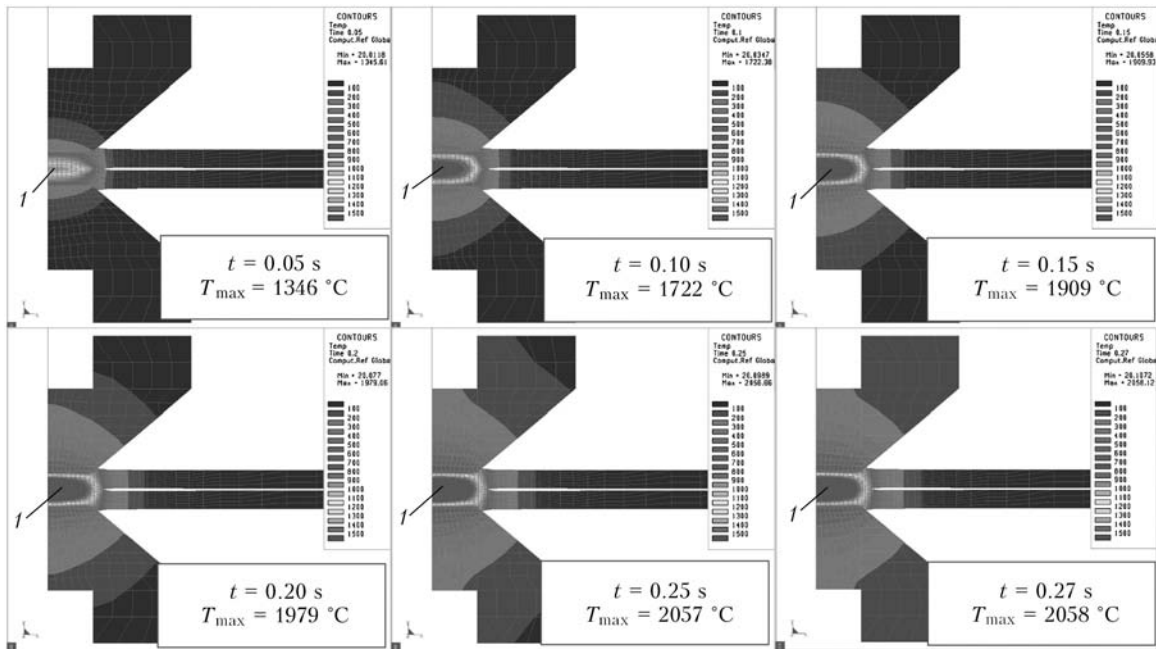


Figure 3. SYSWELD-simulated heating and subsequent growth of weld pool during RSW at  $I = 9$  kA:  $I$  — molten material

thickness. Further heating does correspond to further growth of the weld pool (both in diameter and in thickness), but this growth rate seems to decrease drastically. In fact the growth of total volume of molten material is rather constant, as can be seen in Figure 5. This is due to the fact that volume growth is cubic, whilst growth in diameter or thickness is of first order. Even if the growth in thickness is left out of the equation, the diameter of the weld would only need to increase with 2.15 % to accommodate a volume increase of 10 %.

Aided by the cooling capacity of the electrodes (especially if they are water-cooled) the decrease in temperature as soon as the current is switched of is also very large. Figure 6 shows that to cool the entire work piece below 500 °C (traditionally seen as a boundary value for HAZ effects) does not take more than 0.28 s. In this short period of time the maximum temperature in the workpiece went down by 1500 °C. It is therefore save to state that RSW steel sheet is quenched after welding. In this particular case the electrodes were in contact with the workpiece after

welding for a total of 5 cycles (i.e. 0.10 s). In this period cooling is fastest. Cooling remains fast though after the electrodes have been removed from the steel due to the fact that resistance spot welds are small, whilst the rest of the steel sheet offers a heat sink. As the temperature distribution in the workpiece evens out, the cooling rate slows down. To reach room temperature (important to ensure all transformation processes have stopped) takes quite a while as cooling to the surrounding environment through convection is a much less efficient process than cooling through conduction to the electrodes (Figure 7, welding schedule of 13w 5h).

It is probably impossible to determine the maximum temperature in a workpiece during RSW experimentally, but some remarks on the calculated value for the peak temperature can be made. As the model does not take into account fluid flow in the molten weld pool due to electro-magnetic influences the temperature in the weld pool is much more homogenised during welding than it is in the model. A maximum temperature exceeding 2000 °C for instance would

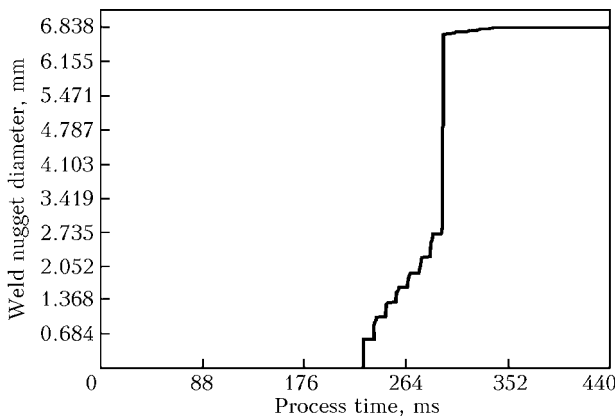


Figure 4. Sorpas-calculated growth of weld pool diameter during RSW

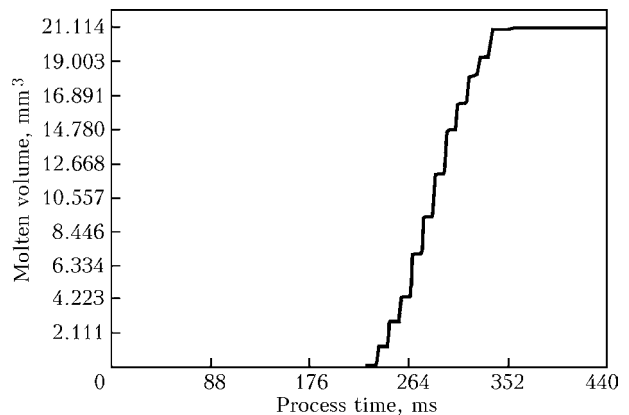


Figure 5. Sorpas-calculated growth of weld pool volume during RSW

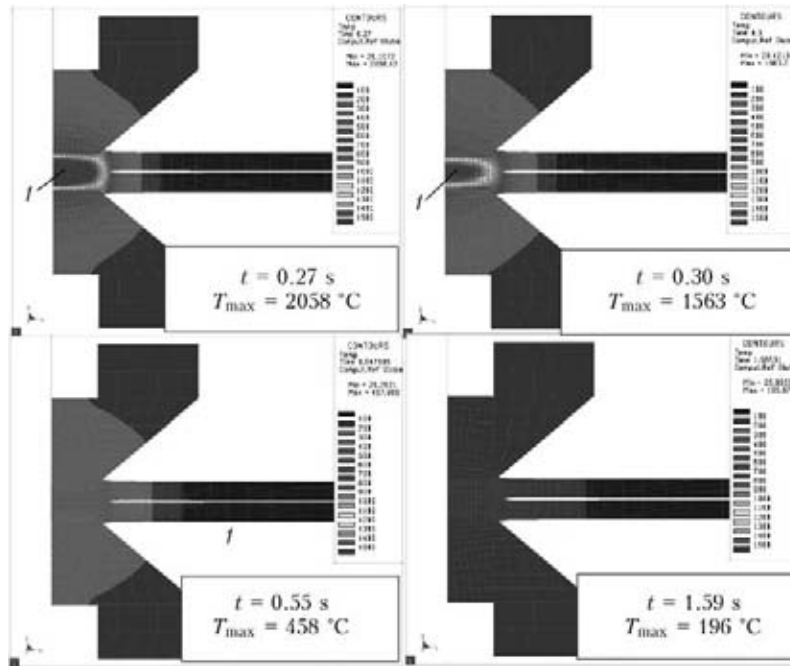


Figure 6. SYSWELD-simulated cooling of workpiece after RSW: / — molten material; dark zones — temperatures below 100 °C

immediately cause the weld pool to expand. The calculated value does however give an indication for the total amount of energy supplied to the material during welding.

Figure 8 shows the temperature profile in the centre of the weld for various spot welds. All these welds were calculated for a weld scheme of 13w 5h (0.26 s of applied current and 0.10 s hold time with the electrodes in contact with the material). The area below the temperature lines gives an indication for the amount of energy supplied to the weld pool. Two phenomena can be seen in this Figure. First of all the fact that the calculated maximum temperature in the weld is reached sooner for higher weld currents. The drop in temperature for higher currents is due to the way certain thermodynamic parameters are defined in the model. For instance, the thermal contact resistance between electrode and workpiece changes at higher temperatures. The other phenomena is much more apparent for the welds calculated for lower currents. After the maximum temperature in the material exceeds 1500 °C, the material melts and the weld pool starts to grow. This can be seen in Figure 8 by a flattening thermal profile for the weld currents of 8.5

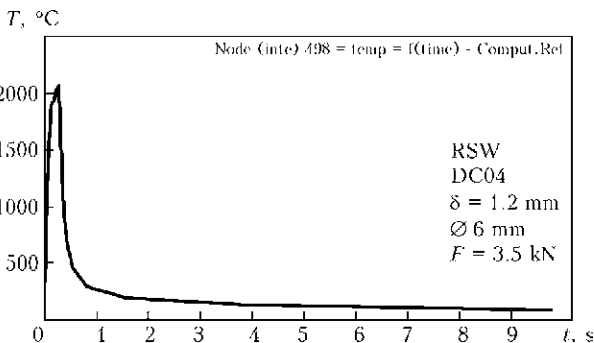


Figure 7. SYSWELD-calculated maximum temperature in workpiece during RSW at  $I = 9$  kA

and 9.0 kA. The same effect can also be seen for the other currents, but less pronounced. This stabilisation of the temperature is caused by the cooling effect of the latent heat needed to melt material during the growth of the weld pool. It can be seen in Figure that the temperature starts to increase again after a while.

This discontinuity is caused by the fact that latent heat acts on a surface (i.e. the melting surface between the molten weld pool and the solid steel), a second order effect. The weld pool is heated due to the Joule effect which acts on a volume, a third order effect. As the weld pool grows, the Joule heating on the molten material is initially checked by the cooling effect of latent heat on the liquid-solid boundary. After a while the weld pool reaches a size after which Joule heating works on a larger volume than the surface latent heat cooling effect, causing a renewed increase in temperature.

Closer inspection of the thermal profile for the centre of a single weld ( $I = 9$  kA) as shown in Figure 9 (welding schedule of 13w 5h) reveals several transi-

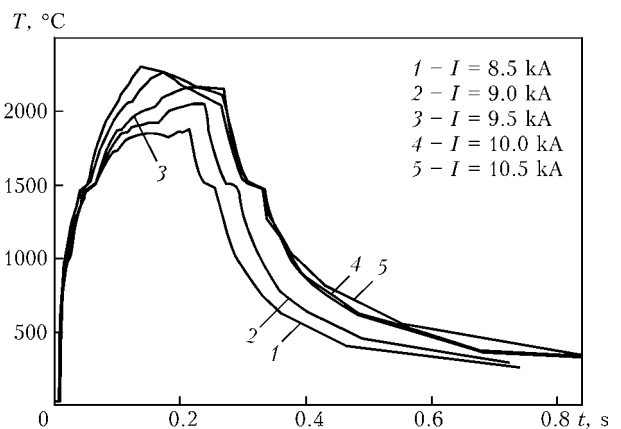


Figure 8. SYSWELD-calculated maximum temperature in workpieces during RSW of mild steel at various welding currents

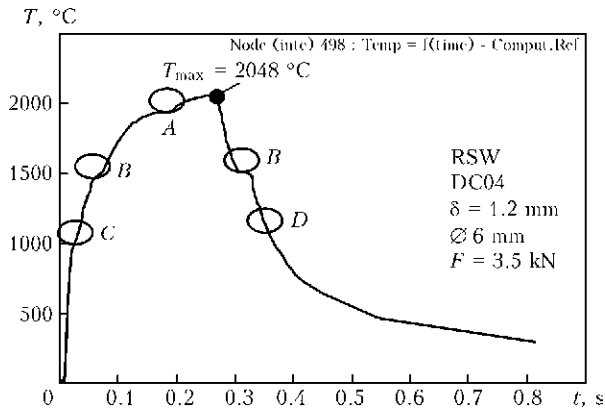


Figure 9. SYSWELD-calculated maximum temperature during RSW at  $I = 9$  kA (for designations see the text)

tion points. The point where Joule heating in the weld pool overtakes the cooling effect of latent heat is identified by point A, point B identifies the effect of latent heat at the transition from solid to liquid during heating and liquid to solid during cooling. Point C identifies the effect of phase change to austenite, while point D shows the change in cooling rate due to the release of the electrodes (thus changing the cooling mechanism).

As stated before, the weld pool is always cooled at such speed during RSW that the resultant microstructure will be the same as if the material was quenched. Figure 10 shows the temperature curves in a point in the HAZ for the same welds as shown in Figure 8. The calculated temperature in the HAZ is not influenced by molten flow phenomena and can therefore be considered the true temperature reached during welding. Again it can be seen that increased welding currents lead to increased temperatures. Also it can be seen that cooling in the HAZ is much less rigorous compared to the centre of the weld (approximately  $1100$  °C/s compared to more than  $5300$  °C/s). It is still very fast though.

Again a discontinuity temperature rate can be seen. The temperature at which this discontinuity occurs gives rise to the idea that this is caused by the change of initial material to austenite. However, a closer look

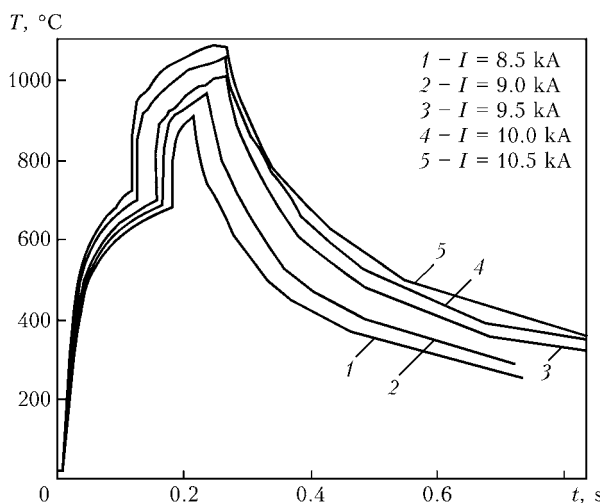


Figure 10. SYSWELD-calculated maximum temperature in the HAZ during RSW of mild steel at various welding currents

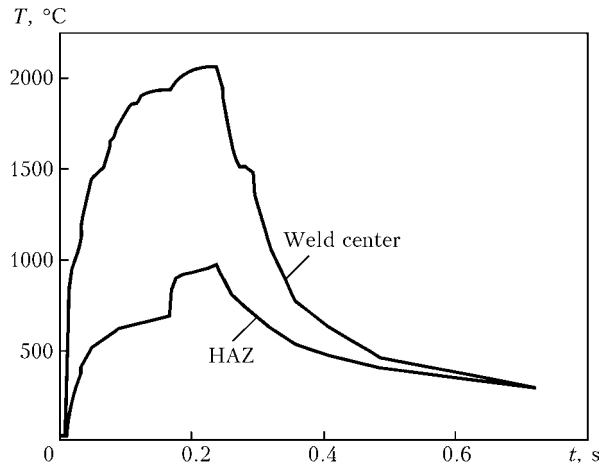


Figure 11. SYSWELD-calculated maximum temperature in the centre of weld and HAZ during RSW of mild steel at  $I = 9$  kA

at the temperature profile for a single weld shows that there may be a combination of effects occurring. Figure 11 shows the temperature profile of the centre of the weld and in the HAZ for a single weld (welding schedule of 13w 5h). Here it can be seen that the sudden rise in temperature coincides with the transition of the latent heat dominated growth of the weld pool to Joule heating dominated weld growth. It is this sudden «boost» in temperature rise that enables the temperature in the HAZ to rise.

#### Phase transformations

**Weld nugget.** The quenching effect caused by rapid cooling of the molten weld pool results in a fully martensitic microstructure in the weld nugget (Figure 12, welding schedule of 13w 5h). As the resultant microstructure is primarily dependent on the cooling rate the energy input is of almost no influence at all (Figure 13). The slight differences in transformation curves between different weld schemes is due to the fact that in welds made with higher welding currents the material will be at a higher temperature after similar periods of cooling (compare Figure 8). As martensitic transformation is temperature-dependent, a higher temperature will force less austenite to transform to martensite. Eventually the entire weld nugget will reach a temperature below the  $M_f$  temperature resulting in a fully martensitic structure.

**Heat-affected zone.** The situation is different in the HAZ. As mentioned before cooling rates in the

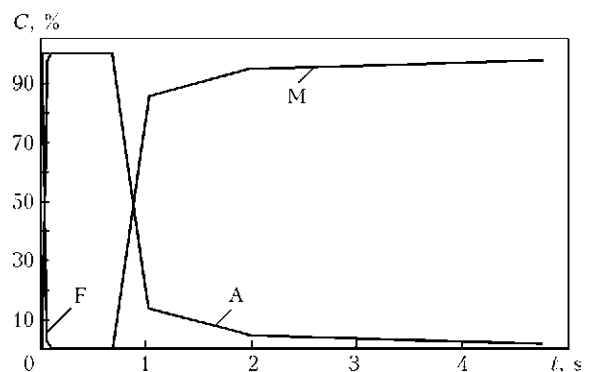


Figure 12. SYSWELD-calculated phase composition C in the weld centre during RSW of mild steel at  $I = 9$  kA

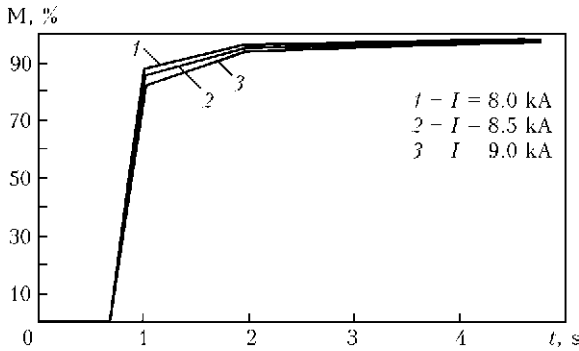


Figure 13. SYSWELD-calculated martensite component in the weld centre during RSW of mild steel at various welding currents

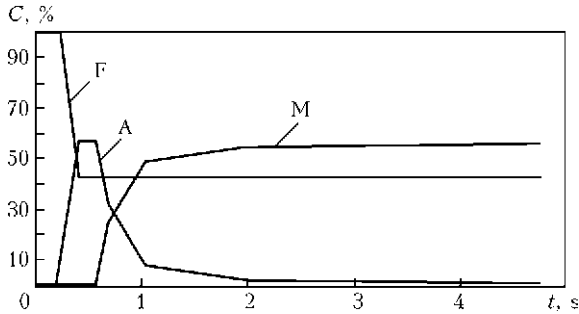


Figure 14. SYSWELD-calculated phase composition C in the HAZ during RSW of mild steel at I = 8.5 kA

HAZ are high (see Figure 11). Even though they are not as high as they are in the weld nugget, they are still sufficiently high to prevent the formation of any other phase but martensite. However, as not all of the material has been transformed to austenite, only a part of the material will be quenched to martensite (Figure 14, welding schedule of 13w 5h). After welding the HAZ will consist of ferrite and martensite with possibly some retained austenite. The resultant percentage of martensite is dependent upon the welding current (Figure 15). Although the examples shown here concern welded mild steels, the results would be similar if another class of steels was welded. If, for instance, dual-phase steel of 50 % ferrite and 50 % martensite would have been welded, the same percentage of initial material would transform, and the final ratio between ferrite and martensite in Figure 14 would have been approximately 1 to 4.

Apart from increased weld nugget size (see Figure 2) and HAZ dimensions, increased welding currents will also result in higher percentages of martensite in the HAZ. Although the transformation lags behind the welding operation, the material will transform rapidly after the temperature has decreased suf-

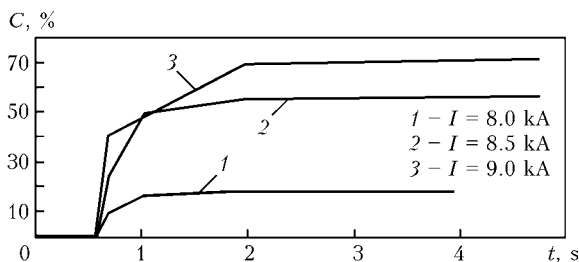


Figure 15. SYSWELD-calculated phase composition C in the HAZ during RSW of mild steel at various welding currents

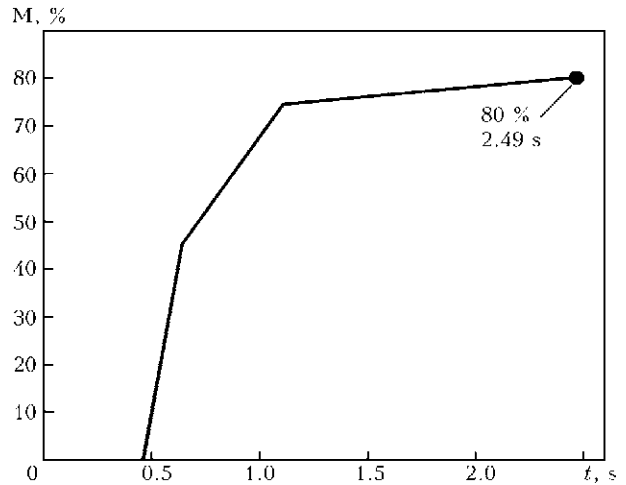


Figure 16. SYSWELD-calculated martensite component in the HAZ during RSW of mild steel at I = 11 kA

ficiently to allow the transformation of austenite into martensite. Figure 16 (welding schedule of 13w 5h) shows the percentage of martensite in the HAZ of an area in the HAZ against temperature for a resistance spot welded joint between two 1.2 mm thick pieces of uncoated mild steel. Just 2.48 s after the start of welding (welding started at  $t = 0.01$  s) 80 % of the original material in the HAZ has been transformed into martensite. Thus the HAZ effectively has become a different class of steel compared to the base material (dual phase instead of ferrite).

**Deformation.** It is also worth noting that the transformation to martensite takes place after the electrodes have been released from the workpiece. At the moment the clamping is released the weld is still rather hot and austenitic. If high strength steels show a lot of springback during assembly, it may be worthwhile to keep the electrode pressure on the workpiece until the weld has cooled down enough for it to gather strength.

Phase transformations will have an influence on the resulting mechanical characteristics of a weld. In Figure 17 it can be seen that maximum stresses decreases with increased supply of energy to the material (mild steel) in RSW. Decreased stress levels do not automatically lead to less deformation as can be seen in Figure 18, which gives the deformation against maximum temperature during welding. The reason for this can be found in the fact that RSW uses heating as well as forging to join materials. As the electrodes

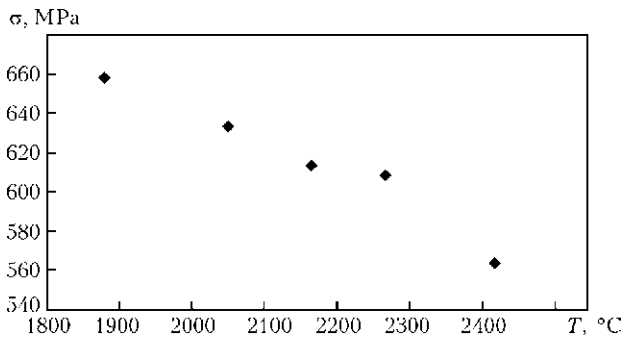


Figure 17. Calculated resultant maximum stresses after RSW against maximum temperature during welding

indent the material when it is soft (i.e. hot) the distortions in the workpiece increase.

When welding mild steel sheet material, the deformation due to the electrodes is actually larger than the deformation due to residual stresses in the workpiece (Figure 19, welding schedule of 13w 5h). Apart from the effects of welding, the total deformation of a workpiece is very much dependent upon a wide range of factors, such as the class of materials involved (e.g. mild steels or high strength steels or a combination of steels), the geometry of the workpiece, welding equipment (stiffness) and welding sequence. Results of mechanical analysis through simulation have to be studied carefully therefore before coming to conclusions.

### Weldability

**Carbon equivalent number.** Weldability of steels is usually described as the reverse of the hardenability of steels. This hardenability is then expressed in terms of a carbon equivalent ( $CE$ ), which should not exceed a certain value. In general a  $CE$  is based upon the amount of carbon present in the material and a range of other elements that influence the hardness of the material after welding with a factor expressing the relative impact of the element compared to the impact of carbon. Probably best known is the IIW formulation:

$$CE = C + Mn/6 + (Cr + Mo + V)/5 + (Cu + Ni)/15 \quad (1)$$

with all amounts expressed in wt.%. The IIW equation is used for steels with carbon content of 0.18 wt.% and more. For lower alloyed steels the Ito-Besseyou formula is well used:

$$CE = Si/30 + (Mn + Cr + Cu)/20 + Ni/60 + Mo/15 + V/10 + 5B. \quad (2)$$

This use of two different  $CE$  numbers highlights a drawback of  $CE$  numbers in general; they are chemistry dependent. The  $CE$  of a steel is in effect nothing

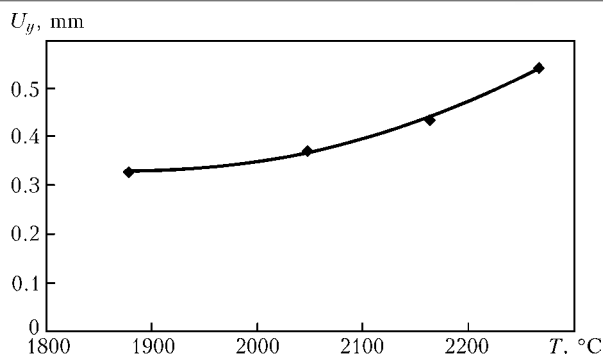


**Figure 18.** Calculated resultant maximum deformation after RSW against maximum temperature during welding

more than an indication in how far the material is capable to form martensite. Although the chemistry of a material and its ability to form martensite are very important factors in determining postweld hardness, it can be assumed that high speed welding processes such as RSW and laser welding of automotive steel sheet (typically 1–2 mm thick) is always going to result in the formation of martensite.

**Postweld hardness.** The challenge in welding thin steel sheet is to keep the hardness of this resultant martensite below a certain value (usually  $HV$  450 is taken) to ensure ductile failure of welded joints. RSW joints that are harder than  $HV$  450 tend to show brittle failure which is undesirable for automotive applications. Therefore models have been built to couple the  $CE$  to actual hardness levels after welding. Generally these models take one of two forms:

- chemistry-dependent models ( $HV = \sum H_i(X_j) V_i$ );
- (cooling) time and chemistry-dependent models

$$(HV = f(H_i(X_j), t_{8/5}),$$

where  $H_i(X_j)$  is the hardness of a certain constituent of the material;  $V_i$  is the amount of the constituent present; and  $t_{8/5}$  is the cooling time (which is often taken between 800 and 500 °C).

As the chemistry-dependent models do not take cooling rates into account they are generally only

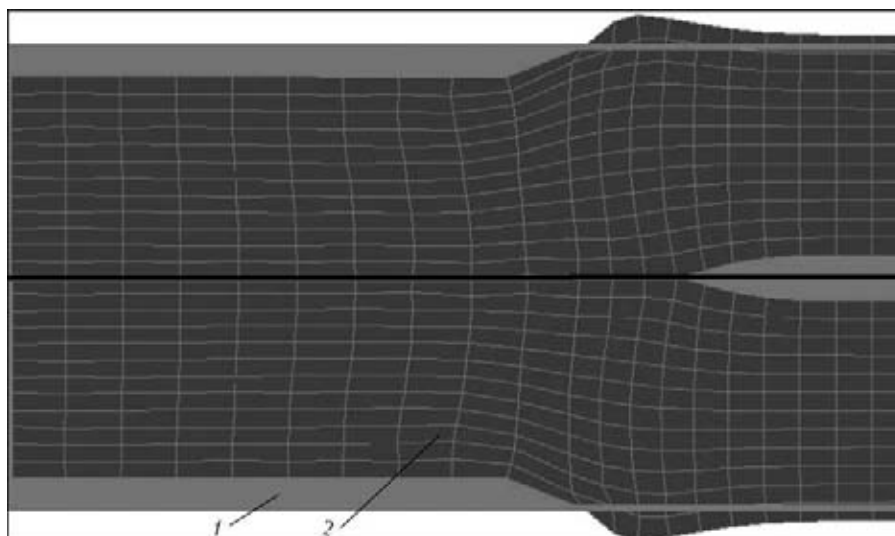


**Figure 19.** SYSWELD-simulated deformation of two RS-welded 1.2 mm thick mild steel sheets: 1 – pre-weld configuration; 2 – postweld shape; deformations are enlarged 10-fold

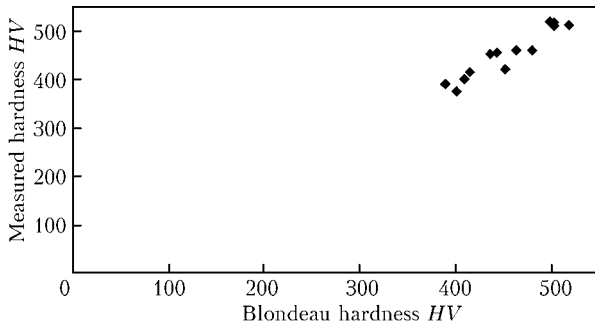


Figure 20. Correlation between experiment and the use of the Blondeau model to calculate maximum hardness values after RSW

applicable to one welding process and for a certain range of thickness of materials. The advantage is that they are «cheap» in calculation costs. The models that do take the cooling time into account are much more suited to be used for a wide range of processes and material thicknesses. The drawback is that the user is often required to use sophisticated finite element modelling to calculate the cooling temperatures. Also these calculations have to be repeated whenever there is a significant change in the welding process or material geometry.

Blondeau [1] developed a model for heat treating low alloyed carbon steels that works surprisingly well for RS-welded steels. Blondeau predicts the maximum hardness of martensite to be dependent upon composition and the cooling rate at 700 °C:

$$127 + 949C + 27Si + 11Mn + 8Ni + 16Cr + 21 \log t_r \quad (3)$$

with all amounts expressed in wt.%;  $t_r$  the cooling rate at 700 °C in °C/h. This model was tested against a series of measured hardness values in RS-welded high strength steels (7 DP and 5 TRIP steels, with thickness ranging from 1.0 to 1.6 mm). The results depicted in Figure 20 show good correlation.

In general chemistry-dependent equations take the shape of

$$HV = A + B \cdot CE, \quad (4)$$

whereas chemistry and cooling rate dependent models take the shape of

$$HV = P + Q \cdot CE + R(t). \quad (5)$$

If the equations are used to predict hardness values of the same process and material combination the equ-

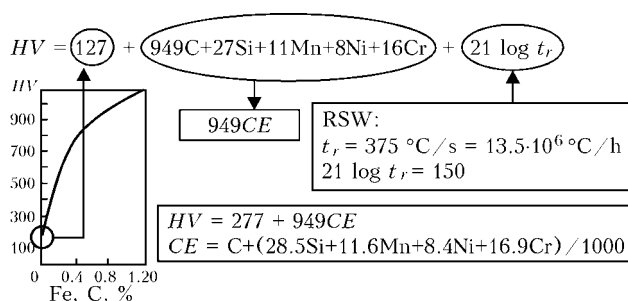


Figure 21. Derivation of simple hardness equation for RSW of steel sheet using Blondeaus model

ations are roughly similar. As long as the cooling range does not change too much, the value of  $R(t)$  can be considered a constant. In that case the second equation becomes

$$HV = (P + R(t)) + Q \cdot CE. \quad (6)$$

In fact  $P$  represents the hardness of unalloyed bcc iron and  $R(t)$  represents the impact of cooling rate upon the hardness of martensite.  $Q$  represents the influence of alloying (itself represented in the carbon equivalence number) on the hardness of martensite.

For example in the case of the Blondeau model (Figure 21) Eq. (3) can be written as

$$HV = (127 + 21 \log t_r) + 949CE, \quad (7)$$

where

$$CE = C + (28.5Si + 11.6Mn + 8.4Ni + 16.9Cr) / 1000. \quad (8)$$

For RSW high strength steel sheet (see Figure 20) an cooling rate of 3750 °C/s ( $13.5 \cdot 10^6$  °C/h) is reached, leading to a value of 150 for the term  $21 \log t_r$ . Although the hardness of martensite is cooling rate dependent, the cooling rate needs to change dramatically to have an impact on the resultant hardness. For instance, doubling the cooling rate will only result in an hardness increase of  $HV 6.3$  ( $\log 2t_r = \log t_r + \log 2 = \log t_r + 0.301$  and  $21 \cdot 0.301 = HV 6.3$ ).

Blondeaus model for RSW steel sheet then becomes

$$HV = 277 + 949CE. \quad (9)$$

**Weldability of high strength steel.** To predict postweld hardness after welding chemistry based models are much more user-friendly than models taking into account both chemistry and cooling rate. Even though they can only be used with restrictions on process and material. It was therefore decided to try and find a simple equation to derive the postweld hardness of high strength steels (DP and TRIP) from the chemical composition of the material. This way a prediction concerning the weldability of the material can be made and possible solutions (e.g. postweld heat treatment, different joining methods) can be found.

Using experimental data available at Corus RD&T (for instance used for Figure 20) together with known information on  $CE$  numbers (as described above), it was possible to derive a simple equation to enable predictions of (resistance spot) weldability for high strength steels:

$$HV = 240 + 855CE, \quad (10)$$

where

$$CE = C + Si/40 + Mn/20. \quad (11)$$

The results can be seen in Figure 22 and correlate very well.



## CONCLUSION

Research is done at Corus RD&T to investigate the influence of RSW on material properties. The outcome of this research serves to increase understanding on weldability of steel sheet for the automotive industry. In this paper results were presented on the thermal analysis and subsequent changes in microstructure of steel sheet during RSW. Also the results of simulation and experimental work were combined to derive relations between chemistry and hardness for RSW of steel sheet material. These relations can be used to estimate the weldability of materials.

It was found that RSW of steel sheet is a very fast process. Cooling rates are fast leading to fully martensitic structures in the weld nugget. At higher welding currents a considerable part of the material in the HAZ becomes martensitic too. Not taking clamping and workpiece geometry into account, residual stresses tend to decrease with increasing welding currents. The deformation of the material increases though. The deformation is caused by indentation of the material by the electrodes and expulsion of material on the side of the electrodes during welding. Combi-

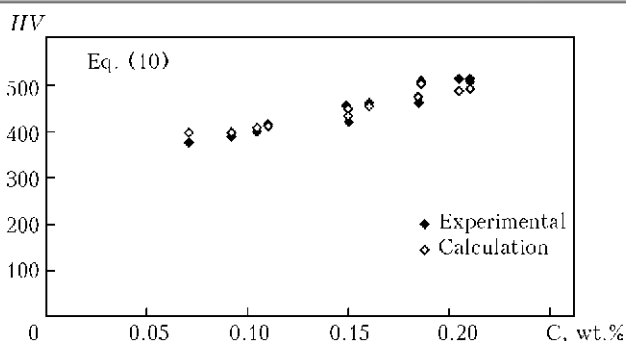


**Figure 22.** Experimentally measured and calculated maximum hardness values for various SR-welded high strength steels

ning the results of the simulations and experimental work it was found that postweld hardness can be calculated accurately using a simple equation (10) with equation (11).

1. Blondeau, R., Maynier, Ph., Dollet, J. (1973) Prevision de la durete, de la resistance des aciers au carbone et faiblement allies d'apres leur structure et leur composition. *Sci. Rev. Metallurgie*, 70(12).

# NUMERICAL STUDY OF THE INFLUENCE OF GROOVE ANGLE OF BUTT, TEE AND CORNER JOINTS ON ANGULAR DISTORTIONS AND LATERAL SHRINKAGE IN ARC WELDING OF LOW-ALLOYED STEELS

E.A. VELIKOIVANENKO<sup>1</sup>, G.F. ROZYNKA<sup>1</sup>, N.I. PIVTORAK<sup>1</sup>, V.A. STARODUBTSEV<sup>2</sup>,  
B.V. STEPANOV<sup>2</sup> and S.V. YAROCKIN<sup>2</sup>

<sup>1</sup>E.O. Paton Electric Welding Institute, NASU, Kiev, Ukraine

<sup>2</sup>Uralmashzavod, Ekaterinburg, Russia

One of the arguments in favor of reducing groove angle in arc welding of various welded joints are lower welding distortions observed, in particular connected with angular distortions and lateral shrinkage. The present numerical study was conducted for samples of butt joints B17 and B25, corner joints C6 and C8, as well as for tee joints T6 and T8, in order to obtain the whole spectrum of qualitative characteristics of the above reduction of welding distortions. On the basis of this study the degree of effect of such reduction for different thicknesses of low-alloyed steels (09G2S, 17G1S, 10KhSND, 12GN2MFAYu) is shown. This work has become a basis for the development of new directional materials on preparation of edges of different welded joints for shielded-gas arc welding.

Development of structural steel welding technology of the considered groups in manufacturing different weldments stimulates creation of efficient technological processes, where required product quality is provided with minimum funds and time consumption. One of the ways of decreasing said consumption lies in the reduction of volume of the deposited metal due to respective preparation of edges of welded joints, namely reduction of groove angles. In a number of cases modern technology of thin wire arc welding in gas mixture enables to provide quality formation of butt, tee and corner joints at reduced groove angles as compared with GOST 14771-76.

Thus, for butt joints in one-sided consumable electrode arc welding in the gas mixture on the basis of argon, meeting GOST requirements for thicknesses below 11 mm, recommended V-groove angle is  $2\alpha = 60^\circ$ . These are one-sided B17 welds, one-sided welds on removable backing B18, one-sided welds on permanent backing B19, one-sided castellated welds B20. For greater thicknesses ( $\delta > 11$  mm) of B17-B20 joints according to GOST, V-groove angle is  $2\alpha = 40^\circ$ .

Similarly, for double-sided butt joints with X-groove B25 for thicknesses below 20 mm  $2\alpha = 60^\circ$ , while with greater thicknesses  $2\alpha = 40^\circ$ .

These recommendations are based on many years of experience producing quality weld formation, however in a number of cases they are quite superfluous, therefore the question of consequences in the case of smaller angle  $2\alpha$  V-grooves is raised, on condition that welding technology provides quality welded joints.

Payoff in reduction of expenses is quite evident. Thus, for V-grooves reduction of the angle from  $60^\circ$  to  $30^\circ$  provides about 2 times reduction of deposited metal, which is quite essential. In the case of V-grooves with  $2\alpha = 40^\circ$ , reduction of angle down to  $30^\circ$  reduces the volume of deposited metal 1.35 times, which is also quite attractive. However, a number of other questions involved with heat effect are raised, concerning microstructure, mechanical properties, residual stresses and distortions.

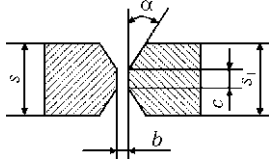
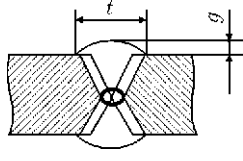
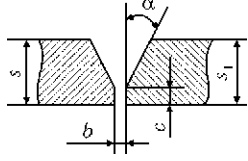
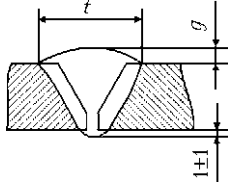
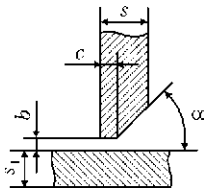
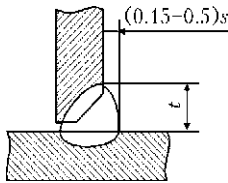
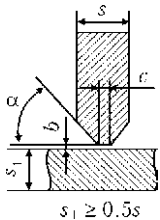
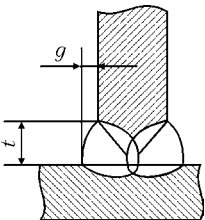
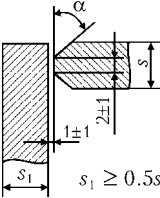
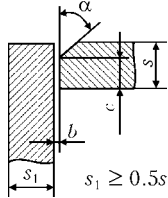
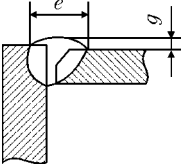
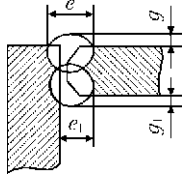
Finding answers to these questions was the task of this work. As objects for investigation were chosen butt joints B17 and B25, corner joints C6 and C8, T-joints T6 and T8 from Table 1.

For evaluation of residual stresses, angular distortions and lateral shrinkage depending on groove angle, calculation technique based on consecutive monitoring of development of plasto-elastic distortions in points  $x$ ,  $y$  of specimen section, as a function of temperature change for each pass with regard for residual stresses and distortions from the previous pass. Plane distortion hypothesis was applied.

To solve such problems, sufficiently well are developed numerical methods, based on finite element method. This type of algorithm is used in the WELD-PREDICTIONS software package, on whose basis studies of residual stresses, angular distortions and lateral shrinkage depending on the V-groove angle for welded joints considered, were conducted.

Investigation of residual stresses and distortions for B17 joints, having thickness 10 and 20 mm, as well as for double-sided B25 joints 40 mm thick, was conducted.

**Table 1.** Joints selected for investigation

Designation of welded joint	Structural elements of welded joints	
	Edges of parts to be welded	Welds
B17		
B25		
T6		
T8		
C6		
C8		

The calculations were performed for carbon steel 20, increased-strength low-alloyed steels 09G2S and 17G1C, as well as for HSLA steel 12GN2MFAYu.

Figures 1–3 show typical results of distribution of normal stresses  $\sigma_{zz}$  (along the weld),  $\sigma_{xx}$  (transverse to the weld) and  $\sigma_{yy}$  (across specimen thickness) in the zone of B17 welded joint 20 mm thick and B25 joint 40 mm thick.

It is seen that prevailing in magnitude are longitudinal stresses  $\sigma_{zz}$ . Transverse stresses  $\sigma_{xx}$  are lower than  $\sigma_{zz}$  longitudinal ones, especially at thickness  $\delta =$

$= 10$  mm (here not shown). Especially sharply  $\sigma_{yy}$  stresses are lowering with decreasing thickness. Even for thickness  $\sigma = 40$  mm they are below 130 MPa (Figure 3). Therefore further consideration of residual stresses is dedicated to  $\sigma_{zz}$  longitudinal stresses. In Figures 4–6, for steel 20, in detail is shown influence of the groove angle  $2\alpha$  on  $\sigma_{zz}$  stress values on  $y = 0$  and  $y = \delta$  specimen surfaces at different thicknesses  $\delta = 10$  and 20 mm of B17 joint, and for B25 joint at  $\delta = 40$  mm. It is seen that at  $\delta = 10$  mm, distribution of  $\sigma_{zz}$  residual stresses across the thickness is approx-

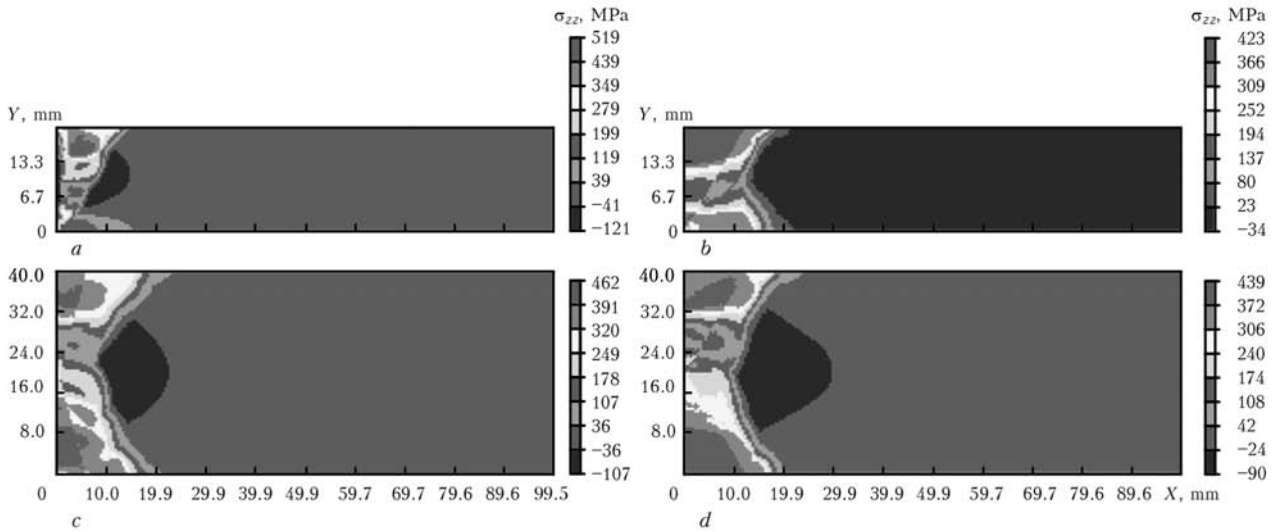


**Figure 1.** Distribution of longitudinal residual stresses  $\sigma_{zz}$  in cross section of joints B17 20 mm thick (variants 3 (a) and 4 (b) with  $2\alpha = 30^\circ$  and  $60^\circ$ , respectively) and B25 40 mm thick (variants 5 (c) and 6 (d) with  $2\alpha = 30^\circ$  and  $60^\circ$ , respectively) of steel 20 welded with wire Sv08G2S

imately uniform. For greater thicknesses the distribution is quite non-uniform, since subsequent passes partially unload the preceding ones.

Characteristically that reduction of groove angle increases non-uniformity (see Figure 5, curves 1-4). In these same Figures 4-6 are shown curves, characterizing residual angular distortions, defined by  $\Delta U_y$  displacement of along the  $y = 0$  surface. It is seen that diminishing  $2\alpha$  groove angle markedly reduces angular distortions. Table 2 shows numerical values of the specified angles for half of the specimens and different cases, including those considered in Figures 4-6. These also contain comparison data on  $\Delta U_{tr}$  transverse shrinkage along median line of joint B17.

It is seen that reduction of groove angle  $2\alpha$  from  $60^\circ$  to  $30^\circ$  decreases angular distortions approximately by half, while transverse shrinkage approximately proportionally to the number of passes.

In calculating transverse shrinkage, the above technique based on the assumption of fast-moving source and plane strain, does not yield real results (es-

pecially for initial passes), therefore a more generalized scheme was used for a 3D specimen with tacks at the beginning and end of the weld, which drastically increased counting time, was used. The results obtained agree fairly with the data of Figures 1-6 on stresses and angular distortions. Transverse shrinkage levels are quite close to those observed in experiments [1] and provide a comparison picture regarding influence of  $2\alpha$  angle.

Plausibility of the calculation results can be evaluated based on known experimental data published in authoritative publications. Thus, in [2] are reported data on experimental study of angular distortions in butt one-sided multilayer welds of B17 type 25 mm thick on steel type 20 in  $CO_2$  welding with 1.2 mm wire.

For the three-pass welding case at  $I = 300$  A,  $U = 32$  and  $v_w = 0.14$  cm/s, angular distortion was  $\beta/2 = (4.5-4.9) \cdot 10^{-2}$  rad. Calculation results using the algorithm of this work give  $\beta/2 = 5.1 \cdot 10^{-2}$  rad, which is quite close to the experimental value. Taking

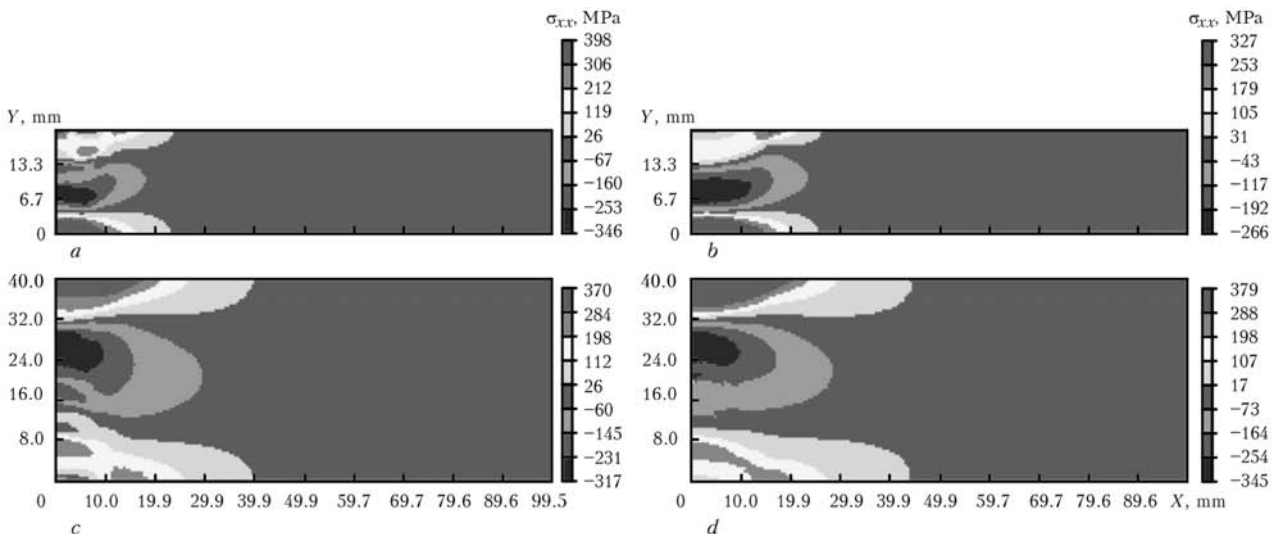


**Figure 2.** Distribution of residual transverse stresses  $\sigma_{xx}$  in cross section of joints B17 20 mm thick (variants 3 (a) and 4 (b) with  $2\alpha = 30^\circ$  and  $60^\circ$ ) and B25 40 mm thick (variants 5 (c) and 6 (d) with  $2\alpha = 30^\circ$  and  $60^\circ$ ) of steel 20 welded with wire Sv08G2S

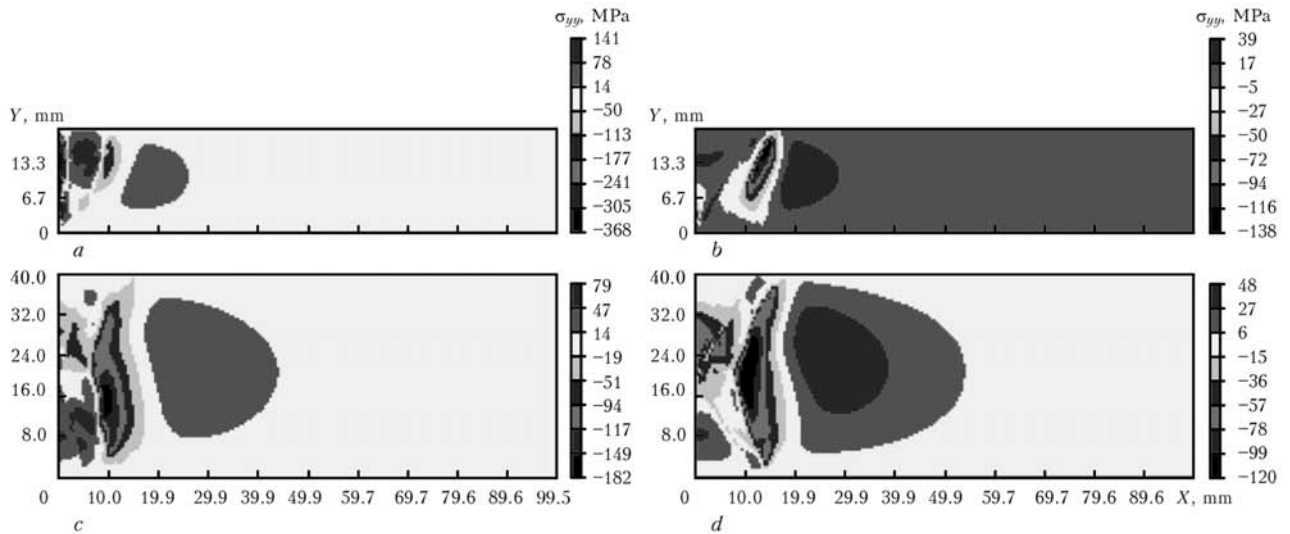


**Figure 3.** Distribution of residual normal stresses  $\sigma_{yy}$  across the thickness in cross section of joints B17 20 mm thick (variants 3 (a) and 4 (b) with  $2\alpha = 30^\circ$  and  $60^\circ$ ) and B25 40 mm thick (variants 5 (c) and 6 (d) with  $2\alpha = 30^\circ$  and  $60^\circ$ ) of steel 20 welded with wire Sv08G2S

into account comparative character of our investigation, one can consider that our data on the influence of  $2\alpha$  angle value on distortions of the butt welds are quite realistic.

For T6, T8 and C6, C8 joints, calculations to determine influence of the bevel angle on residual stresses and distortions were conducted. In thus made assembly one of the two elements has a beveled edge. We shall conditionally call that element the wall, and the second one — the web. Respectively, angular distortion will comprise angular distortion of the wall  $\beta_w$  plus angular distortion of web  $\beta_{web}$  with their respective signs.

Transverse shrinkage for tee and corner joints occurs both in the wall and in the web. It depends on conditions of fastening and geometric dimensions of elements to be welded, and under otherwise equal conditions, is proportional to deposited metal section area [1]. For such joints more important are angular distortions, leading to evident shape deformations,

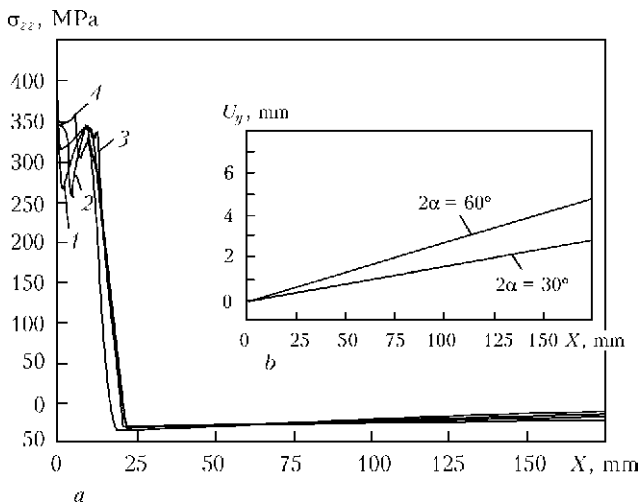


**Figure 4.** Residual longitudinal stresses  $\sigma_{zz}$  in the steel 20 joint B17 10 mm thick (a) on surface  $y = 0$  (1, 3),  $y = \delta$  (2, 4) at  $2\alpha = 30^\circ$  (2),  $2\alpha = 60^\circ$  (4), and residual dislocations  $U_y$  on surface  $y = 0$  for different  $2\alpha$  values (b)

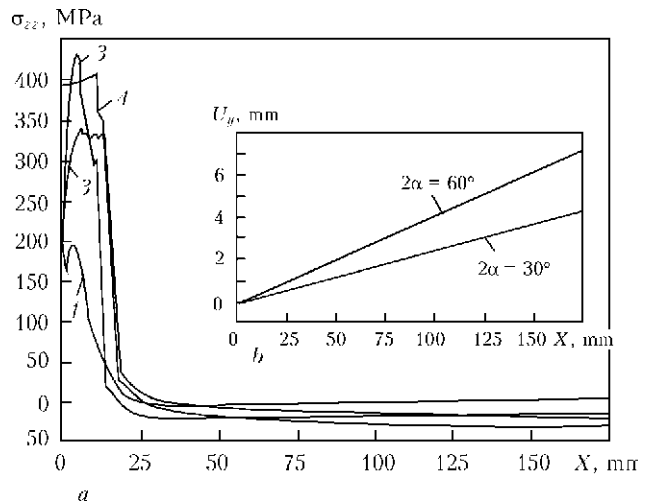


**Figure 5.** Residual longitudinal stresses  $\sigma_{zz}$  in the steel 20 joint B17 20 mm thick (a) on surface  $y = 0$  (1, 3),  $y = \delta$  (2, 4) at  $2\alpha = 30^\circ$  (2),  $2\alpha = 60^\circ$  (4), and residual dislocations  $U_y$  on surface  $y = 0$  for different  $2\alpha$  values (b)

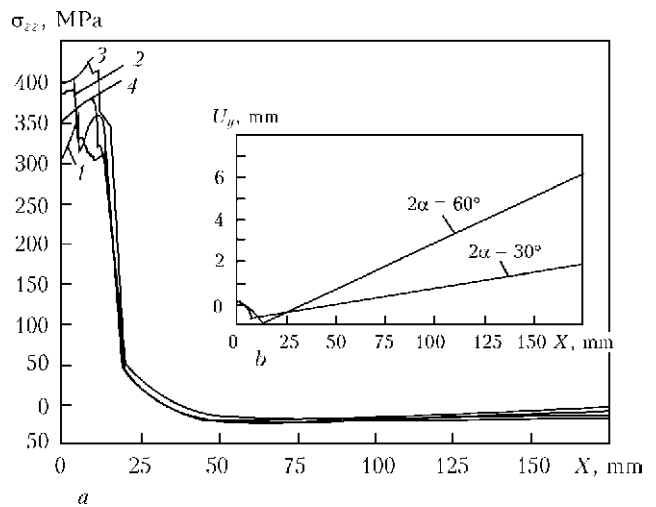


**Figure 6.** Residual longitudinal stresses  $\sigma_{zz}$  in the steel 20 joint B25 40 mm thick (a) on surface  $y = 0$  (1, 3),  $y = \delta$  (2, 4) at  $2\alpha = 30^\circ$  (2),  $2\alpha = 60^\circ$  (4), and residual dislocations  $U_y$  on surface  $y = 0$  for different  $2\alpha$  values (b)

**Table 2.** Aggregate results of calculation of residual distortions (angular distortion  $\beta$  and transverse shrinkage  $\Delta U_{tr}$ ) for butt joints B17 and B25 depending on groove angle  $2\alpha$

Joint type (thickness, mm)	Material	St20		17G1S		09G2S		12GN2MFAYu	
		$2\alpha$ , deg	30	60	30	60	30	60	30
C17 (10)	$\beta/2 \cdot 10^{-2}$ , rad	1.31	2.53	1.264	2.477	1.217	2.459	1.265	2.523
	$\Delta U_{tr}$ , mm	-0.4	-0.62	-	-	-	-	-	-
C17 (20)	$\beta/2 \cdot 10^{-2}$ , rad	2.07	3.92	2.13	4.13	2.088	4.10	2.195	4.316
	$\Delta U_{tr}$ , mm	-0.64	-1.58	-	-	-	-	-	-
C25 (40)	$\beta/2 \cdot 10^{-2}$ , rad	1.017	3.17	0.97	3.19	0.96	3.24	0.96	3.0
	$\Delta U_{tr}$ , mm	-	-	-	-	-	-	-	-

Note. For  $\delta = 10$  mm number of passes is 1 and 2, for  $\delta = 20$  mm – 3 and 8, and for  $\delta = 40$  mm – 6 and 16 at  $\alpha = 30^\circ$  and  $60^\circ$ , respectively.

therefore below particular attention is paid to the influence of bevel angle  $\alpha$  on angular distortions  $\beta = \beta_w + \beta_{web}$ .

Figure 7, *a-d* show typical patterns of distribution of residual stresses for the steel 20 T6 joint with thickness 30 + 30 mm at  $\alpha = 45^\circ$ .

Here too, as with butt joints in Figure 1, it is seen that most significant are longitudinal normal stresses  $\sigma_{zz}$ , whose value in the geometric concentration zone may exceed material yield point 1.5–1.7 times because of volumetric character of stressed state, i.e. when quite significant in value are constituents  $\sigma_{xx}$  and  $\sigma_{yy}$ , which is easily seen in Figure 7, *b* and *c*, where maximum values are  $\sigma_{xx} = 400$ , but  $\sigma_{yy} = 200$  MPa.

More detailed information for this joint on residual stresses  $\sigma_{zz}$  on the wall surfaces (on the back and face of the weld) is entered in Figure 8, *a* and *b*. In Figure 9, *a* for  $\alpha = 45^\circ$ , and in Figure 9, *b* for  $\alpha = 30^\circ$  are entered data on residual dislocations  $U_y$ . Such dislocations define value of angle  $\beta_w$ . It is seen that

increasing wall bevel angle from  $30^\circ$  to  $45^\circ$  markedly increases  $\beta_w$  (Table 3) from  $4.32 \cdot 10^{-2}$  to  $10.96 \cdot 10^{-2}$  rad.

Characteristically that as for the butt joints, steel properties (for the ferrite-pearlite steels considered), produce a marked effect on values of residual stresses, and an insignificant one on distortions.

Based on the data for T-joints T6 and T8, the following conclusions can be drawn:

- residual stresses depend to a small degree on the wall bevel angle within  $\alpha = 45-30^\circ$  range;
- transverse shrinkage, as well as angular distortion of the wall  $\beta_w$ , grows with increasing volume of deposited material, i.e. here minimum value of angle  $\alpha$  is preferred;
- angular distortion of web  $\beta_{web}$  depending on the web thickness, can either grow with increasing  $\alpha$ , or get reduced. The latter occurs at comparatively small thicknesses of the web (compared to wall thickness), i.e. at  $\beta_{web} \leq \beta_w$ .

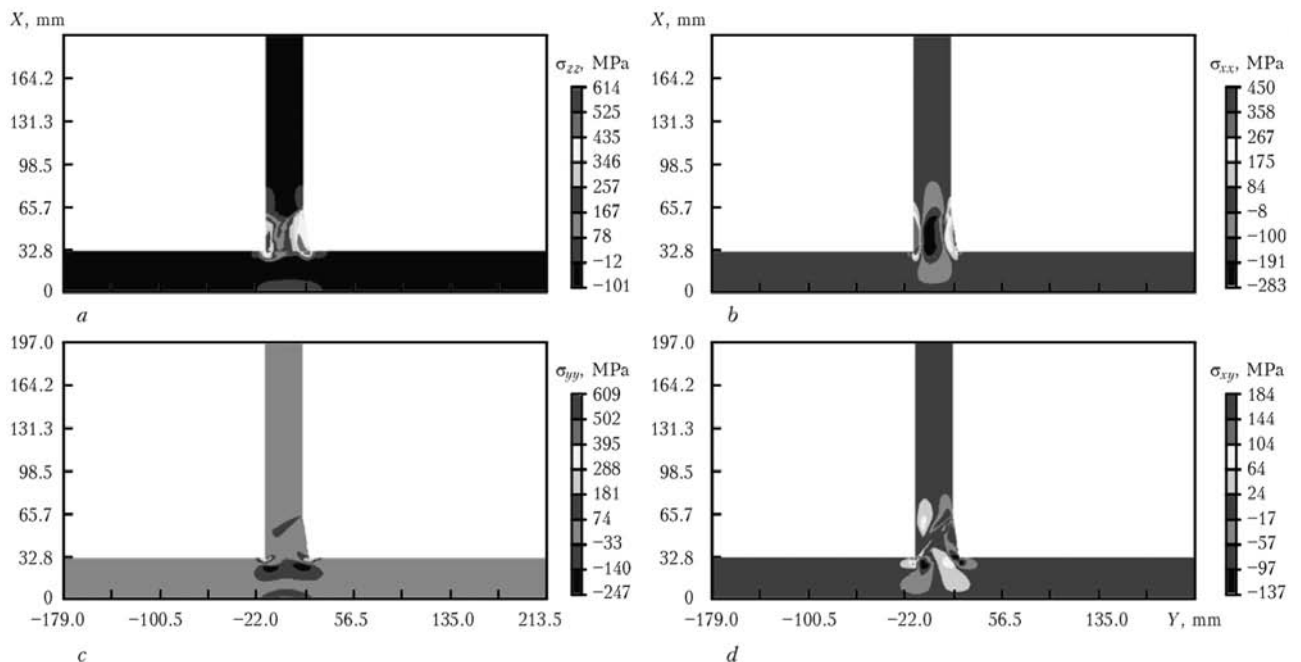


**Figure 7.** Distribution of residual stresses  $\sigma_{zz}$  (*a*),  $\sigma_{xx}$  (*b*),  $\sigma_{yy}$  (*c*) and  $\sigma_{xy}$  (*d*) in section  $z = \text{const}$  for the steel 20 joint T6 with thickness of 30 + 30 mm at  $\alpha = 45^\circ$

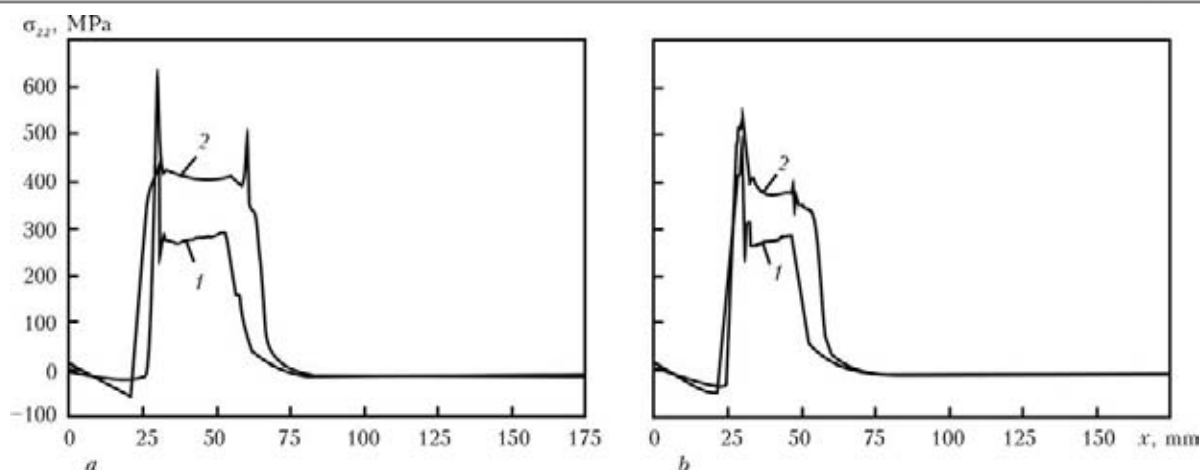


**Figure 8.** Distribution of residual stresses  $\sigma_{zz}$  in the steel 20 joint T6 with thickness of 30 + 30 mm at  $\alpha = 45^\circ$  (a) and  $30^\circ$  (b) on the surfaces corresponding to the weld reverse (1) and face (2) side on wall

Investigation, similar to that for T-joints T6 and T8, was conducted for corner joints C6 and C8.

Figure 10 shows typical results for the  $\sigma_{zz}$ ,  $\sigma_{xx}$ ,  $\sigma_{yy}$ ,  $\sigma_{xy}$  stress distribution in section  $z = \text{const}$  of the steel 20 joint C6 at  $\delta = 20 + 20$  mm and  $\alpha = 40^\circ$ .

Here too, one can note predominance in magnitude of longitudinal residual stresses  $\sigma_{zz}$  in the weld zone. These stresses may exceed yield point of the material, which is due to quite noticeable volumetric character of stressed state observed at  $\delta = 20$  mm and over, when residual normal stresses  $\sigma_{xx}$  and  $\sigma_{yy}$  in the weld zone are of the same sign with  $\sigma_{zz}$ , while values of tangential stresses  $\sigma_{xy}$  are quite small. More detailed consideration of distribution of longitudinal residual stresses  $\sigma_{zz}$  on the wall surfaces (face and reverse) is possible using the data of Figures 11, a and 12, a corresponding to C6 and C8 joints of steel 20. Typical feature of C8 joint as opposed to one-sided C6 joint, is a marked concentration of residual stresses in the zone of transition from the web to the wall on the surface, conditioning deposition of the second series of welds, i.e. from the inner surface of the corner joint. Such a phenomenon can be explained by rather high rigidity of the corner joint C8 at  $\delta = 40 + 40$  mm after welding up the groove from the face (first series welds).

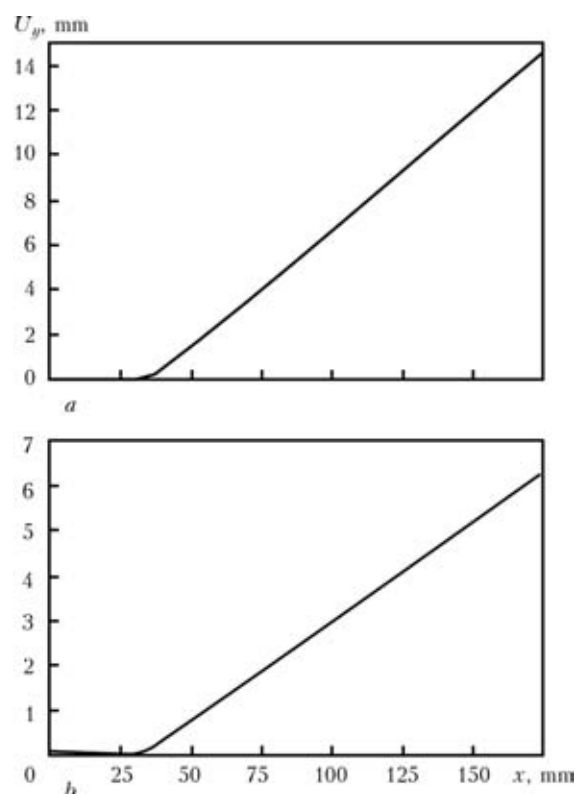


**Figure 9.** Residual dislocations  $U_y$  on surface  $y = \text{const}$  corresponding to the wall reverse side for the steel 20 joint T6 30 + 30 mm thick at  $\alpha = 45^\circ$  (a) and  $30^\circ$  (b)

**Table 3.** Aggregate results of calculation of residual angular distortions for wall and web in tee and corner joints depending on wall bevel angle  $\alpha$

Joint type (thickness, mm)	Material	$\alpha$ , deg	Number of passes	$\beta_w \cdot 10^{-2}$ , rad	$\beta_{\text{web}} \cdot 10^{-2}$ , rad
T6 (30 + 30)	Steel 20	45	15	10.96	0.32
	Same	30	9	4.32	0.43
	Steel 12GN2MFAYu	30	9	4.52	0.42
T8 (40 + 40)	Steel 20	45	14	5.61	0.19
	Same	30	8	2.6	0.26
C6 (20 + 20)	Steel 20	40	6	6.7	–
	Same	30	4	4.15	–
C8 (40 + 40)	Steel 20	40	12	4.15	–
	Same	30	8	2.3	0.13
	Steel 12GN2MFAYu	30	8	2.12	–

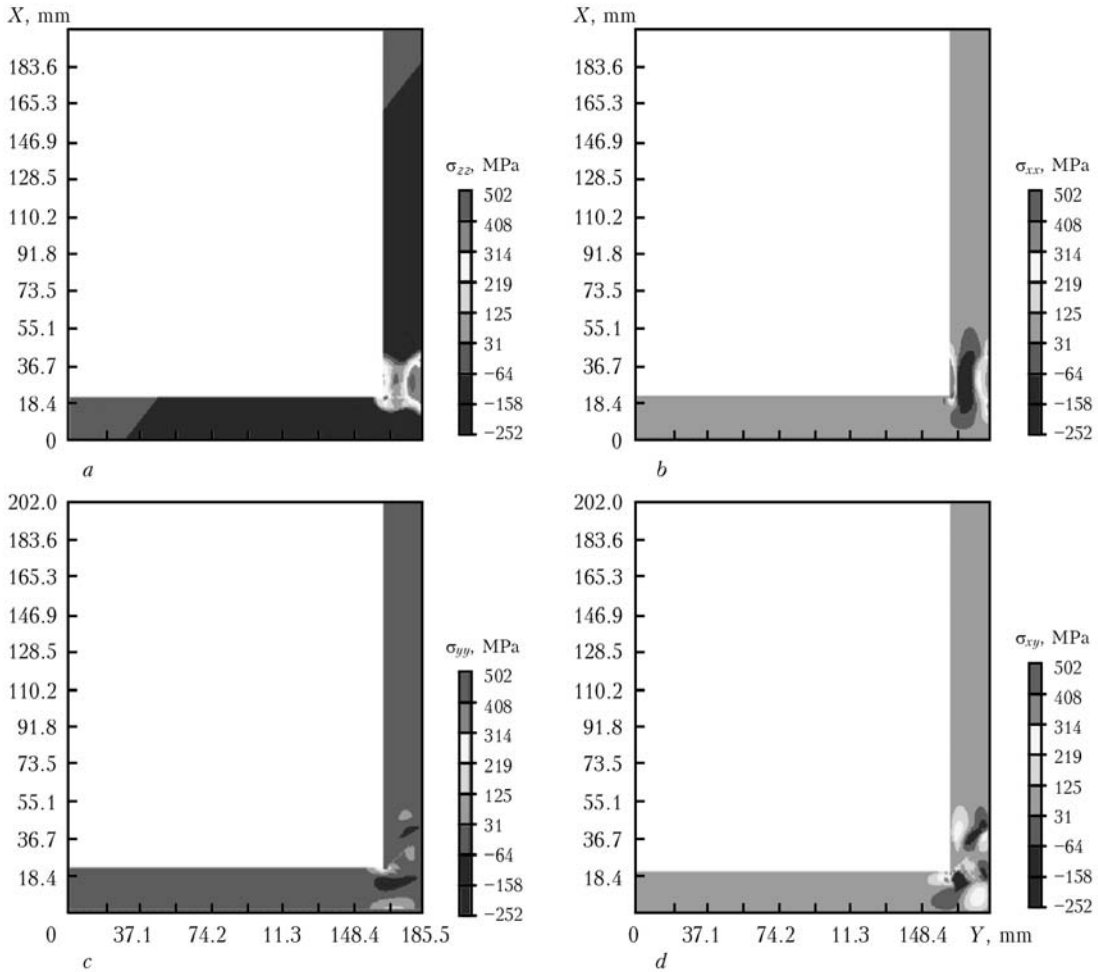


**Figure 10.** Distribution of residual stresses  $\sigma_{zz}$  (a),  $\sigma_{xx}$  (b),  $\sigma_{yy}$  (c),  $\sigma_{xy}$  (d) across section  $z = \text{const}$  for the steel 20 joint C6 20 + 20 mm thick at  $\alpha = 40^\circ$

There too, in Figures 11, b and 12, b are given data on residual dislocations  $U_y$ , controlling angular distortions  $\beta_w$  (see Table 3). It is seen that here wall bevel angle  $\alpha$  is becoming more manifest, i.e. as is the case for the butt and tee joints, value  $\alpha$  is little affecting residual stresses, but essentially residual distortions.

Note also that angular distortions of web  $\beta_{web}$  occur in welding of corner joints, however their values compared with  $\beta_w$  are small, which is well substantiated by data of Table 3. Influence of  $\alpha$  on  $\beta_{web}$  values is ambiguous, as is the case for T-joints.

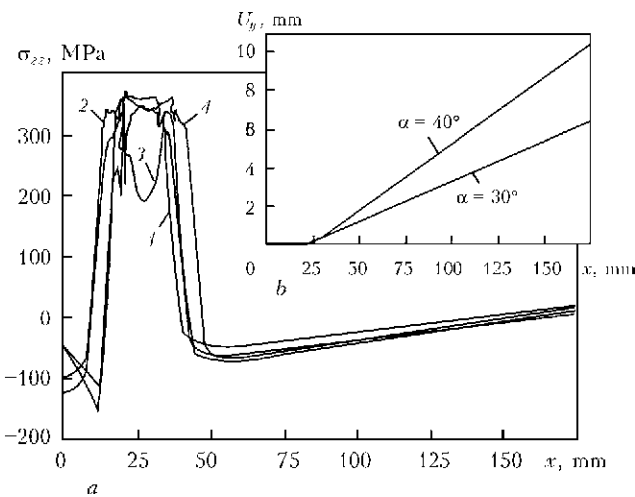


**Figure 11.** Residual stresses  $\sigma_{zz}$  (a) and dislocations  $U_y$  (b) correspond to  $\alpha = 30^\circ$  (1, 2) and  $40^\circ$  (3, 4) on the wall reverse (1, 3) and face (2, 4) for the steel 20 joint C6 20 + 20 mm thick

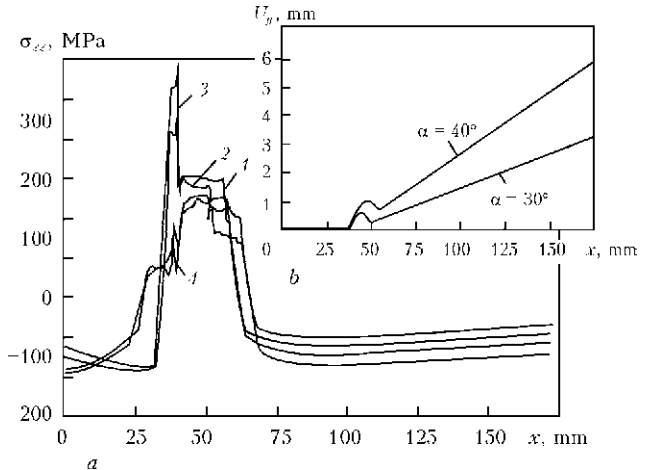


**Figure 12.** Residual stresses  $\sigma_{zz}$  (a) and dislocations  $U_y$  (b) correspond to  $\alpha = 30^\circ$  (1, 2) and  $40^\circ$  (3, 4) on surface after first (2, 4) and second (1, 3) series of filling the groove for the steel 20 joint C8 40 + 40 mm thick



## CONCLUSIONS

Numerical studies of the influence of the groove angle of butt, tee and corner joints types B17 and B25, T6 and T8, C6 and C8 as per GOST 14771-76 from steels VSt3, VSt5, St20, 20GS, 09G2S, 17GS, 17G1S, 10KhSND, 12GN2MFAYu in arc welding in argon-based mixture using wires Sv08G2S, OK Autrod 12.51, OK Autrod 12.64, OK Autrod 13.26, OK Autrod 13.28, OK Autrod 13.29, having 1.2–1.6 mm diameter, for thicknesses of 10–40 mm with groove angles varying within 60–30° range have revealed the following:

1. For B17 and B25 butt joints, reduction of groove angle from 60° to 30° is conducive to reduction of deposited metal volumes by approximately 2 times; in so doing approximately proportionally decreases transverse shrinkage and angular distortions, which is quite essential from the point of view of reducing expenses on welding and provision of accuracy in manufacturing.

2. Residual stresses in B17 and B25 joints with changing angle  $\alpha$  change little. Most notably influ-

ence on residual stresses depends on mechanical properties of the material in welding zone (mainly yield point  $\sigma_{0.2}$ ).

3. For T-joints T6, T8, as well as for corner joints C6 and C8, change in bevel angle  $\alpha$  of «wall», adjacent to the «web», from the point of view of residual stresses and transverse shrinkage, have much in common with butt joints of respective thicknesses.

4. As to the angular distortions, whose magnitude is defined by the sum of wall angular distortion  $\beta_w$  and web angular distortion  $\beta_{web}$ ,  $\beta_w$  value steadily increases with growing bevel angle  $\alpha$ , while  $\beta_{web}$  value with growing heat input into the web first increases, and then diminishes. Within the conditions and thicknesses considered, reduction of angle  $\alpha$  leads to the reduction of heat input into the web and increase of summand  $\beta_{web}$ , whose absolute value is usually much lower than  $\beta_w$ .

1. Masubuchi, K. (1980) *Analysis of welded structures*. Pergamon Press.
2. Murugan, V.V., Gunaray, V. (2005) Effect of process parameters on angular distortion of gas metal arc welded structural steel plates. *Welding J.*, Nov., p. 165–171.

# PHYSICAL-MATHEMATICAL MODEL OF MULTIPLE REFLECTION OF RADIATION IN LASER WELDING, CUTTING AND DRILLING THE METAL\*

A.V. ZAITSEV and O.B. KOVALEV

Institute of Theoretical and Applied Machines, RAS SB, Novosibirsk, Russia

Results of numerical simulation of laser radiation with metals as applied to laser cutting, welding and drilling are described. A mathematical description of interrelated physical processes is suggested in the form of coupled formulations of adjoint problems of mechanics of continuous media with moving boundaries. The effect of radiation polarization (linear, elliptical, and circular) on the absorption factor and surface shape being formed is analyzed. The current methods of modeling of forceful radiation fluxes interacting with metals are based on the assumption that only a single radiation absorption is considered. Therewith, one assumes that a reflected radiation does not substantially contribute into destroying the material and dissipates in metals at the expense of thermal conductivity. Visual observations of the laser processing show that a multiple radiation absorption and reflection take place at its propagation inside the laser cutting or cave, especially in case of thick materials ( $\geq 10$  mm). A physical-mathematical model of multiple reflection of laser radiation propagating in a narrow channel is developed. The model describes the mechanism of radiant energy transfer inward the channel, which is important in simulating laser cutting, welding and drilling of thick materials.

The problem of physical-mathematical simulation of interaction of laser radiation with metals, as applied to laser cutting processes, is complicated by the variety of interrelated physical processes. The most important of them are local heating, material melting, and removal of products by a gas jet [1]. The description of gas-laser cutting of metals involves a number of adjoint heat- and mass-transfer problems: thermal interaction of laser radiation with the metal surface, formation of the melt, and melt flow in the form of a thin liquid film; exhaustion of the gas jet and its dynamic interaction with the melted metal; heat transfer in a solid body, and material melting. Solving these problems in the full formulation seems to be extremely complicated. In the approach proposed in

the present paper, the overall formulation of the problem is divided in terms of physical processes into sub-problems. Each subproblem is considered in 1D, 2D, or 3D approximation.

It has been known that a focused laser radiation is moving as electromagnetic oscillations, and has the form of a Gaussian beam, which corresponds to an approximate particular solution of the Maxwell equations. The Gaussian beam reflecting from an arbitrary surface can significantly change its form, in which case the wave properties of radiation are meaningful. A correct state of the problem on interaction of the electromagnetic emanation with a free metal surface is complicated by the necessity to solve the complete equations of electrodynamics.

By virtue of complexity of the processes one suggests a simplified model allowing one to calculate an influence degree of multiple radiation reflection and absorption on a surface form in the laser drilling, cutting and welding the metals. One obtained an analytical expression for the absorption coefficient of laser radiation and developed a computer program of 3D modeling of laser radiation propagated in the channel with taking into account a multiple reflection. It allows one to describe the process of energy transferring into the depth of the channel and, consequently, to simulate its structure more correctly, especially in welding, cutting and drilling thick sheet materials.

**Gas flow.** A sketch of interaction of a laser beam and a gas jet with the surface of a metal plate is shown in Figure 1.

We consider a simplified formulation of the problem, where the nozzle-exit diameter is much greater than the cut width. In this case, the gas parameters are assumed to be constant in each cross section of the cut front. The gas pressure  $P_0$  in the tank and the

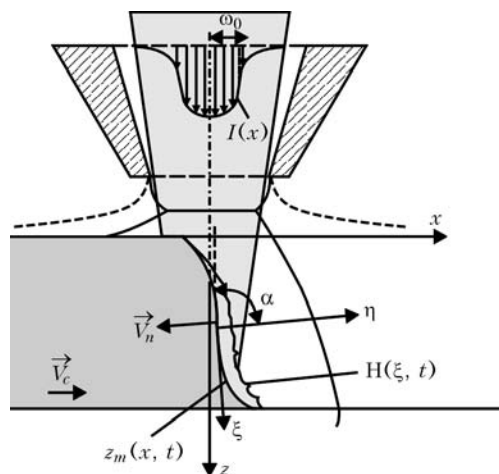


Figure 1. Interaction of a beam and a gas jet with a metal plate

\*This work was supported by the Russian Foundation for Basic Research (Grants No. 04-01-00798, 05-01-00311).

ambient pressure  $P_a$  being known, the gas parameters at the nozzle exit are calculated by the following isentropic formulas:

$$\begin{aligned} P_1 &= P_0 \left( 1 - \frac{k_g - 1}{k_g + 1} \lambda_1^2 \right)^{k_g/k_g - 1}, \\ \rho_1 &= \rho_0 \left( 1 - \frac{k_g - 1}{k_g + 1} \lambda_1^2 \right)^{1/k_g - 1}, \\ T_1 &= T_0 \left( 1 - \frac{k_g - 1}{k_g + 1} \lambda_1^2 \right), \\ \lambda_1^2 &= \frac{k_g + 1}{k_g - 1} \left( 1 - \left( \frac{P_a}{P_0} \right)^{k_g - 1/k_g} \right), \\ V_1 &= \lambda_1 a_c, \quad a_c = \sqrt{\frac{2k_g}{k_g + 1} R_g T_*}. \end{aligned} \quad (1)$$

Here,  $P_1$ ,  $\rho_1$ ,  $T_1$  and  $V_1$  are the gas pressure, density, temperature, and velocity at the nozzle exit, respectively;  $k_g$  and  $R_g$  are the ratio of specific heats and the gas constant;  $\lambda_1$  is the reduced velocity;  $a_c$  is the critical velocity of sound; and  $T_*$  is the stagnation temperature. If  $\lambda_1 > 1$ , the gas flow is supersonic, and a normal shock wave arises between the nozzle and the plate. The parameters behind the shock wave are

$$\begin{aligned} \lambda_2 &= \frac{1}{\lambda_1}, \quad P_2 = P_1 \left( \frac{\lambda_1^2 - \frac{k_g - 1}{k_g + 1}}{1 - \frac{k_g - 1}{k_g + 1} \lambda_1^2} \right), \\ \rho_2 &= \rho_1 \lambda_1^2, \quad T_2 = \frac{P_2}{\rho_2 R_g}. \end{aligned} \quad (2)$$

If the pressure gradient  $-dP/d\xi = k \approx \Delta P/L = 0.5\rho_2 V_2^2/L$  ( $L$  is the plate thickness) is constant, we obtain

$$\begin{aligned} P &= P_2 - 0.5\rho_2 V_2^2 \xi/L, \quad V_g = V_2(1 + 0.5\xi/L), \\ \rho &= \rho_2/(1 + 0.5\xi/L), \quad T_g = P/(\rho R_g). \end{aligned} \quad (3)$$

**Liquid metal flow.** The motion of the melt film is considered in a coordinate system fitted to the cut-front surface (see Figure 1):

$$\frac{\partial U}{\partial \xi} + \frac{\partial V}{\partial \eta} = 0, \quad (4)$$

$$\rho_m \left( \frac{\partial U}{\partial t} + U \frac{\partial U}{\partial \xi} + V \frac{\partial U}{\partial \eta} \right) = -\frac{dP}{d\xi} + \mu_m \frac{\partial^2 U}{\partial \eta^2}, \quad (5)$$

$$\begin{aligned} \rho_m \left( \frac{\partial E}{\partial t} + U \frac{\partial E}{\partial \xi} + V \frac{\partial E}{\partial \eta} \right) &= \\ = U \frac{dP}{d\xi} + \frac{\partial}{\partial \eta} \left( \rho_m \kappa_m \frac{\partial E}{\partial \eta} \right) + \mu_m \left( \frac{\partial U}{\partial \eta} \right)^2. \end{aligned} \quad (6)$$

Here,  $U$  and  $V$  are the velocity-vector components;  $E = c_m T$ ;  $T$  is the temperature;  $\kappa_m$ ,  $\rho_m$ ,  $c_m$  and  $\mu_m$  are the thermal diffusivity, density, heat capacity, and viscosity of the liquid metal, respectively.

The condition of continuous velocity of the liquid and the Stefan condition are satisfied on the moving boundary «solid body–liquid»  $z = z_m(t, x)$ , which moves with a normal velocity  $V_n$ :

$$U(t, \xi, 0) = V_c \cos \alpha, \quad V(t, \xi, 0) = V_c \sin \alpha, \quad (7)$$

$$\lambda_m \frac{\partial T}{\partial \eta} - \lambda_s \frac{\partial T_s}{\partial \eta} = \rho_m H_m V_n, \quad (8)$$

$$T(t, \xi, 0) = T_s(t, \xi, 0) = T_m.$$

Here,  $\lambda_m$  and  $\lambda_s$  are the thermal conductivities of the liquid and solid metal;  $T_m$  and  $H_m$  are the melting point and the phase-transition heat; and  $V_c$  is the cutting velocity.

The other moving boundary «liquid–gas»  $\eta = H(t, \xi)$  is subjected to the conditions  $\eta = H(t, \xi)$ :

$$\mu_m \frac{\partial U}{\partial \eta} = \tau, \quad \frac{\partial H}{\partial t} + U \frac{\partial H}{\partial \xi} = V, \quad (9)$$

$$\begin{aligned} \lambda_m \frac{\partial T}{\partial \eta} &= \frac{2A(\gamma)W \cos(\alpha - \varphi)}{\pi\omega_0^2 \cos \varphi} \times \\ &\times \exp \left( -\frac{2(\xi \cos \alpha + H(\xi) \sin \alpha - \omega_0)^2}{\omega_0^2} \right), \end{aligned} \quad (10)$$

$$\begin{aligned} \cos \alpha &= 1/\sqrt{1 + (z_m)_x^{-2}}, \quad \cos \varphi = 1/\sqrt{1 + H_\xi^2}, \\ \gamma &= \alpha - \varphi. \end{aligned} \quad (11)$$

Here,  $\gamma$  is the angle of incidence of the beam onto the liquid surface;  $A(\gamma)$  is the radiation-absorption factor; and  $\tau = \sqrt{\mu_g \rho_g^* V_g^3}/L$  is the shear stress at the boundary on the side of the gas [2].

**Heat transfer in solid metal.** The scale of material heat conduction in the direction perpendicular to the optical axis of the beam is small as compared with the longitudinal scale. This allows one to ignore heat transfer across the plate and, in addition to (4)–(11), to consider the 1D heat-conduction equation at each point  $\xi$  in the region  $\eta \in (-\infty, 0)$ :

$$c_s \rho_s^0 \left( \frac{\partial T_s}{\partial t} + V_n \frac{\partial T_s}{\partial \eta} \right) = \frac{\partial}{\partial \eta} \lambda_s^0 \frac{\partial T_s}{\partial \eta}, \quad (12)$$

$$\eta = T_s = T_m; \quad \eta = -\infty \quad T_s = T_0. \quad (13)$$

In the steady case, Eqs. (4)–(13) are readily integrated [1], which allows one to evaluate the liquid film thickness (Figure 2), and obtain the temperature distribution in the melt layer and in the solid metal (Figure 3). The normal component of velocity of the melting front  $V_n$  acquires the form [1]

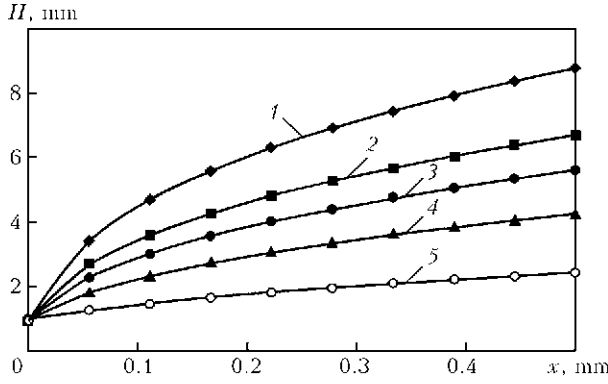


**Figure 2.** Thickness of liquid layer  $H$  versus the cut depth  $\xi$  and cutting velocity  $V_c = 500$  (1), 250 (2), 160 (3), 80 (4) and 20 (5) mm/s

$$v_n = \rho_m H_m + c_s \rho_s^0 (T_m - T_0) + \frac{c_m \rho_m (T_m - T_0)}{\omega_0} \times \left( h - \frac{kh^3}{6(\mu_m V_c \cos \alpha + \tau h + kh^2)} \right), \quad (14)$$

where  $I$  is the density of radiation intensity;  $\omega_0$  is the radius of the Gaussian beam; and  $h = H/\omega_0$  is the dimensionless thickness of the liquid film. As  $h$  tends to zero, the angle  $\varphi$  also tends to zero, the angle  $\gamma$  tends to the angle  $\alpha$  (see Figure 1), and formula (14) transforms to the known local law of conservation [3]  $V_n = A(\alpha)I \cos \alpha / (\rho_m H_m + c_s \rho_s^0 (T_m - T_0))$ .

**Description of the cut-surface shape.** The traditional formulation of the problem with motion of the free surface of a material subjected to laser radiation reduced to the equations [3]

$$\frac{\partial z_m}{\partial t} - V_c \frac{\partial z_m}{\partial x} = -V_n \sqrt{1 + \left( \frac{\partial z_m}{\partial x} \right)^2 + \left( \frac{\partial z_m}{\partial y} \right)^2}, \quad (15)$$

$$\frac{\partial z_m}{\partial x}(t, -a, y) = \frac{\partial z_m}{\partial x}(t, a, y) = 0, \quad -b \leq y \leq b, \quad (16)$$

$$\frac{\partial z_m}{\partial x}(t, x, -b) = \frac{\partial z_m}{\partial x}(t, x, b) = 0, \quad -a \leq x \leq a, \quad (17)$$

$$z_m(0, x, y) = 0, \quad (18)$$

where  $z = z_m(t, x, y)$  is the free-surface equation; and  $a, b$  characterize the plate size.

$T \cdot 10^{-3}, K$

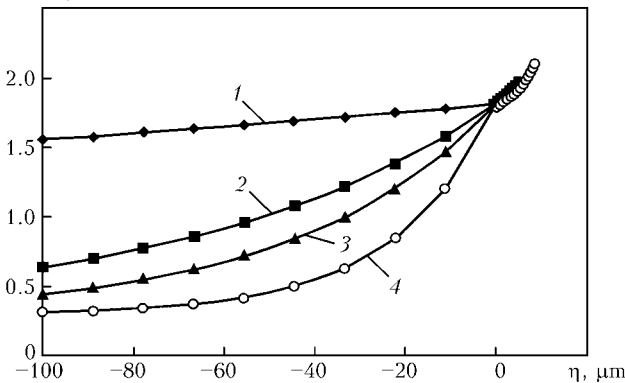


**Figure 3.** Distribution of temperature  $T(\eta)$  in solid metal ( $\eta < 0$ ) and melt layer ( $\eta \geq 0$ ) at  $V_c = 20$  (1), 160 (2), 250 (3) and 500 (4) mm/s

The density of radiation intensity is described by the Gaussian distribution [4]

$$I(x, y, z) = \frac{2W}{\pi\omega_z^2} \exp\left(-\frac{2r^2}{\omega_z^2}\right), \quad (19)$$

$$\omega_z = \sqrt{\omega_0^2 + \left(\frac{z - z_f}{\pi\omega_0}\right)^2}, \quad r = \sqrt{x^2 + y^2},$$

where  $W$  is the radiation power;  $z_f$  is the distance between the focal surface and the plane  $z = 0$ ;  $\omega_0$  is the beam radius in the focal plane; and  $\lambda_0 = 10.6 \mu\text{m}$  is the radiation wavelength.

Let us analyze the effect of radiation polarization on the absorption factor. The wave vectors of the incident  $\vec{k}$  and reflected  $\vec{k}_R$  radiation and the unit normal vector  $\vec{N}$  form the incidence plane. The vector of electric field intensity  $\vec{E}$  is decomposed into two projections. The projection  $\vec{E}_p$  in the incidence plane corresponds to the reflection factor  $R_p$ , and the projection  $\vec{E}_s$  aligned normal to the incidence plane corresponds to the reflection factor  $R_s$ . Let  $\beta$  be the angle between the vector  $\vec{E}$  and the normal to the incidence plane  $\vec{N}_{kn}$ . The expression for the absorption factor is written [5] as

$$A(\beta, \gamma) = 1 - R(\beta, \gamma) = 1 - \cos^2 \beta R_s - \sin^2 \beta R_p.$$

In the case of elliptical polarization of the beam, when the end of the vector  $\vec{E}$  in the plane  $(X, Y)$  describes an ellipse with semi-axes  $a$  and  $b$  ( $a^2 + b^2 = 1$ ), the absorption factor is written as the sum  $A = a^2 A_x + b^2 A_y$ , where  $A_x$  and  $A_y$  are the absorption factors, for studying the linearly polarized radiation parallel to the  $OX$  and  $OY$  axes:

$$A_x(\gamma, \beta_x) = 1 - R_s(\gamma) \cos^2 \beta_x - R_p(\gamma) \sin^2 \beta_x,$$

$$A_y(\gamma, \beta_y) = 1 - R_s(\gamma) \cos^2 \beta_y - R_p(\gamma) \sin^2 \beta_y,$$

where  $\beta_x$  and  $\beta_y$  are the angles between the normal to the incidence plane  $\vec{N}_{kn}$  and the  $OX$  and  $OY$  axes ( $\cos^2 \beta_x = N_y^2$ ,  $\cos^2 \beta_y = N_x^2$ ). In the case of elliptical polarization, we obtain the following generalized formula for the absorption factor:

$$A(\gamma, N_x, N_y) = 1 - R_s(\gamma)(a^2 N_y^2 + b^2 N_x^2) - R_p(\gamma)(a^2(1 - N_y^2) + b^2(1 - N_x^2)). \quad (20)$$

For  $b/a = 0$ , we have a linear  $P$ -wave; for  $b/a = 1$ , there is circular polarization; for  $b/a = \infty$ , we have a linear  $S$ -wave. Eqs. (15)–(20) were solved numerically by a pseudo-transient method with an explicit finite-difference scheme. The calculated maximum cut depth  $L$  is plotted in Figure 4 in dimensionless variables ( $L/\omega_0, b/a$ ) as a function of the ratio  $b/a$ ; the value of the following dimensionless aggregate was varied:

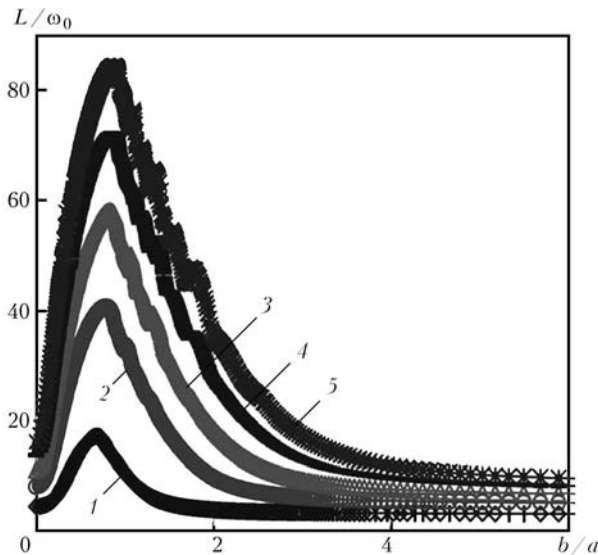


Figure 4. Maximum cut depth  $L/\omega_0$  as a function of beam polarization  $b/a$  at  $\sigma = 50$  (1), 100 (2), 150 (3), 200 (4) and 300 (5)

$$\sigma = 2W/[\pi\omega_0^2 V_c(\rho_m H_m + \rho_s c_s^0(T_m - T_0))].$$

Figure 4 displays a clear maximum corresponding to the value  $b/a = 0.75 \div 0.8$ . Typical shape of the laser cut is shown in Figure 5. The calculations show that radiation with elliptical polarization ( $b/a = 0.75 \div 0.8$ ) aligned with the beam direction is most effective.

**Model of multiple reflection of radiation.** For most materials, the radiation absorption factor is rather low ( $A = 0.01-0.50$ ). In this case, emission of reflected waves can play an important role, especially for deep and thin cuts, where multiple reflections make the main contribution to absorbed energy. Currently available methods for modeling the interaction of laser radiation with metals are based on approximation (15)–(20), which takes into account only

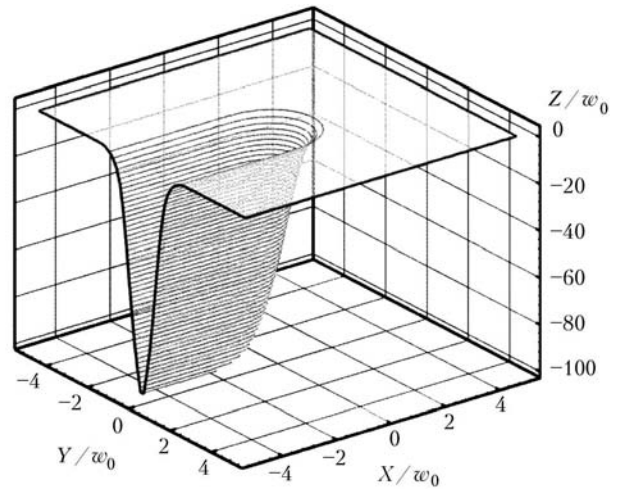


Figure 5. Shape of the cut surface  $z = z_m(\infty, x, y)$  at  $\sigma = 300$ ,  $b/a = 0.75$ ,  $\omega_0 = 100 \mu\text{m}$

single absorption of radiation. Focused laser radiation is known to propagate as electromagnetic oscillations and has the form of the Gaussian beam, which is a particular solution of Maxwell equations [4]. The correct formulation of the problem of interaction of electromagnetic radiation with an arbitrary metal surface is rather complicated because it involves solving full equations of electrodynamics.

The physical model suggested in the present paper for calculating the shape surface, which takes into account multiple reflections of radiation, differs from the traditional model (15)–(20) by the fact that the normal component of velocity of the surface points  $V_n$  is expressed via the sum of the entire power  $Q$  multiply absorbed by each surface point. The function  $Q(x, y, z_m(t, x, y))$  is calculated by a trajectory method, which implies finite-element discretization of the density distribution of the Gaussian beam intensity. Each element is a light beam containing a

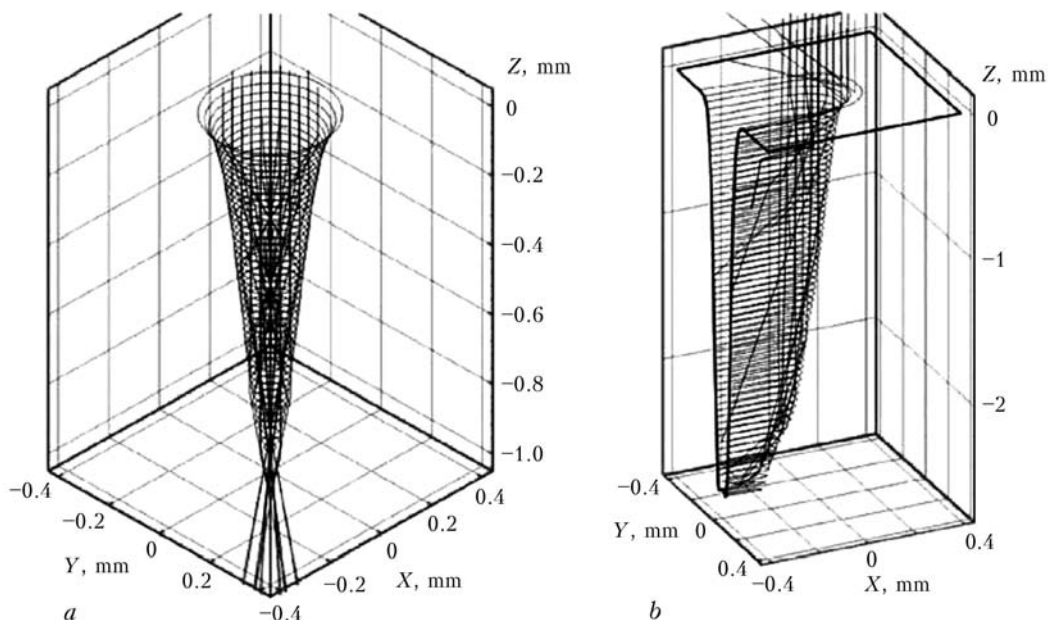


Figure 6. Radiation propagation in channel in laser drilling (a) and cutting (b) at  $W = 1 \text{ kW}$ ,  $V_c = 0.17 \text{ m/s}$ ,  $z_f = 0.25 \text{ mm}$  and  $\omega_0 = 100 \mu\text{m}$

radiation energy  $dE_{k_i} = I(x_{k_i}, y_{k_i}, z_{k_i})dxdy$ , which has coordinates  $x_{k_i}, y_{k_i}, z_{k_i}$  and velocity  $\vec{V}_{k_i}$  along the wave vector  $\vec{k}_i$ . Under interaction with the surface, the trajectory of each light beam changes its direction according to the laws of geometric optics (the angle of incidence equals the angle of reflection). The energy of the light beam decreases by the value of energy absorbed by the surface.

Figure 6 shows a 3D pattern of laser radiation propagating in a channel during laser drilling and cutting of a metal plate. The horizontal level lines correspond to the contour of the resultant surface. It is seen that the light beams are multiply reflected from the inner surface of the channel.

## CONCLUSION

It is shown that the description of gas-laser cutting of metals is complicated by a large number of physical parameters; some of them have to be chosen to ensure optimal performance. For this purpose, the problem is formulated mathematically in the form of adjoint problems of mechanics of continuous media with moving boundaries. Under certain simplifying assumptions (in the 2D case), these problems can be solved analytically. A local law of conservation of energy (14) is derived, which relates the radiation parameters, beam velocity, melt-film thickness, and thermodynamic parameters of the gas and metal to the melting-front velocity.

The influence of radiation polarization (linear, elliptical, and circular) on the absorption factor and

surface shape is analyzed. The effect of radiation parameters on the surface shape and cut depth is considered numerically. It is shown theoretically that elliptical polarization of radiation aligned with the beam direction is most beneficial for practical use because it provides an optimal shape of the cut.

A physical model of multiple reflection of laser radiation propagating in narrow channels is proposed, as applied to laser cutting, welding and drilling processes. It is shown that multiple reflection of radiation is most efficient in cutting thick materials if a beam with the TEM<sub>00</sub> mode and circular polarization is used. The model of multiple reflection of radiation allows one to describe energy transfer inward the channel, which is particularly important in processing thick materials.

The developed numerical algorithms and codes can serve as a basis for computer simulation of laser cutting, welding and drilling of metals.

1. Kovalev, O.B., Orichich, A.M., Fomin, V.M. et al. (2001) Adjoint problems of mechanics of continuous media in gas-laser cutting of metals. *J. Appl. Mech. Tech. Phys.*, 42(6), p. 1014–1022.
2. Schlichting, H. (1979) *Boundary layer theory*. New York: McGraw-Hill.
3. Niziev, V.G., Nesterov, A.V. (1999) Influence of beam polarization on laser cutting efficiency. *J. Phys. D: Appl. Phys.*, 32, p. 1455–1461.
4. Oraevsky, A.N. (1988) Gaussian beams and optical resonators. In: *Transact. of the Lebedev Physical Institute*. Ed. by A.N. Oraevsky. Moscow: Nauka, p. 3–9.
5. Born, M., Wolf, E. (1980) *Principles of optics*. Pergamon Press.

## NAME INDEX

- A**  
Abdullah B.M. 13  
Afonin Yu.V. 123  
Ahrens C. 51  
Aleksandrov S. 130  
Aryus A. 51
- B**  
Bataev A.A. 123  
Berezovsky B.M. 136  
Bikbulatov D.V. 20  
Bolshakov M.V. 143  
Borodianskiy K. 147  
von Breitenbach G. 279  
Brightmore A. 23  
Burov V.G. 123
- C**  
Charles C. 151  
Chawla K. 116  
Cherepanov A.N. 157  
Chinery M. 26  
Christiansson A.-K. 29  
Cuiuri D. 32
- D**  
Demchenko V.F. 184, 258  
Dilthey U. 250, 264  
Di Pietro P. 73  
Dunn L. 95  
Dyachenko V.I. 20
- E**  
Ermolaev G.V. 295  
Erofeev V.A. 295
- F**  
Fomin V.M. 157
- G**  
Gedanken A. 147  
Gorbach V.D. 40  
Gougeon P. 29  
Grigorenko G.M.  
Guy P. 116
- H**  
Habedank G. 100  
Heimerdinger C. 269  
Heins K.-U. 295  
Hole G. 23  
Hulka K. 130
- Hyeong-Soon Moon 46, 113
- I**  
Ilin A. 269
- J**  
Jarvstrat N. 151  
Jong-Cheol Kim 46, 113  
Jong-Joon Kim 46
- K**  
Karkhin V.A. 162, 167  
Karpoushkina N.G. 91  
Keitel S. 51  
Khomich P.N. 162, 167  
Khorunov V.F. 247  
Kolpakov V.V. 55  
Kolyada V.A. 106  
Korepanov A. 68  
Korolyova T.V. 173  
Kovalenko D.V. 258  
Kovalenko I.V. 258  
Kovalenko V.S. 55  
Kovalev O.B. 179, 322  
Krivtsun I.V. 184, 258  
Kunkevich D.P. 20, 58
- L**  
Lesnoj A.B. 184, 258  
Levchenko A.M. 167  
Lomozik M. 188  
Lopota V. 301  
Lucas B. 13  
Lucas J. 63  
Lugovskoy A. 147  
Lukina G.N. 143
- M**  
Makhnenko O.V. 196, 202, 208, 213  
Makhnenko V.I. 202, 219, 227, 234, 240, 286  
Makhutin M. 269  
Maksymova S.V. 247  
Malikov A.G. 123  
Malkin P. 301  
Manajchev K.A. 179  
Mavromatidis P. 63  
Mazurovsky V. 147  
Medvedev S.V. 20, 58  
Melyukov V. 68

- Michailov V.G. 162, 167  
 Mikno Z. 84  
 Milenin A.S. 234  
 Mokrov O. 250, 264  
 Moo-Ryeong Park 46  
 Morozov Yu. 130  
 Muzhichenko A.F. 208  
  
**N**  
 Nazarov A. 130  
 Nicholson A. 73  
 Norrish J. 32, 73, 76, 95  
  
**O**  
 Orishich A.M. 123  
  
**P**  
 Palm F. 269  
 Paton B.E. 258  
 Paute D.G. 91  
 Pavlyk V. 250, 264  
 Petrushina M.V. 80  
 Pietras A. 84  
 Pilnik O.V. 136  
 Pivtorak N.I. 213, 240, 314  
 Ploshikhin V. 269  
 Plotnikov A.M. 91  
 Ponikarovski R.F. 40  
 Pratt A. 95  
 Pretorius T. 100  
 Prikhodovsky A. 269  
 Pujko A.V. 136  
  
**R**  
 Richter K.-H. 295  
 Rozyinka G.F. 240, 314  
  
**S**  
 Saprykina G.Yu. 274  
 Sedlmaier A. 279  
 Semin L.G. 157  
 Semmler U. 279  
 Semyonov A.P. 234  
  
 Seyffarth P. 286  
 Shapeev V.P. 157  
 Shapovalov E.V. 106  
 Shekera V.M. 292  
 Shikakhalev E.G. 123  
 Sinitsky V.A. 110  
 Smith J.S. 13  
 Starodubtsev V.A. 173, 314  
 Stepanov B.V. 173, 314  
 Steshenkova N.A. 40  
 Strachan J. 26  
 Streltsov A.I. 20  
 Sudnik V. 295  
 Sung-Hoon Ko 113  
  
**T**  
 Tapp J. 116  
 Turichin G. 301  
 Tyurin V. 68  
  
 den **U**  
 Uijl N.J. 306  
  
**V**  
 Valdaytseva E. 301  
 Velikoivanenko E.A. 213, 240, 286, 314  
 Vollertsen F. 100  
  
**W**  
 Woitschig J. 100  
  
**Y**  
 Yakovleva Zh.G. 58  
 Yarochkin S.V. 314  
 Yarochkin V.A. 173  
 Yong-Baek Kim 46  
 Yushchenko K.A. 258  
  
**Z**  
 Zadroga L. 84  
 Zaitsev A.V. 322  
 Zelinskaya G.M. 247  
 Zemlyakov E. 301  
 Zinigrad M. 147